REVIEW OF THE VKI DOCTORAL RESEARCH

2016 - 2017



von Karman Institute for Fluid Dynamics

Covert art: Numerical simulation of a magnetically-confined nuclear fusion device.
The twisted magnetic field lines (represented as grey rods) compress the plasma in order to achieve temperatures of 10^7-10^8 K that are necessary to achieve nuclear fusion reactions. Even though nuclear fusion represents a clean and almost unlimited source of energy, magnetic confinement is very difficult to achieve because of the instabilities. In the figure, the electric current (represented as a red surface and plotted on the slices) develops a kink instability that damages the confinement. Within a collaboration between VKI and KU Leuven, a novel multi-fluid model is developed and implemented within the COOLFluiD platform. The model is able to capture new phenomena in astrophysical and nuclear fusion plasmas that are neglected by simplified standard models.

©2017 by the von Karman Institute for Fluid Dynamics
Waterloosesteenweg 72, B-1640 Sint-Genesius-Rode
To order: https://www.vki.ac.be

ISBN 978-2-87516-120-8

D/2017/0238/688, T. Magin, Editor-in-Chief

The contents of this book are the property of the von Karman Institute for Fluid Dynamics. No part of this book may be reproduced or distributed in any form of by any means, or stored in a database or retrieval system, without the prior written permission from the Publisher.

PREFACE

The eighth symposium on the doctoral research of the von Karman Institute for Fluid Dynamics took place during the period March 1 to 3, 2017. The doctoral students have presented the progress of their research work carried out in the three departments: Aeronautics and Aerospace, Environmental and Applied Fluid Dynamics, Turbomachinery and Propulsion. The first year students have presented a poster on their research plans and some preliminary results, while the most advanced students have proposed a presentation followed by a session of questions.

This event was attended by the faculty of the von Karman Institute as well as by colleagues from universities and industrial partners. The Symposium was open to external attendees free of charge. In addition to the presentations of the PhD candidates, we had the pleasure to welcome three prominent keynote lecturers who have opened each day the Symposium:

- Dr. Russell Cummings, Technical Advisor and International Program Officer, Air Force Office of Scientific Research (AFOSR), London, United Kingdom, "*Critical hypersonic aero-thermodynamic phenomenon: a plan for future research,*"
- Prof. Rodney O. Fox, Chemical and Biological Engineering, Iowa State University, USA, *"Eulerian models for disperse multiphase flows,"*
- Dr. Ingrid Lepot, Cenaero, Belgium, *"Turbomachinery Optimization Research at Cenaero."*

A special IFAR virtual conference (International Forum for Aviation Research http://www.ifar.aero) was organized in collaboration with NASA. This virtual conference was broadcasted among the IFAR members and associated universities with interaction during the question session. Three PhD members were selected this year to present their work related to IFAR activities: Yuki Sakamoto, Bogdan Cezar Cernat and Marc Schwalbach.

This year, the best presentation award has been attributed to Alejandro Álvarez Laguna for his research on "*Multi-Fluid Modeling of Magnetic Reconnection in Astrophysical and Laboratory Plasmas*." We would like to congratulate him on this achievement. The illustrated cover art of these proceedings is based on his research results.

This proceedings volume contains 38 papers which are divided into the following topics: "*Numerical Approach for Hypersonic and Plasma Flows*," "*Ground and Flight Experiments,*" "*Multiscale and Multiphase Flow Problems*," "*Noise and Aeroacoustics*," "*Aero-Thermal Investigations in Turbomachinery*," and "*Development of Advanced CFD and Optimization*."

We would like to emphasize that this publication serves as a tool for communication and aims to enhance exchange between the doctoral candidates, the faculty and external attendees. The annual publication of their results in proceedings is of crucial importance to the VKI research providing a thorough review of the different activities within the three departments.

As such, the doctoral candidate students play a key role in strengthening the expertise in experimental research, computational methods, and physical modelling. In addition to basic research, works carried out at the von Karman Institute often leads to implementation of real life industrial applications critical to the fluid dynamics community.

Julien Clinckemaillie	Thierry Magin	Christelle Debeer
Phd Representative	Professor	Organizer / Editor

The contribution of all VKI members who helped with this event is deeply acknowledged in particular the faculty, library and printing office staff.

TABLE OF CONTENTS

Editorial notes i

Table of contents iii

NUMERICAL APPROACH FOR HYPERSONIC AND PLASMA FLOWS

Alejandro ÁLVAREZ LAGUNA 3
Multi-fluid modeling of magnetic reconnection in astrophysical and laboratory plasmas

Federico BARISELLI 15
Development of an ablation model for rarefied flows with application to meteoroid entry

Georgios BELLAS-CHATZIGEORGIS 27
Development of advanced gas-surface interaction models for reusable materials

Joffrey COHEUR (1st year PhD) 35
Uncertainty quantification of aerothermal flow simulations through low-density ablative thermal protection materials

Florian DANVIN (1st year PhD) 37
On the modeling of transition to turbulence for hypersonic flows

Bruno Ricardo DIAS BARROS 39
Development of a melting model for meteors

Koen GROOT 47
BiGlobal stability of shear flows: spanwise and streamwise analyses

Fernando MIRÓ MIRÓ 57
Multi-species equilibrium and non-equilibrium models for hypersonic boundary-layer stability

Sahadeo RAMJATAN (1st year PhD) 69
Blackout analysis of reentry vehicles for Martian missions

Quentin WARGNIER (1st year PhD) 71
Mathematical modeling and simulation of non-equilibrium plasmas for the prediction of magnetic reconnection: application to solar atmosphere

Ludovico ZANUS (1st year PhD) 73
Numerical study of chemically reacting hypersonic boundary layers by means of nonlinear parabolized stability equations

GROUND AND FLIGHT EXPERIMENTS

Zdeněk ILICH 77
Review of test conditions in the VKI Longshot gun tunnel for hypersonic transition experiments

Ivan PADILLA MONTERO (1st year PhD) 91
Analysis of the stability of a flat plate high-speed boundary layer with discrete roughness

MULTISCALE AND MULTIPHASE FLOW PROBLEMS

Andrea ATTAVINO (1st year PhD) 95
Numerical methods for thermal hydraulics simulations of containment buildings

Sophia BUCKINGHAM 99
Turbulent heat transfer of separated flows at low Prandlt number

Nicolas COUDOU (1st year PhD) 109
Numerical and experimental investigations of the meandering phenomenon in wind-turbines wakes

Claudia ESPOSITO 111
Experimental study of cavitating flow and fluid hammer in cryogenic conditions

Charline FOUCHIER 121
Experimental investigation on gram-scale condensed-phase explosion in an urban environment

Sara PORCHETTA (1st year PhD) 135
The impact of the wave wind interaction on the energy harvesting of offshore wind turbines

Yuki SAKAMOTO (1st year PhD) 137
Void fraction measurement during LN2 chill-down by capacitive sensor

Maria Teresa SCELZO (1st year PhD) 139
Study of cryogenic slush flows for future launchers engines

Orkun TEMEL 141
Multiscale and multiphysical modeling of the atmospheric boundary layer

Agustín VILLA ORTIZ 147
Turbulent heat transfer at different Prandtl number fluids in natural convection boundary layer on a vertical plate

NOISE AND AEROACOUSTICS

Nicolas BOUANATI (1st year PhD) 163
Leakage characterization through structural vibration analysis

Lionel HIRSCHBERG 165
SRM aeroacoustics: review of the literature

Yakut Cansev KUCUKOSMAN 175
Blade tip noise prediction by linearized airfoil theory

AERO-THERMAL INVESTIGATIONS IN TURBOMACHINERY

Elissavet BOUFIDI 185
Uncertainty quantification of turbulence statistics measured by hot-wire anemometry

Tânia Sofia CAÇÃO FERREIRA (1st year PhD)..... 195
Influence of gas to wall temperature on bypass transition

Bogdan Cezar CERNAT..... 201
Aerothermal characterization of high pressure turbines rotor tip flows

Gian Luca GORI..... 211
Determination and modeling of the aero-thermal behaviour of a cooling channel

Marco VIRGILIO..... 221
Advanced experimental aero-thermal investigations of wall-bounded swirling flows in three-dimensional ribbed tubes

DEVELOPMENT OF ADVANCED CFD AND OPTIMIZATION

Giacomo ALESSI..... 235
Adjoint surface optimization for internal and external aerodynamics applications by means of OpenFOAM

Arnaud CHÂTEL (1st year PhD)..... 243
Development of a hybrid multi-level optimization method

Ismael SÀNCHEZ TORREGUITART..... 245
Optimization of the LS89 axial turbine profile using a CAD and adjoint based approach

Aude LAHALLE..... 253
Experimentally and numerically driven optimization of high performance instrumentation for real engine testing

Alberto RACCA (1st year PhD)..... 269
Turbocharger design and optimization by adjoint method coupled with CHT analysis

Marc SCHWALBACH..... 271
Adjoint optimization of turbomachinery components under mechanical constraints

Nikolaos STERGIANNIS..... 279
Full HAWT rotor CFD simulations using different RANS turbulence models compared with actuator disk and experimental measurement

NUMERICAL APPROACH FOR HYPERSONIC AND PLASMA FLOWS

Multi-fluid modeling of magnetic reconnection in astrophysical and laboratory plasmas

Alejandro Alvarez Laguna

von Karman Institute for fluid Dynamics, Aeronautics and Aerospace Department, alaguna@vki.ac.be

Supervisors: Herman Deconinck and Andrea Lani

Professor, von Karman Institute for fluid Dynamics, Aeronautics and Aerospace Department,deconinck@vki.ac.be

Research Engineer, von Karman Institute for fluid Dynamics, Aeronautics and Aerospace Department, lani@vki.ac.be

University Supervisor: Stefaan Poedts

Professor, KU Leuven, Centrum voor mathematische Plasma-Astrofysica, stefaan.poedts@wis.kuleuven.be

Abstract

Improved models for characterizing plasmas under the effect of magnetic fields are essential to understand the phenomena taking place in astrophysical and laboratory plasmas. Particularly, scenarios where dissipative processes and thermo-chemical inequilibrium play an important role are beyond the classical single-fluid Magnetohydrodynamics (MHD) representation. Multi-fluid models that consider each particle species as a separate fluid offer an alternative approach especially suitable for those conditions. In the present work, we summarize a novel numerical method that solves the multi-fluid equations coupled to Maxwell's equations. Additionally, a finite volume method for solving the radiative transfer equation (RTE) is presented to be used in future studies of magnetic reconnection. The method is applied to study the magnetic reconnection taking place in the chromosphere with the effect of radiative losses and chemical reactions using a two-fluid model considering neutrals and charged species. In addition, a fully ionized model is used to study the reconnection under magnetospheric conditions and a magnetically-confined nuclear fusion device.

Keywords: Magnetohydrodynamics (MHD), Magnetic Fields, Plasmas, Magnetic Reconnection, Sun: Atmosphere, Radiative Transfer.

1. Introduction

Numerical study of plasma flows continues to be an important area of research in a number of fields ranging from astrophysics to engineering applications. The application of electromagnetic fields to control the dynamics of electrically conducting flows has a long tradition in the aerospace industry that uses different concepts for flight and propulsion including plasma actuators, plasma thrusters or MHD by-pass arrangements in scramjets. In the present work, we will focus in two areas of particular interest for the CFD community, solar physics and laboratory plasmas.

The activity of the Sun has a great impact in our technology and ultimately in today's modern society that strongly depends on communications and satellite operations. From a global socio-economic perspective, the most important manifestations of solar activity are the solar wind and solar eruptions, i.e. solar flares and coronal mass ejection (CMEs). The unsteady but continuous emission of particles at high speed and temperature from the Sun into the space can hinder human activity at different levels. Satellite operations can be seriously affected by plasma ejected during solar storms, producing important damages or the loss of some of them, like the Telstar 401 that was short cut in January 1997. More recently, in 2003, a solar storm caused disruptions in the airplane routes and the CME affected several communication satellites (two were total loss). Additionally, when the

high energetic charged particles ejected from the Sun reach our atmosphere can produce the so-called Geomagnetically Induced Currents (GICs) that cause hazards in oil pipelines and power grid outages. An example of the latter is the magnetic storm that burned a $36 million transformer in New Jersey and left 6 million people more than 10 hours without electrical power in Quebec in winter conditions (March 1989). As a matter of fact, the cost of a severe space storm has been estimated to be trillions of dollars for the first year after the storm with recovery times of 4 to 10 years (an order of magnitude more than that of Hurricane Katrina) [5].

Most of the models of magnetized plasmas are based on the magnetohydrodynamics (MHD) description. It is obtained by combining the multi-fluid equations and simplifying them (making certain assumptions on time and length scales). MHD models consider plasma behaving as one quasi-neutral conducting fluid, usually assuming LTE of all the species. Therefore, the model is sufficient to describe phenomena with characteristic lengths than are much larger than particles characteristic lengths, i.e., the mean free path of the collisions and the Larmor radius of the charged particles. Consequently, the MHD description neglects high frequency waves and other effects that are consequence of the particle interaction, such as, the Hall effect, ambipolar diffusion or diamagnetic effects. However, these effects are seen to play an important role in phenomena such as magnetic reconnection, where the width of the current sheet formed becomes comparable to the ion scales (i.e., the ion skin depth, ion gyroradius, ion-neutral collision mean free path) [9].

It is therefore necessary to improve the understanding and modeling of the phenomena taking place in the Sun for enhancing the tools used for the space weather forecasting and eventually reducing its risk on our technology. Magnetic reconnection is a process especially significant in space weather since it has been long considered as a mechanism for creating transient phenomena in magnetized plasma. It occurs when oppositely directed magnetic field lines in conducting plasma merge due to diffusive processes producing a change of topology. The rearrangement of magnetic field lines produces a change of the magnetic flux that due to the finite conductivity creates a current sheet. In addition, the reconnection process causes a conversion of magnetic energy into kinetic and thermal energy, heating up the flow and accelerating it up to very high speed in very small timescales. It is proposed to be a mechanism to heat the corona [6], trigger the coronal mass ejections [7], in the Earth magnetosphere [8], and magnetically-confined nuclear fusion devices [9].

In the present work, we present a summary of the modeling of magnetic reconnection that focuses on the possible benefits of multi-fluid modeling. The general multi-fluid model is disucussed. A finite volume method that solves the previous equations with the effect of radiative transfer is presented. Applications of the code in different astrosphysical scenarios are presented, i.e., chromosphere and magnetospheric magnetic reconnection, as well as tokamak devices.

2. Modeling of the magnetic reconnection

Magnetic reconnection is a process that occurs as a result of a diffusive mechanism that produces a decay in the electrical conductivity of the plasma. The frozen-in constrain that holds in ideal plasmas (with infinite conductivity) is broken in a small region of width δ and length L. In this region, the magnetic field lines reconnect producing a rate of magnetic flux that results in the formation of a current sheet. Thus, the non-dimensional magnetic reconnection rate is defined [12] as follows:

$$M = \frac{d\Phi/dt}{v_A B_i} \tag{1}$$

where Φ is the magnetic flux per unit length in the direction perpendicular to the plane containing the current sheet , v_A is the Alfven speed and B_i is the magnetic field evaluated upstream of the current sheet.

Therefore, it is obvious to realize that the classical ideal MHD equations that consider the conductivity to be infinite are not able to tackle the physics involved in the reconnection. Nevertheless, the resistive singlefluid theory has developed analytical models for 2D steady magnetic reconnection. The Sweet-Parker model [13] proposes a non-dimensional reconnection rate of the form:

$$M = R_m^{-1/2} \tag{2}$$

where

$$R_m = v_A L/\eta \tag{3}$$

is called the Lundquist number, and η is the resistivity.

However, the model is unable to explain the fast energy released by the solar flares or in chromospheric jets and spicules, providing reconnection rates several orders of magnitude smaller.

On the other hand, the Petschek model [14] predicts faster reconnections suggesting geometry different from the Sweet-Parker one, Eq. 4. However, the model assumes explicitly or tacitly that resistivity gives the configuration setup. Because of this controversial issue, the Petschek model has been gradually thrown back [15].

$$M = \frac{\pi}{8\ln(R_m)} \tag{4}$$

Therefore, it is necessary to consider alternative theories to model the reconnection. The multi-fluid models consider each particle species as a different fluid that interact among each other by means of collisions and chemical reactions, exchanging thus mass, momentum and energy in their interplay. Since the width of the diffusion region can be comparable to the ion scales [8], therefore, the multi-fluid description are considered to capture diffusive effects that are completely neglected by the single-fluid theory, as shown in experimental research [9].

In the literature, one can find several fluid closures accounting for the different behavior of the species of plasmas in presence of electromagnetic fields. Braginskii [16] derives a two-fluid formulation considering separate ions and electrons. In his seminal work, he proposes closures for the transport properties, accounting for the anisotropy introduced by the magnetic field. Similarly, Magin [17] proposes a multicomponent model separating heavy particles and electrons, treating the effect of the magnetic field on the transport properties. Most recently, Meier [18] has proposed a two-fluid model considering the charged particles and neutrals as separate fluids, considering both anisotropic effects in the plasma heat conduction due to the magnetic field and chemical reactions (ionization and recombination).

3. Governing Equations

3.1. Reactive, collisional and diffusive multi-fluid plasma equations

Different plasma models can be used depending on the characteristics studied phenomenon. The most universal description of plasma relies on the Boltzmann equation that, together with Maxwell's equations, describes the evolution of the distribution function for each plasma species. However, solving numerically Boltzmann equation is computationally too expensive since it involves seven dimensions, i.e., physical space, velocity phase and time. Because of this reason, usually, kinetic simulations are confined to limited domains.

The multi-fluid plasma description is obtained by taking moments of the Boltzmann equation for each species. This model is simpler since it averages over the velocity space of each plasma species. Therefore, the microscopic information of the individual particles contained in the Boltzmann equation is lost since only macroscopic quantities are considered by this model. The multi-fluid model considers each species in the plasma as a separate fluid, usually assuming that each fluid is in local thermodynamic equilibrium (LTE). The mass, momentum, energy conservation equations for the species α reads:

$$\frac{\partial \rho_\alpha}{\partial t} + \vec{\nabla}\cdot(\rho_\alpha \vec{u}_\alpha) = \dot{\rho}_\alpha, \tag{5}$$

$$\frac{\partial \rho_\alpha \vec{u}_\alpha}{\partial t} + \vec{\nabla}\cdot(\rho_\alpha \vec{u}_\alpha \vec{u}_\alpha + p_\alpha \bar{\bar{I}}) = \vec{\nabla}\cdot\bar{\bar{\pi}}_\alpha + \vec{F}_\alpha + \sum_\beta \vec{R}_{\alpha\beta}^{elastic} + \vec{R}_\alpha^{react}, \tag{6}$$

$$\frac{\partial}{\partial t}\left[\mathcal{U}_\alpha + \rho_\alpha \frac{u_\alpha^2}{2}\right] + \vec{\nabla}\cdot\left[\left(\mathcal{U}_\alpha + \rho_\alpha \frac{u_\alpha^2}{2}\right)\vec{u}_\alpha\right] = \vec{\nabla}\cdot(\vec{u}_\alpha\cdot\bar{\bar{\pi}}_\alpha - \vec{q}_\alpha - p_\alpha \vec{u}_\alpha) + \rho_\alpha \vec{F}_\alpha\cdot\vec{u}_\alpha + \sum_{\alpha\beta} \dot{Q}_{\alpha\beta}^{elastic} + \dot{Q}_\alpha^{react}. \tag{7}$$

Where $\alpha = i, e, n$ that stand for ions, electrons and neutrals; $\vec{R}_\alpha^{\alpha\beta}$ and $Q_\alpha^{\alpha\beta}$ are the momentum and energy exchange due to elastic collisions between the species; $\vec{R}_\alpha^{react}$ and $\dot{Q}_\alpha^{react}$ are the reactive momentum and energy exchange.

3.2. Maxwell's equations

The electromagnetic influence is tackled with the Maxwell equations:

$$\frac{\partial \vec{B}}{\partial t} + \nabla\times\vec{E} = 0 \tag{8}$$

$$\frac{\partial \vec{E}}{\partial t} - c^2\nabla\times\vec{B} = -\frac{\vec{j}}{\epsilon_0} \tag{9}$$

$$\nabla\cdot\vec{B} = 0 \tag{10}$$

$$\nabla\cdot\vec{E} = \frac{\rho_c}{\epsilon_0} \tag{11}$$

where ρ_c is the charge density that is assumed to be zero.

3.3. Radiative transfer equation

In the results on the chromospheric magnetic reconnection shown hereafter, the radiative effects are neglected. However, in the solar atmosphere, particularly in the lower layers, i.e., photosphere and low-chromosphere, radiation is observed to play an important role [19]. The RTE in a non-scattering medium, neglecting the time derivative which is a lower order term, can be written:

$$\vec{\Omega} \cdot \nabla I_\nu = \kappa_\nu (S_\nu - I_\nu) \tag{12}$$

Where I_ν is the radiative intensity for the frequency ν, $\vec{\Omega}$ is the direction, κ_ν is the opacity of the medium and S_ν is the radiative source.

The radiative heat flux that should be included in the species energy equations 7 is calculated, as follows:

$$\vec{q}_{rad} = \int_\nu \int_\Omega I_\nu \vec{\Omega} \, d\Omega \, d\nu, \tag{13}$$

and the divergence of the flux:

$$\nabla \cdot \vec{q}_{rad} = \int_\nu \int_\Omega \kappa_\nu (S_\nu - I_\nu) \, d\Omega \, d\nu. \tag{14}$$

4. Numerical Modeling

4.1. Finite Volume Method

The scheme presented below is described in [1] and [4]. The results have been obtained using the FV solver for unstructured grids provided by the COOLFluiD platform [20]. The governing equations are written in conservative form, as follows:

$$\frac{d}{dt} \int_{\Omega_i} \mathbf{U} \, dV + \oint_{\partial\Omega_i} \mathbf{F^c} \cdot \mathbf{n} \, dS = \oint_{\partial\Omega_i} \mathbf{F^d} \cdot \mathbf{n} \, dS + \int_{\Omega_i} \mathbf{S} \, dV \tag{15}$$

The conservative form of Maxwell equations is found in [21]. The cell-centered FV discretization applies the integral conservation law to each cell, assuming the solution to be constant over the cell and storing the value at the centroid of it. In order to obtain second order accuracy in space, inverse-distance weighted least square reconstruction [22] is used. The multidimensional limiter of Venkatakhrisnan [23] is used to obtain oscillation free solutions. The discretization of the inviscid fluxes is explained hereafter.

4.2. Modified-CIR scheme for Maxwell equations

The CIR scheme [24] splits the flux at the interface into positive and negative components based on the eigenvalue structure of the system as follows:

$$\mathbf{F^c} = \mathbf{A}_+ \mathbf{U}^L + \mathbf{A}_- \mathbf{U}^R \tag{16}$$

where

$$\mathbf{A} = \frac{\partial \mathbf{F^c}}{\partial \mathbf{U}} = \mathbf{A}_- + \mathbf{A}_+ \text{ and } \mathbf{A}_\pm = \mathbf{R} \Lambda_\pm \mathbf{R}^{-1} \tag{17}$$

where $\mathbf{R}$ is the matrix of right eigenvectors, $\Lambda_\pm$ the diagonal matrix of diagonal matrices with the positive and negative eigenvalues, $\mathbf{U}$ are the conservative variables.

As mentioned in [21], when the Maxwell equations are coupled to the fluid equations, the numerical dissipation is out of balance since some terms are proportional to the speed of light while other are proportional to the speed of the fluid. In the results presented in this work, we use a novel scaling of the numerical dissipation including the two divergence cleaning equations.

4.3. AUSM scheme for fluid equations

AUSM-family schemes [28] split the inviscid flux of each fluid at the cell interface into the convective part and the pressure flux as follows:

$$\mathbf{F^c} = \mathbf{F^{conv}} + \mathbf{P} \tag{18}$$

with

$$\mathbf{F^{conv}} = \dot{m} \mathbf{\Psi}^{L/R} \tag{19}$$

$\dot{m}$ is the numerical mass flux at the interface and $\mathbf{\Psi}^{L/R}$ is a vector with the variables convected. The superindex L/R denotes that the values are taken from the left or the right neighboring cell to the cell interface as follows:

$$\mathbf{\Psi} = \begin{cases} (1, \, u, \, v, \, w, \, h)_L & \text{if } \dot{m} > 0 \\ (1, \, u, \, v, \, w, \, h)_R & \text{if } \dot{m} < 0 \end{cases} \tag{20}$$

The methods to compute the numerical mass flux $\dot{m}$ and the pressure $\mathbf{P}$ at the cell interface are discussed in [28] and [29].

4.4. Implicit time stepping

The resulting set of equations is a very stiff system since it has characteristic speeds ranging from the speed of light to the speed of sound of the different fluids. In order to deal with the strong time step requirements, implicit time stepping is used. The second-order accurate three-point Backward Euler is used:

$$\frac{3}{2}\mathbf{U}^{n+1} - 2\mathbf{U}^{n} + \frac{1}{2}\mathbf{U}^{n-1} = \Delta t\, \mathbf{R}^{n+1} \qquad (21)$$

4.5. Validation of the coupling between Maxwell and fluid equations

4.5.1. Hartmann flow

The coupling of the Maxwell equations with the fluid equations is validated on the Hartmann flow [26]. In this verification, we consider only one conductive fluid. This study is used to analyze the complex coupling between the two systems, i.e., Maxwell and fluid equations, with so different characteristic speeds. The Hartmann flow considers a viscous, electrically conductive, fully developed flow between two parallel plates in the x-direction in presence of an imposed magnetic field in the y-direction ($B_{y_0} > 0$) and an imposed electric field in the direction perpendicular to the plane of the movement ($E_{z_0} < 0$). The electromagnetic field produces forces in the flow that change the velocity profile from the parabolic Poiseuille's one to a fuller profile. Also, the movement of the conductive flow produces a electric current that induces a magnetic field. The solution of the velocity and the magnetic field is compared to the analytical solution for a Hartmann number $\mathrm{Ha} = B_{y_0} L \sqrt{\frac{\sigma}{\mu}} = 10$ is compared in Fig. 1.

The performance of the divergence cleaning method is shown in Fig. 2. One can see that around 5 orders of magnitude of $\nabla \cdot \vec{B}$ are reduced setting $\chi = 1$.

4.5.2. Partially ionized two-fluid magnetic reconnection

In this section we present the results using the two-fluid, reactive collisional model presented in Section 3.1, Eqs. (5)-(7). In the literature, only a few examples of simulations reproducing self-consistent partially ionized reactive and collisional multi-fluid models can be found. From the numerical point of view, the main difference of such system of equations compared to ideal two-fluid plasma model [33]-[36] is the stiffness introduced by the source terms and the complexity of the diffusive terms that depend on the magnitude and direction of the magnetic field. In order to assess the numerical method explained in this work, we reproduce the results of a magnetic reconnection in a weakly ionized plasma comparing our results with those of [10].

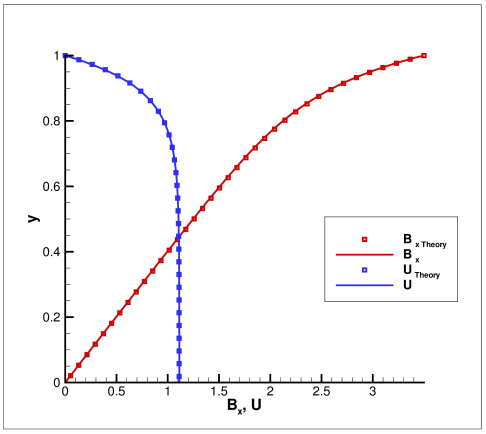

Figure 1: Comparison of non-dimensional velocity and magnetic field solution of Hartmann flow with analytical solution. Solution converged in 500 iterations on a 40×250 cells mesh.

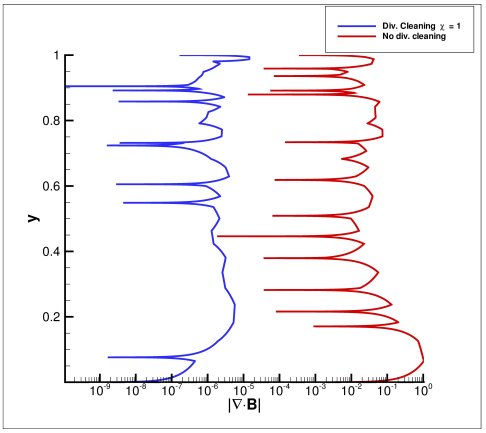

Figure 2: Non-dimensional $\nabla \cdot \vec{B}$ with and without divergence cleaning method

4.6. Parallel scalability of COOLFluiD Finite Volume Solver

We study the scalability of the cell-centered Finite Volume solver of COOLFluiD on an unstructured mesh using implicit time stepping. The parallel performance of the code is carried out using Pleiades supercomputer at NASA Ames Research Center. We test on a 14 M cell mesh up to 4096 processors. The parallel efficiency and speed-up, defined as, $S_p = 64\frac{T_{64}}{T_p}$

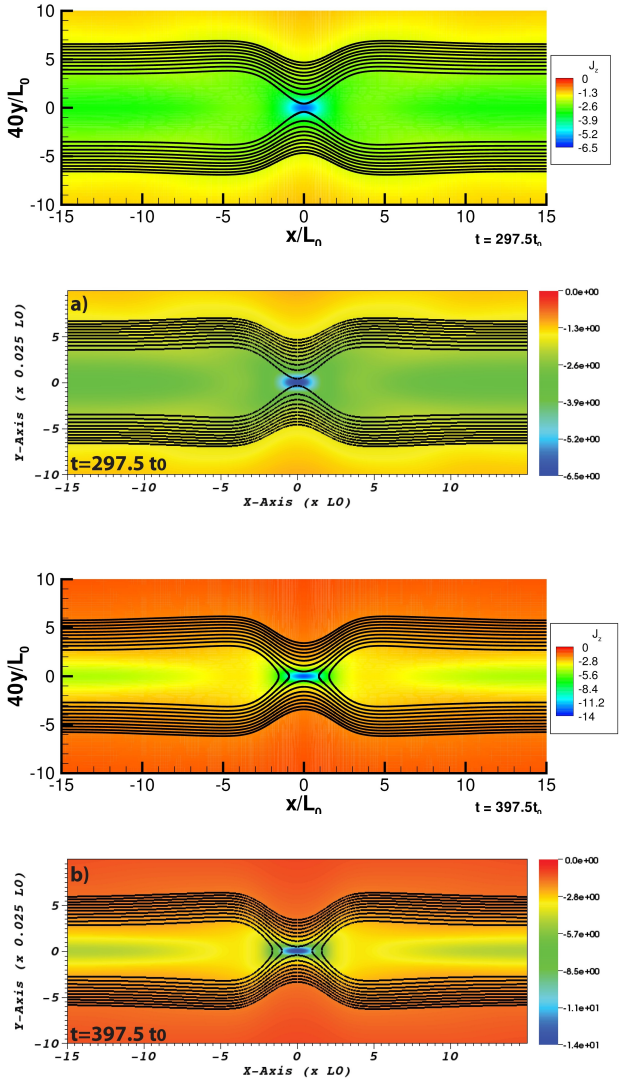

Figure 3: Evolution of the current sheet and magnetic field lines during the magnetic reconnection for different time steps: $297.5t_0$ (top) and $397.5t_0$ (bottom). The results obtained with the present numerical method (top) are compared with the results obtained in [10] (bottom).

and $E_p = \frac{S_p}{p}$ are presented in Figure 4. The result of the test show that almost a speed-up of $S_p = 0.9$ is achieved with 4096 processors. This can be achieved thanks to the parallel architecture of COOLFluiD and it can be considered a strong advantage for the 3D simulations that are presented hereafter.

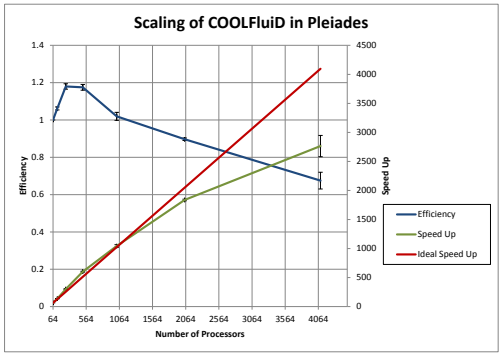

Figure 4: Parallel efficiency and speed-up of COOLFluiD cell-centered Finite Volume

4.7. *Improved finite volume method for the RTE*

The RTE, i.e, Eq. 12, can be also solved using the FV method. In the present work we use the improved method for unstructured grids explained in [27]. The method integrates Eq. 12 over the cell i, as follows:

$$\int_{\Omega_i} \vec{\Omega} \cdot \nabla I_\nu \, dV = \int_{\partial\Omega_i} I_\nu \vec{\Omega} \cdot d\vec{S} = \int_{\Omega_i} \kappa_\nu (S_\nu - I_\nu) \, dV. \tag{22}$$

The latter can be discretized as follows:

$$\sum_j I_{\nu,j}(\Omega)\vec{\Omega} \cdot \vec{n}_{ij} |\partial\Omega|_{ij} = \kappa_\nu (S_{\nu,i} - I_{\nu,i}(\Omega)) \, \Omega_i \tag{23}$$

where $S_{\nu,i}$ and $I_{\nu,i}$ are computed at the center of the cell i and $I_{\nu,j}$ at the center of the face $|\partial\Omega|_{ij}$.

The method explained in [27] approximates the value of $I_{\nu,j}$ at the interface solving the 1-d exact radiative solution for constant κ_ν and S_ν, as follows: considering a distance x along the direction $\vec{\Omega}$

$$I_\nu(x, \Omega) = I_\nu(0, \Omega) e^{-\kappa_\nu x} + (1 - e^{-\kappa_\nu x}) S_\nu \tag{24}$$

At the face where $\vec{\Omega} \cdot \vec{n}_{ij} < 0$, called in the following outgoing face, one can approximate the intensity using the previous solution. In the following expression, we use the superindex *out* for the value computed on an outgoing face and the superindex *in* for the value computed at the center of the incoming cell. Therefore,

$$I^{out}_{\nu,j}(\Omega) = \frac{\sum_{j,\vec{\Omega}\cdot\vec{n}_{ij}<0} I^{in}_{\nu,j}(\Omega)\vec{\Omega}\cdot\vec{n}_{ij}|\partial\Omega|_{ij}e^{-\kappa^{in}_{\nu,j}d}}{\sum_{j,\vec{\Omega}\cdot\vec{n}_{ij}<0}\vec{\Omega}\cdot\vec{n}_{ij}|\partial\Omega|_{ij}} + (1-e^{-\kappa^{in}_{\nu}d})S^{in}_{\nu,j} \quad (25)$$

One can see that the radiative intensity computed at the face center $|\partial\Omega|_{ij}$ is computed in terms of the values at the cell center of cell j and the propagation distance d that is approximated as $d = \left|\frac{\Omega_i}{\vec{\Omega}\cdot\vec{n}_{ij}|\partial\Omega|_{ij}}\right|$.

Using the approximation of the radiative transfer at the interface of the outgoing cells, assuming the source in the cell to be a piecewise-linear function, one can retrieve the radiative intensity at the center of cell i

$$I_{\nu,i}(\Omega) = \frac{\sum_{j,\vec{\Omega}\cdot\vec{n}_{ij}<0} I^{out}_{\nu,j}(\Omega)\vec{\Omega}\cdot\vec{n}_{ij}|\partial\Omega|_{ij}e^{-\frac{1}{2}\kappa^{in}_{\nu,j}d}}{\sum_{j,\vec{\Omega}\cdot\vec{n}_{ij}<0}\vec{\Omega}\cdot\vec{n}_{ij}|\partial\Omega|_{ij}} + \left(1-\frac{1-e^{-\frac{1}{2}\kappa_{\nu,i}d}}{\frac{1}{2}\kappa_{\nu,i}d}\right)S_{\nu,i} + \left(1-\frac{1-e^{-\frac{1}{2}\kappa^{in}_{\nu,j}d}}{\frac{1}{2}\kappa^{in}_{\nu,j}d}\right)S^{in}_{\nu,j} \quad (26)$$

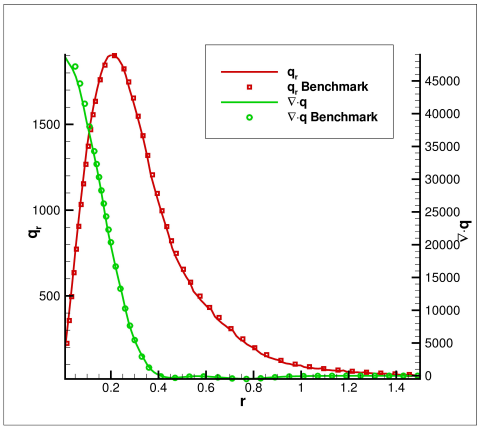

Figure 5: Verification of the RTE finite volume solver with a benchmark solution.

4.7.1. Validation of the RTE solver

We verify the method explained above studying the radiative transfer inside a sphere. We impose a Gaussian temperature profile in the radial direction. We test in a 84000 cells unstructured mesh with 60 mesh points in the radial direction and 20 in the azimuthal direction. For this study, we use the opacity table considering air composition and binning over 100 frequencies. The number of directions used for the azimuthal averaging is 24.

The solution of the heat flux over the radius and the radial heat flux vector compared to the benchmark shows great agreement as it is shown in Figure 5.

5. Summary of applications of the multi-fluid models

The work carried out in this paper is aimed at studying, throughout numerical simulations, a phenomenon know as coronal heating. The distribution of the temperature in the sun atmosphere is still nowadays one of the biggest mysteries in solar physics: it rises from some thousands of Kelvin up to 2 million Kelvin in a very narrow layer called transition region situated around 2Mm above the Sun surface (the surface of the Sun is the layer where the plasma gets opaque). The sudden heating taking place in the transition region is responsible for the acceleration of the solar wind. There are two possible phenomena candidate for causing the coronal heating: magnetic reconnection and wave propagation. We will present a summary of the solutions studying both phenomena with the model presented in Sec. 3.1.

5.1. Propagation of slow magnetoacustic waves in the sun atmosphere

The results shown below are described in detail in [3]. In the Fig. 6 , it is shown some snapshots of the results obtained in our work. At the bottom of the domain, on the Sun surface, the velocity of the plasma is excited. This perturbation travels along the sun atmosphere in form of slow magnetoacoustic waves. The lines of the plot represent the magnetic field corresponding to a magnetic flux that is anchored inside of the sun and expands towards the corona (the upper layer of the Sun, the one that can be seen with a telescope during an eclipse). These simulations propose an innovative formulation that has never been used before, considering partial ionization effects, interaction with the electromagnetic field and thermal and chemical non-equilibrium. We believe that the inclusion of these relevant physical phenomena will help to unveil the reasons of the coronal heating.

5.2. Magnetic reconnection with the effects of radiation in the sun atmosphere

The results presented in this section are described in [2]. We first study a 2D configuration of a Har-

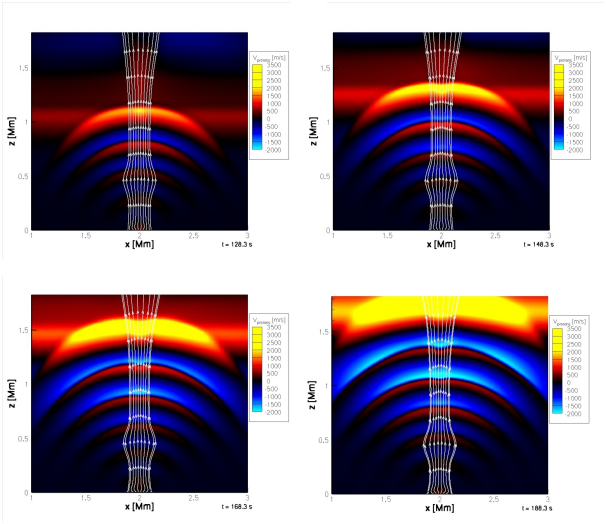

Figure 6: Evolution of slow magnetoacoustic waves in the sun low atmosphere. The plots represent different snapshots of the evolution of the vertical velocity of ions. The lines represent the magnetic field lines corresponding to a flux tube. The perturbation excited on the surface of the sun ravels along the atmosphere accelerating and forming shocks that heat up the plasma. The model used in these simulations allows for studying the effects of partial ionization and thermal and chemical non-equilibrium in the propagation of waves.

ris current sheet under chromospheric conditions corresponding for five different ionization degree levels, from 0.5% to 50%. Under these conditions, collisional effects, chemical reactions and radiation will play a different role in reconnection. We fix the non-dimensional values for all the cases. The characteristic values are:

$$n = 6.6 \times 10^{18} m^{-3}$$
$$T = 8750K$$
$$\Psi = \frac{n_{ions}}{n_{ions} + n_{neutrals}} = 0.5\%$$
$$B = 10^{-3} T.$$

The initial magnetic field topology is chosen to be a Harris sheet, with a small perturbation in order to force the reconnection to occur in the center of the domain. We study the impact of the radiation effect. The chromosphere is known to be optically thin and therefore, radiative cooling plays an important role in the dynamics of the chromosphere. In the present work we compare the results of the reconnection with different radiative models.

In Fig. 7, the reconnection for four different radiation levels is shown. It can be proven analytically that the presence of neutrals help to get thinner the reconnection layer and therefore to speed up the reconnection events. Because of it, as the ionization level increases, the current sheet gets wider and therefore the reconnection rate decreases, as shown in Fig. 8.

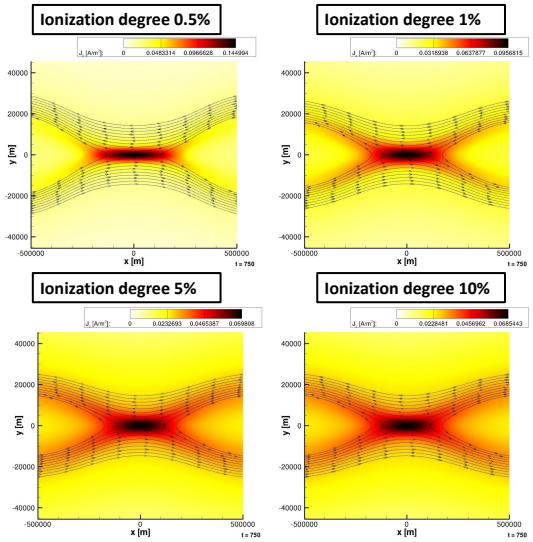

Figure 7: Snapshot of reconnection simulations for four different ionization levels: 0.5% (top left), 1% (top right), 5% (bottom left) and 10% (bottom right). The results are obtained without using any radiative cooling model.

.

When the radiative recombination heat losses are considered, one can see that the results are completely different. As it can be seen it 9, when radiative losses are considered, the width of the current sheet decreases, producing an increase of the reconnection rate, as shown in 10.

6. Study of the magnetic reconnection in the magnetotail with ion+electron collisionless models

Magnetic reconnection plays a fundamental role in the global dynamics of the Earth's magnetosphere. During a geomagnetic substorm, magnetic reconnection takes place in the magnetotail, on the night-side of the magnetosphere, producing heating and acceleration of the particles that travel along the magnetic field lines and can enter the Earth's atmosphere

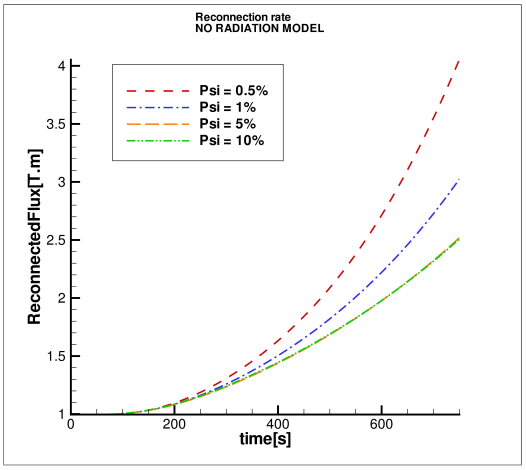

Figure 8: Reconnection rate for different ionization levels without using radiative model

.

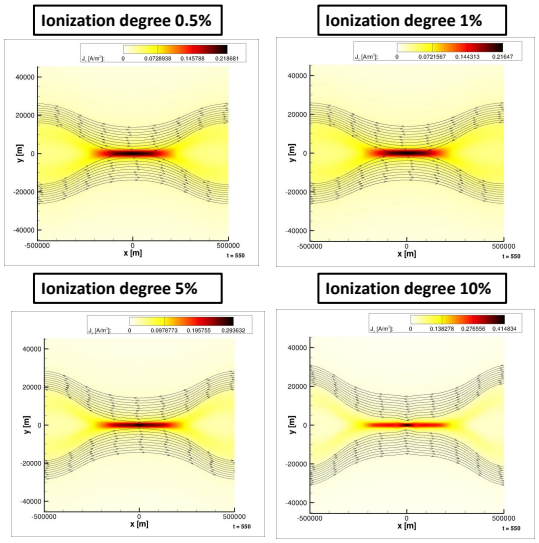

Figure 9: Snapshot of reconnection simulations for four different ionization levels: 0.5% (top left), 1% (top right), 5% (bottom left) and 10% (bottom right). The results are obtained using radiative cooling for the radiative recombination.

.

through the polar caps, producing the Northern lights. Magnetic reconnection in weakly collisional plasmas, as the one in the magnetotail, is a very complex phenomenon, where the reconnection can initiate at scales of the order of the electrons skin depth and that is dominated by the ions scales. Since reconnection is observed to occur faster than the theoretical mod-

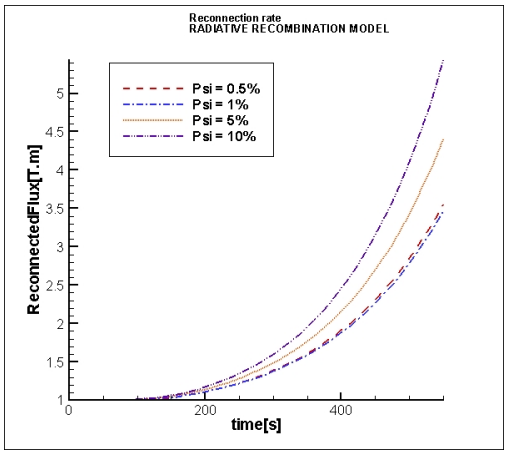

Figure 10: Reconnection rate for different ionization levels using radiative cooling for the radiative recombination.

.

els, the simulation community proposed the Geospace Environmental Modeling (GEM) Reconnection Challenge in order to compare the different models representing a collisionless reconnection. Different models, as resistive MHD, Hall MHD, full-particle and hybrid have been compared in the previous study. Two-fluid model, as it resolves the electromagnetic and the electron scales, is a good candidate to represent the origins of the reconnection. Magnetic field lines are not frozen in the electron fluid, allowing for reconnection. Therefore, unlike Hall-MHD, two-fluid model does not need an artificial resistivity to initiate reconnection.

7. Study of a magnetically-confined nuclear fusion device

Nuclear fusion represents nowadays a clean and almost unlimited source of energy. Magnetic fields are used to confine the plasma in order to achieve temperatures of $10^7 - 10^8$ K that are necessary to achieve nuclear fusion reactions. Magnetic confinement is very difficult to achieve because of the instabilities that are produced by the interaction between the plasma and the magnetic fields. Multi-fluid models are able to study phenomena that is negleted by MHD models, such as drift waves, plasma waves, magnetic reconnection, anisotropic transport produced by the magnetic field, etc. In Fig. 12, the $m = 1, n = 1$ kink instability is studied with an ion-electron two-fluid model.

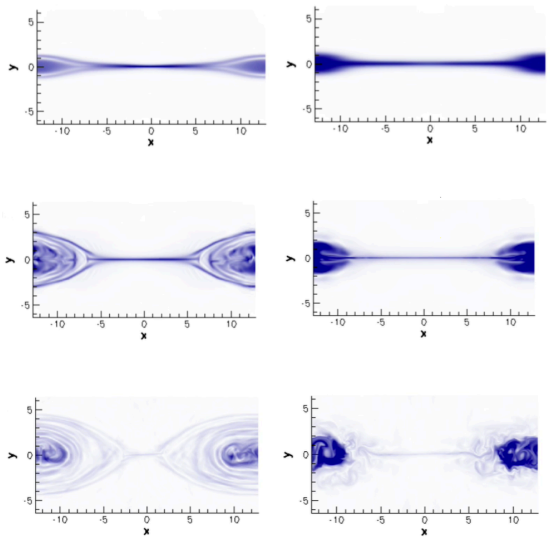

Figure 11: Electron (left) and ion momentum (right) evolution during the magnetic recon- nection. Snapshots at t = 18 (top), t = 26 (middle), t = 45 (bottom) panel.

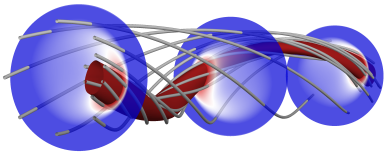

Figure 12: Magnetic field lines (grey) and electric current (red and contour in slices) in the study of the $m = 1, n = 1$ kink instability.

8. Conclusions

The present Ph. D. project is oriented towards the development of numerical tools and models of plasma for representing the magnetic reconnection process in astrophysical and laboratory plasmas. In the present work, we have highlighted the importance of magnetic reconnection process and the necessity of improving the modeling in order to represent this phenomenon more accurately. Multi-fluid models, that consider each species as different interpenetrating fluids, are able to represent microscopic and transport phenomena that is completely neglected in the single-fluid theory. I

Here, we have presented a numerical method solving the multi-fluid equations coupled to Maxwell's equations [1],[4]. The coupling of the equations is validated on the Hartmann flow, showing perfect agreement with the analytical solution and showing the hyperbolic divergence cleaning method to be an efficient way of enforcing the divergence constrains. The parallel scalability of the finite volume solver implemented in COOLFluiD is tested in Pleiades, NASA's supercomputer, showing high efficiency up to 4096 processors. Also, the radiative transfer equation is solved using a finite volume method that improves its accuracy by performing linear-piecewise interpolation along the radiative direction. The verification of the RTE solver was presented showing great agreement with a benchmark solution.

The magnetic reconnection in the chromosphere is simulated using a multi-fluid model considering two fluids, neutrals and charged particles [2]. Magneto-acoustic wave propagation is also studied for the first time with a reactive partially ionized model [3]. The fully-ionized reconnection taking place in the magnetosphere is simulated in [4]. The code is also applied to nuclear fusion plasmas.

Acknowledgments

This research is funded through a fellowship provided by IWT (agentschap voor Innovatie door Wetenschap en Technologie). We would also like to thank Dr. Nagi N. Mansour for the supervision of this work at NASA Ames Research Center and Dr. Andrea Lani, COOLFluiD architect and advisor of this work.

References

[1] Alvarez Laguna, A.; Lani, A.; Deconinck, H.; Mansour, N. N.; Poedts, S. *A fully-implicit finite-volume method for multi-fluid reactive and collisional magnetized plasmas on unstructured meshes*, Journal of Computational Physics, Volume 318, p. 252-276

[2] Alvarez Laguna, A.; Lani, A.; Deconinck, H.; Mansour, N. N.; Poedts,*Effect of radiation on chromospheric magnetic reconnection: reactive and collisional multi-fluid simulations*, Astrophys. J., vol. 842, no. 2. (2017).

[3] Y. Maneva, A. Alvarez Laguna, A. Lani, S. Poedts. *Multi-fluid modeling of magnetosonic wave propagation in the solar chromosphere - effects of impact ionization and radiative recombination* , Astrophys. J., vol. 836, no. 2. (2017).

[4] Alvarez Laguna, A.; N. Ozak; Lani, A.; Deconinck, H.; Mansour, N. N.; Poedts, S. *Fully-implicit finite volume method for the ideal two-fluid plasma model*, Computer Physics Communications, submitted (2017)

[5] Committee on the Societal and Economic Impacts of Severe Space Weather Events, *Severe Space Weather Events Understanding Societal and Economic Impacts: A Workshop Report*, The National Academies Press, 2008.

[6] J. Birn and E. Priest, *Reconnection of Magnetic Fields*, Cambridge University Press, 2007.

[7] F. Zuccarello, *Data analysis and mathematical modeling of the initiation of coronal mass ejections*, PhD thesis, KU Leuven, 2012.

[8] M. Yamada, R. Kulsrud, and H. Ji, *Magnetic Reconnection*, Reviews of Modern Physics vol.82, 2010.

[9] Yamada, M. et al. *Conversion of magnetic energy in the magnetic reconnection layer of a laboratory plasma.* Nature Communications 5:4774 doi: 10.1038/ncomms5774 (2014).

[10] J. E. Leake, V. Lukin, M. Linton and E. Meier, *Multi-fluid simulations of chromospheric magnetic reconnection*, ApJ. 760, 2012.

[11] K. Shibata et al., *Chromospheric Anemone Jets as Evidence of Ubiquitous Reconnection*, Science, Volume 318, Issue 5856, pp. 1591, 2008.

[12] K. Shibata and T. Magara, *Solar Flares: Magnetohydrodynamic Processes*, Living Rev. Solar Phys. 8, 2011.

[13] E. N. Parker, *Sweet's mechanism for merging magnetic fields in conducting fluids*, Geophysical research 62, No. 4, 509-520, 1957

[14] H. E. Petschek. *Magnetic Annihilation*. The Physics of Solar Flares, Proceedings of the AAS-NASA Symposium, October 1963

[15] D. Biskamp, *Magnetic Reconnection in Plasmas*, Cambridge University Press, 2005

[16] S. I. Braginskii, *Transport processes in a plasma*. Reviews of Plasma Physics, Volume 1., pp. 205 311. (1965)

[17] B. Graille , T. E. Magin , M. Massot, *Kinetic theory of plasmas. Translational Energy.* Mathematical Models and Methods in Applied Sciences, Vol. 19, 04 (2009) 527-599

[18] E. T. Meier, U. Shumlak, *A general nonlinear fluid model for reacting plasma-neutral mixtures.* Physics of Plasmas, Volume 19, Issue 7, pp. 072508-072508-11 (2012).

[19] M. Carlsson and J. Leenaarts, *Approximations for radiative cooling and heating in the solar chromosphere.* Astronomy & Astrophysics, Volume 539, March 2012.

[20] A. Lani, *An object Oriented and high perforrmance platform for aerothermodynamics simulations*, PhD Thesis, von Karman Institute for Fluid Dynamics, 2009

[21] R. W. MacCormack. *Numerical Simulation of Aerodynamic Flow Including Induced Magnetic and Electric Fields.* In 39th AIAA Plasmadynamics and Lasers Conference, Seattle, June 2008.

[22] T. Barth. Aspects of unstructured grids and finite volume solvers for the euler and navier-stokes equations. 25th Computational Fluid Dynamics Lecture Series. Von Karman Institute, March 1994.

[23] V. Venkatakrishnan. *Convergence to steady state solutions of the euler equations on unstructured grids with limiters.* Journal of Computational Physics, 118:120130, 1995.

[24] J. Steger, R. F. Warming, *Flux vector splitting for the inviscid gas dynamic equations with application to finite difference methods*, J. Comp. Phys., Vol. 40, No. 2, pp. 263-293, 1981

[25] C.-D. Munz., P. Ommes, R. Schneider. *A three-dimensional finite-volume solver for the Maxwell equations with divergence cleaning on unstructured meshes*. Computer Physics Communications130, 83-117, December,1999.

[26] M. Mitchner and C. H. Kruger, *Partially ionized gases*, Wiley series in plasma physics, 1973.

[27] A. Wray, *Improved Finite-Volume Method for Radiative Hydrodynamics.*, ICCFD7-1003, July 2012.

[28] M. S. Liou, *A sequel to AUSM, part II: AUSM+ -up for all speeds.* J. Comp. Phys., 214:137170, 2006.

[29] A. Alvarez Laguna, A. Lani, N. N. Mansour, A. Kosovichev, and S. Poedts, *A two-fluid computational model to study magnetic reconnection in reactive plasmas under chromospheric conditions*, WCCM XI-ECCM V-ECFD VI, Barcelona (2014).

[30] G. S. Voronov, *A practical fit formula for ionization rate coefficients of atoms and ions by electron impact*, Atomic data nad nuclear data tables 65, 1-35, 1997

[31] B. M. Smirnov, *Physics of Atoms and Ions*, Springer-Verlag New York, Inc., 2003

[32] Vernazza, J. E., Avrett, E. H., Loeser, R., *Structure of the solar chromosphere. III. Models of the EUV brightness components of the quiet Sun*, ApJS45, 635-725, 1981

[33] U. Shumlak and J. Loverich. Approximate riemann solver for the two-fluid plasma model. *J. Comput. Phys.*, 187(2):620–638, May 2003.

[34] A. Hakim, J. Loverich, and U. Shumlak. A high resolution wave propagation scheme for ideal two-fluid plasma equations. *J. Comput. Phys.*, 219(1):418–442, November 2006.

[35] J. Loverich and U. Shumlak. A discontinuous galerkin method for the full two-fluid plasma model. *Computer Physics Communications*, 169(1):251–255, July 2005.

[36] B. Srinivasan and U. Shumlak. Analytical and computational study of the ideal full two-fluid plasma model and asymptotic approximations for Hall-magnetohydrodynamics. *Physics of Plasmas*, 18(9):092113, September 2011.

Development of an ablation model for rarefied flows with application to meteoroid entry

Federico Bariselli

Aeronautics and Aerospace Department, von Karman Institute for Fluid Dynamics, Belgium, federico.bariselli@vki.ac.be

Supervisor: Thierry Magin

Associate Professor, Aeronautics and Aerospace Department, von Karman Institute for Fluid Dynamics, Belgium, thierry.magin@vki.ac.be

University Supervisor: Aldo Frezzotti

Professor, Aerospace Science and Technology Department, Politecnico di Milano, Italy, aldo.frezzotti@polimi.it

University Supervisor: Annick Hubin

Professor, Electrochemical and Surface Engineering Department, Vrije Universiteit Brussel, Belgium, annick.hubin@vub.ac.be

Abstract

An evaporation boundary condition is developed in the framework of the Direct Simulation Monte Carlo method and applied to the study of meteoroid entry. The material is composed by a mixture of metal oxides typically present in ordinary chondritic meteorites. Preliminary results show the formation of the trail and the shielding/condensation effects of the ablated vapors. Chemical reactions in the gas phase are not triggered under strongly rarefied conditions.

Keywords: Ablation, atmospheric entry, meteoroid, rarefied gas dynamics, Direct Simulation Monte Carlo

1. Introduction

Artificial space systems are not the only objects flying in our sky. About 50 tonnes of small meteoroids enter the terrestrial atmosphere every day [1]. These bodies, from one meter diameter to micron-size grains, originate either from sublimating comets or from asteroids. In their rush to the ground, they intersect the atmosphere at velocities up to 72 km/s. As a meteoroid interacts with the atmosphere, its surface temperature can reach several thousands of Kelvins causing its ablation, i.e. fragmentation, melting and evaporation. Due to their small size and tremendous speeds, meteors often burn up at high altitudes, above 80 km, where the atmosphere is rarefied. Here, the gas cannot be treated as a continuous medium and the Navier-Stokes equations usually employed in Gas Dynamics fail. As shown in Figure 1, due to the high energies involved, coupled physico-chemical phenomena (strong departure from thermo-chemical equilibrium, radiative heating, ionization and complex gas-surface interactions) occur both in gas and solid phases, making the prediction of these flows an extremely challenging task.

Recent efforts have been made by the Belgian Institute for Space Aeronomy to predict velocity, trajectory and mass of meteors. The Belgian RAdio Meteor Stations (BRAMS) experiment consists in a series of receivers spread all over Belgium to collect and standardize the meteor observations [2]. Ground radio stations are able to detect the free electron concentration in the wake, which is directly influenced by ablation mechanisms. However, the interpretation of radio data currently relies on phenomenological methods, hence, poorly account for melting and evaporation of the material, chemistry in the meteor trail, and rarefied gas effects.

The classical meteor ablation models are derived under the assumption of free molecular flow and evaporation into vacuum. The simplest among these models assumes that the mass loss rate is proportional to the kinetic energy imparted on the meteoroid, with the

ablation beginning when the surface of the meteoroid reaches the boiling point [3]. In [4], Campbell-Brown et al. inferred that this model is not valid for low density conditions for which the ablation may start before the boiling temperature is reached. They proposed an ablation model applying the Knudsen-Langmuir formula coupled with the Clausius-Clapeyron relation to compute the equilibrium vapor pressure of the melt-vapor phase transition. In [1], Vondrak et al. adopted a similar approach, with the equilibrium properties of the silicate-vapor system computed by means of a mass balance and mass action software [5].

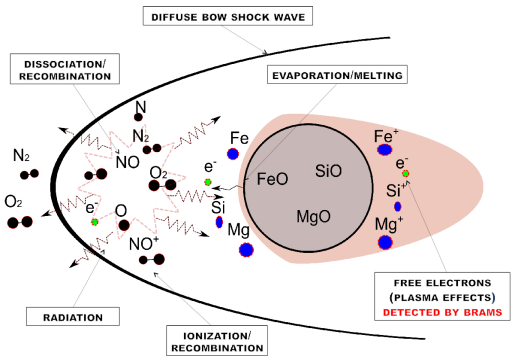

Figure 1: Schematic of the coupled physico-chemical phenomena which can occur during meteoroid ablation in the rarefied regime.

Boyd [6] was the first to address the problem of the ablation of meteors in the rarefied regime by giving a description of the phenomenon from the flow field perspective. He treated the meteor material as a single species, i.e. magnesium, using a phenomenological ablation model accounting for evaporation of the metal and assuming a vaporization temperature of 2500 K. No chemical reactions were considered in the gas phase. Preliminary results indicated that a cloud of ablated material surrounds the meteor and that a large high-temperature region in near-thermal equilibrium is present in the meteor's trail. This result is in qualitative agreement with spectral measurements of meteor wakes but is not able to predict quantitatively their composition and ablation rate. A Direct Simulation Monte Carlo (DSMC) [7] approach was also used by Vinkovic [8] to predict the emission of light by very high altitude meteors detected on the ground, not explainable by means of classical ablation theory. The study focused on the sputtering from the meteoroid surface. Strong assumptions were made, such as no distinction between atomic and molecular species in the gas phase. Other physical processes like vaporization, ionization, dissociation and excitation were not included.

In this work, an evaporation boundary condition is developed in the framework of an open source DSMC software [9]. The material is assumed to be composed by a mixture of metal oxides which are typically present in ordinary chondritic meteorites. Stoichiometric phase change reactions are assumed. The wall emits particles at rates set by the equilibrium vapor pressures of each of the elements evaporating from the meteoroid. The latter are obtained in a similar fashion as in [1]. Particles can be absorbed by the wall in agreement with condensation coefficients and they are computed in such a way that the equilibrium condition can be kinetically retrieved and that the constraint of stoichiometric evaporation is satisfied. In a second step, the flow is coupled with the material response through surface mass and energy balances. The material code models a randomly rotating sphere with the temperature which is uniquely dependent on the radius [10]. The melt-solid phase change is accounted through the equivalent heat capacity method [11].

In the next section, an overview of the meteor phenomenon is given. The employed gas-phase and material models are respectively introduced in Section 3 and 4, while the kinetic interface for the gas-wall coupling is presented in Section 5. Finally, in Section 6, some preliminary results are discussed for a simplified configuration.

2. Overview of the meteor phenomenon

2.1. Typical sizes and physico-chemical properties

The bulk of material vaporizing in the atmosphere every day is formed by particles in the range between 5×10^{-5} and 2×10^{-2} m [10]. Radar and radio waves techniques are able to sample meteoroids smaller than optical systems, but big enough for the generation of a wake of plasma sufficiently intense to be detected. According to Baggaley [12], this corresponds to a rough limit of 10^{-5} m for meteoroids traveling at a speed of about 30 km/s. Particles smaller than several hundredths of a millimeter decelerate before reaching the melting temperature. This class of micrometeoroids, for which the most of the heat is dissipated by radiation, is not detected neither by radar nor optical techniques and disappear into the atmosphere without the possibility of being tracked.

More than the 90% of meteorites collected on the ground is represented by ordinary chondrites. Similarly to magmatic rocks such as basalt, these meteorites are composed by a mixture of metal oxides with

a composition close to the one reported in Table 1. Hence, from here on out, they will be considered as the meteoroid prototype.

Table 1: Typical composition of an ordinary chondrite [1].

Oxide	Mass %	Oxide	Mass %
SiO_2	34.0	CaO	1.9
MgO	24.2	Na_2O	1.0
FeO	36.3	K_2O	0.1
Al_2O_3	2.5	TiO_2	0.01

If the chemical composition of the ordinary chondrites has been widely studied, much less attention has been devoted to characterize their physical properties, especially at high temperatures [13]. In literature, big discrepancies can be found for parameters which turn out to be vital for the predictivity of the models (e.g. latent heat and melting temperature). The list of the properties employed in this work to model the material is given in Table 2.

Table 2: Phisical properties of an ordinary chondrite.

Density	[kg/m^3]	ρ	3500
Conductivity	[W/m/K]	k	1.5
Emissivity	[-]	ϵ	1.0
Specific heat	[m^2/s^2/K]	C_p	1050
Melting temperature	[K]	T_m	1800
Heat of melting	[J/kg]	L_m	4×10^5
Heat of evaporation	[J/kg]	L_e	4×10^6

2.2. Pre-heating phase and onset of evaporation

Ablation only starts after a pre-heating phase in the thermosphere in which the surface of the body is heated up to a melting condition. In this phase, the meteoroid essentially conserves its mass and the density of the atmosphere, ρ_∞, is so low that the particle velocity, V_∞, remains unchanged. The onset of intense evaporation, H_{eva}, is computed as the altitude at which the surface starts melting and it is obtained by solving the heat equation for the body with a boundary condition of the following type:

$$\frac{\rho_\infty V_\infty^3}{8} = k \frac{\partial T}{\partial r}\bigg|_w + \epsilon\sigma(T_w^4 - T_\infty^4) \qquad (1)$$

where the thermal energy received by the meteoroid in the LHS is balanced by the heat conduction and the radiative loss on the RHS. As revealed by Table 3, this altitude is strongly dependent on the velocity and on the dimension of the body, with the smaller and fastest ones vaporized earlier along their trajectory.

The classical equation of ablation [3] can be written as:

$$\phi_e = \frac{\Lambda \rho_\infty V_\infty^3}{2L_e} \qquad (2)$$

where ϕ_e is the mass flux due to evaporation and $\Lambda \leq 1$ represents a free molecular heat transfer coefficient accounting for screening effects. The characteristic time of ablation and the altitude of extinction of the phenomenon, respectively T_{abl} and H_{ext}, can be obtained by integrating Equation 2 over the surface and in time:

$$-\frac{2}{3}\frac{\rho}{\Lambda}\frac{L_e}{V_\infty^3}\int_R^0 \frac{dr^3}{r^2} = \int_0^{T_{abl}} \rho_\infty(t)\, dt \qquad (3)$$

where:

$$\rho_\infty(t) = \rho_0\, exp\left\{-\frac{H_{eva} + V_\infty t}{H^*}\right\} \qquad (4)$$

which implies that the velocity of the particle is kept constant and the impact angle is assumed to be zero. As shown in Table 3, the times go from tens of second to few seconds for slower and bigger bodies. This time is probably underestimated for the latter, reaching the lower layers of the atmosphere where the deceleration of the body starts playing an important role. Although approximate, this analysis provides an overall picture of the phenomenon and it confirms the experimental evidence for which radio observations mostly refer to a sector of the atmosphere going from 130 km to 70 km [12].

Table 3: Estimates of the onset of intense evaporation, altitude of extinction and time of ablation for typical velocities and diameters.

	V_∞ [km/s]	D [m]		
		10^{-4}	10^{-3}	10^{-2}
H_{eva} [km]	12	114	109	100
	32	137	126	119
	72	155	140	136
H_{ext} [km]	12	106	91	73
	32	124	106	89
	72	138	120	102
T_{abl} [s]	12	0.7	1.5	2.3
	32	0.4	0.6	1.0
	72	0.2	0.3	0.5

2.3. Flow regimes

Traveling at geocentric speeds from 12 up to 72 km/s, meteoroids can experience hypersonic velocities which are more than 200 times the speed of sound. For instance, a Leonid at an altitude of 100 km flies at a Mach number above 270 [6]. To give an idea, this velocity corresponds to 8 times the Stardust re-entry speed, which is the maximum speed ever experienced by a spacecraft during its re-entry trajectory into the Earth's atmosphere.

The Knudsen number is the ratio between the mean free path of the gas and the size of the body rushing through it. Flows described by $Kn > 0.1$ show high degrees of thermal non-equilibrium. $Kn > 10$ characterize free-molecular regimes, where the collisions in the gas phase can be disregarded and the dynamics of the gas is fully described by the gas-surface interactions. Figure 2 plots a map of the characteristic conditions encountered by the meteoroids in terms of the Kn with respect to the size and the altitude. Tiny bodies flying at high altitudes reveal $Kn > 10$. However, such an analysis can be misleading. Let us consider, for example, a 1 mm body falling at 72 km/s, detected by a radar at an altitude of 100 km. According to the map, this condition corresponds to free-molecular flight. Since the evaporation has already been triggered, however, this body is ablating at a rate higher than its mass. The latter is described by the contours plotted for the evaporation rates as a percentage of the mass of the object. Forming a high density region around the body, the ablated vapors may have a shielding effect, making the dynamics of the gas more complex and widening the spectrum of regimes which characterize the flowfield.

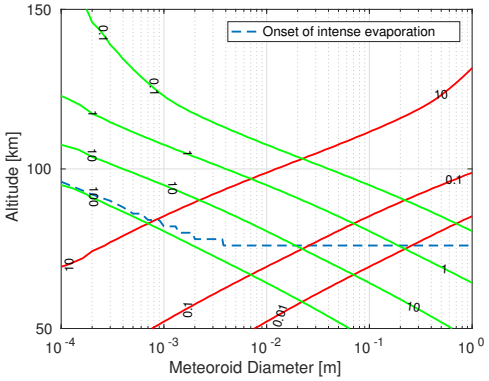

(a) $V_\infty = 12$ km/s

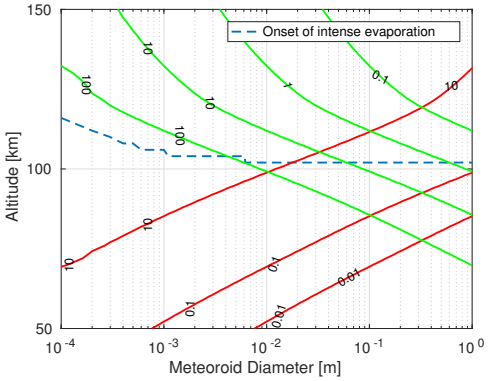

(b) $V_\infty = 72$ km/s

Figure 2: Map of the different rarefaction regimes in terms of the Knudsen number (—) and the normalized ablation rate (—) in relationship to diameter and altitude.

3. Model of the flow

3.1. Physico-mathematical model

As long as the hypothesis of continuum is valid, a hydrodynamic model can be applied. However, under rarefied conditions, the collision rate is too low for the gas to reach local thermodynamic equilibrium, hence, the gas has to be described at a molecular scale. Such a scale does not allow a fully deterministic approach and a statistical description is more suitable. The function $f_i(\boldsymbol{x}, \boldsymbol{\xi}_i, t)$ is defined as the *one-particle velocity distribution function* for the species i and its evolution over time is described by an integro-differential equation. The Boltzmann equation [14] for a gas mixture can be written as:

$$\frac{\partial f_i}{\partial t} + \boldsymbol{\xi_i} \cdot \frac{\partial f_i}{\partial \boldsymbol{x}} + \frac{\boldsymbol{F_i}}{m_i} \cdot \frac{\partial f_i}{\partial \boldsymbol{\xi_i}} = \sum_{j \in S} J(f_i, f_j) \quad i \in \mathcal{S} \quad (5)$$

$$J(f_i, f_j) = \int (f_i' f_j' - f_i f_j) \, |\boldsymbol{\xi}_i - \boldsymbol{\xi}_j| \, \sigma_{ij} \, d\omega \, d\boldsymbol{\xi}_j$$

where the LHS describes the result of macroscopic gradients and external body forces $\boldsymbol{F_i}$ on the velocity distribution function in the physical and velocity space $(\boldsymbol{x}, \boldsymbol{\xi}_i)$, while the integral at the RHS models the effect of the binary collisions characterized by cross section σ_{ij}.

3.2. Numerical method

Direct Simulation Monte Carlo is a particle-based method for the numerical solution of the Boltzmann equation [7]. This technique has been widely used

in the aerospace community over the last 50 years to simulate hypersonic flows [15; 16] with a high degree of thermo-chemical non-equilibrium. The trajectories of a representative number of molecules are simulated in the physical space: the particle advection phase is treated deterministically using finite differences, while the collision integral of Equation 5 is solved by means of Monte Carlo integration.

The SPARTA software is used [9] here. Developed at the Sandia Labs, this is an open-source DSMC tool and its object-oriented philosophy enables extensions.

DSMC employs a phenomenological potential to describe the dynamics of binary collisions. In this work, the Variable Hard Sphere (VHS) model has been chosen for its simplicity [7]. It provides an inter-molecular potential which depends on the relative velocity of the collision and the scattering angle is sampled from an isotropic distribution. It is well known that such a model fails in the attempt of capturing diffusion processes in mixture of gases and that the anisotropy of neutral-charged collisions in weakly ionized gases cannot be described [17]. The internal energy exchanges are modeled according to the classical Larsen-Borgnakke phenomenological model [7]. Chemical reactions from the NASA Air 11 mixture [18] are accounted through the Total Collision Energy (TCE) method [7]. This method consist of assuming an analytic form for the collision-dependent reaction cross-section. When averaging this cross-section over a Maxwellian velocity distribution, it is possible to equate it to known rate coefficients in Arrhenius form. Strictly speaking this method is valid only under the assumption of thermal equilibrium. Chemistry involving the ablated species will not be taken into account.

4. Model of the material

4.1. Physical model

The thermal response of a rapidly and randomly rotating sphere is considered [10]:

$$\frac{\partial T}{\partial t} = \frac{k}{\rho C_p}\frac{\partial^2 T}{\partial r^2} + \frac{2k}{\rho C_p}\frac{1}{r}\frac{\partial T}{\partial r} \tag{6}$$

The heat equation in this form is obtained by applying a transformation into spherical coordinates $T = T(r, \theta, \varphi, t)$ and dropping the angular dependencies due to the symmetry of the problem. The vapor-liquid interface is considered as a moving boundary problem as it is described in Section 5. Here, the interface has to couple the Boltzmann equation for the vapor with the heat conduction in the condensed phase. The liquid-solid transition is dealt through the *equivalent heat capacity method* [11]. In this method, only one equation is solved for both the condensed phases without the need of tracking the melting front which is obtained a posteriori. The latent heat of melting at the interface is taken into account by assuming a temperature dependency of the heat capacity of the following type:

$$C_p = \begin{cases} C_p^s & T < T_m - \Delta T \\ \frac{C_p^s + C_p^l}{2} + \frac{L_m}{2\Delta T} & T_m - \Delta T < T < T_m + \Delta T \\ C_p^l & T > T_m + \Delta T \end{cases} \tag{7}$$

where ΔT defines the range of temperatures in which the molten and solid coexist, typically characterizing melting problems in non-pure substances (also see Figure 3).

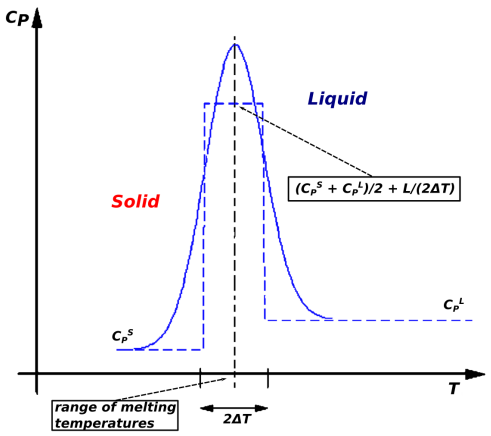

Figure 3: Variation of the heat capacity with respect to the temperature in the equivalent heat capacity method.

4.2. Numerical method

A finite differences scheme is employed to solve Equation 6. The integration over the time is performed via an explicit Euler method. The equation is solved in a fixed reference frame, with a boundary (the vapor-liquid interface), which is moved at each time step in agreement with the velocity of the wall, v_w. This quantity is obtained through a surface mass balance as described in Section 5. At each time step, the mesh is re-generated so that it is kept uniform. If the node at the interface overlaps with its neighbor, a node is dropped, so that the space discretization remains almost constant throughout the simulation. At each time step, the solution previously obtained is re-mapped on

the new grid. The effectiveness of this procedure is evaluated by comparing the numerical solution with an exact one for a 1D semi-infinite slab, initially at uniform temperature, T_0, exposed to a step in the surface temperature, T_w, and in the surface recession rate, v_w. For constant properties, it can be shown that the temperature profile approaches a quasi-steady form:

$$\frac{T - T_0}{T_w - T_0} = exp\left\{ - \frac{\rho C_p}{k} v_w r \right\} \tag{8}$$

Figure 4 shows the comparison between the computed and exact profiles. For the present conditions, after 100 s, the solution has reached the steady-state and the agreement between the profiles is excellent.

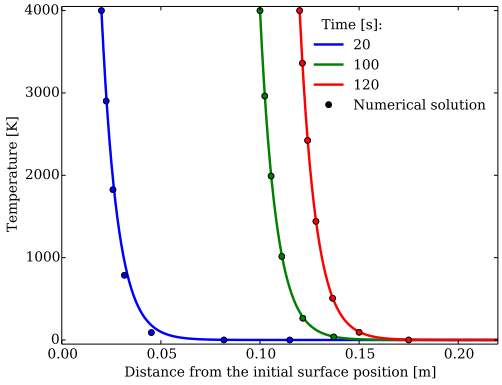

Figure 4: Comparison of the exact and numerical temperature profiles for the verification of the recession procedure.

As shown in Figure 3, the C_p in the equivalent heat capacity method is approximated through a Gaussian shape to avoid numerical instabilities. By solving the Stefan problem, an exact solution of the melting problem for a 1D semi-infinite slab was obtained by Carslaw and Jaeger [19]. The accuracy of the methodology is assessed by comparing the position of the melting front, for which an algebraic equation exists:

$$\frac{T_0 - T_m}{T_w - T_m} \sqrt{\frac{C_p^l}{C_p^s}} \frac{exp\left\{ - C_p^l / C_p^s \, \eta_{ls}^2 \right\}}{erfc\left\{ - \sqrt{C_p^l / C_p^s} \, \eta_{ls} \right\}} + \\ + \frac{exp\left\{ - \eta_{ls}^2 \right\}}{erf\left\{ \eta_{ls} \right\}} - \frac{\sqrt{\pi} \, \eta_{ls} \, L_m}{C_p^l (T_w - T_m)} = 0 \tag{9}$$

where the subscript ls is used to denote the liquid-solid interface and $\eta_{ls} = \frac{r_{ls}}{2\sqrt{k/\rho C_p^l t}}$.

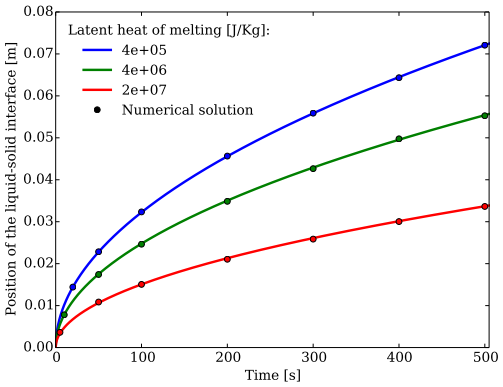

Figure 5: Comparison of the exact and numerical solution for the position of the liquid-solid interface for the verification of the heat equivalent method.

5. Model of the gas-surface interactions

5.1. Kinetic boundary condition for evaporation

From a microscopic point of view, the vapor-liquid interface is a finite region whose thickness is 10-20 nominal molecular diameters [20]. At a kinetic scale, its detailed physical structure is neglected and reduced to a surface, Σ, bounding the vapor. The molecular flux of the species i emerging from Σ, which moves at $\boldsymbol{v_w}$ and is characterized by a normal unit vector, $\boldsymbol{n}$, can be modeled by the following inhomogeneous linear boundary condition:

$$f_i[\boldsymbol{\xi_i} - \boldsymbol{v_w}] \cdot \boldsymbol{n} = g_i[\boldsymbol{\xi_i} - \boldsymbol{v_w}] \cdot \boldsymbol{n} + \\ + \int_{[\boldsymbol{\xi_i'} - \boldsymbol{v_w}] \cdot \boldsymbol{n} < 0} K_{B_i}(\boldsymbol{\xi_i'} \rightarrow \boldsymbol{\xi_i}) f_i[\boldsymbol{\xi_i'} - \boldsymbol{v_w}] \cdot \boldsymbol{n} \, d\boldsymbol{\xi_i'}, \\ [\boldsymbol{\xi_i} - \boldsymbol{v_w}] \cdot \boldsymbol{n} > 0 \quad i \in \mathcal{S} \tag{10}$$

This comprises 2 contributions: i) the particles coming from the liquid and evaporating into the vapor phase with a half-range Maxwellian. At the equilibrium vapor number density, $n_{w_i}^{eq}(composition, T_w)$, and temperature, T_w, this distribution can be written as:

$$g_i = \frac{\alpha_{e_i} \, n_{w_i}^{eq}}{(2\pi R_i T_w)^{3/2}} \, exp\left\{ - \frac{|\boldsymbol{\xi_i} - \boldsymbol{v_w}|^2}{2 R_i T_w} \right\}, \\ [\boldsymbol{\xi_i} - \boldsymbol{v_w}] \cdot \boldsymbol{n} > 0 \tag{11}$$

in which R_i is the gas constant defined as k_B/m_i, k_B being the Boltzmann constant and m_i the atomic mass of species i. Departures from equilibrium are taken into account via an evaporation coefficient $0 \leq \alpha_{e_i} \leq 1$; ii)

the molecules in the gas phase which, interacting with the wall and not condensing, are scattered back and whose velocity is instantaneously changed from $\boldsymbol{\xi}_i'$ to $\boldsymbol{\xi}_i$ with probability driven by the *scattering kernel*:

$$K_{B_i}(\boldsymbol{\xi}_i' \rightarrow \boldsymbol{\xi}_i) = \\ = (1-\alpha_{c_i}) \frac{[\boldsymbol{\xi}_i - \boldsymbol{v}_w] \cdot \boldsymbol{n}}{2\pi(R_i T_w)^2} \, exp\left\{ - \frac{|\boldsymbol{\xi}_i - \boldsymbol{v}_w|^2}{2R_i T_w} \right\} \quad (12)$$

In this case, the kernel is written as if the impinging particles were fully thermalized to the temperature of the liquid. The condensation coefficient $0 \leq \alpha_{c_i} \leq 1$ represents the probability to condense for a molecule of the species i.

The determination of the equilibrium properties of the vapor-liquid system is fundamental since they directly influence the kinetic boundary condition through $n_{w_i}^{eq}$. For this purpose, a multi-phase and multi-species equilibrium solver developed by Fegley and Cameron [5] is used. Using a mass action, mass balance algorithm, MAGMA has been widely used to model silicate lavas and has been extensively validated against experimental data [21]. This software assumes evaporation reactions of this type:

$$\mathrm{M}_x\mathrm{O}_y \, (\mathrm{l}) \rightleftharpoons x \, \mathrm{M} \, (\mathrm{g}) + y \, \mathrm{O} \, (\mathrm{g}) \quad (13)$$

where $\mathrm{M}_x\mathrm{O}_y$(l) is an oxide among the ones reported in Table 1 and Equation 13 can be written for a set of change of phase reactions, $\mathcal{R}$. Although this can be false far from the equilibrium, this type of mechanism is the only considered in our development. This is due to the fact that the thermodynamic equilibrium has to be retrieved by the kinetic approach and, in this sense, the 2 treatments have to be consistent (*detailed balance* condition [22]). A last comment needs to be made on the choice of evaporation and condensation coefficients which are still left as degrees of freedom. Their determination would imply an analysis at the microscopic scale such as the one provided by Molecular Dynamics [20]. This knowledge is still missing for complex systems. For this reason, we assume $\alpha_{e_{\mathrm{M}_i}} = \alpha_{c_{\mathrm{M}_i}} = \alpha_{\mathrm{M}}$ for all the metallic elements which appear in $\mathcal{R}$, and $\alpha_{e_{\mathrm{O}}} = \alpha_{c_{\mathrm{O}}} = \alpha_O$ for oxygen. The 2 remaining parameters have to be chosen in agreement with the following constraints:

$$\begin{cases} \phi_{e_{\mathrm{M}_i}}^{eq} = \phi_{c_{\mathrm{M}_i}}^{eq} & i \in \mathcal{R} \\ \phi_{e_{\mathrm{O}}}^{eq} = \phi_{c_{\mathrm{O}}}^{eq} \;\Rightarrow\; \sum_{i \in \mathcal{R}} \phi_{e_{\mathrm{O}_i}}^{eq} = \phi_{c_{\mathrm{O}}}^{eq} \\ y_i \phi_{e_{\mathrm{M}_i}}^{eq} = x_i \phi_{e_{\mathrm{O}_i}}^{eq} & i \in \mathcal{R} \end{cases} \quad (14)$$

where the first 2 conditions ensure the possibility of retrieving equilibrium (the rate of evaporation has to be balanced by the rate of adsorption of each species), while the third one constraints the molecular fluxes in agreement with Equation 13.

5.2. Flow-material coupling

The Boltzmann and the heat conduction equation are coupled by means of surface mass and energy balances. A schematic of these balances is provided in Figure 6. The surface mass balance can be formally written as:

$$\sum_{i \in \mathcal{S}} \phi_{e_i} - \sum_{i \in \mathcal{S}} \phi_{c_i} = \rho_w v_w \quad (15)$$

while the surface energy balance reads as:

$$\sum_{i \in \mathcal{S}} q_{c_i} + \sum_{i \in \mathcal{S}} q_{r_i} - \sum_{i \in \mathcal{S}} q_{e_i} + \epsilon\sigma T_\infty^4 = \\ \rho h_w v_w + k \left.\frac{\partial T}{\partial r}\right|_w + \epsilon\sigma T_w^4 \quad (16)$$

On the RHS, it appears the contribution coming from the flow side while the LHS consist of all the terms regarding the material. Subscripts e, c and r are used to refer to evaporation, condensation and reflection contributions respectively. The latter does not contribute in the mass balance. The evaporation terms are computed theoretically, while the ones from condensation and reflection are directly obtained by DSMC simulation.

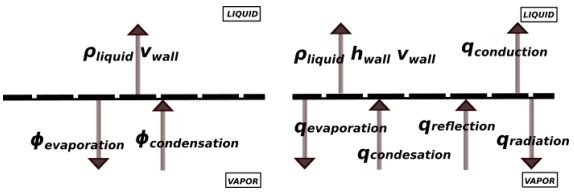

Figure 6: Surface mass (left) and energy (right) balances.

6. Preliminary results and discussion

6.1. Trajectory simulations

Results for the full coupling are still not available. For this reason, the trajectory and the material response are studied separately from the flowfield. The terms due to condensation in Equation 15 and 16 are neglected and the reflection of the particles approximated in the same fashion as in Equation 1.

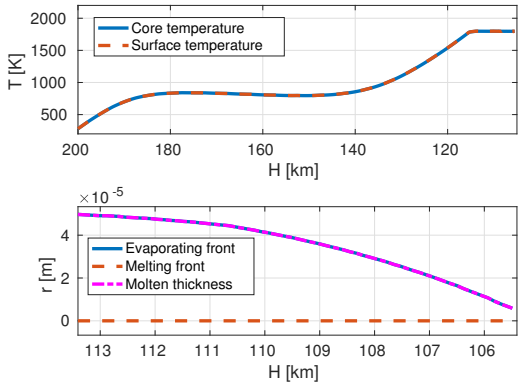

(a) $D = 10^{-4}$ m

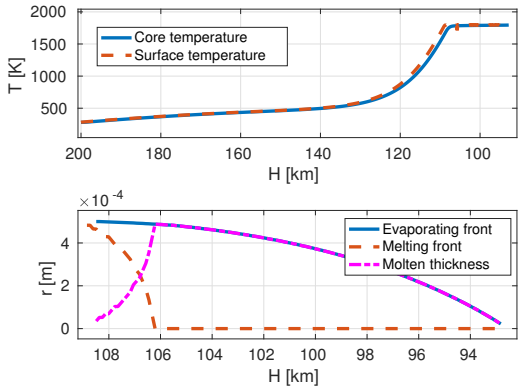

(b) $D = 10^{-3}$ m

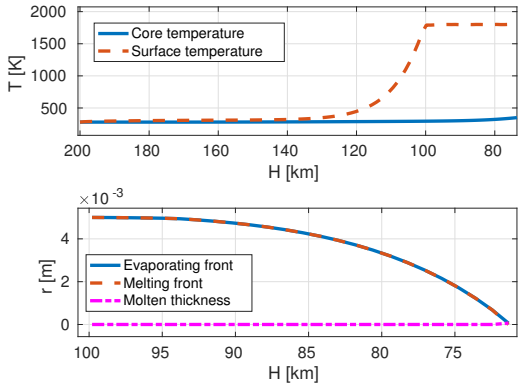

(c) $D = 10^{-2}$ m

Figure 7: Trajectory simulations for $V_\infty = 12$ km/s. The position of the fronts is computed from the core of the body.

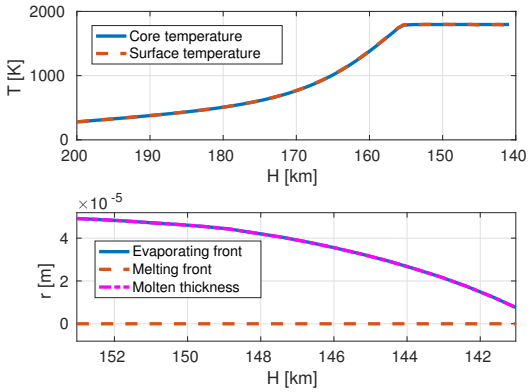

(a) $D = 10^{-4}$ m

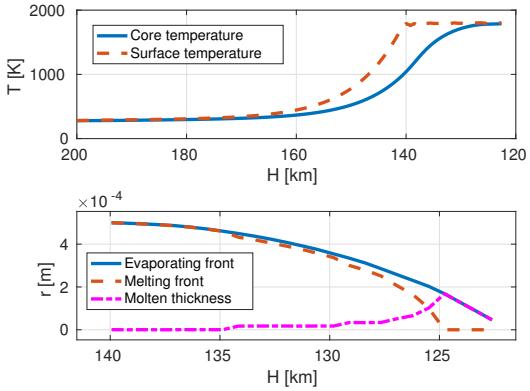

(b) $D = 10^{-3}$ m

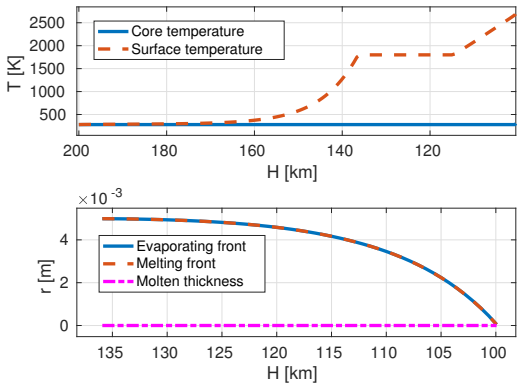

(c) $D = 10^{-2}$ m

Figure 8: Trajectory simulations for $V_\infty = 72$ km/s. The position of the fronts is computed from the core of the body.

When a meteoroid enters the atmosphere, it starts being heated up very soon. However, down to 200 km, the raise in temperature of the body is generally small. Particles of size 10^{-4} m are characterized by a fast and uniform heat up with negligible temperature gradients between the surface and the core of the body (see Figure 7.a and 8.a). The cooling effect due the re-radiation of the surface is evident for the tinier and slower particles, for which the trajectory is characterized by a plateau in the temperature between 180

and 140 km (see Figure 7.a). Moreover, the thermal non-equilibrium inside the material is enhanced by increasing the velocity and by decreasing the size, as shown in Figure 7.b and 8.b.

When the surface starts melting, evaporation can commence. From this point of the trajectory on, the energy is dissipated mostly by evaporation and the material cannot heat up anymore. Only higher heat fluxes (Figure 8.c), encountered at greater velocities, lead the surface temperature to overcome the melting condition. This highlights the overwhelming influence of the melting temperature as input of our modeling.

When small particles start melting, they evolve into molten droplets (see Figure 7.a and 8.a). Hence, the effect of the shear of the flow may play an important role, with the mass being lost mainly through mechanical removal. In particles of intermediate size (see Figure 7.b and 8.b), we detect the development of a liquid layer. The latter is not present in the largest class of bodies under study (see Figure 7.c and 8.c), where the evaporation front consumes the liquid layer and the 2 fronts turn out to coincide. Moreover, in this class of meteoroids, conduction does not have time to level out the temperature inside the body and the core remains unaffected. It is reasonable to think that this class of meteoroids fragments due to the large thermal stresses.

6.2. *Characteristics of the flowfield*

The structure of the flowfield around a 1 cm body is analysed for 2 different altitudes (130 and 90 km) and 2 different velocities (12 and 72 km/s). A simplified configuration of the wall is chosen by assuming an iron meteoroid vaporizing at its melting temperature, 1808 K.

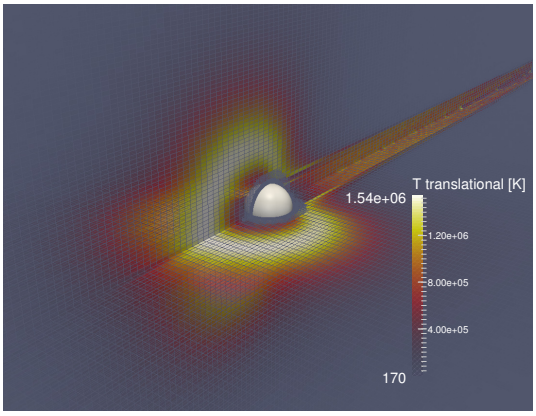

Figure 9: Translational temperature of the gas around a 1 cm body flying at 72 km/s at an altitude of 90 km.

In Figure 9 and 10, we see a diffused bow shock wave developing in front of the body. As result of the thermal non-equilibrium (i.e. the departure of the gas from a Maxwellian velocity distribution), tremendous temperatures can be appreciated at the velocity of 72 km/s. In other words, the free-stream particles, in equilibrium at low temperatures and characterized by formidable kinetic energies, mix in the shock layer with those atoms coming from the material and whose kinetic energy is much inferior. From the DSMC point of view, the temperature is a measurement of the width of the overall velocity distribution function which comes from blending the distributions of 2 different classes of molecules. The result is that no particles are really characterized by such a temperature in the thermal sense [6]. At 130 km, this shock has a thickness of several diameters and the temperature reaches its maximum several lengths upstream of the meteoroid (Figure 10.a). In the same figure, it possible to appreciate how the value of this peak does not depend on the altitude, but it is entirely affected by the flight velocity.

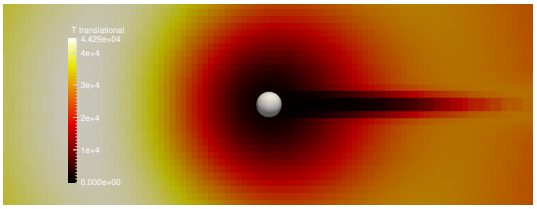

(a) H = 130 km

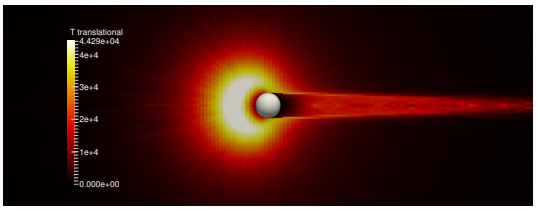

(b) H = 90 km

Figure 10: Translational temperature of the gas around a 1 cm body flying at 12 km/s at altitude of 130 (a) and 90 (b) km.

For all the conditions under study, the excitation of the internal degrees of freedom is minor due to the limited effect of the collisions. Figure 11 displays a delay in the response of the rotational and vibrational levels and the excited molecules are essentially present in the trail. In addition, chemical reactions in the gas phase are not triggered for none of the conditions. O_2 and N_2, coming from the free-stream, do not dissociate. The lack of dissociation results in negligible degrees of ionization. However, ionized trails represent an experimental evidence [12]. In our sim-

ulations, only atomic air species can loose an electron through associative or electron impact ionization. However, at the conditions of interest, other mechanism could play a role, such as the direct impact ionization, the ionization of metals, whose potential is lower than the one of air species, and the excitation of electronic states [23]. Finally, the accuracy of the TCE model for conditions distant from the equilibrium should be questioned [24].

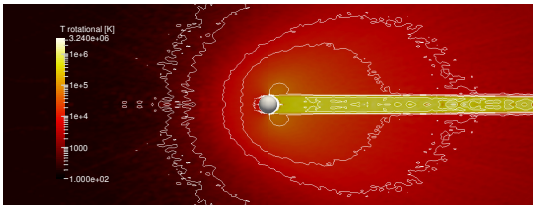

(a) Rotational temperature

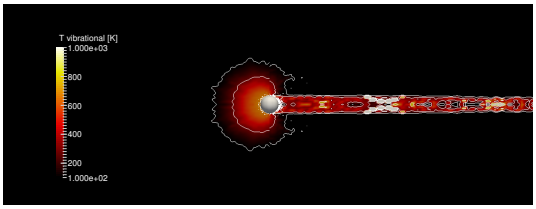

(b) Vibrational temperature

Figure 11: Internal temperatures of the gas around a 1 cm body flying at 72 km/s at altitude of 90 km.

At high altitudes, the atoms leaving the surface screen the meteoroid from the air. This is clear in Figure 12.a, where the concentration of the iron is plotted with values over the 90% in front of the body. The intensity of the collision rates is low enough to allow the iron particles to travel upstream and to create an ablation sphere large few meteoroid diameters. On the other hand, at lower altitudes the vapor pressure is not high enough (Figure 12.b) to overcome the pressure contribution of the molecules of air at the stagnation point. The iron atoms are immediately scattered back and they re-condense so that the concentration of this element ahead of the body is insignificant. High concentration of iron are visible in the trail for both the cases.

7. Conclusion

The models used to describe the entry of meteoroids do not characterize the dynamics of the gas around the body. Hence, an evaporation boundary condition for the vaporization of silicates in a rarefied environment has been developed and applied in the

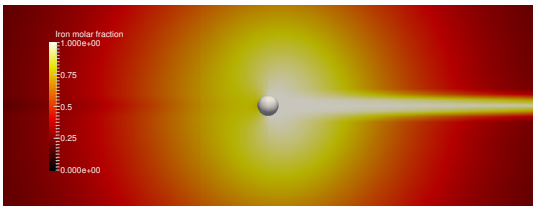

(a) H = 130 km

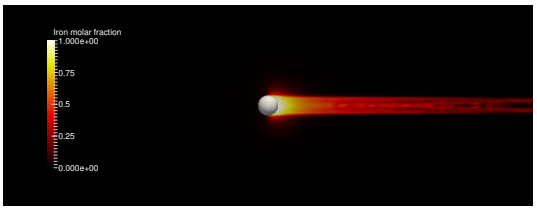

(b) H = 90 km

Figure 12: Molar fraction of iron around a 1 cm body flying at 72 km/s at altitude of 130 (a) and 90 (b) km.

the framework of DSMC. The material-flow coupling is being integrated into a trajectory program which is able to follow the meteoroid along its entry trajectory and track variables of interest such as its velocity, size, material temperature, composition and position of the melting front.

Although they are not conclusive, the results provide a useful insight on the phenomenon. They bring to light the limits of the state-of-art models and open future work perspective. The effect of altitude on condensation and screening of the ablated vapor is evident. The first turns out to be important for the lower points of the trajectory, while the latter for higher altitudes. None of these effects can be accounted by current models.

Finally, simulations did not predict the presence of free electrons in the trail. Although the majority of these may come from the ionization of the metals, which was not included, this aspect deserves further investigation. Future work will be devoted to the understanding of the dynamic of the molten layer and the computation of transport and kinetic properties of the vaporized species.

Acknowledgments

The research presented here was funded by a PhD grant of the Research Foundation Flanders (FWO).

References

[1] T. Vondrak, J. M. C. Plane, S. Broadley, D. Janches, A Chemical Model of Meteoric Ablation, Atmospheric Chemistry and Physics 8 (23) (2008) 7015–7031.

[2] H. Lamy, S. Ranvier, J. De Keyser, E. Gamby, S. Calders, BRAMS: the Belgian RAdio Meteor Stations, in: Meteoroids: The Smallest Solar System Bodies, Vol. 1, 2011, pp. 351–356.
[3] V. A. Bronshten, Physics of meteoric phenomena, D. Reidel Publishing Co., 1983.
[4] M. D. Campbell-Brown, D. Koschny, Model of the Ablation of Faint Meteors, Astronomy and Astrophysics 418 (2) (2004) 751–758.
[5] B. Fegley, A. G. W. Cameron, A Vaporization Model for Iron/Silicate Fractionation in the Mercury Protoplanet, Earth and Planetary Science Letters 82 (1987) 207–222.
[6] I. D. Boyd, Computation of Atmospheric Entry Flow About a Leonid Meteoroid, Earth, Moon and Planets 82 (2000) 93–108.
[7] G. A. Bird, Molecular Gas Dynamics and the Direct Simulation of Gas Flows, Oxford University Press, 1994.
[8] D. Vinković, Thermalization of Sputtered Particles as the Source of Diffuse Radiation from High Altitude Meteors, Advances in Space Research 39 (4) (2007) 574–582.
[9] M. A. Gallis, J. R. Torczynski, S. J. Plimpton, D. J. Rader, T. Koehler, Direct Simulation Monte Carlo: The Quest for Speed, AIP Conference Proceedings 1628 (1) (2014) 27–36.
[10] Z. Ceplecha, J. Borovicka, W. G. Elford, D. O. ReVelle, R. Hawkes, V. Porubcan, and M. Simek, Meteor Phenomena and Bodies, Space Science Reviews 84 (3) (1998) 327–471.
[11] C. Bonacina, G. Comini, A. Fasano and M. Primicerio, Numerical Solution of Phase-Change Problems, International Journal of Heat and Mass Transfer 16 (10) (1973) 1825 – 1832.
[12] E. Murad, I. Williams, Meteors in the Earth's Atmosphere, Cambridge University Press, 2002.
[13] S. Loehle, P. Jenniskens, H. Bhrk, T. Bauer, H. Elsaber, D. W. Sears, M. E. Zolensky, M. H. Shaddad, Thermophysical Properties of Almahata Sitta Meteorites (Asteroid 2008 TC3) for High-Fidelity Entry Modeling, Meteoritics and Planetary Science 52 (2) (2017) 197–205.
[14] J. H. Ferziger, H. G. Kaper, Mathematical Theory of Transport Processes in Gases, Elsevier Science Publishing, 1972.
[15] M. S. Ivanov, G. N. Markelov, S. F. Gimelshein, L. V. Mishina, A. N. Krylov and N. V. Grechko, High-Altitude Capsule Aerodynamics with Real Gas Effects, Journal of Spacecraft and Rockets 35 (1) (1998) 16–22.
[16] G. J. LeBeau, A Parallel Implementation of the Direct Simulation Monte Carlo Method, Computer Methods in Applied Mechanics and Engineering 174 (3–4) (1999) 319–337.
[17] K. Swaminathan-Gopalan, K. A. Stephani, Calibration of DSMC Parameters for Transport Processes in Ionized Air Mixtures, in: 45th AIAA Thermophysics Conference, Dallas, TX, 2015.
[18] C. Park, R. L. Jaffe, H. Partridge, Chemical-Kinetic Parameters of Hyperbolic Earth Entry, Journal of Thermophysics and Heat Transfer 15 (1) (2001) 76–90.
[19] H. S. Carslaw, J. C. Jaeger, Conduction of Heat in Solids, Oxford at the Clarendon Press, 1959.
[20] A. Frezzotti, Boundary Conditions at the Vapor-Liquid Interface, Physics of Fluids 23 (3) (2011) 030609.
[21] L. Schaefer, B. Fegley, A Thermodynamic Model of High Temperature Lava Vaporization on Io, Icarus 169 (1) (2004) 216–241.
[22] C. Cercignani, Mathematical Methods in Kinetic Theory, Plenum Press, New York, 1969.
[23] R. A. Dressler, Chemical Dynamics in Extreme Environments, World Scientific, Advanced Series in Physical Chemistry - Vol. 11, 2001.
[24] M. A. Gallis, R. B. Bond, J. R. Torczynski, A Kinetic-Theory Approach fo Computing Chemical-Reaction Rates in Upper-Atmosphere Hypersonic Flows, The Journal of Chemical Physics 131 (2009) 124311.

Development of advanced gas-surface interaction models for reusable materials

Georgios Bellas-Chatzigeorgis

Aeronautics and Aerospace Department, von Karman Institute for Fluid Dynamics, Belgium, georgios.bellas.chatzigeorgis@vki.ac.be

Supervisor: Thierry E. Magin

Associate Professor, Aeronautics and Aerospace Department, von Karman Institute for Fluid Dynamics, Belgium, thierry.magin@vki.ac.be

University Supervisor: Paolo F. Barbante

Assistant Professor, Department of Mathematics, Politecnico di Milano, Italy, paolo.barbante@polimi.it

Abstract

A framework that provides the boundary condition for a chemically reacting wall to flow solvers has been implemented in a VKI code named *Mutation++*. It solves the mass balance at the wall taking into account the phenomenon of catalysis treated with two models; the *gamma* and the *elementary reaction* one. The gas-surface interaction framework has been coupled with a 2D Navier-Stokes solve in order to reproduce experimental results.

Keywords: Catalysis, *Mutation++*, Gamma model, Finite Rate Chemistry model

1. Introduction

The design of the thermal protection system (TPS) for a spaceship during an atmospheric entry is a challenging task due to the multi-physics phenomena occurring in the shock layer of the space vehicle [1]. These phenomena include strong deviation from thermo-chemical equilibrium and gas-surface interaction (catalysis and ablation) between the vehicle's surface and the surrounding gas. By correctly modeling them, one can more accurately predict the heat load to the vehicle. In this way the sizing of the TPS can be optimized and the available payload can be maximized.

Here we will focus on the phenomenon of catalysis in entry conditions. As the space vehicle enters an atmosphere, it converts its kinetic energy into thermal energy of the gas surrounding it. This thermal energy causes the molecules of the gas to dissociate converting part of the thermal energy into chemical and eventually cooling the gas. For vehicles such as the Space Shuttle, its thermal protection system acts as a catalyst of exothermic recombination reactions, which directly release part of the dissociation energy to the surface of the vehicle, increasing the total heat flux.

Three types of models have been used by the aerospace community in order to numerically study catalysis [2]. The first one treats catalysis from a macroscopic point of view and is named gamma model [3]. It requires only the definition of a probability γ which expresses the probability for recombination to occur. Its simplicity has made the gamma model widely used in the study of thermal protection systems. The second approach, is a mesoscopic one and requires the definition of all the elementary processes that occur on the surface. Even though this approach is in principle more accurate than the previous one, these type of models for aerospace applications have still large uncertainties. The third type of models are the microscopic ones which study catalysis using molecular dynamics, direct simulation Monte Carlo and quantum chemistry calculations, but these approaches go beyond the scope of this paper.

In order to make the study of thermal protection materials more accessible to any CFD solver, a gas-surface interaction framework has been developed in an open source code at the von Karman Institute for fluid dynamics named *Mutation++* [4]. It provides directly the appropriate boundary conditions taking into

account the gas-surface interaction phenomena. The code will be presented below along with the currently implemented models for catalysis.

In parallel, catalysis is also being studied from an experimental point of view, using both ground and in-flight experiments [5; 6; 7; 8]. These experiments are useful not only for their importance in practical applications, but also for the validation and calibration of the catalytic models described above. The presentation of such a process is one of the aims of this paper. The experiments that will be simulated are performed in the Plasmatron facility of the von Karman Institute [9; 10; 11]. A copper flat plate is exposed to a high-enthalpy jet and the heat fluxes along the plate are measured. Using the measurements the catalytic properties of copper will be determined. Even though copper is not directly used as a material for a TPS, it is often used as a catalytic reference for the characterization of other materials.

2. Gas-Surface Interaction Modeling

2.1. Gas Phase Models

The dynamical evolution of the flowfield is governed by the Navier-Stokes equations:

$$\frac{\partial \rho_i}{\partial t} + \nabla \cdot (\rho_i \mathbf{u} + \mathbf{j}_i) = \dot{\omega}_i, \tag{1}$$

$$\frac{\partial \rho \mathbf{u}}{\partial t} + \nabla \cdot (\rho \mathbf{u} \otimes \mathbf{u} + p\underline{\underline{I}} + \underline{\underline{\tau}}) = \mathbf{0}, \tag{2}$$

$$\frac{\partial \rho E}{\partial t} + \nabla \cdot (\rho \mathbf{u} H + \underline{\underline{\tau}}\mathbf{u} + \mathbf{q}) = 0. \tag{3}$$

ρ_i is the partial density of species i, $\rho\mathbf{u}$ and ρE are momentum and total energy of the whole mixture. $\mathbf{j}_i$ is the diffusion flux and $\dot{\omega}_i$ is the chemical production/destruction term of the ith species. The identity matrix is symbolized with $\underline{\underline{I}}$, p is the mixture pressure, $\underline{\underline{\tau}}$ is the stress tensor and $\mathbf{q}$ is the heat flux. If Eqs. (1) are summed up over all the species in the mixture, the total continuity equation will be obtained, since $\sum_i \rho_i = \rho$. By solving the above equations along with the perfect gas law, $p_i = \rho_i R_i T$ the state of the fluid system is totally defined.

In order to close the Navier-Stokes equations expressions for diffusion flux, stress tensor and heat flux should be obtained. The transport properties are computed using the *Mutation++* library, developed by Scoggins and Magin [4] at the von Karman Institute for Fluid Dynamics. The diffusion flux is computed with the Stefan-Maxwell equations:

$$\frac{M}{\rho} \sum_k \left(\frac{x_i \mathbf{j_k}}{M_k \mathcal{D}_{ik}} - \frac{x_k \mathbf{j_i}}{M_i \mathcal{D}_{ik}} \right) = \nabla x_i \tag{4}$$

where x_i and M_i mole fraction and molar mass of species i, and $\mathcal{D}_{ik}$ is the binary diffusion coefficient. The stress tensor reads classically:

$$\underline{\underline{\tau}} = -\mu[\nabla \mathbf{u} + (\nabla \mathbf{u})^T - \frac{2}{3}\nabla \cdot \mathbf{u}\underline{\underline{I}}], \tag{5}$$

where μ is the shear viscosity, and the heat flux:

$$\mathbf{q} = -\lambda \nabla T + \sum_i h_i \mathbf{j}_i \tag{6}$$

where λ is the thermal conductivity associated with the translational temperature T of the gas and the second term is the diffusive heat flux. Both the viscosity and thermal conductivity have been computed by solving the linear transport systems as presented by [12].

2.2. Wall Phase Models

The Navier-Stokes equations in order to be solved require some boundary conditions. Here the general boundary condition for the case of a chemically reacting no slip wall will be presented. Firstly, since it is a no slip wall the tangent component of the velocity should be imposed to zero, $\mathbf{u}_t = \mathbf{0}$. Then, additional information should be provided for the partial densities and energy at the wall. The conditions that will be applied should respect both the conservation of mass and energy. Integrating Eq. (1) over a small volume and by forcing one of its dimensions to zero, and assuming steady state, one obtains:

$$(\rho_i \mathbf{u} + \mathbf{j}_i) \cdot \mathbf{n_w} = \dot{\omega}_{i,chem} + \dot{\Omega}_{surf}, \tag{7}$$

where $\mathbf{n}_w$ is the unit vector normal to the surface, $\dot{\omega}_{i,chem}$ is the mass of species i produced or destroyed per unit of area and unit time due to surface chemical reactions. The term $\dot{\Omega}_{surf}$ includes all the fluxes from the wall (eg. pyrolysis gas for ablation). However, since they are not studied in this project, they are gathered into a single term which will be set to zero. For a wall without mass blowing like in catalysis, the normal velocity is equal to zero.

The set of Eqs. (7) have to be solved for all species to obtain their partial densities at the wall. Coupled with the mass balance the energy balance should be also solved in order to correctly determine the temperature of the wall. The solution of the energy balance will also be provided by Mutation++ in the future, but for the time being the assumption of no-slip isothermal wall has been imposed. It should be mentioned that the energy mass balance for catalysis will also take into account the thermal non-equilibrium effects and the β coefficient as described by [13]. The

importance of thermal non-equilibrium effects for a catalytic wall has been studied by [14; 15].

Focus will be now given for the modeling of the term $\dot{\omega}_{i,chem}$ for the case of catalytic wall.

2.3. Gamma Model

The right hand side can be modeled using a phenomenological approach, the γ model, widely used in the aero-thermodynamics community [3; 16]. In this model the recombination reactions are viewed macroscopically as:

$$A + A \rightarrow A_2, \tag{8}$$

where two atoms of A species are recombining into an A_2 molecule. For every category of this kind of reactions taken into account a probability for recombination needs to be defined. Therefore, the probability of recombination for species i, γ_i, is given as:

$$\gamma_i = \frac{M_{i,rec}}{M_i^{\downarrow}}, \tag{9}$$

where $M_i^{\downarrow}$ is the flux of species i impinging the surface and $M_{i,rec}$ is the flux of species recombining at the surface. This probability is the input parameter for this model. A fully catalytic wall has γ_i equal to 1, which means that all the particles of species i impinging the surface recombine at the wall. γ_i equal to 0 means that no reaction takes place and corresponds to a non-catalytic, or chemically inert wall. Anything between these two extreme cases is a partially catalytic wall. Knowing the probability γ_i, the right hand side of Eq. (7) is equal to [17]:

$$\dot{\omega_{i,chem}} = \dot{\omega}_{i,cat} = \gamma_i m_i M_i^{\downarrow}, \tag{10}$$

with m_i being the mass of species i.

When the translational energy modes of gas species close to the wall have a Maxwellian distribution function and there is no temperature slip, the impinging flux, $M_i^{\downarrow}$, is equal to [17]:

$$M_i^{\downarrow} = n_i \sqrt{\frac{kT_w}{2\pi m_i}} \tag{11}$$

where T_w is the wall temperature.

2.4. Elementary Reactions Model

Even though the gamma approach is widely used in the aerothermodynamics community, a more rigorous way to describe the phenomenon of heterogeneous catalysis is by defining the elementary reactions that occur at the wall. This approach increases the complexity of the system, since it requires the definition of many parameters for the chemical reactions. Such parameters will be seen in the following sections. They are mainly the coefficients of Arrhenius type reaction rates and most of the time their actual value is uncertain [18; 19]. Before defining each of the most important elementary reactions separately, some basic definitions for the model will be given.

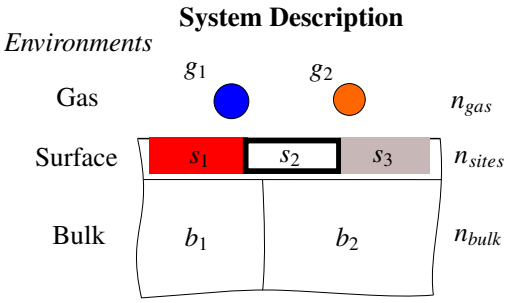

Figure 1: description of the system for the elementary reactions model

2.4.1. Model Definitions

In order to formulate this model some basic definitions about the system itself should be given. The system in question can be seen in Fig. 1. Firstly, three distinct environments can be seen. The first one is the gas environment which is composed by n_{gas} chemically distinct species which participate in the surface and the gas phase reactions. The rate of production and destruction of these species due to the surface are the ones needed in order to compute the term $\dot{\omega}_{i,chem}$ found in Eq. (7).

The second phase is the surface phase and it is composed of n_{sites} categories of active sites. Each category, s_i, covers a part of the surface and has a site density equal to S_i mole per square meter. By definition active sites are the places on the surface where all the surface chemical reactions take place. They can be empty or can accommodate a species from the gas phase. Not all gas species can be accommodated in all types of active sites. The number of different species that can be accommodated in a site i is denoted as $n_{(species\ in\ site\ i)}$. This accommodation is in reality the development of a chemical bond between the species and the surface. Then, the species are said to be adsorbed and will be denoted as A_{s_i}. This bond can be weak (van der Waals)-physisorption or strong (ionic or covalent)-chemisorption.

One chemical species in the gas phase should be

considered different to the same one adsorbed on the surface at each site i. Chemical reactions are the mechanisms that convert one gas species to a surface one and vice versa. Therefore in order to fully define the surface, the total number of species that are needed is equal to:

$$n_{(surface\ species)} = \sum_{i=1}^{n_{sites}} n_{(species\ in\ site\ i)}. \quad (12)$$

The total number of each site S_i is conserved and it is a property of the material. Inert and porous areas of the surface can be included as sites without any chemical species assigned to them. For notation, if a species A has as subscript the symbol s it means that it is adsorbed into the active sites named s.

The last environment is the bulk environment which consists of n_{bulk} phases, but since it is used to describe mainly ablative reactions and porous materials it is not taken into account [20].

The total number of species considered in this model ignoring the bulk are:

$$n = n_{gas} + n_{(surface\ species)}. \quad (13)$$

2.4.2. Adsorption

Adsorption is the elementary process where a gas species, mainly atom creates a chemical bond with one active site of the surface. A chemical reaction can describe this process be expressed as:

$$A + s \rightarrow A_s. \quad (14)$$

For such kind of processes the reaction rate coefficient is given by the formula

$$k_{f,ads} = s_{ads} \sqrt{\frac{kT_w}{2\pi m_A}} \frac{1}{S_{tot}} e^{-\left(\frac{E_{ads}}{k_B T}\right)}, \quad (15)$$

where s_{ads} is a sticking coefficient and expresses the probability for an impinging atom to be adsorbed. It can be taken either as constant or an exponential function of the negative of temperature in order to take into account the fact that if an energetic atom contacts the surface, the probability of it to stick is decreased. For atoms there is no need to take into account any steric effect. Furthermore, adsorption is almost an instant process without the need of activation because of the large difference of energy between the gas and surface species. For this reason $E_{ads} = 0$. S_{tot} is the total number of active sites on the surface.

Molecules have also a probability to be adsorbed by the surface, but they create a weak bond with it making their adsorption important only at very low temperatures. What is more likely to occur is the molecules to dissociate and then the atoms to be adsorbed. Such a process is called dissociative adsorption. Its reaction reads

$$A_2 + 2s \rightarrow 2A_s \quad (16)$$

and the reaction rate coefficient is equal to

$$k_{f,diss-ads} = s_{diss-ads} \sqrt{\frac{kT_w}{2\pi m_{A_2}}} \frac{1}{S_{tot}^2} e^{-\left(\frac{E_{ads}}{k_B T}\right)}, \quad (17)$$

Again the sticking coefficient $s_{diss-ads}$ is taken as constant or as a weak function of temperature and $E_{ads} = 0$, because we deal with a non activated reaction process.

Not all the molecules can be dissociatively adsorbed. For example O_2 is dissociatively adsorbed on a Cu surface, but N_2 is not. This is difference is associated to the vacancies of the orbitals of the atoms, to the energy of the bond between the N_2 atoms, as well as to the size of the N_2 molecule [21].

As a concluding remark, since we treat the surface from a mesoscopic point of view the mean field approximation is assumed meaning that all the adsorbed species are randomly distributed on the surface and they do not interact between each other with a potential while they are adsorbed.

2.4.3. Desorption

Desorption or thermal desorption is the process where the adsorbed atoms on the surface have enough energy to vibrate sufficiently to break its bond with the surface without recombining. It is the reverse process of adsorption and its reaction is

$$A_s \rightarrow A + s \quad (18)$$

Desorption is an activated process, with activation energy E_{des} equal to the energy of the bond of the adsorbed atom with the surface. For a chemisorbed atom this energy can be high and therefore the process becomes important only for high temperatures. The rate coefficient of the desorption is give by the formula

$$k_{f,des} = v_d e^{-\left(\frac{E_{des}}{k_B T}\right)}, \quad (19)$$

with v_d expressing the attempts of the atoms to escape due to their vibrations on the surface. It can be imposed as a constant or get an approximation for it using transition state theory which gives $v_d = \frac{k_B T}{h}$.

2.4.4. Eley-Rideal Mechanism

The Eley-Rideal mechanism is the first of the two mechanisms which cause recombination on the surface. The presence of this mechanism was found by the fact that highly vibrationally excited molecules were found over catalytic surfaces, something that could not be explained by the other recombination mechanism, the Langmuir-Hinshelwood.

The process describes the phenomenon when an atom from the gas phase impinges on an adsorbed atom and they recombine. The produced molecule is instantly released to the gas phase. The process can be seen as a reaction like:

$$A + A_s \rightarrow A_2 + s \tag{20}$$

This mechanism can be either activated or not depending on whether the resulting molecule has a stronger or weaker bond between its atoms compared to the bond between the atom and the surface before recombination [21]. Its rate coefficient is again of the Arrhenius type:

$$k_{f,E-R} = s_{E-R} \sqrt{\frac{kT_w}{2\pi m_A}} \frac{1}{S_{tot}} e^{-\left(\frac{E_{E-R}}{k_B T}\right)}. \tag{21}$$

s_{E-R} expresses the Eley-Rideal reaction efficiency and can be taken as a constant or a slightly increasing function with the temperature [21]. The reaction rate for this process is in fact the rate of impinging atoms on the surface, just like the case of adsorption, multiplied by a recombination probability.

2.4.5. Langmuir-Hinshelwood Mechanism

The last elementary reaction type that has been implemented so far is the mechanism of Langmuir-Hinshelwood. As it has been mentioned before, it is the second mechanism which produces molecules for the gas phase. These molecules are produced due to the sufficiently energetic collision of two already adsorbed atoms. The reaction formula is:

$$A_{s_1} + A_{s_2} \rightarrow A_2 + s_1 + s_2 \tag{22}$$

One of the approaches that is implemented in Mutation++ for the reaction rate comes from the work of Marschall which suggest the following formula, since his model does not take into account the phenomenon of surface diffusion:

$$k_{f,L-H} = \sqrt{\frac{\pi k_B T}{2m_A}} \sqrt{\frac{A_v}{S_{tot}}} s_{L-H} e^{-\left(\frac{E_{L-H}}{k_B T}\right)}, \tag{23}$$

where A_V is the Avogadro number, s_{L-H} is the probability for the L-H recombination to occur and E_{L-H} is the activation energy of the reaction, which is assumed as a constant. Other approaches close to the latter one are also available in the literature, but for different kind of metallic surfaces [21].

3. VKI Flat Plate Experiments

The VKI inductively coupled plasma (ICP) facility provides an ideal test environment for investigating catalytic effects on TPS materials. It is equipped with a high power solid state generator ($1.2MW$, $400kHz$, $2kV$) which is used to produce an impurities-free plasma in the $160mm$ diameter torch. The plasma is injected in the test chamber ($2.5m$ long, $1.4m$ in diameter), where characterization probes and sample holders can be inserted in the flow during the experiment with special displacement mechanisms. All the metallic components that are exposed to the plasma are water cooled to avoid melting. Several different mixtures of gases can be used for the tests, including air. The facility can operate in both subsonic and supersonic conditions, and can provide heat fluxes ranging from from 0.09 to $10MW/m^2$ in pressures between 1000 and $22000Pa$ [22].

Fig. (2) shows a typical experiment of a flat plate probe immersed in the core of the plasma jet of plasmatron. The flat plate is used to study the off-stagnation point heat fluxes for conditions close to the re-entry ones [23]. It is made of copper and it is equipped with an internal water cooling system which keeps its wall temperature constant and equal to $350K$. It has dimensions 240x200x25mm with a rounded nose of $12.5mm$ radius. A linear calorimeter is fitted inside a groove of $30mm$ times $189mm$. The calorimeter is equipped 8 insulated from one another heat sensors which give 8 distinct measuring heat flux points. The measured heat fluxes from such an experiment are going to be used for the comparison with the CFD predicted ones. For more information about the experimental methodologies and some of the actual measured heat fluxes one should refer to [24; 25].

4. Preliminary Results

Figures (3) and (4) show some preliminary results of the flow field around the flat plate for the non and fully catalytic cases. The flow is subsonic, behaves as incompressible and due to the high temperature it can be considered laminar because of the high viscosity. From these simulation the heat flux profiles can be extracted as seen in Fig. (5). At $x = 0mm$ the horizontal

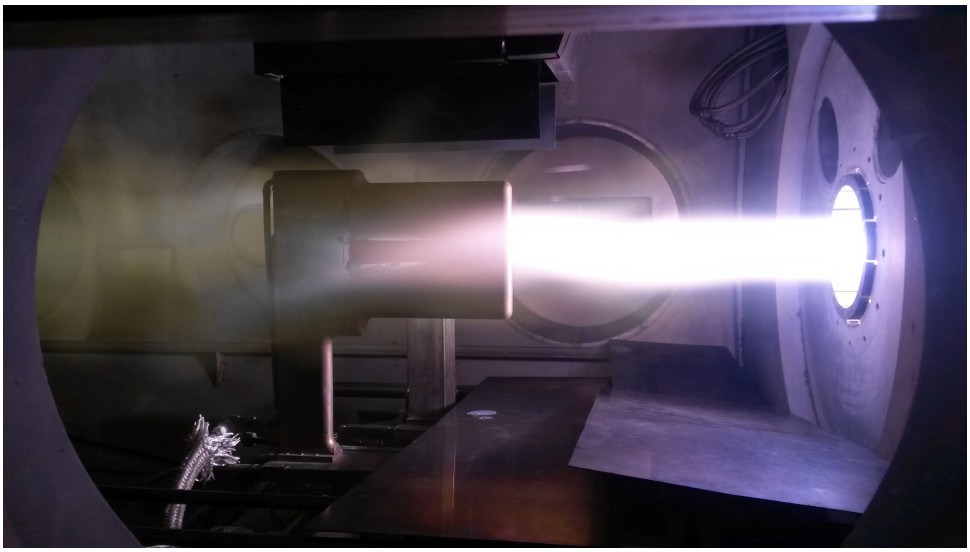

Figure 2: Flat Plate inside Plasmatron's test chamber during experiment. [5]

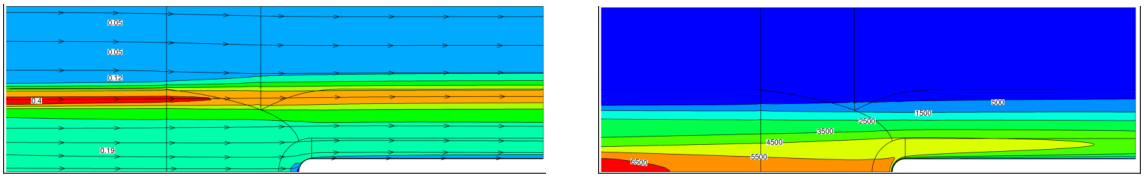

(a) (b)

Figure 3: Stream line and Mach number(left) and Temperature Profiles $[K]$(right) for the flat plate in the Non-Catalytic case (Phenomenological Model).

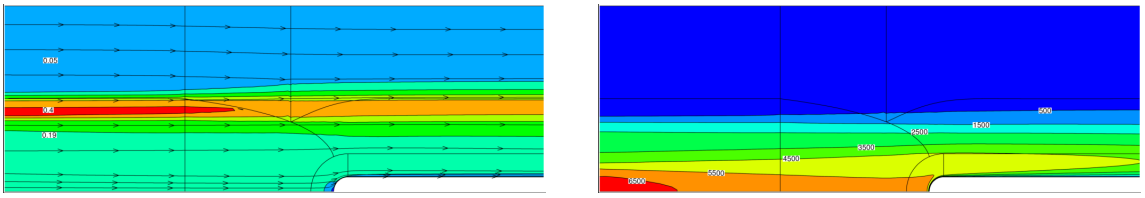

(a) (b)

Figure 4: Stream line and Mach number(left) and Temperature Profiles $[K]$(right) for the flat plate in the Fully-Catalytic case(Phenomenological Model).

part of the flat plate begins while the very first point one the left is the stagnation point heat flux. It can be observed that after a distance along the flat plate the two heat fluxes are almost equal and this can be explained because of the fact that the atomic species have already recombined upstream. The simulations were performed using an in-house finite volume code named cosmic [17]. The convective fluxes are discretized with a preconditioned version of a flux vector splitting scheme named AUFS and second order accuracy has been achieved using total variation diminishing methods. The diffusive fluxes are discretized with a central scheme. The time integration is fully implicit first order till steady state is achieved. The linear systems are solved with the GMRES iterative solver.

In the subsonic inlet a profile of temperature and velocity has been imposed and the flow field is assumed to be in chemical equilibrium. The profiles have been obtained from another in house code which simu-

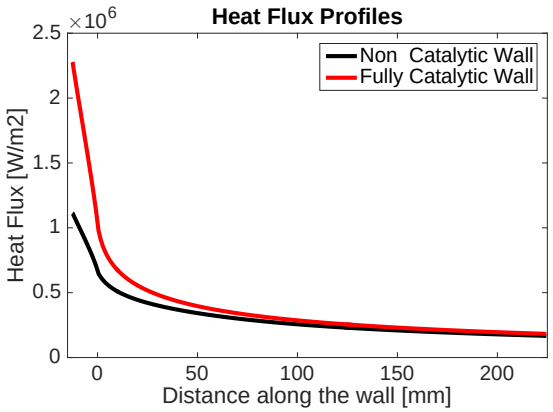

Figure 5: Heat Flux profiles in $[W/m^2]$ along the flat plate. At x=0 the horizontal part of the plate starts. The furthest point to left is the stagnation point heat flux.

lates the whole plasmatron facility by solving Navier-Stokes coupled with the Maxwell equations in chemical equilibrium [12]. Symmetry is imposed on the bottom horizontal boundary and the wall on the bottom right is assumed to be isothermal at temperature equal to $350K$. The compositions on the wall are computed based on the catalytic properties of it using the external library *Mutation++*. The rest of the boundaries are subsonic outlets with pressure equal to the static pressure of the experiments $5000Pa$. The chemical mechanism for the simulation is the one proposed by Park [1]. As mentioned before, all the thermochemical and transport properties for the closure of the Navier-Stokes equations are taken again from *Mutation++* library.

5. Concluding remarks

The flow around a flat plate will be simulated for the high enthalpy conditions occurring inside the inductively coupled plasma facility (Plasmatron) of the von Karman Institute. In order to achieve that, the two dimensional chemically reacting single temperature Navier-Stokes equations will be solved using a second order finite volume method. The flat plate will be assumed to be a catalytic isothermal wall modeled with a phenomenological and a finite rate catalytic model presented above. By comparing the heat flux profiles of the experiments and the simulations the two models will be assessed and further developed. In this way a catalytic model for copper will be available which will help for the more accurate characterization of other thermal protection systems actually used for re-entry applications. The presented catalytic models have been implemented in a general way in order to be extensible for a variety of other applications (ablative surfaces) and the tools presented can be coupled to any of CFD code.

References

[1] C. Park, Review of chemical-kinetic problems of future nasa missions. I: - earth entries, Journal of Thermophysics and Heat Transfer 7-3 (1993) 385–398.

[2] V. L. Kovalev, A. F. Kolesnikov, Experimental and Theoretical Simulation of Heterogeneous Catalysis in Aerothermochemistry (a Review), Fluid Dynamics 40 (2005) 669–693. doi:10.1007/s10697-005-0106-4.

[3] R. Goulard, On catalytic recombination rates in hypersonic stagnation heat transfer, Jet Propulsion 28 (1958) 737–745.

[4] J. B. Scoggins, T. E. Magin, Development of Mutation++: Multicomponent Thermodynamic and Transport Properties for Ionized Plasmas written in C++, American Institute of Aeronautics and Astronautics, 2014. doi:10.2514/6.2014-2966.

[5] A. Viladegut, O. Chazot, Off-stagnation point testing in plasma facility, in: Array (Ed.), EUCASS Proceedings Series Advances in AeroSpace Sciences, Vol. 7, 2015, pp. 113–122.

[6] M. Balat-Pichelin, L. Bedra, O. Gerasimova, P. Boubert, Recombination of atomic oxygen on α-Al $_2$O $_3$ at high temperature under air microwave-induced plasma, Chemical Physics 340 (2007) 217–226. doi:10.1016/j.chemphys.2007.09.019.

[7] J. M. Meyers, W. P. Owens, D. Fletcher, Surface Catalyzed Reaction Efficiencies in Nitrogen and Oxygen Plasmas from Laser Induced Fluorescence Measurements, AIAA 2013-3139, 44th AIAA Thermophysics Conference, Fluid Dynamics and Co-located Conferences.

[8] A. Nawaz, D. M. Driver, I. Terrazas-Salinas, S. Sepka, Surface Catalysis and Oxidation on Stagnation Point Heat Flux Measurements in High Enthalpy Arc Jets , AIAA 2013-3138, 44th AIAA Thermophysics Conference, Fluid Dynamics and Co-located Conferences.

[9] J. Marschall, D. Pejakovic, W. G. Fahrenholtz, G. E. Hilmas, F. Panerai, C. O., Temperature Jump Phenomenon During Plasmatron Testing of ZrB2-SiC Ultrahigh-Temperature Ceramics, Journal of Thermophysics and Heat Transfer 26 (4) (2012) 559–572.

[10] F. Panerai, Aerothermochemistry characterization of thermal protection systems, Ph.D. thesis, Rhode-St-Gense, Belgium (February 2012).

[11] J. Thoemel, Surface catalysis in high enthalpy flows, Ph.D. thesis, RWTH Aachen, von Karman Institute for Fluid Dynamics (January 2013).

[12] T. Magin, A Model for Inductive Plasma Wind Tunnels, Ph.D. thesis, Université Libre de Bruxelles (2004).

[13] B. Halpern, D. Rosner, Chemical energy accomodation at catalyst surfaces, Journal of the Chemical Society, Faraday Transactions, 1987.

[14] E. Kustova, E. Nagnibeda, I. Armenise, M. Capitelli, Nonequilibrium kinetics and heat transfer in O-2/O mixtures near catalytic surfaces, 2002.

[15] G. Bellas-Chatzigeorgis, P. F. Barbante, T. E. Magin, Development of detailed chemistry models for boundary layer catalytic recombination, 8th European Symposium on Aerothermodynamics for Space Vehicles, Lisbon, Portugal.

[16] C. D. Scott, Wall boundary equations with slip and catalysis for multicomponent nonequilibrium gas flows, Tech. rep., NASA Lyndon B. Johnson Space Center, Houston, Texas 77058 (1973).

[17] P. Barbante, Accurate and efficient modelling of high temperature nonequilibrium air flows, Ph.D. thesis, Université Libre de Bruxelles (May 2001).

[18] C. Sorensen, P. Valentini, T. E. Schwartzentruber, Uncertainty analysis of reaction rates in a finite-rate surface-catalysis model, Journal of Thermophysics and Heat Transfer 326:3.

[19] F. Nasuti, M. Barbato, C. Bruno, Material-dependent catalytic recombination modeling for hypersonic flows, AIAA 1993-2840. 28th Thermophysics Conference, Orlando, FL.

[20] J. Marschall, M. MacLean, Finite-Rate Surface Chemistry Model, I: Formulation and Reaction System Examples, AIAA Thermophysics Conference, Honolulu, Hawaii.

[21] M. Barbato, S. Reggiani, C. Bruno, J. Muylaert, Model for Heterogeneous Catalysis on Metal Surfaces with Applications to Hypersonic Flows, Journal of Thermophysics and Heat Transfer 14 (2011) 412–420.

[22] B. Bottin, Aerothermodynamic model of an inductively-coupled plasma wind tunnel, Ph.D. thesis, University of Liege (1999).

[23] G. Ceglia, E. Trifoni, J.-B. Gouriet, O. Chazot, V. Mareschi, G. Rufolo, G. Tumino, Experimental investigation on ixv tps interface effects in plasmatron, CEAS Space Journal 8 (2) (2016) 65–75.

[24] A. Viladegut, U. Düzel, O. Chazot, Diffusion effects on the determination of surface catalysis in Inductively Coupled Plasma facility, Under Review.

[25] Ümran Düzel, Validation of Gas Surface Interaction modeling in Plasmatron facility for in-flight experiment development, Tech. Rep. Project Report 2015-14, von Karman Insititute for Fluid Dynamics, Rhode-Saint-Genèse, B1640 (June 2015).

Uncertainty quantification of aerothermal flow simulations through low-density ablative thermal protection materials

Joffrey Coheur

Aeronautics and Aerospace Department, von Karman Institute for Fluid Dynamics, Belgium, joffrey.coheur@vki.ac.be

Supervisor: Thierry Magin

Associate Professor, Aeronautics and Aerospace Department, von Karman Institute for Fluid Dynamics, Belgium, magin@vki.ac.be

University Supervisor: Maarten Arnst

Assistant Professor, Aerospatial & Mechanical Engineering, Université de Liège, Belgium, maarten.arnst@ulg.ac.be

University Supervisor: Philippe Chatelain

Assistant Professor, Institute of mechanics, materials and civil engineering, Université Catholique de Louvain, Belgium, philippe.chatelain@uclouvain.be

Abstract

For space missions involving atmospheric entry, the thermal protection system (TPS) is essential to shield the vehicle and its payload from the severe aerothermal loads. The enduring challenge for designing and manufacturing TPSs is in minimizing weight while *reliably* ensuring integrity.

Whereas past TPS design relied on experiments and simplified models complemented with large safety margins, current TPS engineering is witnessing a paradigm shift towards a synergistic use of new experiments and new high-fidelity numerical simulations, which hold the promise of affording smaller safety margins. Although new experiments and new high-fidelity numerical simulations are available, the extent to which they are still affected by uncertainty and thus afford reduced safety margins is still unaddressed.

The overarching objective of this project is to contribute to the development of the uncertainty quantification methodology to link new experiments and new high-fidelity numerical simulations for TPS ablation and establish their requisite safety margins. First, physico-chemical models relevant to ablation will be improved and their attendant uncertainties characterized by applying probabilistic inverse methods to recent but still largely unexploited experiments. Next, the improved physico-chemical models will be integrated in a high-fidelity coupled flow-material simulation code of atmospheric entry ablation, specifically, in the ablation-dedicated branch of the Argo code under development at Cenaero, Vki, and Ucl. In addition, nonintrusive probabilistic methods will be developed and implemented for propagating the uncertainty in the physico-chemical models to the predictions. Finally, the improved physico-chemical models and computational methods will be validated through a comparison of predictions with experimental observations stemming from the Vki Plasmatron ground test facility, and the added value brought by the uncertainty quantification methodology will be demonstrated on engineering problems relevant to in-flight performance prediction and TPS design.

Keywords: Atmospheric reentry, ablative material, uncertainty quantification, computational fluid dynamics, aerothermal flows

On the modeling of transition to turbulence for hypersonic flows

Florian Danvin

Aeronautics and Aerospace Department, von Karman Institute for Fluid Dynamics, Belgium, danvin@vki.ac.be

PhD student, CEA-CESTA 15 avenue des Sablières CS 60001 33116 Le Barp Cedex France

Supervisors: Olivier Chazot and Fabio Pinna

Head of department, Aeronautics and Aerospace Department, von Karman Institute for Fluid Dynamics, Belgium, chazot@vki.ac.be

Senior research engineer, Aeronautics and Aerospace Department, von Karman Institute for Fluid Dynamics, Belgium, pinna@vki.ac.be

University Supervisor: Marina Olazabal-Loume

Senior research engineer, CEA-CESTA 15 avenue des Sablières CS 60001 33116 Le Barp Cedex France, marina.olazabal@cea.fr

Abstract

During atmospheric reentry flights a spacecraft will be accelerated at hypersonic speeds from the rarefied to the continuum layer; a laminar boundary layer will develop around the body and may become turbulent. Engineers and researchers aim at constantly improving the spacecraft performances. A better knowledge of the environment allows a more accurate prediction of the physics endured by the spacecraft. To achieve one of the main objective, such as drag reduction and heat flux estimation, laminar boundary layer transition understanding is of paramount importance. At hypersonic speeds a turbulent state is synonym of both wall friction and wall heat transfer increase causing drag augmentation and sometimes surface deterioration.
The main objective of the PhD is to couple a database prediction method with a R.A.N.S. (Reynolds Averaged Navier Stokes) solver. The database construction is based on linear stability results to predict the onset of transition, and is accessed via neural network. Once the laminar flow field has been calculated, the database will be used to predict an approximated position of the onset of transition given some similarity parameters. Afterwards an intermittency function coupled with a turbulence model for the R.A.N.S. calculation is used to give a prediction of the entire flow field.
The project will be decomposed into 4 parts. The first part is to increase the database size to gain in precision, and to increase to domain of applicability. Afterwards an optimization of the neural network method used is required to increase the robustness of the method before coupling it with the R.A.N.S. solver. The last part would be to study in what extent distributed roughness can be taken into account in our stability calculations.

Keywords: Linear stability theory, neural network, hypersonic flow, transition, R.A.N.S.

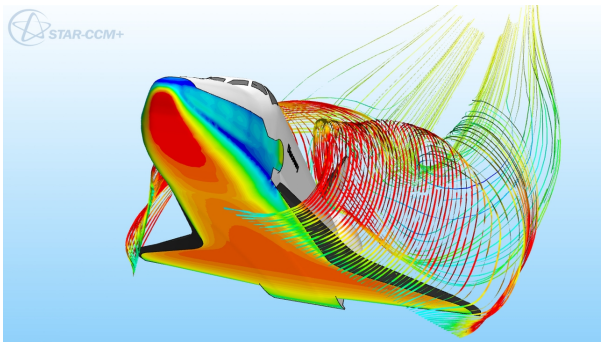

Shuttle reentry, source: Siemens STAR CCM+

Development of a melting model for meteors

Bruno Dias

Aeronautics and Aerospace Department, von Karman Institute for Fluid Dynamics, Belgium, barros@vki.ac.be

Supervisor: Thierry E. Magin

Associate Professor, Aeronautics and Aerospace Department, von Karman Institute for Fluid Dynamics, Belgium, magin@vki.ac.be

University Supervisor: Philippe Chatelain

Assistant professor, Thermodynamics and fluid mechanics - TFL, Université catholique de Louvain, Belgium, philippe.chatelain@uclouvain.be

Abstract

Meteor phenomenon is a frequent event happening on planet Earth. Due to the high entry velocities of these objects, the surface of the material undergoes extreme heat loads. Since the material is mainly composed by several oxides, eventually, the surface temperature will overcome the melting point. In this study we propose a melting model, in order to understand the material behavior, coupled with a flow solver. A detailed study of the flow around the stagnation streamline is also presented.

Keywords: meteors, melting, continuum, CFD

1. Introduction

From 50 to 100 tonnes of meteoroids enter Earth's atmosphere every day. Entry velocities can vary between 11.5 km/s and 72 km/s, and these strong hypersonic conditions lead to extreme temperatures on the surface of these objects. Since most of the meteoroids are composed by oxides, such as SiO_2 and MgO, the extreme heat loads at the surface promotes the material to melt and eventually to evaporate. Overall, this process leads to a huge amount of mass deposition in the upper atmosphere and is the main reason of the growing interest in studying the ablation of these space objects. During the meteoroid disintegration, ablation products interact with the ionized gas surrounding the meteoroids and are driven to the wake giving a signature that can be detected by radars. The detection of meteors aims to answer questions such as: "What is the real meteor incoming flux?" and "What is the influence the mass deposition into the upper atmosphere for aeronomy purposes?"

Recent efforts have been made by the Belgian Institute for Space Aeronomy in order to predict velocity and trajectory of the meteors, by means of an innovative technique based on radio waves. The Belgian Radio Meteor Stations (BRAMS) experiment, consists in a series of receivers spread all over Belgium to collect and standardize the meteor observation data. In brief, a signal sent by a transmitter, is first reflected by the free electrons in the trail of the meteor, and then captured by the ground receivers (Forward Scattering technique) allowing for the study of the meteor atmospheric entry. One of the main objective of this project is the computation of the meteoroid flux densities. However, this quantity is hardly quantifiable from the lone radar observation, and it is necessary to rely on comparison with numerical models to have an estimate of it. In this scenario, the necessity of having the capability to numerically reproduce the meteor entry finds its room.

Current ablation models (1), are based on the Knudsen-Langmuir. These kind of models disregard any melting of the material considering only evaporation once the melting temperatures is reached.

The development of melting models was initially conducted in the 50's by (2). The use of glassy materials as protection of spacecraft vehicles led to deep study of the melting phenomenon. More recently, with the advances of the metallurgic industry

(3), there was a necessity to improve such models. Moreover it has been observed from the meteorites recovered in the ground (4), an importance in considering this phenomenon.

The study of meteor ablation mentioned above, are used to understand the mass deposition in the atmosphere. However, since they were conceived to study the ablation of small particles in the upper atmosphere, they usually rely on a zero dimensional approach and lack of an accurate treatment of the particle interaction with the atmosphere from the fluid dynamic point of view. Therefore, for meteoroids big enough to survive this first phase of the atmospheric entry, a different approach has to be sought. Moreover the study of material melting and its possible removal by mechanical forces is often neglected.

In this work we propose to study the meteor ablation with a numerical approach similar to those used in the aerospace community to model the gas-surface interaction over TPS materials. A material solver has been developed in order to solve the Stefan problem and understand better the melting of meteors. Furthermore, the material solver has been coupled with a 1-D Stagnation-Line CFD solver with an integrated evaporation boundary condition and part of a meteor-entry trajectory has been computed in a coupled fashion.

2. Flow field radiation

At the range of velocities typical of meteor phenomena, radiation becomes highly significant, the intense light observed during a meteor entry is mainly due to the radiation of the air and metallic species, where the latter are coming from ablation products.

By solving the radiative transfer equations (RTE) one can determine the spectral radiative intensity, therefore, the radiative source terms, $\mathcal{P}^{rad}$ and $\mathcal{P}^{rad,VE}$ and $\dot{\omega}_i^{rad}$. The production or destruction of species, $\dot{\omega}_i^{rad}$, due to radiative processes such as photoionization and photodissociation and the radiative source terms are shown in detail by (5). Solving the RTE by conventional methods such as Line-by-Line (LBL) becomes computationally very expensive for complex molecular spectra.

Recently, (6) presented a hybrid statistical narrow band model (HSNB) showing an accurate description of the radiative flux with low CPU costs for non-ablative materials. Later (7), extended this approach for ablative TPS material.

The feature of the HSNB is that if the radiative mechanisms are statistically uncorrelated one can divide the spectra into narrow bands and compute the intensity in terms of averages. The different mechanism can be separated in two 3 contributions: optically thick molecular systems, optically thin molecular systems and continua, atomic lines. Due to the weak spectral density of atomic lines, this contribution has to be solved by LBL methods. (8) presents an atomic spectral mesh to optimize to the LBL method for atomic lines. Details about the HSNB can be found in Refs. (6; 7).

3. Gas-Surface Interaction

The evaporation of a melted layer can be modeled by limiting the control volume to an infinitesimal thin lamina where the surface is located. Typically mass conservation for the generic species i can be written in terms of a surface mass balance (SMB)(9). To solve this balance a suitable model to compute the surface reactions is needed, which in general can be solved by heterogeneous finite-rate chemistry. However, this approach is not always feasible due to the lack of specific data when more exotic surfaces are considered. In this case, a possible solution is then to consider the heterogeneous mixture (hot gas phase and material surface) to be in thermochemical equilibrium at the local conditions of pressure and temperature. As shown by (10), when such an equilibrium approach is considered, it is useful to write the SMB in terms of elements which reads as:

$$J_{k,w} + \dot{m}_{evap} y_{k,s} = (\rho u)_w \, y_{k,w} \quad \forall \, k \in \varepsilon \tag{1}$$

where $(\rho u)_w$ is the gas blowing, $y_{k,w}$ is the mass fraction of element k in the gaseous mixture at the wall, $y_{k,s}$ is the elemental mass fraction of the solid, $\dot{m}$ is the mass blowing rate and $J_{k,w}$ is the elemental mass diffusion. By summing Eq. 1 over all elements, one obtains:

$$\dot{m}_{evap} = (\rho u)_w$$

and finally the mass blowing rate can be computed as:

$$\dot{m}_{evap} = \frac{J_{k,w}}{(y_{k,w} - y_{k,s})} \quad \forall \, k \in \varepsilon \tag{2}$$

where the elemental composition of the solid phase, $y_{k,s}$, is known and the elemental composition of the gas can be computed by solving a multiphase equilibrium problem. Once the equilibrium gas composition is known and the mass blowing rate, $\dot{m}$, is computed, the surface blowing velocity can be easily obtained as:

$$u_w = \frac{\dot{m}_{evap}}{\rho_w} \tag{3}$$

where ρ_w is the density of the mixture in gas phase at the wall. Finally the recession velocity, $\dot{s}$, can be computed as:

$$\dot{s} = \frac{\dot{m}_{evap}}{\rho_s} \tag{4}$$

being ρ_s the density of the solid phase.

The removal of liquid layer due to mechanical forces was first derived by (2). By assuming the steady-state incompressible governing equations, the tangential velocity was derived by the authors as:

$$v = \tau_{flow/melt} \int_0^{\delta} \frac{dr}{\mu(T)} + \frac{1}{R} \frac{\partial P}{\partial \theta}_{flow/melt} \int_0^{\delta} \frac{r}{\mu(T)} dr \tag{5}$$

where by knowing the molten layer thickness, δ, Eq. 5 can be easily integrated. The liquid layer viscosity, for glassy materials, is a function of temperature expressed by:

$$\mu(T) = \exp([(a/T) - b])$$

where the coefficients a and b can be found in (4) for ordinary chondrites. Finally the corresponding mass flux due to mechanical removal is obtained by:

$$\dot{m}_{melt} = \rho_{melt} v$$

The total mass removal of the liquid layer has then contributions from both the evaporation and the mechanical forces.

Analogously one can consider a balance of energy fluxes entering and exiting the surface. The surface energy balance (SEB) is described by:

$$q_{conv} + q_{rad,in} + \left(\dot{m}_{evap} + \dot{m}_{melt}\right) h_c = \epsilon \sigma T_w^4 + \dot{m}_{evap} h_w + k \frac{\partial T}{\partial r} + \dot{m}_{melt} h_c \tag{6}$$

where the terms on the left side represent the incoming convective heat flux (conductive heat flux and diffusive heat flux), shock layer radiation and the energy of the solid due to mass loss. On the right side the fluxes leaving the surface are represented by the re-radiation of the material, the energy of the gas composition at the wall, the material heat conduction and energy lost due to liquid removal. By solving this non-linear equation, one can estimate the surface temperature T_w.

4. Numerical tools

The flow governing equations are solved through a CFD code where the SMB boundary condition, explained the in previous section, is implemented. The flow properties are computed with the VKI physico-chemical library (Mutation^{++}). In order to study the effect of melting and estimate the liquid layer thickness, a 1D material code has been built where SEB and liquid mass removal are solved.

4.1. Stagnation-Line Code CFD Solver

The 1D Stagnation-Line solver developed at the VKI by Munafò (11), resolves the Navier-Stokes equations along the stagnation line of spherical or cylindrical bodies, where an illustration is shown by Fig. 1. This model leads to an efficient way to calculate hypersonic flows with low computational costs.

In this code the three-dimensional Navier-Stokes equations are reduced to a one-dimensional approximation for the stagnation streamline by a system called "Dimensionally Reduced Navier Stokes Equations" (DRNSE). The spatial discretization is done by finite volume method and the time integration is computed by a Backward-Euler method. The stagnation-line equations read as:

$$\frac{\partial}{\partial t}\mathbf{U} + \frac{\partial}{\partial r}\mathbf{F^{inv}} + \frac{\partial}{\partial r}\mathbf{F^{vis}} + \frac{\mathbf{G^{inv}} + \mathbf{G^{vis}}}{r} = \mathbf{S^c} + \mathbf{S^r} \tag{7}$$

Where $\mathbf{U}$ denotes the volume-specific balance quantities, $\mathbf{F^{inv}}$ are the inviscid fluxes, $\mathbf{F^{vis}}$ the viscous terms, $\mathbf{S^c}$ and $\mathbf{S^r}$ are respectively the chemical and radiative source terms:

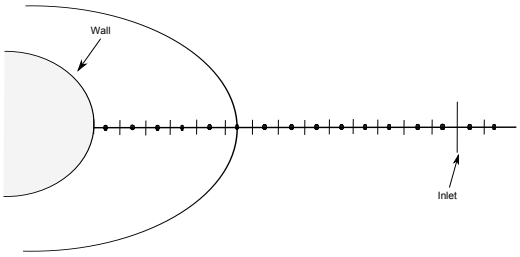

Figure 1: 1D Stagnation-Line illustration

$$
\begin{aligned}
\mathbf{U} &= \left[\rho_i,\ \rho u,\ \rho v,\ \rho E,\ \rho e^{VE}\right]^T \\
\mathbf{F^{inv}} &= \left[\rho_i u,\ \rho u^2 + p,\ \rho uv,\ \rho uH,\ \rho u e^{VE}\right]^T \\
\mathbf{F^{vis}} &= \left[\mathrm{J}_{ri},\ \bar{\tau}_{rr},\ \bar{\tau}_{r\theta},\ q_r + \bar{\tau}_{rr}u,\ q_r^{VE}\right]^T \\
\mathbf{G^{inv}} &= \left[2\rho_i(u+v),\ 2\rho u(u+v),\ 3\rho v(u+v) - 2\bar{p},\ 2\rho H(u+v),\ \rho e^{VE}\right]^T \\
\mathbf{G^{vis}} &= \left[\mathrm{J}_{ri},\ 2(\bar{\tau}_{rr} - \bar{\tau}_{\theta\theta} + \bar{\tau}_{r\theta}),\ -\bar{\tau}_{\theta\theta} + 3\bar{\tau}_{r\theta},\ 2(q_r + \bar{\tau}_{rr}u + \bar{\tau}_{\theta\theta}u + \bar{\tau}_{r\theta}v),\ 2q_r^{VE}\right]^T \\
\mathbf{S^c} &= \left[\dot{\omega}_i^{\mathbf{c}},\ 0,\ 0,\ 0,\ \Omega^{VE}\right]^T \\
\mathbf{S^r} &= \left[\dot{\omega}_i^{\mathbf{rad}},\ 0,\ 0,\ \mathcal{P}^{rad},\ \mathcal{P}^{rad,VE}\right]^T
\end{aligned}
$$

The variables $\mathbf{G^{inv}}$ and $\mathbf{G^{vis}}$ are inviscid and viscous source terms arising from the DRNSE transformation, respectively. The therm ρe^{VE} stands for vibrational-electronic-electron energy. Details regarding the radial heat fluxes, q_r and q_r^{VE} as well the energy transfer source term, Ω^{VE} are given by (7).

4.2. MUlticomponent Thermodynamic And Transport properties for IONized plasmas in C++ (Mutation^{++})

The closure of the multi-temperature Navier-Stokes equations is done by computing thermodynamic and transport properties. Mutation^{++} is a library built at the VKI by (12) where thermodynamic properties are computed by the Rigid Rotor Harmonic Oscillator model while transport properties are derived by the Chapman-Enskog expansion from Kinetic Theory (13).

4.2.1. Multiphase Equilibrium

Accurate chemical equilibrium solutions are necessary to have a proper estimation of the therm $y_{k,w}$ in Eq. 2. As shown in Table 1, the meteor under investigation (Ordinary Chondrites) is composed by three elements.

Recently an equilibrium multiphase solver based on the Gibbs function continuation method was developed at VKI by (14) and implemented inside the library Mutation^{++}. The solver proved to be very robust by converting the minimization of the mixture Gibbs free energy into an initial value problem which can be easily integrated. Furthermore, the solver has the capability of imposing any constraint in order to treat multiple surface components, which becomes a useful approach, when the actual evolution of the surface is unknown.

In brief the ratio between each element in the condensed phase is always respected in the gaseous products. By doing this, it can be ensured that in the case of ablation all the surface elements are changing phase with the same rate and the surface composition is always clearly defined.

4.3. Melting material solver

The study of meteor melting is essentially a Stefan problem. By solving the heat equation in spherical coordinates,

$$\rho c_p(T)\frac{\partial T}{\partial t} = \frac{1}{r^2}\frac{\partial}{\partial r}\left(r^2 k\frac{\partial T}{\partial r}\right) \tag{8}$$

Table 1: Meteors surface properties

Composition[a]		Elemental composition[a]		Density [kg/m^3]
SiO_2	0.606	Si	0.232	3000
MgO	0.394	Mg	0.152	
		O	0.616	

[a] Mole fractions are shown.

one can compute the temperature throughout the material and the melted layer can be estimated. Since the material presents different phases, a thermodynamic property such as the c_p has different values for the corresponding phases. Therefore in order to define accurately the molten interface one must build c_p as a function of temperature. This means that the c_p of the solid region (1050 J kg^{-1} K^{-1}) is different from the liquid (1650 J kg^{-1} K^{-1}) and the corresponding solid/liquid interface will be represented as a discontinuity in the property. Moreover for simplicity it will be assumed symmetry between the polar and azimuthal angles transforming the domain into one dimensional. This hypotheses was posed by (4), where is stated that, due the rotation of the meteor, the surface temperature tends to be uniform. To solve Eq. 8 an unsteady finite differences solver was built. The time integration is done by an explicit method. Since the material is recessing due to evaporation and mechanical removal, the change of the domain must be considered. This is done by building an updated domain at each time step and remapping the solution on the new mesh.

4.4. Solvers coupling strategy

As mentioned before, a coupling between material and flow solver is needed. Once the steady state solution of the flow is reached, convective heat flux and evaporation rate are exchanged with the material solver. Then the material solver is responsible for solving the transient solution in a predefined macro time step where the SEB is computed at each internal time. Once the desired time step is reached the surface temperature is provided to the flow solver for the next trajectory point.

For the presented analysis an implicit coupling was chosen (15). This type of coupling allows for time varying properties into the material solver. In other words, after obtaining the wall temperature from the material solver, the stagnation-line code is run a first time to compute the initial guess of mass blowing rate and convective heat flux. These quantities are linearly interpolated with those computed at the end of the previous trajectory point. The time varying quantities are assigned again to the material solver providing a new solution for the wall temperature. This procedure is repeated until converge is reached, i.e, once the wall temperature difference between two iterations is less than 50 K.

5. Test case and results

We considered a 1 cm radius ordinary chondrite with a constant velocity of 15 km s^{-1} along the trajectory. The trajectory was defined to start at 60 km, ending at 50 km altitude, thus, the total trajectory time for this conditions corresponds to 0.67 s. This trajectory was divided into 10 points where the solvers coupling methodology mentioned before was employed.

The ablation species injected into the flow field were considered frozen due to the lack of specific data on their chemical reaction rates. Differently, air species were modeled with finite rate chemistry with reaction rates taken from (16). A two-temperature model was used for these simulations, i.e., $T = T_{rot}$ and $T_{vib} = T_{ele}$.

Figure 2 shows the temperature profile along the stagnation streamline at 60 and 50 km altitude. From Fig. 2(a) is visible the shock roughly located at 0.2 cm from the surface, being very diffused due to the altitude conditions. The maximum translation temperature reaches values around 70000 K and drops abruptly to the surface. The intense non-equilibrium between translational and internal temperature is also visible around the shock layer. Comparing the previous figure with Fig. 2(b), the latter presents a reduced shock layer thickness. This is due to the increase of the free-stream pressure avoiding the shock layer at 60 km to be as diffused as at the previous altitude. From both figures it is also visible a thermal non-equilibrium in the free-stream region. This process occurs due to photoionization reactions in that region. In other words, due to strong radiative field,

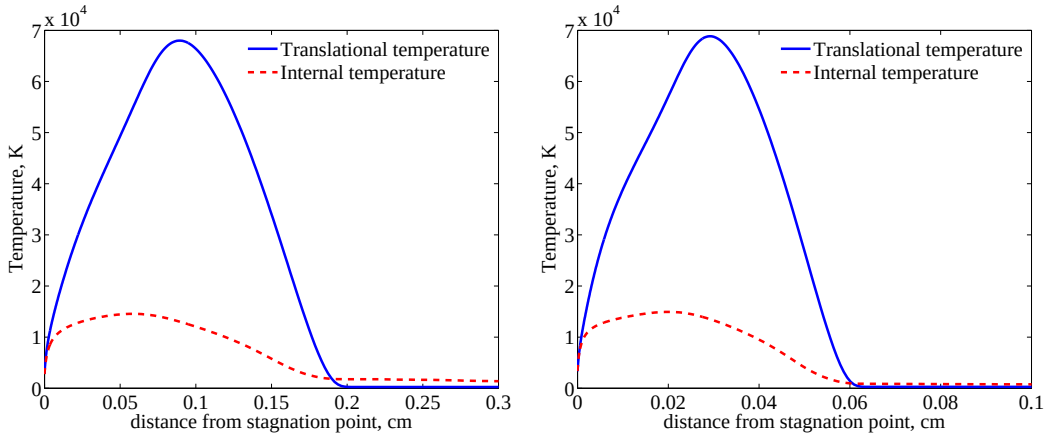

(a) 60 km (b) 50 km

Figure 2: Temperature profile along the stagnation streamline

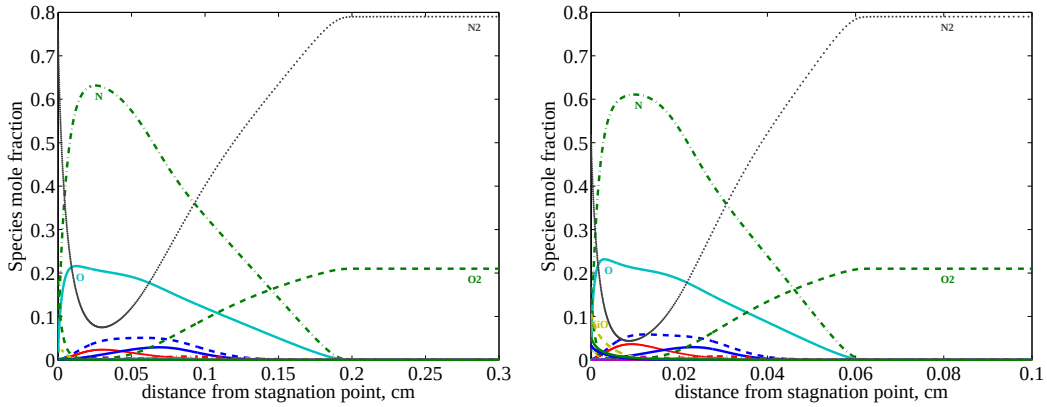

(a) 60 km (b) 50 km

Figure 3: Species concentration along the stagnation streamline

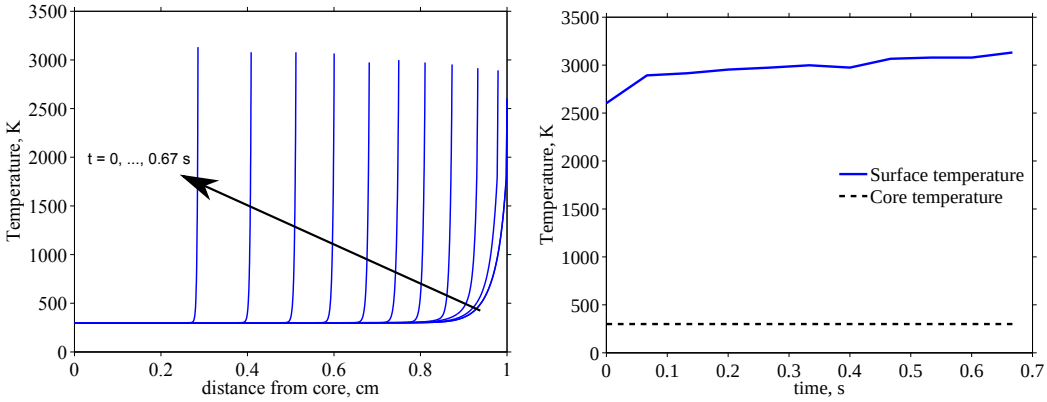

(a) in depth material temperature along trajectory (b)

Figure 4: Material temperature

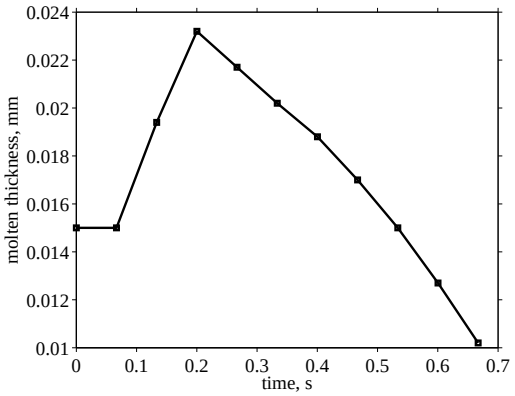

Figure 5: Interface location along the trajectory

the photons cross the shock wave colliding with the neutral species in the free-stream.

Figure 4(a) shows the temperature profile inside the material for the different trajectory points. It is visible that the surface temperature, around 3000 K, remains almost constant along the trajectory. Since the recession of the material is much higher than the thermal diffusion speed of the material, it is noticeable a steep temperature profile around the surface, leading the core of the meteor to remain unchanged at 300 K. One can notice, from the temperature profiles, that the recession of the material due to evaporation and mechanical removal, is around 0.75 cm for the full trajectory.

Then molten thickness along the trajectory is shown in Fig. 5. It is visible a very thin layer mostly due to the high mass removal by mechanical forces as shown by Fig. 6(b). The biggest contribution of the mechanical removal is due to the stress forces, i.e. the term $\tau_{flow/melt}$ in Eq. 5. The mass removal due to evaporation remains limited due to fact that the surface temperature does not reach the material sublimation point.

Finally Fig. 6(a) shows the contributions of heat flux to the surface. The high temperature gradients next to surface drives the convective heat flux to be the major contribution to the total heat flux. The radiative heat flux is rather small when compared to the convective contribution mostly due to the small shock layer thickness.

6. Conclusion

A model to study the meteor ablation at low altitude has been proposed and implemented. The chosen parameters (trajectory, entry velocity and material size) were selected arbitrarily with the purpose of presenting a different approach from the one proposed by the state of the art. The model takes the clue from the strategy used to evaluate the gas-surface interaction on the heat shields of re-entry capsules. In order to study the material response under the harsh entry environment, a material solver was built with the main objective of studying the removal of the molten layer of the meteor. Considering the fact that the material solver requires information from the flow, namely the boundary layer, a coupling with a flow solver was required.

A trajectory (60 km to 50 km altitude) of a 1 cm ordinary chondrite meteor entering at 15 km s^{-1} was studied. Under this conditions it has been observed that the main responsible for the of mass removal is the mechanical removal leading to a very thin molten layer along the trajectory.

It is important to mention that at this conditions double ionized species should be considered, such as N^{++} and O^{++}, which may allow a decrease of the translational temperature in the shock layer. Also the radiation of the ablation products was not considered, the absorption of these species may act as cooling effect of the shock layer.

Further comparison of the proposed melting model with experimental results are needed. The model developed for melting can be used to study larger meteors at altitudes where the continuum assumption is valid, such as fireballs. Most of the BRAMS observations are conducted above 80 km altitude where rarefied gas effects prevail. The melting model can be coupled to a DSMC method to study these conditions (17).

It has also been observed a considerable amount of e^- in the shock layer. This result might not represent the reality since at this range of temperatures it is important to consider double ionized species such as N^{++} and O^{++}.

For detection purposes, to study the electron concentration in the wake is essential. The model presented in this paper can easily be integrated into a multi dimensional CFD solver in order to study the wake of meteors, consequently, the electron concentration in the trail. Moreover reactions rates of the ablation species with air species are required to understand the influence of ablation in the electron concentration. Further comparisons with this model and meteor observations will be done in the future.

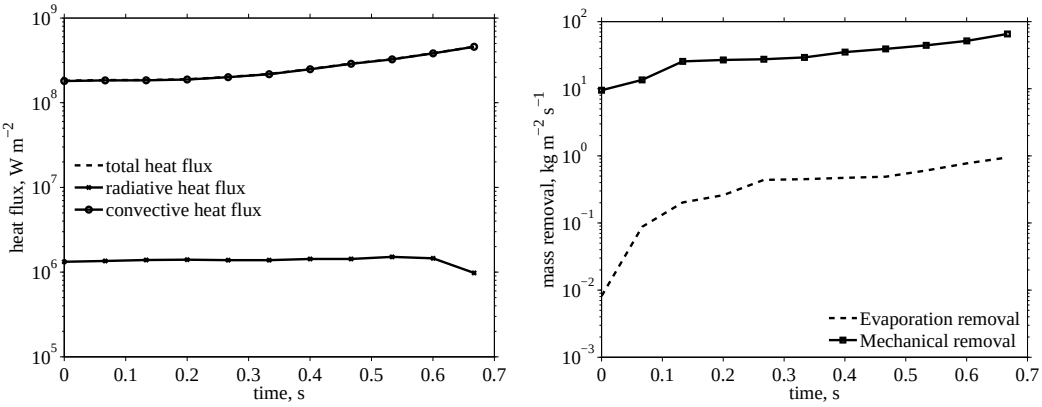

(a) Flow heat flux at the surface

(b) Material mass removal

Figure 6: Heat flux and mass removal

7. ACKNOWLEDGMENTS

This research is sponsored by the Belgian Research Action Through Interdisciplinary Networks "METRO: Meteor trajectories and origins". Research of B. Dias is sponsored by fellowship from the "Fonds pour la Formation la Recherche dans l'Industrie et dans l'Agriculture.".

References

[1] T. Vondrak, J. M. Plane, S. Broadley, D. Janches, A Chemical Model of Meteoric Ablation, Atmospheric Chemistry and Physics 8 (23) (2008) 7015–7031.

[2] H. Bethe, M. C. Adams, A Theory for the Ablation of Glassy Materials, Journal of the Aerospace Sciences 26 (6) (1959) 321–328.

[3] A. Faghri, Y. Zhang, Transport Phenomena in Multiphase Systems, Elsevier, Burlington, MA, 2006.
URL `https://cds.cern.ch/record/1417168`

[4] V. A. Bronshten, Physics of Meteoric Phenomena, D. Reidel Pub. Co., 1983.

[5] L. Soucasse, J. Scoggins, P. Rivire, T. Magin, A. Soufiani, Flow-radiation coupling for atmospheric entries using a hybrid statistical narrow band model, Journal of Quantitative Spectroscopy and Radiative Transfer 180 (2016) 55–69.

[6] J. Lamet, P. Rivière, M. Perrin, A. Soufiani, Narrow-band model for nonequilibrium air plasma radiation, Journal of Quantitative Spectroscopy and Radiative Transfer 111 (1) (2010) 87–104.

[7] J. Scoggins, L. Soucasse, P. Riviere, S. Soufiani, T. Magin, Coupled flow, radiation, and ablation simulations of atmospheric entry vehicles using the hybrid statistical narrow band model, in: 45th AIAA Thermophysics Conference, Dallas, Texas, 2015, AIAA 2015–3112.

[8] J. Scoggins, L. Soucasse, P. Riviere, S. Soufiani, T. Magin, An adaptive hybrid statistical narrow band model for coupled, in: Proceedings of 8th European Symposium on Aerothermodynamics for Space Vehicles, May 2015, ESTEC, Noordwijk, The Netherlands, 2015.

[9] A. Turchi, A Gas-Surface Interaction Model for the Numerical Study of Rocket nozzle flows over pyrolyzing ablative materials, Ph.D. thesis, Università degli Studi di Roma "La Sapienza" (2013).

[10] D. Bianchi, F. Nasuti, E. Martelli, Navier-stokes simulations of hypersonic flows with coupled graphite ablation, Journal of Spacecraft and Rockets 47 (4) (2010) 554–562.

[11] A. Munafò, Multi-Scale Models and Computational Methods for Aerothermodynamics, Ph.D. thesis, Ecole Central Paris (2014).

[12] J. Scoggins, Development of Mutation++: MUlticomponent Thermodynamics And Transport properties for IONized gases library in C++, VKI PhD Symposium (2013).

[13] T. E. Magin, G. Degrez, Transport algorithms for partially ionized and unmagnetized plasmas, Journal of Computational Physics 198 (2004) 424–449.

[14] J. Scoggins, T. Magin, The gibbs function continuation method for linearly constrained multiphase equilibria, Combustion and Flame 162 (12) (2015) 4514–4522.

[15] P. Schrooyen, Numerical simulation of aerothermal flows through ablative thermal protection systems, Ph.D. thesis, Université catholique de Louvain (2016).

[16] C. Park, R. Jaffe, H. Partridge, Chemical-kinetic parameters of hyperbolic earth entry, Journal of Thermophysics and Heat Transfer 15 (1) (2001) 76–90. doi:10.2514/2.6517.

[17] F. Bariselli, E. Torres, T. Magin, State-specific catalytic recombination boundary condition for dsmc methods in aerospace applications, in: 30th International Symposium on Rarefied Gas Dynamics, Victoria, Canada, 2016.

BiGlobal stability of shear flows: spanwise and streamwise analyses

Koen J. Groot

Aerodynamics Section (AWEP), Delft University of Technology, The Netherlands, k.j.groot@tudelft.nl

Supervisors: Olivier Chazot and Fabio Pinna

Professor, Aeronautics and Aerospace Department, von Karman Institute for Fluid Dynamics, Belgium, chazot@vki.ac.be

Research Engineer, Aeronautics and Aerospace Department, von Karman Institute for Fluid Dynamics, Belgium, fabio.pinna@vki.ac.be

University Supervisor: Bas W. van Oudheusden

Associate Supervisor, Aerodynamics Section (AWEP), Delft University of Technology, The Netherlands, b.w.vanoudheusden@tudelft.nl

University Supervisor: Fulvio Scarano

Professor, Aerodynamics Section (AWEP), Delft University of Technology, The Netherlands, f.scarano@tudelft.nl

Abstract

A main project goal is investigating feasibility of applying stability approaches to measured mean flows, a test case being swept-wing boundary layers. Stability results are sensitive to flow details, but represent consistent physical balances. Using the approach the perturbation flow structure and physics can be reproduced. Hence, the method is proposed as a way to extend and enhance experimental measurability.

Keywords: laminar-to-turbulent transition, BiGlobal stability, swept-wing boundary layer

1. Introduction

Laminar-to-turbulent transition of flows causes an increase in the local skin friction and heat transfer. Therefore taking into account this phenomenon is important for the design of airliners, regarding their fuel consumption, and re-entry vehicles, with respect to their thermal protection systems. The classical numerical approach to this phenomenon, originally proposed in 1956 by Van Ingen [1], is the combination of Linear Stability Theory (LST), which determines the growth rate of the eigenmodes (Tollmien-Schlichting (TS) waves) that live on a laminar flow, and the semi-empirical e^N-method, which establishes a correlation between the transition "location" and the total growth (or: gain) that the eigenmodes undergo.

Transition can occur through several paths. Perturbations are entrained into the boundary layer via receptivity mechanisms and experience an amplification phase before they breakdown to turbulence. The amplification kind strongly depends on the disturbance environment. For small perturbations, the most unstable exponentially growing eigenmode will become dominant and lead to parametric instability (path A). In this treatment the main focus will be on the case of swept-wing boundary layers emmersed in low disturbance environments. These flows are dominated by stationary streamwise-oriented crossflow (CF) vortices as the primary instability. This instability is weak and is non-linearly stable, but it causes a mean-flow distortion that gives rise to secondary instabilities. These instabilities dictate the breakdown to turbulence in this particular case. [2; 3; 4; 5]

For this reason, understanding these instabilities is important in understanding, and ultimately predicting, where laminar-turbulent transition will occur. Malik *et al.* [6; 7] established the applicability of the e^N-method to the secondary instability, by incorporating the mean flow distortion induced by the primary instability mode and using the experiments of Kohama *et al.* [8] to verify their results. Kawakami *et al.* [9], Bippes & Lerche [10] and Bippes [11] report on forcing and the receptivity of secondary crossflow instabilities.

The primary CF vortices redistribute the momentum of the undisturbed boundary layer flow by advection about their vortical axis. This causes a spanwise modulation of the steady flow in terms of a sequence of high-speed/low-speed regions. The resulting distorted flow therefore is two-dimensional; it is approximately homogeneous in the streamwise direction. In the remainder, the latter will be referred to as the base flow. The instabilities of such flows can be approached with the BiGlobal stability equations, see Theofilis [12]. Main studies for the application at hand have been performed by Malik *et al.* [6], Högberg & Henningson [13] and Bonfigli & Kloker. [2]

Koch *et al.* [14] classify the most prominent instabilities to the distorted base flow into three catagories. First, the type I mode is generated by the spanwise shear layer in the upwash region to the left of the primary vortex. Second, the type II mode is mainly generated by wall-normal shear and sits on top of the primary vortex. These modes are also referred to as the z- and y-modes respectively, as intorduced by Malik *et al.* [15]. Third, Koch *et al.* define the type III mode, which is the travelling primary crossflow instability subject to the distorted base flow. The modes of type I and II are proper secondary instabilities to the stationary primary crossflow vortex.

The primary CF vortices are subject to receptivity mechanisms such as the disturbance environment, e.g. micron-sized surface roughness near the leading edge and freestream turbulence. The secondary stability, in turn, depends strongly on the primary vortices and the overall disturbance environment, so care must be taken in accurately representing the base flow for the secondary stability analysis. In previous work, the latter is computed by performing NPSE or DNS. However, when to be compared with experimental data, these techniques require careful receptivity calibration for the initial conditions, see Malik *et al.* [7], Fisher & Dallmann [16] and Bonfigli & Kloker. [2]

By directly measuring the distorted base flow one can completely avoid this complication. The main objective of this work is therefore to investigate the feasibility of using experimentally measured base flows for the BiGlobal analysis of secondary instabilities of crossflow vortices. The secondary stability analysis is applied to the experimentally measured "base flow," through the means of tomographic (or tomo-)PIV, which fully resolves the three-dimensional boundary layer flow including the mean flow distortion effect due to the primary vortex. The base flow is represented by the mean flow field under the hypothesis that the difference between the base and mean flow becomes negligible as the number of instantaneous snapshots is increased. Other features related to practical limitations are approached and will be shown to have a negligible impact on the results. This progress communication is in its entirety based on the publication of Groot *et al.* [17]. A similar approach has been deployed to the flow in the aft of micro-ramp vortex generator. [18]

Next to circumventing computationally modelling the primary vortices, this approach is further motivated by the fact that the secondary instability is of inherent interest in this case. Comparing the measured instantaneous signal to the linear mode helps understanding the later transition stages. Furthermore, the approach extends and enhances experimental measurability. The instantaneous flow field is more difficult to resolve than the mean flow. Thus, if the instantaneous field can be decomposed into an eigenmode superposed on a steady flow, the mode can be identified by the current method and the experimental set-up can be further optimized.

The experimental set-up and the pre-processing of the experimental data is discussed in Sec. 2. See Serpieri & Kotsonis [19] for a detailed description of the tomo-PIV experiments. It is worth mentioning the tomo-PIV dataset is the first for this particular application, rendering the application and validation of the current approach feasible for the first time. The numerics of the BiGlobal stability method are discussed in Sec. 3. The focus of the verification lies on the establishment of the convergence limit for the ensemble size for the mean and the handling of the near-wall and freestream regions. A preliminary validation of the proposed methodology is performed in Sec. 4, based on the comparison of instability eigenfunctions with coherent structures obtained with the tomo-PIV measurement. The verification and validation are handled in Secs. 4. The paper is concluded in Sec. 5.

2. Experimental Base Flow

The mean field is obtained with three-dimensional tomo-PIV measurements by Serpieri & Kotsonis [19], performed in the TU Delft LTT facility. The model is a 45° swept wing with an airfoil that is an adaptation of the NACA66018 shape, called 66018M3J, with a small leading edge radius to avoid attachment line instability, see Fig. 1(top). The wing was set under an angle of attack of 3 degrees, so to enhance the crossflow instability at the pressure side. The pressure minimum is attained at $X/c_X = 0.63$ at this angle of

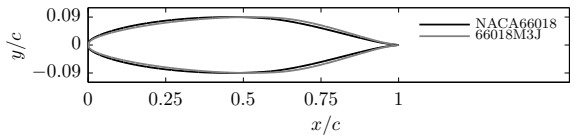

Figure 1: 66018M3J and NACA66018 airfoils, from Serpieri & Kotsonis [19].

attack, where X is parallel to the tunnel walls and c_X the chord in the X-direction. The full C_p-distribution is shown in Fig. 1(bottom). The windtunnel inflow velocity is $\overline{Q}_\infty = 25.6\,[m/s]$, yielding a chord Reynolds number of $2.17 \cdot 10^6$. The measurement is performed about the 45% chord, spanwise center location. There the vortices and inviscid streamline respectively have an angle of 5.0 and 1.74 degrees (clockwise positive) with $\overline{Q}_\infty$.

The relevant coordinate systems are defined in Fig. 2. The first, (X, Y, Z), has X parallel to $\overline{Q}_\infty$, Z in the spanwise direction perpendicular to the tunnel walls and Y normal to the ZX-plane. The second, (x_w, y, z_w), is aligned with the primary crossflow vortices. I.e. x_w is parallel to the vortices, y wall-normal with respect to the airfoil and z_w spanwise, perpendicular to the $x_w y$-plane. Unless otherwise specified, the results will be displayed in this main coordinate system. The related velocity components are indicated with the subscript w. The third (swept-wing) coordinate system, (x, y, z), is obtained by rotating the (X, Y, Z)-system 45° about the Y-axis. x is orthogonal to the leading edge, y wall-normal with respect to the airfoil and z parallel to the leading edge. The origin of the (x_w, y, z_w)- and (x, y, z)-systems is located at the 45% chord, spanwise center position. In the experimental treatments, the y-coordinate normal to the airfoil is also denoted by y_t; at the fixed streamwise station of current interest, $X/c_X = 45\%$, the difference is negligible. The primary instability is fixed by installing a cylindrical roughness element array at $X/c_X = 2.5\%$ parallel to the leading edge, with a spanwise spacing of 9 $[mm]$. The elements' diameter and height are $2.8\,[mm] \times 10\,[\mu m]$. The projection of the roughness spacing on the z_w-direction is $9\cos 40° = 6.89\,[mm]$. This length will be used as the length scale throughout the elaboration and is denoted by λ_r. The velocity scale is taken to be the edge velocity in the direction of the primary vortex at $X/c_X = 45\%$, $\overline{U}_{w,e}$, is equal to $28.0\,[m/s]$. It is referred to as $\overline{U}_e$ in the remainder.

2.1. Tomographic PIV

The tomo-PIV setup consisted of four cameras, that were mounted in an arc arrangement located approximately one meter away from the model. The laser light enters the wind tunnel vertically from below. The final field of view was $35 \times 35 \times 3\,[mm^3]$ and centered at $X/c_X = 0.45$. Volume reconstruction and correlation were performed in a coordinate system aligned with the primary crossflow vortices, i.e. in the x_w-direction. The final interrogation volume size is $2.6 \times 0.67 \times 0.67\,[mm^3]$ in (x_w, y, z_w). This turned out to provide sufficient spatial resolution for both primary and secondary structures. A 75% overlap of adjacent interrogation volumes was used. The final vector field was interpolated on a grid with a uniform spacing of $0.15\,[mm]$ in all three directions, only implying interpolation in x_w. The planes were obtained at $x_w = 0$ by a linear interpolation. The measurements were performed at a sampling frequency of $0.5\,[Hz]$. Proper Orthogonal Decomposition (POD) analysis is applied to identify the most energetic spatially correlated three-dimensional flow structures. [20] See Serpieri & Kotsonis [19] for more details related to the present application. The frequency of the POD mode corresponding to the type I mode was estimated to be $5\,[kHz]$, using the Taylor hypothesis in combination with the observed wavelength and convective velocity.

In total 500 uncorrelated snapshots were obtained. The mean flow field was conceived with different ensemble sizes (number of snapshots): $N_f = 300$, 400 and 500 are used as a base flow for the stability analysis. Previous studies [18] pointed out that using this amount of snapshots is enough to yield converged stability results. Regarding a maximal perturbation magnitude of $0.1\overline{U}_e$, the uncertainties of the mean fields are estimated to be $0.1/\sqrt{N_f} = 5.8{\cdot}10^{-3}$, $5.0{\cdot}10^{-3}$ and $4.5{\cdot}10^{-3}$ in units of $\overline{U}_e$ for the 300, 400 and 500 frame cases. These are relatively high in terms of the expected uncertainty of the stability analysis, but highly sufficient for PIV standards. Despite of this, the stability results are found to be less sensitive than expected, as will be shown in Sec. 4.

The most important feature of the tomo-PIV experiment as opposed to hot-wire measurements, which is the prevalent technique applied in this field [5; 8; 9; 10; 11], is that all 3 velocity components are measured in an entire volume. It is known that the stability results are sensitive to the in-plane velocity components. [2; 6] Preliminary BiGlobal stability tests also indicated that the results deviated significantly when

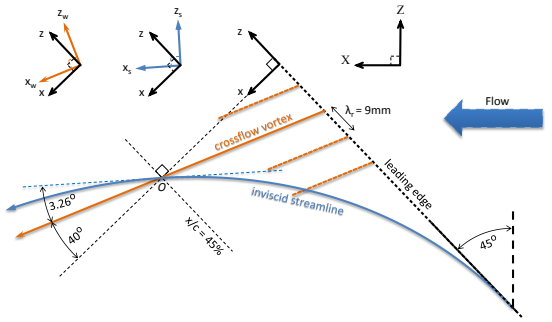

Figure 2: Definition of (left to right) primary crossflow vortex (x_w, z_w), inviscid streamline (x_s, z_s), leading edge (x, z) and freestream (X, Z) coordinate systems. At the 45.0% chord location, the primary vortices have a $-40°$ angle with respect to the leading edge orthogonal x-coordinate ($+5.0°$ with respect to X), in turn the inviscid streamline has a $-3.26°$ angle with respect to the primary vortices ($+1.74°$ with respect to X).

discarding them, despite being an order of magnitude smaller. This is the first occasion where this apparently essential data is available from experiments, rendering the current stability approach feasible.

2.2. *Pre-Processing for BiGlobal Analysis*

Prior to the analysis of the mean flow fields with the BiGlobal stability method, they have to be preprocessed. This processing is mainly related to the limited field of view and problems associated to measuring in close proximity to the wall.

The perturbations need sufficient distance to decay in the wall-normal direction. To this end, the $\overline{U}_w$ and $\overline{W}_w$ base flow velocity components are extrapolated using the Blasius solution in the inviscid streamline direction, i.e. $\overline{W}_{w,e} = \overline{U}_{w,e} \tan 3.26° = 1.59\,[m/s]$. A Falkner-Skan-Cooke profile would be the best approximation, but the difference is negligible as the top of the field of view penetrates the freestream to a significant extent; about 2 undisturbed boundary layer thicknesses. The Blasius and PIV datasets are not continuous at the top of the field of view. Therefore, a cosine weight overlap layer is introduced to make the resulting base flow continuous at the interface. δ_{PIV} and Δy denote the height up to which the PIV data is used solely and the height of the overlap region. $\overline{V}$ is extrapolated to a zero value in the freestream; the exact non-zero value is $O(10^{-5})$ and is neglected.

Near-wall PIV measurements are challenging. [21] Important factors affecting measurement accuracy are laser-light reflections, low particle density and the strong shear. Effectively, these features cause the velocity profile to slope off at a non-zero value instead of representing the no-slip condition. The region where this is prominent is here referred to as the near-wall region. The type III mode is dominant in this region and therefore depends sensitively on the flow's near-wall details. The local measurement noise is therefore expected to be irreversibly affecting mode III. Moreover, artificial inflection points are created that can cause a significant artificial inviscid instability.

This behaviour is mended with the purpose of avoiding the latter solutions and approached in 2 steps. First, the profiles are connected to the wall, the no-slip condition is "added." Visual inspection pointed out the data closest to the wall yields the unwanted inflection points. Therefore, as the second step, the data at the y-position closest to the wall is overwritten with a spline interpolation; so the no-slip condition is connected approximately linearly to the data on the second non-zero y-coordinate with respect to the wall. This removes the artificial shear due to PIV measurement errors. This is analogous to the approach used to suppress the type III mode in the computational literature. [2] The type I and II modes experience negligibly effects by these base flow changes outside their spatial region of dominance, see Sec. 4.

The in-plane $\overline{U}_w$-shear from the resulting mean tomo-PIV flow field is shown in Fig. 3(left) by extracting the plane along the z_w-coordinate. 500 snapshots have been used for the average field. The spanwise extent of the domain covers one primary vortex in the z_w-direction and is equal to $1\lambda_r = 6.89\,[mm]$. Sixth order finite differences are used to determine the derivative fields consistently, i.e. using central differences in the interior and forward/backward differences at the boundaries. The high order was chosen in order to avoid corruption of the derivatives by the finite spatial resolution of the tomo-PIV. Using fourth order differences yields a notable but coherent difference, which indicates that higher order differences do not amplify random oscillations, but rather provide a required higher accuracy. It is observed the derivatives of the small quantities $\overline{V}$ and $\overline{W}_w$, that are difficult to measure, can attain large values in the near-wall region and are sensitive to the ensemble size for the mean. Tests are performed in which these levels are artificially reduced, which led to $O(10^{-4})$ absolute changes in the type I mode's eigenvalues. The height of the measurement domain and the near-wall region is shown by the white and black dashed lines respectively. The color scale is adjusted so to remove the levels pertaining to the near-wall region.

Fig. 3(right) displays the derivative profiles $\partial\overline{U}_w/\partial y$ and $\partial\overline{U}_w/\partial z_w$ extracted at constant $z_w/\lambda_w = 0.378$; the location where the type I mode is identified to be

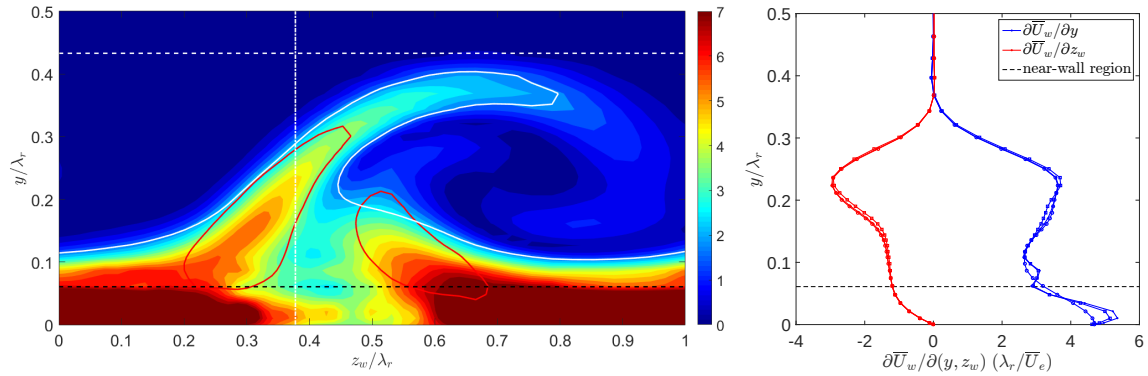

Figure 3: (left) In-plane $\overline{U}_w$-shear magnitude of the 500 frame tomo-PIV dataset, interpolated onto the 55×55 mapped Chebyshev grid. Levels are in units of $\overline{U}_e/\lambda_r$; the maximum encountered above the black dashed line is $7\,\overline{U}_e/\lambda_r$. Red and white thick contours respectively indicate where the z_w- and y-shear magnitudes equal $7/4\,(\overline{U}_e/\lambda_r)$. The horizontal white dashed line ($y/\lambda_r = 0.433$) indicates the highest coordinates captured in the measurement; the black dashed line ($y/\lambda_r = 0.061$) indicates the near-wall region. (right) Shear component profiles for the 500 (solid dots), 400 (circles) and 300 (squares) frame datasets extracted along the vertical dash-dotted line ($z_w/\lambda_r = 0.378$) in the left figure. Black dashed line indicates the near-wall region.

most dominant by the BiGlobal analysis (see Sec. 4). With the exception of the near-wall region, the differences between the profiles are small. The largest relative difference between the 400 and 500 frame cases outside of the near-wall region is 1.9% for both profiles. The shear levels are directly related to the modal growth rates, [22] thus one expects the difference in the growth rates to be of this order of magnitude.

3. BiGlobal Stability Analysis

The BiGlobal stability approach assumes dominant shears in 2 principal directions. The flow is assumed to be independent of the third. The best approximation of such a direction in the case of the primary crossflow vortices is along the wave vector of the primary vortices: the x_w-direction. Implicitly, one neglects the curvature of the vortices, [7; 2] which is *a-posteriori* justified by the small wavelengths of the secondary modes. [12] A single primary vortex wavelength is considered for simplicity. Periodic boundary conditions are applied on the boundaries in the z_w-direction. Regarding the wall-normal direction, no-slip and pressure compatibility conditions [23] are applied at $y = 0$ and Dirichlet conditions are used for all amplitudes on the top boundary as it is located high enough (at $4\lambda_r$) and as it resolves the additive-constant non-uniqueness problem with the pressure.

The $z_w y$-planes are extracted directly from the tomo-PIV data, since the cross-correlation is performed in this direction and hence yields the most consistent representation. Moreover, not having to project the data on a plane minimizes the continuity problems discussed by Bonfigli & Kloker [2]. The data is interpolated to yield the plane with $z_w = 0$ at $x/c = 45\%$. The introduced non-periodicity is assumed to be negligible. The change in the edge velocity is used as a representative quantity and changes less than $10^{-3}\overline{U}_e$. This is a consequence of the small chordwise extent of the domain, it protrudes $6.89 \sin 40° = 4.4\,[mm]$ in the streamwise direction only. Note, in this regard, that the base flow quantities, including the shear, change discontinuously across the boundaries, but no new shear is introduced due to this.

One combines the aforementioned considerations in the BiGlobal ansatz for the perturbation as follows:

$$q' = \tilde{q}(z_w, y)\, e^{i(\alpha x_w - \omega t)} + c.c., \qquad (1)$$

where α is the wavenumber in the x_w-direction and ω the angular frequency. The BiGlobal stability equations are solved for $\omega \in \mathbb{C}$ (given $\alpha \in \mathbb{R}$) or $\alpha \in \mathbb{C}$ (given $\omega \in \mathbb{R}$), in a temporal or spatial framework, respectively. In both approaches solutions are sought for which $\omega_r/(2\pi) \approx 5.0\,[kHz]$, the frequency associated to the tomo-PIV POD mode. The in-plane base flow velocity components $\overline{V}$ and $\overline{W}_w$ appear as coefficients in the BiGlobal equations. [24] The tomo-PIV dataset is the first for this particular application. [19] Capturing those components, it renders the current stability approach feasible for the first time.

The BiGlobal tools of the VKI Extensible Stability and Transition Analysis (VESTA) toolkit are used to set up the stability problem. [25] The problem is discretized using Chebyshev spectral collocation and a BiQuadratic mapping is used to resolve the y- and z_w-directions in specific areas. The BiQuadratic mapping

is defined as follows:

$$y = y_{max}\frac{a\eta^2 + b\eta + c}{d\eta^2 + e\eta + f}, \qquad (2)$$

$$\begin{array}{ll} a = (y_{i2} - 3y_{i1}) & d = 2(2y_{i2} - 2y_{i1} - y_{max}) \\ b = \frac{3}{2}(y_{i2} - y_{i1}) & e = 0 \\ c = (y_{i2} + 3y_{i1})/2 & f = 2y_{max} - y_{i2} + y_{i1} \end{array}$$

where the Chebyshev coordinate $\eta \in [-1, 1]$ and the physical coordinate $y \in [0, y_{max}]$. The mapping is conceived so as to distribute one third of the collocation nodes over the domains $[0, y_{i1}]$, $[y_{i1}, y_{i2}]$ and $[y_{i2}, y_{max}]$, as long as $0 < y_{i1} < y_{i2} < y_{max}$ and $y_{i2} < 9y_{i1}$ and $9y_{i2} < y_{i1} + 8y_{max}$ to ensure a regular one-to-one behaviour. In the current context, the mapping is equipped with specific parameters so to dedicatedly resolve the type I mode. Using $N_z \times N_y = 55 \times 55$ nodes and setting $(z_{i1}, z_{i2}, z_{max}) = (0.30, 0.55, 1.0)\lambda_r$ and $(y_{i1}, y_{i2}, y_{max}) = (0.18, 0.60, 4.0)\lambda_r$ yields type I eigenvalue errors of $O(10^{-5})$ in absolute sense. An example of the mode on the grid is shown in Figure 4. Grid convergence was checked by increasing the resolution using these mapping parameters and checking against a more conventional grid, applying no or standard bilinear mappings. [26] The type II modes, positioned about the point $(z_w, y) = (0.7, 0.35)$ that is depleted from nodes, has yet to overcome $O(10^{-3})$ differences with higher resolution computations. Using the BiQuadratic mapping this way has the main advantage of markedly reducing the computational expenses, in terms of RAM and evaluation time, while maintaining excellent accuracy for the main target at hand: the type I mode. The reduced number of nodes rendered both temporal and spatial problems small enough to be solved on small workstations in mass. A single evaluation requires only several minutes on a standard workstation.

A final step to improve solving efficiency is setting the center of the resolved spectrum; the parameters for the shift & invert transformation in the Arnoldi algorithm. This is done considering specific heuristics: the modes of interest have a high phase speed due to their high position in the boundary layer. Conversely, modes inside the near-wall region are subject to measurement noise. Modes that lie in the near-wall region have low phase speeds corresponding to the low $\overline{U}_w$ values, by inspection smaller than $0.4\overline{U}_e$. Hence, the region with $\omega_r < 0.4\alpha_r$, especially the stable region, is to be avoided. Additionally, the modes of interest are discrete and do not belong to the continuous spectrum. The continuous spectrum contains modes that live in the freestream, those with phase velocity equal to 1. They complete the spectrum, but are very expensive to compute. The shift is oriented so to equally avoid both (stable) regions, but capture all interesting discrete modes. As only the modes of interest are captured and the type I mode is usually most unstable, it suffices to reduce the number of resolved modes to 5.

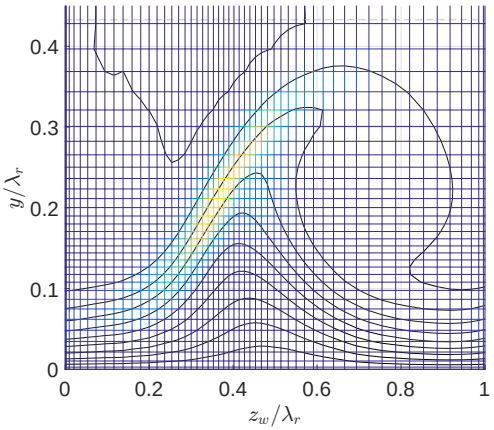

Figure 4: Near wall zoom on optimized grid (55x55 nodes) resolving the type I mode (temporal, $\alpha = 8.2/\lambda_r$) using a BiQuadratic mapping.

4. Results

The temporal and spatial branches corresponding to the type I mode obtained for a range of α and ω, are displayed in Figure 5(left) and -(right), respectively. The temporal problem is solved for the α-range $[1.5, 11.5]/\lambda_r$ with a spacing of half a unit of $1/\lambda_r$. The most unstable, forced and high frequency neutral modes (respectively having $(\alpha\lambda_r, \omega\lambda_r/\overline{U}_e) = (6.1; 4.6)$, $(8.2; 6.2)$ and $(11.4; 8.7)$) are resolved with a spacing of a tenth unit of $1/\lambda_r$. These α-values are based on the 500 frame base flow case specifically and fixed for the other cases. The obtained real parts of the temporal frequencies are used as the input for the spatial problem. The obtained branches display the characteristic shape associated to the Kelvin-Helmholtz mechanism [27] associated to the type I mode and are qualitatively comparable with computational literature. [2] The closest extracted wavenumbers and frequencies for the comparison to the experimental data are: $(\alpha_r\lambda_r, \omega_r\lambda_r/\overline{U}_e) = (9.5; 7.2)$ for the tomo-PIV and $(8.2; 6.2)$ for the hot-wire experiment. Both frequencies are higher than the most unstable frequencies at this location. This is a qualitative indicator for the spatially most amplified mode, as a frequency attaining the maximum N-factor usually is itself not the most unstable wave at that streamwise location. [28]

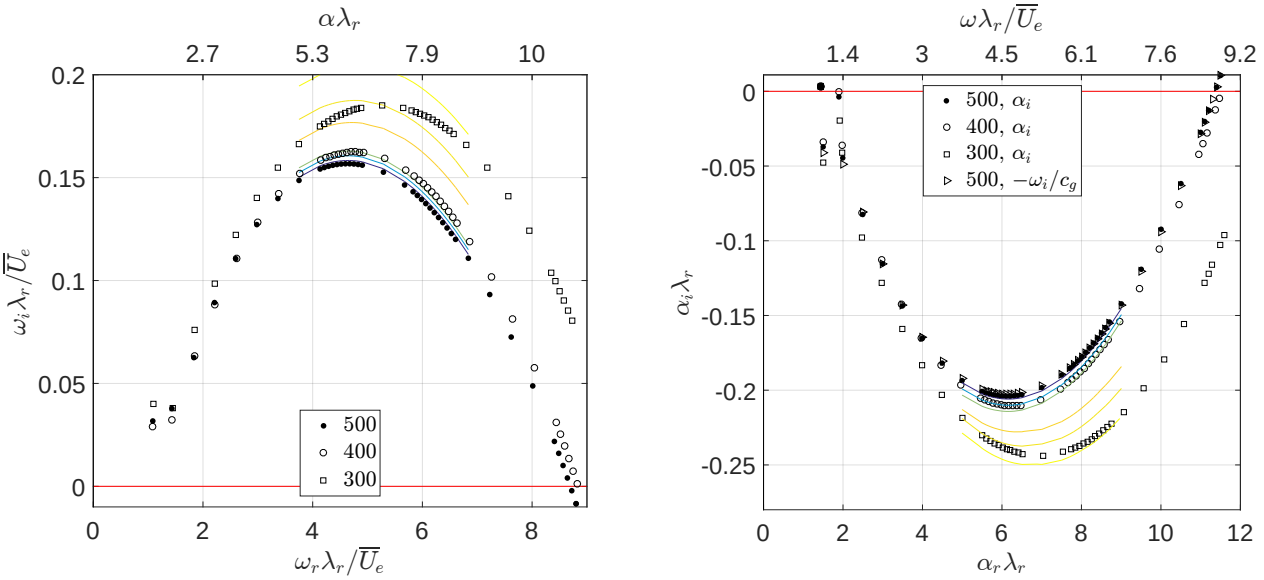

Figure 5: Temporal (left) and spatial (right) eigenvalues associated to the type I secondary instability with varying real α and ω, respectively. The spacing of the latter is chosen so to densely resolve the most unstable and most amplified modes at the $x/c = 45\%$ location. The Gaster-transformed 500 frame temporal spectrum is shown amongst the spatial spectra. Note that the top axes, indicating the input for the 500 frame base flow case, are non-linear. Pseudospectrum levels corresponding to the 500 frame case are superposed, for the temporal spectrum: 10^(−6, −5, −4, −3.1, −3, −2.9) and the spatial spectrum: 10^(−7, −6, −5, −4.1, −4, −3.9).

Although the statistical uncertainties of the mean flows are in the order of $O(10^{-2.3})$, Fig. 5 shows the resulting branches are similar over the covered frequency range. The main change is a vertical shift, that increases for higher frequencies and wavenumbers. The real dispersion parameters pertaining to the phase and group speed differ very slightly, the average group speed found for the spatial 500, 400, 300 and temporal 500 frame cases are 0.7725, 0.7760, 0.7648 and 0.7736 units of $\overline{U}_e$, respectively, indicating convergence and $O(10^{-3})$ errors in the real parameters for the 400 and 500 frame cases. These values agree with the phase speeds observed in the tomo-PIV experiment [19] and those reported by Kawakami *et al.* [9], the values respectively being $0.8\overline{U}_e$ and $0.78\overline{U}_e$. Note that the difference in the group and phase speeds is small for large enough frequencies. [7] The average group speed $c_g = 0.7736\overline{U}_e$ is used for the Gaster-transformation [29] of the 500 frame temporal spectrum shown in Fig. 5(right); which agrees remarkably with the spatial branch, despite the large ω_i-values. The applicability of the Gaster-transformation, used by Malik *et al.* [7] and Koch *et al.* [14], is therefore demonstrated for the current approach as well. As the number of frames increases, the growth rates ω_i and $-\alpha_i$ decrease and saturate. The same applies to the most unstable real frequency and wavenumber.

Absolute eigenfunction profiles at the POD mode frequency are shown in Fig. 6, at the z_w-coordinate where the 500 frame $|\tilde{u}_w|$-amplitude attains its maximum. A first observation is that the profiles are small in the near-wall region and freestream. Second, the temporal and spatial eigenfunctions are found to be virtually identical. The same conclusion is drawn when considering the full two-dimensional absolute amplitude contours for all variables. The combination of the match of the temporal and spatial eigenvalues and -functions demonstrates the Gaster-transformation can be applied with confidence. Third, it is found that the profiles corresponding to the 400 and 500 frame cases closely overlap as well. The only noticeable differences are small depressions in the $\tilde{v}$- and $\tilde{w}$-amplitudes of the 400 frame case. This indicates that the 400 and 500 frame base flows yield nearly identical mode structures, although the eigenvalues have slightly different imaginary parts. With these observations it is concluded that the 400 and 500 frame cases yield a converged stability result. The latter will therefore be used to compare to the experimental data in the remainder of the paper. A significant difference is expected when regarding the 300 frame case. This manifests itself primarily in the eigenfunction's maximum moving relative to the wall.

Also the effect of the Blasius extrapolation parameters to approach the limited field of view has to be quantified. Significant variations in the position (δ_{PIV})

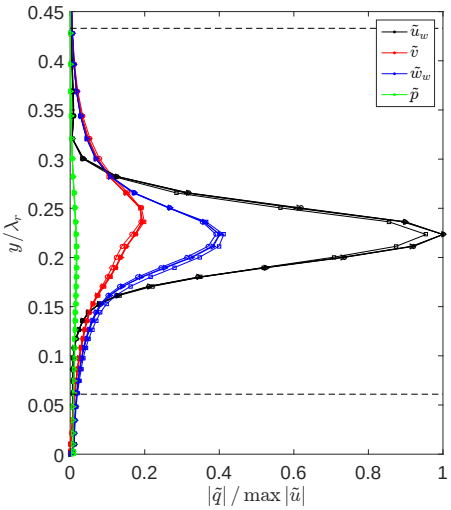

Figure 6: Absolute eigenmode y-profiles at $z_w = 0.378\lambda_r$, where the type I $|\tilde{u}_w|$eigenfunction corresponding to the 500 frame base flow is maximal. The solid dots, circles and squares correspond to the 500, 400 and 300 frame spatial BiGlobal modes (at $(\alpha\lambda_r; \omega\lambda_r/\overline{U}_e) = (9.506 - 0.1191i; 7.228)$, $(9.465 - 0.1319i; 7.228)$ and $(9.572 - 0.1988i; 7.228)$, respectively) and the triangles to the temporal BiGlobal mode for the 500 frame base flow (for $(\alpha\lambda_r; \omega\lambda_r/\overline{U}_e) = (9.500; 7.228 + 0.09318i)$). Black dashed lines indicate the near-wall region and the upper limit of the field of view.

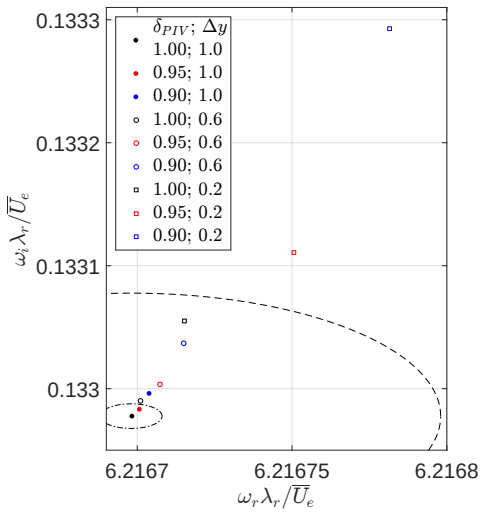

Figure 7: Temporal eigenvalue for different domain extrapolation parameters (in units of $0.433\lambda_r$). Dashed and dash-dotted lines indicate 10^{-4} and 10^{-5} absolute error limits with respect to the $\delta_{PIV} = \Delta y = 0.433\lambda_r$ case; values inside the outer and inner error limits correspond to errors of $O(10^{-5})$ and $O(10^{-6})$.

and size (Δy) of the overlap region causes negligible differences. Increasing δ_{PIV} implies changing the data inside the PIV domain to a lesser extent. Increasing Δy implies reducing the artificially introduced shear. The eigenvalue is expected to converge when both parameters are maximized. The type I eigenvalue displays this and attains $O(10^{-5})$ error levels as shown in Fig. 7. The physical explanation is that the eigenfunctions are small in the freestream regions and are therefore negligibly affected. The used overlap region for the results presented in this paper was set to have zero overlap with the PIV domain ($\delta_{PIV} = 0.433\lambda_r$) and the same wall-normal extent as the PIV domain ($\Delta y = 0.433\lambda_r$). This wall-normal extent ensures the shear magnitude introduced in the extrapolated region is small with respect to that inside the PIV domain for this specific case.

The two-dimensional BiGlobal amplitudes are compared to the (total) r.m.s. of the tomo-PIV experiment in Fig. 8. Due to the expected effect of measurement noise, the near-wall region is cut from the experimental data. The BiGlobal mode is computed at $x_w = 0$, while the experimental contours are extracted at $x_w = 17.55\,[mm] = 2.5\lambda_r$; the measured structures at $x_w = 0$ are too small to have been properly captured. Note that the total r.m.s. data contains all frequency content, while the BiGlobal mode is monochromatic. First of all, the relative velocity component magnitudes are very close. This is unexpected regarding the apparent sensitivity of the relative magnitudes of the local $\tilde{v}$- and $\tilde{w}_w$-profiles compared to $\tilde{u}_w$ in Fig. 6. In addition, the structure of the x_w- and y-components agree well, the largest difference being the spanwise extent. Overall, this clearly indicates that the type I mode is most dominant/amplified at this particular station. The spanwise component shows distinct dissimilarities. An explanation for this could lie in the structure of the most energetic POD mode, reported by Serpieri & Kotsonis; [19] this mode is representative of a relatively low frequency oscillation of the whole primary vortex in the spanwise direction.

The three-dimensional instantaneous x_w-velocity isosurfaces of the BiGlobal mode are compared to those of the POD mode that is representative of the type I mode from the tomo-PIV experiment in Fig. 9. The spatial BiGlobal mode is extrapolated in space, incorporating the calculated spatial growth. Upstream of the $x_w = 0$ station the isosurfaces are absent in the POD mode. This is associated to the limited dynamic range of this particular tomo-PIV experiment. Overall, a qualitative topological match is established between the experimental POD mode and the BiGlobal

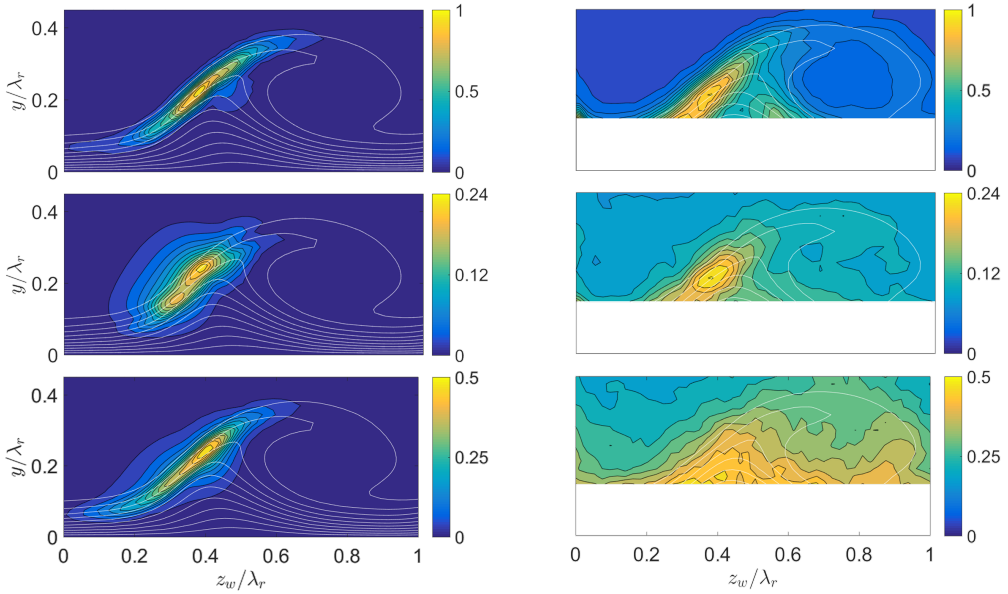

Figure 8: Relative magnitudes of the (top) x_w-, (middle) y- and (bottom) z_w-velocities of (left) the type I spatial BiGlobal mode with $(\alpha\lambda_r; \omega\lambda_r/\overline{U}_e) = (9.506 - 0.1191i; 7.228)$ at $x_w = 0$ and (right) the r.m.s. of the tomo-PIV measurement at $x_w = 17.55\,[mm]$, the region affected by the wall proximity is cut. 15 base flow contours are superposed ranging from 0 to $\overline{U}_e$.

solution. Based on this comparison, it is difficult to conclude whether the linear spatial growth matches with the experiment; further investigations have to be undertaken to pinpoint this.

5. Conclusion

BiGlobal stability theory is applied on an experimentally measured mean flow to resolve secondary instability of swept-wing three-dimensional boundary layers. The treatment is focussed on the type I mode as this is the most dominant. The stability results are found to converge with the ensemble size of the mean tomo-PIV flow. Te treatment of the freestream and, similarly, the near-wall region has negligible effect on the stability results, which is associated to the negligible amplitude of the eigenfunctions in these regions.

Successful validations are performed with the instantaneous tomo-PIV data for the frequency of the POD mode. Comparing the spanwise amplitude distributions, high similarity is observed, despite the apparent sensitivity of the $\tilde{v}$ and $\tilde{w}_w$-profiles. The three-dimensional structures also show good agreement.

These results indicate, at least for this application, that resolving the shear layers associated to the secondary instabilities is sufficient to be able to perform stability analysis. Inherently, this implies that by measuring the primary crossflow vortices to sufficient detail, it is possible to capture the secondary instability via stability analysis.

Usually, stability analysis is performed only on computed base flows.The essential features of the experiment set-up on which the ultimate transition process is critically dependent are captured in the current approach. Therefore, by bringing the stability approach closer to the experiment, making their ever-present relationship more mutual, a better representation and physical understanding can result.

References

[1] J. L. Van Ingen, The e^n-method for transition prediction. historical review of work at tu delft, in: 38th Fluid Dynamics Conference & Exhibit, no. 2008-3830, AIAA, ISBN: 978-1-60086-989-1, Seattle, Washington, 2008.

[2] G. Bonfigli, M. Kloker, Secondary instability of crossflow vortices: validation of the stability theory by direct numerical simulation, Journal of Fluid Mechanics 583 (2007) 229.

[3] H. L. Reed, W. S. Saric, D. Arnal, Linear stability theory applied to boundary layers, Annual Review of Fluid Mechanics 28 (1) (1996) 389–428.

[4] W. S. Saric, H. L. Reed, E. B. White, Stability and Transition of three-dimensional boundary layers, Annual Review of Fluid Mechanics 35 (1) (2003) 413–440.

[5] E. B. E. White, W. W. S. Saric, Secondary instability of crossflow vortices, Journal of Fluid Mechanics 525 (2005) 275–308.

[6] M. R. Malik, F. Li, C.-L. Chang, Crossflow disturbances in three-dimensional boundary layers: nonlinear development, wave interaction and secondary instability, Journal of Fluid Mechanics 268 (-1) (1994) 1.

[7] M. R. M. Malik, F. Li, M. M. M. Choudhari, C.-L. L. Chang, Secondary instability of crossflow vortices and swept-wing boundary-layer transition, Journal of Fluid Mechanics 399 (1999) 85–115.

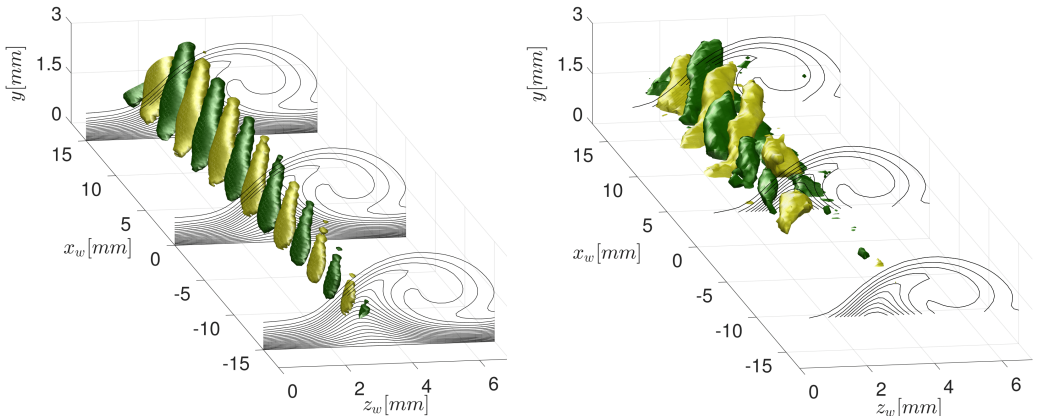

Figure 9: x_w-velocity isosurfaces of (left) the type I spatial BiGlobal mode at the frequency $\omega/2\pi = 5\,[kHz]$ ($\alpha_r = 9.5/\lambda_r$), having maximal amplitude 1 at $x = -17.6\,[mm]$, plotting the ±84% levels, and (right) the tomo-PIV POD mode, plotting the $\pm 0.086\overline{U}_e$ levels, the near-wall region is cut.

[8] Y. Kohama, W. Saric, J. Hoos, A high frequency, secondary instability of crossflow vortices that leads to transition, in: Proc. R. Aeronaut. Soc. Conf. on Boundary-Layer Transition and Control, Cambridge, UK, 1991.

[9] M. Kawakami, Y. Kohama, M. Okutsu, Stability characteristics of stationary crossflow vortices in three-dimensional boundary layer.

[10] H. Bippes, T. Lerche, Transition prediction in three-dimensional boundary-layer flows unstable to crossflow instability, AIAA paper 1906 (1997) 1997.

[11] H. Bippes, Basic experiments on transition in three-dimensional boundary layers dominated by crossflow instability, Progress in aerospace sciences 35 (4) (1999) 363–412.

[12] V. Theofilis, Advances in global linear instability analysis of nonparallel and three-dimensional flows, Progress in Aerospace Sciences 39 (4) (2003) 249–315.

[13] M. Högberg, D. Henningson, Secondary instability of crossflow vortices in falkner–skan–cooke boundary layers, Journal of Fluid Mechanics 368 (1998) 339–357.

[14] W. Koch, F. P. Bertolotti, A. Stolte, S. Hein, Nonlinear equilibrium solutions in a three-dimensional boundary layer and their secondary instability, Journal of fluid mechanics 406 (2000) 131–174.

[15] M. R. Malik, F. Li, C.-L. Chang, Nonlinear Crossflow Disturbances and Secondary Instabilities in Swept-Wing Boundary Layers, Springer Netherlands, Dordrecht, 1996, pp. 257–266.

[16] T. Fischer, U. Dallmann, Primary and secondary stability analysis of a three-dimensional boundary-layer flow, Physics of Fluids A: Fluid Dynamics (1989-1993) 3 (10) (1991) 2378–2391.

[17] K. J. Groot, J. Serpieri, M. Kotsonis, F. Pinna, Secondary stability analysis of crossflow vortices using BiGlobal theory on PIV base flows, AIAA.

[18] K. J. Groot, Q. Ye, B. van Oudheusden, Y. Zhang, F. Pinna, BiGlobal stability analysis of a micro-ramp wake using PIV base flows, AIAA.

[19] J. Serpieri, M. Kotsonis, Three-dimensional organisation of primary and secondary crossflow instability, J. Fluid Mech. 799 (2016) 200–245.

[20] L. Sirovich, Turbulence and the dynamics of coherent structures part i: coherent structures, Quarterly of applied mathematics 45 (3) (1987) 561–571.

[21] F. Scarano, Iterative image deformation methods in piv, Measurement science and technology 13 (1) (2001) R1.

[22] C. Cossu, L. Brandt, On TollmienSchlichting-like waves in streaky boundary layers, European Journal of Mechanics-B/Fluids.

[23] K. J. Groot, F. Pinna, B. W. van Oudheusden, On closing the streamwise biglobal stability problem: the effect of boundary conditions, in: 8th IUTAM-ABCM Symposium on Laminar-Turbulent Transition, Elsevier, Rio de Janeiro, 2014.

[24] F. Pinna, K. J. Groot, Automatic derivation of stability equations in arbitrary coordinates and different flow regimes, in: 44th AIAA Fluid Dynamics Conference, Atlanta, GA, 2014.

[25] F. Pinna, Numerical study of stability of flows from low to high mach number, Ph.D. thesis, Università di Roma-"La Sapienza", Von Kármán Institute, Rhode-Saint-Genèse (2012).

[26] M. R. Malik, Numerical methods for hypersonic boundary layer stability, Journal of Computational Physics 86 (2) (1990) 376–413.

[27] P. G. Drazin, W. H. Reid, Hydrodynamic Stability, Cambridge University Press, New York, ISBN: 978-0521525411, 2004.

[28] D. Arnal, Boundary layer transition: Predictions based on linear theory, in: Special course on Progress in Transition Modelling, no. R-793, AGARD, ISBN: 92-835-0742-8, 1994.

[29] M. Gaster, A note on the relation between temporally-increasing and spatially-increasing disturbances in hydrodynamic stability, Journal of Fluid Mechanics 14 (1962) 222–224.

Multi-species equilibrium and non-equilibrium models for hypersonic boundary-layer stability

Fernado Miró Miró

Aeronautics and Aerospace Department, von Karman Institute for Fluid Dynamics, Belgium, fernando.miro.miro@vki.ac.be

Supervisors: Olivier Chazot and Fabio Pinna

Head of Department, Aeronautics and Aerospace Department, von Karman Institute for Fluid Dynamics, Belgium, chazot@vki.ac.be

Senior Research Engineer, Aeronautics and Aerospace Department, von Karman Institute for Fluid Dynamics, Belgium, fabio.pinna@vki.ac.be

University Supervisor: Gérard Degrez

Professor, École Polytechnique de Bruxelles, Université Libre de Bruxelles, Belgium, gdegrez@ulb.ac.be

Abstract

Boundary-layer transition remains an area limiting the development of hypersonic cruise and entry vehicles. Stability theories aim at predicting transition based on the early development of perturbations in the boundary layer. In this work stability tools are developed to study flows in thermal and chemical non-equilibrium - a common scenario in hypersonic cruise and entry vehicles. The development is error-free, using and extending automatic derivation and implementation tools.

Keywords: Hypersonics, Boundary Layer, Transition, Stability, Thermo-Chemical Non-Equilibrium, Ablation

Nomenclature

Roman Symbols

$\mathcal{A}$	Species name [-]
A	Preexponential reaction rate constant $[(\mathrm{m^3\,mol^{-1}})^{\nu'-1}\,\mathrm{s^{-1}\,K^{-\theta}}]$
$a_\#$	Coefficient in the polynomial expansion of the species enthalpies and Gibbs free energies $[\mathrm{K^{1-\#}}]$
b	Coefficient in the polynomial expansion of the species Gibbs free energies [-]
$\mathscr{D}$	Diffusion coefficient $[\mathrm{m\,s^{-2}}]$
Da	Damköhler number [-]
Da_v	Vibrational-electronic Damköhler number [-]
$\underline{e}^i_j$	i-component of the coordinate system's unit vector in the j direction [-]
E_A	Reaction activation energy $[\mathrm{J\,mol^{-1}}]$
Ec	Eckert number [-]
G	Reaction Gibbs free energy $[\mathrm{J\,mol^{-1}}]$
g	Species Gibbs free energy $[\mathrm{J\,kg^{-1}}]$
h	Total enthalpy $[\mathrm{J\,kg^{-1}}]$
h_v	Vibrational enthalpy $[\mathrm{J\,kg^{-1}}]$
J^i	Mass diffusion fluxes $[\mathrm{kg\,m^{-2}\,s^{-1}}]$
$\mathcal{J}^i$	Energy diffusion fluxes $[\mathrm{J\,m\,s^{-1}}]$
$\mathcal{J}^i_v$	Vibrational energy diffusion fluxes $[\mathrm{J\,m\,s^{-1}}]$
k	Thermal conductivity $[\mathrm{W\,m^{-1}\,K^{-1}}]$
k_b	Backward reaction rate $[(\mathrm{m^3\,mol^{-1}})^{\nu''-1}\,\mathrm{s^{-1}}]$
K_c	Reaction equilibrium constant [-]
k_f	Forward reaction rate $[(\mathrm{m^3\,mol^{-1}})^{\nu'-1}\,\mathrm{s^{-1}}]$

k_{tr} Thermal conductivity due to translational-rotational modes [$\mathrm{W\,m^{-1}\,K^{-1}}$]

k_v Thermal conductivity due to vibrational-electronic modes [$\mathrm{W m^{-1}\,K^{-1}}$]

ℓ_e Blasius length [m]

$\mathscr{M}$ Molar mass [$\mathrm{kg\,mol^{-1}}$]

$\mathcal{M}$ Atomic mass [$\mathrm{kg\,mol^{-1}}$]

N Number of ... [-]

p Pressure [Pa]

Pr Prandtl number [-]

Pr_{tr} Translational-rotational Prandtl number [-]

Pr_v Vibrational-electronic Prandtl number [-]

q Flow variable [various]

Q_{TV} Energy transfer from translational-rotational to vibrational-electronic modes [W]

$\mathscr{R}$ Ideal gas constant (= 8.31447) [$\mathrm{J\,K^{-1}\,mol^{-1}}$]

Re Reynolds number [-]

S Temperature coefficient in Sutherland's formula [K]

Sc Schmidt number [-]

$\mathbb{T}$ Viscous stress tensor [Pa]

T Temperature [K]

t Time [s]

T_v Vibrational temperature [K]

u^i Velocity components [m/s]

X Molar mass fraction [-]

x^i Spatial coordinates [m]

Greek Symbols

α Perturbation wavenumber in the streamwise direction x^1 [$\mathrm{m^{-1}}$]

β Perturbation wavenumber in the homogeneous direction x^3 [$\mathrm{m^{-1}}$]

ϵ Order of magnitude of streamwise derivatives in PSE [various]

ϕ Mixing coefficient in Wilke's rule [-]

θ Temperature exponential reaction rate constant [-]

λ Second viscosity coefficient [$\mathrm{kg\,m^{-1}\,s^{-1}}$]

μ Dynamic viscosity [$\mathrm{kg\,m^{-1}\,s^{-1}}$]

ν' Stoichiometric coefficients for reactants [-]

ν'' Stoichiometric coefficients for products [-]

ρ Density [$\mathrm{kg\,m^{-3}}$]

τ_c Chemical time scale [s]

τ_v Vibrational relaxation time scale [s]

χ Atomic mass fraction [-]

ξ Integration variable for the x^1 direction [m]

$\dot{\omega}_s$ Species source term [$\mathrm{kg\,m^{-3}\,s^{-1}}$]

ω Perturbation frequency [$\mathrm{s^{-1}}$]

Sub- and superscripts

$\overline{q}$ Mean laminar variable

q' Perturbation variable

$\tilde{q}$ Perturbation amplitude

$\hat{q}$ Dimensional quantity

q Non-dimensional quantity

q_e Referred to the boundary-layer edge

q_E, q_F Element quantity

q_n reaction quantity

q_{ref} Reference quantity

q_s, q_ℓ Species quantity

1. Background

The prediction and understanding of boundary-layer transition is a major need in the development and optimisation of hypersonic cruise and entry vehicles. Due to the lack of knowledge still existing on the underlying mechanisms, the design of the vehicle's Thermal Protection System (TPS) is based on experimental correlations. These correlations lack a physicsal understanding, forcing the use of large safety coefficients, and thus reducing the available payload.

The TPS's design will be conditioned by the speeds and heat loads the vehicle will experience, leading to a distinction between ablative and non-ablative TPS [1]. Ablative materials can be used only once, since they protect the payload by evacuating heat through exothermic reactions between the flow and the composite material. These reactions lead first to the pyrolysis of the polymeric matrix, and eventually to the ablation and failure of the fibres, rendering the material unusable [2]. Non-ablative materials are capable of standing the high heat loads without pyrolysing, and are therefore suitable for multiple uses. Fast entry missions featuring high amounts of kinetic energy to be dissipated to the atmosphere, such as those entering Mars, are currently restricted to ablative TPS [3; 4]. Slower entry missions, such as those returning from Low Earth Orbit (LEO), or hypersonic cruise vehicles, do allow the use of non-ablative materials [5]. In them, the amount of energy to be dissipated is lower, and allows for designs without the burning of the TPS.

The modelling of laminar-to-turbulent transition in boundary layers surrounding both types of TPS requires Thermo-Chemical Non-Equilibrium (TCNE) models. This is a consequence of the flow regimes in which they operate, where the characteristic time of the flow is of the same order of magnitude as that of the chemical reactions and the vibrational mode's relaxation [6].

Stuckert [7] and Hudson [8] studied the stability of flat plates in chemical and thermal non-equilibrium regimes using linear stability theory. Li [9] investigated the effect of outgassing on boundary layer stability in perfect gas conditions, observing the rather surprising result that massive outgassing was weakly stabilising. However, these results were not observed in the corresponding experimental investigations [10], leading the authors to speculate that transition in the experiments was caused by mechanisms other than the amplification of the second mode. Johnson [11] looked at the effect of ablation on boundary layer stability by simulating the wall injection of CO_2. Mortensen [12] performed linear stability studies of blunt cones in TCNE with a surface chemistry model to take into account the graphite ablation.

Experimental efforts investigating the effect of ablation on transition have focused on decoupling the outgassing from the surface chemistry and roughness modification induced by ablation. A review of all experimental efforts on ablation-outgassing effects on transition before 2010 can be found in the review by Schneider [13].

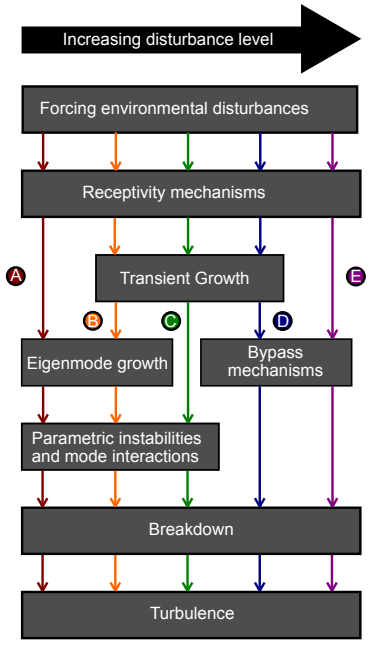

Figure 1: Paths to transition for different disturbance levels. Original by Reshotko [18].

The present work aims at developing thermo-chemical non-equilibrium stability tools to be used in the analysis of ablative flows. It does so by extending the VKI Extensible Stability and Transition Analysis (VESTA) Toolkit [14; 15], and by using highly accurate models for the thermodynamic and transport properties such as those in mutation^{++} [16; 17].

2. Transition modelling

Laminar-to-turbulent transition comprises a series of different mechanisms, which are sketched in Fig. 1. In the first stage, external disturbances enter the boundary layer through a process known as receptivity. These disturbances are then amplified until breakdown and turbulence occur. The amplification stage is strongly dependent on the environmental disturbance level, being possible to distinguish between five paths:

(A) In low-disturbance environments, the most unstable eigenmode will grow exponentially. After reaching a certain amplitude, parametric instabilities will appear and modes will begin to interact with one-another.

(B) For higher disturbance levels, several eigenmodes can have significantly large amplitudes. The superposition of these eigenmodes may dis-

play algebraic transient growth preceding the eigenmode growth.

(C) Even higher disturbance environments will lead to a transient growth that leads directly to parametric instabilities and mode interactions.

(D) When the environment has high disturbance levels, the eigenmode growth and mode interactions are bypassed, leading directly to breakdown.

(E) Very high disturbance levels will produce a bypass of all perturbation growth mechanisms, and will directly produce breakdown.

Further information on the paths to transition can be found in the work of Lees and Reshotko [19].

Boundary-layer stability approaches the study of transition in such a way that the underlying physics prevail. The mathematical treatment consists in decomposing all flow variables into a mean steady laminar component plus a perturbation:

$$q(x^i, t) = \overline{q}(x^i) + q'(x^i, t)\,. \tag{1}$$

Different stability theories will allow to take into consideration some of the aforementioned mechanisms, and will therefore be suitable in different scenarios.

The most extensively studied of these theories is Linear Stability Theory (LST) [20]. In LST, the perturbations are assumed to be significantly smaller than the mean-flow quantities, making possible the discarding of non-linear perturbation terms:

$$q'_1 \cdot q'_2 \approx 0\,. \tag{2}$$

LST also assumes the flow to be parallel, meaning that the mean-flow quantities will only be a function of the wall-normal direction (x^2):

$$\overline{q} = \overline{q}(x^2)\,. \tag{3}$$

Moreover, the perturbation terms will be considered to be periodic in the streamwise and homogeneous directions (x^1 and x^3) and in time, and will have an amplitude term solely dependent on the wall-normal direction:

$$q' = \tilde{q}(x^2) \cdot e^{\alpha x^1 + \beta x^3 - \omega t} + cc.\,, \tag{4}$$

where *cc.* stands for complex conjugate.

Using a more complex set of hypotheses leads to the Parabolic Stability Equations (PSE). PSE assumes an extra degree of freedom on the mean-flow quantities:

$$\overline{q} = \overline{q}(x^1, x^2)\,, \tag{5}$$

and a different ansatz affecting the perturbation terms:

$$q' = \tilde{q}(x^1, x^2) \cdot e^{\int_{x_0^1}^{x^1} \alpha(\xi)\mathrm{d}\xi + \beta x^3 - \omega t} + cc.\,. \tag{6}$$

The physical interpretation is that the flow does not need to be parallel, allowing a weak dependency on the streamwise direction.

Since the dependency on x^1 can be absorbed by both the amplitude or the exponential term, it is necessary to impose a normalization condition on the perturbation amplitude:

$$\int_0^\infty \tilde{q}^* \cdot \frac{\partial \tilde{q}}{\partial x^1} \mathrm{d}x^2 = 0\,. \tag{7}$$

One can see from the previous that it is a set of hypotheses that gives more freedom to the amplitude term. Unlike in LST, in PSE the shape function is let free not only in the wall-normal, but also in the streamwise direction. This is however only a weak dependency, meaning that:

$$\frac{\partial \tilde{q}}{\partial x^1} \sim O(\epsilon) \quad , \quad \frac{\partial \tilde{q}}{\partial x^2} \sim O(1)\,, \tag{8}$$

with $\epsilon << 1$.

Finally in BiGlobal stability analyses [21] the mean-flow variables and perturbation source terms are both assumed dependent on two spatial directions. It is thus possible to distinguish between spanwise (where these two directions define a plane normal to the streamwise) or streamwise BiGlobal (where these two directions are the streamwise and the wall-normal). In both cases, the oscillatory term will model the dependency on the remaining spatial direction and time. The mean-flow-variable dependency and the ansatz for the perturbation quantities for spanwise BiGlobal are therefore:

$$\overline{q} = \overline{q}(x^2, x^3)\,, \tag{9}$$

$$q' = \tilde{q}(x^2, x^3) \cdot e^{\alpha x^1 - \omega t} + cc.\,, \tag{10}$$

whereas for streamwise BiGlobal they are:

$$\overline{q} = \overline{q}(x^1, x^2)\,, \tag{11}$$

$$q' = \tilde{q}(x^1, x^2) \cdot e^{\beta x^3 - \omega t} + cc.\,. \tag{12}$$

Due to the aforementioned set of hypotheses assumed in LST, BiGlobal and PSE, they may be used to analyse the eigenmode growth phase in Fig. 1. Despite this, the modelling is already very acceptable and, coupled with semiempirical methods, such as the e^N [22; 23], allows for a first prediction of transition based on the underlying physics.

More complex stability approaches, such as nonlinear PSE, are capable of also modelling, up to a certain level, the transient growth and mode interactions.

3. Governing equations

Three different flow assumptions are considered and developed in this work: Chemical Equilibrium with element diffusion (CEel), Chemical Non-Equilibrium (CNE) and TCNE. The system equations are expressed in invariant form, such that it enables usage in a broad variety of reference systems.

The superscript/subscript notation refers to contravariant/covariant vectorial variables. A vectorial variable is contravariant q^i when its components vary with the inverse transformation with respect to the basis change, i.e. they "contra-vary". On the other hand, it is covariant q_i if its components vary with the same transformation, i.e. they "co-vary". The metric tensor g_{ij} will allow to keep track, not only of the variable value changes, but also of the modification of the space itself. It is defined as:

$$g_{ij} = \sum_{k=1}^{3} \frac{\partial y^k}{\partial x^i} \frac{\partial y^k}{\partial x^j}, \tag{13}$$

where y^i corresponds to the Cartesian coordinates, and x^i to the curvilinear. For more details on tensorial algebra, see the work of Brillouin [24] and Aris [25].

Also, with this notation, a spatial covariant derivative is expressed with a comma followed by an index corresponding to the spatial direction with respect to which one is deriving: $\partial q^i/\partial x_j = q^i_{,j}$. When dealing with species, element and boundary-layer-edge indices it is common to use also commas separating them. For this reason, the spatial subindices are strictly kept to be i, j & k. Whatever other index appears after a comma will not denote a derivative.

3.1. Non-dimensionalization

In order to allow for a simplified general analysis of the physical phenomena taking place, a non-dimensional formulation is chosen. Throughout this text, hat variables $\hat{q}$ denote dimensional quantities and standard variables q denote non-dimensional quantities. Subindices s or ℓ refer to species quantities and subindices E and F refer to element quantities. The corresponding unknowns are non-dimensionalized the same way as the mixture quantities. Most of the variables are non-dimensionalized with respect to the boundary-layer edge values q_e. The different variables together with their non-dimensionalization references are summarized in table 1, which is an extension of the convention used by Pinna [26].

Variable	Reference
x^i	ℓ_e
t	ℓ_e/U_e
u^i	U_e
T, T_v	T_e
p	$\rho_e U_e^2$
ρ, ρ_s, ρ_E	ρ_e
μ, λ	μ_e
k	k_e
k_{tr}	$k_{tr,e}$
k_v	$k_{v,e}$
$\mathscr{M}, \mathscr{M}_s$	$\mathscr{M}_e$
$\mathcal{M}, \mathcal{M}_s$	$\mathcal{M}_e$
h, h_s, h_v, h_{vs}	h_e
$\mathscr{D}_{s\ell}, \mathcal{D}_s$	$\mathscr{D}_e$
$\dot{\omega}_s$	$\rho_e/\tau_{c,e}$
Q_{TV}	$\rho_e h_e/\tau_{v,e}$

Table 1: Nondimensionalization convention used in VESTA.

ℓ_e is the Blasius length, and it is denoted with the subindex e for consistency with the other quantities, even though it can only be defined from boundary-layer-edge quantities, and to distinguish it from the species subindex ℓ used very often:

$$\ell_e = \sqrt{\frac{\mu_e \hat{x}}{U_e \rho_e}}. \tag{14}$$

$\mathscr{M}_e$ and $\mathcal{M}_e$ are the mixture molar mass and mixture atomic mass at the boundary-layer edge, $\mathscr{D}_e$ is a reference diffusion coefficient, $\tau_{c,e}$ is a reference time scale of the chemical reactions and $\tau_{v,e}$ is a reference vibrational relaxation time.

3.2. Chemical non-equilibrium

The Navier-Stokes equations in CNE will include N_s species-, three momentum- and one energy-conservation equations:

$$\frac{\partial \rho_s}{\partial t} + (u^j \rho_s)_{,j} = -\frac{1}{ReSc} J^j_{s,j} + Da\, \dot{\omega}_s\,, \tag{15}$$

$$\rho \frac{\partial u^i}{\partial t} + \rho u^j u^i_{,j} = -g^{ij} p_{,j} + \frac{1}{Re} \mathbb{T}^{ij}_{,j}, \qquad (16)$$

$$\rho \frac{\partial h}{\partial t} + \rho u^j h_{,j} = Ec \left(\frac{\partial p}{\partial t} + \rho u^j p_{,j} \right) + \frac{1}{RePr} \left(k g^{ij} T_{,i} \right)_{,j} - \\ - \frac{1}{ReSc} \mathcal{J}^j_{,j} + \frac{Ec}{Re} g_{ik} \mathbb{T}^{kj} u^i_{,j}, \qquad (17)$$

where the diffusion mass fluxes of each species J^j_s can be obtained in three different ways: from the exact diffusion coefficients, from the averaged diffusion coefficients, or from a constant Schmidt number. The viscous stress tensor is:

$$\mathbb{T}^{ij} = \lambda g^{ij} u^k_{,k} + \mu \left(g^{jk} u^i_{,k} + g^{ik} u^j_{,k} \right), \qquad (18)$$

and the energy fluxes due to species diffusion are defined as:

$$\mathcal{J}^i = \sum_{s=1}^{N_s} \left(h_s J^i_s \right). \qquad (19)$$

Due to the non-dimensionalization, several non-dimensional reference parameters appear in the equations, such as the Reynolds, the Eckert or the Prandtl number. It is important to point out that these non-dimensional parameters are **reference values**, since they are calculated based on the boundary-layer-edge quantities. Their value within the boundary layer will obviously change. For instance, the Schmidt number ($\mu / \rho \mathscr{D}_{s\ell}$) will not be constant for all species at all locations (unless it is fixed as such). The appearance of these non-dimensional parameters is therefore due to the chosen non-dimensionalization (table 1). If the variables would have been otherwise non-dimensionalized, they could have not appeared. For instance, in the non-dimensionalization followed by Stuckert [27], the diffusion coefficients $\mathscr{D}_{s\ell}$ are non-dimensionalized with μ_∞/ρ_∞, and therefore the Schmidt number does not appear in his equations. This may give the impression that they are therefore unnecessary, but having them allows for a better analysis of the problem's physics, since different phenomena can be associated with different non-dimensional parameters.

3.3. Thermo-chemical equilibrium with element diffusion

Chemical non-equilibrium can become a computationally very expensive assumption, since it requires N_s species equations. This may not be a major issue when studying air chemistry without ionization – five species. However, if there is surface ablation (release of carbon species), or if there is pyrolysis coming from the phenolic resin (release of hydrocarbon species), the number of species needed to model the system, and therefore the number of equations grows very rapidly.

For this reason it is very interesting to use thermo-chemical equilibrium models with element diffusion. In them, since the reactions are in equilibrium in all the domain, it is possible to retrieve the species mass fractions as a function of pressure, temperature and the element fractions $X_s = X_s(p, T, \chi_E)$. Therefore, it is only necessary to solve for the N_E element densities ρ_E, rather than the N_s species densities ρ_E. Since, in general, there are less elements than species, the number of equations needed, and therefore the computational cost, is significantly reduced.

This simplification comes at an obvious price – the effect of chemical non-equilibrium on stability is no longer considered. However, this does not mean that chemical reactions are not considered at all. What is assumed is that they reach equilibrium infinitely fast, i.e. $\tau_c >> \tau_{flow} = \ell_e / U_e$.

Summing over the species conservation equations multiplied by the elemental coefficient $E_{E,s}$ (the number of atoms of each element in each species) one reaches the element conservation equation:

$$\frac{\partial \rho_E}{\partial t} + (u^i \rho_E)_{,i} = \frac{1}{ReSc} J^j_{E,j}. \qquad (20)$$

The form of the momentum- and energy-conservation equations (Eq. 16 and 17) will be the same as for CNE, the only difference will be the expression of the diffusion energy fluxes $\mathcal{J}$.

3.4. Thermo-chemical non-equilibrium

Depending on the temperature ranges of interest, considering the flow to be modelled exclusively by one temperature may not be enough. Fig. 2 shows that after a certain temperature, the vibrational energy modes of the molecules in air start to be excited. This motivates the use of multi-temperature models, where the behaviour of the different energy modes are packed into groups, being each group modelled by one temperature.

A two-temperature model is explored here, with a translational-rotational temperature T and a vibrational-electronic-electron temperature T_v. In the case of ionization, the contribution of the electron species will be absorbed by T_v, which is why it is

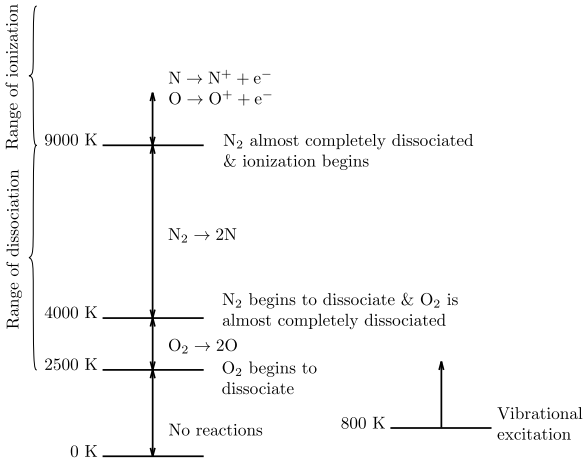

Figure 2: Temperature ranges of vibrational excitation, dissociation and ionization for air at 1-atm pressure. Original by Anderson [28].

called vibrational-electronic-*electron*. Nevertheless, for simplicity, they will hereafter be referred to as the temperature and vibrational temperature respectively.

In this two-temperature model, the species- and momentum-conservation equations will remain the same as those for CNE (Eqs. 15 and 16). Having two temperatures will only affect the way in which the dependent quantities appearing in them are computed. However, the energy-conservation equation will change:

$$\rho\frac{\partial h}{\partial t}+\rho u^j h_{,j}=Ec\left(\frac{\partial p}{\partial t}+\rho u^j p_{,j}\right)+\frac{1}{RePr_{tr}}\left(k_{tr}g^{ij}T_{,i}\right)_{,j}+ \\ +\frac{1}{RePr_v}\left(k_v g^{ij}T_{v,i}\right)_{,j}-\frac{1}{ReSc}\mathcal{J}^j_{,j}+\frac{Ec}{Re}\,g_{ik}\mathbb{T}^{kj}u^i_{,j}\,. \tag{21}$$

The main difference with respect to its CNE counterpart is that the thermal conductive heat fluxes are decomposed into the contributions of the two temperatures. This also motivates the introduction of two Prandtl numbers (Pr_{tr} and Pr_v), based on each of the thermal conductivities (k_{tr} and k_v respectively). The expressions of the mass and energy heat fluxes (J^j_s and $\mathcal{J}^j$) appearing in the species- and energy-conservation equations will also change in this two-temperature model.

Finally, an additional equation must be introduced to account for the vibrational temperature – the vibrational-electronic-electron-energy-conservation equation (for simplicity hereafter referred to as the vibrational-energy-conservation equation):

$$\rho\frac{\partial h_v}{\partial t}+\rho u^j h_{v,j}=\frac{1}{RePr_v}\left(k_v g^{ij}T_{v,i}\right)_{,j}-\frac{1}{ReSc}\mathcal{J}^j_{v,j}+ \\ +Da_v\,Q_{TV}+\sum_{s=1}^{N_s}Da\,\dot{\omega}_s\,h_{vs}\,, \tag{22}$$

where Q_{TV} is the energy flux between translational-rotational and vibrational-electronic modes, and $\mathcal{J}_v$ is the diffusion vibrational energy flux – defined analogously to the diffusion energy flux $\mathcal{J}$:

$$\mathcal{J}^i_v=\sum_{s=1}^{N_s}\left(h_{vs}J^i_s\right). \tag{23}$$

3.5. Boundary conditions

The same way in which a set of boundary conditions is imposed on the mean flow variables $\overline{q}$, they also need to be defined for the perturbation amplitude terms $\tilde{q}$. Traditionally [26], Calorically Perfect Gas (CPG) stability analyses fix all perturbations to zero, both at the wall and in the freestream, except for the pressure perturbation, which does not necessarily have to be zero. To account for these two extra variables ($\tilde{p}(0)$ and $\tilde{p}(x^2_{max})$), the wall-normal-momentum-conservation equation is evaluated at the wall and in the freestream, and used as a compatibility condition.

In the present multi-species/multi-element approach, the pressure is no longer an independent variable – it is depending on the species densities and the temperatures. It is reasonable to assume the temperature perturbation to be equal to zero at the wall. It is trivial that this is the case for an isothermal wall, whereas for an adiabatic wall its thermal inertia is so big that its temperature perturbations are negligible [29]. Therefore, in order to maintain the pressure perturbation different than zero, the species density perturbations at the wall cannot be zero.

Their boundary condition is obtained by imposing a non-catalytic condition at the wall:

$$\underline{e}^i_2\left(\frac{\rho_s}{\rho}\right)_{,i}=0\,. \tag{24}$$

Note that this expression is valid for whatever coordinate system, since it includes the unit vector in the wall-normal direction $\underline{e}^i_2$.

In order to preserve the system's global mass continuity, this non-homogeneous wall boundary condition must have a counterpart in the freestream boundary. For this reason, the velocity perturbation is assumed

different than zero ($\tilde{v}(x^2_{max}) \neq 0$), obtaining it from imposing the global continuity equation:

$$\frac{\partial \rho}{\partial t} + (\rho\, u^i)_{,i} = 0\,, \tag{25}$$

in the freestream boundary.

Following the same idea used for CPG stability codes, another set of boundary conditions is proposed, consisting in imposing each species-conservation equation (Eq. 15) both at the wall and in the freestream. This approach is more consistent with the way in which the pressure-perturbation boundary conditions are obtained in classic stability codes [26].

The ablation-specific boundary conditions – the surface chemistry models, are still to be developed. However, they will be very similar to those used by Mortensen [30].

Note that these boundary equations are expressed as a function of the total quantities. The same linearisation process followed by the flow equations, which will depend on the stability theory as described in section 2, will have to be applied to these in order to obtain the stability boundary equations.

3.6. Thermodynamic and transport properties

Within the system equations, it is possible to distinguish between dependent and independent variables. A set of independent variables is such that it has the minimum number of variables giving the system of partial differential equations closure. In CNE for instance, a valid set of independent variables would be the three velocity components u^i, the N_s species densities ρ_s and the temperature T. All other variables (viscosity μ, pressure p, enthalpy h, etc.) may be obtained from them, and are therefore referred to as dependent variables.

Two ways of computing these dependent variables are available in VESTA: from the coupling with mutation^{++} [17], and from a set of analytical expressions implemented into VESTA. It currently counts only with a built-in CNE model with constant-Schmidt-number diffusion, but it is being extended to TCNE. The expressions used to retrieve each of the dependent variables of interest are:

- Mixture density – adding over the different species densities:

$$\hat{\rho} = \sum_{s=1}^{N_s} \hat{\rho}_s\,. \tag{26}$$

- Pressure – assuming a mixture of ideal gases:

$$\hat{p} = \hat{\mathscr{R}}\,\hat{T} \sum_{s=1}^{N_s} \frac{\hat{\rho}_s}{\hat{\mathscr{M}}_s} = \hat{\rho}\,\frac{\hat{\mathscr{R}}}{\hat{\mathscr{M}}}\,\hat{T}\,. \tag{27}$$

- Species enthalpies – polynomial expansion:

$$\hat{h}_s = \frac{\hat{\mathscr{R}}}{\hat{\mathscr{M}}_s} \cdot \left(\hat{a}_{0,s} + \hat{a}_{1,s}\hat{T} + \hat{a}_{2,s}\frac{\hat{T}^2}{2} + \right. \\ \left. + \hat{a}_{3,s}\frac{\hat{T}^3}{3} + \hat{a}_{4,s}\frac{\hat{T}^4}{4} + \hat{a}_{5,s}\frac{\hat{T}^5}{5}\right). \tag{28}$$

- Mixture enthalpy – the sum over the species enthalpies weighed by the species mass fraction:

$$\hat{h} = \sum_{s=1}^{N_s} \hat{h}_s\,\frac{\hat{\rho}_s}{\hat{\rho}}\,. \tag{29}$$

- Mixture molar mass – by definition:

$$\mathscr{M} = \Big(\sum_{s=1}^{N_s} \frac{1}{\mathscr{M}_s}\,\frac{\rho_s}{\rho}\Big)^{-1}. \tag{30}$$

- Mixture viscosity – using Wilke's mixing rule [31] on the species viscosities:

$$\hat{\mu} = \sum_{s=1}^{N_s} \frac{X_s\,\hat{\mu}_s}{\sum_{\ell=1}^{N_s} X_\ell\,\phi_{s,\ell}}\,, \tag{31}$$

where each species viscosity is obtained from Sutherland's law:

$$\hat{\mu}_s = \hat{\mu}_{ref,s}\left(\frac{\hat{T}}{\hat{T}_{ref,s}}\right)^{1.5}\,\frac{\hat{T}_{ref,s} + \hat{S}_{\mu,s}}{\hat{T} + \hat{S}_{\mu,s}}\,, \tag{32}$$

and where the mixing coefficient is:

$$\phi_{s,\ell} = \frac{\left(1 + \left(\frac{\hat{\mu}_s}{\hat{\mu}_\ell}\right)^{1/2}\left(\frac{\hat{\mathscr{M}}_\ell}{\hat{\mathscr{M}}_s}\right)^{1/4}\right)^2}{\left(8\left(1 + \frac{\hat{\mathscr{M}}_s}{\hat{\mathscr{M}}_\ell}\right)\right)^{1/2}}\,. \tag{33}$$

- Thermal conductivity – analogous to that of the dynamic viscosity.

- Species source terms for a set of N_r chemical reactions of the form:

$$\sum_{s=1}^{N_s} \nu'_{sn}\,\mathscr{A}_s \leftrightarrow \sum_{s=1}^{N_s} \nu''_{sn}\,\mathscr{A}_s \qquad \forall n \in N_r\,, \tag{34}$$

are obtained from:

$$\hat{\dot{\omega}}_s = \hat{\mathscr{M}}_s \sum_{n=1}^{N_r} (\nu''_{sn} - \nu'_{sn}) \left(\hat{k}_{f,n} \prod_{s=1}^{N_s} \left(\frac{\hat{\rho}_s}{\hat{\mathscr{M}}_s} \right)^{\nu'_{ns}} - \right.$$
$$\left. - \hat{k}_{b,n} \prod_{s=1}^{N_s} \left(\frac{\hat{\rho}_s}{\hat{\mathscr{M}}_s} \right)^{\nu''_{ns}} \right), \quad (35)$$

with the forward and backward reaction rates defined as:

$$\hat{k}_{f,n} = \hat{A}_n \, \hat{T}^{\theta_n} \, e^{-\frac{\hat{E}_{A,n}}{\hat{\mathscr{R}} \hat{T}}}, \quad (36)$$

$$\hat{k}_{b,n} = \frac{\hat{k}_{f,n}}{\hat{K}_{C,n}}, \quad (37)$$

and equilibrium constant being:

$$\hat{K}_{C,n} = \left(\frac{\hat{p}_{atm}}{\hat{\mathscr{R}} \hat{T}} \right)^{\sum_{s=1}^{N_s} (\nu''_{sn} - \nu'_{sn})} e^{-\frac{\Delta \hat{G}_n}{\hat{\mathscr{R}} \hat{T}}}, \quad (38)$$

where the Gibbs free energy of each reaction n is:

$$\Delta G_n = \sum_{s=1}^{N_s} (\nu''_{sn} - \nu'_{sn}) \, \hat{\mathscr{M}}_s \, \hat{g}_s \quad (39)$$

and the species Gibbs free energies also come from a polynomial expression similar to that for the species enthalpies:

$$\hat{g}_s = \frac{\hat{\mathscr{R}}}{\hat{\mathscr{M}}_s} \left(\hat{a}_{0,s} + \hat{a}_{1,s} (\hat{T} - \log \hat{T}) - \hat{a}_{2,s} \frac{\hat{T}^2}{2} - \right.$$
$$\left. - \hat{a}_{3,s} \frac{\hat{T}^3}{6} - \hat{a}_{4,s} \frac{\hat{T}^4}{12} - \hat{a}_{5,s} \frac{\hat{T}^5}{20} - \hat{b}_s \hat{T} \right) \quad (40)$$

For information on what each of these terms represent please refer to the initial nomenclature.

Note that all these expressions are in dimensional form ($\hat{q}$).

4. Methodology

4.1. Automatic Derivation and Implementation Tool

In order to develop the required stability solvers, VESTA's Automatic Derivation and Implementation Tool (ADIT) [14] is extended and used. The ADIT is a collection of functions in Maxima and Matlab that effectively pass from the Navier-Stokes equations to functions building the necessary system matrices for stability analyses free of errors.

The derivation tool operates symbolically with the system's equations for a variety of flow assumptions, and coordinate systems, applying the necessary hypotheses corresponding to the different stability theories. It currently allows for solvers to be generated for incompressible, compressible, Local-Thermodynamic-Equilibrium (LTE), CEel, CNE and TCNE flow assumptions. It also features a range of coordinates systems (3D-cartesian, polar-cylindrical, spherical and six ortho-curvilinear systems), and three stability theories (LST, PSE and BiG).

Once the stability equations are derived, the implementation tool translates the symbolical expressions into a script to be used to build the system's matrices with the required boundary conditions. This implementation tool has been extended in such a way that it is completely transparent to the set of equations and variables that it receives from the derivation tool.

4.2. Derivatives of the dependent variables

Multi-species stability codes require the computation of, not only the mean-flow dependent variables, but also their derivatives up to the third order with respect to the independent variables they depend on. This is due to two mathematical artefacts appearing in the derivation of the stability equations. Firstly, there is the appearance of second-order spatial derivatives in the diffusion terms. When applying the chain rule, these spatial derivatives are passed to the independent variables, and bring up second-order derivatives of the dependent variables with respect to the independent. This can be easily exemplified by taking the mean-flow species enthalpy $\overline{h}_s$ – a dependent variable depending only on the temperature:

$$\frac{\partial \overline{h}_s}{\partial x^i} = \frac{\partial \overline{h}_s}{\partial \overline{T}} \frac{\partial \overline{T}}{\partial x^i}$$
$$\frac{\partial^2 \overline{h}_s}{\partial x^{i\,2}} = \frac{\partial^2 \overline{h}_s}{\partial \overline{T}^2} \left(\frac{\partial \overline{T}}{\partial x^i} \right)^2 + \frac{\partial \overline{h}_s}{\partial \overline{T}} \frac{\partial^2 \overline{T}}{\partial x^{i\,2}}$$

Secondly, due to the expansion around zero of the perturbation terms of dependent variables, an additional derivative will appear. Taking the same example, and bearing in mind that due to the stability hypotheses (section 2) $h_s = \overline{h}_s + h'_s$, with $h'_s << \overline{h}_s$:

$$h'_s = \frac{\partial \overline{h}_s}{\partial \overline{T}} T'$$

Therefore, second-order spatial derivatives of perturbation dependent variables will lead to third-order

derivatives of mean dependent variables with respect to the independent. For the same example:

$$\frac{\partial^2 h_s'}{\partial x^{i\,2}} = \frac{\partial^3 \overline{h}_s}{\partial \overline{T}^3}\left(\frac{\partial \overline{T}}{\partial x^i}\right)^2 T' + \frac{\partial^2 \overline{h}_s}{\partial \overline{T}^2}\frac{\partial^2 \overline{T}}{\partial x^{i\,2}} T' + \\ + \frac{\partial^2 \overline{h}_s}{\partial \overline{T}^2}\frac{\partial \overline{T}}{\partial x^i}\frac{\partial T'}{\partial x^i} + \frac{\partial^2 \overline{h}_s}{\partial \overline{T}^2}\frac{\partial \overline{T}}{\partial x^i}\frac{\partial T'}{\partial x^i} + \\ + \frac{\partial \overline{h}_s}{\partial \overline{T}}\frac{\partial^2 T'}{\partial x^{i\,2}}$$

Note that this is a very simple case, since the species enthalpy only depends on one independent variable. For variables such as the diffusion coefficients or the viscosity, which depend on the temperature(s) and on the N_s species densities, the number of terms of such an expansion grows exponentially. This is yet another proof of the advantages of the ADIT, which carries out all this derivation free of the more-than-likely human error.

These third-order derivatives are not directly obtainable from mutation^{++}, motivating the usage of a forward finite-difference method to approximate them numerically. However this increases significantly the number of points for which mutation^{++} must be run. For an air-5 mixture in CNE, every spatial point requires of 86 computational points in order to approximate all these derivatives. For a 16-species mixture such as that used by Mortensen [12] to study ablation in TCNE, this number rises to 1330.

The main advantage of the analytical expressions built into VESTA, is that they also offer all the necessary analytical derivatives with respect to independent variables. This is done through a module of the ADIT that can obtain the analytical derivatives of the expressions in section 3.6, and then automatically generate functions to compute them from the independent variables' fields and the required tabulated values and constants.

5. Preliminary results

As a preliminary step towards the verification of the multi-species LST tools against the work of Stuckert [7] and Hudson [8], simulations have been run for the same conditions (table 2) but for CPG and LTE. Fig. 3 compares the non-dimensional perturbation growth rates (α_i) as a function of the non-dimensional perturbation frequency ω for the different literature cases and with VESTA. The agreement is well within the expected numerical error.

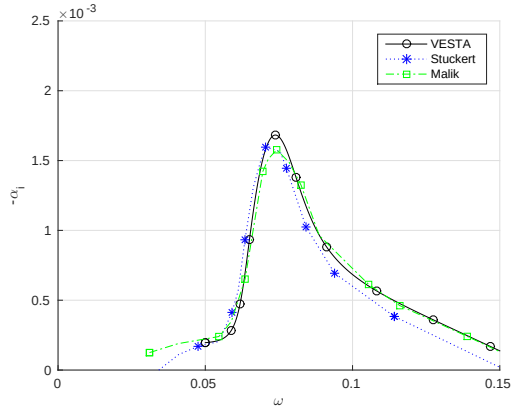

(a) CPG

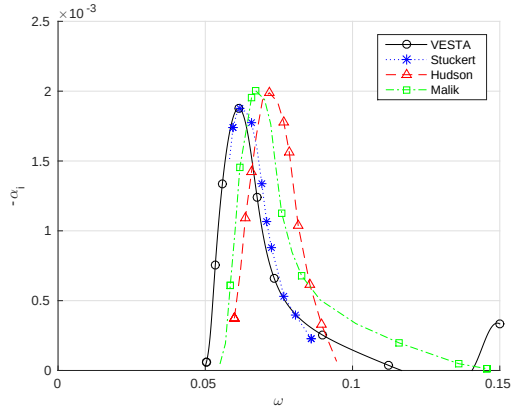

(b) LTE

Figure 3: Maximum amplification rate comparison against Stuckert [7], Hudson [8] and Malik [32] for different flow assumptions and for the conditions in table 2.

6. Conclusions

Stability models have been developed for CEel, CNE and TCNE flows, using VESTA's ADIT to carry out the process error-free.

The system's equations are expressed in their invariant form, such they are valid in all reference systems. They are also in non-dimensional form, such that non-dimensional reference parameters appear and allow for a quantification of the relative importance of the different physical phenomena.

Two different sets of boundary conditions are proposed for the perturbation terms – a set of non-catalytic conditions, such as those used by Stuckert [7], Hudson [8] and Mortensen [30], and a set of compatibility conditions, similar to those used in classic stability models [26].

M_∞	Re_1 (1/m)	$\hat{T}_\infty$ (K)	wall b.c.	$X_{N_2,\infty}$	$X_{O_2,\infty}$
10	9.8425×10^6	278	adiabatic	0.767	0.233

Table 2: Flow conditions for all simulations.

Two different ways of computing the mean dependent variables and their derivatives with respect to independent variables are developed – coupling VESTA with mutation^{++} and approximating the derivatives with a forward finite-difference method, or using VESTA's built-in analytical expressions and derivatives.

Preliminary results show a good agreement between the literature and VESTA's CPG and LTE solvers. VESTA's CNE and TCNE solvers remain in the verification/validation phase.

Acknowledgements

This research is made possible thanks to the financial support provided by the Fonds de la Recherche Scientifique through their FRIA fellowship program.

References

[1] B. Laub, E. Venkatapathy, Thermal protection system technology and facility needs for demanding future planetary missions, Proceedings of the International Workshop Planetary Probe Atmospheric Entry and Descent Trajectory Analysis and Science, Lisbon, Portugal.

[2] F. S. Milos, Y. K. Chen, Ablation, thermal response, and chemistry program for analysis of thermal protection systems, Journal of Spacecraft and Rockets 50 (1).

[3] J. M. Bouilly, F. Bonnefond, L. Dariol, P. Jullien, F. Leleu, Ablative thermal protection systems for entry in mars atmosphere. a presentation of materials solutions and testing capabilities, 4th International Planetary Probe Workshop, Pasadena California.

[4] E. Venkatapathy, C. E. Szalai, B. Laub, H. H. Hwang, J. L. Conley, J. Arnold, . Co-authors, Thermal protection system technologies for enabling future sample return missions, NASA, White Paper to the NRC Decadal Primitive Bodies Sub-Panel, Washington DC.

[5] Y. Liu, Z. Jiang, Concept of non-ablative thermal protection system for hypersonic vehicles, AIAA Journal 51 (3).

[6] J. D. Anderson, Modern Compressible Flow with Historical Perspective (2nd edition), McGraw Hill, 2003.

[7] G. K. Stuckert, H. L. Reed, Linear disturbances in hypersonic, chemically reacting viscous flows, AIAA Journal 32 (7).

[8] M. Hudson, N. Chokani, G. Chandler, Linear stability of hypersonic flow in thermochemical nonequilibrium, AIAA Journal 35 (6) (1997) 958–964.

[9] F. Li, M. Choudhari, C.-L. Chang, J. White, Effects of injection on the instability of boundary layers over hypersonic configurations, Physics of Fluids 25.

[10] J. G. Marvin, C. M. Akin, Combined effects of mass addition and nose bluntness on boundary-layer transition, American Institute of Aeronautics and Astronautics 8 (1970) 857–863.

[11] H. B. Johnson, J. E. Gronvall, G. V. Chandler, Reacting hypersonic boundary layer stability with blowing and suction, 47th AIAA Aerospace Sciences meeting.

[12] C. H. Mortensen, X. Zhong, Numerical simulation of graphite ablation induced outgassing effects on hypersonic boundary layer receptivity over a cone frustum, 51st AIAA Aerospace Sciences Meeting.

[13] S. P. Schneider, Hypersonic boundary-layer transition with ablation and blowing, Journal of Spacecraft and Rockets 47 (2010) 225–237.

[14] F. Pinna, K. Groot, Automatic derivation of stability equations in arbitrary coordinates and for different flow regimes, 44th AIAA Fluid Dynamics Conference, Atlanta.

[15] F. Pinna, VESTA toolkit: a software to compute transition and stability of boundary layers, 43rd AIAA Fluid Dynamics Conference, San Diego, California.

[16] T. E. Magin, G. Degrez, Transport of partially ionized and unmagnetized plasmas, Journal of Computational Physics 198 (2).

[17] J. B. Scoggins, T. E. Magin, Development of mutation++: Multicomponent thermodynamic and transport properties for ionized plasmas written in c++, 11th AIAA/ASME Joint Thermophysics and Heat Transfer Conference. number AIAA 2014-2966.

[18] E. Reshotko, Paths to transition in wall layers, in: Advances in laminar-turbulent transition modeling, von Karman Institute for Fluid Dynamics, 2008.

[19] L. Lees, E. Reshotko, Stability of the compressible laminar boundary layer, Journal of Fluid Mechanics 12 (4) (1962) 555–590.

[20] D. Arnal, Boundary layer transition: Predictions based on linear theory, Tech. Rep. 793, AGARD, VKI, Brussels (1993).

[21] V. Theofilis, Advances in global linear instability analysis of nonparallel and three-dimensional flows, Progress in Aerospace Sciences 39 (4) (2003) 249–315.

[22] A. M. O. Smith, N. Gamberoni, Transition, pressure gradient and stability theory, Tech. Rep. ES 26388, Douglas Aircraft Co., El Segundo, California (1956).

[23] J. L. van Ingen, A suggested semi-empirical method for the calculation of the boundary layer transition region, Tech. Rep. VTH-74, Univ. of Delft. Dept. Aerospace Engineering, Delft, the Netherlands (1956).

[24] L. Brillouin, Tensors in Mechanics and Elasticity, Academic Press, 1964.

[25] R. Aris, Vectors, Tensors and the Basic Equations of Fluid Mechanics, Dover - Prentice Hall, 1962.

[26] F. Pinna, Numerical study of stability flows from low to high mach number, Ph.D. thesis, von Kármán Institute for Fluid Dynamics and Universitá "La Sapienza" di Roma (2012).

[27] G. K. Stuckert, Linear stability theory of hypersonic, chemically reacting viscous flows, Ph.D. thesis, Arizona State University (1991).

[28] J. D. Anderson, Hypersonic and High-Temperature Gas Dynamics, AIAA Education, 2002.

[29] L. M. Mack, Boundary Layer Stability Theory, Jet Propulsion Laboratory, California Institute of Technology, Pasadena, California, 1969.

[30] C. Mortensen, Effect of thermochemical nonequilibrium on hypersonic boundary-layer instability in the presence of surface ablation or isolated two-dimensional roughness, Ph.D. thesis, University of California Los Angeles (2015).
[31] C. Wilke, A viscosity equation for gas mixtures, The Journal of Chemical Physics 18 (4).
[32] M. R. Malik, Transition in hypersonic boundary layers, Fourth Symposium on Numerical and Physical Aspects of Aerodynamics Flows, California State University, Long Beach, CA.

Blackout analysis of reentry vehicles for Martian missions

Sahadeo Ramjatan

Aeronautics and Aerospace Department, von Karman Institute for Fluid Dynamics, Belgium, sahadeo.ramjatan@vki.ac.be

Supervisor: Thierry Magin

Assistant Professor, Aeronautics and Aerospace Department, von Karman Institute for Fluid Dynamics, Belgium, magin@vki.ac.be

Co-Supervisor: Jan Thoemel

Managing Scientist, Belgium Institute for Space Aeronomy, jan.thoemel@aeronomie.be

University Supervisor: David Hahn

Professor and Department Chair, Mechanical and Aerospace Engineering, University of Florida, United States, dwhahn@ufl.edu

Abstract

The spacecraft atmospheric reentry process is one of the most challenging aspects of the design phase for space missions. Due to Martian reentry flight conditions, high velocities approximately on the order of 5-8 km/s imply strong shock waves and extreme aerodynamic heating of the vehicle. These high temperatures lead to an increase in collisions of the molecules, that result in the disruption of the electronic structure producing free electrons and ions. This production of electrons and ions creates a region of ionized flow or plasma around the vehicle that attenuates the radio frequency signal from the spacecraft, and transmission is only possible at radio frequencies greater than the characteristic plasma frequency. During blackout, vehicles cannot receive guidance or maneuvering information from a control center and cannot transmit signals that would enable monitoring of the flight trajectory. As a result, radio blackout is a potential mission killer since loss of communication with the spacecraft results in high risk for the crew or success of a mission. Current blackout prediction methods can be improved by an enhanced understanding of the flow physics, which is a highly interdisciplinary problem involving non-equilibrium gas physics, electromagnetic wave analysis, and plasma physics. For example, radio signals are bent by electron density gradients in the flow field thereby affecting radar and radio communication systems. This research aims to perform a comprehensive modeling of blackout by accounting for electron-heavy particle collisions, the plasma frequency, and their effects on a ray-tracing model. This will provide a more realistic estimate of the blackout period during the reentry phase of future space missions. Therefore, the objectives of this research is to implement and apply tools for predicting blackout duration and validating these tools on data from previous space missions. Lastly, a flight experiment will be designed to measure the electron concentration during reentry. The methodology in performing this research will involve generating maps of the plasma distribution and collision frequencies around the reentry vehicle by non-equilibrium hypersonic CFD simulations and subsequently involve examining the electromagnetic wave interactions with the plasma. The electromagnetic wave propagation through the plasma will be investigated using Appleton theory accounting for the plasma frequency, collision frequency, refraction index, and the absorption coefficient. In addition, the propagation of the field radiated by the antenna through the plasma will be modeled using ray tracing. Previous research performed at the Von Karman Institute for Fluid Dynamics (VKI) involved using the plasma cut-off frequency to assess the blackout period for small cone-shaped reentry vehicles. Current research efforts involve examining the radio blackout of ESA's recent ExoMars mission, which involves the coupling of the VKI's MUTATION++ library for reacting flows to the COOLFLuiD CFD code.

Keywords: radio blackout, reentry, hypersonic flight

Mathematical modeling and simulation of non-equilibrium plasmas for the prediction of magnetic reconnection: application to the solar atmosphere

Quentin WARGNIER

Ecole Centrale-Supelec, France, quentin.wargnier@vki.ac.be

Supervisor: Marc MASSOT

Professor, Laboratoire EM2C, Ecole CentraleSupelec, France, marc.massot@ecp.fr

Supervisor: Thierry MAGIN

Aeronautics and Aerospace Department, von Karman Institute for Fluid Dynamics, Belgium, thierry.magin@vki.ac.be

Abstract

The ability to model, simulate and predict magnetic reconnection (MR) is a stumbling block in order to predict space weather and geomagnetic storms, which can lead to great perturbation of satellites. Some fundamental aspects of MR are not yet well understood. The scientific issue at stake is the proper description of the unsteady energy transfer from magnetic energy to kinetic and thermal energy, which is still out of reach for the standard Magneto-hydrodynamics (MHD) models. The first objective of the present project is to develop a coherent fluid model for magnetized plasmas out of thermal and chemical equilibrium with a detailed description of the dissipative effects based on kinetic theory of gases, which thus inherits a proper mathematical structure. The second goal is the development of a new numerical strategy, with high accuracy and robustness, based on a massively parallel code with adaptive mesh refinement able to cope with the full spectrum of scales of the model and related stiffness. The whole set of transport coefficients, thermodynamics relations and chemical rates in this magnetized two-temperature setting will be studied and compared to the one in the literature used in the field. Then, we will show that the model and related numerical strategy, obtained from this transdisciplinary work involving engineering, plasma physics, solar physics, mathematics, scientific computing and HPC, is able to properly reproduce the physics of MR. The validation of the approach through a series of test-cases relevant for the application to the dynamics of solar atmosphere in connection with VKI and NASA will provide a tool, open to the community, capable of resolving several critical scientific and technological issues.

Numerical study of chemically reacting hypersonic boundary layers by means of Nonlinear Parabolized Stability Equations

Ludovico Zanus

Aeronautics and Aerospace Department, von Karman Institute for Fluid Dynamics, Belgium, ludovico.zanus@vki.ac.be

Supervisors: Olivier Chazot and Fabio Pinna

Professor, Head of Aeronautics and Aerospace Department, von Karman Institute for Fluid Dynamics, Belgium, chazot@vki.ac.be

Senior Research Engineer, Aeronautics and Aerospace Department, von Karman Institute for Fluid Dynamics, Belgium, pinna@vki.ac.be

University Supervisor: Gérard Degrez

Professor, Dean of the École polytechnique de Bruxelles - ULB, Université Libre de Bruxelles , Belgium, Gerard.Degrez@ulb.ac.be

Abstract

The study of stability and laminar-turbulent transition is one of the most relevant problems in fluid dynamics. Accurate predictions of the transition location have a fundamental importance in many applications, being directly related to trustworthy heat flux and skin friction estimations. This is a particularly delicate aspect when related to hypersonic flows, where the physics complexity and the lack of experiments often lead to large uncertainty design margins. The common and widely used e^N method based on Linear Stability Theory (LST) results presents some limitations related to the local assumption underlying this theory. These deficiencies can be overcome by using the so called Nonlinear Parabolized Stability Equations (NPSE) technique. In this way, the streamwise development of the instability can be captured and effects like nonparallelism and curvature can be taken into account. Moreover and most importantly, by considering physical nonlinearities the analysis can be conducted up to the final stages of the transition process, thus determining with a quite good accuracy the turbulence onset. The goal of this project is to study the stability and predict transition of a realistic hypersonic flow such the one faced by space vehicles during an atmospheric re-entry or by future high speed spaceplanes. In order to have an accurate and reliable description of the investigated phenomenon high temperature gas effects have to be taken into account, such for example Thermo-Chemical Non-Equilibrium conditions (TCNEQ). The NPSE method in TCNEQ will be developed inside the framework of the VKI Extensible Stability and Transition Analysis (VESTA) toolkit. The results obtained by the numerical investigation will be compared against the in-flight data collected by the re-enty Intermediate eXperimental Vehicle (IXV), developed by a partnership of European countries and launched by ESA in 2015. This project may exploit the IXV data and provide new knowledge on similar applications.

Keywords: Hypersonic stability, transition, Parabolized Stability Equations, Thermo-Chemical Non-Equilibrium, atmospheric re-entry

GROUND AND FLIGHT EXPERIMENTS

Review of test conditions in the VKI Longshot gun tunnel for hypersonic transition experiments

Zdeněk Ilich

Aeronautics and Aerospace Department, von Karman Institute for Fluid Dynamics, Belgium, zdenek.ilich@vki.ac.be

Supervisor: Olivier Chazot

Professor, Aeronautics and Aerospace Department, von Karman Institute for Fluid Dynamics, Belgium, chazot@vki.ac.be

University Supervisor: Herbert Olivier

Professor, Shock Wave Laboratory, RWTH Aachen University, Germany, olivier@swl.rwth-aachen.de

Abstract

This paper presents the last research activities related to an improvement of the test conditions in the VKI Longshot facility in the framework of a design of transition experiments. Three main points are reviewed, namely the effective operation of the facility, determination of free-stream conditions, and assessment of disturbance levels. Specifically, experimental and numerical work resulting in a reliable operational map of the facility is presented. Regarding free-stream conditions, the most appropriate formula for the velocity gradient at the stagnation point needed to rebuild free-stream flow properties is identified thereby reducing uncertainties on the flow characterization of the tunnel. Drawn conclusions are supported by independent experimental measurements. Moreover, a design of new free-stream probes is introduced.

Keywords: Hypersonic, Longshot, test conditions

Nomenclature

Symbols

h	specific enthalpy, J/kg
$\bar{h}$	reduced enthalpy, $\bar{h} = h/(rT_{ref})$, $T_{ref} = 273.15$ K
M	Mach number
p	pressure, Pa
Pr	Prandtl number
$\dot{q}$	heat flux, W/m^2
R_N	nosetip radius, m
Re	Reynolds number
T	temperature, K
u	velocity, m/s
y	distance along meridian profile, m

Greek Symbols

$\bar{\Delta}$	dimensionless shock stand-off distance
γ	specific heat ratio
ρ	density, kg/m^3
μ	dynamic viscosity, Pa.s

Subscripts

c	along a conical surface
e	at the edge of the boundary layer
t	stagnation condition
unit	based on a unit length of 1 m
s	stag. condition at the edge of the boundary layer
w	at the wall
0	stagnation conditions in the reservoir
1	condition upstream a normal shock
2	condition downstream a normal shock
∞	free-stream value

Abbreviations

DRNSE	Dimensionally Reduced Navier-Stokes Eq.
EOS	Equation of State
FLDI	Focused Laser Differentail Interferometry
LST	Linear Stability Theory
LHS	Latin Hypercube Sampling
VKI	von Karman Institute for Fluid Dynamics

1. Introduction

1.1. Background

Despite decades of intense investigation, the boundary-layer transition from laminar-to-turbulent flow is still an open research problem - especially for hypersonic regimes. For such flows of large Mach numbers, an experiment represents valuable means to acquire the basic knowledge about the corresponding physics.

At the von Karman Institute for Fluid Dynamics (VKI), instability and transition measurements on a smooth slender cone at Mach numbers about 10 have been already performed by Grossir (2015) [1]. Among others, this work has demonstrated ability of the VKI Longshot gun tunnel to be used for transition experiments. Based on this conclusion, there is the ongoing research aiming to continue investigation of the boundary-layer transition in the Longshot wind tunnel by including both new measurement techniques as well as other aspects influencing the transition process, e.g. bluntness, roughness or blowing.

As a part of the design of such an oncoming transition experiment, first, the concern is turned to the facility itself – mainly to its test conditions.

1.2. Objectives

The test conditions in the Longshot facility will be reviewed from the transition study point of view. The review is organized into three main sections:

- Effective operation of the wind tunnel
- Reliable determination of the free-stream conditions
- Assessment of disturbance levels

2. The VKI Longshot gun tunnel

The VKI Longshot hypersonic wind tunnel (Fig. 1) belongs to the gun tunnel family. It is designed to provide hypersonic short duration (about 20 ms) flows of large Reynolds numbers[1] whereas stagnation temperatures remain low enough not to have high-temperature gas effects such as dissociation of the test gas [1]. Thus, the Longshot wind tunnel is sometimes referred to as a "cold hypersonic" facility. Nowadays, nitrogen is used as a test and driver gas. The state-of-the-art Longshot wind tunnel with its detailed description can be found in [1].

The design of the VKI Longshot wind tunnel consists of a system of driver/driven tubes, and a test section with a hypersonic nozzle. It relies on a nearly adiabatic compression by a high-velocity piston moving in the driven tube and generating high-pressure and high-temperature gases in a reservoir, which are subsequently expanded through hypersonic nozzles. The Longshot nozzle flow can be tuned by altering the *initial conditions* (i.e. the pressure in the driver and driven tubes, and the mass of the piston). However, the selection of these initial conditions is not arbitrary as it must ensure both desired test free-stream conditions and a safe maximal piston position which is sufficiently far from the end of the driven tube.

3. Effective operation of the wind tunnel

Experimental transition investigations usually require conducting series of experiments with different combinations of parameters. Regarding free-stream conditions, this typically includes different Mach and Reynolds numbers. To fulfill this task efficiently, the operation and behavior of the wind tunnel have to be well understood. This knowledge of the facility is represented by a so-called *operational map*, which relates the settings of the initial conditions to the resulting gas conditions obtained in the nozzle reservoir. With such a map in hand, the selection of appropriate initial conditions can be done rapidly without successive trials and errors.

To obtain the operational map, the compression process taking place inside the system of driver/driven tubes must be accurately physically described and modeled. Such attempts can be tracked up to the early development of the facility by R.W. Perry and his team [2] at the Republic Aviation Corporation (U.S.). Continuing efforts relying on an analytical solution were also made after the relocation of the facility to the VKI in 1967. Although the resulting operational map [3] provided correct trends of the dependency of the reservoir conditions on the settings of the initial wind-tunnel parameters, it was not accurate enough to be directly used for the operation of the tunnel. Therefore, the current approach to the representation the Longshot compression process relies on an effective quasi-one-dimensional numerical solver introduced at the VKI by Bensassi (2014) [4]. However, since this solver strongly depends on several engineering corre-

[1] The final test conditions depend on initial parameters according a desired test regime and on a nozzle used. General range is $Re_{\infty,unit} = (3 - 13) \cdot 10^6$ /m.

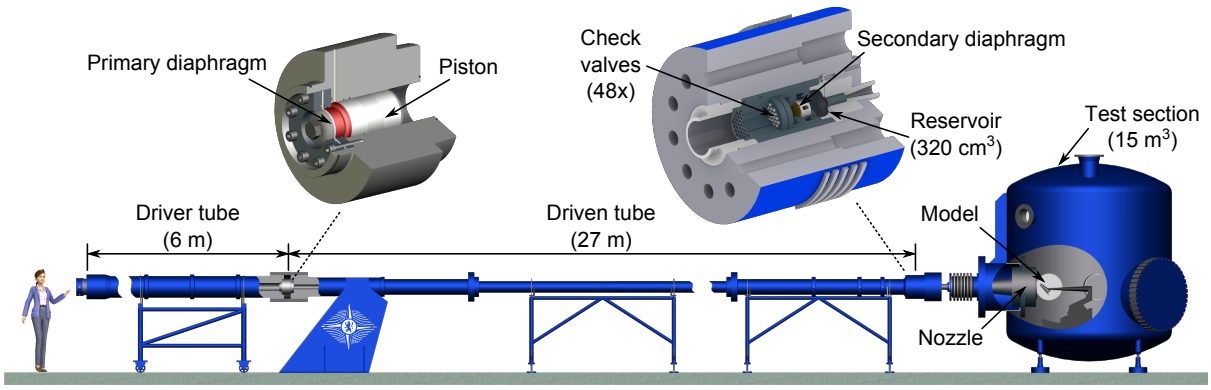

Figure 1: The VKI Longshot hypersonic gun tunnel.

lations, it is necessary to validate it against experimental data.

3.1. *Experimental investigation of the compression process*

To overcome the lack of reliable experimental data related to the compression process, temperature and pressure sensors have been installed to monitor precisely the initial conditions of the driver and driven gases prior to each experiment. Moreover, six fast-response pressure sensors (Kistler 601H and 6215) are fitted at discrete locations along the driven tube. Measurements are performed to determine the pressure evolution during a test and to partially characterize the motion of the piston.

An example of the pressure profile measured by *fast-response* sensors during a test is depicted in Fig. 3 (for the location of 26.8247 m measured from the driver/driven-tube interface). Several kinds of different events, usually appearing as a sudden jump, are distinguished. Based on the basic knowledge of the compression process, these events can be identified as primary or reflected shocks, piston passages, etc. and collected to a so-called space-time diagram (Fig. 2), where they appear as black discrete dots.

The present set of reliable experimental data gives the sound basis for the successful numerical simulation of the compression process in the VKI Longshot facility which is discussed in the following. For more details, see [5]

3.2. *Quasi-1D numerical solver*

As a good compromise between accuracy and numerical cost, the L1d code has been chosen for the

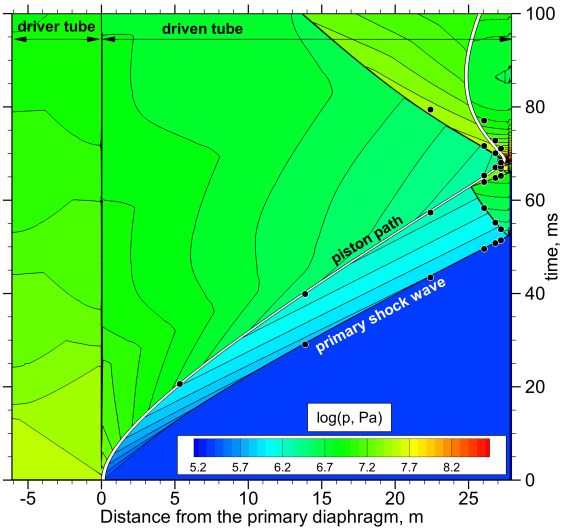

Figure 2: Space-time diagram of the compression process with iso-pressure contours (log-scale) resulting from the L1d simulation. Symbols (•) denote characteristic events measured experimentally along the driven tube [7].

simulation of the compression process. It is a quasi-one-dimensional Lagrangian solver developed by Jacobs (1999) from the University of Queensland (Australia) [6]. The space discretization of gas slugs is performed only along the longitudinal coordinate using a number of cells (control-mass elements) but gradual changes of the tube diameter can be taken into account.

Limitations of the original version of the L1d code available at the VKI did not allow its direct use for determination of the operational map. To this point, several improvements had to be brought to the code. The crucial ones were:

- use of the real-gas EOS via the Span&Wagner

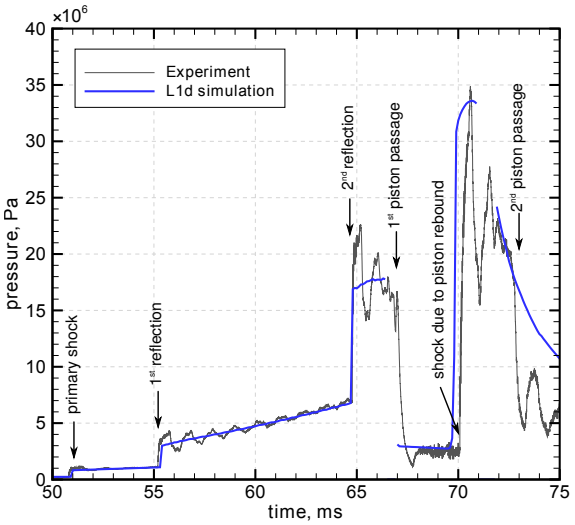

Figure 3: Pressure measured at distance of 26.8247 m from the driver/driven-tube interface.

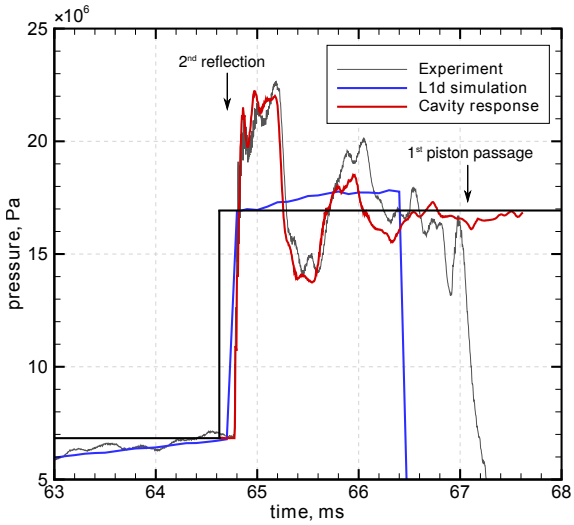

Figure 4: Cavity response for the pressure step corresponding to the second reflection. The L1d solver is used for the calculation.

equations for nitrogen,

- identification of a suitable correlation for the viscosity effects,
- designing of simplified geometry for representation of the entire system of driver/driven tubes including check valves and the reservoir,
- evaluation of losses through check valves,
- methodology for calculation of the final reservoir conditions.

Currently, all these points have been successfully implemented resulting in the state-of-the-art version of the code available at the VKI [7]. An example of the numerical results is illustrated in Fig. 2 representing the space-time diagram of the compression process. The agreement with the experimental data (Section 3.1) is excellent.

The comparison of the pressure profile is shown for the location of 26.8247 m in Fig. 3. Once again, the very good match is obtained. Discrepancies occurred after the piston rebound are expected as the closure of the check valve is not modeled.

Due to large pressures involved, the driven-tube wall is rather thick. This leads to a non-negligible length of cavities connecting the fast-response pressure sensors, which are not flush-mounted, with the tube inside. This cavity effect, resulting in clearly visible wiggles in Fig. 3, is evaluated using the same L1d numerical solver.[2] Numerical computations for such a tube/cavity exposed to a pressure step accurately reproduce the low-frequency oscillations and the harmonics observed experimentally. Therefore, the sensors themselves play a minor role on the observed oscillations. Figure 4 shows the results for the step corresponding to the second reflection in Fig. 3. It can also be shown that the delay introduced by the cavity is on the order of $0.1-0.3$ ms depending on the length of the tube and on the local flow temperature.

To conclude this section, the powerful and accurate numerical tool is currently available for prediction of the reservoir conditions. For standard Longshot operating conditions, predictions of the peak reservoir pressure remain within 5.6% of the experimental measurements. A preliminary operational map has been already computed and is available for operation of the tunnel. For more details, see [7]

4. Longshot free-stream conditions

Characterization of free-stream properties is an essential task not only for transition experiments but generally for each wind-tunnel test. However, it may be very challenging. This is especially true for hypersonic facilities where relatively short test times may

[2] Previous attempts to assess the cavity effect by the theory developed by Bergh & Tijdeman [8] failed mainly due to its limited range of applicability. For its justified use, pressure steps have to be small compared to absolute pressure, which is definitely not the case.

be associated with specific phenomena such as dense gas effects, high temperatures, chemistry, or non-equilibrium effects. Moreover, a direct measurement of free-stream quantities is limited by the measurement techniques available. Instead, rebuilding methods are required to determine all quantities of interest.

For the Longshot gun tunnel, a new rebuilding method involving only measurements performed in the test section has been developed by Grossir [1] improving the accuracy with respect to previous methodologies.

In the following, attention will be paid successively to the instrumentation used, to an improvement of the rebuilding method, and to an estimation of uncertainties on the free-stream quantities.

4.1. Instrumentation

The current rebuilding method requires measurements of the stagnation point heat flux $\dot{q}_w$, the pitot pressure p_{t_2}, and the free-stream static pressure p_∞ in the free-stream [9][3]. These three experimental inputs are obtained using a *static pressure probe* of the Nagamatsu type [10] and a *stagnation double probe*, which allows combined measurements of the pitot pressure and of the heat flux.

In order to extend available instrumentation and to possibly improve measurements of stagnation quantities, two new dedicated probes have been designed (Fig. 5). Decoupling the stagnation point heat flux measurement from the pitot one enables to optimize the design of the probes and improve the embedded instrumentation.

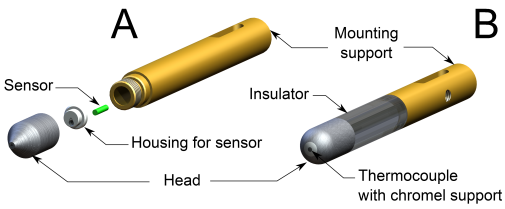

Figure 5: New family of the stagnation probes of: A) pitot pressure B) heat flux.

4.1.1. New pitot probe

The tip of the probe, with the outer diameter equaled to 15 mm, is optimized for the pressure measurement. It consists of the metallic head of a conical shape of 30° half-angle. This is used to minimize the sensitivity to flow pollution by deflecting particles far from the measurement location. An absolute piezo-resistive pressure transducer (Kistler XCQ-093)[4] is mounted in a cavity following a pressure tap (⌀1 mm), within a Teflon housing and sealed. The pressure sensor is located slightly off the axis to avoid any potential impact with flow seeding particles. The volume of the cavity has been reduced over the previous design, and the diameter of the tubing has been enlarged, hence improving the response of the probe.

Comparison of the pitot pressure measured by the new probe and the previous double probe is shown in Fig. 6. As expected, the level of pressure is the same whereas the signal from the new probe contains less noise. This can be seen more precisely in Fig. 16 where the power spectral density is plotted for both probes together with an acoustic probe which will be discussed later on.

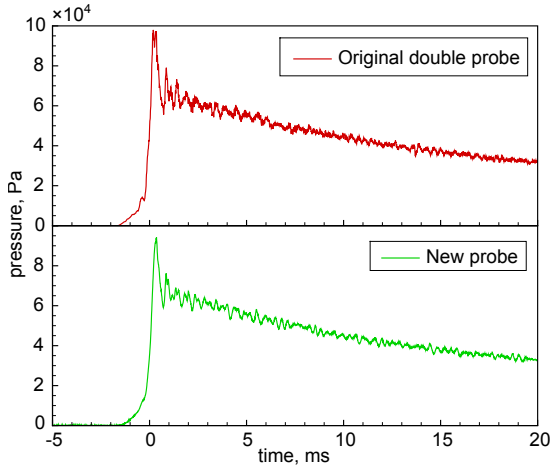

Figure 6: Comparison of the pitot pressure measured by new and old probes.

4.1.2. New stagnation point heat flux probe

The outer diameter of the probe has been reduced from 25 mm to 15 mm. The heat flux at the stagnation point being proportional to $1/\sqrt{R_N}$, the sensitivity of the probe is enhanced by 29%. A fast-response coaxial type-E thermocouple (Chromel-Constantan), manufactured at the Shock Wave Laboratory (RWTH Aachen University, Germany), is flush-mounted at the stagnation point and shaped to match the local curvature radius. In order to ensure a 1-dimensional heat

[3]The reservoir pressure p_0 is still monitored for the assessment of the repeatabilities between successive experiments but is no longer involved in the determination of free-stream conditions.

[4]A differential sensor of the same type (Kistler XCQ-093) is used for the original double stagnation probe.

flux through the thermocouple, a chromel insert with identical thermal properties surrounds the sensor. The diameter of the active junction of the thermoclouple has been reduced from 1.9 mm to 0.5 mm, which ensures a better-localized measurement and therefore an improved response time.

Due to an ongoing modernization of the tunnel, only two measurements with new probes, where non-standard test conditions were used for a specific purpose, could be performed. More tests are needed to finally conclude on benefits over the previous double probe.

4.2. *Rebuilding method*

The determination of the free-stream flow properties in the Longshot gun tunnel is achieved using the VKI *Mutation* library [11] and three experimental inputs discussed above. The aim is to find two of the unknown free-stream quantities (the velocity u_∞, and the static temperature T_∞) which provide a satisfactory set of free-stream conditions to match the measured stagnation point heat flux $\dot{q}_w$ on a hemispherical probe, and the pitot pressure p_{t_2}. This matching is obtained iteratively. For more details about the rebuilding method, see [1]

Although the assumptions used by the current rebuilding method are relatively limited[5], it still relies on the Fay-Riddell equation [12] in order to relate the wall heat flux at the stagnation point to the free-stream total enthalpy. This has been identified as a remaining weak point [1]. The original Fay-Riddell equation can be expressed in simplified form (eq. 1) for the specific case of the Longshot wind tunnel as the stagnation temperature is limited to $T_0 \lesssim 2500\,\mathrm{K}$ so that nitrogen dissociation is not expected. Under such conditions, the Lewis number (which is the ratio of the thermal diffusivity and the mass diffusivity) is assumed to be equal to 1. The corresponding nomenclature is depicted in Fig. 7.

$$\dot{q}_w = 0.763 \times \mathrm{Pr}^{-0.6}\ (\rho_w \mu_w)^{0.1}\ (\rho_s \mu_s)^{0.4} \times (h_s - h_w) \sqrt{\left(\frac{du}{dy}\right)_s} \quad (1)$$

The use of the Fay-Riddell equation raises a question about the suitable choice of a required formula for

[5] Apart from the use of the Fay-Riddell equation, the method assumes thermal equilibrium in the free-stream as well as after a normal shock.

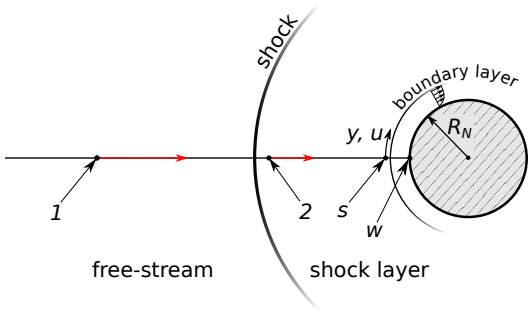

Figure 7: Nomenclature used in the Fay-Riddell equation [1].

the tangential velocity gradient at the stagnation point $(du/dy)_s$. Several expressions available in the literature [13; 14] considerably differ in a level of their complexity. The summary of considered methods for determination of the velocity gradient detailed in [15] are listed in Table 1 together with phenomena accounted for. Whereas the Newton method represents a crude approximation based on the Newtonian theory for hypersonic velocities, the Olivier method is the most complex one including the following phenomena: the density ratio across the shock depending on M_∞, the compressibility – varying density through the shock layer, the shock stand-off distance, the vorticity produced by the curved shock, and high-temperature gas effects [15].

Nevertheless, a priori selection of the most suitable methods for Longshot conditions appears to be rather difficult. An example of rebuilt free-stream Mach (M_∞) and Reynolds unit ($\mathrm{Re}_{\mathrm{unit},\infty}$) numbers using different methods is shown in Fig. 8. Note a large scatter on the Reynolds number, which is more than 30% and makes the choice even more critical. The influence on the free-stream Mach number is indiscernible since this quantity essentially depends on the pressure ratio p_∞/p_{t_2}.

Table 1: List of considered methods for the tangential velocity gradient.

Method	$\frac{\rho_2}{\rho_\infty}$	$\frac{\rho_2}{\rho_s}$	$\bar{\Delta}$	vorticity	high T
Newton	-	-	-	-	-
Linnell	+	-	-	-	-
Stokes	+	-	+	-	-
Olivier	+	+	+	+	+

In the following, several cases covering the range of the Longshot free-stream conditions are calculated by the rebuilding method using different expressions for

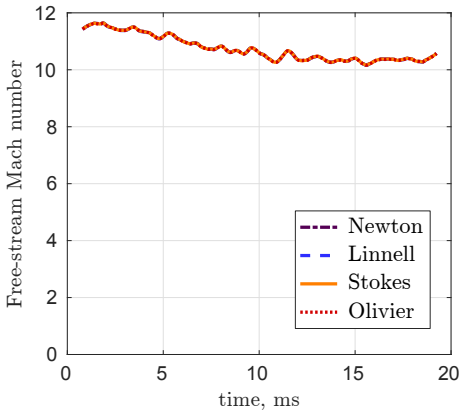

(a) Free-stream Mach number M_∞.

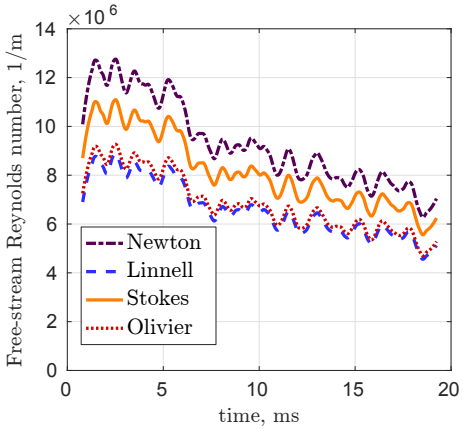

(b) Free-stream Reynolds number $Re_{unit,\infty}$.

Figure 8: Influence of the velocity gradient expression on some free-stream flow properties.

the tangential velocity gradient (entering the rebuilding method through the Fay-Riddell equation) as well as by a numerical stagnation-line code. This enables comparison of flow properties between these two approaches and identification of the most suitable expression for the velocity gradient.

Note that the Stokes and Olivier method require determination of the shock stand-off distance. By default, the Stokes and Olivier methods in the current rebuilding method use different correlations. Namely, the Lobb [16] and Freeman [17] expressions are employed for the Stokes and Olivier methods, respectively, see Section 4.2.3. To make the comparison more representative, the Stokes method with the Freeman expression for the shock stand-off distance will be also considered (dashed line in Figs. 9 and 11).

4.2.1. Stagnation-line code

The Stagnation-line code is a quasi-1D code enabling the determination of flow properties along the stagnation streamline of hypersonic (generally non-equilibrium) flows over spheres or cylinders. This solver developed by Munafò [18] can be coupled with the VKI *Mutation* thermodynamic library [19; 11]. Results obtained using this numerical tool will be referred to as the "stagline" data.

In order to determine stagnation-streamline quantities in hypersonic flows over a spherical probe, the two-dimensional Navier-Stokes equations must be solved. Based on the local similarity of the flow field, the 2D governing equations are reduced to a 1D approximation for the stagnation streamline. This reduction of independent spatial variables proposed by Klomfass and Müller [20] is called DRNSE (Dimensionally Reduced Navier-Stokes Equations). An implicit finite-volume numerical method with second order accuracy in space is then used to solve these dimensionally reduced equations [18].

Main limitations of the DRNSE approach pointed out in [20], namely a limitation to flows where the thickness of the shock wave is small compared to the thickness of the shock layer, specifically chosen functional dependencies which are favorable for isothermal, fully catalytic wall, and an assumption of a Newtonian-like pressure distribution, may be tolerated for the present investigations.

4.2.2. Results

The specific cases covering the standard Longshot conditions[6] have been calculated by the rebuilding method using different expressions for the tangential velocity gradient listed in Table 1 as well as by the Stagnation-line code detailed in Section 4.2.1.

The comparison of the stagnation point heat flux, which is of main interest, is shown in Fig. 9 in terms of reduced variables.

In order to better quantitatively evaluate the methods for determination of the velocity gradient, Fig. 10 presents percentage differences against reference values obtained from the numerical code. A large scatter is observed among the different methods confirming that the velocity gradient has an important influence on the stagnation point heat flux. The Newtonian theory exhibits the largest difference against the numerical results (more than 30%) as it was expected due to

[6]Three standard operating regimes of the tunnel are commonly used and referred to as "Low", "Medium", and "High" Reynolds regimes [1].

its simplicity. The Linnell and Stokes methods give the results with the difference about 5% and 15%, respectively. The best agreement between the numerical results and the theoretical predictions is obtained by using the Olivier method [14]. Differences are less than 3% for all test cases. Therefore, the Olivier expression should be preferred for the Longshot rebuilding method.

The previous comparison of heat fluxes is valuable since it quantifies the accuracy of the investigated methods on the final quantity ($\dot{q}_w$) which is directly used in the rebuilding method. However, a direct comparison of the velocity gradient itself can be carried out. Then, the Fay-Riddell equation is not needed. Figure 11 depicts the reduced velocity gradient as a function of the density ratio through the shock. For numerical results, the velocity gradients have been retrieved at the boundary-layer edge defined as 99% of the free-stream total enthalpy h_{t1}.

The Olivier method gives again the best agreement with the numerical results, which, however, seem to have different slope and dependence on the Reynolds-number regime. Although the use of the Freeman expression for the shock stand-off distance brings the Stokes method closer to the numerical prediction, it still remains somewhat worse than the Olivier method. This is also true for the previous comparison of the wall heat flux where differences decrease to a level of 7.5% (dashed line in Fig. 9), which is about half of the original values using the Lobb expression.

The present numerical results correspond very well with calculations of the hypersonic flow around a sphere for perfect gas performed by Sagnier and presented in [14]. This might be expected as the Longshot conditions are close to the theoretical limit of the density ratio for perfect gases $\rho_\infty/\rho_2 = 1/6$ (for $\gamma = 1.4$).

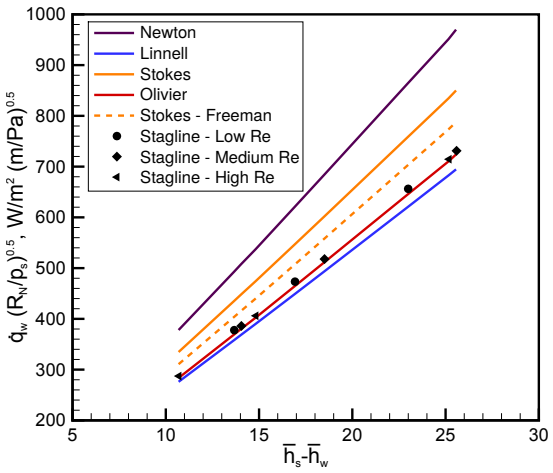

Figure 9: Reduced stagnation point heat flux vs. reduced enthalpy difference.

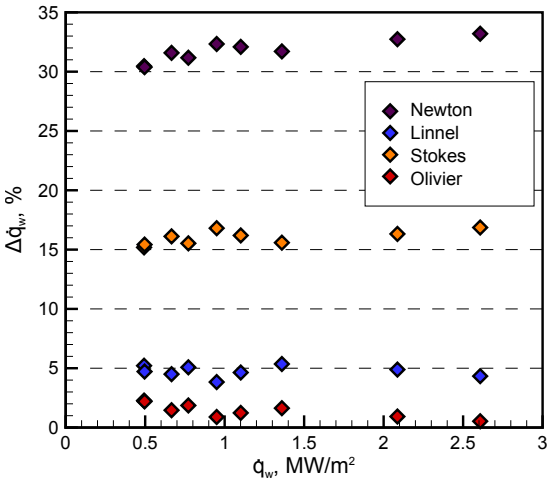

Figure 10: Percentage difference of investigated engineering methods for the velocity gradient against the numerical results.

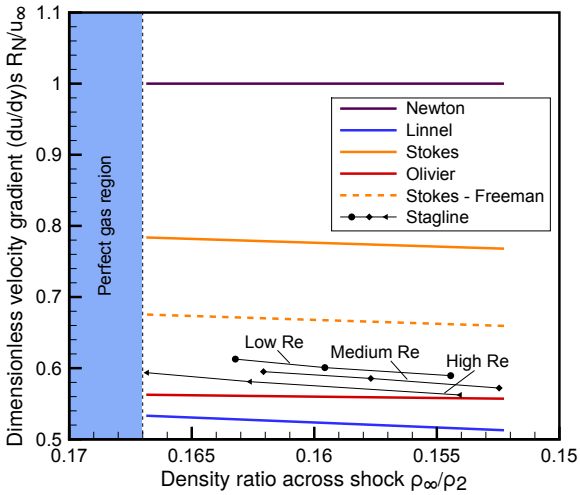

Figure 11: The tangential velocity gradient as a function of the density ratio across the shock.

4.2.3. *Shock stand-off distance*

The shock stand-off distance is presented in Fig. 12 redrawn from [14]. The present numerical data for the Longshot facility calculated by the Stagnation-line code are added. However, the DRNSE approach used in the Stagnation-line code is well known to underestimate the shock stand-off distance [20][7]. There-

[7]The differences have been found to increase with the decreasing Mach number and probably attributed to the Newtonian theory

fore, it is not possible to rely on the Stagnation-line code for the selection of a suitable correction for the shock stand-off distance. The differences against two-dimensional, inviscid, perfect-gas calculations are reported to be about -10% in [20]. This agrees well with the current 2D axisymmetric calculations considering nitrogen as a thermally perfect gas and using the commercial CFD++ solver. Experimental values retrieved from Schlieren pictures for a single Longshot test are also indicated in Fig. 12. Nevertheless, they are flawed by large uncertainties and must be regarded only as indicative.

For a reason which still remains unclear, the Freeman expression performs best for both of the Stokes and Olivier methods, even though it does not agree with the shock position determined numerically and experimentally. It may be also possible to consider $\bar{\Delta}$ as a simple density ratio which agrees well with numerical simulations. However, such an interpretation of $\bar{\Delta}$ does not correspond to the way the Stokes and Olivier methods have been derived.

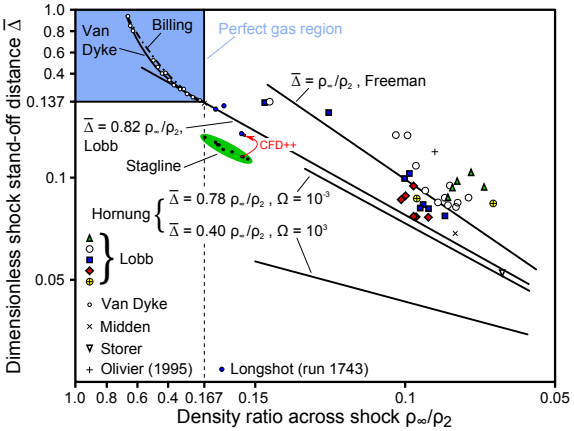

Figure 12: Shock stand-off distance, redrawn from [14].

4.2.4. *Experimental validation*

Experimental data acquired during boundary-layer transition studies along a 7° half-angle cone carried out by Grossir [1] in the VKI Longshot tunnel give an opportunity to experimentally evaluate the accuracy of the numerical and theoretical results discussed above. The idea is to measure the convection velocity of boundary layer instabilities along a model and to compare these values to theoretical ones determined from the set of free-stream flow properties issuing from the rebuilding method.

used for a prescribed pressure distribution on a sphere [20].

In hypersonic regimes, the boundary-layer transition phenomenon along a slender sharp cone typically exhibits the presence of second mode instabilities [21]. From an experimental point of view, these instabilities can be visualized using flow visualization techniques (e.g. LIF-Schlieren [1]), and their group velocities can then be inferred using successive images separated by a short amount of time. Figure 13 illustrates such instabilities, and red arrows highlight their displacement after 1 µs. Similarly, the cross-correlation of pressure traces (obtained from streamwise sensors along the surface, Fig. 13) can be used to determine their group velocities. These velocities can then be compared with theoretical predictions. Note that such an analysis is fully independent of the free-stream flow conditions derived from the rebuilding method.

From a theoretical point of view, the group velocity of the boundary layer instabilities differs from the local flow velocity along the cone, but can be estimated from linear stability theory (LST). Within the Longshot environment, and for the conical geometry considered here, the group velocity for the second mode instabilities is about $u_c \approx 0.93 u_e$, where u_e is the theoretical boundary layer edge velocity. This relationship is only weakly dependent upon free-stream conditions. The boundary layer edge velocity u_e is about 98.8% of the free-stream velocity, as determined from a Taylor-Maccoll solution [22] knowing free-stream flow properties and the conical half-angle.

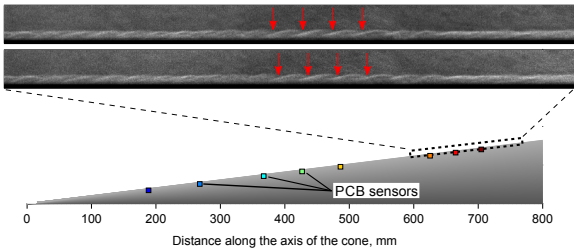

Figure 13: Positions of pressure sensors on the cone (7° half-angle, $R_N = 1.75$ mm) with illustrative LIF-Schlieren pictures of second mode waves (separation time 1 µs), redrawn from [1].

Experimental and theoretical group velocities can then be compared to each other. Using the Stokes formula for the stagnation point velocity gradient leads to a poor agreement as illustrated in Fig. 14a: the free-stream velocity, and therefore the group velocity of the instabilities is underestimated regardless of the time instant considered. On the other hand, a much better agreement can be obtained if the Olivier formula is used (Fig. 14b). This results in larger free-

stream velocities and larger group velocities which are then closely matching experimental values.

Therefore, the present comparison supports the conclusions drawn earlier using the Stagnation-line code, namely that the stagnation point velocity gradient within the VKI Longshot low enthalpy environment is accurately described by the Olivier expression using the shock stand-off distance equal to the density ratio across the shock. This equation should, therefore, be preferred for the Longshot free-stream rebuilding method.

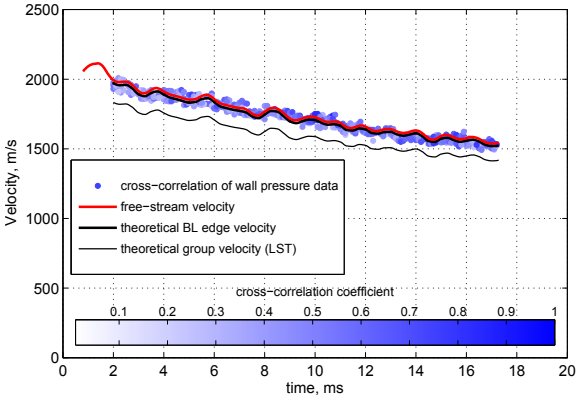

(a) Using Stokes expression.

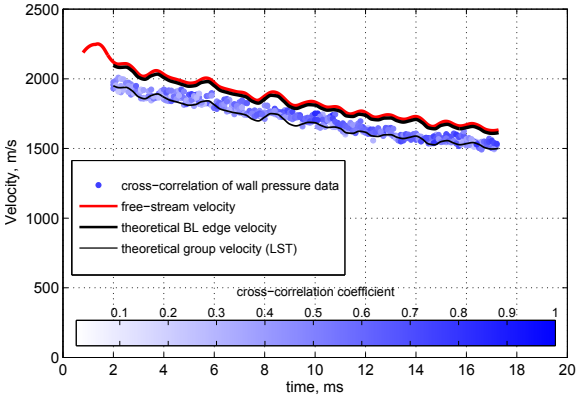

(b) Using Olivier expression.

Figure 14: Experimental convection velocities (symbols: ●) for hypersonic boundary layer instabilities and comparison with theoretical results (thin line: ——) based on different expressions for the stagnation point velocity gradient.

4.3. Uncertainty quantification

Uncertainty analysis of Longshot free-stream conditions has been carried out by Grossir in [1]. First, input uncertainties on the measured quantities (p_{t2}, $\dot{q}_w$, and p_∞, see Section 4.1) were determined taking into account two sources:

- uncertainty on the linearity and sensitivity of the sensors used,
- uncertainties due to flow fluctuations at the exit of the nozzle.

Then, each input was separately perturbed and corresponding outputs of the rebuilding method were combined to estimate the uncertainties on final free-stream quantities of interest. This allowed identification of the most critical measurements.

In order to improve the analysis, the Dakota code from the Sandia National Laboratories with Monte Carlo and Polynomial Chaos methods [23] can be employed instead of the perturbation method. Whereas Polynomial Chaos methods are suitable to determine the sensitivities on inputs, one of various sampling-based approaches can be used to determine the final uncertainties. These techniques generate sets of samples according to the probability distributions of the uncertain variables (inputs) and map them into corresponding sets of response functions (final quantities of interest). In the present case, Latin hypercube sampling (LHS) is preferred over Monte Carlo one since, in general, it requires fewer samples. The Dakota code has been coupled with the rebuilding method using the fork simulation interface [23].

The present analysis has been performed using the same input uncertainties as in [1]. An example for the "Low Reynolds" regime is shown in Table 2 together with the previous results from [1]. All uncertainties are evaluated for 68.3% confidence level.

Table 2: Summary of typical Longshot uncertainties for the "Low Reynolds" regime.

		Uncertainties	
		LHS	Grossir [1]
inputs	p_{t2}	2.60	2.60
	$\dot{q}_w$	8.00	8.00
	p_∞	7.10	7.10
derived	u_∞	3.00	3.20
	ρ_∞	7.00	7.60
	T_∞	9.76	10.10
	h_{t1}	5.99	6.30
	M_∞	3.84	4.10
	$Re_{unit,\infty}$	12.65	13.10

No correlations between inputs are assumed. The derived uncertainties are relatively close to the original values. The largest difference is obtained for the

free-stream density (0.6%). Therefore, a nonlinearity of the system is rather limited and all conclusion drawn in [1] are valid, mainly that the largest uncertainty is observed for the free-stream Reynolds number. Since it is a crucial parameter to be followed during transition experiments, effort should be put to reduce it by decreasing the uncertainties on the free-stream static temperature and wall heat flux measurements.

5. Disturbance levels

For boundary-layer transition experiments, an additional requirement on free-stream conditions (discussed in the previous section) regarding disturbance levels arises. The effect of free-stream disturbances on the boundary-layer transition is well-known even though the receptivity mechanism by which the disturbances enter a boundary layer is not yet fully understood [24].

It is possible to distinguish three main origins (modes) of wind tunnel disturbance levels [25]: *vorticity* (velocity fluctuation), *entropy fluctuations* (temperature/entropy spottiness) and *pressure fluctuations* (often referred to as noise levels). The latter ones, which are believed to mainly come from a turbulent boundary layer developed on the nozzle wall, are usually identified to be dominant in supersonic and hypersonic wind tunnels ($M_\infty > 2.5$). Since the flight noise levels are much lower than wind-tunnel ones [24], many efforts have been made to design "quiet" wind tunnels [26]. In conventional hypersonic ground testing facilities such as the VKI Longshot tunnel[8], it is necessary to characterize the disturbance levels as much as possible (i.e. their amplitude, spectrum, and direction) in order to allow correct interpretation of the acquired data.

The full characterization of disturbance levels in a hypersonic facility is not an easy task, mainly due to the fact that the shock interaction with one of three types of disturbance waves creates all of them downstream from the shock wave [27; 28]. Thus, the noise measured by an intrusive probe may not be the same as in the free-stream and the pitot pressure fluctuations alone are not sufficient to perform a modal analysis. Besides use of one of the optical techniques, for instance FLDI [29], two methods can be currently found in literature, namely the classical hot-wire-pitot-probe method [30] and new cone/wedge-probe-DNS method [31; 32].

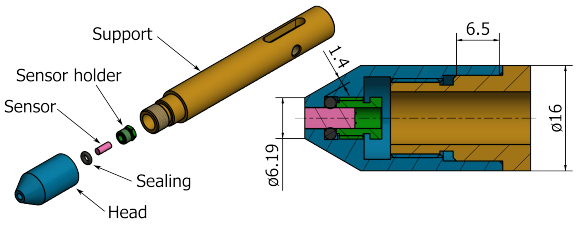

Figure 15: Acoustic probe [33].

As a first step, a new acoustic probe has been designed in [33] to measure the conventional fluctuation level of the pitot pressure (Fig. 15). The probe with the outer diameter of 16 mm has a 30° half-angle conical head, which front part is truncated to a diameter of 6.19 mm. A fast-response piezoelectric pressure sensor (PCB 132A31) with an external diameter of 3.18 mm is flush-mounted at the tip of the probe. The frequency bandwidth of such a sensor goes up to 1 MHz.

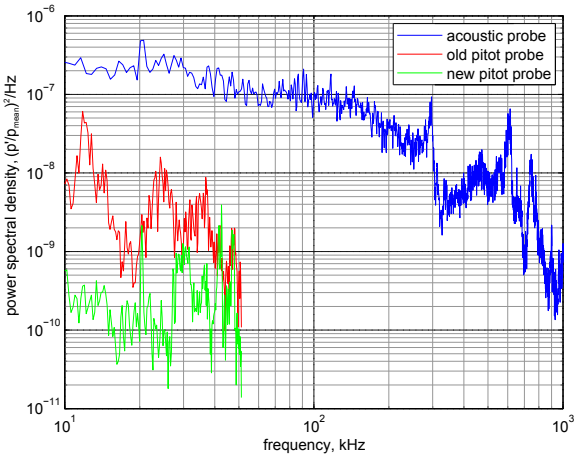

Figure 16: PSD of normalized pitot pressure.

The power spectral density of normalized pitot pressure for the new pitot-pressure and the acoustic probes are compared with results from the original double probe in Fig. 16. The *acoustic probe* clearly enhances the ability to measure the free-stream noise. The peak at 300 kHz corresponds to a natural frequency of the PCB sensor. Other two harmonics can be distinguished at frequencies close to the multiple of the fundamental ($f_1 \approx 300$ kHz, $f_2 \approx 600$ kHz, $f_3 \approx 900$ kHz). The peak at about 750 kHz remains of unknown origin.

The comparison of the *pitot probes* illustrates the

[8] The conventional pitot pressure fluctuations have been estimated to be about 7% at the nozzle exit [1].

effect of their different design, mainly the dependency of dynamic pitot pressure measurements on the forebody shape of the stagnation probe reported also in [34]. Note that both probes use the same type of sensor (Kulite XCQ-093 with natural frequency about 240 kHz) only differing on the operational mode (new probe - absolute, old probe - differential).

6. Conclusion

Effective operation of the VKI Longshot gun tunnel, required by transition parametric studies, is now possible thanks to the new accurate operation map, which has been computed using the numerical L1d solver. To this point, several major improvements had to be brought to the code through research at the VKI and extensive experimental investigation of the Longshot compression process had to be carried out. Benefits of such a reliable code simulating the facility go beyond the determination of the operational map as it could also help to predict the facility behavior during its modernization/modification, e.g. a planned removing the check valves.

Free-stream flow characterization has been enhanced by the new family of the stagnation probes including the fast acoustic probe for measurements of the conventional fluctuation level of the pitot pressure. However, more experiments are needed to fully characterize them and to evaluate their benefits over the current instrumentation.

It has been shown that using the Fay-Riddell equation within the rebuilding method of free-stream conditions raises the question about the suitable choice of the formula for the tangential velocity gradient at the stagnation point since its effect on the rebuilt free-stream properties is considerable (variations more that 30% on the Reynolds number). The four different expressions for determination of the velocity gradient have been described and evaluated for typical Longshot conditions using the quasi-1D numerical solver. The best agreement has been found for the Olivier method which gives differences on the stagnation point heat flux against the numerical results less than 3% for all test cases. It is, therefore, preferable to be used in the current rebuilding method.

Experimental validation has been obtained indirectly by comparing convection velocities of boundary layer disturbances along a slender cone (derived from a streamwise array of pressure sensors) against Linear Stability Theory predictions (based on free-stream flow properties and conical geometry). Since the convection velocity of these disturbances directly scales with the free-stream velocity, and since the latter is very sensitive to the expression used for the stagnation point velocity gradient, it is relatively easy to determine the most accurate expression for the velocity gradient to match predictions with experimental measurements. For the Longshot flow conditions, the Olivier method [14] is accurate to within 1.6% of the experimental observations.

Acknowledgments

The author wishes to thank Dr. Grossir for introducing him to the problematics related to Longshot test conditions and for his effort during the development of the final version of the L1d code.

The support of this activity by the European Space Agency (ESA) through grant 4000114170/15/NL/KML is gratefully acknowledged.

References

[1] G. Grossir, Longshot hypersonic wind tunnel flow characterization and boundary layer stability investigations, Ph.D. thesis, von Karman Institute for Fluid Dynamics - Université Libre de Bruxelles (July 2015).

[2] R. W. Perry, The Longshot type of high-Reynolds number hypersonic tunnel, in: Third hypervelocity techniques symposium, Advanced experimental techniques for study of hypervelocity flight, 1964.

[3] G. Simeonides, The performance of the VKI Longshot hypersonic wind tunnel, Technical Note TN-161, von Karman Institute for Fluid Dynamics (June 1987).

[4] K. Bensassi, Contribution to the numerical modeling of the VKI Longshot hypersonic wind tunnel, Ph.D. thesis, von Karman Institute for Fluid Dynamics - Université Libre de Bruxelles (January 2014).

[5] Z. Ilich, G. Grossir, S. Paris, O. Chazot, Experimental investigation of the VKI Longshot gun tunnel compression process, in: EUCASS, to be published, 2017.

[6] P. A. Jacobs, Quasi-one-dimensional modeling of a free-piston shock tunnel, AIAA Journal 32 (1) (1994) 137–145.

[7] G. Grossir, Z. Ilich, Modeling of the complete VKI Longshot compression process using a quasi-1D approach, Technical Note, von Karman Institute for Fluid Dynamics, to be published (2017).

[8] H. Bergh, H. Tijdeman, Theoretical and experimental results for the dynamic response measuring systems, NLR-TR F.238, 1965.

[9] G. Grossir, B. Van Hove, S. Paris, P. Rambaud, O. Chazot, Free-stream static pressure measurements in the Longshot hypersonic wind tunnel and sensitivity analysis, Experiments in Fluids 57 (5) (2016) 64.

[10] G. Grossir, S. Paris, P. Rambaud, B. Van Hove, Design of static pressure probes for improved free-stream characterization in hypersonic wind tunnels, in: 52nd AIAA Aerospace Sciences Meeting, no. AIAA 2014-1410, 2014.

[11] T. E. Magin, A model for inductive plasma wind tunnels, Ph.D. thesis, von Karman Institute for Fluid Dynamics - Université Libre de Bruxelles (June 2004).

[12] J. A. Fay, F. R. Riddell, Theory of stagnation point heat transfer in dissociated air, Journal of the Aeronautical Sciences 25 (2) (1958) 73–85.
[13] H. Olivier, An improved method to determine free stream conditions in hypersonic facilities, Shock Waves 3 (3) (1993) 129–139.
[14] H. Olivier, Influence of the velocity gradient on the stagnation point heating in hypersonic flow, Shock Waves 5 (4) (1995) 205–216.
[15] Z. Ilich, G. Grossir, O. Chazot, Evaluation of the stagnation point velocity gradient in low-enthalpy hypersonic flows, in: 33rd AIAA Aerodynamic Measurement Technology and Ground Testing Conference, 2017 AIAA Aviation Forum, to be published, 2017.
[16] R. Lobb, Experimental measurement of shock detachment distance on spheres fired in air at hypervelocities, in: W. Nelson (Ed.), The high temperature aspects of hypersonic flow, Oxford: Pergamon press, 1964, pp. 519–527.
[17] N. C. Freeman, On the theory of hypersonic flow past plane and axially symmetric bluff bodies, Journal of Fluid Mechanics 1 (4) (1956) 366–387.
[18] A. Munafò, Multi-scale models and computational methods for aerothermodynamics, Ph.D. thesis, von Karman Institute for Fluid Dynamics - École Centrale Paris (2014).
[19] J. B. Scoggins, T. E. Magin, Development of Mutation++: Multicomponent thermodynamic and transport properties for ionized plasmas written in C++, in: AIAA AVIATION Forum, no. AIAA 2014-2966, American Institute of Aeronautics and Astronautics, 2014.
[20] A. Klomfass, S. Müller, A quasi-one dimensional approach for hypersonic stagnation-point fows, Internal Report 121, RWTH Aachen (1996).
[21] L. M. Mack, The stability of the compressible boundary layer according to a direct numerical solution, in: Recent development in boundary layer research, Vol. AGARDograph 97, AGARD, 1965, pp. 329–362.
[22] G. I. Taylor, J. W. Maccoll, The air pressure on a cone moving at high speeds. I, Proceedings of the Royal Society 139 (1933) 278–297.
[23] B. M. Adams, M. S. Ebeida, M. S. Eldred, J. D. Jakeman, L. P. Swiler, J. A. Stephens, D. M. Vigil, T. M. Wildey, W. J. Bohnhoff, K. R. Dalbey, J. P. Eddy, R. W. Hooper, K. T. Hu, L. E. Bauman, P. D. Hough, A. Rushdi, Dakota, a multilevel parallel object-oriented framework for design optimization, parameter estimation, uncertainty quantification, and sensitivity analysis: Version 6.3 users manual, Tech. Rep. SAND2014-4633, Sandia (July 2014).
[24] S. P. Schneider, Effects of high-speed tunnel noise on laminar-turbulent transition, Journal of Spacecraft and Rockets 38 (3) (2001) 323–333.
[25] S. R. Pate, Effects of wind tunnel disturbances on boundary-layer transition with emphasis on radiated noise: a review, in: 11th AIAA Aerodynamic testing conference, no. AIAA paper 1980-0431, 1980.
[26] I. E. Beckwith, Development of a high Reynolds number quiet tunnel for transition research, AIAA Journal 13 (3) (1975) 300–306.
[27] H. S. Ribner, Spectra of noise and amplified turbulence emanating from shock-turbulence interaction, AIAA Journal 25 (3) (1987) 436–442.
[28] T. Schilden, W. Schröder, S. R. C. Ali, R. Radespiel, Interaction of acoustic and entropy waves with shocks, in: 44th AIAA Fluid Dynamics conference, no. AIAA paper 2014-2352, 2014.
[29] N. J. Parziale, Slender-body hypervelocity boundary-layer instability, Ph.D. thesis, California Institute of Technology (May 2013).
[30] D. Masutti, E. Spinosa, O. Chazot, M. Carbonaro, Disturbance level characterization of a hypersonic blowdown facility, AIAA Journal 50 (12) (2012) 2720–2730.
[31] T. Schilden, W. Schröder, S. R. C. Ali, A.-M. Schreyer, J. Wu, R. Radespiel, Analysis of acoustic and entropy disturbances in a hypersonic wind tunnel, Physics of Fluids 28 (5) (2016) 056104.
[32] A. Wagner, E. Schülein, R. Petervari, K. Hannemann, S. R. C. Ali, High frequency free-stream disturbance measurements in hypersonic wind tunnels by means of a slender wedge probe, in: 46th AIAA Fluid Dynamics Conference, AIAA AVIATION Forum, no. AIAA 2016-3192, 2016.
[33] G. Grossir, Z. Ilich, Design of intrusive probes for enhanced Longshot flow characterization, Technical Note 3100 CR 2016-19, VKI (2016).
[34] S. R. C. Ali, R. Radespiel, T. Schilden, W. Schröder, High-frequency measurements of acoustic and entropy disturbances in a hypersonic wind-tunnel, in: 44th AIAA Fluid Dynamics conference, no. AIAA paper 2014-2644, 2014.

Analysis of the stability of a flat plate high-speed boundary layer with discrete roughness

Iván Padilla Montero

Aeronautics and Aerospace Department, von Karman Institute for Fluid Dynamics, Belgium, ivan.padilla@vki.ac.be

Supervisors: Olivier Chazot and Fabio Pinna

Head of department and professor, Aeronautics and Aerospace Department, von Karman Institute for Fluid Dynamics, Belgium, olivier.chazot@vki.ac.be

Senior research engineer, Aeronautics and Aerospace Department, von Karman Institute for Fluid Dynamics, Belgium, fabio.pinna@vki.ac.be

University Supervisor: Gérard Degrez

Dean of the faculty and professor, Aero-Thermo-Mechanics Department, Université Libre de Bruxelles, Belgium, gdegrez@ulb.ac.be

Abstract

Transition to turbulence is a critical aspect in the design of high-speed vehicles. Turbulent boundary layers are characterized not only by increased skin friction, and hence drag, but also for larger heat transfer rates that lead to challenging aerothermodynamic loads. Isolated roughness elements present on the surface of a body, such as those encountered during atmospheric entries due to factors like misaligned heat shield tiles, rivets or remains of contaminants, among others, are known to have an important impact in the transition process. The presence of these elements can accelerate the growth of incoming disturbances and introduce additional instability mechanisms in the flow field, eventually leading to a premature occurrence of transition.

Experimental investigations of roughness-induced transition in hypersonic flow have been recently performed at the von Karman Institute for Fluid Dynamics. The work mainly focused on different three-dimensional roughness elements mounted on top of a flat plate in a Mach 6 freestream. The results repeatedly showed the generation of different families of long streamwise structures in the vicinity of the roughness and their persistence in the transitional wake, characterized by strong counter-rotating vortices that give rise to low velocity streaks. These vortical structures appear to follow a cascade behaviour, so that secondary vortices are generated by the primary roughness-induced structures in the widening of the wake. Although the topology of the structures is well identified, their physical nature is, at present time, only partly understood. The main objective of this project is to numerically analyse the stability of the wake induced by isolated roughness elements. Because of the strong inhomogeneity of the flow field in the spanwise and wall-normal directions, mainly due to the streamwise vortical structures, a BiGlobal linear stability analysis will be performed in different spanwise planes along the wake, so to be able to track the streamwise evolution of the instabilities. The laminar base flow will be computed by means of a perfect gas Navier-Stokes simulation using a second-order finite volume scheme. Then, the partial differential eigenvalue problem resulting upon the application of the BiGlobal ansatz will be discretized by means of the Chebyshev collocation method and solved with the Arnoldi algorithm. The resulting spectrum and two-dimensional eigenfunctions will be used to assess the nature of the instability modes present in the roughness-induced wake, their regions of development and their interaction downstream. Varicose and sinuous instability modes developing in the high-shear regions located at the interface between the low velocity streak behind the element and the surrounding flow are expected to be the most unstable ones, accompanied by Mack modes evolving in the lateral, low-disturbed boundary layer. The results of this primary stability calculation will also be used as a basis for a linear secondary instability analysis, useful to assess whether the generation of secondary vortices in the widening of the wake is a consequence of the linear instability of the primary structures or not. Furthermore, besides investigating the new instability modes triggered by the presence of the roughness, the BiGlobal solver will also be used to explore the influence of the element on the linear growth of second mode instabilities already present in the upstream laminar boundary layer.

MULTISCALE AND MULTIPHASE FLOW PROBLEMS

Numerical methods for thermal hydraulics simulations of containment buildings

Andrea Attavino

Environmental and Applied Fluid Dynamics Department , von Karman Institute for Fluid Dynamics, Belgium, andrea.attavino@vki.ac.be

Supervisor: Philippe Planquart

Research Manager, Environmental and Applied Fluid Dynamics Department, von Karman Institute for Fluid Dynamics, Belgium, philippe.planquart@vki.ac.be

University Supervisor: Alessandro Parente

Associate Professor, Aero-Thermo-Mechanics Department, Université Libre de Bruxelles, Belgium, alessandro.parente@ulb.ac.be

Abstract

The aim of this PhD research is to develop and validate a numerical method for the simulation of hydrogen stratification and deflagration in containment buildings of nuclear reactors. The validation of the code will be performed using the database provided by the OECD-NEA THAI-3 Project.

Keywords: multiphase flows, reacting flows, hydrogen stratification, hydrogen deflagration

1. Introduction and Motivation

During a sever nuclear accident in water cooled nuclear reactors, a large amount of hydrogen can be generated as a result of the zircaloy oxidation. Leakage of hydrogen from the reactor into the containment building can lead to the formation of a combustible mixture that, in the event of ignition and subsequent deflagration, can cause relevant damage to many safety systems and challenge the integrity of the containment. In the worst scenario the safety function of the containment get lost and radioactive material, like I-131 and Cs-137, can be released in the atmosphere.

Even if many efforts have been taken in order to mitigate and reduce the potential risk of the hydrogen, the Fukushima Daiichi accident showed that it is still a key safety issue for nuclear power plants. [1]

The aim of this project, born from the collaboration of VKI and BelV, is to develop models for simulating the thermohydraulics behaviour of containment buildings during sever nuclear accidents.

2. State of the art

A sever nuclear accident is a complex event involving several physical phenomena, including particle and radiation transport, multiphase fluid dynamics and chemical reactions. This project will focus on the study of the hydrogen accumulation and deflagration in a containment atmosphere, typically in presence of steam and water.

In the past years, many lumped parameter codes (eg. MELCOR, APROS) and system codes (eg. CATHARE, COCOSYS) have been developed to model the progression of severe accidents in nuclear power plants [2]. The main advantage of these codes is their robustness and short computation time, nevertheless they are unable to accurately predict what happens in regions of the reactors characterized by a complex geometry. Due to these restrictions and the enhanced speed of the modern computers, CFD codes have become more attractive for a detailed analysis of different components of a reactor.

However, most of the commercial CFD codes do not include all the models needed for the simulations and prediction of hydrogen risk in nuclear accidents. These models have to be implemented in the code by the mean of user defined functions. These models are not always performant and optimized, resulting in poor prediction capabilities [3].

3. Methodology

For this work a CFD code will be developed with the use of OpenFOAM libraries. OpenFOAM offer extensive features for the development of multiphase and reacting solvers and it includes excellent libraries for linear algebra solvers and parallel computing.

The first solver that will be developed will feature a two-fluid three-field model [4]-[5]-[6] to describe the two phase flow. This model describes the liquid as two different fields, one as a continuous media and the other as a dispersed phase, representing the liquid droplets entrained in the liquid. The gaseous phase is modelled as a multicomponent field, composed of nitrogen, oxygen, steam and hydrogen. The challenge of this model will be to correctly describe the turbulent mass transport of the different gas components, the interaction of turbulence and the liquid droplets and the heat transfer at the walls of the containment.

The second solver will feature a combustion model to describe the hydrogen deflagration. The combustion can be modelled by two different approaches. The first one is to describe the combustible atmosphere as a mixture of all the components involved in the reactions and use a chemistry model to evaluate the production and consumption of each component. This method is useful for evaluating the production of dangerous reaction products during the combustion. The second model describes the combustible gas as two different mixtures, the unburned one and the exhaust one. The advancement of the flame front is represented by a progress variable whose behaviour is governed by the properties of the unburned mixture and the turbulence field [7]-[8].

The codes will be validated using a vast experimental database created in the framework of the OECD-NEA THAI-3 project. The aim of the THAI project is to investigate issues specific for Water Cooled Reactors under severe accident conditions: fission product behaviour, hydrogen mitigation and combustion. The experiments that investigates those topics will be performed in the THAI+ facility operated by Becker Technologies GmbH in Frankfurt [9], and are planned for the year 2018.

4. Planning

After reviewing the literature and the state of the art, the plan for the first year is to develop a solver that can predict the hydrogen stratification in a closed atmosphere in the absence of a liquid phase. Afterwards the solver will be validated by means of a suitable benchmark.



Figure 1: THAI+ test facility

In the second year, the two-phase three-field model will be implemented in the solver and validated using the THAI database.

In the last two years, a solver will be developed to predict the hydrogen deflagration in the containment building. The solver can be then validated by taking part in the blind simulation exercises proposed by the analytical group of the THAI-3 project.

5. Conclusion

The final aim of this PhD project is to create a CFD solver that is able to predict the distribution of hydrogen and the overpressure caused by its deflagration during a severe nuclear accident. However the models that will be investigated and further improved could also be useful for completely different application, like dispersion of gaseous pollutants simulations and hydrogen combustion simulations in engines.

Acknowledgments

This research is sponsored by BelV, a subsidiary of the FANC (Federal Agency for Nuclear Control), and is carried at the von Karman Institute for fluid dynamics.

References

[1] D.C. Visser, M. Houkema, N.B. Siccama, E.M.J. Komen, Validation of a FLUENT CFD model for hydrogen distribution in a containment, Nuclear Engineering and Design 245 (2012) 161–171.

[2] M. Freitag, E. Schmidt, S. Gupta, G. Poss, Simulation benchmark based on THAI-experiment on dissolution of a steam stratification by natural convection, Nuclear Engineering and Design 299 (2016) 37–45.

[3] D.C. Visser, N.B. Siccama, S.T. Jayaraju, E.M.J. Komen, Application of a CFD based containment model to different large-scale hydrogen distribution experiments, Nuclear Engineering and Design 278 (2014) 491–502.

[4] Hyungrae Kima, Soo Hyoung Kima, Seung-Jun Leea, Ik Kyu Parka, Han Young Yoona, Hyoung Kyu Chob, Jae Jun Jeongc, Development of CUPID-SG for the analysis of two-phase flows in PWR steam generators, Progress in Nuclear Energy 77 (2014) 132–140.

[5] J.J. Jeong, H.Y. Yoon, H.K. Cho, J. Kim, I.K. Park, A semi-implicit numerical scheme for a transient two-fluid three-field model on an unstructured grid , International Communications in Heat and Mass Transfer 35 (5) (2008) 597–605.

[6] Cesare Frepolia, John H. Mahaffyb, Katsuhiro Ohkawaa, Notes on the implementation of a fully-implicit numerical scheme for a two-phase three-field flow model, Nuclear Engineering and Design 225 (2-3) (2003) 191–217.

[7] J. Yaneza, A. Kotchourko, A. Lelyakin, KYLCOM Model for the Calculation of Under-Resolved Hydrogen Combustion Problems, Sixth International Seminar on Fire and Explosion Hazards.

[8] A. Cutrono Rakhimova, D.C. Vissera, T. Hollerb, E.M.J. Komena, , The role of CFD combustion modelling in hydrogen safety management VI: Validation for slow deflagration in homogeneous hydrogen-air-steam experiments, Nuclear Engineering and Design 311 (2017) 142–155.

[9] S. Guptaa, E. Schmidta, B. von Laufenberga, M. Freitaga, G. Possa, F. Funkeb, G. Weberc, THAI test facility for experimental research on hydrogen and fission product behaviour in light water reactor containments, Nuclear Engineering and Design 294 (2015) 183–201.

Turbulent heat transfer of separated flows at low Prandtl number

Sophia Buckingham

Environmental and Applied Fluid Dynamics Department, von Karman Institute for Fluid Dynamics, Belgium, sophia.buckingham@vki.ac.be

Supervisor: Jeroen van Beeck

Professor, Environmental and Applied Fluid Dynamics Department, von Karman Institute for Fluid Dynamics, Belgium, vanbeeck@vki.ac.be

University Supervisor: Yann Bartosiewicz

Professor, Institute of Mechanics, Materials and Civil Engineering, Universit catholique de Louvain, Belgium, yann.bartosiewicz@uclouvain.be

University Supervisor: Grégoire Winckelmans

Professor, Institute of Mechanics, Materials and Civil Engineering, Universit catholique de Louvain, Belgium, gregoire.winckelmans@uclouvain.be

Abstract

After presenting the project, this paper focuses on the turbulence generation method that will be used in the LES simuations that are foreseen. The existing temperature perturbation method (TPM) is applied for the first time to incompressible wall bounded flows. This requires fundamental changes in the formulation of the technique to insure the formation of turbulent structures.

Keywords: Large-Eddy simulation, low Prandtl number, turbulent inflow, buoyancy.

1. Introduction

1.1. Problematic

Liquid metal cooled reactors have been relying on CFD analyzes for their design and safety evaluation. However, the major challenge of these numerical simulations is the modeling of the turbulent heat transfer in the low Prandtl number (Pr) coolant. The classical Reynolds analogy fails to correctly predict the local heat transfer of such fluids, which may jeopardize the structure integrity of the reactor components. More advanced models have been developed but these require to be tested, calibrated and validated for a wide variety of flows to make them applicable to Liquid Metal Reactors.

Up to now, studies in forced convection have been limited to confined channel flows, which are not representative of turbulent thermal behavior of pool flows. Pool thermal-hydraulics regroups many challenges that are mainly concentrated in the upper plenum of the reactor, particularly important for turbulent heat transfer phenomena such as jet mixing, shear-layer and separations in a non-confined environment. These separated flow areas will be the focus of this PhD project.

1.2. Objectives

In the frame of the Horizon 2020 MYRTE project, the purpose of this work is to generate numerical validation data of separated flows at low Prandtl number, that can be used to validate more advanced turbulent heat transfer models. For this, the primary objective is to set-up an efficient wall resolved LES simulation able to accurately reproduce flow separation. The backward-facing step (BFS) is selected as test case to run these high fidelity simulations. It reproduces the fundamental flow mechanisms since it exhibits a detached shear-layer and a recirculation zone.

A validation of the LES simulation over the BFS is foreseen by comparison to experimental data acquired in the newly designed MYRTE wind tunnel of the VKI. A gas mixture composed of Helium and Xenon

will be tested, which enables to reduce the Prandtl number down to 0.2. This is the lowest achievable value for gases, since testing liquid metals (i.e. LBE, characterized by Pr = 0.025) is not conceivable if one wants to acquire detailed turbulence information. The LES simulation will then be used to generate data at three different Prandtl numbers, i.e. Pr = 0.025, Pr = 0.2 and Pr = 0.71. In depth-analysis will provide further insight into the influence of the molecular Prandtl number and in particular into the turbulent heat transfer behavior of low Prandtl number fluids in separated flows. Based on this data, the performance of turbulent heat transfer models in CFD can be later assessed.

2. Turbulent inflow generation for LES

2.1. Existing methods

The proper specification of turbulent inflow conditions for both Large Eddy Simulation (LES) and Direct Numerical Simulation (DNS) remains a considerable challenge. For developing flows, the most straightforward approach is to impose a laminar profile with small perturbations and to compute the transition to turbulence. However, simulating the transition process itself is very costly, and coupling this with a simulation of the downstream turbulent flow would be extremely expensive. The most common approach is to impose an already turbulent flow at the inlet. This too is a difficult task since turbulent flows are coherent in both space and time. Thus, imposing inflow conditions that are physically "almost correct" remains a considerable challenge. The flow needs to adjust until an equilibrium is reached where the governing equations are satisfied. The key requirement for a turbulent inflow technique is to be as "efficient as possible" in order to minimize the recovery length and reduce the computational cost.

The most common techniques to generate inflow turbulence can be grouped into two main categories: precursor simulation methods and synthetic methods.

Among the precursor simulation methods, two variants exist where the first consists in running an auxiliary calculation on a separate domain with periodic inlet-outlet boundary conditions, used for instance in [1] and [2]. The velocity in a section is stored at each time step; it is then fed at the inlet of the main domain that simulates the flow of interest. An important limitation, in addition to the need for an extensive database so that different flow regimes can be simulated, is that this approach is restricted to fully developed flows that rarely occur in reality. Moreover, the auxiliary simulation introduces "spurious" periodicity into the inflow as observed by Spille-Kohoff and Kaltenbach [3].

Cyclic or recycling methods are the second variant; these eliminate the necessity of generating a precomputed library by placing a cyclic plane in the inflow region of the actual computational domain. In the case of developing boundary layers, Lund et al. [4] proposed a procedure to rescale the velocity profile according to similarity laws before re-introducing it at the inlet. The computational effort of this second approach is reduced but, as precursor methods, contamination due to periodicity should not be overlooked.

Synthetic turbulence methods generate a pseudo-random coherent field of fluctuating velocities that tries to reproduce certain aspects of a turbulent flow. This requires the velocity field to be correlated both in time and space, with given first and second order moments, an assigned spectra, and the appropriate phase information between modes. An option to generate these random perturbations is to use digital filtering. Xie and Castro [5] developed a digital filter that is constructed based on the assumption that in most turbulent shear flows, turbulent velocity correlations can be approximated by an exponential function both in time and in space [6]. LES of a plane channel provided satisfactory validation of the technique. However, *a priori* detailed information about the flow is needed such as second order moments and integral length scales; something that is unknown in a majority of cases.

These shortcomings have motivated the development of alternative approaches that would be less complex and more flexible. In the frame of atmospheric boundary simulations, Mirocha et al. [7] introduced a new method based on the inclusion of random temperature perturbations. Thorough testing of the technique was carried out by Muñoz-Esparza [8] summarized in [9]. This technique relies on the principle that the seeded perturbations help to speed up turbulence generation by inducing local buoyancy effects. These vertical accelerations induce the creation of three-dimensional motions that eventually form turbulent structures. This method presents major advantages over the classical velocity perturbations. Instead of trying to impose realistic turbulence as boundary condition, turbulence is triggered through buoyancy, hence making the process naturally divergence-free. Moreover, it requires very limited information regarding the inlet flow specifications.

2.2. The TPM applied to wall bouded flows

2.2.1. Similarity parameters

Up to now, the temperature perturbation method has been applied to atmospheric boundary layer flows using the Weather Research and Forecasting (WRF) LES model [10]. The objective of this study is to apply the concept to incompressible wall bounded flows. The solver of OpenFOAM *buoyantBoussinesqFoam* is chosen to accommodate this technique as it models the buoyancy effects that will provoke the formation of turbulent structures by converting the seeded temperature gradients into velocity perturbations. A detailed description of the governing equations used by the solver can be found in [11]. Their non-dimensional form can be obtained by scaling the variables as follows:

$$\overline{u}_i^* = \overline{u}_i/U_0;\ x_i^* = x_i/L_0;\ t^* = tU_0/L_0;\ \tilde{P}^* = \tilde{P}/U_0^2;\\ (\Delta\overline{T})^* = (\overline{T} - T_0)/(\Delta T)_0;\ g_i^* = g_i/g_0\ , \tag{1}$$

with U_0, L_0, $(\Delta T)_0$ and g_0 that are reference quantities for velocity, length scale, temperature and gravity respectively.

This results in the dimensionless form for the momentum equation:

$$\frac{\partial\overline{u}_i^*}{\partial t^*} + \frac{\partial}{\partial x_j^*}(\overline{\overline{u}_i^*\overline{u}_j^*}) = -\frac{\partial\tilde{P}^*}{\partial x_i^*} + \frac{1}{Re}\frac{\partial}{\partial x_j^*}\left[\left(1 + \frac{\nu_{sgs}}{\nu_0}\right)\left(\frac{\partial\overline{u}_i^*}{\partial x_j^*} + \frac{\partial\overline{u}_j^*}{\partial x_i^*}\right)\right] - Ri\left(\Delta\overline{T}\right)^* g_i^*\ , \tag{2}$$

where the Reynolds number, *Re*, gives the ratio between advective and viscous forces:

$$Re = \frac{U_0 L_0}{\nu_0}\ , \tag{3}$$

and the Richardson number, *Ri*, gives the ratio between inertial and convective forces:

$$Ri = \frac{g_0\beta(\Delta T)_0 L_0}{U_0^2}\ . \tag{4}$$

Similarly for the temperature equation, one obtains its dimensionless form as

$$\frac{\partial\overline{T}^*}{\partial t^*} + \frac{\partial}{\partial x_j^*}\left(\overline{\overline{T}^*\overline{u}_j^*}\right) = \frac{1}{Pe}\frac{\partial}{\partial x_j^*}\left[\left(1 + \frac{\alpha_{sgs}}{\alpha_0}\right)\frac{\partial\overline{T}^*}{\partial x_j^*}\right]\ , \tag{5}$$

where the Peclet number, Pe, is defined as

$$Pe = Re\ Pr = \frac{U_0 L_0}{\alpha_0}\ , \tag{6}$$

with the Prandtl number, Pr, giving the ratio between the momentum diffusivity and the thermal diffusivity, previously defined.

Referring to the momentum equation Eq. (**??**), one understands how the inclusion of temperature gradients can generate a buoyancy force that will induce the development of turbulent structures. The importance of these buoyancy effects are governed by the Richardson number, identified as a key parameter of the TPM.

2.2.2. Computational settings

The cell perturbation method proposed by Muñoz-Esparza [9] imposes random temperature perturbations along square bidimensional groups of cells. This research was extended by the same author [12] with the objective of identifying and optimizing the governing parameters in order to reduce the recovery length. These recommendations serve as main guidelines in this work, in order to help define the key parameters of the TPM.

Firstly, the perturbation time scale defines the frequency at which the perturbation values are changed. Thus, a dimensionless perturbation time scale (Γ) is proposed by Muñoz-Esparza [12], based on the perturbation time t_p:

$$\Gamma = \frac{t_p U_1}{d_c}\ . \tag{7}$$

This parameter represents the time taken by the flow to be advected across a perturbation cell in the most adverse flow conditions. This is considering that the flow direction is along the diagonal of the perturbation cell, $d_c = \sqrt{2}n_c\Delta x$, with n_c the number of grid cells per perturbation cell side and Δx the cell size in the streamwise direction, for a velocity U_1 taken at the first vertical grid point. The study highlighted that the performance of the method can be optimized by leaving sufficient time for the flow to assimilate the perturbations before imposing the next perturbations, such that $\Gamma \simeq 1$. Consequently,

a value of $\Gamma = 1$ will here be taken to calculate the perturbation frequency.

Secondly, the temperature perturbations are distributed over a so-called "seeding zone" that starts from the inflow boundary. A uniform value is randomly attributed to tridimensional perturbation cells of $8\Delta x$ in the streamwise (x) direction and $8\Delta z$ in the wall-normal (y) and spanwise (z) directions. The seeding zone of length L_s, shown in Fig. 1, extends three perturbation cells parallel to the inflow boundary, thus covering 24 grid cells in the streamwise direction.

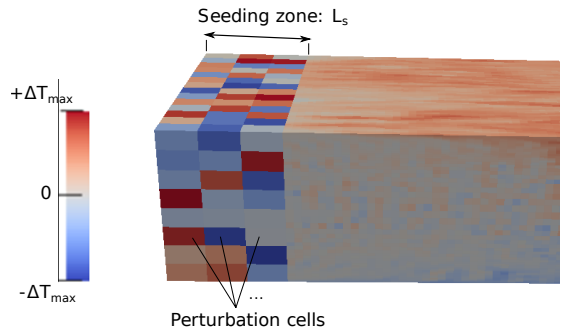

Figure 1: 3D contours of temperature, cell average values obtained with $\beta(x) = +linX$

The perturbation cell size is chosen based on the study of Muñoz-Esparza [12] that recommends choosing a minimum size of $8\Delta x$ to avoid the energy from rapidly dissipating when applied to higher wavelengths.

A major difference compared to the previous application concerns the length scales involved. In atmospheric flows, even at a microscale level these may range from an order of magnitude of 10^{-1} to 10^{2} m, such that buoyancy effects are naturally present in these types of flows, with a typical Richardson number of $Ri = 0.3$. Wall bounded flows though involve smaller length scales (¡ 10^{-1} m) and typically for air and limited gradients ($\Delta T < 1$ K), a plane channel flow simulation at $Re_\tau = 395$ is characterized by $Ri << 1$ and hence negligible buoyancy effects. Let us recall how the buoyancy force of Eq. (2) is defined in the current framework:

$$-\beta\left(\overline{T} - T_0\right) g_i \;\Leftrightarrow\; -Ri\left(\Delta\overline{T}\right)^* g_i^* \,. \tag{8}$$

Since the purpose of the temperature method is to generate inflow turbulence without affecting the downstream flow in a significant way, some modifications of the temperature perturbation method are needed to fulfill both of these criteria. In particular, the buoyancy force needs to play an active role only close to the inflow region. To fulfill this requirement, the solution is to manipulate the local thermal expansion ratio (β field), or equivalently the local Richardson number (Ri field), by artificially increasing its value within a so-called perturbation zone near the inflow. This will enable the seeded perturbations to induce vertical accelerations that are sufficient to trigger the onset of three-dimensional motions and eventually accelerate the formation of turbulent structures. By setting Ri back to zero outside of the perturbation zone, these effects will be rendered inactive downstream. The maximum local artificial Richardson number that is applied within the fully active zone is defined according to guidelines formulated in [12]. A value of 0.2 is fixed here initially, representative of a mixed convection regime.

3. Presentation of the results

3.1. Validation on a plane channel flow

3.1.1. Numerical description

A plane channel flow is simulated with a domain size of $30\,\delta \times 2\,\delta \times 3.5\,\delta$, with δ the half channel height. The Reynolds number is set to $Re_\tau = 395$ based on δ and the friction velocity u_τ. A mesh of 1.68 Million cells is generated, with a number of grid points of $300 \times 80 \times 70$. The mesh is uniform in the streamwise and spanwise directions with resolutions of $\Delta x^+ = 39.5$ and $\Delta z^+ = 19.8$ respectively. A vertical stretching is applied in the wall-normal direction with an expansion ratio of 1.1 resulting in a first cell center at $y^+ = 0.9$. The Smagorinsky sub-grid scale model is applied with a coefficient $C_s = 0.065$ [13] combined with a van Driest near wall damping [14]. Second order schemes are used for the time and spatial discretization.

No-slip wall boundary conditions are applied to the top and bottom walls while periodic boundary conditions are applied in the spanwise direction. A zero velocity gradient is imposed at the outlet while the mean velocity profile extracted from a periodic inlet/outlet channel simulation is applied at the inlet. This reference case, referred to as "case PBC", provides a straighforward validation while testing the TPM since a fully developed turbulent solution is obtained thanks to streamwise periodicity.

3.1.2. *Improvement of the TPM for faster turbulence development*

A preliminary study [11] was performed where special emphasis was brought on the specifications of the perturbation zone. We recall that the purpose of this zone is to trigger turbulence by manipulating the thermal expansion coefficient. By doing so, the buoyancy force becomes sufficiently strong to perturbate the flow, while keeping the temperature gradients negligible. The results of [11] highlighted the necessity of introducing a transition region of length L_{tr} between the fully active region of length L_a , where Ri_a was applied from the inlet, to the rest of the domain that is characterized by zero buoyancy ($Ri = 0$). Therefore, the perturbation zone has a total length of $L_p = L_a + L_{tr}$. Moreover, the main conclusion that could be drawn is that a simple linear function within the transition region was found to be most beneficial. This first function, denoted $Ri\,(X) = linX$, and initial characteristic lengths of the perturbation zone are shown in Fig. 2 a).

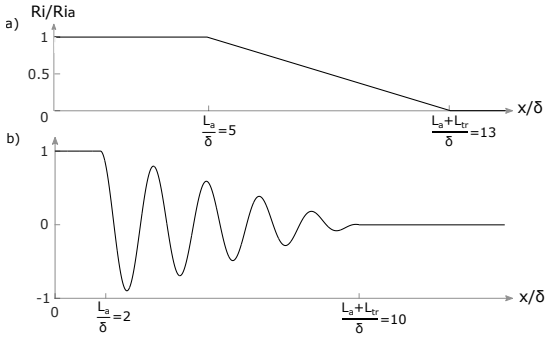

Figure 2: Streamwise variation of the local artificial Richardson number - fully active region of length L_a and transition region of length L_{tr} a) $Ri\,(X) = linX$ b) $Ri\,(X) = linX \cdot cosX$

In addition, by examining more the details of the turbulent flow solution, the normal stresses in the spanwise direction, $< w'w' >^+$, and particularly in the wall normal direction, $< v'v' >^+$, suggested that a minimum length of 20 δ was required for the stratification effects to fully dissipate. These vertical flow motions are caused by a perturbation function, $Ri\,(X) = linX$, that remains linearly positive along the streamwise direction, and uniform in the vertical direction. Consequently, the fluid stratifies as observed in Fig. 3 a).
In the continuaton of this work, several alternative perturbation functions were superposed to the linear decrease of Ri along the streamwise direction, with the aim of efficiently reducing stratification effects. Among these, the superposition of a cosine function

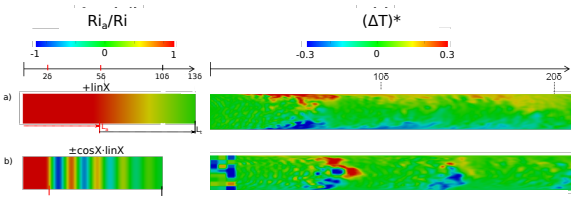

Figure 3: 2D contour fields in the vertical symmetry plane, obtained with different perturbation functions

in the streamwise direction, referred to as $Ri\,(X) = cosX \cdot linX$ and plotted in Fig. 2 b), insures satisfactory mixing of the thermal field as shown in Fig. 3 b). For simplicity, the fully active region is kept equal to the seeding zone ($L_a = L_s$), which roughly measures 2 δ, while initially the transition region extends until 10 δ.
The contour plots give a first indication of how efficient each of these perturbation functions may be in preventing the establishment of stratification. However, they may affect the flow behavior in various ways. For a quantitative measure of their performance, we should refer to how quickly the flow recovers from this perturbation. For this, the recovery length is assessed based on the dimensionless wall shear stress, $\overline{\tau}_w^+ = \overline{\tau}_w/(u_\tau^2)$. An error criteria of 5% around the reference value of 1 is added to the graphs. This parameter is plotted in Fig. 4 for each of the different perturbation functions.

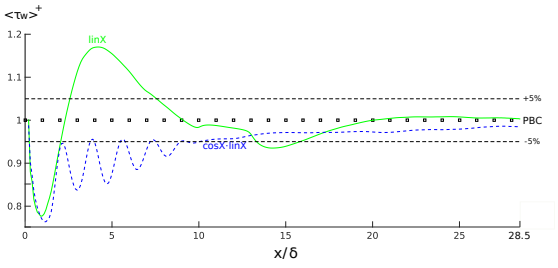

Figure 4: Effect of the perturbation function on the wall shear stress recovery

As suspected, in the case where a linear damping ($linX$) is applied, the presence of stratification effects results in a longer fetch of about 20 δ for the flow to actually stabilize at equilibrium. This stabilization length is related to the fact that the flow still requires a certain fetch downstream of the perturbation zone to mix thanks to turbulence and de-stratify.

Already temperature contours had suggested that superposing a cosine variation streamwise could help promote mixing of the thermal field. Indeed, the func-

tion ($cosX \cdot linX$) appears to be much more efficient. In addition to a shorter development length, the perturbation felt by the wall shear stress is reduced in amplitude. This enables the flow to converge faster along the channel towards a stabilized solution, reducing the flow recovery to roughly 10 δ based on an error criteria of 5%.
We may conclude from this first study that the perturbation function must provide sufficient mixing to eliminate stratification effects, but without perturbing the flow excessively. The use of a cosine variation coupled with a linear transition in the streamwise direction appears to constitute a most efficient way of manipulating the artificial local Richardson number Ri inside the transition region of the perturbation zone.

3.1.3. Optimization of the TPM

Several parametric studies have been performed to try and enhance the performance of the TPM. The Richardson number was identified in Section 2.2.1 as the key parameter governing the strength of the buoyancy effects. Its influence on the results is investigated in Fig. 5. Various values are tested around the initial value of 0.2, keeping Ri within the range $[0.1 - 0.4]$.

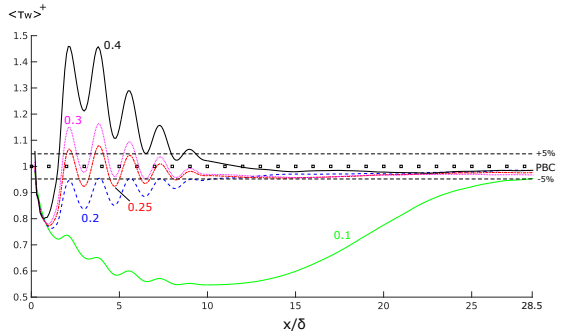

Figure 5: Effect of the Richardson number on the wall shear stress recovery with $Ri\,(X) = cosX \cdot linX$

The variations observed by the wall shear stress are directly related to the Richardson number. For $Ri = 0.1$, the imposed perturbations are not sufficiently strong and the buoyancy triggering mechanism is less effective. A much greater fetch of roughly 30 δ is needed for turbulence to fully develop. The initial value of $Ri = 0.2$ is within an optimal perturbation range that goes up to $Ri = 0.3$. Within this interval, the buoyancy effects are just enough to insure a rapid development of turbulence with a minimum recovery length of approximately 10 δ. Stronger perturbations, represented by the case where $Ri = 0.4$, will induce a further distortion of the velocity field near the inlet, characterized by a perturbation of stronger amplitude in the wall shear stress. This additional energy will take longer to dissipate, thus requiring a longer fetch for the flow to stabilize. In conclusion, an optimum Richardson number of 0.25 has been identified, for which the flow distortion is the least and the recovery length is reduced down to 10 δ.

Another aspect concerns the spatial frequency of the perturbation function ($cosX \cdot linX$). Up to now, it was adjusted so that five periods (5T) would appear throughout the transition region. The aim is to further optimize this modulation by changing the cosine frequency and analyzing its effect on the results. The transition length and the Richardson number are kept equal to 8 δ and 0.2 respectively.
Two additional configurations are tested, where the number of periods is reduced to four (4T) and increased to six (6T). Above this limit, a mesh refinement would be required in the streamwise direction to correctly capture the cosine variation. A slight influence is observed on the evolution of the wall shear stress plotted in Fig. 6. Although the recovery length reduces with the number of periods, nevertheless, the distance to reach a more stable behavior appears similar.

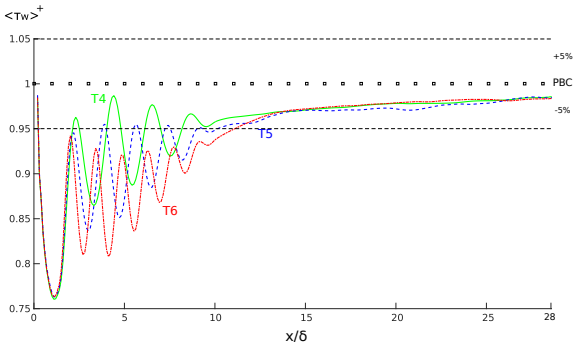

Figure 6: Effect of the frequency of perturbation on the wall shear stress recovery

Therefore, to truly evaluate the frequency effect, one should refer to the turbulent flow solution by analyzing the turbulent statistics. Firstly, the mean velocity profiles are compared in Fig. 7 at every 5 δ along the channel. We recall that this profile is imposed at the inlet, thus the turbulent inflow method has very little influence on this quantity. Although "case 4" is the closest to the reference at 5 δ, one should refer to second moment statistics that will take longer to equilibrate as the turbulent structures develop. Looking at

the vertical stresses plotted in Fig. 8, this first position is still too close to the inlet perturbation. Furthermore, considering the streamwise and shear stresses shown in Fig. 9 and 10 respectively, the streamwise position at 10 δ is more representative since close to flow recovery and indicates that "case 5T" performs just as well as "case 4T", while the peak values are slightly over-estimated by "case 6T".

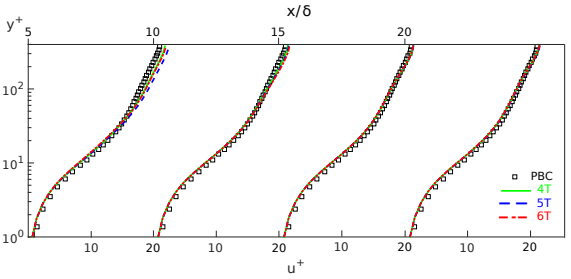

Figure 7: Effect of the frequency of perturbation on the mean velocity profile

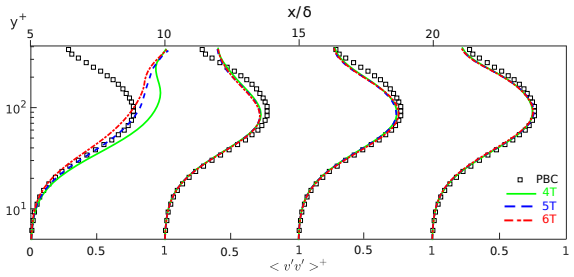

Figure 8: Effect of the frequency of perturbation on the Reynolds vertical stress profile

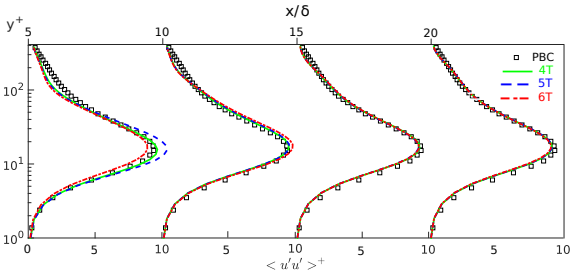

Figure 9: Effect of the frequency of perturbation on the Reynolds streamwise stress profile

To conclude, adjusting the frequency of perturbation to five periods within the transition region appears to be appropriate. Moreover, a satisfactory recoveryis obtained in terms of both the wall shear stress and the

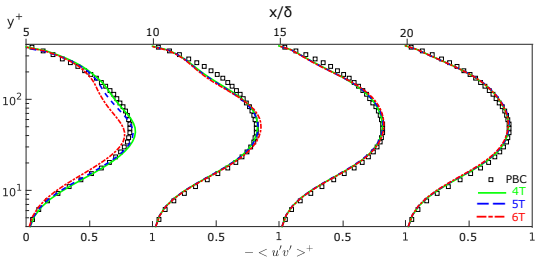

Figure 10: Effect of the frequency of perturbation on the Reynolds shear stress profile

Reynolds stresses by 10 δ. Yet, the TPM should be compared with a competing method before drawing final conclusions. For this, an optimized set-up will be used for which the perturbation function ($cosX \cdot linX$) undergoes five periods within a transition region of L_{tr} = 8 δ. The Richardson number is set to 0.25.

3.2. *Comparison to results obtained with a synthetic turbulence generator*

The results presented in the previous section have demonstrated that the optimized TPM is able to generate realistic turbulence shortly after the inlet boundary. However, to further evaluate the efficiency of the method, a comparison with results obtained using the synthetic turbulence generator method of Xie and Castro [5] is performed on the plane channel flow test case. Kim et al. [15] proposed a modification to insure constant mass flux at the inlet, denoted as "XCMC", for "Xie and Castro with Mass Correction". The original implementation was kindly provided by the authors [5], such that a true comparison of the two methods could be performed using the same numerical set-ups (see Section 3.1.1).

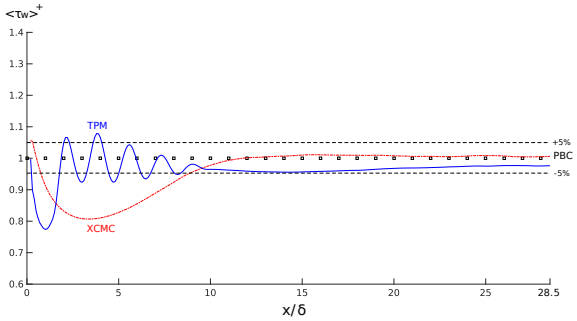

Figure 11: Dimensionless wall shear stress obtained with the TPM (full line) and XCMC (dash-dot line), compared to the reference "case PBC" (square symbol).

First, the dimensionless wall shear stress is plotted along the channel in Fig. 11. The development distance of the two methods are similar and appear to be approximately 10 δ. At this location, the error on the wall shear stress is within 5%, and both curves are stabilizing around equilibrium.

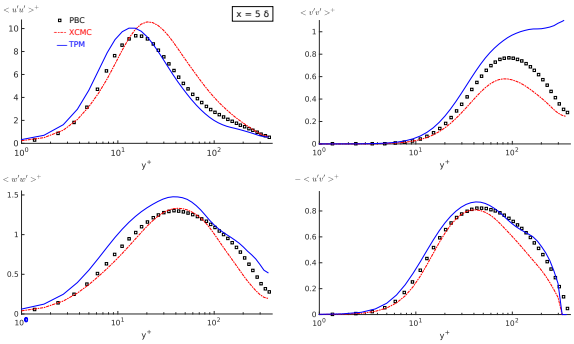

Figure 12: Reynolds stresses obtained at $x = 5\,\delta$ with the TPM (full line) and XCMC (dash-dot line), compared to the reference "case PBC" (square symbol).

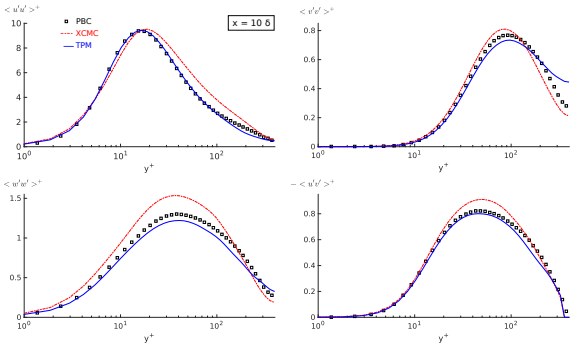

Figure 13: Reynolds stresses obtained at $x = 10\,\delta$ with the TPM (full line) and XCMC (dash-dot line), compared to the reference "case PBC" (square symbol).

A more detailed comparison is proposed in Fig. 12 to 14, where the Reynolds stresses are plotted at 5, 10 and 15 δ along the channel. At the first location, the flow still shows signs of being strongly affected by the inlet perturbation, particularly the wall normal stress $< v'v' >^+$. However, in agreement with the previous statement based on the wall shear stress, a fetch of twice this length, that is 10 δ, is sufficient for the turbulent structures to develop and approach an equilibrium state. Indeed, both the XCMC approach and the optimized TPM exhibit a very good agreement with the reference "case PBC". Moreover, the discrepancies observed by the optimized TPM proposed in this

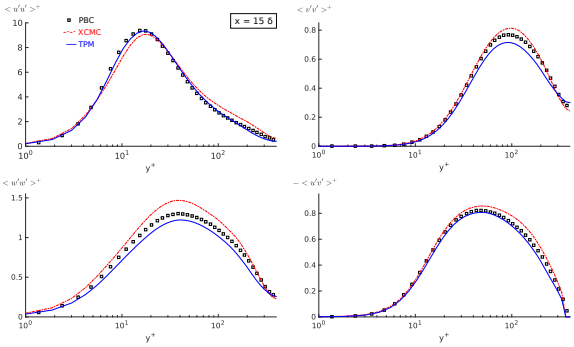

Figure 14: Reynolds stresses obtained at $x = 15\,\delta$ with the TPM (full line) and XCMC (dash-dot line), compared to the reference "case PBC" (square symbol).

work are reduced compared to the XCMC, which confirms the efficiency of the method. An excellent agreement is reached by the time the flow reaches 15 δ. In terms of CPU time, around 5-6 flow throughs were sufficient for the optimized TPM to reach statistical convergence. Yet, if one considers the recovery length based on both wall shear stress and Reynolds stresses, it remains similar in both cases. However the XCMC requires non-trivial input data such as second moment statistics and integral length scales, whereas the optimized TPM only requires the mean velocity profile at the inlet.

4. Conclusion

The temperature perturbation method has been optimized to efficiently generate inflow turbulence for LES (or DNS) simulations of wall-bounded flows. As previously developed for atmospheric flows, the flow is seeded with random temperature perturbations applied to groups of mesh cells placed at the inlet of the domain. The principle relies on the creation of turbulent structures via artificial buoyancy effects.

For this, the incompressible solver of OpenFOAM v2.3 with the Boussinesq approximation is used to account for buoyancy. A plane channel flow is chosen as test case to validate this new approach, as it provides straightforward validation data by using periodic inlet/outlet boundary conditions. For the method to be applicable to wall-bounded flows, the key modification that is proposed consists in creating a perturbation zone at the entrance of the domain. A local artificial Richardson number is applied within the perturbation zone, so as to enhance buoyancy. This zone is divided into a fully active region of 2 δ, where buoyancy effects reach a maximum, followed

by a transition region that is essential to insure a smooth progression of the Richardson number back to zero. A preliminary study [11] demonstrated that using a linear variation as transition is able to efficiently limit the flow distortion compared to an abrupt change. However, the stratification effects that are created by a simple linear transition proved to be detrimental.

Consequently, the focus of this latest work has been to propose an appropriate modulation that would help pre-mix the flow and avoid stratification effects from slowing down the flow recovery length. Among the different functions that were tested, the most efficient one consists in adding a cosine variation of five periods to the linear decrease observed by the artificial local Richardson number within a transition region of $8\,\delta$. By the end of the perturbation zone of $10\,\delta$, a satisfactory flow recovery is obtained, both in terms of the wall shear stress and of the Reynolds stresses.

A comparison of the results obtained using the optimized TPM with those obtained using the synthetic turbulence generator method of Xie and Castro with mass correction [15], shows that the TPM is as efficient, with a slight improvement in the Reynolds stresses that are in excellent agreement with the reference fully developed turbulent state at $10\ \delta$. Even though similar performance is achieved, the major advantages of the optimized TPM over existing turbulent inflow methods is that, other than the mean velocity profile at the inlet, it does not require any second order moments or integral length scales as input. Therefore, in addition to it simplicity, it appears to be very flexible and potentially applicable to a wide variety of flows.

Future work will consist in applying the optimized TPM to generate turbulence at the inlet of the LES simulation over the heated BFS. Indeed, the temperature variations inserted by the optimized TPM do not influence the flow downstream of the perturbation region. Therefore, the turbulent heat transfer within the separated flow region will remain unaffected.

Acknowledgments

This work has been partially funded by the European MYRTE Horizon 2020 project (Contract number: 662186). The authors would like to thank Yusik Kim and Zheng-Tong Xie for providing the original OpenFOAM implementation of the XCMC.

References

[1] N. Li, E. Balaras, U. Piomelli, Inflow conditions for large-eddy simulations of mixing layers, Phys. Fluids 12 (2000) 935–938.

[2] U. Piomelli, E. Ballaras, A. Pascarelli, Turbulent structures in accelerating boundary layers, J. Turbul. 1 (2000) 001.

[3] A. Spille-Kohoff, H.-J. Kaltenbach, Third AFOSR International Conference on DNS/LES Arlington, TX, 5-9 August 2001, in: Generation of turbulent inflow data with a prescribed shear-stress profile, 2001, in DNS/LES Progress and Challenges, edited by C. Liu, L. Sakell, and T. Beutner.

[4] T. S. Lund, X. Wu, K. D. Squires, Generation of turbulent inflow data for spatially-developing boundary layer simulations, J. of Computational Physics 140 (1998) 233–258.

[5] Z.-T. Xie, I. P. Castro, Efficient generation of inflow conditions for large eddy simulation of street-scale flows, Flow Turbulence and Combustion 81 (3) (2008) 449–470.

[6] N. Mordant, P. Metz, O. Michel, J.-F. Pintonk, Measurement of Lagrangian velocity in fully developed turbulence, Phys. Rev. Lett. 87.

[7] J. Mirocha, B. Kosovic, G. Kirkil, Resolved tubulence characteristics in large-eddy simulations nested within mesoscale simulations using the Weather Research and Forecasting model, Mon. Weather Rev. 142 (2014) 806–831.

[8] D. Muñoz-Esparza, Multiscale modelling of atmospheric flows: towards improving the representation of boundary layer effects, PhD Thesis, Université Libre de Bruxelles - von Karman Institute for Fluid Dynamics, Brussels, Belgium (2013).

[9] D. Muñoz-Esparza, B. Kosovic, J. Mirocha, J. van Beeck, Bridging the transition from mesoscale to microscale turbulence in numerical weather prediction models, Boundary Layer Meteorol. 153 (2014) 409–440.

[10] W. Skamarock, J. Klemp, J. Dudhia, D. Gill, D. Barker, M. Duda, X. Huang, W. Wang, J. Powers, A description of the advanced research WRF version 3, NCAR Tech. Note NCAR/TN-475+STR (2008).

[11] S. Buckingham, L. Koloszar, C. Garcia-Sanchez, Y. Bartosiewicz, G. Winckelmans, Temperature perturbation method to generate turbulent inflow conditions for LES/DNS simulations, 9th International Conference on Computational Fluid Dynamics, Istanbul, Turkey, 2016.

[12] D. Muñoz-Esparza, B. Kosovic, J. van Beeck, J. Mirocha, A stochastic perturbation method to generate inflow turbulence in large-eddy simulation models: Application to neutrally stratified atmospheric boundary layers, Physics of Fluids 27 (035102).

[13] P. Moin, J. Kim, Numerical investigation of turbulent channel flow, J. Fluid Mech. 118 (1982) 341–377.

[14] E. R. van Driest, On turbulent flow near a wall, AIAA 23 (1956) 1007–1011.

[15] Y. Kim, I. P. Castro, Z.-T. Xie, Divergence-free turbulence inflow conditions for large-eddy simulations with incompressible flow solvers, Computers and Fluids 84 (2013) 56–68.

Numerical and experimental investigations of the meandering phenomenon in wind-turbines wakes

Nicolas Coudou

Environmental and Applied Fluid Dynamics Department, von Karman Institute for Fluid Dynamics, Belgium, nicolas.coudou@vki.ac.be

Supervisor: Jeroen van Beeck

Professor, Environmental and Applied Fluid Dynamics Department, von Karman Institute for Fluid Dynamics, Belgium, vanbeeck@vki.ac.be

University Supervisor: Laurent Bricteux

Assistant professor, Department of Fluids-Machines , Université de Mons (UMONS), Belgium, laurent.bricteux@umons.ac.be

University Supervisor: Philippe Chatelain

Assistant professor, Institute of Mechanics, Materials and Civil Engineering (iMMC), Université catholique de Louvain (UCL), Belgium, philippe.chatelain@uclouvain.be

Abstract

Between the years 2000 and 2015, the cumulative wind-power installations in the European Union increased from 12.9 GW to 141.6 GW. Based on the European Wind Energy Association's central scenario, wind-energy installations could amount to over 320 GW in 2030. This important rise in the use of wind energy over the years results in more and larger clustered wind farms. It is therefore fundamental to have an in-depth knowledge of wind-turbines wakes, and especially a better understanding of the well-known but less understood wake-meandering phenomenon which causes the wake to move as a whole in both horizontal and vertical directions as it is convected downstream. Because this phenomenon causes the wake to be swept in and out of the rotor disk of downstream turbines, it is critical to understand it to predict mechanical fatigue and loading on the downstream turbines.

The aim of this project is to study in-depth the wake meandering phenomenon using a combination of advanced experimental and numerical tools. The phenomenon will be studied on a 3×3 scaled wind farm composed of three-bladed rotating wind-turbine models and located in the VKI atmospheric-boundary-layer wind tunnel L-1B, inside which atmospheric boundary layers (ABLs) developing on *slightly rough* and *moderately rough* terrains will be modeled. The influence of the incoming velocity profile and turbulence intensity as well as the influence of the wind turbines operating point will be investigated. The experimental campaigns will involve stereoscopic Particle Image Velocimetry (2D3C-PIV), 2D time resolved PIV (2D TR-PIV) and three-component hot-wire anemometry (3C-HWA). The numerical studies will rely on a high-performance implementation of a vortex particle-mesh (VPM) method with immersed lifting lines. The advanced turbulence models (Large Eddy Simulation, LES) implemented will allow to capture very fine physical details of the wake turbulence and as such help to create and validate low-fidelity wake meandering models, and to investigate scaling effects of small-scale wind tunnel modeling of wind farms in order to establish confidence in this approach.

A spectral analysis performed with the spatial and temporal signals obtained respectively from preliminary 2D2C-PIV and 1C-HWA measurements performed in the wake of the three wind turbines constituting the mid row (in stream-wise direction) of the wind farm, led to Strouhal number $St = fD/U_{hub} \approx 0.20 - 0.22$.

Keywords: 2D3C-PIV, 3C-HWA, Neutral-ABL wind tunnel, Wake meandering, Wind-turbines wakes

Experimental study of cavitating flow and fluid hammer in cryogenic conditions

Claudia Esposito

Environmental and Applied Fluid Dynamics Department, von Karman Institute for Fluid Dynamics, Belgium, claudia.esposito@vki.ac.be

Supervisor: Maria Rosaria Vetrano

Associate Professor, Department of Mechanical Engineering, KU Leuven, rosaria.vetrano@kuleuven.be

Associate Professor, Environmental and Applied Fluid Dynamics Department, von Karman Institute for Fluid Dynamics, Belgium, vetrano@vki.ac.be

University Supervisor: Johan Steelant

Associate Professor, Department of Mechanical Engineering, KU Leuven - ESA-ESTEC, Johan.Steelant@esa.int

Abstract

This report presents a research work on cavitating flows in cryogenic conditions. An orifice configuration is chosen at this purpose. Thermodynamic effect will be addressed by using a thermosensitive fluid such as LN_2. The first task of the project is the determination of the technical requirements for the cryogenic experimental set-up and the test conditions. To do that, preliminary measurements on an isothermal test bench, namely with water, have been carried out and they are presented here.

Keywords: cavitation, orifice, thermodynamic effect

1. Introduction

1.1. Motivation

Cryogenic multiphase phenomena are easily induced within the propulsion system of liquid rocket engines. In fact, the activation of spacecraft propulsion systems generally consists of four phases. The first two are the main responsibles of multiphase cryogenic flow. The first phase includes the launch and the separation of the spacecraft from the launcher vehicle. During this phase, the propulsion system is inactive and the propellant tanks are isolated from the combustion chamber by means of a set of valves. The second phase starts with the pressurization of the tanks and the opening of the latch valve, which results in the filling and pressurization of the propellant lines of the spacecraft. Those are initially vacuum pumped or filled with a non-condensable gas at low pressure. This operation is called *priming* and, once done, the propulsion system is fully operational. It is during this phase that a bubble flow is produced by the combination of several phenomena such as boiling (due to the chilldown of the propellant line), cavitation (due to the passage of the fluid through a valve) or to other phenomena such as fluid hammer.

Pipelines and subsystems, which constitute the feeding system, must be properly designed to avoid alterations in the proper operation of the whole system. Thus, a correct characterization of these phenomena is essential. Unfortunately, their prediction and control is still hampered by the unavailability of validated theoretical models for each sub-process. The limiting factor is the difficulty of describing highly non-equilibrium thermodynamic processes in terms of simplified and computationally efficient models, based on equilibrium thermodynamic assumptions.

In this context, the creation of a reliable and consistent experimental database is crucial for assessing the accuracy of model predictions and their range of validity. Nevertheless, the physical properties of the propellant used, generally cryogenic fluids, and the complexity of the multiphase process strongly limits the possible measurement techniques to use. The

most common measurements are about stationary and unstationary temperature and pressure. Both are usually performed with ad-hoc cryogenic sensors, sometimes flush mounted. Even if many non-intrusive techniques, optical based, already exist for two-phase flows, their use is limited to rather standard situation in which the temperature, the velocities and the void fraction level are not extreme.

1.2. Objectives

This work is aimed at characterizing one of the subprocesses happening during the priming operation of a spacecraft propulsion system, namely cavitation. This study will address cavitation both in stationary condition and unstationary one. In particular, the second case refers to the effect of fluid hammer on a cavitating flow. The outcome of this experimental campaign will be the creation of a cryogenic experimental database in terms of pressure, temperature, velocity and flow topology. The purpose is to provide a database that can be used to validate the numerical codes developed to determine damages of valves and pipes due to pressure peaks linked to cavitation and fluid hammer.

Preliminary tests in isothermal environment are carried out as well. Tests with isothermal fluids, such as water, are not considered representative of the cryogenic phenomenon. However, a comparison has already been performed by Pinho [1]. Both water and liquid nitrogen were used as working fluids to test performances of an orifice. Based on his experimental results, he concluded that hydraulic similarity exists between different fluids at single phase condition. Unfortunately, the two-phase cavitating regime has not been investigated experimentally.

The final objective of this work is to experimentally characterize cryogenic cavitation. At this purpose, non intrusive measurement techniques will be used. Finally those data could allow to develop empirical or semi-empirical models for engineering design.

2. Cavitation

Cavitation is commonly defined as the breakdown of a liquid medium under very low pressures [2]. Consequently, vapor cavities appear inside the liquid leading to an unstable two-phase flow. The pressure threshold which induces this phase change is assumed to be the saturation pressure, P_{sat}. It is a property of the liquid and a function of the temperature. Fig. 1 shows the saturation curve for water. Above this pressure, water is in its liquid phase, below it becomes vapor.

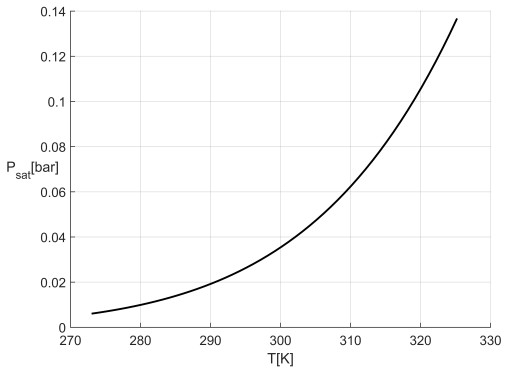

Figure 1: Saturation curve for water

A practical way to include cavitation in the design process and to characterize its extent is provided by the *Cavitation number*,σ. It is a dimensionless parameter given by the ratio of the pressure which provokes cavitation and the actual pressure of the system. Different definitions exist in literature. They depend on the particular flow to study: external jets, flows around bodies or through valves or orifices. The definition we are going to use is the one in Eq. 1 proposed by [3] and also used by [4].

$$\sigma = \frac{P_{up} - P_{sat}}{\Delta P} \tag{1}$$

In Eq. 1 P_{up} is the pressure upstream the orifice and ΔP the pressure drop through it.

2.1. Thermodynamic effect

The thermodynamic effect is a localized cooling process which takes place during the cavitation mechanism [5]. To form and to sustain a vapor bubble, the latent heat is extracted from the surrounding liquid. This effect is usually neglected and cavitation is considered as an isothermal process. However, such an approximation is not always correct. To understand why and when this effect must be taken into account, it is useful to look at the heat balance, Eq. 2, as suggested by [2].

$$\rho_v \cdot V_v \cdot \Delta H = \rho_l \cdot V_l \cdot C_{pl} \cdot \Delta T \tag{2}$$

where C_{pl} is the specific heat of the liquid phase, ΔH is the latent heat of vaporization and the subscripts v and l refer to vapor and liquid phase respectively. A non-dimensional temperature difference, given in Eq. 3, is commonly used [6]. It stands for the temperature drop to apply to a fixed volume of liquid to

produce the same volume of water.

$$\Delta T^* = \frac{\rho_v \cdot \Delta H}{\rho_l \cdot C_{pl}} \tag{3}$$

This temperature drop ΔT^* depends only on the physical properties of the liquid. Table 1 shows characteristic properties of water and three cryogenic liquids, namely, nitrogen, hydrogen and oxygen. These values are all referred to a pressure of 5 bar. It appears that the order of magnitude of ΔT^* for water is much smaller than for the cryogenic liquids. This justifies the distinction into two different kinds of liquids. On the one hand, liquids as water, are isothermal. Cavitation occurs at a constant temperature. On the other hand cryogenic fluids are called thermosensitive. Temperature depression is much more significant and cannot be neglected anymore. This thermal delay also affects the definition of the cavitation parameter. The new expression is written in Eq. 4.

$$\sigma = \frac{P_{up} - P_{sat}(T)}{\Delta P} \tag{4}$$

Table 1: Characteristic values for water compared to cryogenic liquids, [7]

	H_2O	LOx	LN_2	LH_2
T [K]	303.16	108.81	93.99	27.24
C_{pl} [J/g · K]	4.18	1.80	2.20	16.41
ρ_v/ρ_l	$3.05e-5$	0.02	0.03	0.10
ΔH_{vap}	2429.82	191.38	173.32	372.76
ΔT^*	**0.02**	**0.95**	**1.12**	**2.81**

Experimental studies on the thermal effects in cavitating inducers have been performed in [6; 8]. Measurements mainly concern pressure fluctuations. A result was that the temperature depression due to cavitation was increasing with the cavity length.

The importance of the mass-convection across the liquid-vapor interface is discussed in the work by Hosangadi [9]. A cavitating cryogenic flow is simulated over a hydrofoil. As for isothermal cavitation, the vapor bubble has a sharp and distinct interface due to the gap in density across the liquid-vapor interface. It behaves like a limiting streamline and the liquid flows around it. On the contrary, when thermal effects become preponderant, the flow becomes frothy and the vapor volume fraction inside the cavity strongly drops. Since the cavity is more porous, the streamlines flow into it. A small portion of liquid is locally vaporized when it convects into the cavity. The oncoming liquid faces a lower gradient at the interface. The flow slowly deviates and the low pressure region spreads laterally. So the bubble are shorter but they spread laterally allowing a larger entrainment of the liquid.

The rate of this vaporization process is affected by the local geometry and flow conditions. Therefore the shape and the size of the vapor bubble depend on the physical properties of the working fluid as well as on local fluid pressure, temperature and velocity [10].

2.2. Cavitation modeling

Cavitation modeling presents non-negligible difficulties. The flow undergoes to important changes in local density and speed of sound. Moreover the large variance in nuclei number and size and the interaction with turbulence makes cavitation to be a stochastic process. Up to now different models have been proposed in literature [11; 12; 13].

A Hybrid Model will be considered following the approach used by [14; 15]. This model considers the two-phase mixture as a whole. However, Hybrid Models aim to take thermodynamic non-equilibrium into account. Non-equilibrium phenomena within cavitation are vapor bubble nucleation and interphase heat, mass and momentum transfer. Drawback of these models is that they require specific assumptions linked to the particular geometry and conditions. In fact, source terms for the phase change, the evaporation and condensation rates, can be very different according to the specific problem to deal with.

The set of governing equations consists of the conservative form of the Favre-averaged Navier-Stokes equations, a transport equation for the phase change, the enthalpy-based energy equation and the turbulence closure.

$$\frac{\partial \rho_m}{\partial t} + \frac{\partial \left(\rho_m U_j\right)}{\partial x_j} = 0 \tag{5}$$

$$\frac{\partial \left(\rho_m U_j\right)}{\partial t} + \frac{\partial \left(\rho_m U_i U_j\right)}{\partial x_j} = -\frac{\partial p}{\partial x_j} + \frac{\partial}{\partial x_j}\left[(\mu_m + \mu_T)\left(\frac{\partial U_i}{\partial x_j} + \frac{\partial U_j}{\partial x_i} - \frac{2}{3}\frac{\partial U_k}{\partial x_k}\delta_{ij}\right)\right] \tag{6}$$

$$\frac{\partial}{\partial t}\left(\rho_m \left(f_L L\right)\right) + \frac{\partial}{\partial x_j}\left(\rho_m U_j (f_L L)\right) = \frac{\partial}{\partial x_j}\left[\left(\frac{\mu_m}{Pr_L} + \frac{\mu_T}{Pr_T}\right)\frac{\partial h}{\partial x_j}\right] \tag{7}$$

$$\frac{\partial \rho_l \alpha_l}{\partial t} + \frac{\partial \left(\rho_l \alpha_l U_j\right)}{\partial x_j} = \dot{m}^+ + \dot{m}^- \tag{8}$$

In Eqs. 5,6,7,8 the subscripts l and v stand for the liquid and vapor phase respectively. ρ_m is the mixture density, whose expression is written in Eq. 9. α is the volume fraction, U is the velocity and p the pressure. The mixture laminar viscosity is indicated as μ_m and the turbulence one as μ_T. L is the latent heat, h is the enthalpy, Pr_L and Pr_T are the laminar and turbulent Prandtl number respectively.

$$\rho_m = \rho_l \alpha_l + \rho_v \alpha_v \tag{9}$$

Finally $\dot{m}^+$ and $\dot{m}^-$ are the source and the sink term which represent the condensation and evaporation rate, respectively, during the mass transfer process. The equations for the mass transfer are Eqs. 10 and Eqs. 11, where C_{dest} and C_{prod} are two empirical constants. Their values differ significantly from one work to another, [15; 16; 17].

$$\dot{m}^- = \frac{C_{dest} \alpha_l}{t_\infty} \frac{\rho_l}{\rho_v} \frac{MIN(p - p_v(T), 0)}{(0.5 \rho_l U_\infty^2)} \tag{10}$$

$$\dot{m}^+ = \frac{C_{prod}(1 - \alpha_l)}{t_\infty} \frac{MAX(p - p_v(T), 0)}{(0.5 \rho_l U_\infty^2)} \tag{11}$$

Within this model the impact of thermodynamic effect on evaporation and condensation rates is also included [15]. Taylor's series is used at this purpose. The sink and source expressions become functions of the temperature drop. Due to the non-linear relations, the impact of the thermal effects will change according to the working temperature and pressure.

3. Methodology

As stated in the previous sections, this work is aimed at studying peculiarities of cavitation due to the cryogenic nature of the working fluid. To do that, an orifice configuration is used. First a global characterization of this orifice is performed using water as working fluid. Its behavior in both fully liquid condition and two-phase flow is taken into account. Pressure, temperature and flowrate sensors are used. High Speed Imaging is used as well to retrieve information about the two-phase flow topology. Afterward, the same methodology will be used with a cryogenic facility. A hydraulic similitude between the two facilities has to be guaranteed. The objective is to focus only on the effect of fluid properties.
In the following further details on the chosen configuration are provided. Two theoretical models are briefly presented as well. The goal is to have correlations for orifice discharge.

3.1. Orifice configuration

The reasons for the choice of an orifice to induce cavitation are explained in this Section. Orifices are practical and effective. In fact, it has a simple geometry and it allows to reach very high velocity at the section which is called *vena contracta*. Moreover it is not just a didactic case since the orifices are quite common in the feeding system of liquid propulsion systems.
The three flow conditions to be reached are: fully liquid flow, cavitating flow and super-cavitating flow. To give an idea of the meaning of these three flow conditions a schematic of the pressure trend through the orifice is illustrated in Fig. 2.

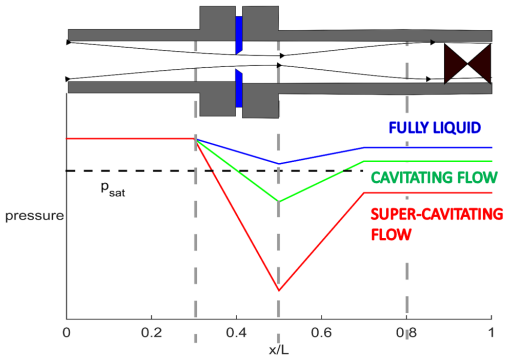

Figure 2: Schematic of pressure trend through an orifice

Because of the contraction, pressure will decrease through the orifice. Then it recovers but without reaching initial conditions because of the head losses. An overall pressure drop is reached. The swirling flow and turbulent motion near the orifice induce a head loss which cannot be calculated theoretically [18]. This maximum head loss occurs at the *vena-contracta*.

When the saturation pressure P_{sat} is reached at the *vena-contracta*, cavitation starts occurring. The vapor pressure is a physical limit. Further reductions in the downstream pressure have no effect on the orifice dicharge. This condition is called Choked cavitation. The only result in reducing downstream pressure is the elongation of the vapor cavity. This lads to the super-cavitating condition [19].

A useful dimensionless parameter to describe orifices is the diameter ratio β, Eqs. 12.

$$\beta = \frac{d_{orifice}}{D_{pipe}} \tag{12}$$

where $d_{orifice}$ is the inner diameter of the orifice and D_{pipe} is the inner diameter of the pipe. It allows the comparison of different geometries.

Two semi-empirical models will be considered: Tullis' [4] and Chisholm's model [20]. The relationship between the flowrate and the pressure drop can be written by applying Bernoulli equation. A discharge coefficient C_d is introduced to take viscous effects into account, see Eqs. 13.

$$Q = C_d \cdot Q_{ideal} = C_d \cdot A \cdot \sqrt{\frac{2 \cdot \Delta P}{\rho \cdot \left(\frac{D_{pipe}^4}{d_{orifice}^4} - 1\right)}} \tag{13}$$

where A is the area of the pipe section.

The way to correct the ideal flowrate relation and so to consider the viscous effects distinguishes among different models. Various coefficients and correlations can be found in literature. Mainly they come from empirical results.

3.1.1. Tullis' model

This model is illustrated in Tullis cavitation guide [4]. It is a semi-empirical model oriented to design both orifices and valves by determining their cavitation potential and to avoid damages.

The empirical data concern orifices which are:

- circular
- concentric
- sharp-edged
- thin

An orifice is usually referred to as thin when its thickness is smaller than the half of the diameter of its section, $s/d \leq 0.5$.

For the design purpose Tullis defines some cavitation limits to cover the full range of possible instabilities. Four limits are defined:

- **Incipient cavitation**: the cavitation is classified as incipient when an intermittent popping sound starts to be barely audible above the background turbulent noise of the flow;
- **Critical cavitation**: the intensity is the same as for the Incipient cavitation but here the phenomenon is constant rather than intermittent;
- **Incipient damage**: the intensity of the noise and vibration could cause damage to the structure;
- **Choking cavitation**: the flow through the orifice is choked.

Empirical relationships between these limits and the β parameter have been computed within this model and they are given in Fig. 3.1.1

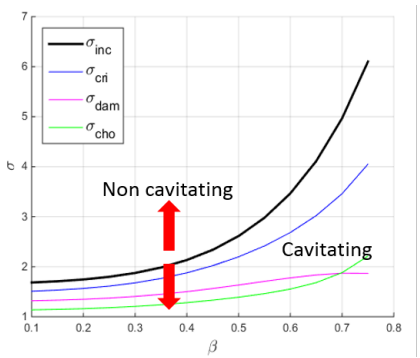

Figure 3: Cavitation parameter as a function of the orifice geometry

As seen by applying Bernoulli equation, a linear relation exists between the flowrate and pressure drop. This relation is true in fully liquid condition. When choking occurs, it is not valid anymore. Of course, this choking condition is gradually reached. However, just relations for the linear behavior and the choked one are available in literature. A law to describe the transition between the two has not been found yet.

The equations for the two regimes are Eq. 14 and Eqs. 15:

1. Linear behavior

$$Q = K_v \cdot \sqrt{\frac{\Delta P_{net}}{\rho/\rho_w}} \tag{14}$$

   where K_v is the flow coefficient, ΔP_{net} is the pressure drop due only to the orifice and ρ_w is the density of water.

2. Choked behavior

$$Q = F_L \cdot K_v \cdot \sqrt{\frac{2 \cdot (P_{up} - F_F \cdot P_{sat})}{\rho/\rho_w}} \tag{15}$$

   where F_L is the liquid pressure recovery factor and F_F is the liquid critical pressure ratio factor.

The liquid critical pressure ratio factor F_F takes into account the fact that liquid vaporizes at a pressure lower than the saturation one because of thermodynamic non-equilibrium effects.

$$F_F = 0.96 - 0.28 \cdot \sqrt{\frac{P_{sat}}{P_{cri}}} \tag{16}$$

In Eq. 16, P_{cri} stands for the critical pressure of the liquid.

As for the liquid pressure recovery factor F_L, it has been introduced by Baumann [21]. It is defined as the ratio between the overall pressure drop through an orifice and the drop between the static pressure at the inlet and the static pressure at the *vena contracta*. In choking conditions it will have the expression shown in Eq. 17:

$$F_L = \sqrt{\frac{\Delta P_{chok}}{P_{up} - F_F \cdot P_{sat}}} \tag{17}$$

3.1.2. Chisholm model

Kojasoy [20] and Fossa et al. [22] compute the pressure drop through the orifice by means of Bernoulli equation applied first, between the inlet and the *vena contracta* and, then, between the *vena contracta* and the outlet. A distinction is foreseen between thin and thick orifices. In fact, within a tick orifice, $s/d > 0.5$, flow can reattach to the wall. A boundary layer can even develop until it finally expands back into the pipe, Fig. 4.

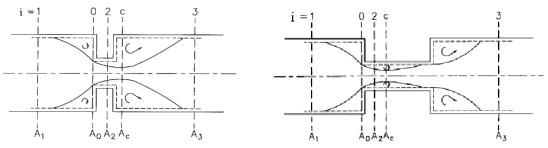

Figure 4: a.Flow through a thin orifice [20]; b. Flow through a thick orifice [20]

a)

$$\Delta P = \frac{1}{2} \cdot \rho \cdot V^2 \cdot [\frac{\sigma_a}{\sigma_c} - 1] \tag{18}$$

b)

$$\Delta P = \frac{1}{2} \cdot \rho \cdot V^2 \cdot [(\frac{\sigma_a}{\sigma_c})^2 - 1 - 2 \cdot \sigma_a^2 \cdot (\frac{1}{\sigma_c} - 1) - 2 \cdot (\sigma_a - 1)] \tag{19}$$

where σ_a is the area ratio: $\sigma_a = (D_{pipe}/d_{orifice})^2$ and σ_c is the contraction ratio, that is the ratio between the *vena contracta* section and the orifice one.

However, when dealing with this formulation the *vena contracta* section must be known and its determination is not trivial at all. To overcome this problem Chisholm relation is used. It links the contraction ratio to the area ratio:

$$\sigma_c = \frac{1}{0.639 \cdot (1 - \frac{1}{\sigma_a})^{0.5} + 1} \tag{20}$$

4. Water experimental facility

A schematic of the facility used for tests with water is shown in the Fig. 5. It works in a closed loop. Water is stored in a 750 l tank which feeds the system. It can be heated through an electrical resistance. The maximum operating pressure is limited to 6 bar. This prevents any damage to the test-section which is built in plexiglass to allow an optical access. The test-section is 600 mm long with an inner diameter, D_{pipe}, of 40 mm. The orifice is at the height of 190 mm of the test section and it can be dismantled.

The back pressure is adjusted either slightly by a valve located downstream the test section or by the vacuum pump which is connected to the top of the reservoir. A minimum back pressure of around 0.1 bar(a) has been achieved. A smaller reservoir is located just after to pump to calm the water flow after the pump and before entering the test section. The facility is equipped with an electromagnetic flowmeter. It is placed after the calming reservoir upstream the test section to guarantee that just liquid is present. Pressure drop through the orifice is measured with a differential Validyne sensor. The downstream static pressure is measured far enough from the orifice to allow the flow to re-stabilize. In the specific case, pressure is measured $15D_{pipe}$ far from the orifice. Three Kulite unsteady transducers are placed downstream the orifice to measure pressure fluctuations. Temperature is controlled with two K-type thermocouples placed in the calming reservoir and downstream the test section respectively. High speed imaging is realized thanks to a Phantom *v*7.0 CMOS camera. Images are acquired at 14035 fps with an exposure time of 68 μs. The goal is to investigate the flow in the region immediately downstream the orifice section. Finally a dissolved oxygen probe is used to monitor the dissolved oxygen concentration in water during the experiments.

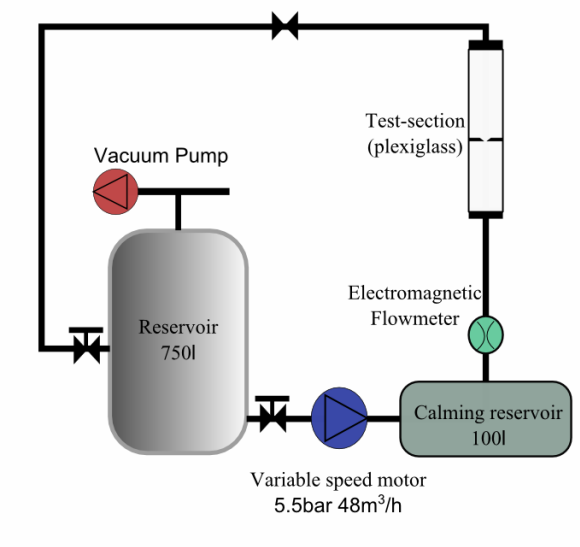

Figure 5: Schematic of the water facility

5. Flow topology through the orifice

5.1. Fully liquid flow

When pressure drop is small enough, the discharge of the orifice is linearly proportional to the square root of the ΔP, as already stated in Eq. 13 . Experimental results for four different geometries are illustrated in Fig. 6. Specifically, they refer to β ratios of: 0.15, 0.20, 0.25 and 0.30.

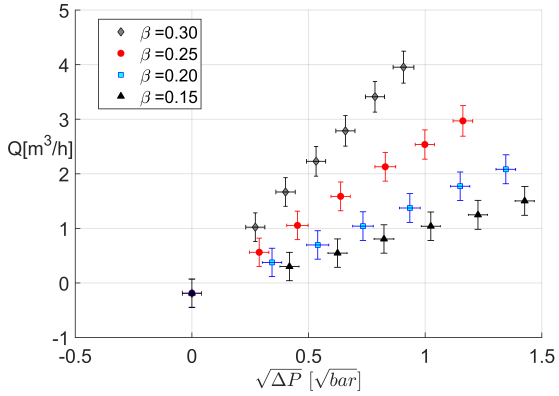

Figure 6: Orifice discharge at different β ratios

These ratios correspond to the following orifice diameters: 6 mm, 8 mm, 10 mm and 12 mm. All the tested orifices are 4 mm thick. This means that the orifice of 6 mm is classified as thick ($s/d = 0.67$), Subsection 3.1.2. On the opposite, all the other are considered thin. A comparison with the two theoretical models introduced in Subsections 3.1.1 and 3.1.2 is here provided for two cases. Fig. 7 depicts the case of thin orifice with $\beta = 0.30, s/d = 0.33$. On the other hand, Fig. 8 is about the thick orifice with $\beta = 0.15, s/d = 0.67$. Indeed, the experimental K_v for the thin orifice is in a good agreement with both Chisholm and Tullis correlations. Percentage error results bigger for the thick orifice, in particular for Tullis model, whose validity is limited to thin orifices. In fact, deviation of experimental results for the 6 mm orifice from Tullis relation is around 50%.

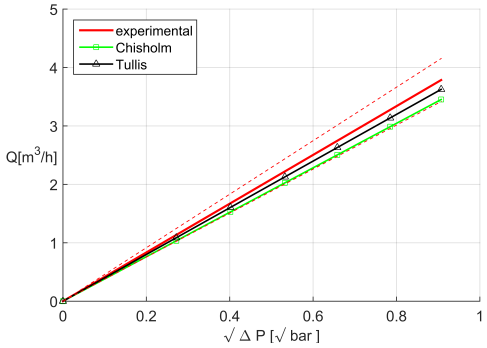

Figure 7: 12*mm* orifice

Table 2: K_v coefficient for the 12*mm* orifice

	K_v $m^3/h \cdot \sqrt{bar}$	Err %
Experimental	4.17 ± 0.40	
Chisholm model	3.81	9.65
Tullis model	3.99	4.41

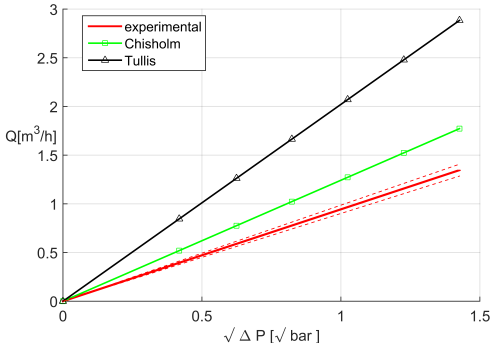

Figure 8: 6*mm* orifice

Table 3: K_v coefficient for the *6mm* orifice

	K_v $m^3/h \cdot \sqrt{bar}$	Err %
Experimental	0.94 ± 0.04	
Chisholm model	1.24	24.03
Tullis model	2.02	53.31

5.2. Incipient Cavitation

Cavitation Inception indicates the boundary between a non-cavitating and a cavitating flow. The way to define this transition is still matter of discussion. As for Tullis correlation, cavitation inception is determined on the basis of acoustic measurements. At this stage, cavitation is not observable yet. On the contrary, Yan et al. [19] defined the Inception condition when the first very small bubbles could be seen intermittently at the *vena contracta*. In both cases, they found that cavitation inception starts with a downstream pressure higher than the saturation pressure (P_{sat}).

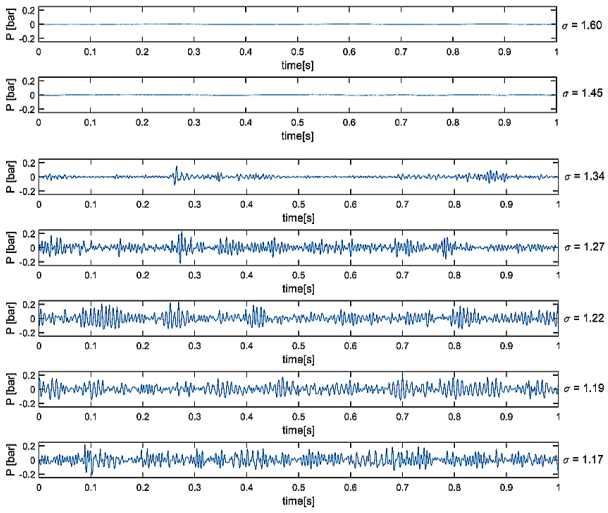

Figure 9: Pressure fluctuations in time at different cavitation numbers

At the inception condition the flow rate continues to increase with $\sqrt{\Delta P}$. However, a deviation from the linear dependency can be noticed. Within this work cavitation inception has been identified by looking at unsteady pressure measurements. Fig. 9 shows the pressure signals in time recorded downstream the orifice. For each signal the average was removed to present only the pressure fluctuations. On the right of each signal the cavitation parameter is specified. The first two sets of data appear almost flat. They correspond to a fully liquid condition. When $\sigma = 1.34$ the first fluctuations start to be observed. The Incipient cavitation has been so identified. By reducing the cavitation parameter, fluctuations become stronger in these transient data.

5.3. Developed cavitation

Further reductions in the downstream pressure make cavitation to be stronger. The cavity size increases progressively.

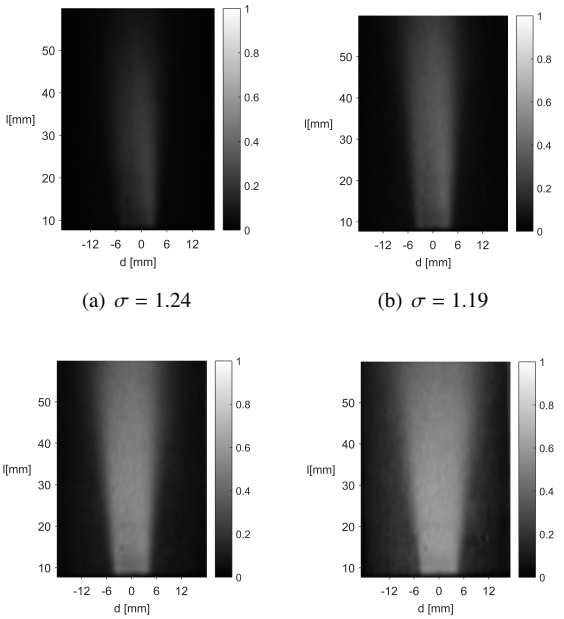

(a) $\sigma = 1.24$ (b) $\sigma = 1.19$

(c) $\sigma = 1.14$ (d) $\sigma = 1.09$

Figure 10: Mean aspects of cavitating flow

The average aspect of the cavitating flow is depicted in Fig. 10. It has been obtained by averaging the 5349 images recorded during the tests. Each image corresponds to a different cavitation number, from the incipient cavitation ($\sigma = 1.24$) up to a fully developed one ($\sigma = 1.09$). The cavity width has been measured according to the gray-scale level which goes from 0 in fully liquid to 1 for fully vapor. A threshold has been imposed to distinguish the liquid phase from the vapor one. It has been chosen equal to 0.1. This value seemed small enough to properly recognize the cavity but also sufficiently high to not detect noise. From these images the width of the cavitation cloud has been measured at eight different distances far from the orifice exit. These measures are shown in Fig. 11. The

value of $\sigma = 1.24$ corresponds to an Incipient Cavitation stage, according to Tullis definition. Here the pressure appears to recover after a length equal to the pipe diameter, 40 mm, see Fig. 11. The maximum thickness is below the 30% of the test section diameter.

When $\sigma = 1.09$, the pressure downstream the orifice is almost equal to the vapor pressure. The cavity reaches its maximum width occupying the 80%of the test section diameter.

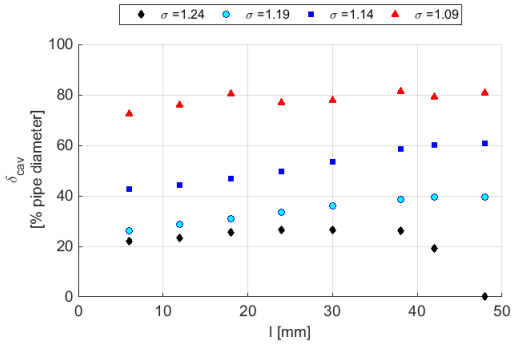

Figure 11: Cavitation thickness evolution

5.4. Super-cavitation

Super-cavitation is the evolution of a choked flow. Once the downstream pressure looses its control on the orifice flow rate, vapor cavity expands itself. Fig. 12(a) illustrates a picture of the flow just before super-cavitation takes place and Fig. 12(b) the condition immediately after. The submerged liquid jet becomes visible at the center of the test section. A thick vapor cavity surrounds it. On the walls of the test section a film of water is falling down due to the finite length of the super-cavitating region.

This condition has already been observed by [19]. An attempt to simulate a super-cavitating flow has been carried out by [23]. In their work the computational domain was too short and the cavity was periodically collapsing. On the contrary, during the experiments the water jet surrounded by vapor was stable enough.

To summurize, super-cavitation is a more stable phase than developed cavitation. Pressure fluctuations drastically reduce due to the presence of the big vapor cavity close to wall. In fact, the cavitation parameter σ keeps almost constant at 1. This means that the downstream pressure is very close to the water saturation pressure.

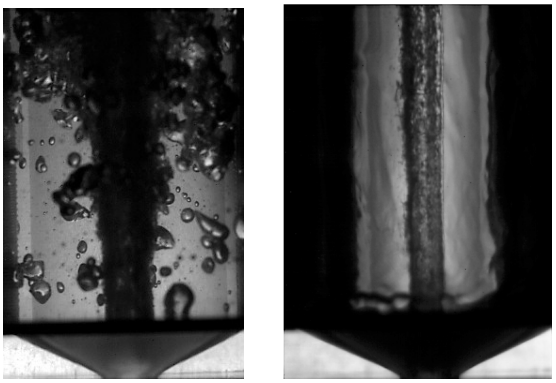

(a) Developed cavitation (b) Supercavitation

Figure 12: Transition from two kinds of cavitating flow

6. Conclusion

The first part of this work was devoted to create a test bench in water to characterize a cavitating flow. Firstly, the aim was to have further insights into the physics of the phenomenon. At this purpose, pressure measurements together with flow visualizations have been considered. Hydraulic behavior of the orifice has been analyzed from the fully liquid condition up to the super-cavitation. Moreover these tests in water will be used to validate theoretical models. This validation will help for the extension to the cryogenic experiments. Within this experimental campaign, the parameters which allow a hydraulic similitude between isothermal and cryogenic cavitation have been defined. The new cryogenic test-section will be designed in such way that this similitude is guaranteed.

Acknowledgments

This research is supported by the ESA's Networking/Partnering Initiative (NPI).

References

[1] J. Pinho, J.-M. Buchlin, S. Chabane, B. Haut, Experimental investigation of cavitation in a safety relief valve using water: extension to cryogenic fluids.

[2] J.-P. Franc, J.-M. Michel, Fundamentals of Cavitation (fluid mechanics and its applications), Kluwer Academic, Dordrecht, The Netherlands, 2004.

[3] W. Nurick, Orifice cavitation and its effect on spray mixing, ASME, Transactions, Series I-Journal of Fluids Engineering 98 (1976) 681–687.

[4] J. P. Tullis, Cavitation guide for control valves, Tech. rep., Nuclear Regulatory Commission, Washington, DC (United States). Div. of Engineering; Tullis Engineering Consultants, Logan, UT (United States) (1993).

[5] M. BILLET, D. WEIR, Thermodynamic effects on developed cavitation, Journal of Fluids Engineering (1975) 507.
[6] J.-P. Franc, C. Rebattet, A. Coulon, An experimental investigation of thermal effects in a cavitating inducer, Transactions of the ASME-I-Journal of Fluids Engineering 126 (5) (2004) 716–723.
[7] P. Linstrom, W. Mallard, NIST Chemistry WebBook, NIST Standard Reference Database Number 69, National Institute of Standards and Technology, Gaithersburg MD, 20899, retrieved February 11, 2017. doi:10.18434/T4D303.
[8] Y. Yoshida, K. Kikuta, S. Hasegawa, M. Shimagaki, T. Tokumasu, Thermodynamic effect on a cavitating inducer in liquid nitrogen, Journal of Fluids Engineering 129 (3) (2007) 273–278.
[9] A. Hosangadi, V. Ahuja, Numerical study of cavitation in cryogenic fluids, Transactions of the ASME-I-Journal of Fluids Engineering 127 (2) (2005) 267–281.
[10] J. Feng, C. L. Merkle, Numerical modeling of the thermodynamic effects of cavitation, Journal of fluids engineering 119 (1997) 421.
[11] E. Goncalves, R. F. Patella, Numerical simulation of cavitating flows with homogeneous models, Computers & Fluids 38 (9) (2009) 1682–1696.
[12] E. Lauer, X. Hu, S. Hickel, N. A. Adams, Numerical modelling and investigation of symmetric and asymmetric cavitation bubble dynamics, Computers & Fluids 69 (2012) 1–19.
[13] E. Giannadakis, M. Gavaises, H. Roth, C. Arcoumanis, Cavitation modelling in single-hole diesel injector based on eulerian-lagrangian approach, in: Proc. THIESEL International Conference on Thermo-and Fluid Dynamic Processes in Diesel Engines. Valencia, Spain, 2004.
[14] C. C. Tseng, W. Shyy, Turbulence modeling for isothermal and cryogenic cavitation, in: 47th AIAA Aerospace Sciences Meeting including The New Horizons Forum and Aerospace Exposition, 2009, p. 1215.
[15] T. Chen, G. Wang, B. Huang, K. Wang, Numerical study of thermodynamic effects on liquid nitrogen cavitating flows, Cryogenics 70 (2015) 21–27.
[16] R. F. Kunz, D. A. Boger, D. R. Stinebring, T. S. Chyczewski, J. W. Lindau, H. J. Gibeling, S. Venkateswaran, T. Govindan, A preconditioned navier–stokes method for two-phase flows with application to cavitation prediction, Computers & Fluids 29 (8) (2000) 849–875.
[17] A. K. Singhal, M. M. Athavale, H. Li, Y. Jiang, Mathematical basis and validation of the full cavitation model, Transactions-American Society of Mechanical Engineers Journal of Fluids Engineering 124 (3) (2002) 617–624.
[18] B. R. Munson, D. F. Young, T. H. Okiishi, Fundamentals of fluid mechanics, New York 3 (4).
[19] Y. Yan, R. Thorpe, Flow regime transitions due to cavitation in the flow through an orifice, International journal of multiphase flow 16 (6) (1990) 1023–1045.
[20] G. Kojasoy, F. Landis, P. Kwame-Mensah, C. Chang, Two-phase pressure drop in multiple thick-and thin-orifice plates, Experimental thermal and fluid science 15 (4) (1997) 347–358.
[21] H. D. Baumann, The introduction of a critical flow factor for valve sizing, ISA Transactions 2 (2).
[22] M. Fossa, G. Guglielmini, Pressure drop and void fraction profiles during horizontal flow through thin and thick orifices, Experimental Thermal and Fluid Science 26 (5) (2002) 513–523.
[23] J. KOZÁK, P. RUDOLF, D. ŠTEFAN, M. HUDEC, M. GRÍGER, Analysis of pressure pulsations of cavitating flow in converging-diverging nozzle, in: 6th IAHR International Meeting of the Workgroup on Cavitation and Dynamic Problems in Hydraulic Machinery and Systems, 2015.

Experimental investigation on gram-scale condensed-phase explosion in an urban environment

Charline Fouchier

Environmental and applied fluid dynamics, von Karman Institute for Fluid Dynamics, Belgium, charline.fouchier@vki.ac.be

Supervisors: Jean-Marie Buchlin and Delphine Laboureur

Professor and Head of Department,Environmental and applied fluid dynamics, von Karman Institute for Fluid Dynamics, Belgium, buchlin@vki.ac.be

Research Engineer, Environmental and applied fluid dynamics, von Karman Institute for Fluid Dynamics, Belgium, delphine.laboureur@vki.ac.be

University Supervisor: Alessandro Parente

Professor, Aero-Thermo-Mechanical Department, Université Libre de Bruxelles, Belgium, alparent@ulb.ac.be

Abstract

Conducting experimental investigations on condensed phase explosions is a notorious difficult task, especially to measure properly the blast wave propagation. While studies on air blast propagation exist, it is difficult to find a work detailed enough to conduct investigations for the first time without having to face typical technical problems such as parasite vibrations in the blast pressure signal. The objective of this paper is to provide a solid technical knowledge on gram-scale condensed-phase explosion. Experimental investigations on blast wave measurements are conducted at the von Karman institute on a 2.8 m diameter wood table with pressure sensors flush mounted. The blasts generated by three kind of explosive are investigated in free field and inside typical street configurations. Technical recommendations are given and an overview of impacts of a complex environment on the blast wave characteristics is proposed.

Keywords: Blast Wave, Explosion, Detonation, Free Field, Pressure measurements, Safety

1. Introduction

Explosions, whether accidental or not, are a major concern in the security and safety fields. Understanding its mechanisms and its consequences in cities and industries helps to protect goods and people from disasters. Examples of tragedies caused by explosions are numerous. The accident of the west fertilizer company explosion, West Texas, 2013 is one of them. A charge of more than 28 tons of ammonium nitrate detonated in a storage, causing 15 deaths, more than 200 injured and around 100 MUSD of damages [1].

Strong explosions will result in a pressure wave, also called blast wave. The Chapman-Jouguet theory defines a blast wave as a discontinuity of pressure which propagates with a supersonic speed. When this discontinuity propagates in free field, it is followed by a pressure decrease and a return to the atmospheric pressure by oscillations. The theoretical shape of a blast wave is depicted in Figure 1.

The wave is composed by a sudden jump of pressure, called shock front followed by a decay, described as quasi-exponential in character [2]. The positive pressure phase is shorter in duration than the negative pressure phase. As the negative pressure has a limit of one atmosphere under-pressure (complete vacuum), the negative phase is often ignored by investigators, giving priority to the positive phase, which represents, in most of the cases, a more significant hazard [3]. Two main characteristics are used to describe a blast : the overpressure peak (P) and the positive impulse (integral of the time signal between the start of the blast and the end of the positive phase). In free field, the

positive impulse and the negative impulse are equal [2].

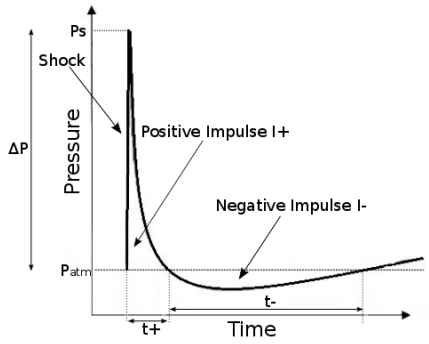

Figure 1: General shape of a blast wave
(ΔP: overpressure peak, P_s: maximal pressure of the shock, Patm: atmsopheric pressure, t+: duration of the positive phase, t-: duration of the negative phase)

The propagation of a blast wave in free-field has been widely studied for many explosives [4][5][6] and calculation is generally straightforward. However, the prediction of the propagation becomes much more difficult as the number of obstacles interacting with the wave increases. Research on the blast propagation in free field and complex environments has been performed, like the study of T. Rose *et al.* about the influence of straight city streets on the blast impulse [3], the investigation of M. Johansson *et al.* on an explosion at an intersection [7] or the study of T. Kisters *et al.* about the characterization of a detonation in the near field [8]. However, only the work of K. Cheval *et al.* [9], describing a methodology for proper measurement in lab-scale, could be found in the literature. Moreover, the blast measurement technical knowledge is not yet available at the von Karman institute (VKI), where the project is conducted.

The global objective of the PhD project is the investigation of pollutant dispersion driven by a condensed-phase explosion in an urban environment. In order to achieve this goal, a first investigation has been conducted on three kinds of explosive used to acquire a technical knowledge on air-blast wave measurement. The present paper summarizes the experimental set-up used and the characteristics of the explosives in free field. An overview of impacts of a complex environment on the blast wave characteristics is proposed. The urban configurations investigated are the straight street, the T-junction, the cross junction, and the channeling.

2. Materials and Methods

This chapter describes the experimental set-up used for the investigation of the propagation of a blast wave in free field and in a complex environment.

2.1. Free field propagation

The setup has been designed to conduct non-destructive studies of air blast three dimensions propagation in free field. Experiments have been performed on a 2.8 m diameter wood table. For each test, the explosive is placed at the center of the table. A metal plate of 55 x 55 cm replaces the wood in the middle of the table to protect it against the explosion.

The effects of the explosive source are studied through three kinds of condensed-phase explosives: one pyrotechnic device (Nitrate Banger Tristar, black panther collection, S1225 - C20) and two exploding-bridge-wire (EBW) detonators (RP80 and RP83, distributed by RISI [10]). The pyrotechnic device is a cylinder of 53 mm height and 17 mm diameter, composed by 1.4 g of black powder, a mixture of potassium perchlorate KClO4, sulfur S and aluminum Al. It is taped directly on the center of the test table and lighted manually. The detonators are metal cylinders of 7 mm diameter and 21 mm or 40 mm length, respectively for the RP80 or RP83. They are filled with 0.08 g of Pentaerythritol tetranitrate PETN as initiating explosive and 0.123 g or 1.031 g of cyclotrimethylenetrinitramine RDX as output explosive, respectively for the RP80 or RP83. The explosive charges are stored in an aluminum cup with a plastic molded head. Detonators are set inside a solid foam block of 5 x 5 cm in the center of the test table, standing out from a given height (*i.e.* 9 mm for the RP80, 25 mm for the RP83) to have only the secondary explosive (RDX) outside the support. From past experiments, these heights correspond to the optimal position for an hemispherical blast. The foam support is destroyed by the explosion and has to be changed after each test. The detonators are activated using a FM150 firing module and a FD201 firing system. Pictures of the pyrotechnic device and a RP83 inside its foam support are proposed in Figure 2 while the characteristics of each explosive are gathered in Table 1.

The TNT equivalent of the explosives used can be estimated using their composition. The TNT equivalents of the detonators have been estimated by summing the TNT mass equivalent of the two components (*i.e.* RDX and PETN), themselves evaluated from past experiments (*i.e.* 1.3 for the RDX and 1.27 for the PETN). The energy theoretically released by the

Explosive	Distributor	Composition
Pyrotechnic device	Tristar SD	0.7 g KClO4 0.42 g S 0.28 g Al
RP-80 EBW detonator	RISI	0.08 g PETN
		0.123 g RDX
RP-83 EBW detonator	RISI	0.08 g PETN
		1.031 g RDX

Table 1: Characteristics of explosives used (EBW: exploding-bridge-wire)

Explosive	TNT eq		
Pyrotechnic device	1.16	1.63 g	7.62 kJ
RP-80 EBW detonator	1.29	0.261 g	1.22 kJ
RP-83 EBW detonator	1.3	1.44 g	6.74 kJ

Table 2: TNT equivalent estimated of explosives used (EBW: exploding-bridge-wire) : TNT equivalent, mass equivalent of TNT and energy released

explosives has been obtained using the energy of a TNT explosion (4686 J/g [11]) and the TNT equivalent mass. The Table 2 gathers the obtained values.

As the interactions between the three compounds of the pyrotechnic device are difficult to predict, a differential scanning calorimetry analysis (TG/DSC) has been performed to characterize the black powder. According to the TG/DSG, the powder releases 2723 J/g during its combustion. To estimate the energy released by the deflagration of the pyrotechnic device at ground level, a factor 2 has to be applied to take into account the ground effect [11]. A total of 7.62 kJ is theoretically released during the deflagration of the pyrotechnic device at the ground level, leading to a TNT equivalent of 1.16 and the TNT mass equivalent of 1.63 g. It has to be noticed that these values are a rough estimation of the deflagration energy, as the energy released by a slow combustion is not equal to the energy released by the fast combustion of all the compounds of the pyrotechnic device. Moreover, the energy should also depends on the confinement of the explosive powder, that is not taken into account during the TG/DSG analysis.

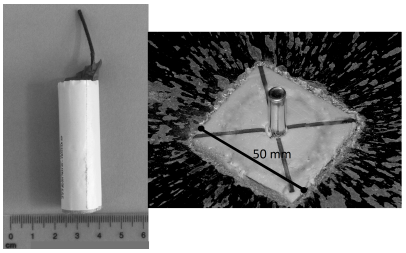

Figure 2: Left picture : Pyrotechnic device, Right : RP83-EBW inside the foam support

The test table is perforated with 1 cm diameter holes to mount sensors flush to the surface. Ten flush mounted sensors are used to record the blast: seven piezoresistive transducers (five PCB 116 and two Kistler 603B) and three piezoelectric transducers (two Kistler 4043A5, one Kistler 4043A2). Each sensor is statically and dynamically calibrated with its measurement chain (amplifier and cables). The characteristics of sensors and amplifiers used are respectively summarized in Table 3 and Table 4. The resonance frequencies are provided by the manufactor. The rise times have been estimated from measurements of pressure steps inside a shock tube. The pressure variations of all sensors are recorded with a sample frequency of 8 MHz, using a NI PXIe 7962R system with an acquisition module NI-5751. The sample size is equal to 40.10^6 points per channel.

Name	Type	Range bars	Resonance kHz	Rise Time
PCB 106	Piezo-electric	0 - 3.45	> 100	4 μs
Kistler 603 B	Piezo-resistive	0 - 200	> 400	2 μs
Kistler 4043A2	Piezo-resistive	0 - 5	> 30	14 μs
Kistler 4043A5	Piezo-resistive	0 - 5	> 80	10 μs

Table 3: Sensor characteristics

Sensor	Amplifier	Low pass filter frequency
PCB 106	Kistler 5011	200 kHz
Kistler 603 B (1)	Kistler 5007	330 kHz
Kistler 603 B (2)	Kistler 5001	180 kHz
Kistler 4043A2	VKI	200 kHz
Kistler 4043A5	VKI	200 kHz

Table 4: Amplifier characteristics

The effects of the support of the explosive and the

sensors are studied using three experimental systems (Figure 3):

1- a metal plate to support the explosive and the sensors directly screwed on the test table,

2- a foam plate instead of the metal plate and sensors screwed on the table,

3- a metal plate to support the explosive and the sensors supported by elastics, to allow a vertical movement.

Figure 4 shows schematics of the two types of fixation that have been used for the sensors. For the three systems, the sensors are screwed in an aluminum cylinder ("sensor support" in Figure 4), which is fixed to the table using one of the two fixation systems. The Figure 5 gives a picture of the support 2 holding a sensor.

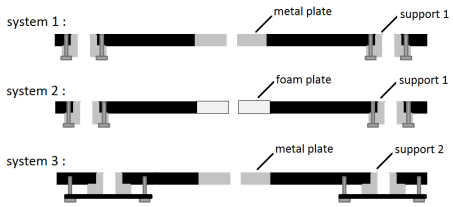

Figure 3: Three setups tested (sectional view)

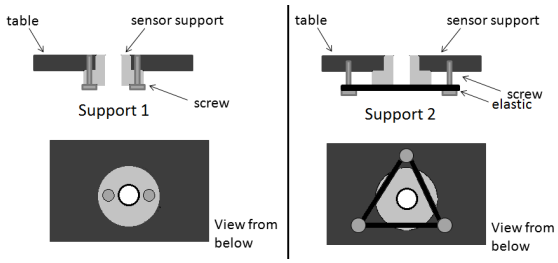

Figure 4: Two types of sensor fixations tested

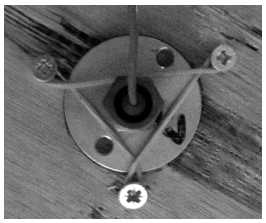

Figure 5: Picture of the support 2 with the sensor

Tests have been conducted inside a room of approximately 5 x 10 x 6 m, allowing an assumption of a free field propagation. The system 1 (metal plate and sensors screwed on the table) has been tested only with the pyrotechnic device because it induced strong vibrations inside the test table, making the post-processing of the blast impossible. The systems 2 and 3 (foam plate with sensors screwed and metal plate with sensors supported by elastics) have been tested by the three kinds of explosives. Each configuration has been realized at least two times in order to investigate the repeatability. The system 3 has been tested three times for the detonators and four times for the pyrotechnic device. In total, ten pyrotechnic devices and five of each detonator have been used. The Table 7 summarizes the tests conducted.

Explosives	System	Number of tests
Pyrotechnic device	1	3
Pyrotechnic device	2	3
RP80	2	2
RP83	2	2
Pyrotechnic device	3	4
RP80	3	3
RP83	3	3

Table 5: Experimental matrix

2.2. Propagation in a complex environment

Once the three studied explosives have been characterized in free field, the effect of the urban environment around the explosion on the blast propagation can be investigated.

The effects of the obstacles configurations on the blast propagation are studied through six experimental configurations. Each configuration is built with 1 cm thick wood boxes. If not specified, the obstacles height is equal to 10 cm. The configurations, depicted in Figure 6, are:

1- The free-field, with no obstacles;

2- The 10 cm width straight street;

3- The 10 cm width straight street with buildings of 20 cm height;

4- Part A: The 25 cm width straight street; Part B: The 25 cm width T-junction.

The part A and B are supposed independent concerning the propagation of the incident blast wave;

5- The cross junction, with a 10 cm width street and 25 cm width street;

6- The channeling, built with 15 cm x 10 cm wood boxes, separated from each other by 5 cm.

The position of the explosive and sensors are respectively indicated by a circle and crosses in the Figure 6. The exact positions of the sensors are summarized in Table 6. While all the configuration have been

Sensor	Number	Conf. 1	Conf. 2 and 3	Conf. 4	Conf. 5	Conf. 6
PCB 106	1	475 mm	725 mm	450 mm/s6	725 mm	¢
PCB 106	2	725 mm	¢	725 mm	725 mm	¢
PCB 106	3	725 mm	¢	1250 mm	1250 mm	525 mm
Kistler 603B (1)	4	350 mm	525 mm	350 m	350 mm	¢
Kistler 603B (2)	5	350 mm	¢	350 mm	350 mm	¢
PCB 106	6	725 mm	¢	725 mm	725 mm	¢
PCB 106	7	725 mm	¢	800 mm/s6	1250 mm	¢
Kistler 4043A5	8	975 mm	725 mm	450 mm/s6	525 mm	725 mm
Kistler 4043A5	9	1079.8 mm	1250 mm	800 mm/s6	1250 mm	1250 mm
Kistler 4043A2	10	1225 mm	1250 mm	1250 mm	1250 mm	¢

Table 6: Positions of sensors for each configuration (the position .../s6 represents the distance from the sensor 6)

investigated, the effects of the configurations 4-Part B and 5 on the blast propagation are not presented in this paper.

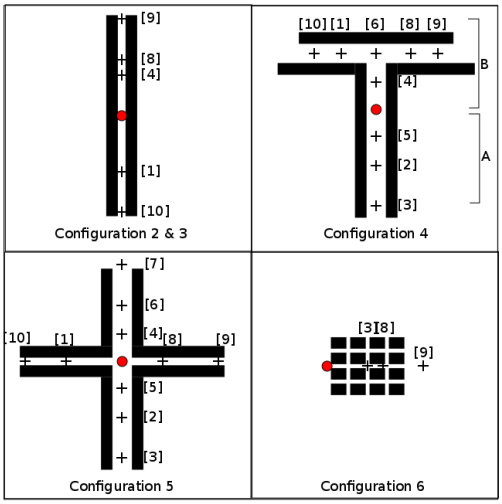

Figure 6: Configurations tested (configuration 1 : free field)

The configurations 1, 2, 3 and 4 have been tested with the three types of explosive. The other configurations have only been tested with the firecracker and the RP80 detonator. In total, 24 tests have been conducted. The Table 7 summarizes the tests conducted.

Configurations	Firecracker	RP80	RP83
Conf. 1	4	2	2
Conf. 2	1	1	1
Conf. 3	2	1	1
Conf. 4	2	1	1
Conf. 5	1	1	-
Conf. 6	2	1	-

Table 7: Experimental Matrix

To study the effect of the obstacles on the blast propagation, the positive impulse and the overpressure peak of the blast are compared between different configurations.

3. Results and Discussion

3.1. Free Field Propagation

3.1.1. Blast wave measurement optimization

Three types of sensors and three experimental systems have been studied to optimize the quality of the blast wave measurement. This section presents the analysis of these setups.

Three types of sensors are used to measure the propagation of the blast wave : PCB 106, Kistler 603B and Kistler 4043 (cf. Table 3 for the characteristics). Figure 7 gives the pressure signal of a blast generated by a RP83 detonator recorded by the different types of sensor from different distances. The three sensors properly record the blast. However, the Kistler 4043 shows a slower rise time (>10 s), inducing a smoother signal but also a loss of information regarding the overpressure peak.

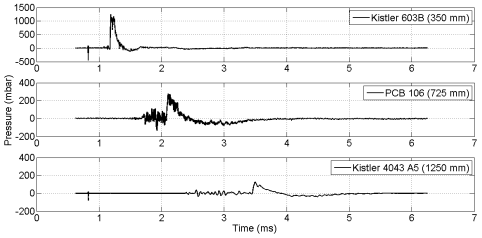

Figure 7: Comparison of the different types of sensors used - blast from a RP83 detonator at 350mm, 725 mm and 1250 mm from the explosion - 200 kHz filtered

The three different experimental system, described in Figures 3 and 4 are compared by comparing the blasts generated by the three explosives and measured at a given distance. Figure 8 proposes a comparison between blasts generated by the explosion of a pyrotechnic device and a RP83 detonator recorded 1250 mm away from the explosion for the different systems. The results concerning the detonator RP80 are not presented here as they are similar to the results from the detonator RP83. During tests using the system 1, pressures oscillations are measured before and during the blast wave. These vibrations disturb the proper measurement of the blast. After a Fast Fourier transform investigation, it appears that the main frequency of these oscillations decreases with the distance. The origin of these vibrations is suspected to be the propagation of the shock inside the experimental table. Due

to the complexity of the construction of the experimental plate (*i.e.* assembly of metal plate and wood plates, connection with wooden boards, holes for sensors and for further studies using the table), further investigations using an accelerometer have to be conducted to confirm this hypothesis. A first way to reduce the vibration is to isolate the explosive from the test table by using a foam plate instead of a metal one (system 2). This method shows a good attenuation of the vibrations amplitude as observed in Figure 8 (74 % of reduction for the pyrotechnic device).

A second way to reduce vibrations is to isolate the sensors from the test table by creating a mechanical band-pass filter. This has been done using elastics instead of screws to maintain sensors flush on the test table (system 3). A quasi-total suppression of the oscillations due to vibrations inside the table can be observed for the pyrotechnic device (almost 97 % of amplitude reduction) and a significant diminution for the detonator RP83 (Figure 8). In both types of explosives, the general shape of the blast wave is recovered. Although the experimental data obtained in the present project can not attest of the absence of energy absorption by the metal plate, the energy loss due to the ground is reduced by 20 % compared to the use of a foam plate. However, it should be noticed that the metal plate is not deformed by the explosion. On the other hand, the foam block used as detonator support is destroyed and has to be changed after each tests. Further tests in free field with the charges suspended at a sufficient height above the ground in order to neglect its effect have to be conducted to study the real effect of the metal plate on the explosion.

The three types of sensor used during the study are suitable to properly record the pressure signal of a blast wave from a gram-scale condensed phase explosion. The last experimental system tested (system 3) shows the best quality of measurement. The authors, therefore, recommend this system for gram-scale condensed phase explosion experiments such as pyrotechnic devices or detonators investigations.

3.1.2. Characteristics of the explosives

This section is dedicated to the characterization of the explosives. The symmetry and repeatability of each explosive are investigated through free field tests. The characteristics of each explosive are given and the blasts generated are compared.

Three tests with detonators and four tests with pyrotechnic devices are conducted to investigate the repeatability of the explosion. Figure 9 depicts the variation regarding the distance of the pressure peaks and

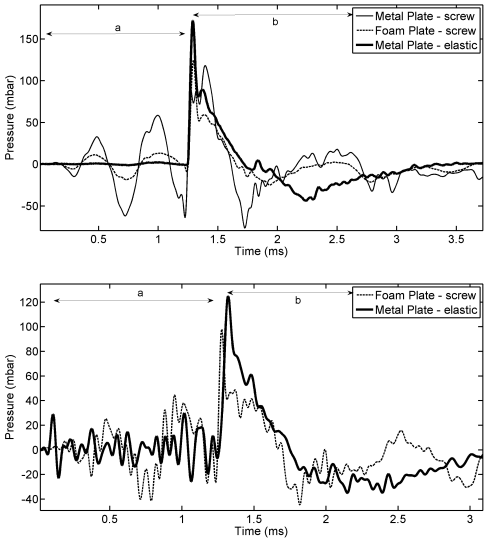

Figure 8: Signals at 1250 mm from a Kistler 4043A2, 200 kHz filtered (up: 1.4g pyrotechnic device, down: RP83 detonator)

the positive impulses of blasts generated by the three types of explosives. The standard deviation, based on 3 tests for the detonators and 4 tests for the pyrotechnic device, is also added. In general, the standard deviation is higher for the pyrotechnic device, attesting a lower repeatability.

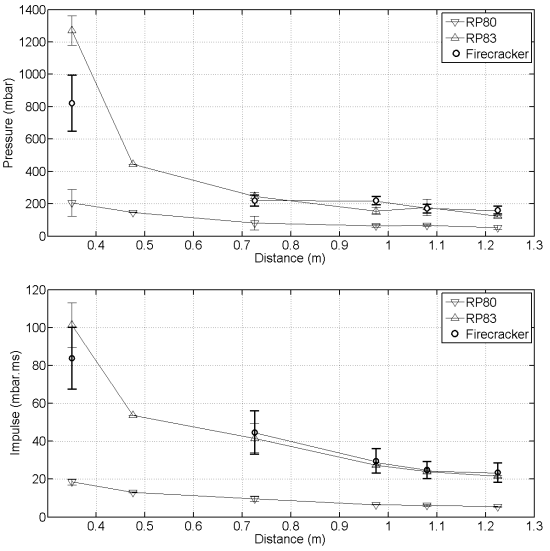

Figure 9: Variation of the overpressure peak and the impulse of blasts generated by a pyrotechnic device, a detonator RP80 and a detonator RP83

Figure 10 presents the pressure signal of blasts ob-

tained from two pyrotechnic devices tests (top figure) and two RP83 detonators tests (bottom figure) at 1225 mm from the explosion. As the RP80 detonator presents similar results than the RP83 detonator, it is not presented here. The signals from the RP83 detonators have been superposed by taking as the initial time the impulse of the firing system. As the initial time of the explosion of the pyrotechnic device is unknown, the blast signals have been superposed manually using the blast arrival time at pressure sensor closest to the explosion source (350 mm from the source). The results confirm the previous observation: the detonators show a good repeatability between different tests, contrary to the pyrotechnic devices. A small difference of overpressure peaks can be sometimes observed for the detonator. It is due to the response of the sensor itself. Nonetheless, the shapes of the blasts after the pressure peak are similar, highlighting the fact that the study of the positive impulse is more reliable than the study of the overpressure peak as it depends less on the response time of the sensors. Contrary to the detonators, the significant difference of overpressure peak of the blasts generated by the pyrotechnic devices can not be explained by the sensor response. During the test 1, a stronger blast has been generated in the direction of the sensor used, involving a higher overpressure peak and a faster propagation of the blast. This difference highlights the lack of repeatability of the pyrotechnic device. The observation is possible for every distance from the explosion.

In the present study, the explosion geometry has been measured systematically using four pressure sensors at 725 mm from the center of the explosion and at different angles. Polar plots of one explosion of each type of explosive are proposed in Figure 11. The characteristics (positive impulse and overpressure peak) of blasts recorded by the sensors equidistant to the explosion are given. In order to highlight the symmetry of each explosion, a mean value has been added and corresponds to the average of the characteristics obtained in the four directions. A good circularity of detonator explosions is observed. The pyrotechnic device explosion presents a non-circularity, with a random predominant direction.

The difference of repeatability and geometry between detonators and pyrotechnic devices can be explained by the high quality of fabrication and ignition of the detonators, while pyrotechnic devices are not always exactly identical and present a weakness point that leads in a random energy release direction.

The pyrotechnic device is supposed to be composed

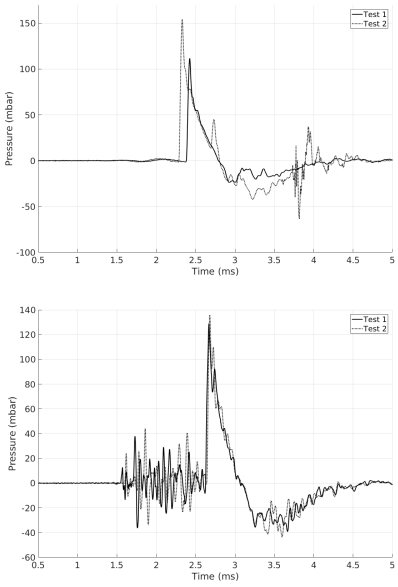

Figure 10: Repeatability of explosions of pyrotechnic devices (top) and RP83 detonators (down)- signal from a Kislter 4043A2 at 1225 mm from the explosion - 200 kHz low-pass filtered

of black powder. As a consequence, this device deflates and, by definition, does not generate a blast wave similar to the one driven by a detonation. However, the limit between deflagration and detonation is not well defined and pressure wave similar to a shock wave has been already observed from pyrotechnic devices [12]. The Figure 12 depicts the comparison between a blast generated by a pyrotechnic device and a blast generated by a RP83 detonator, highlighting the similarities between the two blasts. The variation of the characteristics of the two blasts are similar, as well as their shapes. It can be also noticed that a detonator induces more electronic noise and vibrations inside the test table than a pyrotechnic device, complicating the post-processing.

The blasts generated by a detonator and the pyrotechnic device are comparable. However, the explosion of the pyrotechnic device differs from a detonator explosion for producing a larger fireball and many projectiles. Pictures of the fireball and the projectiles just after the explosion of a pyrotechnic device are proposed in Figure 13. These phenomena cause noise on the pressure signal and affect the quality of the measurement. The investigation near the center of the explosion is then difficult. While the PCB 106 pressure sensors do not provide a good pressure signal due to the fireball heat flux and have to be placed

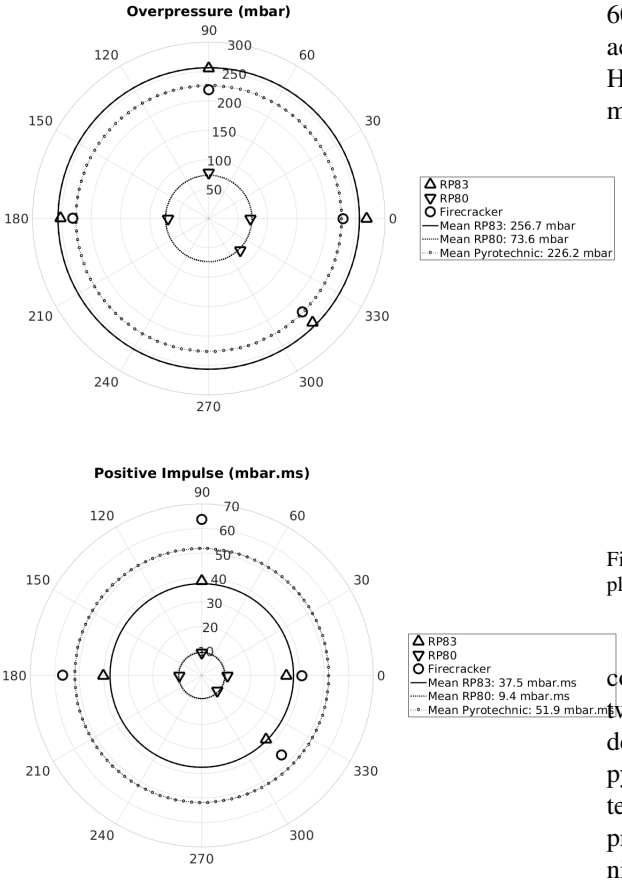

Figure 11: Polar plot : symetry of the explosion at 725mm from the explosion

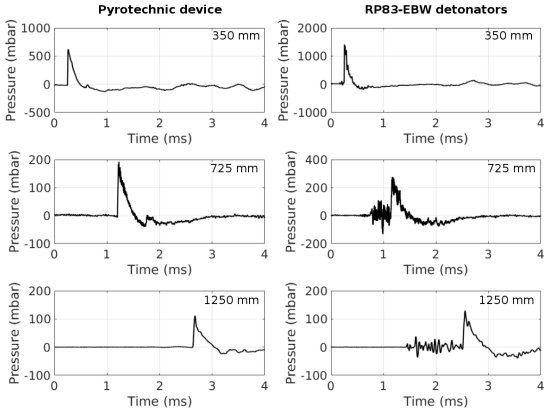

Figure 12: Comparison of blasts from a pyrotechnic device and a RP83-EBW detonator (20 kHz low-pass filtered)

at minimum 700 mm from the explosion, the Kistler 603B pressure sensors seem to be able to provide an accurate measurement at 350 mm from the explosion. However, these sensors do not provide good measurements if mounted closer to the explosion center.

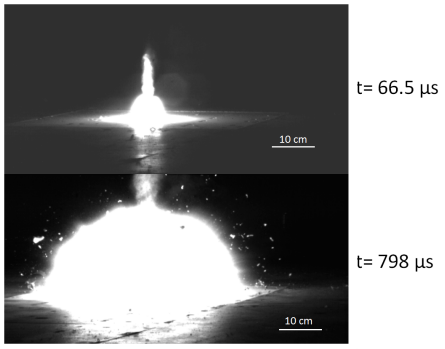

Figure 13: Fireball and projectiles from the pyrotechnic device explosion

The pyrotechnic device shows a bad repeatability compared to detonators. However, similarities between the characteristics of blasts from pyrotechnic devices and detonators can be observed. Moreover, pyrotechnic devices induce fewer vibrations on the test table and electronic noise, which make the post-processing easier. It is then advised to use pyrotechnic device to conduct preliminary gram-scale tests and qualitative studies of the phenomenon studied. Thereafter, tests have to be conducted with detonators to perform quantitative analysis.

Moreover, the positive impulse shows a better reliability than the pressure peaks, as it depends less on the response of the sensor. Therefore, the authors recommend the use of the positive impulse characteristic for quantitative studies.

3.1.3. Experimental TNT equivalent

The TNT equivalent is used to characterize the blast produced by an explosion. This chapter describes the investigation on the TNT equivalent of the three explosives used.

The variation of the positive impulse regarding the distance, scaled using the theoretical TNT equivalent estimated for each explosive (Table 2) is proposed in Figure 14 (top graph). Reference curves for hemispherical TNT explosions at the ground from Kinney and Graham [13] and GEMO [14] are included. It appears that the experimental points do not fit the reference curves. The actual TNT equivalents of the explosives are not equal to the theoretical ones. An experimental TNT equivalent can be estimated by curve

fitting the experimental results to the reference curves [14]. Figure 14 (down graph) represents the variation of the impulse regarding the distance scaled with the new equivalents obtained.

The estimated TNT mass equivalents, the actual values and the difference between the two are gathered in the Table 8. The difference visible between the experimental and the theoretical estimations for the pyrotechnic device mainly comes from the difference of confinement of the powder between the TG/DSC analysis and the pyrotechnic device and the speed of combustion, as discussed in section 2. However, the small difference between the theoretical and the experimental energies shows the utility of a TG/DSC analysis.

The same amount of energy difference between the theoretical estimation and the experimental results is visible for the detonators, suggesting that this energy is absorbed by the plastic deformation of the metal cylinder of the detonator and the ground. The absorption of energy by the casing of the explosion has been observed in the litterature [15], as well as the ground effect [11][13]. The results presented here confirm the importance of conducting tests to characterize the explosive studied and its support.

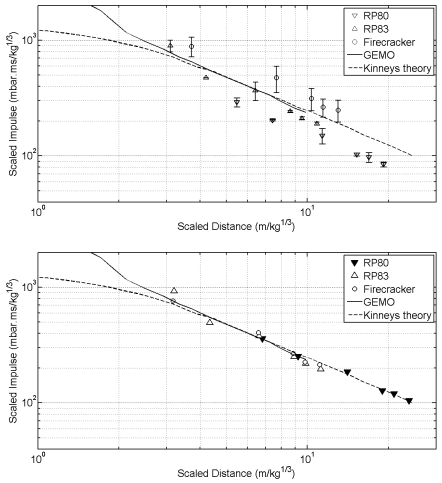

Figure 14: Variation of the positive impulses regarding the distance (scaled by the theoretical TNT equivalent 1 (up) and experimental TNT equivalent (down)

Energy is absorbed by the plastic deformation of the casing of the detonators and the ground. These results shows the importance of conducting tests to characterize an explosive and not only use the estimation of the TNT equivalent of each explosive compound.

Explosive	Theoretical TNT eq.	Experimental TNT eq.	Difference	
			mass	energy
Pyrotechnic device	1.63 g	1.34 g	-0.29 g	-1.35 kJ
RP80	0.261 g	0.136 g	-0.125 g	-0.59 kJ
RP83	1.44 g	1.31 g	-0.13 g	-0.61 kJ

Table 8: Theoretical and Experimental TNT mass equivalent

3.2. Propagation in a complex environment

Once the three explosives are characterized in free field, the effect of typical street configuration on the blast propagation is investigated. In this section, the effect of the width of a straight street, the building height of a straight street and the repetition of buildings (*i.e.* channeling) are presented.

3.2.1. Straight Street

The straight street effect on the blast propagation is studied through the comparison of the characteristics of a blast (positive impulse and overpressure peak) propagating in free field, inside a 25 cm straight street and inside a 10 cm straight street (configurations 1, 2 and 4-Part A, cf. Figure 6).

The Figure 15 depicts the variation of the characteristics of blasts generated by a RP83 detonator propagating in the three studied configurations. A general increase of the characteristics is observed when the width of the street decreases. However, the blast at 350 mm from the center of the explosion in the 25 cm straight street (first left circle point on the overpressure graph) presents the same pressure than a free field blast. Two blast waves are propagating inside the straight street : the incident blast and the blast reflected on the walls of the street. At 350 mm from the center of the explosion, the reflected blast did not merge yet with the incident blast. The signals of blasts propagating in free field and in the 25 cm straight street are superposed in the Figure 16 using the time of the impulse from the firing system as the initial time of the explosion. Two peaks are visible on the 25 cm straight street blast. These peaks correspond to the incident blast and the reflected one. The first peak is equal to the blast in free field, from the pressure variation and the speed of propagation. The second blast propagates faster than the first one, merges with it at a given distance and induces the increase of the blast characteristics.

Concerning the variation of the impulse, presented in Figure 15, the positive impulse decreases faster when the street width is smaller. This observation was also made by T. Rose et al. [16] by investigat-

ing the propagation of a blast from a 11.09 g of DEMEX 100 plastic explosive inside different configurations of straight streets using sensors on the walls of the buildings. The experimental results from the two closest configurations to the configurations studied in this paper have been superposed to the experimental variation of the positive impulse in Figure 15. They correspond to straight streets of 1.6 $m/kg^{1/3}$ and 2.4 $m/kg^{1/3}$, built with 0.8 $m/kg^{1/3}$ high buildings. The experimental data and the T.Rose data are different due to the different position of the sensors (wall of the buildings v.s. flush at the ground) and the difference of configuration dimensions. However, a similarity of decrease is observed far from the center of the explosion.

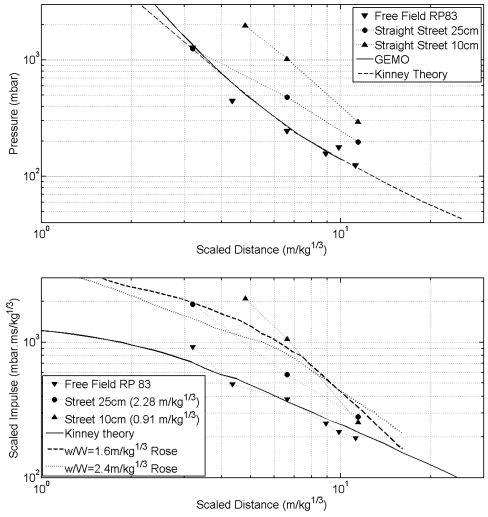

Figure 15: Impact of the street width on the scaled characteristics variation of a blast produced by a RP83 regarding the scaled distance (left : overpressure peak, right : scaled positive impulse)

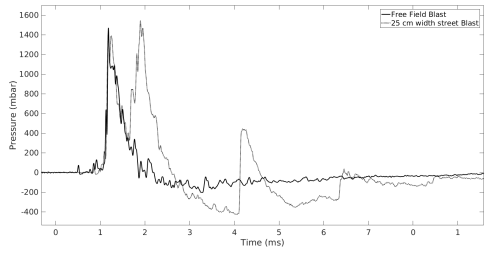

Figure 16: Blast at 350 mm from the center of the explosion in a 25cm width street (RP83) and in free field (signals from C4, 200kHz filtered)

The Figure 17 depicts the variation of characteristics of the blast generated by a RP80 detonator and propagating in the configurations 1,2 and 4-Part A. As for a blast generated by a RP83 detonator, the characteristics are increased by the confinement of the straight street. As the blast generated by a RP80 detonator is less powerful than the one generated by a RP83 detonator, the reflected blast takes more time to merge with the incident one. At 350 mm from the center of the explosion, the positive phase of the incident and the reflected blast are totally distinct as shown in the Figure 18. As a consequence, the positive impulse of the first incident blast correspond to the positive impulse of a blast propagating in free field, as depicted by the "incident blast" marker on the Figure 17 left. The full impulse (total blast) corresponds to the characteristic of a blast propagating inside the 25cm width straight street. The experimental results from Rose et al. [16] from the closest configurations have been superposed to the positive impulse experimental variation in Figure 17. They correspond to straight streets of 1.6 $m/kg^{1/3}$ and 4.8 $m/kg^{1/3}$, built with 1.6 $m/kg^{1/3}$ high buildings. As observed for the RP83 detonators, the experimental data and the data from Rose et al. are different due to the different position of the sensors and the difference of configuration dimensions. However, a similarity of decrease is observed far from the center of the explosion.

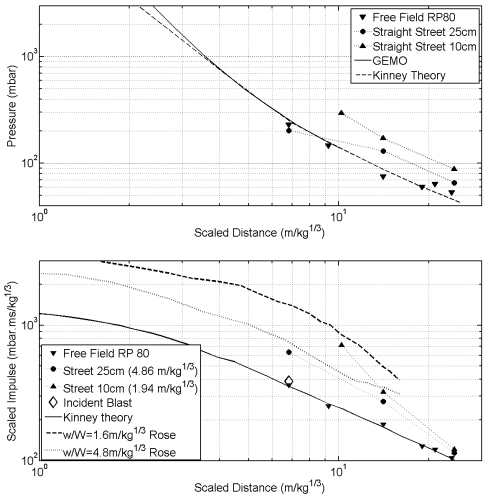

Figure 17: Impact of the street width on the scaled characteristics variation of a blast produced by a RP80 regarding the scaled distance (left : overpressure peak, right : scaled positive impulse)

Before the merging of the incident blast and the reflected blast, the incident blast is not affected by the confinement and is similar to a blast propagating in

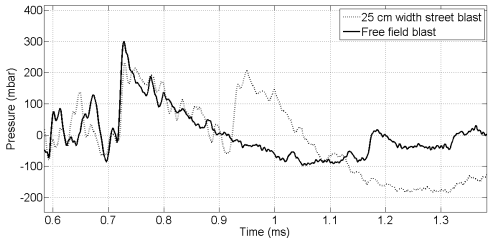

Figure 18: Pressure signal of a blast 350mm from the center of the explosion, RP80, configuration 4-Part A (C4-200kHz filtered)

free field. The merging of the incident and reflected waves increases the characteristics of the blast. The time the blasts need to merge depends on the explosion energy: the more powerful the explosive, the faster the merge between the two blast happens. The straight street configuration increases the blast characteristics : the characteristics are higher when the blast propagates in narrow street. While the overpressure is translated to higher values when the street width decreases, the impulse decreases faster in narrow streets. The comparison of the experimental results with results from Rose et al. [16] shows a good coherence with the decrease of the positive scaled impulse regarding the scaled distance.

3.2.2. Buildings height

The effect of the building height on the blast propagation is investigated through the configurations 1, 2 and 3 (cf. Figure 6). Only the results concerning the RP83 detonators are presented here. The blasts from firecrackers and RP80 detonators present similar results and, as a consequence, is not described here.

The Figure 19 depicts the variation of the scaled characteristics of a blast generated by a RP83 detonator for different buildings heights and street widths. A general increase of the overpressure and the scaled positive impulse is observed. A similar observation was made by Rose et al. [16]. The experimental results from the closest configurations to the configurations studied in this paper have been superposed to the positive impulse experimental variation in Figure 19. The corresponding scaled dimensions are written in the legend of the figure. As observed in the section focused on the effect of straight streets on the blast propagation, the experimental data and the T.Rose data are different due to the different position of the sensors (wall of the buildings v.s. flush at the ground) and the difference of configuration dimensions. However, a similar slope of decrease is observed for the propagation inside the configuration 3 (10 cm straight street with 20 cm high buildings) and the results of Rose et al. [16] for a $1.6m/kg^{1/3}$ width straight street with $1.6m/kg^{1/3}$ high buildings.

A similar decrease of the blast characteristics can also be observed between the blast propagation inside the configuration 4-Part A (25cm straight street with 10cm buildings) and inside the configuration 3 (10cm straight street with 20cm buildings). While the blast characteristics decrease fast inside the configuration 2 (10cm straight street with 10cm buildings), the decrease of the blast inside the configuration 3 is similar to the one inside the configuration 4-PartA. This observation can be explained by the fact that the configuration 2 does not confine enough the blast and the energy of the explosion is lost. In the opposite, the configurations 3 and 4-Part B presents a degree of confinement enough to maintain the energy of the blast.

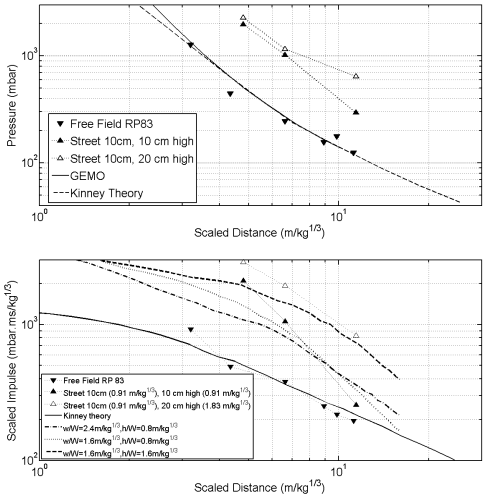

Figure 19: Impact of the street width and building heights on the scaled characteristics variation of a blast produced by a RP83 (left : overpressure peak, right : scaled positive impulse)

The propagation of the blast depends on the street width but also the height of the buildings. When the buildings of a narrow street are not high enough, the blast characteristics decrease fast. In the opposite, if the buildings are high enough, the energy of the blast is kept inside the configuration and the blast characteristics decrease as it would do in free field.

3.2.3. Channelling

The effect of repetition of buildings, called channelling effect, is studied using the configuration 6 (schematized in Figure 6). The configuration 1 (free field) is used as a reference.

The Figure 20 depicts the variation of the overpressure peak and the scaled positive impulse of a blast propagating inside the studied configurations. The RP80 and the firecracker are represented in the same figure. Between the spaced buildings that decreases the blast characteristics and the confinement that increases them, the blast propagation is similar to a free field propagation. However, at the exit of the channelling configuration, the blast positive impulse and overpressure are reduced of about 80 % from the free field values.

On the contrary, the blast propagation speed inside the configuration channelling increases : the blast arrives 0.07 ms earlier than the free field blast at a given distance (0.1 ms at the end of the propagation). This difference of speed can be visualized in the Figure 21, depicting the signals of blast from a RP80 detonator propagating inside the channelling configuration and the free field configuration at 725 mm from the explosion.

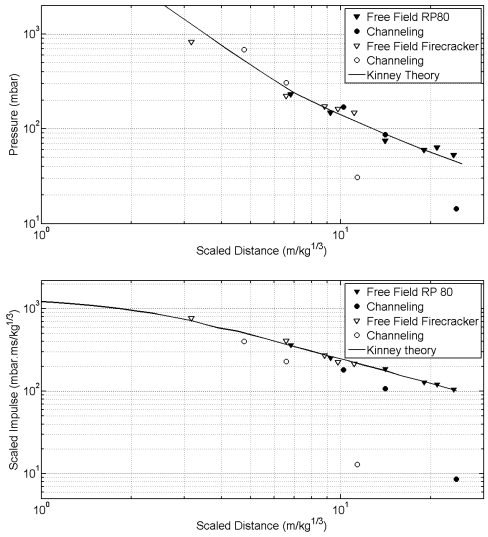

Figure 20: Variation of the overpressure peak and scaled impulse inside and outside the channeling configuration

The Figure 22 depicts the blast signal at 525 mm, 725 mm (inside the channelling) and 1250 mm (outside the channelling) from the explosion of a firecracker. The observations made above can be validated : the amplitude of the blast at the exit of the configuration (C9) is really reduced compared to the one of the blast inside the configuration. Several reflection peaks can be observed. The superposition of signals in free field and inside the configuration at 725 mm confirm the increase of the speed of propagation

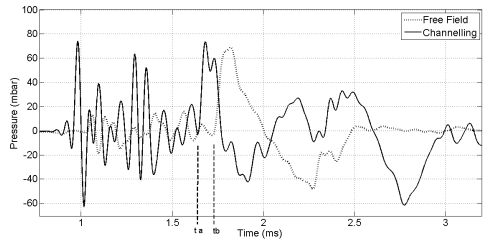

Figure 21: Blast signal in free field and inside the channelling at 725 mm from the center of the explosion - C8 - 200kHz filtered - RP80 detonator. ta: arrival time of the blast propagating inside the channelling, tb: arrival time of the blast propagating in free field

inside the configuration, as the blast inside the channelling arrives sooner at the sensor at 725 mm from the explosion.

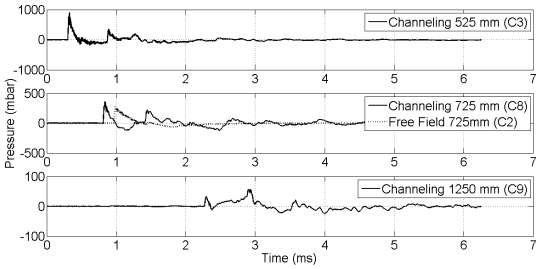

Figure 22: Pressure signal of a blast propagating inside the channelling configuration (distance from the explosion : C3: 525 mm, C8: 725 mm, C10: 1250mm (outside of the channelling configuration) - 200kHz filtered) - firecracker (The superposition of signals in the channelling configuration and the free field has been done using the arrival time on a sensor at 350 mm from the explosion, outside of the configuration)

Between the effect of the confinement and the effect of gaps between buildings, the blast propagating inside a channelling configuration is similar to the one propagating in free field. However, the blast is accelerated. By contrast, the blast characteristics are highly reduced at the exit of the configuration.

4. Conclusion and perspectives

The objective of this study is to gain a solid technical knowledge about blast propagation in an urban environment at laboratory scale.

This paper presents gram-scale experimental investigations on blast wave measurement using three types of explosive : 1.4 g pyrotechnic device, RP80-EBW detonator and RP83-EBW detonator. Three experimental setups have been compared. It appears that

fixing the sensors with an elastic allows reducing vibrations due to the explosion and makes the post-processing easier. The use of foam to disconnect physically the explosive from the test table is not advised as it absorbs a part of the energy released by the explosion.

The pyrotechnic device appears to produce a similar blast than the RP83. However, the first explosive generates an explosion with a poor repeatability and circularity. It is then advised to use a pyrotechnic device for preliminary studies and use detonators for quantitative analysis.

A methodology to study the characteristics of a blast has been applied. It has been showed that the theoretical TNT equivalent differs from the experimental one because of the plastic deformation of the set-up. However, it appeared that the characteristics of the blasts, once scaled by the appropriate TNT mass equivalent have a similar variation regarding the distance than the characteristics of a blast generated by a TNT explosion.

The effect of some selected configurations on the blast propagation is given in the paper. Studies about the straight street configuration show an increase of the blast characteristics when the confinement increases (*i.e.* decrease of the width or increase of the buildings heights). Concerning the channeling effect, between the confinement of the buildings and the gaps between them, the blast propagating inside the configuration is similar to a blast in free-field. However, a reduction of about 80 % of the characteristics is observed at the exit of the configuration.

Through this investigation, a solid technical knowledge has been acquired. The next stage of the project will be to install the experimental table inside the subsonic wind tunnel L1-b of the von Karman institute in order to investigate the dispersion after the explosion. The dispersion will be simulated using micro talc powder and different atmospheric condition will be tested.

Acknowledgments

This work has been conducted with the collaboration of the Direction des applications militaires (DAM) of the Centre d'Etudes de Gramat (CEG), from the Commissariat à l'énergie atomique et aux énergies alternatives (CEA).

The authors thank G. Glabeke, engineer at the von Karman Institute, for the TG-DSC of the pyrotechnic device and for his assistance during the experimental campaigns.

References

[1] D. Laboureur, Z. Han, B. Harding, A. Pineda, W. Pittman, C. Rosas, J. Jiang, S. Mannan, Case study and lessons learned from the ammonium nitrate explosion at the west fertilizer facility, Journal of Hazardous Materials, Volume 308, 5 May 2016, Pages 164-172.

[2] G. Kinney, K. Graham, Explosive shocks in air, Second Edition, Spring Science Business Media New York, 1985.

[3] T.A.Rose, P. Smith, Influence of the principal geometrical parameters of straight city streets on positive and negative phase blast wave impulses, International journal of impact engineering, 27 (2002), Pages 359-376".

[4] G. Ben-Dor, O. Igra, T. Elperin, Handbook of shock waves, volume 1-2. 2001.

[5] S. Mannan, Lees Loss prevention in the process industries, volume 2 2012. Fourth edition.

[6] US Department of the Army Navy and Air Force, Tm5-1300. the design of structures to resist the effects of accidental explosions., Tech. rep. (Washington DC, 1990).

[7] M. Johansson, O. Larsen, L. Laine, Explosion at an intersection in an urban environment - Experiments and analyses, Shock and Vibration, Vol. 78, 2007.

[8] T. Kisters, J. Kuder, Experimental Characterization of a near-field HOB-detonation, 22nd International MABS Symposium, Bourges, France, 2012.

[9] K. Cheval, O. Loiseau, V. Vala, Laboratory scale tests for the assessment of condensed-phase explosive blast effects. part i: Free-field test campaign, journal of loss prevention in the process industries 23, pages 613-621, 2010.

[10] Risi, data base - risi - subsidiary of reynolds industries incorporated.

[11] S. mannan. lees loss prevention in the process industries, volume 2 2012, fourth edition.

[12] G. Settles, A. Brandt, J. Miller, Full-scale schlieren imaging of shock waves for aviation security research.

[13] Explosive shocks in air, Second Edition., s.l. : Spring Science Business Media New York, 1985., ¢.

[14] Groupe d′étude des Modes Opératoires, Détermination des équivalents tnt par effet de souffle des explosifs, november 2013 edition.

[15] P. Cooper, Comments on tnt equivalence, 20th international pyrotechnics seminar, colorado springs, colorado july 24-29, 1994.

[16] T.A.Rose, P. Smith, Influence of the principal geometrical parameters of straight city streets on positive and negative phase blast wave impulses, International journal of impact engineering.

The impact of the wave wind interaction on the energy harvesting of offshore wind turbines

Sara Porchetta

Environmental and Applied Fluid Dynamics Department, von Karman Institute for Fluid Dynamics, Belgium, sara.porchetta@vki.ac.be

Supervisor: Jeroen van Beeck

Professor, Environmental and Applied Fluid Dynamics Department, von Karman Institute for Fluid Dynamics, Belgium, vanbeeck@vki.ac.be

University Supervisor: Nicole van Lipzig

Professor, Earth and Environmental Sciences, KULeuven, Belgium, nicole.vanlipzig@kuleuven.be

Abstract

A future without renewable energy resources has become unrealistic. One of the more promising renewable energy resource is wind energy, especially offshore wind energy. This because of the many advantages compared to onshore wind energy like less societal complications, more space availability and more energy extraction among multiple other advantages. Moreover, there is estimated that if approximately 5% of the area of the North Sea would be covered with offshore wind turbines this would be enough to provide one fourth of Europes energy demand. However, little is known about the effect of wind, waves and their interaction on the performance of offshore wind turbines. In this PhD this effect will be studied both experimentally and numerically. First, experiments will be conducted in a wind tunnel which is provided with a wave flume. This enables us to simultaneously control the wind and/or the waves and even the current. Measurements of PIV will quantify the velocity profile above the water and the surface parameters of the waves will be captured. Different wind speeds, wave speeds, current speeds and directions between the wind and waves will be tested. From this a more sophisticated roughness model than the commonly used Charnock relation can be found. Secondly, this wind-wave roughness model will be included in numerical models to find high fidelity wind and wave fields for specific sites both for the long and short term. Numerical Weather Prediction models, like WRF and COSMO, are CFD models which solve the momentum equations on a large spatial scale including mesoscale effects like weather fronts. These models will be used in a later stage to obtain the inflow conditions for small scale CFD models, like OpenFOAM, to investigate the effect on offshore wind turbines. This coupling ensures to have the advantage of both large and small scale models, which on the one hand take into account the large scale effects and on the other hand include small scale wind turbines. Both WRF and COSMO can be coupled with ocean and wave models. During this PhD I will focus on the implementation of the wind-wave roughness and try to improve this by the relation found during the experimental campaign. The effect on the wind profile, which in the final stage will be used for the small scale simulation, will be investigated thoroughly. Once the best implementation for the wind-wave roughness is found and the best use of the coupling of the atmospheric-ocean-wave models, the inflow conditions for the small scale simulation can be extracted and the effect of the wave wind interaction on offshore wind turbines can be studied.

Void fraction measurement during LN2 chill-down by capacitive sensor

Yuki Sakamoto

Environmental and Applied Fluid Dynamics Department, von Karman Institute for Fluid Dynamics, Belgium, yuki.sakamoto@vki.ac.be

Supervisors: Maria Rosaria Vetrano and Laura Peveroni

Professor, Environmental and Applied Fluid Dynamics Department, von Karman Institute for Fluid Dynamics, Belgium, vetrano@vki.ac.be

Engineer, Environmental and Applied Fluid Dynamics Department, von Karman Institute for Fluid Dynamics, Belgium, peveroni@vki.ac.be

University Supervisor: Tetsuya Sato

Professor, Department of Applied Mechanics, Waseda university, Japan, sato.tetsuya@waseda.jp

Abstract

The chill-down is one of the most important phenomena to develop a cryogenic liquid-propellant engine. Even if chill-down is a well known phenomenon, there is not a reliable characterization model for cryogenic fluids. Void fraction is one of the important parameters of gas-liquid two phase flows, however, there is no established measurement method. The author focuses on the capacitive void fraction measurement technique as non-interactive method and applies to analyze the cryogenic chill-down phenomena at the high accuracy measurement. The specification of the sensor is compared with the optical technique in room temperature and cryogenic conditions.

Capacitive void fraction sensor uses the difference of dielectric constants between liquid and gas. Measurement capacitance changes depend on the gas/liquid distribution, then the void fraction can be calculated by capacitance change. The shape of the electrodes are optimized by electric field analysis (EFA).

EFA and capacitive sensor accuracy are verified in advance of chill-down experiment. The accuracy is estimated by comparison between optical and capacitive techniques by silicone-oil/air bubble column experiment. The two phase state occurred by injecting air to the pipe filled with silicone-oil in atmosphere. The optical void fraction error is within 13%, it is estimated by comparing to air injection speed. The time averaged optical/capacitive/EFA void fractions are compared, they have a good agreement in low fraction region. The current results and author's previous results propose that EFA can estimate the sensor accuracy. EFA shows that the maximum error is within 30% in imaginary conditions such as block flow and sheet flow. However, the error in probable conditions is within 10% in LN2/GN2 flows.

Cryogenic chill-down experiment is conducted in a vacuum chamber with flowing LN2/GN2. Its temperature range is from 100K to 300K and its phenomena is very fast, so *temperature drift problem* and *time responsiveness* are focused on. The capacitance is dependent on the sensor/fluid temperature/pressure even if the gas/liquid distribution is the same, due to the sensor parts shrinking and fluid dielectric constant change. In present work, the capacitance modification formula is developed by comparison of pipe temperature and pressure. As a result, it is succeeded to reduce the influence from more than 3% to less than 1%. The time response is estimated by comparing with the light intensity history acquired by high speed camera data. 1200Hz capacitive signal and time averaged 250Hz optical signal(from 1000Hz) have a good agreement and both of the FFT results have peaks at the same frequency. The results propose that the responsiveness is more than 250Hz and it is enough to know the fluctuations. In addition, it is found that the light intensity and void fraction have a strong correlation, so the conversion formula from light intensity to void fraction is tried to be developed.

Keywords: chill-down, liquid nitrogen, gas-liquid two phase flow, void fraction, capacitance

Study of cryogenic slush for future launchers engines

Maria Teresa Scelzo

Environmental and Applied Fluid Dynamic Department, von Karman Institute for Fluid Dynamics, Belgium, mariateresa.scelzo@vki.ac.be

Supervisors: Maria Rosaria Vetrano and Laura Peveroni

Associate Professor, Environmental and Applied Fluid Dynamic Department, von Karman Institute for Fluid Dynamics, Belgium, vetrano@vki.ac.be,
Associate Professor, Mechanical Department, KU Leuven, Belgium, rosaria.vetrano@kuleuven.be

Research Engineer, Environmental and Applied Fluid Dynamic Department, von Karman Institute for Fluid Dynamics, Belgium, laura.peveroni@vki.ac.be

University Supervisor: Herman Deconinck

Professor, Aero-Thermo-Mechanics Department, Université libre de Bruxelles, Belgium, hdeconink@ulb.ac.be

Abstract

Liquid hydrogen is widely used as fuel in rocket engines due to the high specific impulse provided. However, several problems are related to this choice, such as low density (requiring larger storage tank), temperature stratification and short holding time due to its low latent heat. On the other hand, strong sloshing can occur due to the liquid state.

A promising solution to these problems is to replace liquid propellant with slush hydrogen, a solid-liquid mixture with higher density and heat capacity. The employment of this form of propellant mails to the development of new concept rocket engines. However, the presence of solid particles in the liquid suspension changes the flow properties: the rheological behavior becomes non-Newtonian for high particle concentration and, due to the heat transfer, the solid fraction may partially melt changing slush features. This implies that the standard correlations for the liquid flow in tubes are no longer valid. Therefore, the optimization of the slush transport through circular pipelines, valves orifices and narrowing, requires the measurement of the slush physical features, along with their modeling.

The goal of this research project is to provide a complete understanding of the slush behavior at different flow conditions such as velocity, mass fraction concentration and particles diameter distribution. An extensive experimental campaign will furnish a complete database concerning pressure drops, heat transfer and rheological behavior. This database will be used to develop improved engineering correlations along with revised models for Eulerian-Eulerian numerical approaches available in existing softwares, to be used in the design of propulsion systems.

The project is divided in two parts. The first part concerns the experimental study of an iso-thermal slurry in flow similarity with slush hydrogen. The similarity is based on Reynolds number and density ratio, in the working range of a typical feeding line of rocket engines. At the end of this task, the design, manufacturing and commissioning of the experimental facility is expected to be achieved. In parallel, experimental and numerical tools will be chosen and validated for isothermal slurries. During the second part, cryogenic slush will be produced: because of the high safety risks involved with hydrogen and consequent extremely high costs, the experimental campaign will take place employing slush nitrogen. The experimental tools calibrated during the first tasks will be validated in non iso-thermal conditions. Finally, numerical model and empirical correlations for slush nitrogen will be designed and validated by means of the experimental database.

Multiscale and multiphysical modeling of the atmospheric boundary layer

Orkun Temel

Environmental and Applied Fluid Dynamics Department, von Karman Institute for Fluid Dynamics, Belgium, orkun.temel@vki.ac.be

Supervisor: Jeroen van Beeck

Professor, Environmental and Applied Fluid Dynamics Department, von Karman Institute for Fluid Dynamics, Belgium, vanbeeck@vki.ac.be

University Supervisor: Laurent Bricteux

Professor, Departement Mecanique, Universite de Mons, Belgium, laurent.bricteux@umons.ac.be

Abstract

The atmospheric boundary layer is one of the mostly studied topics in the field of the environmental fluid dynamics due to many engineering applications including air quality, emergency response, heavy gas dispersion and wind engineering related studies and this study is devoted to develop a convenient numerical modelling methodology for the computational fluid dynamics simulations sustained by the inflow conditions acquired by the numerical weather prediction simulations.

Keywords: Atmospheric boundary layer, turbulence modelling, mesoscale modelling

1. Introduction

Conventionally, the atmospheric boundary layer is modeled by using one of two main numerical approaches which are being classified based on the spatial length scale associated with the physics governed by the numerical approach. One of them is to apply numerical weather prediction (NWP) codes on a global scale or on a regional scale, which is so called as mesoscale modeling. These NWP models are used for both operational and research purposes. However, even for the applications with fine grids, the mesh size can go down to close to a kilometer for mesoscale simulations, therefore the spatial resolution reached with mesoscale simulations is limited. Hence, the other approach is to apply computational fluid dynamics (CFD) codes at the micro-scale range by using a grid size that can be as fine as a meter so that the three-dimensional turbulent phenomenon can be modeled properly. Even though using the CFD codes for the modeling of the atmospheric boundary solves the spatial resolution problem that arised for the mesoscale models. Since the inflow conditions of the micro-scale CFD simulations still depend on large-scale physical processes that the microscale models are not designed to work with. Nevertheless, the results of the mesoscale simulations can not be used directly as inflow conditions for CFD simulations unless the turbulence models coherently developed with the atmospheric physics are employed. On this framework, the doctoral thesis on the mesoscale/microscale coupling and which this present study is a part of it, is divided into three main parts which are the development of RANS closures based on the physics of the atmospheric boundary layer, reformulation of the developed models for the utilization with the inflow conditions acquired from the mesoscale simulations and finally the extension of the proposed methodology for non-neutral conditions. Finally, mesoscale simulations have been performed by using the Weather Research and Forecasting (WRF), which is an open source numerical weather prediction code, and the microscale simulations have been performed with the open source CFD toolbox, OpenFOAM.

2. The inconsistency of standard RANS closures with the physics of ABL

The inconsistency fo the closure coefficients of the standard $k-\epsilon$ model had been pointed out by some studies in the literature [1],[2] and the development of

RANS closures coherent with the physics of the atmospheric boundary layer is still an open field. For neutral ABL, which is an idealized state where the buoyancy effect on the transport phenomena is negligible, variants of standard $k-\epsilon$ models, which employ convenient turbulence closure coefficients for neutral ABL [2], or an additional source term for the realistic representation of ABL physics [3], have been proposed in literature and some further improvements have been proposed within the wake region of a hill or an obstacle [4]. In order to include non-neutral effects, Alinot and Masson [5] proposed modified closure coefficients for standard $k-\epsilon$ model [6]. Unlike Alinot and Masson [5], Pontiggia [7] followed an analytic approach to define an additional source term to the transport equations and applied it to a heavy gas dispersion case for nocturnal ABL. The methodology applied in the present study is similar to the one applied by Alinot and Masson [5] because it is based on the determination of the closure coefficients but also similar to Pontiggia's approach [7] due to the analytic derivation carried out. Finally, unlike the previous similar studies, not only the standard $k-\epsilon$ but also the RNG $k-\epsilon$ [8] and a variant of the $k-\omega$ [9] where the dissipation term is slightly differs from the standard version, are modified for non-neutral ABL. The advantage of the developed closures is the fact that instead of defining an additional source term or keeping distinct closure coefficients for shear, buoyancy and dissipation related terms, new closures employ only one user-defined constant, which is C_1. The other two coefficients C_2 or β and C_3 are computed as a function of C_1. Therefore with less coefficients to be tuned, the new models contain reduced level of epistemic uncertainty. The new closure coefficients for $k-\epsilon$, RNG $k-\epsilon$ and $k-\omega$ model are as given [10]:

$$u_j\frac{\partial k}{\partial x_j}=\frac{\partial}{\partial x_j}\left[\left(\frac{\nu_t}{\sigma_k}\frac{\partial k}{\partial x_j}\right)\right]+P+P_b-\epsilon \tag{1}$$

$$u_j\frac{\partial \epsilon}{\partial x_j}=\frac{\partial}{\partial x_j}\left[\left(\frac{\nu_t}{\sigma_\epsilon}\frac{\partial \epsilon}{\partial x_j}\right)\right]+C_1\frac{\epsilon}{k}P+C_3\frac{\epsilon}{k}P_b-C_2\frac{\epsilon}{k}\epsilon \tag{2}$$

where the shear production term, P is modeled as $\nu_t S_{ij}$. For standard [6] and RNG $k-\epsilon$ [8] models, the closure coefficients are as given respectively:

$$C_2=C_1+\frac{\kappa^2}{\sigma_\epsilon\sqrt{C_\mu}} \tag{3}$$

$$C_3=\frac{L\phi_m}{\kappa z\phi_\epsilon}\left[C_1\left(\phi_m-1\right)-C_2\left(\phi_\epsilon-1\right)\right] \tag{4}$$

$$C_2=(C_1^0-R)+\frac{\kappa^2}{\sigma_\epsilon\sqrt{C_\mu}} \tag{5}$$

$$C_3=\frac{L\phi_m}{\kappa z\phi_\epsilon}\left[(C_1^0-R)\left(\phi_m-1\right)-C_2\left(\phi_\epsilon-1\right)\right] \tag{6}$$

Similarly, the transport equations and the closure coefficients for the $k-\omega$ model is as follows:

$$u_j\frac{\partial k}{\partial x_j}=\frac{\partial}{\partial x_j}\left[\left(\alpha_k\nu_t\frac{\partial k}{\partial x_j}\right)\right]+P+P_b-\omega C_\mu k \tag{7}$$

$$u_j\frac{\partial \omega}{\partial x_j}=\frac{\partial}{\partial x_j}\left[\left(\alpha_\omega\nu_t\frac{\partial \omega}{\partial x_j}\right)\right]+\alpha\frac{\omega}{k}P+C_3\frac{\omega}{k}P_b-\beta C_\mu\omega^2 \tag{8}$$

$$\beta=\alpha+\frac{\alpha_w\kappa^2}{\sqrt{C_\mu}} \tag{9}$$

$$C_3=\frac{L}{\phi_\epsilon\kappa z}\left(\alpha\left(\phi_m^2-1\right)-\beta\left(\phi_\epsilon\phi_m-1\right)\right) \tag{10}$$

The implemented models had been tested for the homogeneous non-neutral atmospheric boundary layer in comparison to standard models and the theoretical results [11]. The results show the importance of the

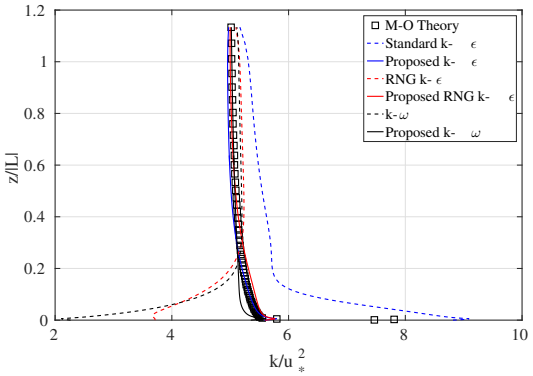

Figure 1: Comparison of the standard and proposed models with the Monin-Obukhov theory under stable stratification: Normalized turbulence kinetic energy

new closure coefficients which prevents the unphysical production/dissipation of turbulence with respect to the only universally acceptable theory for the atmospheric boundary layer, the Monin-Obukhov theory.

3. Updated RANS closures based on mesoscale turbulence schemes

Even though the developed RANS models are on agreement with the Monin-Obukhov theory, the inflow conditions acquired from the mesoscale simulations can not be used directly for the RANS simulations because the turbulent viscosity coefficient, C_μ

must be equivalent for the mesoscale and microscale turbulence closures. Otherwise the results turbulent fluxes of momentum and heat would be completely different what is supposed to imposed from mesoscale simulations to microscale simulation as inflow conditions. Hence, the formulation proposed by Detering and Etling [12] is applied to the models developed and the closure coefficients are updated based on the mesoscale turbulence parameterisation schemes. First the mesoscale simulations have been performed for the Askervein Hill and the microscale simulations have been conducted by using the results of the mesoscale simulations as inflow conditions. Simulations have been performed by using 8 different $k-\epsilon$ closures based on different mesoscale turbulence closures. C_μ coefficient is updated as stated as well as the C_1 formulation. The selected test case is the Askervein Hill and the time period of interest had been considered to be near-neutral, so that the following C_2 and C_μ relationships have been used.

$$C_1 = C_1^0 + C_f Ro^{-1} \tag{11}$$

$$C_2 = C_1^0 + C_f Ro^{-1} + \frac{\kappa^2}{\sigma_\epsilon}\sqrt{\frac{B_1}{C_q S_m}} \tag{12}$$

$$C_\mu = \frac{C_q S_m}{B_1} \tag{13}$$

The configuration of the mesoscale domain, validation of mesoscale results with the weather balloon measurements and finally the comparison of the computed near-surface wind speed and turbulence kinetic energy profiles of microscale results with the observations are as presented [13]:

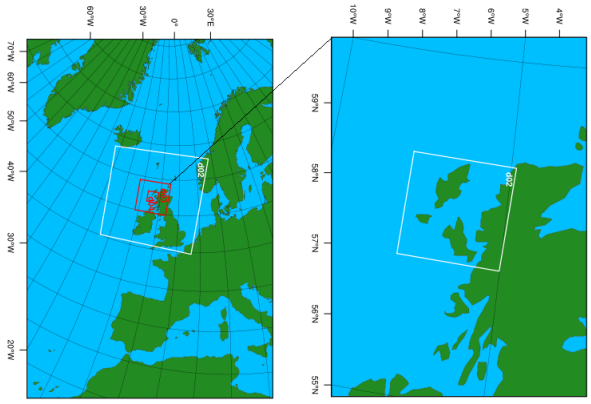

Figure 2: Mesoscale domain setup

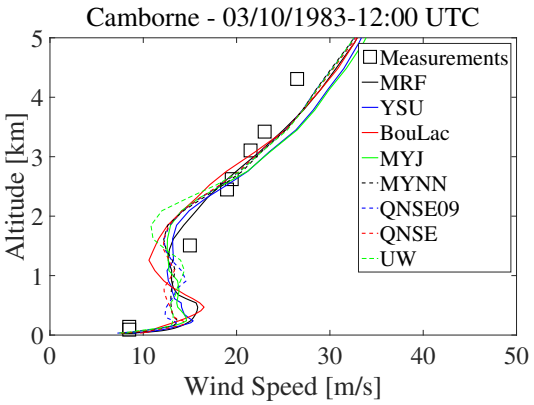

Figure 3: Computed wind speed vs weather balloon observations

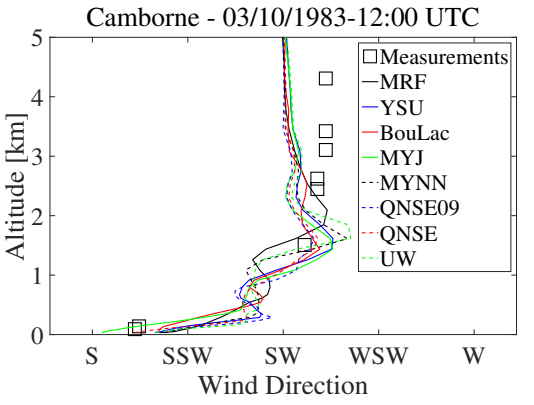

Figure 4: Computed wind direction vs weather balloon observations

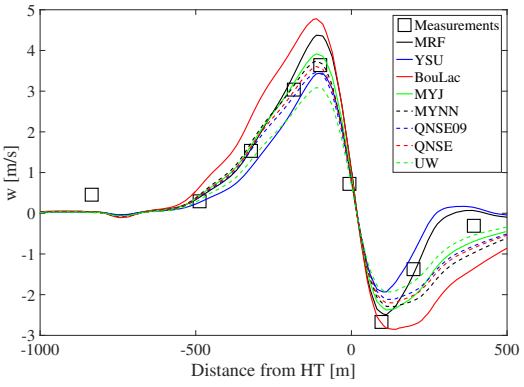

Figure 5: Computed wind speed vs weather balloon observations

4. Extension of the developed methodology to non-neutral conditions

Even though the mesoscale models calculate the wind speed, wind direction, potential temperature and

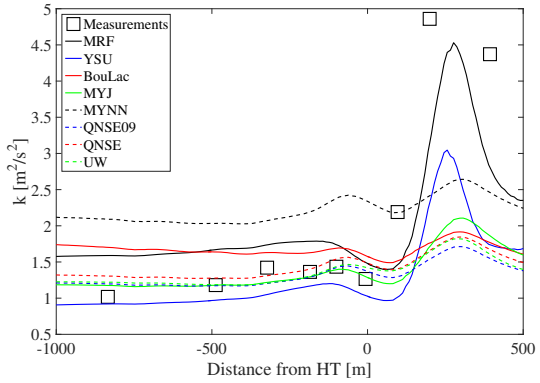

Figure 6: Computed wind direction vs weather balloon observations

any other atmospheric quantities, the mesoscale results can not be directly used as inflow conditions for microscale RANS simulations.

First of all, the turbulent scalars must be determined for the turbulence closures which are not based on the $k-\epsilon$ formulations. For the closures based on turbulence kinetic energy closures like MYJ scheme is rather simpler but for the algebraic closures turbulent scalars must be determined using a theoretical or analytical derivation.

Second point is that even the turbulent scalars are determined correctly, CFD simulations sustained with mesoscale inflow conditions can not be performed with the standard closures. Assuming that the turbulent scalars, k and ϵ, are equivalent for microscale and mesoscale simulations, if the C_μ and Pr_t are not defined consistently with the mesoscale turbulence closures, the turbulent viscosity for momentum or heat would be completely different for mesoscale and microscale simulations.

In addition to the correct determination of C_μ and Pr_t, the closure coefficients (C_1, C_2, C_3) for the transport equation of the ϵ transport equation must also be determined consistently with the physics of the atmospheric boundary layer so that the turbulence would not be produced or dissipated unphysically.

Finally, standard wall functions can not be used for the atmospheric boundary layer because of the fact that the near-surface winds and turbulent transport is governed by different mechanisms which can be modelled with the Monin-Obukhov similarity theory [11].

These stated problems had been investigated and a new methodology had been proposed in our previous study [13] only for the neutral boundary layer. Even though this present study follows a similar approach, the models developed for the neutral atmospheric boundary layer is updated to non-neutral conditions. In the extend of the current literature survey, it is possible to state that this approach is really one of few studies dealing with the bridging the gap between the mesoscale and microscale approaches and proposing a proper turbulence modelling approach.

Based on some analytical derivations [14], following closure coefficients are determined for two different RANS closures based on the best performing two mesoscale turbulence parameterisation in the previous studies.

$$C_1 = C_1^0 + C_f Ro^{-1} \tag{14}$$

$$C_2 = C_1^0 + \frac{\kappa^2}{\sigma_\epsilon \sqrt{\frac{C_q S_m}{B_1}}} \tag{15}$$

Where C_μ is set to 0.085 for stable and unstable conditions for YSU scheme and 0.17 and 0.13 for MYJ scheme. Turbulent Prandtl numbers are also set to 0.9 and 1.16 for YSU scheme and 0.57 and 1.5 for MYJ scheme. Similar to the study performed for the Askervein Hill, first the mesoscale simulations have been performed over Oklahoma region for four different time periods corresponding to different atmospheric stability conditions, which are denoted as IOP2, IOP4, IOP9 and IOP10. Finally the microscale results in comparison to near-surface wind speed, wind direction and temperature measurements are as given:

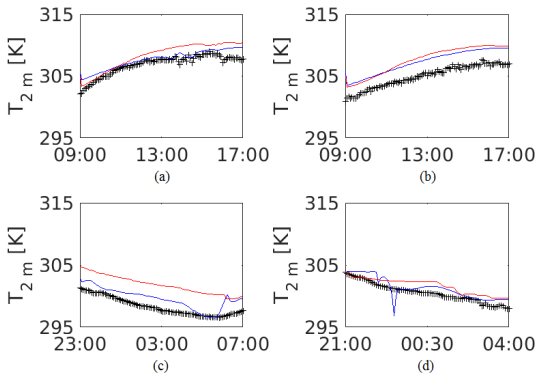

Figure 7: Comparison of temperature at 1.5 meters with near-surface observations: Black marker - observations, blue solid line - Microscale/YSU, red solid line - Microscale/MYJ, (a):IOP2, (b):IOP4, (c):IOP9, (d):IOP10

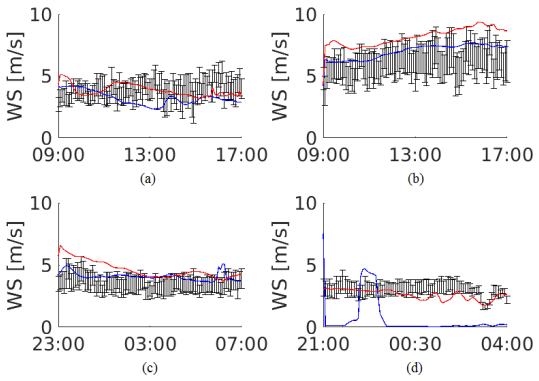

Figure 8: Comparison of wind speed at 10 meters with near-surface observations: Black marker - observations, blue solid line - Microscale/YSU, red solid line - Microscale/MYJ, (a):IOP2, (b):IOP4, (c):IOP9, (d):IOP10

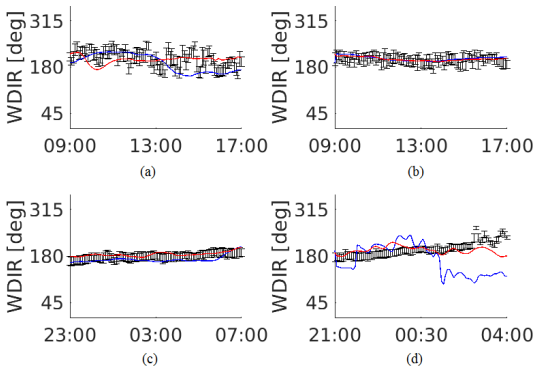

Figure 9: Comparison of wind direction at 10 meters with near-surface observations: Black marker - observations, blue solid line - Microscale/YSU, red solid line - Microscale/MYJ, (a):IOP2, (b):IOP4, (c):IOP9, (d):IOP10

5. Conclusion and future work

New closures constants are derived for three different RANS closures and applied for the homogeneous atmospheric boundary layer. Results have shown the importance of using modified turbulence closures to be coherent with the physics of turbulence within the atmospheric boundary layer. However, it must be noted that due to the fact that the models are based on the MoninObukhov theory, the applicability is also limited with the assumptions of MoninObukhov theory. In order to overcome this drawback, turbulence models are updated by using the features of the mesoscale turbulence parameterisation schemes and tested for the Askervein Hill by performing coupled mesoscale/microscale simulations and finally the proposed methodology is extended to the non-neutral conditions. Finally, the coupled simulations are still being performed for the heavy gas dispersion case in the Oklahoma City for the final validation of proposed models.

Acknowledgments

This study has been supported and funded by the Fonds de la Recherche Scientifique de Belgique (FRS-FNRS). NCEP Reanalysis data provided by the NOAA/OAR/ESRL PSD, Boulder, Colorado, USA, from their Web site at http://www.esrl.noaa.gov/psd/.

References

[1] Blocken, B., Stathopoulos, T. and Carmeliet, J. (2007). *CFD simulation of the atmospheric boundary layer: wall function problems.* Atmospheric environment, 41(2), 238-252.

[2] Richards, P. J. and Hoxey, R. P. (1993). *Appropriate boundary conditions for computational wind engineering models using the $k-\epsilon$ turbulence model.* Journal of wind engineering and industrial aerodynamics, 46, 145-153.

[3] Parente, A., Gorl, C., van Beeck, J. and Benocci, C. (2011). *A comprehensive modelling approach for the neutral atmospheric boundary layer: consistent inflow conditions, wall function and turbulence model.* Boundary-layer meteorology, 140(3), 411-428.

[4] Balogh, M., Parente, A. and Benocci, C. (2012). *RANS simulation of ABL flow over complex terrains applying an enhanced $k-\epsilon$ model and wall function formulation: Implementation and comparison for Fluent and OpenFOAM.* Journal of wind engineering and industrial aerodynamics, 104, 360-368.

[5] Alinot, C. and Masson, C. (2002, January). *Aerodynamic simulations of wind turbines operating in atmospheric boundary layer with various thermal stratifications.*, In ASME 2002 Wind Energy Symposium (pp. 206-215). American Society of Mechanical Engineers.

[6] Jones, W. P. and Launder, B. (1972). *The prediction of laminarization with a two-equation model of turbulence.* International journal of heat and mass transfer, 15(2), 301-314.

[7] Pontiggia, M., Derudi, M., Busini, V. and Rota, R, (2009). *Hazardous gas dispersion: a CFD model accounting for atmospheric stability classes.* Journal of hazardous materials, 171(1), 739-747.

[8] Speziale, C. G. and Thangam, S. (1992). *Analysis of an RNG based turbulence model for separated flows.* International Journal of Engineering Science, 30(10), 1379-IN4.

[9] Wilcox, D. C. (1988). *Reassessment of the scale-determining equation for advanced turbulence models.* AIAA journal, 26(11), 1299-1310.

[10] Temel, O. and van Beeck, J. (2017). *Two-equation eddy viscosity models based on the Monin-Obukhov similarity theory.* Applied Mathematical Modelling 42, 1-16

[11] Foken, T., et al., *50 years of the MoninObukhov similarity theory.*, Boundary-Layer Meteorology, 119(3), 431–447.

[12] Detering, H., and Etling, D., (1985). *Application of the E- turbulence model to the atmospheric boundary layer.* Boundary-Layer Meteorology, 33(2), 113-133.

[13] Temel, O. and van Beeck, J. (2016). *Adaptation of mesoscale turbulence parameterisation schemes as RANS closures for ABL simulations.* Journal of Turbulence, 17(10), 966-997.

[14] Temel, O., Porchetta, S., Bricteux, L. and van Beeck, J. (2017). *RANS closures for non-neutral microscale CFD simulations sustained with inflow conditions acquired from mesoscale simulations.* submitted to Applied Mathematical Modelling

Turbulent heat transfer at different Prandtl number fluids in natural convection boundary layer on a vertical plate

Agustín Villa Ortiz

Environmental and Applied Fluid Dynamics Department, von Karman Institute for Fluid Dynamics, Belgium, villaortiz@vki.ac.be

Supervisor: Jean-Marie Buchlin

Head of Department, Environmental and Applied Fluid Dynamics Department, von Karman Institute for Fluid Dynamics, Belgium, buchlin@vki.ac.be

University Supervisor: Tony Arts

Professor, Institute of Mechanics, Materials and Civil Engineering, Université Catholique de Louvain, Belgium, arts@vki.ac.be

Abstract

In the context of the Generation IV of nuclear power reactors, liquid metals (whose Prandtl number $Pr \ll 1$) are proposed as coolant agents. The thermal design of such reactors depends on the proper thermo-hydraulic characterization. However, the actual Reynolds Averaged thermal turbulence models have problems to reproduce accurately the thermal field of this sort of fluids, especially in natural convection flows. Therefore, the effect of Pr on heat transfer needs to be further analyzed to improve this modeling.

The scope of the present paper is the characterization of a turbulent natural convection boundary layer at a $Pr = 0.71$ through Large Eddy Simulations, and establish a high fidelity simulation environment to study such flows. The Nusselt number along the boundary layer and the non-dimensional velocity and temperature are compared against experimental and numerical data. Preliminary results of a Large Eddy Simulation at a low Prandtl number $Pr = 0.025$ is presented.

Keywords: turbulence, heat transfer, natural convection, low Prandtl number, boundary layer, LES, turbulence modelling, OpenFOAM

1. Introduction

1.1. Context of the project

The MYRRHA reactor (**M**ulti-purpose h**Y**brid **R**esearch **R**eactor for **H**igh-tech **A**pplications) is a fast reactor under design in Belgium by SCKCEN, which can operate in critical and subcritical modes [1]. It contains a proton accelerator of 600 MeV, a spallation target and a multiplying medium with MOX fuel, cooled by a eutectic of lead and bismuth.

When MYRRHA is operated in subcritical mode, it is piloted by an ADS (accelerator driven system), which provides the high energy protons that are used in the spallation target to produce neutrons which feed the core. Neutrons impact in fuel atoms, producing new atoms, neutrons and energy (heat).

In normal operating conditions, MYRRHA works in forced convection. The liquid metal transports the produced heat in the core to the external heat exchangers. During the maintenance of the reactor, the pump system is shut down, and there is still heat production. The heat exchangers, which are operative, remove this heat, creating then a natural convection loop. During the design phase of MYRRHA natural convection plays an important role, where its behavior must be taken into account for the structural design.

1.2. Natural convection

Natural convection flows are driven by buoyancy forces. These forces are originated by the gravitational acceleration and density variations (due to changes in the temperature field), and both momentum and thermal fields are coupled. For non-

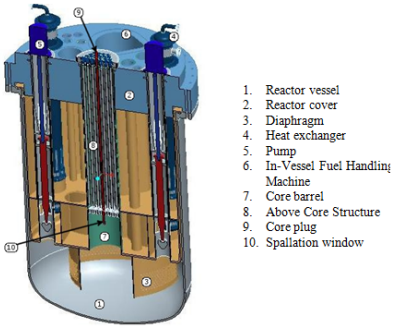

Figure 1: MYRRHA reactor cross section.

isothermal flows, such as in natural convection, the Prandtl number Pr relates the diffusion of the momentum and thermal fields. It is expressed as:

$$Pr = \frac{\nu}{\alpha} \tag{1}$$

where ν is the kinematic viscosity and α is the thermal diffusivity.

The influence of the Prandtl number in natural convection flows is evident when the thickness of momentum and thermal boundary layers δ_U and δ_T are compared. Both of them develop when a wall is heated. Figure 2a presents the case of a high Prandtl number fluid. As it is observed, the kinematic viscosity is larger than the thermal diffusivity. There is a balance between viscous and buoyancy forces near the wall, but out of the thermal boundary layer, where there is no buoyancy effect, the viscous forces are balanced with the inertial ones. Since the thermal boundary layer is thinner than the momentum one, the balance viscosity-inertia is present in almost the momentum boundary layer.

At low Prandtl number, shown in fig. 2b, the thermal diffusivity is larger than the kinematic viscosity. It results in a thicker thermal boundary layer in comparison with the previous case. The viscous forces are only significant near the wall, and their influence decreases after the peak of velocity. The buoyancy forces are then balanced with the inertial forces up to the end of the boundary layer. Out of the thermal boundary layer, since there are no buoyancy forces to produce motion, there is no velocity. This is why the momentum and thermal boundary layers have the same thickness.

A natural convection flow can be characterized by different dimensionless numbers. The Grashof number relates the buoyancy and viscous forces. At big values it is observed that turbulence features appear in

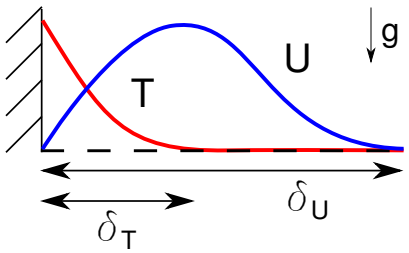

(a) $Pr > 1$

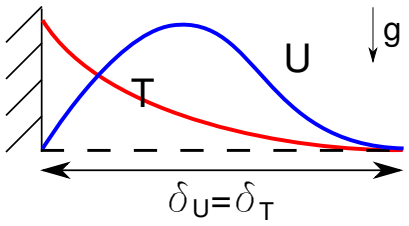

(b) $Pr < 1$

Figure 2: Velocity and temperature boundary layers in natural convection.

the flow. This is the reason why the Grashof number has the same role as the Reynolds number in forced convection. Its expression is:

$$Gr_L = \frac{g\beta\Delta T L^3}{\nu^2} \tag{2}$$

where g is the gravity acceleration, β the thermal expansion coefficient, ΔT the representative difference of temperature of the flow, and L a characteristic length.

The combination of the Grashof and Prandtl number leads to the Rayleigh number, which relates the buoyancy forces with the thermal ones. It is the analogous dimensionless number in natural convection of the Peclet number.

$$Ra_L = Gr_L \cdot Pr = \frac{g\beta\Delta T L^3}{\nu\alpha} \tag{3}$$

The Nusselt number defines the ratio between the convective and the conductive heat flux in the wall. It is usually expressed as:

$$Nu_L = \frac{(\partial T/\partial y|_w)\, L}{T_w - T_0} = \frac{hL}{k} \tag{4}$$

where h is the convective heat transfer coefficient, and k the thermal conductivity of the fluid.

1.3. State of the art of natural convection simulation

In the literature several numerical simulations of turbulent natural convection boundary layers (TNBL)

are found, specially inside the Reynolds Averaged Navier Stokes simulations (RANS) context. In 1986, To [2] developed two buoyant low Reynolds turbulence models: a $k-\varepsilon$ and an algebraic stress model. The obtained results predict well the mean flow quantities. A posterior comparison between different turbulence models was performed in 1989 by Henkes [3]. Different low Reynolds $k-\varepsilon$ models are compared with the standard $k-\varepsilon$ model and an algebraic model. Henkes sentenced that accurate simulations require the use of low Reynolds modifications in the $k-\varepsilon$. Further investigations were done by Peeters and Henkes under the same flow configuration [4]. They indicated that the k- assumptions are not capable to describe the different turbulent structures due to the isotropic nature of this model. The turbulent diffusion is predicted correctly if a Reynolds Stress Model (RMS) is used, but a differential model is needed to predict in detail the turbulence structures.

The increase of computing power has allowed to perform in since the last decade Large Eddy Simulations (LES) and Direct Numerical Simulations (DNS) for natural convection cases. In 2005, Yan [3] used LES to study the dynamics of a TNBL and the associated convective heat transfer at $Pr = 0.71$, with the sub-grid scale turbulence modeled with the Smagorinsky approach. A space-developing technique was used, where the whole boundary layer is simulated. Simulations in 2D and 3D were performed, and two different wall functions were compared. There is a good agreement with the experimental data of Tsuji [4]. The flow transition is well captured. The comparison of the wall functions shows that in the 2D computation, both wall functions give similar results. However, in the case of the 3D simulation, all turbulence characteristics are included, and differences about 15% were found between both wall functions.

A natural boundary layer over a cylinder was studied by Barhaghi [5] in 2006. Similarities were found between this surface and the flat plate of Tsuji [4] using Large Eddy Simulations. Barhaghi estimated the region y^+ where the linear law of the wall is hold.

Later in 2009, Zoinal [6] performed DNS in a vertical boundary layer for $Pr = 0.71$ and 6. A time-developing technique is used, where a correlation is used in order to express the flow as if the space-developing was used. This technique offers the advantage that a lower computational effort is needed, since the boundary layer can be studied by using a shorter computational domain. In both Prandtl number cases, the transition to turbulence was observed at the same Grashof number Gr_δ. A good agreement with the experimental data was found. Discrepancies in the turbulent heat fluxes are present, and a lack of accuracy is indicated by the author due to the use of the Boussinesq approximation for buoyant flows.

Similar discrepancies were found by Abramov [7] during his DNS in a TNBL, but the explanation was the absence of convective entrainment, since the time-developing technique does not allow a good estimation of the inflow from the far field. A comparison with experiments showed an agreement between the performed simulations and the experimental data for $Pr = 0.71$.

Recently, Nakao [8] have performed *LES* of a TNBL at $Pr = 0.71$. The transition from laminar to turbulence regime was observed to change in function of the mesh resolution. In one case, they needed to introduce velocity perturbations to produce the transition. Nevertheless, a good agreement between numerical simulations and the experiments of Tsuji [4] was shown.

1.4. Objectives

The simulation of the thermo-hydraulics of MYRRHA needs the use of proper models that can deal with the present fluid and flow conditions. It has been shown that the usual turbulence models cannot handle the simulation of flows when low Prandtl numbers fluids are present. This is why in the last years a great effort has been done to improve the existing turbulence models. High fidelity simulations, such as DNS and LES, provide relevant information to improve the different model. Nevertheless, most of this effort has been focused in forced convection flows, not in natural convection ones.

The objective of this PhD project is the contribution to the state of the art of thermal turbulence modeling at low Prandtl numbers in natural convection flows. The understanding of the physics beyond these phenomena is required. LES will be performed to study the Prandtl number effect in natural convection, and to test the available turbulence models. In the future, these models will be used in the design phase of the MYRRHA reactor.

1.5. Summary

In the current paper, an introduction to LES simulations and thermal turbulence modeling is present in section 2. The investigated test cases and their results are explained in section 3. A summary with conclusions and the future work is detailed in section 4.

2. Methodology

2.1. LES equations

Large Eddy Simulations are characterized by resolution of large turbulent motions and the modeling of the smaller ones. Continuity, momentum and energy equations are filtered in space. The filtered Navier Stokes equations for incompressible flows using the Boussinesq approximation are then expressed as:

$$\sum_j \frac{\partial \overline{U_j}}{\partial x_j} = 0 \tag{5a}$$

$$\frac{\partial \overline{U_i}}{\partial t} + \sum_j \frac{\partial \left(\overline{U_i}\,\overline{U_j}\right)}{\partial x_j} = -\frac{1}{\rho}\frac{\partial \overline{p}}{\partial x_i} + \sum_j \frac{\partial}{\partial x_j}\left(\nu \frac{\partial \overline{U_i}}{\partial x_j} - \tau_{ij}\right) + g_i(1 - \beta(\overline{T} - T_0)) \tag{5b}$$

$$\frac{\partial \overline{T}}{\partial t} + \sum_j \frac{\partial \left(\overline{U_j}\,\overline{T}\right)}{\partial x_j} = \sum_j \frac{\partial}{\partial x_j}\left(\alpha \frac{\partial \overline{T}}{\partial x_j} - \pi_j\right) \tag{5c}$$

where the filter operator is represented as $\overline{\ }$. τ_{ij} denotes the sub-grid stresses, appearing after the filtering process. π_j appears as well, due to the filtering, taking into account the sub-grid heat fluxes. The term containing the gravity acceleration g_i and the thermal expansion coefficient introduces the buoyancy forces in the momentum equation.

Several sub-grid scale models are available to model the sub-grid scale stress. A common way is to express it as a stress:

$$-\tau_{ij} = 2C\Delta^2 \overline{|S|S}_{ij} \tag{6}$$

where C is a constant provided by the sub-grid model, Δ is the size of the filter, and $\overline{S}$ is the symmetric part of the tensor of the velocity gradient $\overline{S}_{ij} = 1/2\left(\partial \overline{U_i}/\partial x_j + \partial \overline{U_j}/\partial x_i\right)$.

If an analogy between the momentum exchange and the energy exchange is applied, then a sub-grid thermal diffusivity α_{sgs} is defined, and is used to model the sub-grid heat flux as:

$$-\pi_j = \alpha_{sgs}\frac{\partial \overline{T}}{\partial x_j} \tag{7}$$

and the definition of a sub-grid Prandtl number indicates the ratio between the turbulent momemtum and energy exchanges as $Pr_{sgs} = \nu_{sgs}/\alpha_{sgs}$. The use of a sub-grid Prandtl number of $0.4 - 0.5$ is very common in literature.

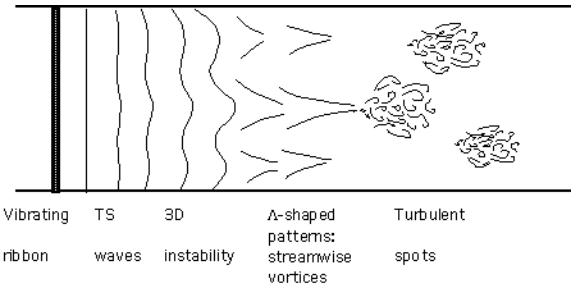

Figure 3: Transition to turbulence over a flat plate, University of Colorado Denver

2.2. Triggered transition to turbulence

A flow becomes turbulent when complex flow patterns appear, due to perturbations given by the initial conditions, boundary conditions and material properties. Every laminar flow will, eventually, become turbulent when some conditions are reached. This fact is evidenced in experiments, and also during numerical simulations. In the first case, small variations in the imposed boundary conditions, the roughness of the surfaces, or inserted elements are the responsible of transition to turbulence. However, in the case of numerical simulations, the origin of perturbations is numerical. It means that, eventually, the flow will become turbulent, due to the numerical schemes, the proposed boundary conditions, or just because of the domain discretization. This transition to turbulence is totally random, and the numerical reproduction of experiments would be affected for this uncertainty.

The use of transitions methods allows to provoke turbulence in a desired region, and not as a response to the simulation setup. In this report, the introduction of a vibration in the wall is proposed, whose objective is to excite the natural frequency of the Tollmien-Schlichting (TS) waves of the boundary layer. This technique has been used in the past in forced convection flows, but the principles are the same for natural convection flows. This natural frequency can be obtained through a Fourier analysis in the boundary layer. The obtained results with this technique are compared with the case without its application.

3. LES of natural convection boundary layer

3.1. Test cases at $Pr = 0.71$

The simulation of a TNBL at $Pr = 0.71$ is shown in this section. The validation of the numerical code and setup is done by comparing with experimental data.

The computational domain is shown in fig. 4. A constant temperature T_h has been imposed at the heated wall, where a no slip condition has been considered for velocity. The boundary below the wall is a symmetry plane, ensuring that the boundary layer will have a vertical entrainment from its beginning. The bottom plane consist in a slip patch, forbidding the entrance of flow through. In both cases, adiabatic conditions are imposed. The upper plane is considered as the outlet. A zero gradient is specified for all the fields, and the entrance of fluid is not allowed. Hence, all the mass flow that leaves the domain is recirculated with a constant temperature T_c. The spanwise sides are defined as periodic patches.

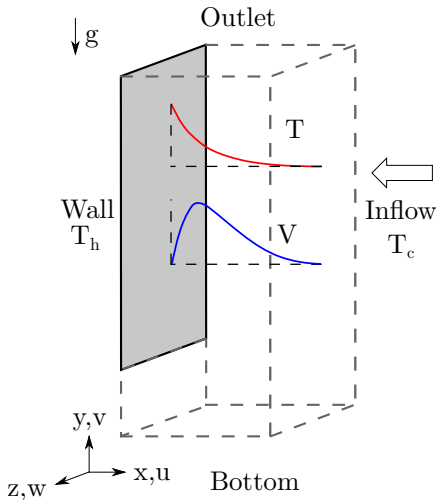

Figure 4: Computational domain of the TNBL.

Three characteristic parameters are computed with the different information of both flow and fluid:

$$u_b = (g\beta\Delta T\nu)^{1/3} \tag{8a}$$

$$t_b = (g\beta\Delta T)^{-2/3}\,\nu^{1/3} \tag{8b}$$

$$l_b = (g\beta\Delta T)^{-1/3}\,\nu^{2/3} \tag{8c}$$

Four different test cases are defined and their parameters are given in table 1, where the different lengths are normalized with l_b. The length L_y of the symmetry plane below the wall is a 20% of the length of the wall.

The time averaged results of the cases are compared against the experimental data of Tsuji [4]. The velocity and temperature are normalized with u_τ and T_τ, defined at the wall as:

$$u_\tau = \frac{\tau_w}{\rho} \tag{9a}$$

$$T_\tau = \frac{q_w}{\rho c_p u_\tau} \tag{9b}$$

As subg-grid models, the Coherent structure Smagorinsky [9] and a sub-grid Prandtl number of $Pr_{sgs} = 0.5$ have been used to model the sub-grid kinematic viscosity and thermal diffusivity, respectively.

3.2. *Results for Pr* = 0.71

The Nusselt number along the boundary layer is shown in fig. 5. There, the numerical results are also compared with Nusselt correlations in laminar and turbulent natural convection. Case 1 presents a smooth transition to turbulence, starting at $Gr \approx 10^7$. The numerical noise introduce through the grid specifications increases the numerical perturbations in the beginning of the boundary layer, producing the transition. On the other hand, case 2 shows a very late transition after $Gr \approx 10^{10}$. The flow becomes turbulent at $Gr = 2 \cdot 10^{10}$, very late compared to the experimental data. The fine mesh resolution avoids the apparition of numerical disturbances that eventually would turn the flow into a turbulent one.

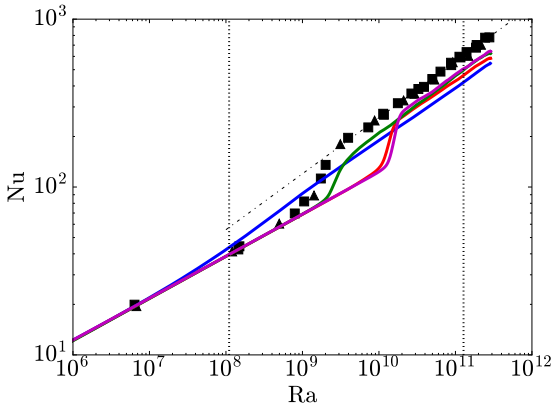

Figure 5: Nusselt number along the boundary layer for case 1 (blue), 2 (red), 3 (green) and 4 (magenta) compared with experiments of Tsuji [4] (■ and ▲) and correlations for laminar and turbulent natural convection (– · –).

A perturbation has been introduced in case 3 to provoke transition at a lower Grashof number, starting from case 2 setup. Perturbations are introduced in the

Case	L_x^*	L_y^*	L_z^*	N_x	N_y	N_z	x_1^*	Gr	Pr	Ra
1	3920	7430	930	100	256	64	0.076	$4.1 \cdot 10^{11}$	0.71	$2.9 \cdot 10^{11}$
2	3920	7430	930	100	512	96	0.076	$4.1 \cdot 10^{11}$	0.71	$2.9 \cdot 10^{11}$
3	3920	7430	930	100	512	96	0.076	$4.1 \cdot 10^{11}$	0.71	$2.9 \cdot 10^{11}$
4	3920	7430	930	120	640	128	0.076	$4.1 \cdot 10^{11}$	0.71	$2.9 \cdot 10^{11}$

Table 1: Information of cases: dimensions of the boundary layer L_i^*, number of cells on i-direction N_i, first grid point distance x_1^*, and maximum Grashof, Prandtl and Rayleigh numbers for the simulations at $Pr = 0.71$.

flow with a given amplitude and a frequency, that corresponds to the natural frequency of the TNBL. The excitation of that frequency increases the amplitude of the flow disturbances, leading to turbulence. This technique is normally used in the forced convection context, but it can be used as well in natural convection. In this simulation, the same perturbation technique than the one of Sayadi [10] for forced convection is used. A FFT was applied after a sampling of 1 kHz during an observation time of 19 s at three different heights. The velocity and temperature power spectrum are observed in fig. 6. As one can see, the same frequency peak is found at different heights for velocity and temperature. This peak corresponds with a frequency of $f_n = 1.37\ Hz$, and it has been used in the perturbation of the boundary layer.

The perturbation was introduced at $Gr = 10^5$, taking into account a 15% of the maximum velocity of the laminar profile at that location. The procedure is explained in [10], where the perturbation is set in the wall as:

$$\begin{cases} A \cdot f_{xi} \cdot \sin \omega_n t & \text{if } y_i < y < y_m \\ A \cdot f_{xf} \cdot \sin \omega_n t & \text{if } y_m < y < y_f \end{cases} \tag{10}$$

where A is the amplitude of the perturbation, $\omega = 2\pi f_n$ is the angular velocity of the perturbation, y_m is the height at $Gr = 10^8$, y_i and y_f are the initial and final heights of the perturbation, estimated as $y_m \pm \lambda$, where $\lambda = U/\omega_n$. f_{xi} and f_{xf} follow the expression

$$f_x = 15.1875y^5 - 35.4375y^4 + 20.25y^3 \tag{11}$$

It is observed that the flow transition starts at $Gr \approx 2 \cdot 10^9$, and it becomes turbulent at $Gr \approx 4 \cdot 10^9$. However, the imposed perturbation is not as close as desired to experiments. Therefore the mastery of the technique is then needed to set the transition close to the experimental observation. For case 4, a late transition is also observed, becoming turbulent at $Gr = 1.8 \cdot 10^{10}$.

For all the cases, the turbulent Nusselt number is underestimated. One can see that the mesh refinement reduces the error in the prediction, but still is

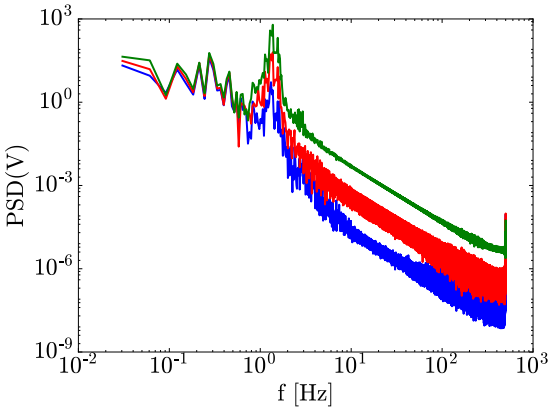

(a) Velocity FFT

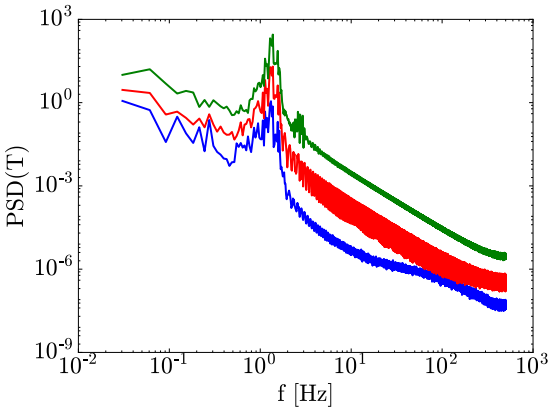

(b) Temperature FFT

Figure 6: Power spectra of the natural boundary layer at $Pr = 0.71$, at $y^* = 1600$ (blue), $y^* = 1850$ (red) and $y^* = 2050$ (green).

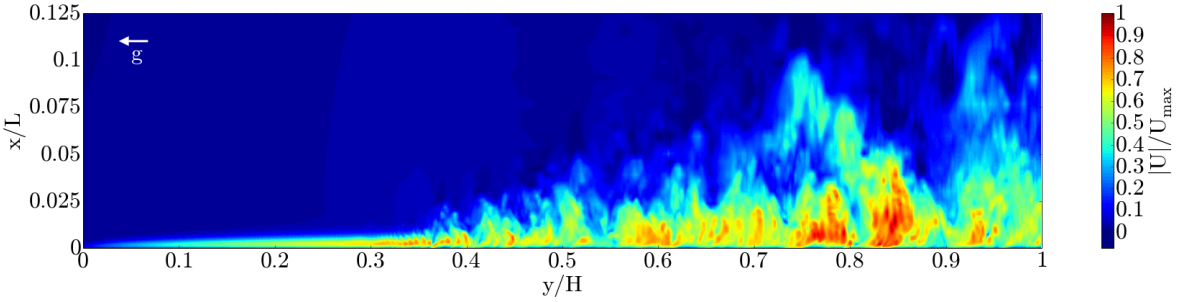

(a) Non perturbed boundary layer (case 2)

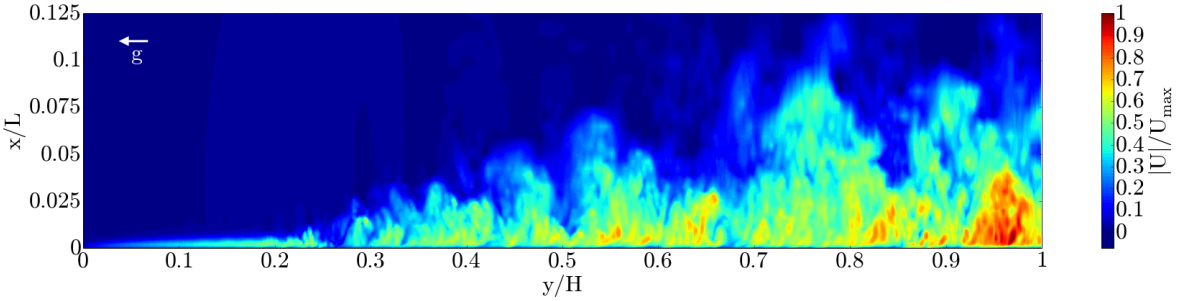

(b) Perturbed boundary layer (case 3)

Figure 7: Instantaneous velocity field for a TNBL at $Pr = 0.71$

not enough to reach the experiments. It can be seen that fixing the transition improves the numerical prediction, as case 3 shows compared to case 2. Also, the turbulent Nusselt prediction improves with the use of the perturbation technique. When it is used, the turbulent heat transfer is similar for cases 3 and 4.

The effect in the transition to turbulence of the perturbation is shown in figs. 7 and 8. In fig. 7 the velocity field for both cases 2 and 3 is shown. When perturbations are applied, at a very low height y/H, the velocity starts to fluctuate, to finally pass to a turbulent regime. This situation is seen in the Nusselt number of fig. 5, where the transition to turbulence is very smooth, as equal as for case 1. It means that the boundary layer is strongly excited, introducing an early transition to turbulence. In fig. 8 the temperature fields are compared for these two cases. The reduction of the laminar region is observed as well in the instantaneous temperature fields.

The mean velocity and temperature, and their turbulent statistics are studied in two different positions: a laminar position at $Gr = 1.52 \cdot 10^8$, and a turbulent one, $Gr = 1.80 \cdot 10^{11}$. Their location is indicated in fig. 5 with vertical lines.

The non-dimensional vertical velocity profiles are shown in fig. 9. The velocity boundary layer is characterized by three regions: an inner one at low x^+, a maximum velocity zone at moderate x^+, and an outer one where the velocity decays after the peak. Case 1 is underestimating the laminar profile in fig. 9a. It is due to the already present turbulent diffusion. The rest of cases shows similar results in the laminar part, since the transition is not observed there. In the turbulent region of fig. 9b, the velocity prediction is well captured for all the cases, though for case 4. The transition method of case 3 allows to improve the velocity prediction in the outer region of the boundary layer if compared with case 2.

The dimensionless temperature profiles are shown in fig. 10. It is possible to recognize three zones in the different profile, just like in the velocity boundary layer: an inner region at low x^+, a logarithmic region at moderate x^+, and finally a constant temperature region, which is already the free-stream temperature. In the case of the laminar profile, only the inner and free-stream regions are present. For case 1, the laminar temperature profile of fig. 10a is not well captured, as it was observed for the velocity, due to the early transition, the effective thermal diffusion is overpredicted, increasing the mixing. The rest of the simulations capture very well the laminar temperature field, but the turbulent profile is not consistent with the experiments

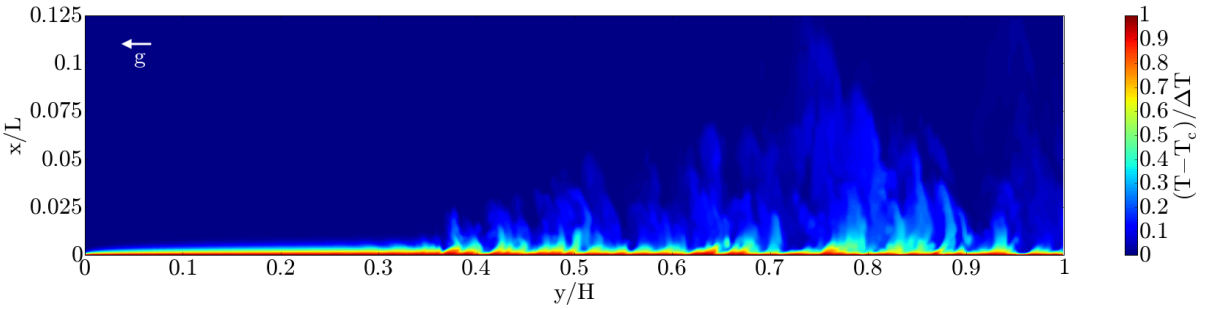

(a) Non perturbed boundary layer (case 2)

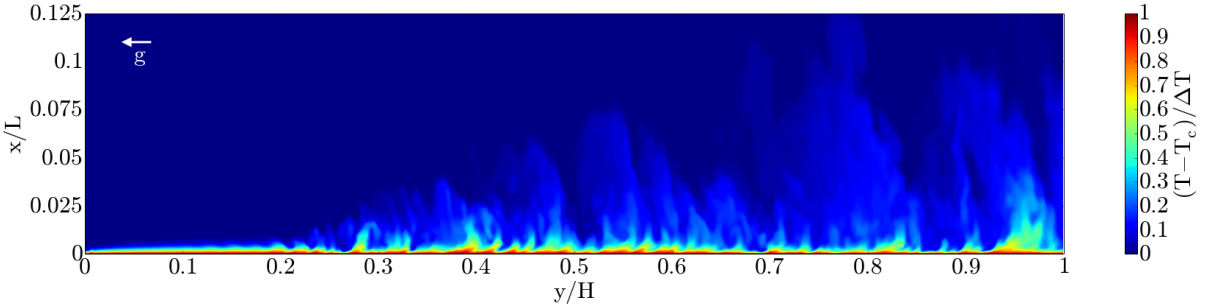

(b) Perturbed boundary layer (case 3)

Figure 8: Instantaneous temperature field for a TNBL at $Pr = 0.71$

for any simulation. A trend is captured, but the temperature values overestimate the measured ones, as it is observed in fig. 10b. The estimation of the heat flux in the wall seems to be the responsible of these results. Nusselt number and the heat flux are linked, so the better is the Nusselt prediction, the better would be the calculated heat flux. This is why the gap between simulations and experiments is lower when the mesh is refined, or the transition is forced to a certain location. As one can see, a slight difference is found in the predictions of cases 3 and 4, as equal as for the Nusselt number in the turbulent region.

The turbulence statistics at $Gr = 1.80 \cdot 10^{11}$ are also presented. The velocity fluctuations are shown in fig. 11. The four cases are able to reproduce fairly the velocity fluctuations. Case 4 provides the best solution, especially in the intermediate and outer sublayer. The maximum magnitude of the fluctuations is given by case 3 at $x^+ = 250$.

The temperature fluctuations $\langle T' \rangle^+$ are shown in fig. 12. A similar behavior as the one of the temperature profile is found here: there is an overprediction in the estimation of the fluctuations, but the refinement of the mesh procures a better approximation. The use of a perturbation allows also to improve the results. The numerical perturbations of the coarse mesh of case 1 produces the highest temperature fluctuations, whose peak is found at the end of the inner layer, the same place as for the experiments.

In addition, the Reynolds stress $\langle u'v' \rangle^+$ of fig. 13 is under-predicted in all the simulations. This fluctuation is a good indicator of turbulence, and it has been used to assess the characteristics of the boundary layer. The four cases provide a similar prediction, but they underestimate the values compared to the experiments. Case 3 shows the highest value of $\langle u'v' \rangle^+$ for all the simulations. In the inner sub-layer region, one can see some negative values of the stress, whereas in experiments, a positive value is found. This phenomenon has been observed in LES and DNS in the past by Abramov [7] and Nakao [8]. The maximum value is reached in the same location than the maximum RMS velocity fluctuation.

Figure 14 shows the turbulent heat flux $\langle u'T' \rangle^+$, whose prediction is slightly overestimated for all the simulations. Cases 3 and 4 slightly differ from cases 1 and 2 in their peak and the estimation of the inner layer. If the results for $\langle v'T' \rangle^+$ in fig. 15 are observed, one can see that cases 1 and 2 deviate more from the experiments, while cases 3 and 4 have a closer approximation to the experiments. Negative values are found at a low x^+, especially for case 3, where the

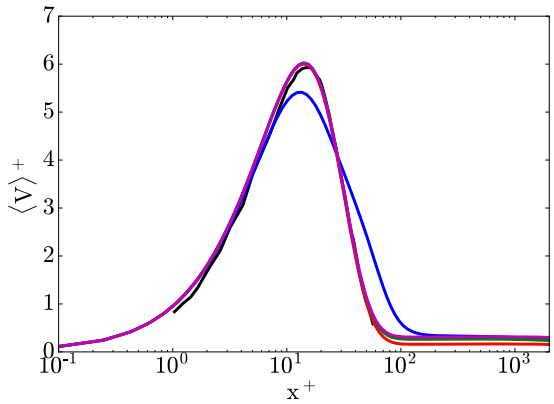

(a) $Gr = 1.52 \cdot 10^8$

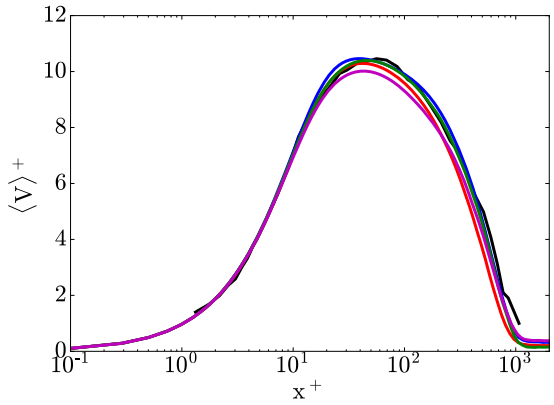

(b) $Gr = 1.80 \cdot 10^{11}$

Figure 9: Dimensionless velocity profiles $\langle V \rangle^+$ for case 1 (blue), 2 (red), 3 (green) and 4 (magenta) compared with experiments of Tsuji [4] (black).

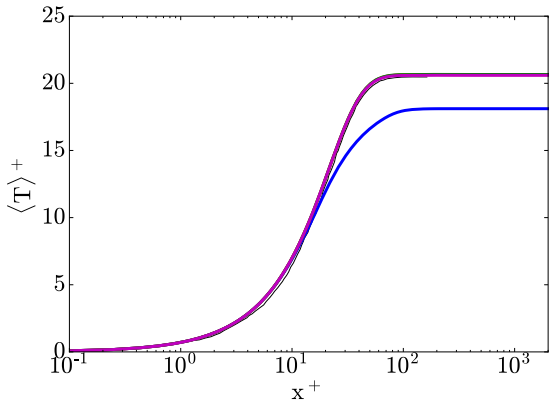

(a) $Gr = 1.52 \cdot 10^8$

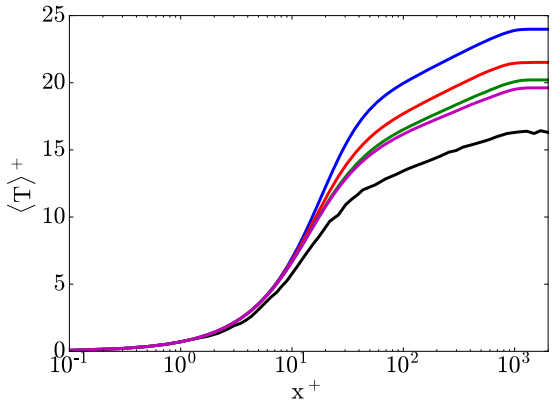

(b) $Gr = 1.80 \cdot 10^{11}$

Figure 10: Dimensionless temperature profiles $\langle T \rangle^+$ for case 1 (blue), 2 (red), 3 (green) and 4 (magenta) compared with experiments of Tsuji [4] (black).

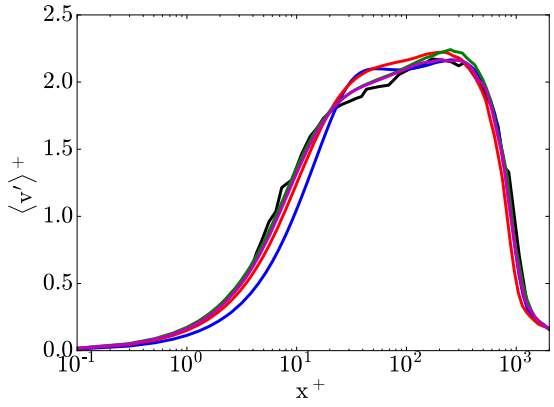

Figure 11: Dimensionless RMS of the stream-wise velocity $\langle v' \rangle^+$ for case 1 (blue), 2 (red), 3 (green) and 4 (magenta) compared with experiments of Tsuji [4] (black) at $Gr = 1.80 \cdot 10^{11}$.

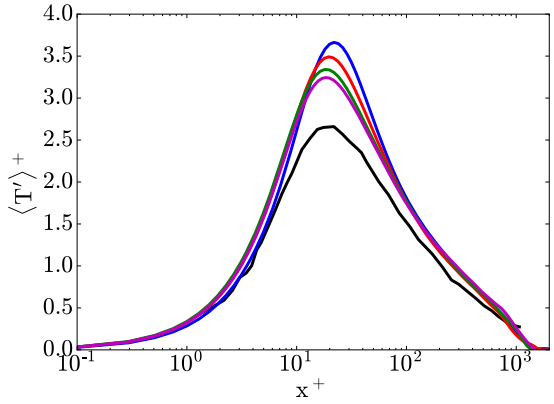

Figure 12: Dimensionless RMS of the temperature fluctuation $\langle T' \rangle^+$ for case 1 (blue), 2 (red), 3 (green) and 4 (magenta) compared with experiments of Tsuji [4] (black) at $Gr = 1.80 \cdot 10^{11}$.

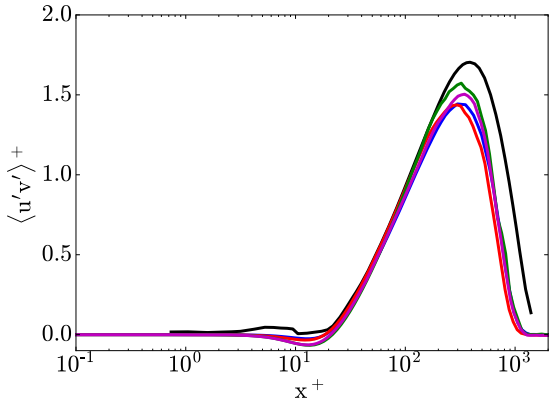

Figure 13: Dimensionless sub-grid scale stress $\langle u'v' \rangle^+$ for case 1 (blue), 2 (red), 3 (green) and 4 (magenta) compared with experiments of Tsuji [4] (black) at $Gr = 1.80 \cdot 10^{11}$.

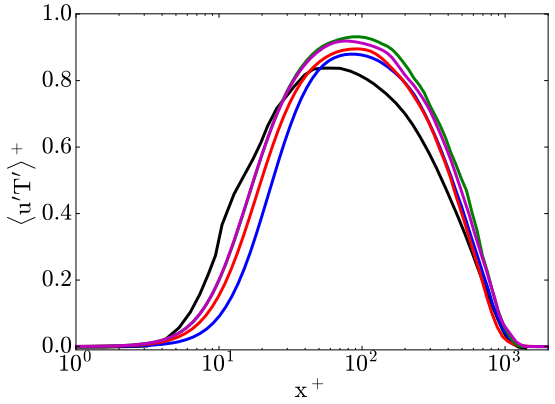

Figure 14: Dimensionless sub-grid scale heat flux $\langle u'T' \rangle^+$ profiles for case 1 (blue), 2 (red), 3 (green) and 4 (magenta) compared with experiments of Tsuji [4] (black) at $Gr = 1.80 \cdot 10^{11}$ (–).

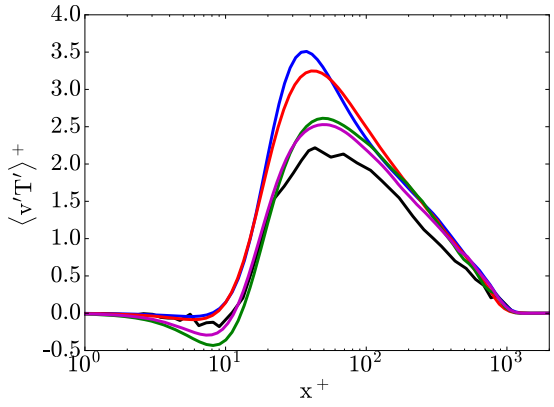

Figure 15: Dimensionless sub-grid scale heat flux $\langle v'T' \rangle^+$ profiles for case 1 (blue), 2 (red), 3 (green) and 4 (magenta) compared with experiments of Tsuji [4] (black) at $Gr = 1.80 \cdot 10^{11}$ (–).

perturbation influence is inducing this behavior. It appears in case 4, but its magnitude is closer to the one of experiments. This negative region is due to the development of the turbulent boundary layer, in a similar way than in forced convection boundary layers. As Tsuji proposed, the gradient of the stream wise velocity is positive, and the temperature gradient is negative, giving as a result the negative value of the heat flux. Nevertheless, the magnitude of this negative heat flux is much lower than the observed one in forced convection boundary layers.

3.3. Preliminary results for a natural convection boundary layer at $Pr = 0.025$

Preliminary results for a natural convection boundary layer at $Pr = 0.025$ are shown in this section. The simulation setup is shown in table 2. A similar approach than the previous case 3 has been chosen, but the number of cells in the span wise direction has been increased. The motivation of this increase comes from the thermal results of case 4, expecting to improve the heat flux prediction. In the other hand, the chosen perturbation frequency is the same than the one for $Pr = 0.71$ as an initial guess.

Instantaneous velocity and temperature fields are shown in figs. 16 and 17 respectively. If the thickness of both velocity and temperature boundary layer are compared with the ones of air, it is observed that at a lower Prandtl number, the boundary layers are much thicker than in case of a higher Prandtl number. Indeed, the higher thermal diffusion increases the thickness of the thermal one, and since the velocity one is linked to the thermal one, the same order of magnitude is observed between both.

It is possible to see that the frequency of the perturbation is not exciting the boundary layer. A transition to turbulence is observed at the end of the domain, as like the previous cases 2 and 4, due to the numerical error that excites a wider range of frequencies. The perturbation effect is visible at the beginning of the boundary layer, but then disappears, indicating that the selected frequency is damped by dissipation. The ongoing work consists in the investigation of the natural frequency of this boundary layer, and the analysis of the mean and turbulent statistics once the transition is controlled.

4. Conclusion

The Large Eddy Simulation of natural convection boundary layers at $Pr = 0.71$ and $Pr = 0.025$ has been performed. Comparable velocity and temperature statistics have been obtained for $Pr = 0.71$ to the experiments of Tsuji [4]. The study of the Nusselt number shows that there is an underprediction on the convective heat flux, leading to an overestimation of the temperature field. As well, it is observed that the transition to turbulence under the selected numerical configurations is not the same as observed in the experiments. This issue affects the estimation of the turbulent heat fluxes. Nevertheless, the application of a perturbation technique in the boundary layer allows to induce transition and an enhancement of the predictions. A modification on the parameters of the perturbation is needed to obtain a better approximation to the experiments.

In the other hand, the preliminary results of the ongoing simulation of a natural convection boundary layer at $Pr = 0.025$ have been presented. The application of the perturbation method will be needed, where a proper perturbation frequency for low Prandtl numbers must be set to induce turbulence. The ongoing work for the transition of turbulence of this boundary layer will be followed by a posterior analysis of the mean statistics, though here no experimental comparison is possible.

The next tasks in the PhD are related with the transition to turbulence for a low Prandtl number boundary layer. The cross comparison of mean and turbulent statistics for $Pr = 0.71$ and 0.025 will allow to analyze its effect in turbulent natural convection. The LES of an intermediate Prandtl number of $Pr = 0.2$ is also planned in order to have an intermediate value between the two previous ones.

L_x^*	L_y^*	L_z^*	N_x	N_y	N_z	x_1^*	Gr	Pr	Ra
3920	7430	930	100	512	128	0.076	$4.1 \cdot 10^{11}$	0.025	10^{10}

Table 2: Dimensions of the boundary layer L_i^*, number of cells on i-direction N_i, first grid point distance x_1^*, and maximum Grashof, Prandtl and Rayleigh numbers for the simulation at $Pr = 0.025$.

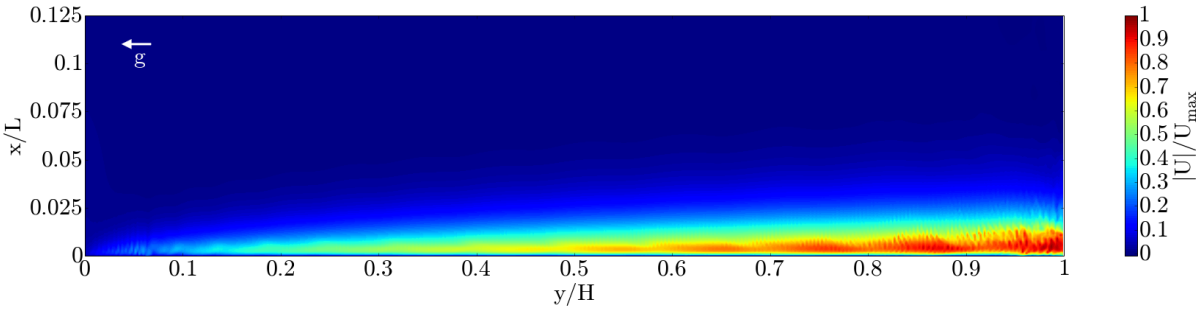

Figure 16: Instantaneous velocity field for a natural convection boundary layer at $Pr = 0.025$

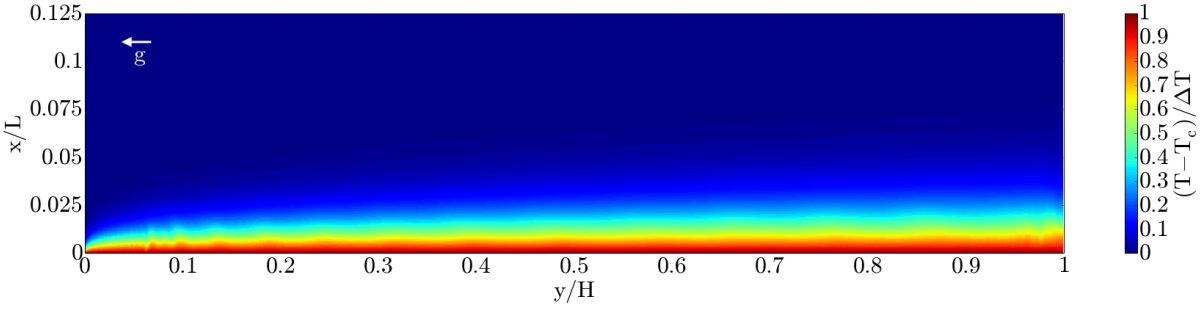

Figure 17: Instantaneous temperature field for a natural convection boundary layer at $Pr = 0.025$

References

[1] MYRRHA Project http://myrrha.sckcen.be/.

[2] W. To, J. Humphrey, Numerical simulation of buoyant, turbulent flow-i. free convection along a heated, vertical, flat plate, International journal of heat and mass transfer 29 (4) (1986) 573–592.

[3] Z. Yan, E. Nilsson, Large eddy simulation of natural convection along a vertical isothermal surface, Heat and Mass Transfer 41 (11) (2005) 1004–1013.

[4] T. Tsuji, Y. Nagano, Characteristics of a turbulent natural convection boundary layer along a vertical flat plate, International Journal of Heat and Mass Transfer 31 (8) (1988) 1723–1734.

[5] D. G. Barhaghi, L. Davidson, R. Karlsson, Large-eddy simulation of natural convection boundary layer on a vertical cylinder, International journal of heat and fluid flow 27 (5) (2006) 811–820.

[6] M. Z. Abedin, T. Tsuji, Y. Hattori, Direct numerical simulation for a time-developing natural-convection boundary layer along a vertical flat plate, International Journal of Heat and Mass Transfer 52 (19) (2009) 4525–4534.

[7] A. G. Abramov, E. M. Smirnov, V. D. Goryachev, Temporal direct numerical simulation of transitional natural-convection boundary layer under conditions of considerable external turbulence effects, Fluid Dynamics Research 46 (4) (2014) 041408.

[8] K. Nakao, Y. Hattori, H. Suto, Numerical investigation of a spatially developing turbulent natural convection boundary layer along a vertical heated plate, International Journal of Heat and Fluid Flow.

[9] H. Kobayashi, The subgrid-scale models based on coherent structures for rotating homogeneous turbulence and turbulent channel flow, Physics of Fluids 17. doi:10.1063/1.1874212.
URL http://gen.lib.rus.ec/scimag/index.php?s=10.1063/1.1874212

[10] T. Sayadi, C. Hamman, P. Moin, Direct numerical simulation of h-type and k-type transition to turbulence, Center for Turbulence Research Annual Research Briefs (2011) 109–121.

NOISE AND AEROACOUSTICS

Leakage characterisation through structural vibration analysis

Bouanati Nicolas

Environmental and Applied Fluid Dynamics Department, bouanati.nicolas@vki.ac.be

Supervisor: Schram Christophe

Professor, Environmental and Applied Fluid Dynamics Department, christophe.schram@vki.ac.be

University Supervisor: Pezerat Charles

Professor, Acoustics Department, Charles.pezerat@univ-lemans.fr

Abstract

Gas and liquid circuits are common in many industrial fields such as chemical processing and energy production. These fluid circuits always feature numerous and various valves for daily operations or safety purposes. Wear and impurities may lead to valve leakages which can necessitate an intervention and the halt plant operations if the mass flow rate passing through the leakage is estimated too important. The measurement of the mass flow rate is therefore important.

Different methods and technologies have been developed in order to permit the detection of a leakage in a valve, for example based on the measurement of the vibrations induced by the unsteady leakage jet flow on the structure of the valve and neighbouring pipe segments. Acoustic Emission (AE) sensors can be used to measure these vibrations at high frequency, i.e. from 100 kHz to 1 MHz, in order to avoid the contamination by the background noise at lower frequency and to be independent of the structural boundary conditions of the pipeline. The current state-of-the-art permits detecting the occurrence of a leakage using empirically-determined thresholds, which requires a priori calibration, and does in any case not foresee the quantification of the leak mass flow rate. This last point constitutes the main objective of this research.

The structural excitation of the valve is due to the wall pressure field fluctuations, which are of hydrodynamic and acoustic nature. The first contribution is associated to the unsteady flow field and boundary layer that are in the immediate vicinity (more precisely within an acoustically compact distance) of the structure and the acoustic component is due to acoustic radiation from remote turbulent sources. The characteristics of the wall pressure field depend on the leak topology and mass flow rate, which constitutes the basic rationale for the development of a leakage quantification method based on the analysis of the vibrations.

The objective of this thesis is to develop analysis tools processing the recorded vibrations of the structure, a priori in the AE frequency range, to determine relevant information about the leakage characteristics and specifically the mass flow rate. The problem is divided in two parts: *i*) the analysis of the hydrodynamic and acoustic pressure perturbations that are induced by the leak jet flow on the structure, and *ii*) the structural response and associated vibrations. A test bench is being developed for the measurement of the flow and structural quantities for different leakage topologies and controlled mass flow rates.

SRM Aeroacoustics:
review of the literature

Lionel Hirschberg

Environmental and Applied Fluid Dynamics Department, von Karman Institute for Fluid Dynamics, Belgium, lionel.hirschberg@vki.ac.be

Supervisor: Christophe Schram

Associate Professor, Environmental and Applied Fluid Dynamics Department, von Karman Institute for Fluid Dynamics, Belgium, christophe.schram@vki.ac.be

University Supervisor: Thierry Schuller

Professor, IMFT, France

Airbus Safran Launchers: Jean Colinet

Mr., Airbus Safran Launcher, France

Abstract

The literature reflects that vortex shedding in large SRMs is a significant source of sustained pressure pulsations. No analytical model is available to predict vortex induced pulsations in SRMs. This text contains a review of the state of the art. In this text the most promising modeling strategies are discussed. The scientific strategy adhered to is described.

Keywords: SRM, Aeroacoustics, Internal Flow.

1. Introduction

Ariane 5 uses large solid rocket motors (SRMs) as boosters for takeoff. After approximately one minute of flight, spurious sustained low frequency pressure pulsations are observed in the SRMs. These pulsations are due to standing longitudinal acoustic waves in the combustion chamber of the SRMs. The force associated with these pressure pulsations is approximately 5% of the thrust [1; 2]. To avoid that pulsations damage the payload, mechanical damping devices are installed, levying a cost on the amount of payload transported per flight. It is thus imperative that the nature of these pressure pulsations be understood. Indeed, a good grasp of what fundamentally drives these pulsations will allow one to take remedial action.

The main objective of this project is to formulate and develop simplified analytical models. This implies the fundamental study of key physical phenomena. The study involves the use and formulation of a theoretical framework.

No single analytical model will encompass all possible contributions to sustained pressure pulsations. It does, however, provide a framework to understand their general behavior and their origin [3].

Culick states [4]: "The purpose of theory is to provide a framework for interpreting observations, both in laboratory and full-scale device; to suggest experiments to produce required ancillary data or to improve the empirical base for understanding; to formulate guidelines for designing full-scale systems; and globally to serve, like any good theory, as the vehicle for understanding the fundamental principles governing the physical behavior, thereby having predictive value as well."

Sustained pressure pulsations are self-excited. I.e. a feedback loop is created in which a source is coupled to the acoustics of the system, see Figure 1. The source can be purely due to combustion or to hydrodynamics or it can be a hybrid of the two. Combustion as a source has been the main focus of study as established in the literature (see section 2). However,

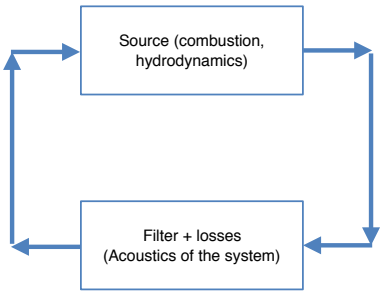

Figure 1: Feedback loop in self-excited systems.

research by ONERA, SNPE and the von Karman institute (VKI) have demonstrated using scale model experiments [5], numerical simulations [6; 7; 8] and cold gas scale experiments [9], that hydrodynamics involving vortex shedding followed by vortex nozzle interaction can induce pulsation amplitudes of the order of pulsations observed in full scale SRMs. Thus the initial focus of this project is to model sustained pressure pulsations due to vortex nozzle interaction (pure hydrodynamic source).

It should be noted that only a small part of the available energy produced in the SRM is involved in the establishment of sustained pressure pulsations. The complicated chemical and flow processes hinder the construction of a complete theory from first principles. It is therefore essential that theoretical work be closely allied with experimental results and vice versa.

In absence of empirical data detailed computational fluid dynamic (CFD) simulations using a numerical code could be used for validation. However, CFD cannot accurately capture all physical processes that exist in a SRM and describe the geometry in all its details. Furthermore, CFD has the tendency to become prohibitively expensive in terms of computation time when many details are considered. Numerical models can, however, provide access to particular aspects of the flows which cannot be observed experimentally. Simplified analytical models should serve as complementary predictive tools, providing fast results which can suggest if an envisioned costly detailed numerical run is indeed beneficial, potentially saving time. Simple models also complement the use of CFD by providing a framework for interpretation of simulation results. These could eventually be used for interpolation or extrapolation of experimental or numerical results. At least simple models should provide scaling rules for the interpretation of reduced scale experiments.

Scientific strategy. The scientific strategy in which the doctoral student is engaged is as follows.

- Analytical models are developed. The following modeling strategies will be used in this project (for a detailed discussion of modeling strategies see section 3):
  - Energy balance approach,
  - Lumped model approach (also referred to as amplitude equation or Culick model).
- The analytical models will be validated with:
  - available empirical data,
  - CFD simulations.

It should be noted that under available empirical data, the following is understood:

1. Cold (without combustion) gas scale model experiments,
2. Hot (with combustion) gas scale experiments.

As the initial focus of the project is on the hydrodynamic contribution to sustained pressure pulsations, validation will be done first with cold flow scale experiments.

In the **second year** of the PhD project emphasis on the formulation of a more precise hydrodynamic source model due to vortex nozzle interaction is placed. To do this a CFD tool called EIA (Euler Internal Aeroacoustics code), provided by Dr. Hulshoff of the Aerospace engineering faculty of the Technische Universiteit Delft (TU Delft) will be used. This study could as a byproduct provide valuable insight into this system. Possibly allowing for the formulation of design rules leading to nozzles with less sound production due to vortex nozzle interaction.

In **year three** this improved hydrodynamic source model will be incorporated in a lumped model. As a source of sound due to combustion the simplified analytical model due to combustion obtained by Mr. Genot[1] will be used i.e. if this model is available. The model which is thus ultimately produced will be validated using available hot gas empirical data.

[1] doctoral candidate focused on simplified combustion models for sustained pressure pulsations in SRMs in a CNES/ASL/CentraleSupélec project

2. Literature

If the feedback loop Figure 1 is linearly unstable, after an initially exponential growth stage at low amplitudes, an essentially nonlinear process saturates growth causing the system to reach a limit cycle. Linear models predict the experimental growth but cannot predict a limit cycle. When the limit cycle is stable it corresponds to periodic pulsations. At the limit cycle there is a balance between acoustic power produced time averaged over a period[2] $\langle \mathcal{P}_{source} \rangle$ and the corresponding time averaged acoustic power dissipated $\langle \mathcal{P}_{loss} \rangle$. In most cases a stable limit cycle involves a single dominant acoustic standing wave (mode of the combustion chamber) and the oscillation frequency is close to the natural frequency of this mode (acoustical oscillation frequency without sources nor losses).

In the literature the application of linear theory receives most attention. In small SRMs the pressure pulsations reach such high amplitudes (pulsation amplitudes of the order of 10% of the static pressure) that nonlinear wave propagation leads to the formation of traveling shockwaves. The thermal-viscous dissipation in the shockwaves provides a nonlinear amplitude limiting process to reach a limit cycle [10; 11; 12]. This effect is negligible in large SRMs where the ratio of pressure fluctuation p' to absolute pressure p is of order $O(10^{-3})$. Hence, in large SRMs the nonlinearity of the source is essential to reach a limit cycle.

The feedback loop can be due to coupling of the longitudinal acoustic standing wave and the following sources:

- surface combustion of the propellant grain [3; 13],
- volume combustion of Aluminum particles [3; 14; 13],
- vortex shedding leading to vortex nozzle interaction [9; 3].

The literature focusses on combustion as a source [3; 13]. Apart from the pioneering work by Hulshoff et al. [15], no conclusive systematic study on vortex nozzle interaction as a source exists. That is to say, a profound lack of understanding of this source is apparent. Studying this source will thus be an important focus of the project.

There are three possible causes of vortex shedding in SRMs (see Figure 2).

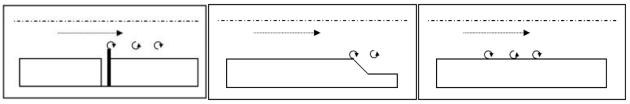

Figure 2: From left to right: obstacle vortex shedding (OVS), angle vortex shedding (AVS) and surface vortex shedding (SVS).

- Obstacle vortex shedding (OVS), which occurs at thermal inhibitors placed between segments of propellent grain [9; 3; 13]
- Angle vortex shedding (AVS), occurs in case of an abrupt increase of combustion chamber cross section in the main flow direction [16].
- Surface vortex shedding (SVS), due to the intrinsic instability of the Taylor-Culick flow generated by surface combustion of the propellant [17; 16; 8].

Regardless of the mechanism by which the vortices are created the formation of vortices triggered by the acoustic oscillation implies sound absorption. The vortices are then convected towards the nozzle and it is their interaction with the nozzle that produces sound, which can drive self sustained oscillations. The convection time from the point where vortex formation is initiated, to the nozzle, plays a similar role as the delay in combustion change due to acoustic perturbation. For critical ratios of delay time to acoustic oscillation period[3], the sound generated by the source reinforces the oscillations. Any contribution to the understanding of the vortex nozzle interaction as a source of sound is thus of paramount importance. As shown in Figure 3 (results for Titan 4) the pulsation amplitudes display several maxima around the first longitudinal acoustic mode (chamber length is half a wavelength). The frequency decreases around each maximum with decreasing Mach number at the inlet of the nozzle (this corresponds with increasing time). Similar hydrodynamic modes appear in scale experiments with hot gases carried out by ONERA [5] and in P230 Ariane 5 boosters see figure 4.

Each maximum corresponds to a hydrodynamic mode. The ratio of Mach number M and the difference ΔM between two successive modes provides an estimate of the number of vortices $m_h \simeq M/\Delta M$ present between the vortex shedding location and the nozzle

[2] The brackets $< \ldots >$ indicate time averaging over a period of oscillation.

[3] This corresponds to so-called hydrodynamic modes m_h of the system.

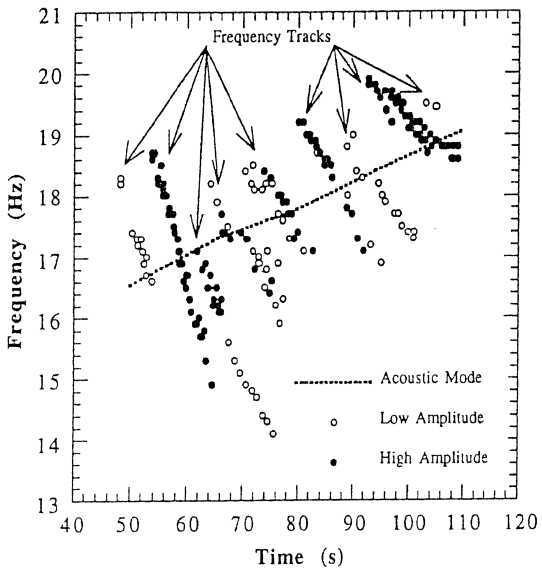

Figure 3: Titan 4 results, figure taken from [13]. The Strouhal lines (frequency tracks) crossing acoustic mode line are evidence of the presence of vortices i.e. of the importance of hydrodynamic effects. Each frequency track line corresponds to a fixed number of vortices traveling down stream from the point of shedding to the inlet of the nozzle. The Mach number at the nozzle inlet decreases as a function of time due to the increase of combustion chamber diameter. These effects are common and have been observed and published recently e.g. see Figure 13a in [5].

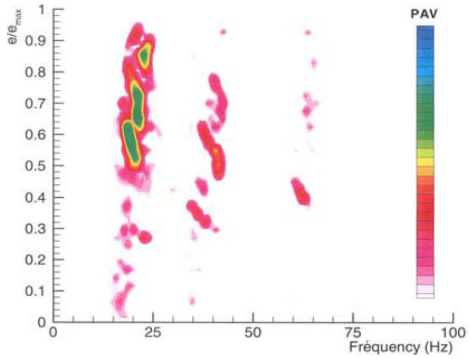

Figure 4: Figure taken from [13]. Strouhal lines in Ariane P230 boosters. According to Anthoine [9] the lowest Strouhal (green lines around the first acoustic mode $20\,Hz$) line corresponds to $M = 0.13$ and the top one to $M = 0.07$.



Figure 5: Figure taken from [8]. Simulation of obstacle vortex shedding (OVS) in a LP3 A motor, leading to five vortices traveling down stream from the inhibitor to the nozzle. This situation corresponds to $m_h \simeq 5$.

inlet. From Figure 4 which show frequencies in a Ariane 5 P230 booster (according to Anthoine [9] the lowest Strouhal line corresponds to $M = 0.13$ and the top one to $M = 0.07$), one deduces that there are initially approximately five vortices ($m_h = 0.07/\frac{0.06}{4} \simeq 5$) at onset of the pulsations. This is indeed confirmed by numerical simulations [8], in the case of OVS [8] find five vortices see Figure 5.

Seminal cold flow experiments were carried out by Anthoine [9] on a $1/30$ scale model for Ariane 5. In cold flow experiments combustion is replaced by injection of air through a porous wall. Anthoine [9] carried out two types of experiments:

1. axial injection experiments (air is injected through a porous head end wall of the "combustion" chamber, a sketch is shown in Figure 6),
2. radial injection experiments (air is injected through a porous side wall of the chamber).

Anthoine [9] observed pressure pulsation amplitudes p' of the order of one thousandth of the static pressure p in the "combustion" chamber. This is of the order of pulsations observed in actual large SRMs [1; 2].

The key feature of these experiments is an integrated nozzle with variable cavity volume was fixed on the downstream end. This corresponds to the actual configuration of SRMs in Ariane 5. At the ignition the cavity is filled with solid propellant. After about a minute a large part of this propellant has burned and the cavity is filled with gas. Later aluminium-oxide dropplets captured by the cavity reduce the acoustically accessible cavity volume. Anthoine [9] found that the relative pressure pulsations p'/p (pressure fluctuations over the static pressure in the chamber) where proportional to the volume of the integrated cavity volume. This could explain the appearance of pulsations after one minute of combustion and part of the reduction of pulsations in the later phase of combustion [1; 2].

Other cold flow experiments are mentioned in the literature e.g. VALDO and VECLA experiments by ONERA [1; 17; 18]. These experiments confirm the intrinsic instability of Taylor-Culick flow and the existence of SVS. However, the available data is for a chamber without nozzle.

While cold flow experiments confirm that sound generated by vortices is essential, one can expect that combustion will also contribute. Hence a coupling between combustion response and vortex nozzle interaction can be essential to understand pulsations in actual

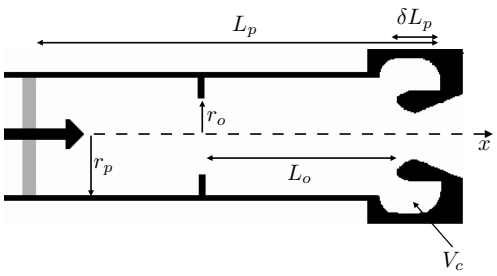

Figure 6: Scale model with axial injection through the upstream porous wall and an integrated nozzle at the downstream side. Figure taken form [9]. In these experiments the volume V_c around the nozzle inlet was varried. Anthoine also studied the effect of the chamber length L_p, orifice radius r_o, orifice position L_o and Mach number M. The Mach number was varied by partial obstruction of the nozzle throat by means of a needle.

SRM.

No ready made analytical "plug and play" models that can predict limit cycles are available in the literature for vortex driven pulsations. Viz. a new model will have to be formulated from the basics using a to be investigated theoretical framework. In the next section we describe different promising strategies.

3. Modeling strategies

To formulate a predictive model three modeling strategies are available to us:

1. The "energy balance" approach, which assumes that the system has reached a limit cycle. The limit cycle is taken to be dominated by a single estimated acoustic mode in its fundamental harmonic. I.e. a standing wave is assumed to exist allowing the user to estimate the amplitude. In first approximation one can assume that the oscillation frequency ω is equal to the natural frequency ω_n of the mode. A problem with the energy in acoustics is that one should consider all relevant second order terms. This makes the approach difficult [3; 19]. However, a simplified model can be used for order of magnitude estimates.
2. The formulation of a lumped model viz. the Culick [3] approach. This is an established method in the field of combustion instabilities. The acoustic field is expanded in a series of orthogonal acoustic modes of the chamber. The system is described by a set of coupled ordinary differential equations for the modes amplitudes. This allows a prediction of the evolution of the pulsations in time (dynamics of the system). When used for the limit cycle the method predicts the deviation of the oscillation frequency from the natural mode frequency ω_n. The first order approximation in which one assumes that a single mode is dominant and that the oscillation frequency is equal to the natural mode frequency is simple to use and robust. It can be used to initiate an iterative solution to find a limit cycle solution. The alternative is an integration in time of the amplitude equation.

3.1. Energy balance approach

The energy balance approach has been used to study the linear stability of a Taylor-Culick flow [20; 21] and for combustion processes [8]. For that purpose all source terms are linearized, thusly this linear approach is not appropriate to study the limit cycle. It only predicts the condition at the threshold for linear instability. As already stressed, the aim of the project is a prediction of limit cycle amplitudes.

As a first step for this project a simple model using the nonlinear energy balance approach was formulated. The model assumes the limit cycle has been reached and is stable. The acoustic field is taken to be dominated by a single mode in its fundamental frequency (one ignores deviation from harmonic oscillation).

The analysis can be repeated for each mode and it provides an estimation of the pulsation amplitude that can be reached. It however does not predict which of the potentially unstable modes will be dominant. For engineering purposes it can be very useful as only the lowest longitudinal modes appear in practice. Hence, calculations for the first three modes does provide an order of magnitude of the amplitudes, which might occur.

The method has been tested for the limit cycle due to a coupling between vortex shedding at an orifice (OVS) triggered by the acoustic longitudinal mode, as observed in cold gas experiments of Anthoine [9] with axial injections.

Sound is assumed to be produced by the interaction of a ring vortex with an uniform acoustic field created by compact cavity volumes placed around the nozzle inlet. Contribution due to vortex nozzle ingestion is neglected. A caricatural model is used for the vortex flow and acoustical field involving two empirical parameters for adjustment to experimental results. This model was compared to available axial injection cold flow scale experiment obtained by Anthoine [9] at the VKI. The results of this work have been peer

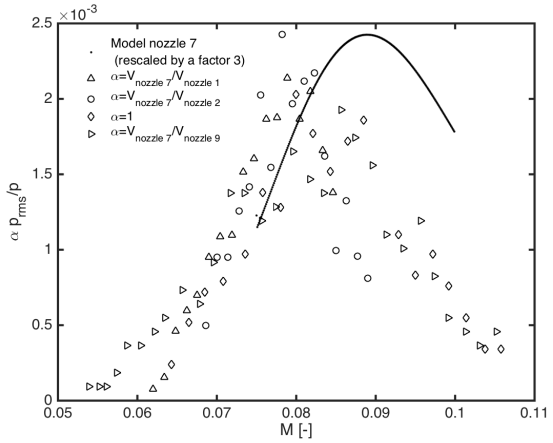

Figure 7: Rescaled (by a factor 3) theoretical prediction of the relative pulsation amplitude p_{rms}/p as a function of the Mach number M. The predictions are compared to the empirical data obtained by Anthoine [9] ($L_p = 393\,mm$, $r_0 = 29\,mm$, $L_o = 71\,mm$, $n = 2$ and $1.00 \times 10^{-4}\,m^3 \leq V_c \leq 2.18 \times 10^{-4}\,m^3$). The scaling coefficient α is the ratio of the reference volume (nozzle 7 in Anthoine's experiments [9]) $V_{ref} = 1.84 \times 10^{-4} m^3$ to the cavity volume V_c. Figure taken from [22].

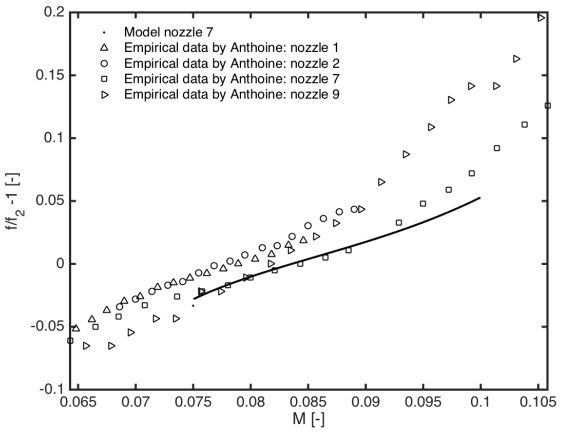

Figure 8: The oscillation frequency $f = \omega/2\pi$ increases monotonously for each acoustic mode, passing the resonance frequency $f_n = \omega_n/2\pi$ around the maximum pulsation level as observed in the experiments ($L_p = 393\,mm$, $r_o = 29\,mm$,$L_o = 71\,mm$, $n = 2$ and $1.00 \times 10^{-4}\,m^3 \leq V_c \leq 2.18 \times 10^{-4}\,m^3$). The slope of the frequency as a function of the Mach number is quite well predicted by the theory, indicating that the losses are well evaluated. Figure taken from [22].

reviewed, published and presented [22; 23] as conference proceedings. These contributions are the first to analytically take into account a simplified nonlinear vortex nozzle source model, giving a reproduction within the order of magnitude of measured pressure pulsations in cold gas scale models. As illustrated in Figure 7 the pulsation amplitudes for different cavity volumes collapse, when divided by the cavity volume and the theory predicts the Mach number evolution of the amplitude fairly well. The predicted amplitudes have been divided by a factor 3 in order to ease comparison with experiments. The model assumes quasi-steady linear losses (viscous losses in porous wall, vortex shedding losses at inhibitor and nozzle radiation losses) which appear to agree with experimentally determined losses within 20% accuracy. This conclusion is atained by comparison of the slope of the ratio ω/ω_n as a function of the Mach number shown in Figure 8. The slope $d\omega/dM$ is inversely proportional to the quality factor Q of the acoustic resonator, which is determined by the acoustic losses of the system. The quality factor is inversely proportional to the damping coefficient due to losses.

To proceed further with the energy balance approach and obtain a predictive model, it is essential to develop a less caricatural model for the vortex flow. This will be discussed in section 4.1.

3.2. Lumped model

The formulation of a lumped model for the amplitudes of the acoustic modes, as suggested by Culick [4; 3], with combustion as a source is an established method in the literature. This analysis is commonly used to study the linear stability of SRM systems. The use of this method with nonlinear source terms for the prediction of limit cycles remains undeveloped. The method yields a set of coupled ordinary differential equations for the amplitude of acoustic modes as a function of time. Next to limit cycle solution one can obtain approximations for slow time evolution using the method of van der Pol (method of averaging) [3].

Preliminary steps have been taken to incorporate nonlinear vortex nozzle interaction in the Culick approach, starting from an integral equation using the pulse response of the combustion chamber (Green's function).

4. Vortex Nozzle interaction

Apart from pioneering work by Hulshoff et al. [15], vortex nozzle interaction as a source of sound has not been studied quantitatively. As a preliminary step in the present study, an analytical model has been formulated to do a preliminary study of the vortex ingestion by the nozzle as a source of sound. More information about this study is given in 4.1. There are limits

to what is possible analytically. Basically only a 2-D planar flow can be considered. Thus CFD studies on vortex nozzle interaction will be needed. The use of numerical simulations to do computational Aeroacoustics (CAA) is discussed in section 4.2.

4.1. Analytical model

Previous work has shown that the presence of an acoustic field due to the compact cavities around the inlet of the integrated nozzle is of major import [9; 22; 23]. The effect of ingestion of a vortex by a nozzle had previously been neglected [22; 23]. To study the effect of ingestion, an analytical model is proposed without the presence of cavities. The purpose of this model is to do a preliminary investigation. The ingestion process is described by a model considering the interaction of a line vortex pair with a contraction in a 2-D planar flow a channel.

The flow is described by 2-Dimensional incompressible potential flow theory. Using conformal mapping, an analytical solution is found for the potential describing the flow and the convection velocity of the vortex. Given the flow, the low frequency and low Mach number approximation of Vortex Sound Theory [24] is used to deduce the sound wave generated by this flow for a contraction (going from a cross-section S_1 to a cross-section S_2) in an infinitely long channel. Results are compared to results obtained by Hulshoff et al. [15] using the numerical solution of an Euler model. A conference proceeding manuscript [25] has been submitted for peer review . In Figure 9 the results of our analytical model are compared side by side with the results of Hulshoff et al. [15] at low Mach numbers. It is interesting to note that a single point vortex model does capture most of the features observed for the interaction between a vortex of finite core size and a contraction in a channel.

Sound appears to be mainly produced in the approach phase, where the flow is essentially subsonic. This suggests that a low Mach number incompressible flow approximation is meaningful even when considering a choked nozzle. Hence, the use of relatively cheap incompressible codes to study vortex nozzle interaction is justified. This will be discussed in more detail in section 4.2. In the study of Hulshoff et al.[15] and the analytical model results are only presented for the case of the ratio $S_1/S_2 = 3$. This work should be extended to arbitrary ratios. Furthermore axis symmetrical flow simulations should be carried out to investigate the effect of a transition from a 2-D planar to a 2-D axis symmetrical configuration.

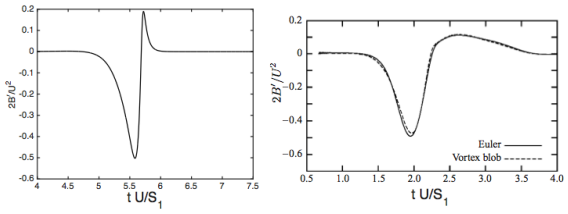

Figure 9: The acoustic stagnation enthalpy pulse generated, $\Gamma/(S_1U) = 1.5$ and $h/S_1 = 0.4$ on the lefthand side compared to figure 17 from Hulshoff et al. [15] on the righthand side $\Gamma/(S_1U) = 1.5$. The circulation Γ of the vortex is made dimensionless by division by the channel height S_1 and the steady flow velocity U, upstream of the contraction. The vortex is released at height h at some distance upstream from the contraction. Note that the absolute times are arbitrary as these depend on where the vortex was released. Figure taken from [25].

This model can be used as a test case for more complex numerical models and provides some insight into the influence of parameters on the sound production.

4.2. Numerical simulation

Aeroacoustics is the study of the generation of sound by flows and interaction of flows with acoustic fields. In section 4.2.1 general remarks on computational Aeroacoustics (CAA) are made. Two approaches to CAA are discussed: the hybrid method (section 4.2.2) and direct simulation (section 4.2.3). The use of CAA is relevant to study the interaction of ring vortices with the nozzle in SRMs. The need for this CAA study is discussed in section 4.2.4. The formation of mature vortices through a nonlinear process due to SVS, is a point of interest for which numerical simulation would be helpful (discussed in 4.2.5). Finally in section 4.2.6, comments are made about challenges faced in finding appropriate CAA tools

4.2.1. Numerical method and CAA

The physics of the flow in a SRM involves scales from microscopic phenomena controlling combustion to the acoustic standing waves over the length of the combustion chamber. At each scale simplifications have to be introduced to allow a mathematical model. After a model has been chosen, one usually has to choose a numerical method to obtain a solution.

With the availability of modern computers and seemingly ever increasing computational power, some are tempted to develop all encompassing numerical codes. This approach has the ambition to mimic the real world. I.e. by modeling all possible physical process present in a system, thus increasing the complexity of the problem considerably. It is assumed that one essentially performs a “numerical experiment”.

It is naive to assume that the more complex a model is the better its results are. Instead of trying to model all physics possibly involved in a system. It is better to find the most simple model allowing the study of the impact of variation of specific parameters on a certain phenomenon.

The present project focuses on self sustained oscillations and the prediction of limit cycle amplitudes. Self sustained oscillations are controlled by several effects:

- the delayed response of combustion to fluctuations in flow conditions (pressure or/and velocity),
- global hydrodynamic instabilities triggered by acoustic perturbations, leading to the formation of large scale vortices which produce sound due to interaction of the vortices with the nozzle.

In the present project the most simple model which describes these phenomena is sought, starting with vortex dynamics.

Part of such a model will be analytical but one can also use dedicated numerical solutions as input. Finding adequate numerical results is challenging. For example the simultaneous solution of hydrodynamic phenomena (vortex dynamics, turbulence) and acoustic wave generation and propagation with a single model is very difficult. Numerical models resolving the dissipative scales of turbulence [16] and the acoustic viscous wall boundary layer involve a fine discretization, hence a huge number of cells. To resolve turbulence Fabignon et al. [16] used numerical simulations with one billion (10^9) cells in a simplified geometry. To obtain meaningful acoustical predictions a large grid refinement is not sufficient. Most solvers tend to dissipate or disperse acoustic waves, which could lead to spurious numerical damping. Only very special dedicated numerical integration methods with a particular choice of numerical parameters can be used to predict the interaction between a flow and acoustic waves. This is a subject of study called Computational Aeroacoustics (CAA) .

There are two basic approaches in CAA [26]:

- hybrid method,
- direct simulation.

The hybrid method recognizes that sound is generated in a compact region (small compared to the acoustic wavelength) and that acoustic waves have a negligible impact on this flow. This is certainly the case of sound production by vortex nozzle interaction because the chamber length is large compared to the nozzle inlet diameter. While the moment at which vortex formation is initiated is confronted by the acoustic flow, once vortices have been formed they are quite insensitive to the acoustic perturbations. Details about the hybrid method can be found in section 4.2.2. Direct simulation, discussed in section 4.2.3, is an attempt to describe the entire flow including acoustic waves with a single numerical model.

4.2.2. The hybrid method

Central to the hybrid method is the idea to use full computational power to describe the details of the hydrodynamic flow (incompressible flow) in the source region. This flow information is then injected in a source term h of a wave equation, a so-called "analogy". A formal solution for the pressure fluctuation p' can then be obtained in the form of an integral equation, which is the convolution of a pulse response $G(\vec{x}, \vec{y}, t-\tau)$ (called a Green's function) of the acoustic (linear) system with the volume sound source h:

$$\begin{aligned} p'(\vec{x},t) &= \int_{-\infty}^{\infty}\int_{V} G h d^3y d\tau \\ &+ \int_{-\infty}^{\infty}\int_{S} (G\nabla p' - p'\nabla G)\cdot\vec{n} d^2y d\tau. \end{aligned}$$

Where V is the volume of the combustion chamber enclosed by the surface S with outer normal $\vec{n}$. The Green's function is the linear pulse response of a user chosen ideal system approximating the system under investigation. The surface integral represents the effect of reflections of the acoustic wave G at the surface S due to the difference between the actual system and the idealized configuration used to calculate G. The surface integral vanishes, when the physical problem and the Green's function G satisfy the same local linear boundary conditions on S. This corresponds to a so-called Tailored Green's function. The user can choose between such a complicated Green's function or a more simple one leading to a more complex integral equation. As stressed by Culick [3] the choice between a tailored or non tailored Green's function is problem dependent. When the Green's function satisfies loss free boundary conditions such as ($G = 0$ or $\nabla G \cdot \vec{n} = 0$) it can be expanded in orthogonal modes of the idealized geometry. This makes the mathematical formulation easier, but does not always provide a fast convergence when truncating at a finite number of modes.

This formal solution should in the present form in principle be solved iteratively because the source h and the boundary conditions on the surface S depend on the solution. An advantage of an integral solution is that it reduces random errors in the solution. As a consequence even simplified models for the source h can provide reasonable results. One can e.g. assume that when the limit cycle is reached only the phase of the source term is influenced by the acoustic field p' while the amplitude of the source is independent of p'.

4.2.3. Direct simulation

In spite of their complexity and of the large computational effort required numerical solutions based on a direct simulation approach have been used to study some aspects of flow instabilities in SRMs. A review of such work is provided by Guéry [27]. Fabignon et al. [16] discuss recent numerical simulations involving 10^9 cells, which allows the capture of the dissipation scale of turbulence in a particular experiment.

It should be noted that while some results are very encouraging, a careful test of the model is needed before calculations can be trusted. For example, an acoustic oscillation induced by a pulse in a combustion chamber of a SRM will typically decay by a factor e in twenty oscillation periods of the fundamental acoustic mode. This implies a propagation of the acoustic waves over twenty wave lengths. One should therefore check whether in the absence of source terms and losses (friction, radiation) the chosen numerical scheme describes acoustic wave propagation with negligible numerical dissipation and dispersion over distances of the order of forty times the length of the SRM. Without such tests results should not be trusted.

4.2.4. Numerical simulation of vortex nozzle interaction

Some insight into the interaction of vortices with the nozzle has been obtained by considering a point vortex pair in a 2-D incompressible channel flow section 4.1 and [25]. This analytical model should now be compared to a 2-D axis-symmetric or 3-D models of a vortex ring interaction with a nozzle. This is necessary because a vortex ring has a different behavior than its 2-D planar counterpart (a pair of point vortices with opposite circulation). The ring vortex has a self induced velocity which depends significantly on the thickness of its (viscous) core. This is not the case for the 2-D planar vortex pair.

Using such calculations one can investigate whether the vortex ring path is strongly affected by changes in the geometry of the nozzle such as variation in volume of the cavities around the nozzle.

The aim would be to find a parametric model of the path of the vortex for different variations in nozzle geometry. This can be used as input for a calculation of the vortex sound source h (section 4.2.2).

4.2.5. Surface vortex shedding

Analytical models have been developed to describe SVS in the linear regime.

However, it is obvious that the vorticity wave soon results in the formation of large coherent structures (vortices). In some numerical simulations [9] one observes merging of successive vortices before they reach the nozzle. This process should be investigated numerically. The findings should be synthesized into a simplified model that can be incorporated in a lumped model.

4.2.6. Available software

For the study of vortex nozzle interaction as a source of sound Dr. Hulshoff's (TU Delft) compressible Euler code (EIA) has been made available.

5. Conclusion

Literature indicates that vortex shedding in large SRMs is a significant source of sustained pressure pulsations (section 2). No analytical model (lumped or 1-D wave propagation) is available to predict vortex induced pulsations in SRMs. There are three vortex shedding mechanisms:

- obstacle vortex shedding (OVS),
- angle vortex shedding (AVS),
- surface vortex shedding (SVS).

The vortex shedding process itself absorbs sound reducing acoustic pulsations. It is the interaction between the vortices and the nozzle which is a source of sound.

As a modeling strategy the lumped model approach of Culick is focused on (section 3). Encouraging preliminary results for OVS in cold gas scale model experiments with axial injection (peer reviewed, published and presented as conference proceedings [23; 22]). A two dimensional plane analytical model for vortex ingestion by the nozzle has been proposed (manuscript [25] submitted for peer review). A next

step is to include this in a predictive energy balance or a lumped model based on Culick's approach. In both cases it is expected that a linear model for the losses can be used, in some cases this model can even be quasi-steady [22]. Modeling of AVS and SVS should follow the conclusion of OVS study. Numerical simulations needed for the development and validation of an energy balance or a lumped model will be done. A Euler Internal Aeroacoustics code (EIA), for the study of vortex nozzle interactions as a sound source, has been made available to us by Dr. Hulshoff of TU Delft.

Acknowledgments

This project is funded by ANRT and ASL in the form of a CIFRE grant. This is acknowledged and appreciated by the doctoral candidate. Support by Mr. Serge Radulovic of ASL is greatly appreciated.

References

[1] J. Anthoine, Solid Propellant Pressure Oscillations, STO-EN-AVT-206, NATO-RTO, 2014.

[2] Y. Fabignon, J. Dupays, G. Avalon, F. Vuillot, N. Lupoglazoff, G. Casalis, M. Prévost, Instabilities and pressure oscillations in solid rocket motors, Aerospace Science and Technology 7 (3) (2003) 191–200. doi:10.1016/S1270-9638(02)01194-X.

[3] F. E. C. Culick, Unsteady Motions in Combustion Chambers for Propulsion Systems, AG-AVT-039, RTO/NATO, 2006.

[4] F. E. C. Culick, Combustion instabilities in solid propellant rocket motors, in: Internal aerodynamics in solid rocket propulsion RTO-EN-023, RTO/NATO, 2004.

[5] J. Anthoine, P. Jézéquel, M. Prévost, P. Prévot, Variable fuel grain burn velocities to reduce solid-rocket-motor pressure oscillations, Journal of Propulsion and Power 31 (1) (2015) 342–351.

[6] J. Anthoine, J.-M. Buchlin, J.-F. Guery, Effect of nozzle cavity on resonance in large srm: Numerical simulations, Journal of Propulsion and Power 19 (3) (2003) 374–384.

[7] F. Vuillot, Vortex- shedding phenomena in solid rocket motors, Journal of Propulsion and Power 11 (4) (1995) 626–639.

[8] F. Vuillot, G. Casalis, Motor flow instabilities - part 1, in: Internal aerodynamics in solid rocket propulsion RTO-EN-023, NATO-RTO, 2004.

[9] J. Anthoine, Experimental and numerical study of aeroacoustic phenomena in large solid propellant boosters, with application to the Ariane 5 solid rocket motor, Ph.D. thesis, ULB (2000).

[10] G. A. Flandro, S. R. Fischbach, J. Majdalani, Nonlinear rocket motor stability prediction: Limit amplitude, triggering, and mean pressure shift, Physics of Fluids 19 (9). doi:10.1063/1.2746042.

[11] D. R. Greatrix, Simulation of axial combustion instability development and suppression in solid rocket motors, International Journal of Spray and Combustion Dynamics 1 (1) (2009) 143–167. doi:10.1260/175682709788083399.

[12] D. R. Greatrix, Scale Effects on Solid Rocket Combustion Instability Behaviour, Energies 4 (1) (2011) 90–107. doi:10.3390/en4010090.

[13] P. Kuentzmann, V. Yang, J. W. Murdock, W. A. Johnston, G. Lengelle, J. Duterque, J. F. Trubert, M. W. Beckstead, M. Salita, F. Vuillot, J. Guery, F. E. C. Culick, Internal Aerodynamics in Solid Rocket Propulsion, RTO EDUCATIONAL NOTES EN-023 AVT-096, RTO NATO, 2004.

[14] S. Gallier, F. Godfroy, Aluminum Combustion Driven Instabilities in Solid Rocket Motors, Journal of Propulsion and Power 25 (2) (2009) 509–521. doi:10.2514/1.37664.

[15] S. Hulshoff, A. Hirschberg, G. Hofmans, Sound production of vortex-nozzle interactions, Journal of Fluid Mechanics 439 (2001) 335–352.

[16] Y. Fabignon, J. Anthoine, D. Davidenko, R. Devillers, J. Dupays, D. Gueyffier, Hijlkema, N. Lupoglazoff, J. M. Lamnet, L. Tessé, A. Guy, C. Erades, Recent advances in research on solid rocket propulsion, Journal AerospaceLab 11.

[17] G. Casalis, F. Vuillot, Motor flow instabilities - part 2: intrinsic linear stability of the flow induced wall injection, in: Internal aerodynamics in solid rocket propulsion RTO-EN-023, NATO-RTO, 2004.

[18] J. Griffond, G. Casalis, On the nonparallel stability of the injection induced two-dimensional Taylor flow, Physics of Fluids 13 (6) (2001) 1635–1644. doi:10.1063/1.1367869.

[19] J. Majdalani, S. R. Fischbach, G. A. Flandro, Improved energy normalization function in rocket motor stability calculations, Aerospace Science and Technology 10 (6) (2006) 495–500. doi:10.1016/j.ast.2006.06.002.

[20] S. R. Fischbach, J. Majdalani, Volume-to-surface reduction of vorticoacoustic stability integrals, Journal of Sound and Vibration 321 (3-5) (2009) 1007–1025. doi:10.1016/j.jsv.2008.10.001.

[21] G. A. Flandro, Aeroacoustic Instability in Rockets, AIAA Journal 41 (3).

[22] L. Hirschberg, C. Schram, A. Hirschberg, Prediction of pulsations in a cold-gas scale-model of a solid rocket motor, in: 22nd AIAA/CEAS in Lyon, 2016.

[23] L. Hirschberg, C. Schram, A. Hirschberg, Self-sustained vortex shedding in a cold-gas scaled model of a large solid rocket motor, in: Congres Français d'Acoustique 2016, 2016.

[24] M. S. Howe, Acoustics of fluid-structure interactions, Cambridge university press, 1998.

[25] L. Hirschberg, T. Schuller, C. Schram, J. Collinet, M. Yiao, A. Hirschberg, Interaction of a vortex with a contraction in a 2-dimensional channel: incompressible flow prediction of sound pulse, in: submitted for peer review 23rd AIAA/CEAS Aeroacoustics confrence 2017.

[26] T. Colonius, S. K. Lele, Computational aeroacoustics: progress on nonlinear problems ofsoundgeneration, Progress in Aerospace Science 40 (2004) 345–416.

[27] J.-F. Guery, Nummerical modeling of internal flow aerodynamics part 1 and 2, in: Internal aerodynamics in solid rocket propulsion, RTO EDUCATIONAL NOTES EN-023 AVT-096, RTO NATO, 2004.

Blade tip noise prediction by linearized airfoil theory

Yakut Cansev Kucukosman

Environmental and Applied Fluid Dynamics Department, von Karman Institute for Fluid Dynamics, Belgium, y.c.kucukosman@vki.ac.be

Supervisor: Christophe Schram

Associate Professor, Aeronautics and Aerospace Department & Environmental and Applied Fluid Dynamics Department, von Karman Institute for Fluid Dynamics, Belgium, christophe.schram@vki.ac.be

Supervisor: Jeroen van Beeck

Professor, Environmental and Applied Fluid Dynamics Department, von Karman Institute for Fluid Dynamics, Belgium, jeroen.vanbeeck@vki.ac.be

Abstract

A far-field noise prediction of a wind turbine airfoil section is carried out by using Amiet's semi-analytical model to predict far-field noise emitted at the trailing edge. Two-dimensional steady Reynolds Averaged Navier-Stokes computations are performed for DU-96-180 type airfoil at 4° angle of attack with a Reynolds number of $Re = 1.13x10^6$. A statistical wall pressure spectrum is evaluated by using the boundary layer information obtained from the Reynolds Averaged Navier-Stokes computations.

Keywords: Wind Turbine Noise, Wall Pressure Spectra, RANS simulations

1. Introduction

As a result of the demand in the utilization of sustainable and clean energy resources, there is an increasing interest in the field of wind engineering. However, the noise emission from the wind turbines establish a hindrance for the public acceptance [1; 2; 3]. Therefore, low-cost and precise noise prediction tools are needed in the process of the wind turbine design and the wind farm planning.

Noise prediction approaches can be distinguished along three categories; semi-empirical methods, direct methods and hybrid methods. Semi-empirical methods such as Brooks, Pose and Marcolini (BPM) model [4] and TNO model [5] are based mostly on experimental data. The BPM model expresses the far field noise in 1/3-octave band based on the velocity and scaling laws. The model is tuned based on a generic airfoil profile, which can lead to poor prediction for other airfoil profiles [6]. The TNO model is based on turbulent boundary layer and the wall pressure wavenumber frequency spectrum developed by Parchen [5]. The Blakes equation is used [7] for the prediction of the wall pressure wavenumber frequency spectrum. This model was observed to yield an underprediction of the noise level compared to some experimental results [8; 9] even though it shows a correct behavior with respect to incoming velocity and angle of attack.

In direct methods, the flow and the sound fields are computed together by solving the compressible flow equations. Direct Numerical Simulation (DNS) [10] resolves all turbulence scales, while Large Eddy Simulation (LES) [11] utilizes sub-grid scale to model small eddies. In theory, both can be used to calculate the radiated noise directly. However, in terms of computational cost, DNS or LES techniques are still too costly to be applied for industrial design purposes. These approaches are however well suited to provide a better understanding of surface pressure spectrum behavior, supporting the development of simplified models.

Hybrid methods offer an interesting compromise in terms of accuracy vs. CPU cost, by decoupling the flow and acoustic calculations. Hybrid methods usually consist in the following two steps: first, the unsteady flow field is computed in the region of

the source term; secondly, an acoustic propagation method is used to compute the acoustic source radiation towards the far-field. In order to further reduce the computational cost, Reynolds-Averaged Navier-Stokes (RANS) simulations can be preferred over scale-resolved simulations to provide a source model. In that case, complementary stochastic methods are necessary to synthesize the missing unsteady information about the flow. The Stochastic Noise Generation and Radiation (SNGR) [12] was developed to this end. Finally, purely statistical methods (not involving any stochastic reconstruction) offer the cheapest solution amongst the hybrid methods. The RANS-based Statistical Noise Model (RSNM) [13] follows this path, the acoustic far field being computed by using semi-infinite half plane Green s function combined with a model for the turbulent velocity cross-spectrum in the vicinity of the trailing-edge. Alternatively, wall pressure based models compute the acoustic far field using a diffraction analogy technique [14] or Amiet's theory [15]. In this paper, the acoustic far field prediction is performed by theory of Amiet.

2. Amiet's Analytical Model For Trailing Edge Noise

Amiet's theory provides an analytical model to compute the far-field acoustic noise of an airfoil subjected to a periodic gust [15]. This model was extended to predict trailing-edge noise [16], considering the scattering of a wall pressure gust convected past the trailing edge. The derivation is performed by solving the scattering problem iteratively at the trailing edge. A leading-edge back-scattering correction is performed by considering the finite length chord by Roger & Moreau [17] as the original method assumes that airfoil extends infinity in the upstream direction. The far-field acoustic PSD (S_{pp}) for trailing edge in the midspan plane at a given observer location, $x = (R, \theta, z = 0)$ can be written as:

$$S_{pp}(\mathbf{x}, \omega) = \left(\frac{sin\theta}{2\pi R}\right)^2 (kC)^2 d\,|\mathcal{L}|\,l_y(\omega)\phi_{pp}(\omega) \qquad (1)$$

where C is the chord length, d is the semi-span, ω is the angular frequency, l_y is the spanwise correlation length, $\mathcal{L}$ is the aeroacoustic transfer function [17], and ϕ_{pp} is the wall pressure spectrum. The spanwise correlation length based on the convection velocity, U_c and the spanwise wavenumber k_y and a model constant b is computed by the Corcos model [18] as:

$$l_y(\omega) = \frac{\omega/(bU_c)}{k_y^2 + (\omega/(bU_c))^2} \qquad (2)$$

The wall pressure spectrum is computed by a statistical model proposed by Panton & Linebarger [19] and later revisited by Remmler et al. [20]. The formulation is based on Navier-Stokes equation by reforming it as a Poisson equation for pressure. With the assumption of statistically stationary and homogeneous flow in streamwise and spanwise directions, the Poisson equation can be solved by using the Green's function technique as:

$$\phi(k_1) = 8\rho^2 \int\int\int_0^\infty \frac{k_1(\omega)^2}{|k|(\omega)^2} e^{-|k|(\omega)(y+\widetilde{y}_2)} S_{22}(y, \widetilde{y}, \omega) \times \frac{\partial \langle U_1 \rangle}{\partial y} \frac{\partial \langle U_1 \rangle}{\partial \widetilde{y}} dy d\widetilde{y} dk_3 \qquad (3)$$

where $|k| = \sqrt{k_1^2 + k_3^2}$, U_1 is the streamwise velocity and y is the wall normal direction. The energy spectrum of the vertical velocity fluctuations S_{22} is given as:

$$S_{22}(y, \widetilde{y}, \omega) = \frac{\overline{u_2'}(y)\overline{u_2'}(\widetilde{y})}{\pi^2} \Lambda^2 \int\int_0^\infty R_{22} cos(\alpha \widetilde{k_1}(\omega)\widetilde{r_1}) cos(\widetilde{k_3}\widetilde{r_3}) d\widetilde{r_1} d\widetilde{r_3} \qquad (4)$$

where u_2' is the crosswise velocity fluctuations, Λ is the integral length scale and α an anisotropy scaling for the streamwise structures compared to the spanwise structures. The velocity correlation function R_{22} is modeled according to Panton & Linebarger[19]:

$$R_{22} = [1 - \frac{\widetilde{r}^2}{2\sqrt{\widetilde{r}^2 + \widetilde{y}^2}}] e^{-\sqrt{\widetilde{r}^2 + \widetilde{y}^2}} \qquad (5)$$

with $\widetilde{r}^2 = \widetilde{r_1}^2 + \widetilde{r_3}^2$. The non-dimensional parameters were used by modifying the integration coordinates and the wave numbers with the integral length scale, $\widetilde{r_i} = r_i/\Lambda$, $\widetilde{k_i} = k_i\Lambda$ and $\widetilde{y} = (y - \widetilde{y})/\Lambda$. Monte Carlo method was used to perform the integration in Eq. 3 since it is hard to perform a fivefold integration numerically.

The time-averaged quantities can be obtained through a RANS simulation, however, some quantities such as R_{22}, α and U_c need to be modeled. The two-equation turbulence models provide the turbulent kinetic energy, $k = 0.5 \sum \overline{u'}_i^2$, with the combination of the streamwise and spanwise velocity fluctuations components not the $\overline{u'}_2^2$ directly. It has been demonstrated by Klebanoff [21] that in a zero pressure gradient boundary layer, the velocity fluctuation components, $\overline{u'}_i^2$, are not constant fractions of $2k$. Therefore, an anisotropy factor ,which is obtained from a

flat plate boundary layer using a Reynolds stress transport model, is defined for each component as $\beta_i = \frac{\overline{u'_i}^2}{2k}$ [20].

Panton & Linebarger [19] was specified the length scale, Λ, 1.5 times the Prandtl mixing length, l_m. However, this approach is not suitable for most of the turbulence models since the Reynolds Stress $-\langle u'_1 u'_2 \rangle$ is not computed. Another approach to calculate the length scale is to use the turbulent kinetic energy and turbulent dissipation rate obtained directly from the numerical simulation, $L = \frac{l_m}{C_m}$ where L is calculated as

$$L = C_\mu \frac{k^3/2}{\epsilon} \tag{6}$$

C_m is a turbulence model constant and was chosen as 1.9 for $k-\omega$ SST [20], C_μ is given as 0.09 and the turbulent dissipation, ϵ, is calculated as $\epsilon = k \cdot \omega$.

3. Numerical Setup

The two dimensional (2D) steady RANS computations are performed by the open source OpenFOAM with DU96-W-180 wind turbine airfoil with zero thickness at the trailing edge. The operating conditions are chosen from the BANC benchmark [22] as the following; the freestream velocity, $U_\infty = 60$ m/s, the Reynolds number, $Re = 1.13 \times 10^6$, the density $_\infty = 1.164$ kg/m^3, the chord of the airfoil is $C = 0.3$ m and the angle of attack, $\alpha = 4°$. θ is the view angle for noise prediction, and equals to 90° when it is orthogonal to the streamwise direction. Far-field noise predictions were computed at an observer distance of $r = 1$ and a wetted span of $b = 1$ m.

The experiment was conducted with laminar inlet flow and the flow was forced to the transition by using a tripping device located at 0.12% C on the suction side and 0.15% C on the pressure side [22]. However, the inlet flow field assumed to be turbulent for the simulation and $k-\omega$ SST model, proposed by Menter [23], was used since only the global variables are needed for the semi-analytical noise prediction method. At inlet, flow properties are calculated based with a weak turbulence intensity of %0.5. Zero flux boundary conditions are imposed at outlet. On the airfoil surface, no slip condition for velocity, the adaptive wall functions are used for k, ν_t and ω. Pressure is set to be zero at inlet. At top and bottom boundaries of the domain, symmetric boundary conditions are applied. The summary of the boundary conditions are given in Table 1. The simulations were performed by an incompressible OpenFOAM solver called *simpleFOAM* with second order accurate schemes and applying the relaxation for all the variables.

Table 1: Boundary Conditions

	Inlet	Outlet	Airfoil
U	U_∞	$\nabla\overrightarrow{U} = 0$	$\overrightarrow{U} = 0$
p	$\nabla P = 0$	P = 0	$\nabla P = 0$
k	fixedValue	$\nabla k = 0$	wallFunction
ν_t	fixedValue	$\nabla \nu_t = 0$	wallFunction
ω	fixedValue	$\nabla \omega = 0$	wallFunction

The grid was generated by using *snappyHexMesh* utility in OpenFoam. This utility creates an unstructured mesh with hexahedral cells and introduces additional layers of hexahedral cells aligned to the boundary surface. The actual domain was determined as 5C upstream of the leading edge, 10 C downstream of the trailing edge and 5C in normalwise direction in both directions. The mesh refinement was achieved by adding layers on the surface so as to ensure $y+ < 1$ for the first few cell on the airfoil surface.

3.1. Mesh Dependency

The domain and grid dependency tests were performed as preliminary investigation.

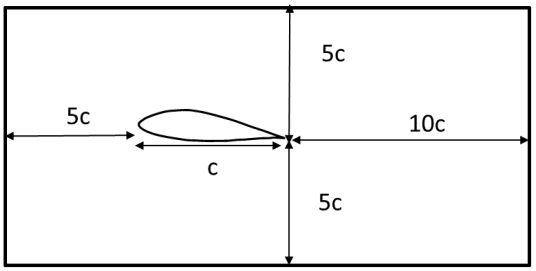

Figure 1: The main domain configuration (Case 1)

The domain dependency was tested with two different configuration, the main case (Case 1) shown in Fig. 1 has a 10C length in the wall normal direction and the second is increased to 20C (Case 2), the upstream and downstream dimensions being identical. The pressure coefficient along the airfoil and the velocity profile at the 0.02 % from the trailing edge are shown in Fig. 2 and Fig. 3. The pressure coefficient distributions are very similar using both computational domains, and agree reasonably well with results obtained using the XFOIL solver [24], excepted

close to the trailing edge. The velocity profiles also confirm the fact that the domain with 10C lateral extent is sufficient.

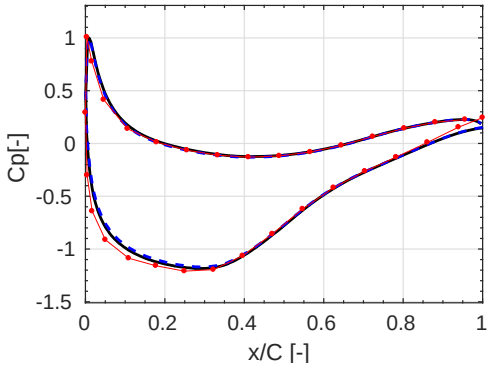

Figure 2: Pressure Coefficient for different domain size; 10C(—), 20C (- -) and XFOIL (-●-)

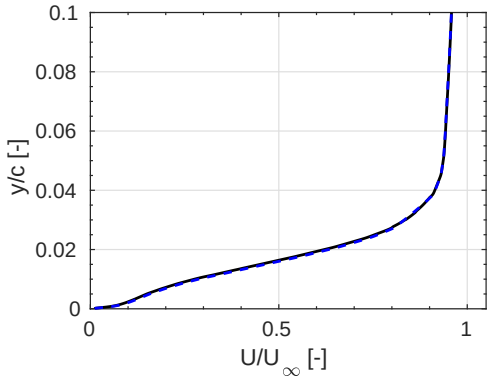

Figure 3: Boundary Layer Velocity Profile for different domain size at 98%c of the suction side; 10C (—), 20C (- -)

The mesh dependency check was performed using three different mesh refinements $y+ > 1$, $y+ \simeq 1$ and $y+ < 1$ listed in Table 2 where *Fine* is denoted by the main configuration, Case 1, in Fig. 1. The finest refinement was determined to achieve $y+ < 1$ to capture the more cells in the inner region of the boundary layer.

When the grid size dependency criteria was performed regarding the pressure distribution, Fig. 4, appears rather insensitive to the mesh refinement for the investigated cases. However, when the boundary layer velocity profile is extracted at the 0.01 % both sides from the trailing edge, they exhibit much more sensitivity to the grid size, as can be seen in Fig. 5 & 6. When the suction side is considered, the grid refinement affects the velocity profile mainly near the wall, on the other hand, the pressure side is affected mostly by the outer part.

Table 2: Test conditions matrix for the Grid Independency

Case	Background Grid Size (m)	y^+ Min	y^+ Max	y^+ Average
Coarse	0.2	0.14	5.74	2.9
Fine	0.1	0.06	3	1.4
Finest	0.05	0.014	1.5	0.7

The same interference can be done for the turbulent kinetic energy as well as the dissipation. The suction side appears to be more sensitive to the grid size than the pressure side. The turbulent kinetic energy profile for the pressure side changes as the same position as the velocity profile, $y/c \sim 0.02$. Moreover,an additional deviation is observed at the peak of the turbulent kinetic energy (Fig. 8). On the other hand, the turbulent kinetic energy for the suction side appears to be more sensitive to the grid size (Fig. 5). Even though, the turbulent kinetic energy is insensitive to the grid size on the pressure side, more refinement is needed for the suction side. Likewise, the specific dissipation profile in Fig. 10 shows that the solution is independent to the grid size but the suction side needs further investigation (Fig. 9).

As a conclusion, the grid dependence is achieved for the pressure side, however, it appears that the suction side is more sensitive to the grid size. Capturing well the boundary layer profiles are important as the acoustic prediction relies on the details of the velocity profile close to the trailing edge.

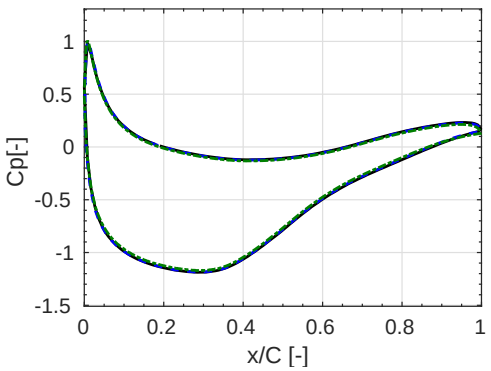

Figure 4: Pressure Coefficient for different grid size at 99%c ; Coarse(—), Fine (- -) and Finest (-·-)

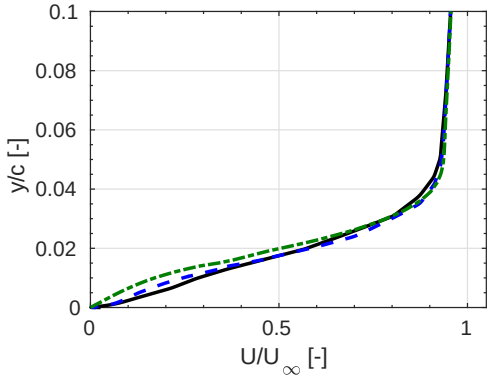

Figure 5: Boundary Layer Velocity Profile for different grid size at 99%c of the suction side; Coarse(—), Fine (- -) and Finest (-·-)

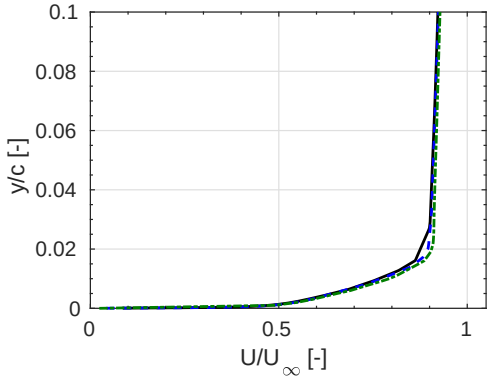

Figure 6: Boundary Layer Velocity Profile for different grid size at 99%c of the pressure side; Coarse(—), Fine (- -) and Finest (-·-)

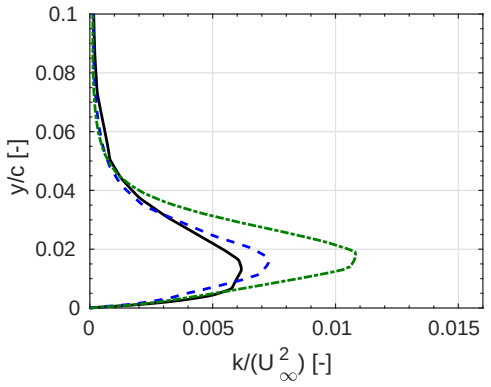

Figure 7: Boundary Layer Turbulent Kinetic Energy Profile for different grid size at 99%c of the suction side; Coarse(—), Fine (- -) and Finest (-·-)

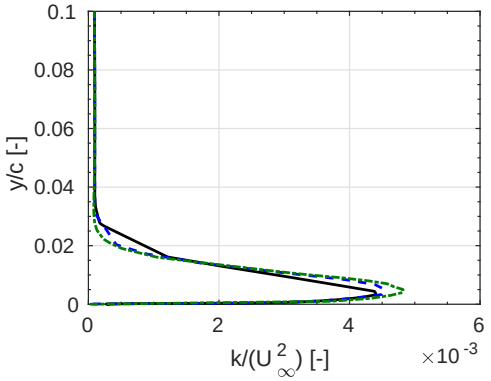

Figure 8: Boundary Layer Turbulent Kinetic Energy Profile for different grid size at 99%c of the pressure side; Coarse(—), Fine (- -) and Finest (-·-)

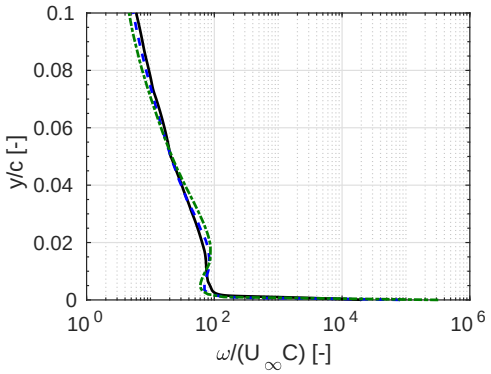

Figure 9: Boundary Layer ω Profile for different grid size at 99%c of the suction side; Coarse(—), Fine (- -) and Finest (-·-)

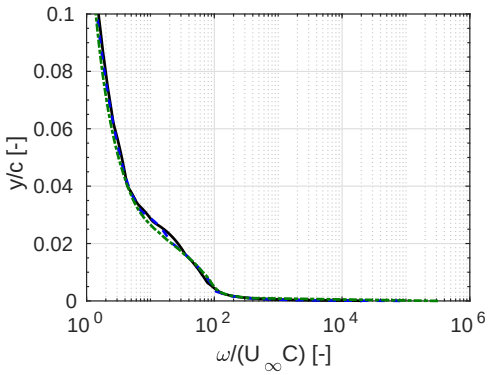

Figure 10: Boundary Layer ω Profile for different grid size at 99%c of the pressure side; Coarse(—), Fine (- -) and Finest (-·-)

4. Preliminary Results

The prediction of the wall pressure spectra and the far-field noise prediction are investigated with three different grid sizes to point out the importance of the well refined boundary layer profiles.

The improvement of the wall pressure spectra is given in Fig. 11 with different grid size refinement. It has been observed that the grid refinement increases the level of wall pressure spectra density. When the

Fine and *Finest* grid size are compared, it has been seen that the grid independence was achieved for the pressure side as the results deviate negligibly for the higher frequency range. Moreover, the behavior of the wall pressure spectra on the pressure side is changing significantly from *Coarse* grid size to a finest grid size. A jump is observed near the 1 kHz which is not present in the *Coarse* grid size.

However, the grid independence performs poor for the suction side of the airfoil. When the grid size is halved, the wall pressure spectra is appeared to be increasing $\sim$ 5 dB for the frequencies lower than 8 kHz. On the other hand, the mesh independence is observed with the finest mesh for the higher frequencies. Due to that the slope of the wall pressure spectra for the *Finest* grid size has a sharp slope since the lower frequencies are sensitive to the grid size and increases $\sim$ 5 dB but the higher frequencies are insensitive to the grid size.

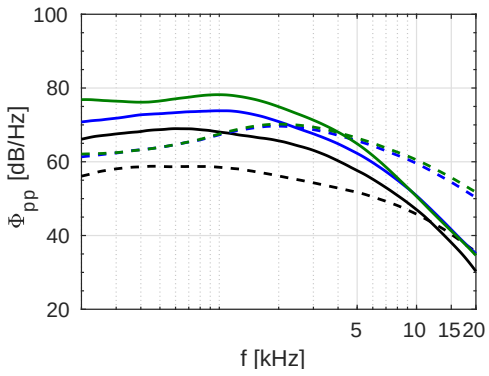

Figure 11: Wall Pressure Spectra for different grid size at 99%c ; Coarse(—), Fine (—) and Finest (—); Suction Side (—), Pressure Side (- -)

The far-field one-third-octave-band trailing edge noise prediction was performed by Amiet's theory at a 1 m observer distance is shown in Fig. 12 and compared with an experimental data [22]. Decreasing the grid size by half for $y+ > 1$, performs an increase starting from $\sim$ 5 dB for lower frequencies to $\sim$ 10 dB for higher frequencies. When the grid size is halved again, the grid independence is achieved for only the higher frequencies which is mentioned for the wall pressure spectra. For the lower frequencies $\sim$ 2 dB difference is observed. When the *Finest* grid configuration is compared with the experimental data, it is observed that the prediction stays in the limit of $\mp$3 dB. However, the trend of the curve is not capturing the whole behavior.

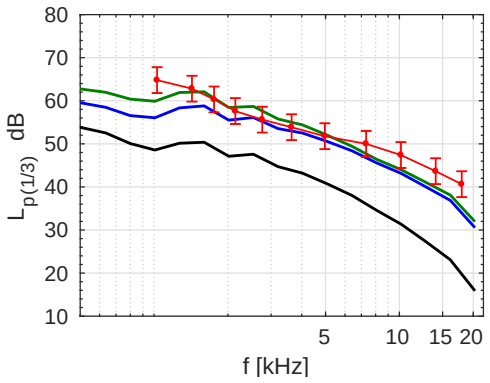

Figure 12: Amiet's Trailing Edge Noise Prediction by different grid size at 99%c of the suction side; Coarse(—), Fine (—) and Finest (—) with experimental data (—●—).

5. Conclusion

A domain and grid study is performed for DU96-W-180 airfoil. The domain independence was achieved with 10C lateral distance. For the grid study, three different cases have been selected where the first cells are $y+ > 1$, $y+ \simeq 1$ and $y+ < 1$. It has been verified that the pressure coefficient is not a reliable parameter in terms of grid dependency. Therefore, the boundary layer profiles at the trailing edge are considered such as the velocity, the kinetic energy and the specific dissipation profile along normal to the surface for both suction and pressure side. It has been concluded that the mesh refinement is sufficient for the pressure side if $y+ \simeq 1$. However, this mesh refinement is not sufficient for the suction side. Therefore, further mesh refinement is needed to verify the grid independence for the suction side.

Grid refinement appears to be an important key parameter for the prediction of the wall pressure spectra and far-field noise. The wall pressure spectra is insensitive for the pressure side of the airfoil when the first cell is located $y+ < 1$, however, this is not sufficient for the suction side when the low frequency part is concerned. Even though it could have been expected that the far-field noise predictions of *Fine* and *Finest* grids would be quite similar, $\sim$ 2 dB of difference is observed between these two grids due to the previous statement on the wall pressure spectra. Nevertheless, it is possible to state that the noise prediction by the finest grid corresponds to a range of $\mp$3 dB with respect to experimental value. For the future studies, a further refinement will be performed to achieve the grid insensitivity for the suction side of the airfoil.

Acknowledgments

The authors gratefully acknowledge the support of the European Commission's Framework Program "Horizon 2020", through the Marie SkÅodowska-Curie Innovative Training Networks (ITN) "AEOLUS4FUTURE - Efficient harvesting of the wind energy" (H2020-MSCA-ITN-2014: Grant agreement no. 643167).

References

[1] A. Bockstael, L. Dekoninck, B. De Coensel, D. Oldoni, A. Can, D. Botteldooren, Wind turbine noise: annoyance and alternative exposure indicators, in: Forum Acusticum, European Accoustics Association (EAA), 2011, pp. 345–350.

[2] J. H. Schmidt, M. Klokker, Health effects related to wind turbine noise exposure: A systematic review, PLOS ONE 9 (12) (2014) 1–28.

[3] K. Waye, E. hrstrm, Psycho-acoustic characters of relevance for annoyance of wind turbine noise, Journal of Sound and Vibration 250 (1) (2002) 65 – 73.

[4] T. Brooks, D. Pope, M. Marcolini, Airfoil Self-noise and Prediction, NASA reference publication, National Aeronautics and Space Administration, Office of Management, Scientific and Technical Information Division, 1989.

[5] R. Parchen, T. P. D. TNO-TH., Progress report DRAW: a prediction scheme for trailing edge noise based on detailed boundary layer characteristics, TNO-report HAG-RPT, TNO Institute of Applied Physics, 1998.

[6] P. Moriarty, P. G. Migliore, N. R. E. L. (U.S.), Semi-empirical aeroacoustic noise prediction code for wind turbines [electronic resource] / P. Moriarty and P. Migliore, National Renewable Energy Laboratory Golden, Colo, 2003.

[7] W. K. Blake, Mechanics of flow-induced sound and vibration Volume I, General concepts and elementary sources, Academic Press, 1986.

[8] M. Kamruzzaman, A. Herrig, T. Lutz, W. Wurz, E. Kramer, S. Wagner, Comprehensive evaluation and assessment of trailing edge noise prediction based on dedicated measurements, Noise Control Engineering Journal 59 (1) (2011) 54. doi:10.3397/1.3531794.

[9] F. Bertagnolio, Trailing edge noise model applied to wind turbine airfoils, Danmarks Tekniske Universitet, Ris Nationallaboratoriet for Bredygtig Energi, 2008, ris-R-1633(EN).

[10] R. D. Sanderg, N. D. Sandham, Direct numerical simulation of turbulent flow past a trailing edge and the associated noise generation, Journal of Fluid Mechanics 596.

[11] X. Gloerfelt, T. Le Garrec, Trailing edge noise from an isolated airfoil at a high reynolds number, AIAA Journal0.

[12] R. Ewert, Broadband slat noise prediction based on CAA and stochastic sound sources from a fast random particle-mesh (RPM) method, Computers & Fluids 37 (4) (2008) 369–387.

[13] C. J. Doolan, C. A. Gonzalez, C. H. Hansen, Statistical Estimation of Turbulent Trailing Edge Noise, in: Proceedings of 20th International Congress on Acoustics, American Institute of Aeronautics and Astronautics, 2010.

[14] K. L. Chandiramani, Diffraction of evanescent waves, with applications to aerodynamically scattered sound and radiation from unbaffled plates, The Journal of the Acoustical Society of America 55 (1) (1974) 19.

[15] R. Amiet, Acoustic radiation from an airfoil in a turbulent stream, Journal of Sound and Vibration 41 (4) (1975) 407–420.

[16] R. Amiet, Noise due to turbulent flow past a trailing edge, Journal of Sound and Vibration 47 (3) (1976) 387–393.

[17] M. Roger, S. Moreau, Back-scattering correction and further extensions of Amiet's trailing-edge noise model. Part 1: theory, Journal of Sound and Vibration 286 (3) (2005) 477–506.

[18] G. M. Corcos, The structure of the turbulent pressure field in boundary-layer flows, Journal of Fluid Mechanics 18 (03) (1964) 353.

[19] R. L. Panton, J. H. Linebarger, Wall pressure spectra calculations for equilibrium boundary layers, Journal of Fluid Mechanics 65 (02) (1974) 261. doi:10.1017/S0022112074001388.

[20] S. Remmler, J. Christophe, J. Anthoine, S. Moreau, Computation of wall pressure spectra from steady flow data for noise prediction, AIAA Journal 48 (9) (2010) 1997–2007.

[21] P. S. Klebanoff, Characteristics of turbulence in boundary layer with zero pressure gradient, Tech. Rep. 19930092249 (January 1955).

[22] M. Herr, R. Ewert, C. Rautmann, M. Kamruzzaman, D. Bekiropoulos, R. Arina, A. Iob, P. Batten, S. Chakravarthy, F. Bertagnolio, Broadband Trailing-Edge Noise PredictionsOverview of BANC-III Results, in: 21st AIAA/CEAS Aeroacoustics Conference, American Institute of Aeronautics and Astronautics, Reston, Virginia, 2015. doi:10.2514/6.2015-2847.

[23] F. R. Menter, Two-equation eddy-viscosity turbulence models for engineering applications, AIAA Journal 32 (8) (1994) 1598–1605. doi:10.2514/3.12149.
URL http://dx.doi.org/10.2514/3.12149

[24] M. Herr, C. J. Bahr, M. Kamruzzaman, Problem Statement for the AIAA/CEAS Second Workshop on Benchmark Problems for Airframe Noise Computations (BANC-II), AIAA Journal.

AERO-THERMAL INVESTIGATIONS IN TURBOMACHINERY

Uncertainty quantification of turbulence statistics measured by hot-wire anemometry

Elissavet Boufidi

Turbomachinery and Propulsion Department, von Karman Institute for Fluid Dynamics, Belgium, boufidi@vki.ac.be

Supervisor: Fabrizio Fontaneto

Assistant Professor, Turbomachinery and Propulsion Department, von Karman Institute for Fluid Dynamics, Belgium, fontaneto@vki.ac.be

University Supervisor: Tony Arts

Professor, Head of Department, Turbomachinery and Propulsion Department, von Karman Institute for Fluid Dynamics, Belgium
iMMC, Université Catholique de Louvain, Belgium, arts@vki.ac.be

Abstract

Instantaneous velocity measurements have been performed at the core of a subsonic non-isothermal jet using Hot-Wire Anemometry and the turbulence intensity has been computed. A detailed uncertainty analysis has been executed using both the Taylor Series Method (TSM) and the Monte Carlo Method (MCM) for the propagation of uncertainties. The two methods are compared and their differences are explained.

Keywords: uncertainty analysis, Monte Carlo Method, turbulence measurement

1. Introduction

A rigorous characterization of flow turbulence (i.e. turbulence intensity, time and length scales, spectrum) is needed to better understand loss mechanisms and heat transfer phenomena in complex turbomachinery flows. Moreover, the increasing use of CFD, as both a design and an investigation tool, requires reliable experimental data for validation of turbulence models and input of boundary conditions (which normally include turbulence kinetic energy and length scales at the inlet of the computational domain). It is therefore evident, that the reliable measurement of turbulence parameters is critical for the reliable and cost-effective design of turbomachinery components.

Hot-Wire Anemometry (HWA) is one of the most popular techniques for measuring velocity fluctuations and, therefore, turbulence quantities, thanks to its high frequency response (up to 50 kHz) and high spatial resolution (wire diameters up to 5 μm) [1]. The operating principle of the HWA is based on the convective heat transfer over heated wires. In incompressible, isothermal flows the output voltage of the anemometer can be directly related to the flow velocity and well known relationships like Kings Law can be used. It is thus widely used in low speed turbomachinery research facilities: Ames and Plesniak [2] characterized the exit turbulence parameters (turbulence intensity, length scales, dissipation) of a HPT vane cascade under different inlet turbulence characteristics, Satta et al. [3] characterized the turbulence parameters of the wake of a LPT blade, Camp & Shin [4] measured the length scales and turbulence intensity in an embedded stage of three multistage low speed compressors. However, in the most general case, in which turbomachinery flows usually lie, the HWA output is sensitive to the velocity, density and total temperature of the flow. To take into account all these effects, different methodologies have been proposed by researchers like Cukurel et al. [5] and Boyle et al. [6].

In order to use any experimentally obtained information, an estimation of their "goodness" should be made. This is critical, for example, in order to compare experimental data with simulation results or when data are used for decision-making. Therefore, every experimental value should be always accompanied by the associated uncertainty at a specified confi-

dence level. This is also true for turbulence parameters, such as turbulence intensity, time and length scales, and energy dissipation, though their related uncertainties are rarely reported in the literature.

The uncertainty of turbulence parameters can be divided in two parts: the uncertainty due to the experimental process (uncertainty of measuring equipment, environmental effects, human error etc.) and the uncertainty due to the sampling of a correlated time series [7]. The current work deals only with the former: the experimental uncertainty assessment of turbulence statistics measured by HWA. The measurements were performed at the core of a subsonic, non-isothermal jet. A calibration methodology based on non-dimensional numbers was used, developed by Cukurel et al. [5], in order to account for the temperature variations.

The two widely used standards for estimating experimental uncertainty are the ASME Test Uncertainty [8] and the ISO Guide to the Expression of Uncertainty in Measurement (GUM) [9]. The two methodologies produce the same results, but differ in the categorization of the uncertainty sources. In the ASME method the uncertainty sources are divided in 'systematic' and 'random', depending on their effect on the measurement data, while in the ISO GUM in 'Type A' and 'Type B', depending on the availability of statistical data for their estimation.

In order to determine the uncertainty of the final result of an experimental campaign, the uncertainties of the different variables need to be propagated through the data reduction algorithm. The propagation of the uncertainties is usually approximated by the first order terms of a Taylor Series expansion, as proposed in both the ISO and ASME standards. Nevertheless, the Taylor Series Method (TSM) for uncertainty propagation is based on the linearization of the measurement model and assumes that the output quantity is characterized by a Gaussian or a scaled and shifted t-distribution [9],[10]. When one of these points is not valid, the resulting uncertainty values and confidence intervals will be unreliable. This led to the issue of a supplement to the GUM guide [10], providing guidelines for the propagation of probability distributions using a Monte Carlo Method (MCM).

In the current work, the nomenclature of the ASME method for the categorization of uncertainty sources is followed. Both the TSM and MCM methods for uncertainty propagation are used and their results are compared, following the guidelines provided in [8], [9], [10], and [11].

2. Experimental setup and methodology

A single Hot-Wire probe was used during the measurement campaign, featuring a platinum-coated tungsten wire of 9 m diameter and 1 mm active sensor length. The Hot-Wire Anemometer was operated by the Dantec Streamline 90N10 Frame. The Frame includes 4 CTA modules, each of them consisting of a CTA bridge and a signal conditioner. The system is configured and operated with the Dantec StreamWare software.

The measurements were carried out at an open-jet facility. The nozzle is connected to the 7 bar pressure supply through a heater, which is used to vary the flow temperature. The head of the HW probe was placed inside the potential core of the jet exiting the nozzle. The total temperature and total pressure inside the nozzle are measured by means of a thermocouple and a validyne transducer.

The calibration methodology proposed by Cukurel et al. [5] was followed in this study. This method consists in the use of an effective wire temperature and of empirical correlations to eliminate the dependency of the calibration on total temperature and Mach number of the flow respectively, which allows establishing a unique Nu-Re calibration curve. The procedure will be briefly described here, as more details can be found in [5].

Taking into account the recovery factor effect, the heat transfer balance over the wire is given by:

$$I^2 R_w = \pi l k (T_w - \eta T_0) Nu \tag{1}$$

By expressing the power supplied in terms of bridge voltage, the Nusselt number can be rearranged as:

$$Nu = \frac{E_b^2 R_w}{k(T_{wire} - \eta T_0)\pi l (R_t + R_l + R_w)^2} \tag{2}$$

The Reynolds number is defined by:

$$Re = \frac{\rho u d_w}{\mu} \tag{3}$$

The viscosity μ and the thermal conductivity k of the flow are evaluated on the total temperature of the flow.

The wire temperature is defined as the temperature which collapses a set of Nu-Re data obtained at different flow temperatures on a single curve. As in incompressible continuum flows there is no compressibility effect, the Nusselt number is a unique function of Reynolds. The R^2 of a 4th order polynomial fit is used as the selection criterion. The wire temperature defined this way is the temperature that better represents

the convective heat transfer process from the wire to the flow. In Fig. 1, a set of data obtained at different flow total temperatures is presented. When plotted in terms of voltage and velocity, a different curve is created for each temperature level. But when plotted in terms of Nu_w and Re with the effective wire temperature in Eq. 2, all the data collapse in a single curve. A single $Nu_w - Re_w$ calibration curve is thus obtained and can be employed to retrieve velocity from non-isothermal flows using HWA.

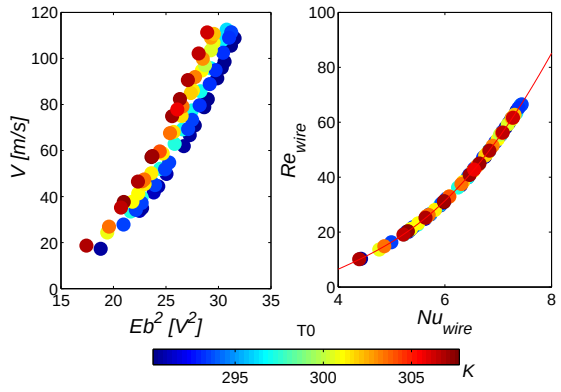

Figure 1: A single Nu-Re curve when the effective wire temperature is used

3. Uncertainty estimation methodology

As mentioned before, the nomenclature of the ASME methodology [8] is followed in the present study, and the uncertainty sources are categorized as 'systematic' and 'random'. Random sources vary randomly during the measurement period and cause scatter in the measurement data, while systematic sources cause a constant deviation from the true value and they do not cause any variability in the measurements.

For a finite number of measurements N of a value X, the sample mean and the sample standard deviation can be calculated by Eq. 4 and 5 respectively:

$$\bar{X} = \frac{1}{N}\sum_{i=1}^{N} X_i \tag{4}$$

$$s_X = \left[\frac{1}{N-1}\sum_{i=1}^{N}(X_i - \bar{X})\right]^{1/2} \tag{5}$$

The random standard uncertainty is calculated as the standard deviation of the sample mean:

$$s_{\bar{X}} = \frac{s_X}{N} \tag{6}$$

When the population is normally distributed and the sample size is large enough ($N > 30$), the interval $\bar{X} \pm s_{\bar{X}}$ is expected to contain the true mean of the population with a 68 % confidence.

As systematic sources do not cause any variability in the measurement data, their effect can not be estimated by successive measurements. Therefore, they are evaluated using available data (e.g. manufacturing specifications, calibration data) and engineering judgement.

When all systematic b_{Xi} and random s_{Xi} standard uncertainties have been evaluated, the total standard uncertainty of X can be calculated by:

$$U_X = \left(\sum_{i=1}^{N_b} b_{Xi}^2 + \sum_{i=1}^{N_s} s_{Xi}^2\right)^{1/2} \tag{7}$$

3.1. Taylor Series Method (TSM)

In the TSM for the propagation of uncertainties, the first order terms of a Taylor series expansion are considered and the propagation takes place at the standard uncertainty level. A detailed derivation of the TSM propagation equation can be found in [11].

If a variable f is a function of two variables x and y ($f = f(x, y)$), then the standard uncertainty in f is calculated by the following equation:

$$u_f = \left[\left(\frac{\vartheta f}{\vartheta x}\right)^2 b_x^2 + \left(\frac{\vartheta f}{\vartheta y}\right)^2 b_y^2 + 2\frac{\vartheta f}{\vartheta x}\frac{\vartheta f}{\vartheta y} b_{xy} + \left(\frac{\vartheta f}{\vartheta x}\right)^2 s_x^2 + \left(\frac{\vartheta f}{\vartheta y}\right)^2 s_y^2\right]^{(1/2)} \tag{8}$$

where b_x and b_y are the systematic standard uncertainties of x and y, and s_x and s_y the random standard uncertainties. The third term in Eq. 8 is the correlated systematic uncertainty term which contains the covariance factor b_{xy}, when the systematic uncertainties of x and y are not independent and share common error sources. An equivalent term for the random uncertainties is not included, since random uncertainties are usually considered uncorrelated [11].

In order to expand the standard uncertainty u_f at a specified confidence level, we need to use an appropriate coverage factor. For most engineering applications, it can be assumed that the error distribution of f will approach a Gaussian distribution and the appropriate Student's t coverage factor can be used for the desired confidence level. The expanded standard uncertainty will be then calculated as:

$$U_f = t_{\%} u_f \tag{9}$$

In order to choose the t value for any confidence interval, the degrees of freedom for the combined system must be known. For most applications, the degrees of freedom can be considered high enough, in order to have a constant t for any confidence level. For the 95% confidence level, $t = 2$ when the degrees of freedom are higher than 30 [8],[11].

3.2. Monte Carlo Method (MCM)

The MCM for uncertainty propagation consists in propagating probability distributions instead of standard uncertainty values. Initially, the probability distribution functions for all uncertainty sources are defined. Random sources are usually assumed to have a Gaussian distribution, while for systematic sources the PDFs are defined based on available data and engineering judgement. In order to define the input variables, a sample is randomly chosen from each PDF and added to the expected value (which is usually the measured value). This procedure is illustrated in Fig. 2 for two variables X_1 and X_2, which are affected by uncertainty sources s_1, b_1, b_2 and b_2, b_3 respectively. For each iteration i, a random sample is selected from each PDF and the input variables for this iteration are defined as: $X_{1i} = \bar{X}_1 + s_{1i} + b_{1i} + b_{2i}$ and $X_{2i} = \bar{X}_2 + b_{2i} + b_{3i}$, where $\bar{X}_1$ and $\bar{X}_2$ are the expected values. The values $X_1 i$ and $X_2 i$ constitute the inputs to the measurement model $Y = f(X_1, X_2)$ for this iteration. Common error sources are taken into account as depicted in Fig. 2, where the uncertainty source b_2 is common to both variables. An advantage of the MCM is that when input uncertainty sources are correctly defined, the implementation of correlated uncertainties is quite straightforward.

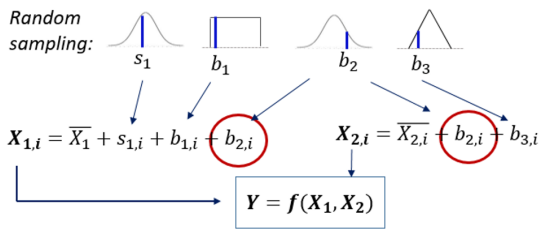

Figure 2: Definition of input variables

Once the input variables are defined, they are fed into the measurement model and the output quantities are computed. This process is repeated M times and results in a certain distribution of the output quantities. Then, the uncertainty values at the desired confidence level (e.g. 95%) can be easily computed. This procedure is described schematically in Fig. 3.

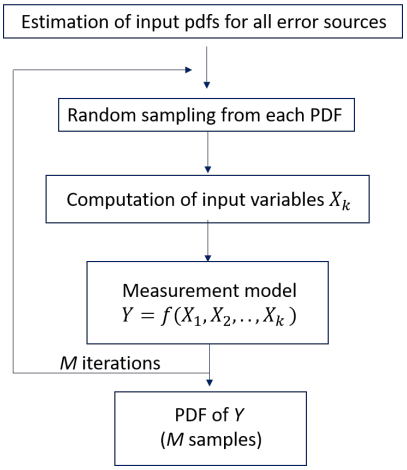

Figure 3: MCM prodedure

Increasing number of M simulations ensures a better approximation of the desired uncertainty values but also increases significantly the simulation time. According to the guidelines of the GUM supplement [10], the number of samples M can be either selected adaptively or a priori. In the first case, the number of samples is continuously increased until the results stabilize in the statistical sense. In the latter case, which is employed in the current study, the number of samples is selected a priori, following the empirical criterion suggested by [10]:

$$M \geq 10^4 \frac{1}{1-p} \tag{10}$$

where p is the desired confidence level. For a confidence level of 95%, M should be equal or higher to $2 \cdot 10^5$.

4. Uncertainty analysis results

In this section, the application of the methodology for uncertainty estimation presented in section 3 on HWA measurements is presented step by step. The final uncertainties are expressed at a 95% confidence level. The number of trials M for the MCM is selected at $2 \cdot 10^5$. It has to be noted that only instrumentation uncertainties are considered in the present analysis and other uncertainty sources like environmental effects and probe positioning are not taken into account.

4.1. Total temperature and total pressure uncertainty

The total temperature and total pressure of the jet are measured by a thermocouple and a validyne transducer respectively. The calibration curves of both instruments have been obtained by a linear regression of the calibration data. The uncertainty analysis of the thermocouple calibration is presented in detail to illustrate the procedure. The thermocouple calibration curve is given by the following equation:

$$T = m \cdot V + c \tag{11}$$

where m and c are the slope and intercept. The temperature T of the calibration points is measured by a PT100 thermometer, whose accuracy is noted by the manufacturer to be $\pm 0.1^{\circ}$. As no more information is provided, the error is assumed to follow a uniform distribution and the related systematic standard uncertainty is computed as:

$$b_T = \frac{0.1}{\sqrt{3}} = 0.058 \tag{12}$$

The random uncertainty of the temperature measurement is not taken into account, due to lack of sufficient successive measurements ($s_T = 0$). The systematic standard uncertainty of the voltage measurement is again estimated considering the manufacturer's accuracy and a uniform distribution, resulting in $b_V = \pm 0.0128\ V$. The systematic standard uncertainty b_V is present also during the measurements, since the same instrument is used in both cases. The random standard uncertainty s_V is computed using Eq. 5 and is different for every calibration and measurement point.

In order to estimate the uncertainty of the total temperature T_0 values measured during the experimental campaign, both the uncertainty of the calibration and the uncertainty of the measured voltage V_{meas} should be considered. The calibration uncertainty consists of the uncertainty of the calibration points $(V, T)_i$ and of the uncertainty due to the regression. Correlated uncertainties between the calibration points (since they are all obtained by the same instrument) and between calibration and experiment should also be considered.

Therefore, for the TSM, the procedure proposed by Coleman & Steele [11] is used. When the thermocouple is used during the experiment, Eq. 11 takes the form:

$$T_0 = m \cdot V_{meas} + c \tag{13}$$

and the standard uncertainty of T_0 for each measurement point is given by:

$$\begin{aligned} u_{T_0} = [&\sum_{i=1}^{N}(\frac{\partial T_0}{\partial T_i})^2(s_{T_i}^2 + b_{T_i}^2) + \sum_{i=1}^{N}(\frac{\partial T_0}{\partial V_i})^2(s_{V_i}^2 + b_{V_i}^2) \\ &+ 2\sum_{i=1}^{N-1}\sum_{k=1+1}^{N}\frac{\partial T_0}{\partial T_i}\frac{\partial T_0}{\partial T_k}b_{T_iT_k} + 2\sum_{i=1}^{N-1}\sum_{k=1+1}^{N}\frac{\partial T_0}{\partial V_i}\frac{\partial T_0}{\partial V_k}b_{V_iV_k} \\ &+ (\frac{\partial T_0}{\partial V_{meas}})^2(b_{V_{meas}}^2 + s_{V_{meas}}^2) \\ &+ 2\sum_{i=1}^{N}(\frac{\partial T_0}{\partial V_{meas}})(\frac{\partial T_0}{\partial V_i}b_{V_{meas}V_i})]^{1/2} \end{aligned} \tag{14}$$

The first two terms account for the measurement uncertainty of the calibration data (N pairs of (V_i, T_i). The third and fourth terms account for the correlated uncertainties between calibration points, since all points were acquired using the same instruments. The fifth term expresses the uncertainty due to the voltage measurement during the experimental campaign and, finally, the last term expresses the correlated uncertainty between the voltage of the calibration data and the experimental measurement. The derivatives $\frac{\partial T_0}{\partial T_i}$, $\frac{\partial T_0}{\partial V_i}$ are computed numerically.

For the MCM, the prodedure is illustrated in Fig. 4. The output is a distribution for each T_0 value comprised of M samples. Then, the uncertainty for the desired confidence level can be computed numerically. The distribution of T_0 for one measurement point is presented in Fig.5 , with the 95% confidence interval. The distribution is Gaussian, which validates the assumption used in the TSM.

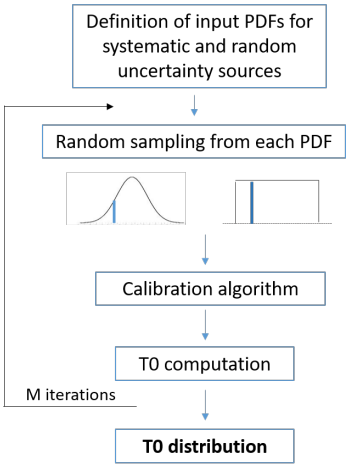

Figure 4: MCM prodedure

The expanded uncertainties at the 95% confidence level computed both by the TSM and the MCM are

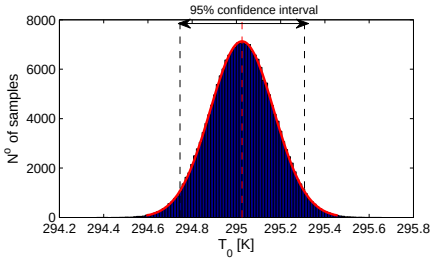

Figure 5: T_0 distribution for one measurement point

presented in Fig. 6. The two methods give similar results, as was expected, since the TSM assumptions are valid for linear models. The TSM seems to overestimate the uncertainty by approximately 0.01°. The uncertainty calculated by the TSM is between ±0.29 − 0.3° and the uncertainty calculated by the MCM is between ±0.28 − 0.29° for all measurement points.

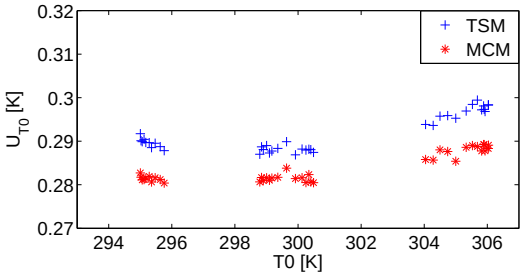

Figure 6: 95% uncertainty of T_0 for all measurement points

The total pressure for each measurement point is calculated by applying the validyne calibration to the measured voltage and adding the ambient pressure:

$$P_0 = dP + P_{amb} = (m_{val}(V - V_0) + c_{val}) + P_{amb} \quad (15)$$

The uncertainty of P_0 is computed following the procedure described for the thermocouple. The expanded uncertainties at the 95% confidence level computed both by the TSM and the MCM are presented in Fig. 7. The two methods give again similar results. The TSM seems to underestimate the uncertainty by approximately 0.1 *mbar*.

4.2. T_{wire}

As described in section 2, the first step of the calibration methodology is to define the effective temperature of the wire as the temperature that collapses the $Nu - Re$ calibration data on a single curve, with the

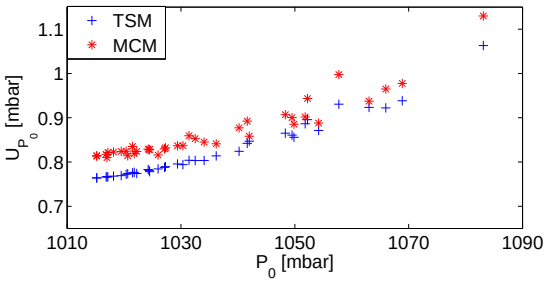

Figure 7: 95% uncertainty of P_0 for all measurement points

best fitting (highest R^2). The value of T_{wire} is a constant during calibration and measurement, and it is assumed that it does not contribute to the uncertainty of the results.

4.3. Velocity measurement uncertainty

The Nusselt and Reynolds numbers are computed by Eq. 2 and 3 respectively. The elemental uncertainty sources considered in this study are the uncertainties due to the measurement of the thermocouple(T_0), the validyne transducer (dP), the ambient pressure (P_{amb}) and the output voltage of the HWA bridge. These elemental uncertainties are propagated in the computation of Nu and Re.

The uncertainty is computed following the procedure outlined for the thermocouple in section 4.1. The uncertainty of the output Reynolds number is due to the uncertainty of the calibration data (N pairs of (Nu_i, Re_i), the uncertainty due to the measurement of Nusselt Nu_{exp} during the experiment, and the uncertainty due to the 4th order polynomial regression. An equation similar to Eq. 14 is used, where the derivatives expressing the sensitivities are computed numerically. The uncertainty of the calibration polynomial, is presented in Fig. 8. It can be seen that its uncertainty is higher in the lower velocity range.

The velocity is computed by the Reynolds number obtained by the calibration curve. The 95% expanded uncertainty computed by both methods is presented in Fig. 9. The TSM underestimates the uncertainty at the lower velocity range, while for higher velocities the results demonstrate a good agreement. To better understand this behaviour, the probability distributions of two different operating points, Point A and Point B, are presented in Fig. 10, as computed by the MCM. Point B is at the high velocity range ($V_m = 106.5$ m/s), where there is a good agreement between the uncertainy results computed by the two methods and its distribution is almost normal. For the low ve-

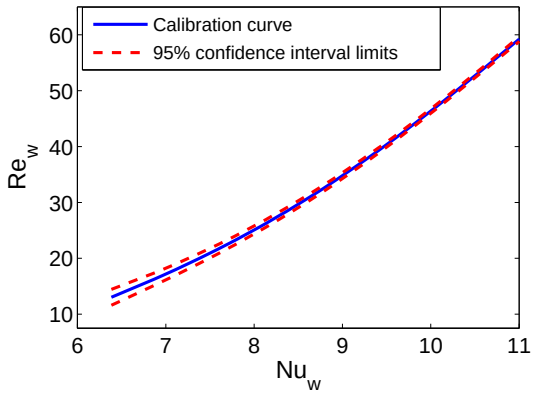

Figure 8: 95% uncertainty of the calibration polynomial

locity Point A though ($V_m = 23\ m/s$), the pdf exhibits a higher deviation from the normal distribution ($skewness = -0.11$). This implies that the assumptions of the TSM are no more valid in this case, and the method fails to predict correctly the confidence intervals. This certainly contributes to the disagreement of the two methods in the low velocity range.

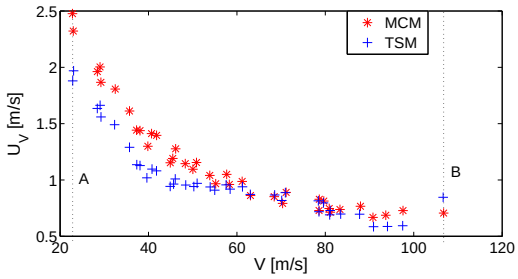

Figure 9: 95% uncertainty of V for all measurement points

When instantaneous voltage measurements are used for the computation of the Nusselt number (Eq. 2), the instantaneous Reynolds number is acquired from the calibration and the instantaneous velocity is computed by:

$$V' = \frac{Re'\mu}{\rho d_w} \tag{16}$$

The uncertainty of the instantaneous velocity is the same as the uncertainty of the mean velocity when considering only the uncertainty sources present in the current study and ignoring effects related to high turbulence intensity, probe geometry etc.

4.4. Turbulence intensity uncertainty with HWA

The difference in the velocity uncertainty computed by the TSM and MCM implies that the same difference will appear in the turbulence intensity uncertainty. For this reason, only the uncertainty computed by the MCM is presented, since it is considered more reliable.

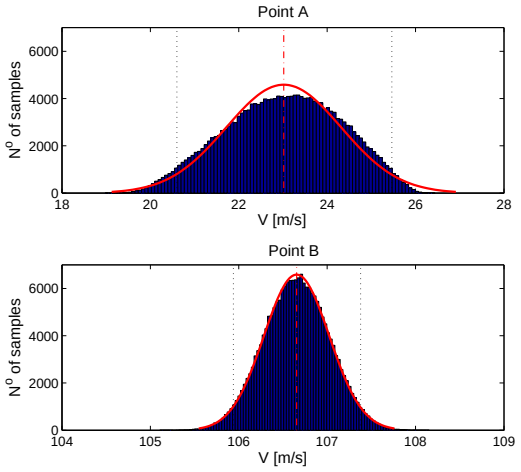

Figure 10: Probability distributions of mean velocity for two different operating points

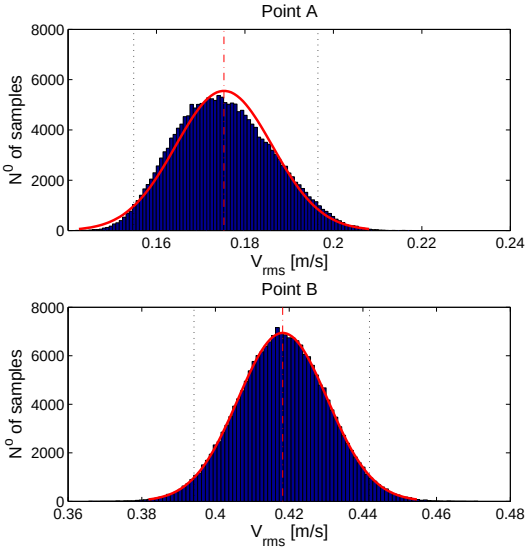

Figure 11: Probability distribution of velocity rms for Points A and B

In Fig. 10, 11 and 12 the probability distributions for the mean velocity, the velocity rms and the turbulence intensity for the operating points A and B are presented respectively. For the Point A, the distributions for all three quantities deviate from the normal distribution. The highest deviation is observed for the turbulence intensity pdf, which has a right skewness

of 0.4. This implies that the assumption of a normal distribution employed by the TSM is not valid, which makes the method unreliable in this case. For Point B, on the other hand, all three distributions are very close to normal.

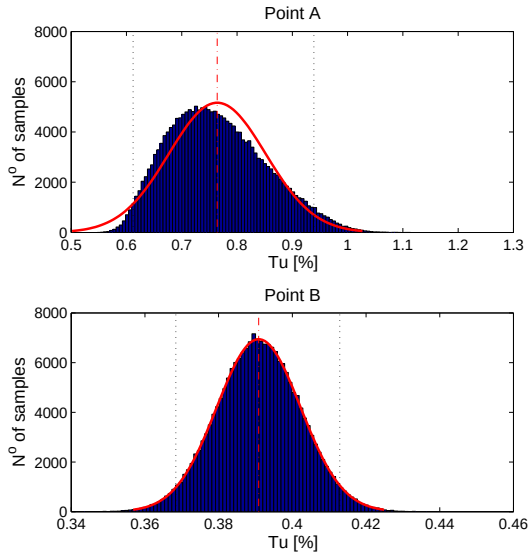

Figure 12: Probability distribution of turbulence intensity for Points A and B

It should be noted that although the absolute uncertainty is high for the mean velocity (4.8 m/s for Point A and 1.5 m/s for Point B), the uncertainty of the V_{rms} is significantly lower (0.054 m/s and 0.045 m/s for Point A and B respectively). This can be explained by the definition of this quantity:

$$V_{rms} = \sqrt{\bar{u^2}} \tag{17}$$

, where $u = V' - V_m$ is the fluctuating velocity component. Due to the subtraction of the mean velocity from the instantaneous velocity, the systematic uncertainty is cancelled out and only the random uncertainty affects the output.

4.5. Convergence of output quantities

As mentioned in Section 3.2, the MCM iterations were selected a priori equal to $2 \cdot 10^5$, following the quidelines of the GUM supplement [10]. The number of iterations is adequate, when the output quantities of interest have converged to the final value. In this case, the quantities of interest are the 95% confidence interval limits of the turbulence intensity estimate. In Fig. 13, the evolution for the upper and lower interval limits for Point B are presented, with increasing number of samples. It can be seen that the values converge for the selected number of samples.

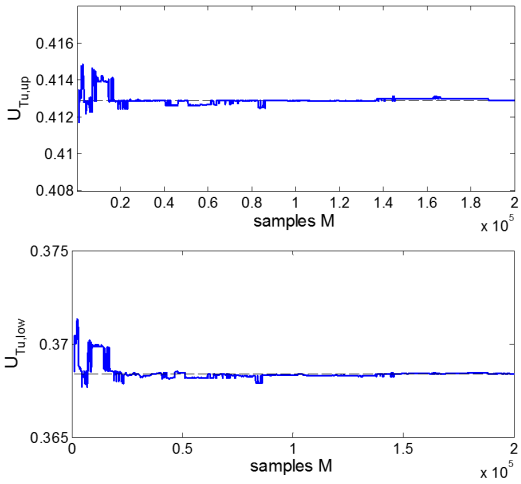

Figure 13: Covergence of 95% confidence interval limits for the Tu, Point B

5. Conclusions

The reliable estimation of the uncertainty of experimentally obtained turbulence parameters is necessary, in order to critically use this information. The Monte Carlo Method can be a useful tool for uncertainty assessment in certain cases. As demonstrated in this work, when complex data reduction procedures are used, the assumptions of the Taylor Series Method may no longer be applicable. Indeed, for certain operating points the turbulence intensity computed by the MCM demonstrates a rightly skewed distribution, which makes the assumption of a normal distribution employed by the TSM no longer valid. Moreover, the application of the MCM is quite straightforward and even simpler than the TSM when correlated uncertainties need to be considered. The main drawback of the method is the computation time, which increases with increasing number of samples.

In future work, the methodology for uncertainty estimation using the MCM will be further developed to include more uncertainty sources (e.g. probe positioning uncertainty) and will be applied in more complex flows.

Acknowledgments

The support of the Fonds de la Recherche Scientifique-FNRS, through the award of a FRIA doctoral grant, is greatly acknowledged.

References

[1] H. H. Bruun, Hot-Wire Anemometry: Principles and Signal Analysis, Oxford University Press, 1995.

[2] F. E. Ames, M. W. Plesniak, The influence of large-scale, high-intensity turbulence on vane aerodynamic losses, wake growth, and the exit turbulence parameters, Journal of Turbomachinery 119 (2) (1997) 182–192.

[3] F. Satta, M. Ubaldi, P. Zunino, Unsteady Inflow Effects on the Wake Shed from a High-Lift LPT Blade Subjected to Boundary Layer Laminar Separation, Journal of Thermal Science 21 (97-108).

[4] T. R. Camp, H.-W. Shin, Turbulence intensity and length scale measurements in multistage compressors, Journal of Turbomachinery 117 (1) (1995) 38–46.

[5] B.Cukurel, S. Acarer, T. Arts, A Novel Perpesctive to High-Speed Cross-Hot-Wire Calibration Methodology, Experiments in Fluids 53 (4) (2012) 1073–1085.

[6] R. Boyle, B. L. Lucci, R. G. Senyitko, Aerodynamic performance and turbulence measurements in a turbine vane cascade, in: ASME Turbo Expo 2002: Power for Land, Sea and Air, no. GT2002-30434, Amsterdam, The Netherlands, 2002.

[7] L. H. Benedict, R. D. Gould, Towards better uncertainty estimates for turbulence statistics, Experiments in Fluids 22 (2) (1996) 129–136.

[8] American Society of Mechanical Engineers, ASME PTC 19.1-2005 Test Uncertainty, ASME, 2005.

[9] Joint Commitee for Guides in Metrology, Evaluation of Measurement Data-Guide to the Expression of Uncertainty in Measurement , JCGM 100:2008, 2008.

[10] Joint Commitee for Guides in Metrology (JCGM), Evaluation of Measurement Data- Supplement 1 to the ”Guide to the Expression of Uncertainty in Measurement” - Propagation of Distributions using a Monte Carlo Method , JCGM 101:2008, 2008.

[11] H. W. Coleman, W. G. Steele, Experimentation, Validation and Uncertainty Analysis for Engineers, John Wiley & Sons Inc., 2009.

Influence of gas-to-wall temperature on bypass transition

Tânia Sofia Cação Ferreira

PhD Candidate, Turbomachinery and Propulsion Department, von Karman Institute for Fluid Dynamics, Belgium, tania.sofia.cacao.ferreira@vki.ac.be

Supervisor: Tony Arts

Professor and Head, Turbomachinery and Propulsion Department, von Karman Institute for Fluid Dynamics, Belgium, arts@vki.ac.be
Professor, Institute of Mechanics, Materials and Civil Engineering, Université Catholique de Louvain, Belgium, tony.arts@uclouvain.be

Abstract

Heat transfer effects on bypass transition are not yet well characterized, particularly for turbomachinery applications, since most experimental studies on transition are based on external flows.

The objective to improve the details of the numerical prediction of this transition mode will be met by wall temperature and heat flux measurements on a linear high pressure turbine vane cascade for a range of flow conditions with varying gas-to-wall temperature ratio, global freestream turbulence intensity, isentropic exit Mach and Reynolds numbers representative of engine conditions.

Further experiments should also include the evaluation of losses and the evolution of the wall static pressure for a thermal and momentum boundary layer comparison.

Keywords: boundary layer transition, turbulence, heat transfer measurements, high pressure turbines

1. Introduction

Boundary layer transition in turbines generates high levels of shear stresses and heat transfer rates leading to an increase in losses and influencing the overall performance of the engine. The assumption of a constant turbulent Prandtl number is commonly applied to turbulence modelling under the Boussinesq approximation. However, very few experimental results indicate that the thermal boundary layer behaves differently than the momentum one under different pressure gradients [1][2]. Considering the highly varying pressure gradients in gas turbine components, such an assumption ought to be verified.

The aim of the project is primarily the investigation of the gas temperature effect on bypass transition on a high-pressure turbine vane by testing in the short duration CT-2 facility, Figure 1.

Heat transfer effects are known to affect natural transition. However; from open literature, the effect is not clear at all for the bypass transition. Moreover, the present research builds-up on previous work performed at the VKI [3] for which the Local Correlations-based Transition Model not always succeeded to predict the measured transition evolution.

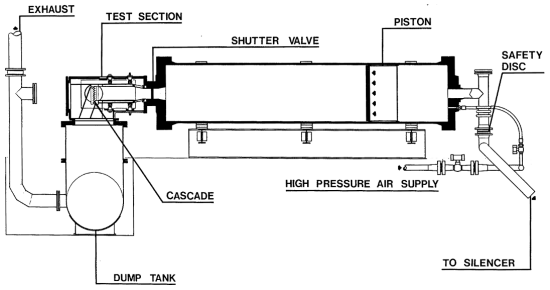

Figure 1: Illustration of the CT-2 facility [3].

2. Goals of the research

The complexity of transition from a laminar to a turbulent boundary layer is still under investigation and the steep increase it induces in wall shear stress and heat flux urges to a more complete understanding of this phenomenon. The heat transfer effects on bypass transition are not yet well characterized, especially for turbomachinery applications, since most of its experimental studies are based on external flows. The objective to improve the details of the numerical

prediction of this transition mode will be met by wall temperature and heat flux measurements in a linear high pressure turbine vane cascade for a range of flow conditions with varying gas-to-wall temperature ratio, global freestream turbulence intensity, isentropic exit Mach and Reynolds number representative of engine conditions. Since the development of losses depends on transition onset and length, further experiments should also include their evaluation as a function of the above-mentioned flow parameters. Complementary measurements of the evolution of the wall static pressure will lead to a thermal and momentum boundary layer comparison, to contribute to the studies that demonstrated a difference in transition length when the flow was subject to distinct pressure gradients [1][2]. The present project also aims to increase the available inlet freestream turbulence intensity in the testing facility which currently provides a maximum of 5.3% [4], to achieve values closer to the ones found in real gas turbines, experimentally showed to be up to 30% [5].

3. State of the art

3.1. Transition: theory and numerical modelling:

Transition is a stochastic, three-dimensional, and unsteady phenomenon characterized by the coexistence of laminar and turbulent flows. Regarding boundary layer transition, it can be categorized as natural, bypass, separated-flow, wake-induced or reverse transition, all described by Mayle [6]. Transition can be also almost instantaneously triggered in the presence of shocks [7] or film cooling [8]. The operating conditions of the turbomachinery component dictate the transition mode and more than one mode can be found along the blade surface. In HP turbines the most predominant transition mode is bypass transition whereas at lower operation Reynolds numbers, separated-flow transition is more likely to occur.

The object of the present study is a highly loaded uncooled turbine guide vane previously tested for an exit Reynolds number range of 0.5-2.0x10^6 and transonic exit Mach numbers [3]. An important result for the present project is one case for highest level of freestream intensity where transition is triggered before the shock position on the suction side. This transition mode is of the bypass type, known to be induced by flow disturbances such as high turbulence intensities, stream-wise pressure gradients, surface roughness and curvature which bypass the initial linear stages of natural transition to the breakdown of turbulent spots that grow and coalesce to form a fully turbulent flow. Their appearance, growth and convection will be the focus of the present study since their behavior will allow the evaluation of the different flow conditions on the bypass transition process. As one is aware of the difficulties present in turbulence modelling, it is easy to understand the struggle in predicting transition due to its different modes and not yet fully characterized sensibility to the flow parameters.

Addressing transition with DNS or LES has been proved successful in some turbomachinery applications, however, the grid and computational time requirements are too high for engineering applications whereas approaches based on linear stability theory fail to predict bypass transition due to the non-linear effects, such as high turbulence intensity and surface roughness [9].

The local correlations-based transition model (LCTM) [10] uses transport equations for the intermittency factor and transition onset momentum thickness Reynolds number and the transition criterion also takes advantage of the van Driest and Blumer's concept of vorticity Reynolds number function [11]. The formulation of this criterion considered freestream turbulence and pressure gradient effects as well as the new empirical correlations developed based on Abu-Ghannam and Shaw's work [12] and similar to the one proposed by Mayle [6]. LCTM uses the Boussinesq approximation, an effective viscosity approach which assumes the Reynolds stresses uniquely related to the rates of strain and local scalar quantities. Transport equations are solved for the turbulent kinetic energy, dissipation and eddy viscosity. However, for the energy equation, a constant turbulent Prandtl number is assumed to retrieve the eddy diffusivity. The physics of this model lies solely on empirical correlations and the accuracy is the key for the transition prediction [9]. LCTM has succeed in several tests cases, even away from the turbomachinery environment [13]. Nevertheless, this model not always succeeded to predict the measured transition onset and development the present work baseline results [3].

3.2. Thermal effects on bypass transition

Wall heating is regarded as a destabilizing effect due to the fluid's viscosity dependence on temperature [14]. If the fluid is a gas, the viscosity will increase with temperature and if the wall is heated a negative viscosity gradient may induce inflection points in the mean boundary layer velocity profile of a laminar attached flow without pressure gradient and thus alter the transition onset.

Furthermore, Driest and Blumer's [11] theoretical study of boundary layer transition under the vorticity Reynolds number criterion points towards the increase of transition Reynolds number for a decreasing wall temperature.

Liepmann and Fila's [15] measurements on a heated flat plate verified that decreasing the wall temperature ratio induces an earlier transition onset. However, this data was acquired at very low freestream turbulence intensities and transition occurred in the natural mode.

The need for bypass transition measurements was later met by Rued and Wittig [16] for a cooled flat plate under wall to gas temperature ratios of 0.53-1.00 and freestream turbulence intensities from 1.6 to 11%. Results indicate that wall cooling is secondary with respect to freestream turbulence intensity however the boundary layer integral parameters and the shape factor ratio indicated a destabilizing effect in decreasing the wall to gas temperature ratio.

Moreover, a longer transition length is observed for the thermal boundary layer than for the momentum one in flows developing under favorable pressure gradients, while the reverse is true for adverse pressure gradients [2]. If one considers the definition of the Prandtl number, the assumption of a constant value for the turbulent analogy falls short when facing flows with varying pressure gradients, present in turbomachinery cascades.

Nealy et al. [17] observed that a lower T_w/T_∞ in the range 0.7-0.8 led to reduced heat transfer levels in the laminar stagnation region and the opposite for the turbulent one. A thorough study of the transition phenomena in turbomachinery is reported by Mayle [6] the effects of surface roughness, surface curvature, compressibility and heat transfer on transition in gas turbines are considered by the author's to be secondary with respect to those induced by the freestream turbulence and the pressure gradient. These statements are later are criticized in a discussion of this paper by Walker [18] nonetheless, no data is presented to contradict it.

The optimal growth theory for compressible boundary layers found cooling to be destabilizing at M=0.5 and almost negligible at M=3.0 [19] however, for the transonic range no results are presented.

A small decrease of T_w/T_{aw} considerably lowered the turbulent spots production in the experiments of Costantini et al. [20]. Nonetheless, the bypass transition indicated by these wedges is due to surface disturbances and not to the freestream turbulence intensity. The effect of T_w/T_{aw} on transition was found more pronounced for favorable and null pressure gradients than for positive pressure gradients which agrees with data presented in [2].

3.3. Heat transfer measurements in an isentropic compression tube facility

The measurement campaign is carried out in the CT-2 short duration testing facility of the von Karman Institute as a follow-up on a previous test campaign which has been extensively used for validation of CDF codes. The facility is an isentropic light piston compression tube (ILPCT) able to simulate full scale engine-like values of gas to wall temperature ratio as well as Mach and Reynolds numbers and freestream turbulence. The concept of this type of facility is described in Ref. [7] and the heat transfer measurements in Ref. [21][22].

The current turbulence grid is made of parallel horizontal bars (d=3 mm, s/d=4) and generates different intensities of inlet freestream turbulence upstream of the cascade according to its stream-wise position. The turbulence intensity value is defined in the streamwise direction and was measured using a constant temperature hot wire probe [3], confirmed by recent measurements in Ref. [4]. The need for higher turbulence levels led to the design of a new grid and the preliminary research is presented in the following subsection.

3.4. Turbulence production in a wind tunnel

Inlet guide vanes are subjected to the flow exiting the combustion chamber where experimental studies have indicated to have turbulence intensities up to 30% [23]. Generating such high values in wind tunnels is quite hard for isotropic turbulence and the degree of nonuniformity is can be of relevance as well as the pressure losses.

Polanka et al. [23] present a horizontal grid with 12 rods of 38 mm each positioned 505 mm upstream the cascade. The test section inlet dimensions are 550x1020 mm. A turbulence intensity of 22% is measured 89 mm upstream the airfoil leading edge and this high value can be achieved due to the flow conditions, a low mainstream inlet velocity of 6.2 m/s. In fact, Frenkiel's correlation estimates almost half of the measured value of turbulence intensity.

For higher operating velocities, Giel et al. [5] use an active grid with three 25.4 mm square tubes placed 876 mm from the measurement passage. The blockage area is only 26% and the operating Mach number is 0.38. Measured turbulence levels are of 7%. Based

on this work, due to the inlet Mach number similarity (M=0.40), Nix et al [24] designed a 25.4 mm square bar turbulence grid with a blockage area of 40%; reporting a total pressure drop of 7% with uniformity of ±1%. The high flow uniformity is attributed to the presence of 2:1 area contraction just downstream of the grid. Turbulence intensities of 10-12% are reached with integral length scale of 20 mm. Later, on the same facility, Carullo et al. [25] designed two passive grids with high blockage area of 50%, achieving turbulence values of 12-14%.

3.5. Intermittency factor

The intermittency factor (γ) is a practical tool for the assessment of transition. It defines the fraction of time over which the flow is turbulent from the point of view of a chosen flow quantity [27]. Intermittency functions are regarded in literature as the favoured tool in predicting transition amongst the turbomachinery community [9] as they can quantify the turbulence evolution within a laminar flow and result solely from experimental data. The power spectral density Integral method [26], the conditional sampling technique and the variable interval time-averaging technique are examples of studied approaches that can be applied to the heat flux data experimentally obtained in the present project.

4. Results

Last year, during the VKI Research Master project, a test campaign was carried out in this facility to address the gas-to-wall temperature effect on bypass transition [27]. Measurements by means of fast response thin films provided the time-resolved wall heat flux under accurately defined inlet and outlet flow conditions. The onset of transition was found from the fluctuations of the heat flux signals and the results indicated that the current instrumentation was not discretized sufficiently for an accurate evaluation of the temperature effect. In fact, for the tested flow conditions, the isentropic outlet Mach number appeared to be the main driver of the onset of transition, Figure 2.

The preliminary results also illustrate the need to understand not only the thermal but also the aerodynamic flow field, considering the dominance of the pressure gradients in the boundary layer transition. Hence, wall static pressure measurements will be carried out for the same flow conditions of the wall temperature measurements so that the transition phenomenon can be understood in terms of both the momentum and the thermal boundary layer evolution.

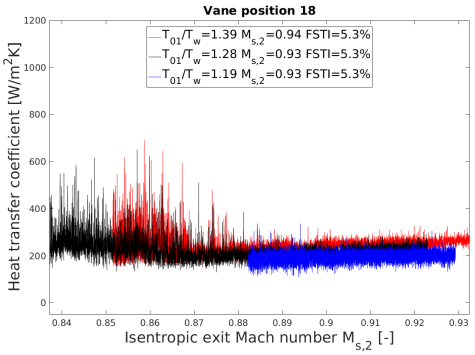

Figure 2: Heat transfer coefficient vs isentropic exit Mach number variation at T_{01}/T_w = [1.19, 1.28, 1.39], $Re_{s,2} = 10^6$ and $FSTI$ = 5.3% for vane position 18 [27].

An initial step of the PhD project is the increase of the inlet freestream turbulence intensity inside the facility, to achieve values closer to the ones found in real gas turbines, with are in the order of 10-30% . The present turbulence grid provides a maximum of 5.3% [4]; hence, a new grid has been designed and is currently being manufactured. Measurements will address not only the turbulence intensity and decay downstream the turbulence grid but also flow uniformity and losses.

The transition modelling in industry mostly uses the two equation $\gamma - Re_\theta$ model which is based on experimental data for the intermittency (γ) correlations. These correlations are usually taken from Abu-Ghannam and Shaw [12] and are sensitive to the freestream turbulence intensity and the pressure gradients, both considered as first order effects on transition. Upon the deeper investigation of the gas to wall temperature ratio effect, if it is proven to be relevant under other flow conditions, this effect, could be included in the intermittency correlations to provide more accurate predictions of transition onset and length. Since the facility can achieve also different levels of isentropic exit Mach and Reynolds number and freestream turbulence intensity, the obtained data can be checked against the intermittency correlations and, in case miss-matches are observed, help in the calibration of these correlations for said flow parameters.

As it has been mentioned in the first paragraph, the underlying importance of the deep understanding of the triggering of the transition process lies in the consequential increase of aerodynamic and thermal losses. Possessing the tools to accurately predict the onset and length of transition would allow a more efficient design of turbine blades. The present PhD project also aims at the evaluation of losses on the

blade and on the downstream wake.

5. Conclusion

In conclusion, this PhD thesis will allow the increase of the available data on transition from an intermittency point of view. The main application will be the LS89 vane, which is widely used for validation of CFD codesregarding the past experimental campaign for the mean values of heat transfer ([3]); and help the improvement of transition/turbulent models. Time-resolved static pressure and temperature measurements will provide a deep insight on the momentum and thermal boundary evolution from laminar to turbulent. A broad range of flow conditions can be used for this investigation in terms of isentropic exit Mach and Reynolds number, freestream turbulence intensity and gas-to-wall temperature ratio.

References

[1] W. M. Kays, Turbulent prandtl number–where are we?, Journal of Heat Transfer 116 (2) (1994) 284–295.

[2] O. P. Sharma, Momentum and thermal boundary layers on turbine airfoil suction surfaces, AIAA (Paper 87-1918).

[3] T. Arts, M. Lambert de Rouvroit and A. W. Rutherford, Aero-thermal investigation of a highly loaded transonic linear turbine guide vane cascade, Technical Note 174, von Karman Institute for Fluid Dynamics, Rhode-Saint-Genèse, Belgium (1990).

[4] F. Fontaneto, Aero-thermal performance of a film-cooled high pressure turbine blade/vane: a test case for numerical codes validation, Ph.D. thesis, von Karman Institute for Fluid Dynamics/Universitá degli Studi di Bergamo, Rhode-Saint-Genèse, Belgium (2014).

[5] P. W. Giel, G. J. Van Fossen, R. J. Boyle, D. R. Thurman, K. C. Civinskas, Blade heat transfer measurements and predictions in a transonic turbine cascade, in: ASME 1999 International Gas Turbine and Aeroengine Congress and Exhibition, no. 78606, 1999, p. V003T01A029. doi:10.1115/99-gt-125.
URL http://dx.doi.org/10.1115/99-GT-125

[6] R. E. Mayle, The role of laminar-turbulent transition in gas turbine engines, Journal of Turbomachinery 113 (4) (1991) 509–536.

[7] H. Consigny, B. E. Richards, Short duration measurements of heat-transfer rate to a gas turbine rotor blade, Journal of Engineering for Power 104 (3) (1982) 542–550.

[8] C. Camci, Experimental and theoretical study of film cooling on a gas turbine blade, Phd thesis, Katholieke Universiteit Leuven, Rhode-Saint-Genèse, Belgium (1985).

[9] D. Di Pasquale, A. Rona, S. Garrett, A Selective Review of Transition Modelling for CFD, AIAA Paper 2009-3812.

[10] R. B. Langtry, F. R. Menter, S. R. Likki, Y. B. Suzen, P. G. Huang, S. V'olker, A correlation-based transition model using local variables–part ii: Test cases and industrial applications, Journal of Turbomachinery 128 (3) (2004) 423–434.

[11] E. R. van Driest, C. B. Blumer, Boundary layer transition: Freestream turbulence and pressure gradient effects, AIAA Journal 1 (6) (1963) 1303–1306.

[12] B. J. Abu-Ghannam, R. Shaw, Natural Transition of Boundary Layers - The Effects of Turbulence, Pressure Gradient, and Flow History, Journal of Mechanical Engineering Science 22 (5) (1980) 213–228.

[13] R. Langtry, F. Menter, Transition Modeling for General CFD Applications in Aeronautics, AIAA Paper 2005-522.

[14] H. Schlichting, K. Gersten, Boundary Layer Theory, 8th Edition, Springer, 2000.

[15] H. W. Liepmann, G. H. Fila, Investigation of effects of surface temperature and single roughness elements on boundary-layer transition, Technical Note 1196, NACA (1947).

[16] K. Rued, S. Wittig, Laminar and transitional boundary layer structures in accelerating flow with heat transfer, Journal of Turbomachinery 108 (1) (1986) 116–123.

[17] D. A. Nealy, M. S. Mihelc, L. D. Hylton, H. J. Gladden, Measurements of heat transfer distribution over the surfaces of highly loaded turbine nozzle guide vanes, Journal of Engineering for Gas Turbines and Power 106 (1) (1984) 149–158.

[18] G. J. Walker, The role of laminar-turbulent transition in gas turbine engines: A discussion, Journal of Turbomachinery 115 (2) (1993) 207–216.

[19] D. Arnal, O. Vermeersch, Compressibility effects on laminar-turbulent boundary layer transition, in: 45th Symposium of Applied Aerodynamics, Marseille, France, 2010.

[20] M. Costantini, U. Fey, U. Henne, C. Klein, Nonadiabatic surface effects on transition measurements using temperature-sensitive paints, AIAA Journal 53 (5) (2015) 1172–1187.

[21] D. L. Shultz, T. V. Jones, M. L. G. Oldfield, L. C. Daniels, A new transient cascade facility for the measurement of heat transfer rates, High Temperature Problems in Gas Turbine Engines AGARD CP 229.

[22] M. L. G. Oldfield, R. Kiock, A. T. Holmes, C. G. Graham, Boundary layer studies on highly loaded cascades using heated thin films and a traversing probe, Journal of Engineering for Power 103 (1) (1981) 237–246.

[23] M. D. Polanka, V. C. Witteveld, D. G. Bogard, Film cooling effectiveness in the showerhead region of a gas turbine vane: Part i – stagnation region and near-pressure side, in: ASME 1999 International Gas Turbine and Aeroengine Congress and Exhibition, no. 78606, 1999, p. V003T01A022. doi:10.1115/99-gt-048.
URL http://dx.doi.org/10.1115/99-GT-048

[24] A. C. Nix, A. C. Smith, T. E. Diller, W. F. Ng, K. A. Thole, High intensity, large length-scale freestream turbulence generation in a transonic turbine cascade, in: ASME Turbo Expo 2002: Power for Land, Sea, and Air, no. 36088, 2002, pp. 961–968. doi:10.1115/gt2002-30523.
URL http://dx.doi.org/10.1115/GT2002-30523

[25] J. S. Carullo, S. Nasir, R. D. Cress, W. F. Ng, K. A. Thole, L. J. Zhang, H. K. Moon, The effects of freestream turbulence, turbulence length scale, and exit reynolds number on turbine blade heat transfer in a transonic cascade, Journal of Turbomachinery 133 (1) (2010) 011030–011030–11. doi:10.1115/1.4001366.
URL http://dx.doi.org/10.1115/1.4001366

[26] T. Coton, T. Arts, M. Lefebvre, N. Liamis, Unsteady and calming effects investigation on a very high-lift lp turbine blade–part i: Experimental analysis, Journal of Turbomachinery 125 (2) (2003) 281–290.

[27] T. S. Cação Ferreira, T. Arts, Influence of gas-to-wall temperature on bypass transition, in: ASME Turbomachinery Technical Conference & Exposition, ASME International Gas Turbine Institute, Charlotte, North Carolina, 2017.

Aerothermal characterization of high pressure turbines rotor tip flows

Bogdan Cezar Cernat

Turbomachinery and Propulsion Department, von Karman Institute for Fluid Dynamics, Belgium, cernat@vki.ac.be

Supervisor: Sergio Lavagnoli

Assistant Professor, Turbomachinery and Propulsion Department, von Karman Institute for Fluid Dynamics, Belgium, lavagnoli@vki.ac.be

University Promoter: Tony Arts

Professor, Universite catholique de Louvain / von Karman Institute for Fluid Dynamics, Belgium, arts@vki.ac.be

Abstract

This paper addresses the investigation of the highly unsteady, three-dimensional HP turbine rotor tip flows in a short-duration rotating test-rig. The rainbow rotor setup, allowing the simultaneous test of different optimized tips, is described, together with the steady and time-accurate measurement techniques employed for the aerothermal flow characterization. Time-averaged results on the pressure fields at the rotor casing and inlet/outlet planes are presented.

Keywords: HP Turbine, Tip Flows, Aerothermal, Measurements, Pressure, Heat Transfer, Rainbow Rotor

1. Introduction

Modern research in gas turbine aero-engines aims at maximizing the propulsion efficiency and components lifetime while reducing fuel consumption, polluting emissions and overhaul expenses. This performance-driven design strategy implies ever-increasing aerothermal and mechanical loads on the engine components, with the high pressure (HP) turbine unquestionably representing the most critical part during engine operation [1].

This research addresses the investigation of the flow physics in the inevitable gap between the HP rotor blade tips and the stationary casing, where unsteady hot gas leakages are induced by the pressure difference between both sides of the airfoil [2]. As a result, considerable aerodynamic and thermal loads fluctuations are produced on the blade extremity [3], with highly detrimental effects on the component integrity and stage aerodynamic efficiency [4]. The by-pass spillage does not contribute to the work production and, once injected in the primary flow, gives rise to significant mixing losses [5].

Periodic disruption of the endwall boundary layer and high velocities associated to the leakage flow markedly contribute to an increase in heat transfer rates towards both the rotating airfoil and the stationary casing. As underlined in previous studies [6], even a 10 K increase in blade metal temperature can reduce by 50% the lifespan of the component. A thorough understanding of the over-tip flow physics is therefore of paramount importance to enhance components lifetime and aerothermal performance in unshrouded rotor configurations.

Various experimental investigations devoted to the study of the unsteady heat transfer and pressure fields in the over-tip area were performed in linear cascades [7]. Nevertheless, the importance of stator-rotor interactions [8; 9] and rotor-casing relative motion [10] on the unsteady turbine flow physics has been extensively assessed. A lack of reliable experimental data at engine representative conditions still prevents from a thorough validation of the multiple numerical studies on this topic [11].

The present work pursues a detailed aerothermal characterization of the pressure and temperature fields in the tip gap region of an HP turbine test rig operating at engine-like conditions. The Reynolds and Mach numbers, as well as the gas-to-wall temperature ratios, are representative of real HP turbine stages. Furthermore the rotating nature of the one-stage rig allows to prop-

erly reproduce turbine flows interactions in terms of vane wakes, secondary flows and rotation effects.
The investigated rainbow rotor configuration allows the simultaneous aerothermal testing of different blade tip geometries (carved and squealer-like tips) arranged in distinct sectors. Particular emphasis is dedicated to quantify the influence of the distinct clearance levels on the tip flows topology, with time-accurate monitoring of the tip gap dimension. Fast-response capacitive probes are deployed for this purpose at distinct axial and circumferential positions along the rotor casing [12]. The blade tip geometries result from a previous optimization process, aimed at the blade tip heat transfer minimization and at the increase of rotor aerodynamic efficiency. [13]
Time-resolved and time-averaged pressure patterns at the rotor casing are evaluated in different circumferential positions by means of fast-response piezoresistive sensors and pressure taps arrays. Temperature and pressure fields are characterized at the inlet and outlet of the turbine stage by performing probe traverses at different pitchwise positions, assessing the test boundary conditions and outflow topology.

2. Experimental test rig

The experimental campaign for the aerothermal characterization of the optimized blade tips was carried out in CT-3, the short-duration compression tube facility of von Karman Institute [14].
The test section presents a 34 blades vane and a 48 blades rotor, scaled-up in dimensions with respect to a real HP stage as presented in Table 1. The test rig allows to establish engine-like flow conditions for a testing period between 300 and 500 ms. More specifically, non-dimensional flow parameters, as Mach and Reynolds numbers, are preserved during the test. Furthermore stator-rotor interactions and rotation effects, of fundamental importance for a correct representation of real engine tip flows, are properly reproduced. The transient character of the test rig allows the establishment of representative gas-to-wall temperature ratios (circa 1.5-1.6) and therefore the measurement of wall heat transfer distributions.
In Fig. 1 the short-duration facility is presented. The compression tube is characterized by a pressurized air supply in the rear part and an internal free-moving lightweight piston. A fast-actuation titanium shutter valve separates it from the test section. This latter is connected to the downstream vacuum tank by a variable-area sonic throat .
At the beginning of the test the shutter is closed and

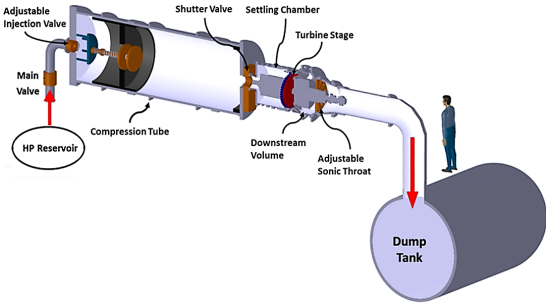

Figure 1: CT-3 Short Duration HP Turbine Test Rig

the appropriate pressure level is set in the tube, based on the required inlet flow conditions. The test section and vacuum tank are evacuated down to 30 mbar (absolute pressure). After activating the bearings lubrication system, an auxiliary pneumatic turbine is operated to spin up the rotor to 90 - 95 % of the nominal rotational speed (5900 rpm). Vibrations are constantly monitored in proximity of the front and rear bearings by means of two accelerometers.
High-pressure cold air is then injected in the tube through sonic throats, forcing the piston forward and realizing a quasi-isentropic compression of the air in front of it. When the required conditions of gas temperature and pressure are reached inside the tube, the fast-actuation shutter valve opens in 70 ms and allows the blow-down of hot compressed air through the annular cascade.

Table 1: Test Rig Operational Specifications

HP Stage	Vane	Rotor
Blade Span (H_{in}) [mm]	70.1	53.4
Blade Count	34	48
Test Parameter	**Value**	**Units**
Reynolds (rotor outlet - C_{ax})	$2.4{\cdot}10^5$	-
$Mach_{rel,out}$	0.73	-
Tip Gap - Nominal value	1.38	% H_{rot}
Tip Gap - Tight value	0.85	% H_{rot}
Rot. Speed (ω)	5900	rpm
$\omega/\sqrt{T_{0,inlet}}$	21	-
Blade Passing Frequency	4720	Hz
Pressure Ratio	2.2	-

The turbine pressure ratio is controlled by the variable area sonic valve, which sets the mass flow when the HP stage is tested at subsonic regimes. A careful adjustment of the tube pressurized air supply and of the sonic throat allows to avoid gas accumulation

in the test section and to keep constant aero-thermal parameters during the test duration. Detailed reviews of the CT-3 design and operational characteristics are given by [15] and [16], while a meridional view of the test section is presented in Fig. 2.

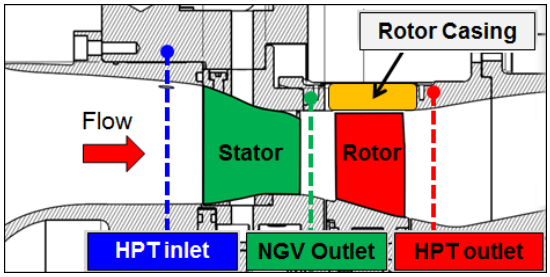

Figure 2: HP Stage - Meridional View

3. Rainbow rotor setup

Several different optimized blade tip profiles are tested simultaneously in the short duration facility by employing a "rainbow rotor" setup, presented in Fig. 3. The 48 airfoils of the HP stage rotor are arranged in seven different sectors, each one consisting of blades of equal tip seal geometry to assure flow periodicity. Five high-performance squealer-like and one contoured tip profile are investigated, with five sectors running at a nominal clearance of 1.38% of the blade span and the remaining two at a "tight" value of 0.85%.
The rainbow rotor strategy, besides drastically reducing the costs of the campaign, is highly time efficient and assures a consistent and precise performance comparison between the optimized blade tip seals. The multiple clearance effect is investigated by coupling the time-resolved aerothermal flow information with time-accurate casing-to-tip distance measurements [17].

4. Tip Clearance Measurement

Wear gauges and capacitive probes are used to measure the distance between the rotating airfoil tips and the external stationary casing. Three inserts are positioned at equally spaced locations along the casing, resulting flush mounted on the inner abradable surface. Each insert presents 5 wear gauges and one fast-response probe, all facing directly the over-tip area.
The wear gauges consist of abradable pins and are

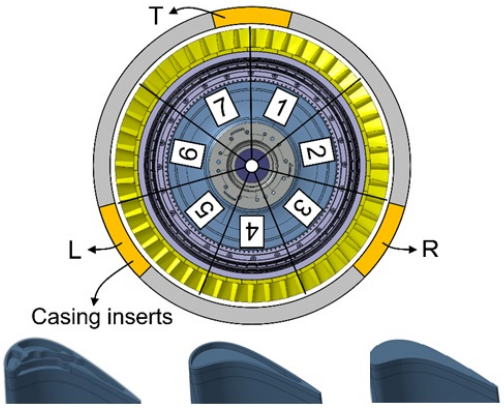

Figure 3: Rainbow Rotor Setup

gradually machined during operation by the rotating blade tips. Consecutive tests are performed at increasing rotational speeds and the length of the pins is measured each time by using a dial gauge. The minimum clearance level at each speed is then retrieved, assessing an absolute reference for the calibration of the capacitance-based proximity sensors. Fig. 4 shows one of the three inserts mounted on the CT-3 rotor casing.

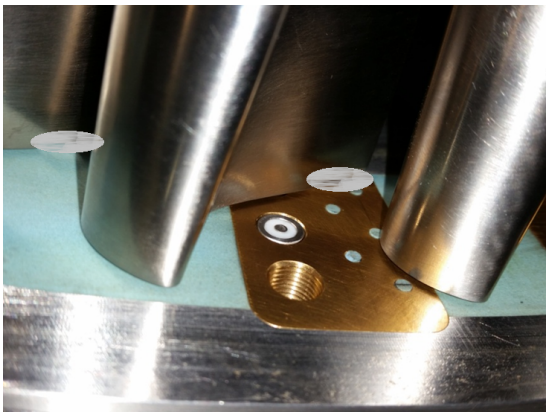

Figure 4: Tip Clearance Insert at Rotor Casing

The fast-response clearance probes are connected to a dedicated conditioning unit by a coaxial cable. The output voltage is proportional to the capacitance variation between the probe head and the passing blade tip. The reliability and performance of such sensors for high-speed annular cascade testing were already proven in a previous experimental campaign [18]. The maximum operating range of each probe is roughly assumable as the sensor radius, while the resolution is 10 μm.

In the present measurement setup, two probes were designed with a sensor diameter of 5.5 while the third one presents a diameter of 2.5 mm. The larger sensors allow the correct detection of the squealer tips cavities (about 3 mm distance from casing wall), while the small one is employed for the detection of the small-scale geometrical features, given its increased spatial resolution. The measuring bandwidth of the fast response probes exceeds 60 kHz, which is more than one order of magnitude higher than the blade passing frequency (approximately 5 kHz). A comprehensive description of the measurement setup, in-situ calibration technique and data-processing can be found in [12].

5. Aerothermal Measurements Setup

The main objective of the experimental test campaign is the quantitative evaluation of the flow aerothermodynamics related to each of the seven sectors. An accurate aerothermal comparison of the different blade seals requires reliable, time-resolved information on the pressure and temperature fields. The flow information is complemented with real time monitoring of the blade passage event and tip clearance size. Fast response instrumentation is needed to correctly detect the blade-to-blade flow variations at frequencies in the order of 5 kHz. Time-averaged aerothermal measurements are used for the characterization of the overall turbine stage characteristics (i.e. boundary conditions, average casing pressure distribution, thermal fields).
The resulting data allow a thorough characterization of each blade tip seal effectiveness, while providing a valuable support to the validation of CFD computations and tip design strategies.

5.1. HP Stage Inlet

The turbine inlet boundary conditions are characterized half axial chord upstream of the NGV leading edge plane. Flow properties are both investigated at the endwalls and as radial profiles in different circumferential locations in order to assess the incoming flow uniformity.
The inltet static pressure distribution over one stator pitch is measured on both endwalls by means of metallic inserts with five pressure taps each. Each tap has a diameter of 0.8 mm and is connected to the pressure transducer by a flexible pneumatic pipe. Due to design constraints, two different transducer systems are used to retrieve the pressure information. The hub taps are connected to dedicated slow-response piezoresistive differential pressure transducers (Sensym 240-PC-006D), providing a measurement accuracy of ± 1 mbar. The tip pressure information is sent to a pressure scanner (Scanivalve controller DSM4000 and ± 15 psid differential 64-port scan module ZOC 33/64PX) with a measurement accuracy of ± 0.5 mbar.
Midspan total temperature and total pressure represent the reference flow properties for the inlet flow. The aerothermal probes employed for these measurements present a bare type-K thermocouple and a Kiel pitot head, as shown in Fig.5-a. The optimized probe design allowed to achieve a recovery factor higher than 99% for both probes at the nominal inlet conditions (Mach number 0.1 and gas temperature 440 K).

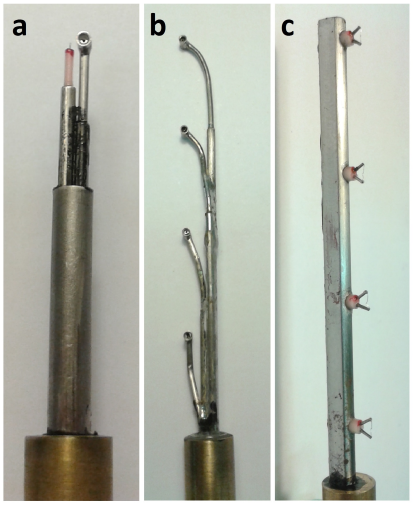

Figure 5: Inlet Plane Aerothermal Probes

Total pressure radial profiles are measured by a probe presenting four Kiel pitot heads, with an internal tube diameter of 0.6 mm (Fig.5-b). The Kiel heads are characterized by a shroud protected inlet, providing a smaller flow angle sensitivity compared to normal pitot tubes. A pressure recovery factor higher than 99.9% was retrieved during the calibration in a range of 30 degrees of yaw angle and 20 degrees of pitch angle (Mach 0.1).
Three K-type thermocouple rakes were employed for the investigation of total temperature radial profiles, with a wire diameter of 50 μm and a length-to-diameter ratio above 80 (Fig.5-c). This design allows to neglect unsteady conduction effects during the tesing period, while sill providing a reasonably fast re-

sponse measurement. A dedicated nozzle calibration assessed the temperature recovery factor of the rake (99.96%) and the related correction to be applied at the typical flow conditions of plane 01 (about 0.15 K over a temperature value of 440 K).
Turbulence intensity and lengthscales at the stage inlet were measured by hot-wire anemometry. Two rakes were employed to this aim. As represented in Fig. 6, each probe presents two hot-wires spaced by 37 mm and a central thermocouple to retrieve the local gas temperature. The hot-wires are made of a special Nickel-Platinum alloy, that guarantees the safe operation at temperatures around 550 K (respecting the wire-to-flow temperature difference of 100 K). To further prevent aging effects a wire diameter slightly larger than the typical was adopted (9 μm against the usual 5 μm, which would offer higher spatial resolution but less structural reliability). The 1 mm active length is chosen to minimize the heat transfer by conduction to the prongs, so that the heat loss rate depends only on the velocity component orthogonal to the wire. According to the maximum cut-off frequency, assessed by measuring the flow in test conditions and equal to 30 kHz, the sampling frequency was set at 65 kHz.



Figure 6: Hot Wire Rake at Stage Inlet

5.2. Nozzle Guide Vane

The HP stator airfoils are instrumented with pneumatic taps arrays both on suction and pressure side, connected by means of flexible tubes to the Scanivalve system. The 1.00 mm diameter holes allow to measure the time-average static pressure distribution at 50% (Fig. 7) and 90% of the blade span.

A hub insert equipped with 18 pressure taps is adopted at the NGV outlet to measure both time-averaged (12 pneumatic taps) and time resolved (6 Kulite sensors) static pressure distributions. The fast-response sensors are mounted 0.2 mm recessed in the insert, this depth representing a trade-off between the necessary frequency response and sensor protection.

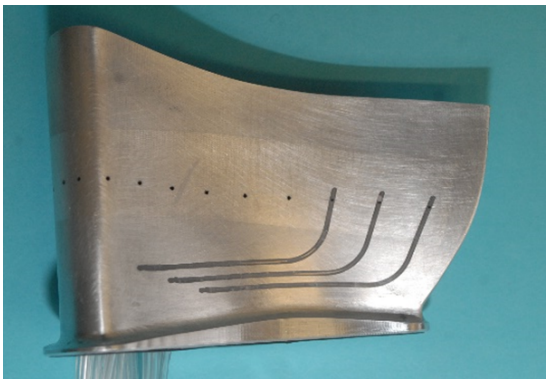

Figure 7: Vane Airfoils Static Pressure Array

5.3. HP Rotor Outlet

The measurement plane at the outlet of the turbine stage lies half axial chord downstream of the rotor blades trailing edge. A slow-response four-head Kiel pitot rake is employed, together with two double-head Kulite rakes, to characterize the total pressure field in this area.
The fast response transducers, directly facing the flow, are covered by a thin elastomer that assures a good protection and negligible influence on the frequency response (Fig.8-a). The probes are displaced at several spanwise and pitchwise positions to fully resolve one blade passage section.
Miniaturized fast-response single hole probes (tap diameter 0.2 mm) are employed for the time-resolved measurement of flow velocity, pressure and yaw angle in the outlet plane (Fig.8-b). Five of these probes are mounting an integrated Measurement Systems sensor (type EPIH-113-1.5B, 1.3 mm external diameter) while one of them is equipped with a Kulite transducer (type XCQ-062 25A, 1.7 mm external diameter). The probe diameters are respectively 1.6 and 2 mm, allowing an appropriate resolution of the outlet flow, generally affected by large gradients and non-uniformities in terms of pressure and flow angles. All the probes were calibrated in a range of ±60 degrees of yaw angle and ±20 degrees of pitch angle (Mach 0.1 to 0.5).

By changing the angular orientation of the probe with respect to the flow direction, but maintining the same radial position, the probes were operated in ”virtual three-hole probe” mode. Therefore each radial point in the test matrix required three distinct angular orientations, operated through three consecutive tests.
In the case under investigation, ”low frequency” physical phenomena, mainly due to the blow-down transient and rotor acceleration, are combined with flow oscillations at frequencies of the order of several kHz, that is the blade passing frequency and its harmonics.
To properly resolve both time-scales, the output voltage, amplified by a factor 100, is processed by analog filters. The time-average signal is obtained by low-pass-filtering the Kulites at a cut-off frequency of 500 Hz, sampling then the signal at 10 kHz with 16 or 14-bits resolution.
The time-resolved signal is retrieved instead by applying a further gain factor of 10 and a band-pass filter between 60 Hz and 180 kHz. The resulting signal is then sampled at 1 MHz, with a resolution of 16 bits. The acquisition periods of the two filtered signals are respectively 7 and 4 seconds.

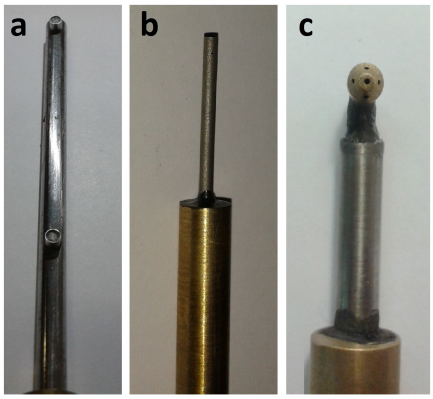

Figure 8: Outlet Plane Aerothermal Probes

In order to perform quasi-steady measurements of flow direction, velocity and static pressure, two pneumatic five hole probes are also employed (Fig.8-c). They are designed to have different measurement ranges, each one covering half of the blade span. The conical heads (60° aperture) present an external diameter of 3.2 mm and holes perpendicular to the surface. The measured total pressure sensitivity to the flow angle is decreased by drilling the central hole with a conical shape. The calibration was performed in a free-jet nozzle in a range of ±30 degrees of yaw angle and±20 degrees of pitch angle (Mach 0.1 to 0.5).
The quasi-steady thermal field is investigated by means of a thermocouple rake similar to the one presented in Fig.5-c.

5.4. Rotor Casing Static Pressure Field

The over-tip flow aero-thermodynamics presents unsteady, high-frequency, three dimensional physical phenomena. To characterize the large pressure gradients from an absolute frame of reference (i.e. rotor casing) it is therefore fundamental to employ fast response measurement techniques, able to resolve the flow field variations at the blade passing frequency of about 5 kHz.



Figure 9: Static Pressure Casing Array

The time-resolved pressure field at the rotor casing is investigated by means of an integrated metallic insert presenting an array of 66 pressure taps, combining both fast-response sensors and slow-response pneumatic tubes. The 0.6 mm diameter taps allow the correct resolution of the static pressure variations due to the passage of the small-scale rims and narrow cavities typical of the squealer-like tips. The 6 circumferential measurement points cover one vane pitch, while the 11 in axial direction extend from -5% to 105% of the rotor axial chord.
The high frequency sampling is performed by means of 33 subsurface mounted Kulite sensors (type XCQ-062 25A), recessed under the insert wall of 0.2 mm for safety reasons and providing a frequency response above 90 kHz. The remaining 33 taps, also employed in the in-situ calibration of the Kulites, are connected to the pressure scanner system (Scanivalve) by flexible pneumatic tubes.
The insert shape (Fig.9) is symmetrical, allowing to

switch its positioning of 180° and swap the measurement points of Kulite sensors and pneumatic taps.
The pressure field is analysed in three distinct circumferential locations along the rotor casing, in order to evalute the influence of stator-rotor interactions. Furthermore, static eccentricity of the rotor with respect to the casing axis and casing shape tolerances are exploited to study the effect of three different clearance levels on the over-tip flows.

6. Results

6.1. Inlet Boundary Conditions

The radial pressure distribution measured at the inlet of the HP stage is presented in Fig. 10. A good agreement between experimental data and numerical predictions is achieved, with uniform pressure levels along the channel span. The repeatability of the measurements is within ± 0.5 mbar, in the same order of magnitude of the Kiel rake uncertainty.
The measurement range extends from 0.5% to 95% of the channel span, limited near the endwalls by the probe head diameter.

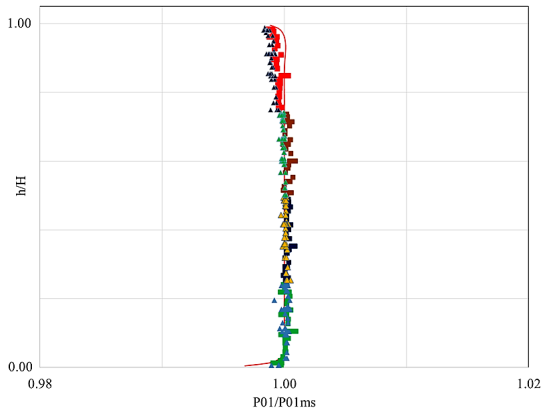

Figure 10: Inlet Total Pressure Profile

The non-dimensional total temperature profiles, presented in Fig. 11, show a markedly higher data scatter, resulting in a measurement repeatability of 1.5% with respect to the mid-span value (corresponding to about ±4 K). This is mainly due to the fact that these measurements are performed by three K-type thermocouple rakes, located in distinct circumferential positions. The measured distribution matches the temperature profile imposed for the numerical computations in the central part of the channel, while a notable difference is present in the endwalls proximity. Indeed, due to the initial absence of reliable data from the experimental facility, a typical engine temperature distribution was considered for the first computations.

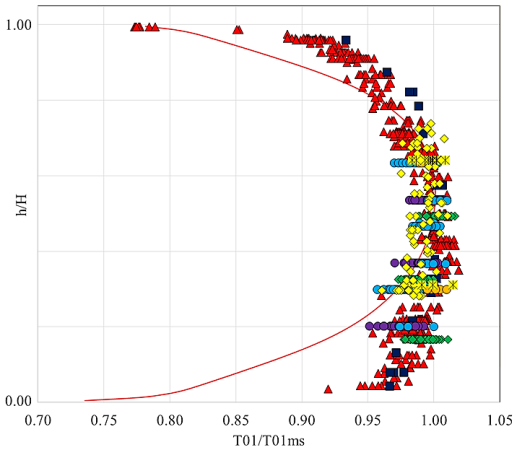

Figure 11: Inlet Total Temperature Profile

6.2. Casing Static Pressure Distribution

The pressure field of the over-tip area has been investigated through both time-resolved and time-averaged measurements. The plot in Fig. 12 shows the axial distribution of pitchwise-average static pressure between -5% and 105% of the rotor axial chord. In order to evaluate the clearance variation effect on the pressure drop, the measurement was performed in three distinct circumferential locations, equally spaced around the rotor. As clearly shown in the plot,

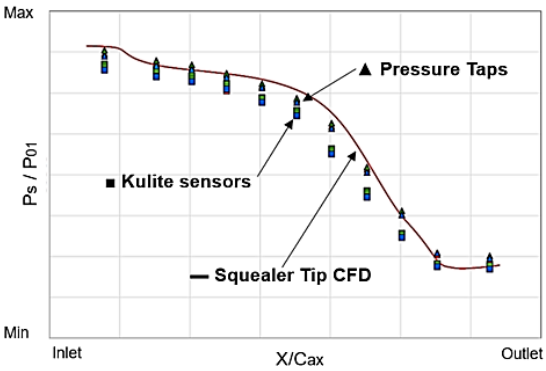

Figure 12: Rotor Casing Static Pressure

a tip gap variation of about 15% of the nominal value induces a quite modest variation on the average static pressure (≤1% P_{01}).
Compared to the numerical predictions, referring in this case to a ”simple squealer” tip geometry, a

slightly lower pressure level is observed experimentally. This effect is particularly evident for the fast-repsonse measurements, which are able to resolve the passage of the "tight clearance" tips. This event corresponds to a lower value in casing static pressure, i.e. higher tip flow velocity, and therefore provokes a bias in the overall average values.

7. Conclusions

This paper presented the measurement setup employed for the aerothermal characterization of the flow field in a one-stage HP turbine test rig. The transient character of the facility allows to correctly reproduce engine-like conditions for the duration of a test, typically ranging between 300 and 400 ms.

The main purpose of the experimental campaign is the evaluation of the pressure and thermal fields in the over-tip region for 6 different optimized blade seal geometries, operating at two values of clearance. A "rainbow rotor" setup was employed in order to simultaneously test the different blade tips performance, with sectors of 6 to 7 blades of the same type to assure flow periodicity.

Time-average total pressure and temperature profiles were acquired at the inlet of the HP vane, in order to provide a thorough characterization of the stage boundary conditions. With the exception of total temperatures in near-endwall zones, a general good agreement with CFD computations was demonstrated. The time-average outlet profiles of temperature and pressure are not shown in this paper for confidentiality reasons.

Steady and time-accurate measurements of pressure and thermal fields at the rotor casing were performed in order to characterize the highly unsteady over-tip flow physics. The experimental results show a general lower level of pitchiwise-average pressure with respect to the "simple squealer tip" CFD predictions. This general offset may be due to the different sectors averaging. In particular, the time-resolved pressure measurements are markedly influenced by the tight-clearance blade tips, which cause a slight decrease of the casing average static pressure.

Further analysis of the high-frequency, time-accurate measurements will allow to characterize the flow field of each of the seven rotor sectors, assessing the individual performance of the optimized airfoil tips.

References

[1] J. P. Bindon, Pressure distributions in the tip clearance region of an unshrouded axial turbine as affecting the problem of tip burnout, in: ASME 1987 International Gas Turbine Conference and Exhibition, American Society of Mechanical Engineers, 1987, pp. V001T01A085–V001T01A085.

[2] T. Booth, Tip clearance effects in axial turbomachines: Importance of tip clearance flows in turbine design, Von Karmin Institute for Fluid Dynamics Lecture Series 5 (1985) 15–19.

[3] R. S. Bunker, A review of turbine blade tip heat transfer, Annals of the New York Academy of Sciences 934 (1) (2001) 64–79.

[4] J. D. Denton, Loss mechanisms in turbomachines, in: ASME 1993 International Gas Turbine and Aeroengine Congress and Exposition, American Society of Mechanical Engineers, 1993, pp. V002T14A001–V002T14A001.

[5] T. Booth, P. Dodge, H. Hepworth, Rotor-tip leakage: Part ibasic methodology, Journal of Engineering for Power 104 (1) (1982) 154–161.

[6] N. Cumpsty, A. Heyes, Jet propulsion, Cambridge University Press, 2015.

[7] P. Newton, G. Lock, S. Krishnababu, H. Hodson, W. Dawes, J. Hannis, C. Whitney, Heat transfer and aerodynamics of turbine blade tips in a linear cascade, Journal of Turbomachinery 128 (2) (2006) 300–309.

[8] R. Dénos, G. Paniagua, Effect of vane-rotor interaction on the unsteady flowfield downstream of a transonic high pressure turbine, Proceedings of the Institution of Mechanical Engineers, Part A: Journal of Power and Energy 219 (6) (2005) 431–442.

[9] R. Miller, R. Moss, R. Ainsworth, C. Horwood, Time-resolved vane-rotor interaction in a high-pressure turbine stage, Transactions-American Society of Mechanical Engineers Journal of Turbomachinery 125 (1) (2003) 1–13.

[10] S. Thorpe, S. Yoshino, R. Ainsworth, N. Harvey, An investigation of the heat transfer and static pressure on the over-tip casing wall of an axial turbine operating at engine representative flow conditions.(ii). time-resolved results, International journal of heat and fluid flow 25 (6) (2004) 945–960.

[11] V. Shyam, A. Ameri, J.-P. Chen, Analysis of unsteady tip and endwall heat transfer in a highly loaded transonic turbine stage, Journal of Turbomachinery 134 (4) (2012) 041022.

[12] S. Lavagnoli, G. Paniagua, M. Tulkens, A. Steiner, High-fidelity rotor gap measurements in a short-duration turbine rig, Mechanical Systems and Signal Processing 27 (2012) 590–603.

[13] C. De Maesschalck, S. Lavagnoli, G. Paniagua, T. Verstraete, R. Olive, P. Picot, Heterogeneous optimization strategies for carved and squealer-like turbine blade tips, Journal of Turbomachinery 138 (12) (2016) 121011.

[14] C. Sieverding, T. Arts, The vki compression tube annular cascade facility ct3, in: ASME 1992 International Gas Turbine and Aeroengine Congress and Exposition, American Society of Mechanical Engineers, 1992, pp. V005T16A001–V005T16A001.

[15] G. Paniagua, C. Sieverding, T. Arts, Review of the von karman institute compression tube facility for turbine research, in: ASME Turbo Expo 2013: Turbine Technical Conference and Exposition, American Society of Mechanical Engineers, 2013, pp. V03CT14A031–V03CT14A031.

[16] V. Andreoli, S. Lavagnoli, G. Paniagua, V. F. Villace, Robust model of a transient wind tunnel for off-design aerothermal testing of turbomachinery, Measurement 82 (2016) 323–333.

[17] S. Lavagnoli, C. De Maesschalck, V. Andreoli, Design con-

siderations for tip clearance control and measurement on a turbine rainbow rotor with multiple blade tip geometries, Journal of Engineering for Gas Turbines and Power 139 (4) (2017) 042603.

[18] S. Lavagnoli, G. Paniagua, C. De Maesschalck, T. Yasa, Analysis of the unsteady overtip casing heat transfer in a high speed turbine, Journal of Turbomachinery 135 (3) (2013) 031027.

Determination and modeling of the aero-thermal behaviour of a cooling channel

Gian Luca Gori

Turbomachinery and Propulsion Department, von Karman Institute for Fluid Dynamics, Belgium, gian.luca.gori@vki.ac.be

Supervisor: Tony Arts

Professor, Turbomachinery and Propulsion Department, von Karman Institute for Fluid Dynamics, Belgium, arts@vki.ac.be

Abstract

Internal Cooling technology for Gas Turbines, although supported by wide literature, still present possible important improvements. The classical CFD codes, based on constant Pr_t and isotropic turbulence, present a limited fidelity for the convective heat transfer prediction (at best 10-15%). The innovative contribution of flow temperature data by Laser-Induced Fluorescence will bring important information and likely help the development of the current numerical tools.

Keywords: turbomachinery, convective heat transfer, internal cooling

1. Introduction

The present research on cooling channels focuses on an aeronautical application (gas turbine), but is of definite interest to many other fields of engineering (oil industry, automotive, nuclear environments). The performance, in terms of thermal efficiency and specific power of a gas turbine cycle, increases with the TIT (Turbine Inlet Temperature). The limits are set by the blades and endwalls material resistance against thermal and mechanical loads. The life time of these components will increase by using efficient cooling techniques, cutting down the high costs for parts replacements. An example of an air cooled blade and its cross section is given in Fig. 1. A major contribution to the heat extraction is given by forced convection in internal passages.

The main objective of internal cooling channels is to maximize the wall heat transfer while keeping the channel pressure drop as low as possible. Initially designed with smooth walls, their surface has rapidly been equipped with various obstacles to increase the thermal exchange area and the local mixing. The resulting flow field is strongly 3D and unsteady [1] [2]; it becomes even more heterogeneous when the channel is put into rotation (rotor blades application)[3]. The strong assumptions of isotropic turbulence and constant Pr_t limit the accuracy of the heat transfer prediction (at best 10-15%) by CFD. The lack of experimental data due to the complexity and the availability of representative facilities, certainly, does not help for numerical improvements. The present research wants to contribute at providing high quality and high resolution experimental data acting directly on the causes of the CFD low fidelity.

Unlike most of the investigations available in literature, not only the wall heat transfer and velocity fields, but also the flow temperature distribution will be object of this experimental study. Although for velocity and surface heat transfer measurements, Particle Image Velocimetry (PIV) and Liquid Crystal Thermography (LCT) are already consolidated and largely used techniques [4], a few Cold Wire measurements were strongly dependent on the position of the probe [5]. They are also able to measure only temperature fluctuations related to the small vorticies. Therefore, Laser-Induced Fluorescence (LIF) has been selected for two dimensional non-intrusive temperature measurements. The technique is a spectroscopic method based on the spontaneous emission of molecules after the excitation by a laser pulse. Never applied for internal cooling research so far, it will need to be developed for this specific application.

Neglecting the fluorescence re-absorption and the

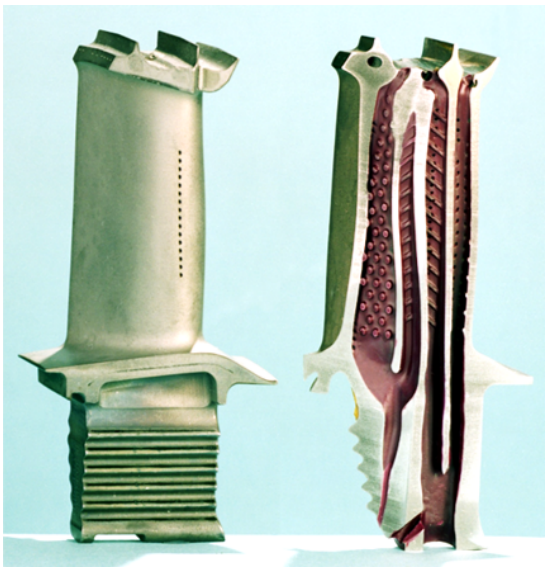

Figure 1: An air-cooled HP turbine blade and its cross-section.

Beer's attenuation, a simplified expression of the signal intensity I_f in function of the emitted wavelength λ and absolute temperature T is given by Eq. 1 [6] :

$$I_f(\lambda) = K_{opt}(\lambda)K_{spec}(\lambda)V_c I_1 C e^{\beta(\lambda)/T} \quad (1)$$

where K_{opt} is an optical constant, V_c the measuring volume, I_1 the incident laser intensity, C the molecular concentration of the fluorescent tracer, K_{spec} and β constants related to the spectroscopic and physical properties of the target molecule. More details on the different contributions and parameters dependencies are presented in Ref. [7]. The final output, registered by a detector, is an image with a signal given by the integral of the expression in Eq. 1 all over the spectra.

The signal obtained by a single camera, therefore, does not depend only on temperature but also on the intensity of the laser pulse and the concentration of the tracer. Information of the local temperature might be retrieved by the so called single-line approach. However, problems occur if concentration and/or laser intensity vary in space and/or in time and these variations can not be neglected or properly taken into account. The latter issues disappear when two or more ground states are observed. The method is called multi-line approach. It requires two or more excitations and/or two or more spectral channels. A double detection and single excitation, the so-called two-color method, is normally a good compromise for keeping the set-up as simple as possible. On the other hand, approaches which use more than two ground states are usually considered worthless [7]. Compared to dual-excitation (e.g. [8]) two-color LIF requires only one laser source [9]. The ratio calculated between the intensity recorded of two different spectral bands cancels out the dependence of I_1 and C (Eq. 2).

$$R_f(T) = \frac{I_{f,1}}{I_{f,2}} = \frac{K_{opt,1}}{K_{opt,2}} exp\left(\frac{\beta_1 - \beta_2}{T}\right) \quad (2)$$

The $I_{f,1}$ and $I_{f,2}$ are the intensity of the light seen by the two cameras provided by two different colored filters. A temperature calibration is still required for determining the constant $K_{opt,1}/K_{opt,2}$. The technique takes into account two different spectral bands of the emitted fluorescence for the two cameras, taking the name of two-color LIF. The selection of these two spectral bands defines respectively the parameters β_1 and β_2. They represent the single temperature sensitivities of the spectral bands 1 and 2. Therefore, as discussed in [10], in order to obtain a high temperature dependence of R_f, the difference $(\beta_1 - \beta_2)$ should be as large as possible. Although the two-color approach looks always more convenient than one-color measurements, the relative uncertainty at least doubles due to the lower temperature dependence [11]. Therefore, it is important to evaluate the real need of two ground states by looking at the uniformity of the fluorescent molecule within the field of view.

If the flow under investigation does not contain any fluorescent molecules, a proper dye must be added to the main flow. The objective is to create a well-mixed flow which allows the measurements without modifying the physics. For heat transfer and temperature determination both Re and Pr numbers of the experiments should match the real operating ones. Although Re can be adjusted by modifying the flow velocity, Pr is a property of the working fluid that needs to be carefully taken into account. For the specific application of air-cooled HP turbine blades the working fluid is represented by part of air bled from the compressor. Although in literature liquid-phase PLIF is more developed than gas-phase PLIF, the latter is preferable in order to represent correctly the same physics. The choice of the fluorescent tracer influences the accessible temperature range as well as the evaluation procedure. Toluene and acetone are the most used tracers for gas-phase LIF thermography (e.g. [12][13][14][15]). Acetone started to be used for its high signal, low toxicity and low cost [16]. The absorption (between 200 and 350 nm) was measured in 1992 by Lozano [17] and in 1996 again by Thurber [8]. The emission, instead, occurs between

300 and 550 nm [18]. The air-acetone vapor mixture *Pr* has been investigated numerically by the NASA CEA algorithm [19] based on equilibrium and assuming frozen reaction. With a maximum tracer concentration of 15% in volume the computed *Pr* varies less than 5% to the one of air at ambient condition. Toluene have been characterized later in [20] [21] with his absorption (240-290 nm) and the emission (250-350 nm) as well as the oxygen quenching (not present for acetone). In this case the concentration needs to keep lower than 9% in volume in order to limit the variations of *Pr*. The red shift of toluene made this tracer suitable for two-color thermography. For both acetone and toluene, the time required for the vapor sublimation is relative short which makes the seeding procedure simple [22] [14]. In particular, the discussion of the preliminary results will analyse pro and cons of acetone and toluene. Details of the characteristics of fluorescent tracers used for gas-phase thermography are referred to Ref. [23].

Acetone vapor mixed with air was selected as the working fluid for the preliminary study for simplicity as well as the aforementioned advantages. Toluene present possible re-absorption of the emitted light, quenching by oxygen and deeper UV fluorescence spectra. However, the discussion of the preliminary results will show the low relevance of this drawbacks compared to the possible improvements.

Since most of the studies are performed in internal combustion engines or other applications where a calibration in situ is really difficult in order to retrieve the correct temperature some alternative methods were developed [24]. However, the field does not require accurate absolute temperature [25]. For the specific application, instead, a proper temperature calibration needs to be carried out. The methods of image processing are explained, discussed and compared for one- and two-color LIF thermography in [11].

2. Preliminary study

In a first step, a static cell was built in order to investigate suitable LIF tracers (Fig. 4). The test section is $50x50mm^2$, $90mm$ height. The structure is composed by two main parts in order to have a complete access inside (manly for spatial calibration and cleaning). In the bottom part a small tap allows to introduce the tracer with a syringe. On top of that a fan take place (black rectangle) in order to mix properly the air with the vaporized tracer. The pressure was monitored by a water manometer to estimate the vapor concentration inside the cell. Four thermocouples probes, previously calibrated, were installed to monitor the temperature at the same high of the laser beam. The top part is composed by five aluminum walls. The four lateral ones have a quartz window for the laser and the cameras optical accesses, each of them sealed with two o-rings and a thin screwed plate. The 2 parts were fixed by a clamp in order to press the lateral walls on the seal gum placed in the groove of the bottom part. Then, all the external walls were thermally insulated by a 15 mm thickness foam.

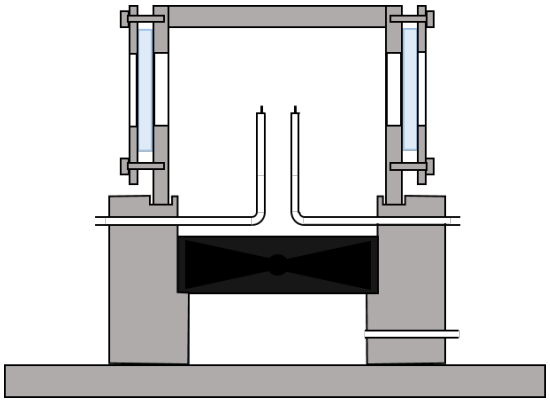

Figure 2: Sketch of the measurement cell.

2.1. Two-color acetone calibration measurements

The objective of the present campaign was to link an intensity ratio to the assumed uniform temperature inside the cell; this defines the sensitivity of the measurements. According to some available data of the emission spectra of acetone and toluene, two-color acetone LIF thermography was performed. An analysis was conducted to select the proper filters to place in front of the two cameras of the experimental set-up in Fig. 4. The two spectral bands were selected in the way suggested in [10] to maximize the sensitivity $(\beta_1 - \beta_2)$. Different possible couples of filters were first evaluated numerically and finally the SHX350 and the XUL0385 units from Asahi Spectra were used.

The two-color technique requires two detectors (Lavision Imager Intense) and one excitation source (Fig. 3). The latter was provided by a Nd:Yag laser (Quantel Big Sky Laser) with 266 nm wavelength pulses of 33 mJ and 532 nm wavelength pulses of 180 mJ. Two dichroic mirrors at 45° allow to decrease the green component of the beam entering in the test section. Acetone, as the majority of organic molecules, does not feature absorption at 532 nm and additional high energy light only produces undesirable reflections. After the dichroic mirrors the beam

passes through a fused-silica spherical lens in order to focus the beam in the center of the cell. An important consideration goes to the location of the two cameras. Indeed, they should observe as better as possible the same area of interest. This is not a big issue for these uniform static measurements but it will be really important for the 2D temperature distribution where accurate temperature gradients are required. In order to decrease the number of degrees of freedom and to use only one camera lens, the detection is sketched in Fig. 4. The light coming from the investigated area is focused by an UV 100 mm camera lens and divided by a ND filter positioned at 45°. The two colored filters are mounted directly in front of the 2 sensors. Camera 2 is also provided with a stopband filter (500-600 nm) in order to cut down the remaining green laser scattered light. A bellow mounted between the splitter cage and the Camera 1 allows the focusing of both detectors at the same time. A series of 400 pictures were taken at a 3 Hz repetition rate of the laser for every different temperature inside the cell. Binning of 8 by 8 pixels was used to maximize the signal. Temperature was increased by heating up the aluminum bottom wall. During the measurements an acquisition system recorded the signal of the four thermocouples triggered by the first flash lamp of the laser with a frequency of 300 Hz. The required data was derived, finally, through the processing of the images and the thermocouple signals.

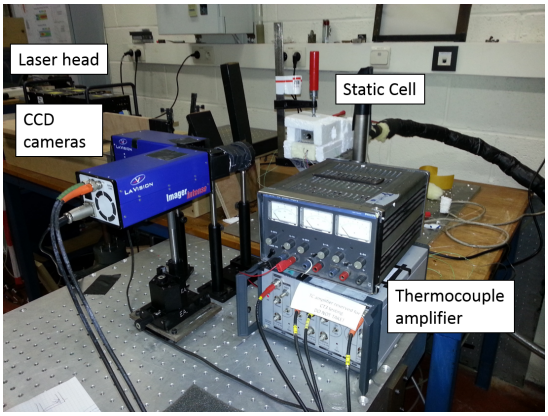

Figure 3: Experimental set-up used for two-color acetone PLIF for uniform temperature measurements.

The image processing is always more relevant in optical techniques for high quality data. It was performed entirely in Matlab. The first operation was the background subtraction where 10 averaged images were taken in the absence of the tracer. Although the signal was corrected by undesirable reflections of the

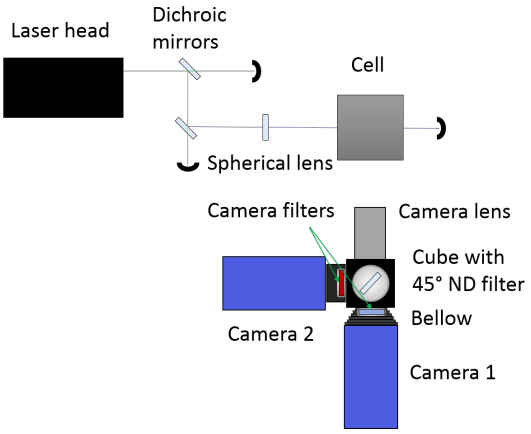

Figure 4: Set-up sketch.

laser light, possible scattering of acetone vapor and internal fluorescence reflections were not taken into account. After that, the spatial calibration was applied thanks to the pictures of a target placed at the same position of the laser beam. Translation, rotation and magnification were used to match exactly the two fields of view. In order to have the corresponding pixels at the same location, a linear interpolation was applied to all the images. It have been seen that, in these measurements, the more accurate the calibration is, the more uniform R_f gets in the field of view. If there is not exact matching of the two pictures the calibration formula for the determination of the temperature in function of R_f must change within the region of interest. A secondary effect is represented by the real spatial resolution of the measurements which increases with higher mismatch. After this operation, the intensity ratio was computed in every location of the laser beam. The mean and the standard deviation were obtained both for spatial and time dimensions. Mean and standard deviation of the thermocouples were also computed in order to assess the spatial uniformity and the variation of temperature during the single experiments. The methodology was designed to evaluate the performance of the measurement technique.

The results of the experimental campaign are summarized by Fig. 5. The ratio between the two camera intensities is represented for a specific position in function of the mean temperature inside the cell during the specific experiment. The location was chosen in the middle of the laser beam where the fluorescence intensity is higher and the data are more reliable. A strong dependence with temperature can be seen be-

tween the six experiments. At the maximum investigated temperature ($98°C$) the value of the intensity ratio drops by 46% of the one recorded at $48°C$. The uncertainty on the intensity ratio was computed by the standard deviation recorded by the 400 images taken for each experiment. This results in 7.3% of the intensity ratio for a confidence level of 95%. It turns that temperature may be determine, inversely, with an uncertainty of $\pm 8°C$. This value of uncertainty needs to be compared with the measurement range in a specific application. The bigger the range, the smaller the effect of the uncertainty on the measurements. Thus, for a measured range of $100°C$ the uncertainty will count 8%. The main contribution on the error is given by the so-called camera *shot noise*. Its effect on the measurements can be limited only by increasing the signal itself. The energy fluctuations of the laser pulses were not quantified. However, the method is theoretically not affected by these variations. During the experiments the thermocouples have shown variations between 1 and $1.8°C$, whereas dis-uniformity in the spatial dimension are at maximum $0.8°C$.

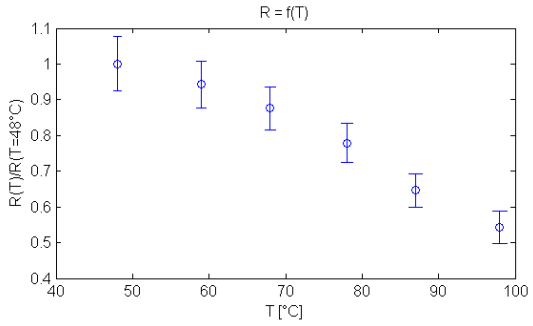

Figure 5: Normalized Intensity Ratio in function of the operating temperature inside the cell.

The presented results represent a starting point for the final objectives of this research project. The presence of an important temperature dependence of the intensity ratio is encouraging for detecting the thermal boundary layer in internal flow applications. Furthermore, the experiments put in evidence some aspects which needs to be discussed:

- the signal is very low (order of 200/4065) and, therefore, the noise acts an important role for the determination of the measurement uncertainty;
- there is not scientific evidence about the dependence with temperature discovered. The filters applied for these measurements were expected to provide a maximum variation of 10% of the signal within $100°C$ variation. The data present in literature of acetone do not show different shape of the spectral emission at different temperatures. Further investigations are, therefore, required to give an explanation to the phenomenon encountered.

For what concerns the low signal, it needs to be amplified. Therefore, either the cameras will be provided by two intensifiers or they will be replaced by ICCDs. In this way, although the *shot noise* will be amplified together with the signal, the *read out noise* will account less to the measurement uncertainty. The second point opened the will of testing more accurately the acetone emission spectra in order to improve the understanding of the spectroscopic features of the selected tracer.

2.2. Acetone spectral measurements

Concerning the unexpected behavior of acetone during the previous experiments and ignoring possible other physical effects, the investigation of the fluorescence emission spectra of acetone was needed in order to explain what was found in the previous section. The measurement cell was kept exactly the same. The detection system of Fig. 4 was replaced by a spectrometer (PI Acton Sp2750) connected to an ICCD camera (PI-MAX 3). In addition to that, a laser energy monitor was added to the system (Fig. 6). A small portion (15%) is reflected by a quartz plate. More attenuation optics were placed in front of a photodiode as well as a filter in order to get rid of the remaining green component. The photodiode produces a current proportional to the incident light. The output signal is synchronized with the laser Q-switch, gated and averaged by a Boxcar Averager (Stanford Research Systems). The laser provides high-energy pulses within 8 ns and it is impossible to detect the amount of light only by recording signal samples at less than 500 MHz. Therefore,the signal generated by the photodiode was integrated around the pulse. The output from the Boxcar Averager goes to an acquisition system to store the data. A reference of the laser power is provided for each pulse and this value was used to normalized the image intensities.

The wavelength full range recorded by the specific grating was about 100 nm. Four ranges were used to cover the entire spectral emission of acetone from 300 nm to 600 nm with an overlap of 20 nm. Binning of 2x2 was used leading to a resolution of 0.1

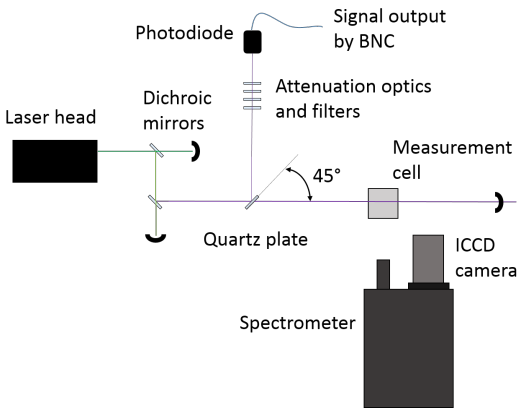

Figure 6: Spectral measurements set-up.

nm and 100 images were averaged. The temperature was kept at the same level while the four set of data were acquired. Together with the images, temperature from the four thermocouples, pressure and energy levels were recorded. The variation of pressure inside the cell is less than 2 Pa and, therefore, its effect on the measurements was neglected. The calibration of the system was performed using a halogen and deuterium lamp. Knowing the theoretical and the recorded signals the spectral calibration was applied after the background subtraction as described by Eq. 3:

$$S = (S_{rec} - BG)\frac{Cali_{rec} - BG}{Cali_{the}} \tag{3}$$

where S and S_{rec} are the calibrated and the recorded LIF signals, $Cali_{the}$ is the theoretical emission of the calibration lamp, $Cali_{rec}$ its recorded signal and BG the background image taken without tracer and related to the different spectral range used for the measurements.

All the measurement sets are taken to reconstruct the emission spectra of acetone. The plot in Fig. 7 represents the latter normalized with the peak value at each temperature. Except for some errors in the curve of $60°C$, the curves collapse in one. This plot explains that the shape of the fluorescence emission does not change with the temperature and neither a significant red shift (as for tracers like toluene and anisole) was recorded. Theoretically, acetone is not a proper tracer for two-color thermography since it shows the same temperature dependence at every wavelength. On the other hand, it does not explain the behavior observed in the previous experiments.

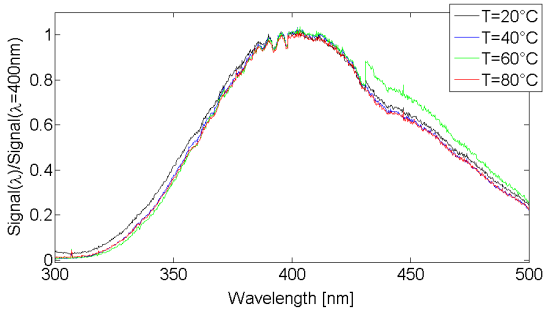

Figure 7: Acetone emission spectra normalized with ambient temperature in function of the cell temperature.

2.3. Discussion and Conclusions

There is no scientific evidence before these measurements of the encouraging trend of the acetone intensity ratio with temperature. Unfortunately, the experiment is not able to explain the observed phenomena and further assessments are required. However, the latter go out of the specific goal to bring a suitable tool for accurate temperature measurements in a cooling channel. It will be more useful to test the detection set-up for a continuous flow, out of phenomena as tracer aging and significant variation of concentration during the experiments. A calibration in situ, required for accurate measurements, may reveal its real feasibility. The one-color approach and toluene as a tracer are the alternatives already tested and used in literature. The reason why this project did not consider them before is given by the more toxicity and the signal quenching by oxygen related to toluene together with the necessity to take into account the laser power fluctuations and the possible variation of tracer concentration. However, these difficulties are already overcome by looking at the toluene signal in air and the energy monitor built for the present campaign.

3. Facility

According to the conclusions of the preliminary study a more complex set-up was required to test the technique in a continuous flow. The global work of the design is represented by the 3D view of the facility in Fig 8.

The purpose is to perform experiments in an internal 2D flow. The test rig is an already existing model which presents a cross section of $240x40mm^2$, therefore, with a *channelaspectratio* of 6. Figure 9 shows it combined with some additional ducts, the settling chamber and the contraction designed at VKI for the

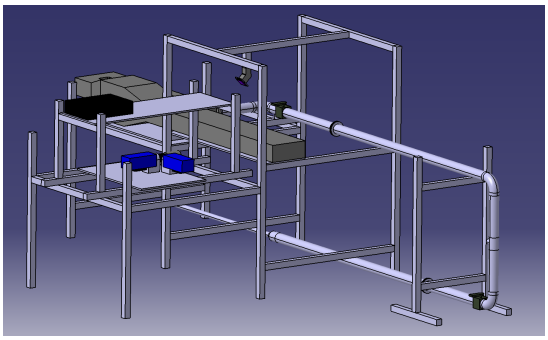

Figure 8: PLIF facility.

RC-1 facility. The channel, as all the structure of the wind tunnel, is made of aluminum. Four optical windows allow the accesses of the light source and the camera. The decision of their streamwise location allows characterizing both the inlet and the fully developed region. Originally made of plexiglass, they have been replaced with quartz plates for the UV components of the laser light and the emitted fluorescence. The bottom wall will be heated up with thin resistances (Minco HAP6949). The goal is to obtain the temperature profiles in order to compare the data with DNS available in literature and some cold wire measurements. In order to match the *Reynolds number* based on the *momentum thickness* of the DNS data ($Re_\theta = 400$), the obtained bulk velocity is 2.63 m/s leading to a mass-flow about 1.8 kg/min. It is, therefore, required to generate the flow inside the test section including the selected fluorescent dye.

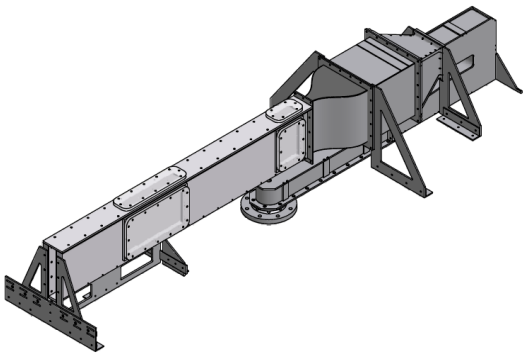

Figure 9: Wind tunnel.

As discussed in the introduction it is also important to monitor the concentration of the tracer in order to keep the *Prandtl number* as close as possible to the real case. Thus, two mass-flow meters will be required to control both the mass-flow and the dye concentration. The LIF flow generator is sketch in Fig. 10. The air is taken from the 7 bar compressed line of the VKI. The flow splits in two branches. One of those passes through the seeder and the other one has the purpose to dilute the mixture. They merge and are connected to the inlet of the wind tunnel. The pipes are made of PE100 Black, resistant to pressurized air up to 16 bars and able to withstand both acetone and toluene vapors. The internal diameter is a DN50 mm. The length of the pipes is determined by the upstream and downstream constraints for the mass-flow meters given by the British Standards [26]. In order to measure such low mass-flow, orifice plates with a diameter ratio of 0.6 have been selected [27], producing pressure drops of the order of 10 mbar. The latter is measured by Validynes Differential Pressure Transducers which also monitor the pressure upstream each orifice plate. Together with the temperature obtain by a thermocouple far downstream, the air density is computed. The NI cDAQ-9174, through the modules NI 9215 and NI 9212, acquires all these data. With a home written LabView code the mass-flow and the tracer concentration can, therefore, be monitored in real time. By changing the position of the valves iteratively these two values are adjusted.

The supports hold both pipes, test section and the required equipment for the measurements. The laser is mounted on a plate supported by posts fixed to the camera structure. The advantage is, once the set-up is aligned, the illumination moves horizontally with the field of view of the detectors. On the laser support the required optics are placed and the laser beam is projected vertically by a UV enhanced mirror hanged on a horizontal support.

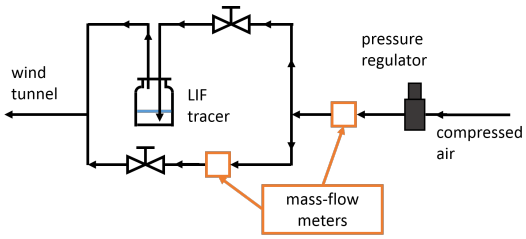

Figure 10: Flow sketch.

In order to characterize the flow inside the test section some PIV measurements have been performed. Fig. 11 represent the streamwise velocity profile non-dimensionalized by the maximum velocity in the middle of the channel. A shape factor of 1.4 is the confirmation of a fully turbulent boundary layer. In order to see if the flow was fully developed the Reynolds

stresses are plotted in Fig. 12. The linear behavior verifies the statement. This plot also allowed to determine the friction velocity and to represent the boundary layer with the u^+ and y^+ coordinates. Fig. 13 shows a good agreement with the logaritmic law obtained with typical constants for internal flows (k=0.37, B=5.1).

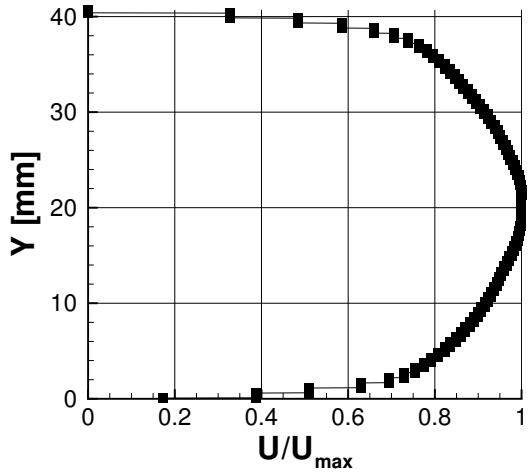

Figure 11: Non-dimensional streamwise velocity inside the channel.

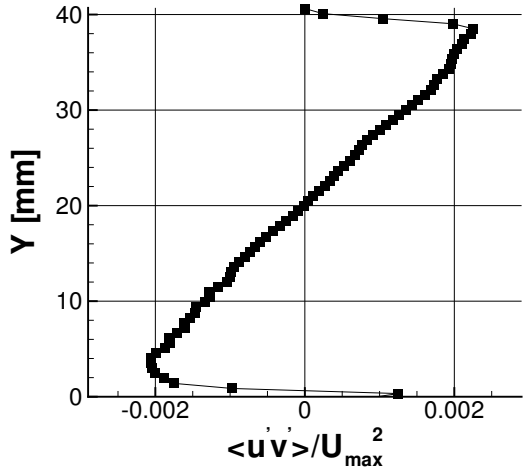

Figure 12: Non-dimensional Reynolds stresses profile inside the channel.

The facility have been recently used for one-color LIF thermography and traverse measurements with a probe thermocouple in order to compare immediately the temperature profiles. However the data acquired still need a further post processing in order to be presented. The other approaches presented in the document will be tested as well to evaluate advantages and drawbacks of both. Considering the high cost of the image intensifiers it is possible to split the camera sensor of the ICCD (previously used in the spectral measurements) to provide the two path with the LIF filters. The in-situ calibration will be also introduced. Once the temperature measurements are optimized the system will be embedded with PIV set-up before going for a more realistic geometrical configuration.

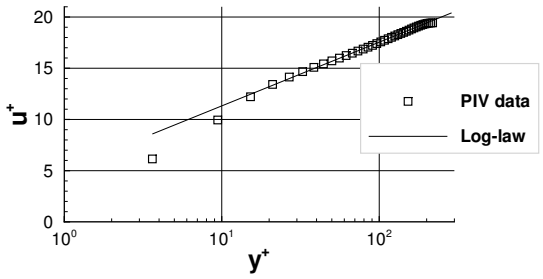

Figure 13: Comparison of the velocity boundary layer with the logaritmic law.

4. Conclusion

Evidence of the importance of flow temperature measurements in cooling technology have been discussed. LIF thermography will be introduced being 2D and non intrusive measurement technique. Some preliminary results, in a static and uniform temperature cell, showed the feasibility the method. Remarks and possible improvements of the measurements were largely treated in the present documents. Constraints and difficulties of the application have been discussed identifying suitable alternatives for the next step. The investigation of the thermal boundary layer for a 2D internal flow needs to be carried out at the moment. A facility have been designed completely for the purpose. Soon after, the set-up will be embedded with the PIV equipment in order to obtain the turbulent heat transport term $\overline{v'T'}$, required for the determination of Pr_t.

Both one-color and two-color approaches will be used and compared in order to select the most performant methodology. A parametric study of the measurement settings will be required, optimizing the appropriate time and spatial resolution together with the accuracy and measurement constraints. The final results will be compared with the available DNS data in literature. It is also in the plan to perform some Cold Wire measurements in the same test section. For

the latter, the test rig will need some modification. It will be also important to evaluate the feasibility of the measurements in the case of a rib-roughened wall (real application). Some obstacles will be introduced in the smooth channel to enhance the mixing.

Considering the encountered issues of the measurement technique in the early research as well as in literature, an in-situ calibration methodology will be introduced. The latter will require an adaption of the facility in order to produce a flow characterized by uniform and adjustable temperature. The test are expected to improve considerably the results quality and measurement uncertainty.

The PIV system will be embedded just after and another measurement campaign will be performed. As before, a careful data processing and analysis will be required. The turbulent Prandtl number determination will be attempted afterwards. Data will be analyzed with the purpose of the modeling contribution already underlined several times.

In summary, the present investigation will cope with the issues on heat transfer prediction by looking directly at the major causes of the numerical and experimental data discrepancies. The aerodynamic and thermal analysis will provide a physical explanation of the complex phenomena of forced convection. The innovative, high quality and high resolution data of the present research will represent a suitable tool for CFD codes validation and modeling improvements.

Acknowledgments

The funding of this PhD research project through a FRIA grant, delivered by the Fonds de la Recherche Scientifique (FNRS), is gratefully acknowledged.

References

[1] L. Casarsa, T. Arts, Experimental investigation of the aerothermal performance of a high blockage rib-roughened cooling channel, Journal of Turbomachinery 127 (2005) 580–588.

[2] N. D. Cardwell, P. P. Vlachos, K. A. Thole, Developing and fully developed turbulent flow in ribbed channels, Exp Fluids 50 (2011) 1357–1371.

[3] I. Mayo, G. Luca Gori, A. Lahalle, T. Arts, Aerothermal characterization of a rotating ribbed channel at engine representative conditions–part i: High-resolution particle image velocimetry measurements, Journal of Turbomachinery 138 (10) (2016) 101008–101008–9. doi:http://dx.doi.org/10.1115/1.4032926.

[4] P. Ligrani, Heat transfer augmentation technologies for internal cooling of turbine components of gas turbine engines, International Journal of Rotating Machinery 2013.

[5] T. Arts, M. T. Abad-Lozano, Y. Kinoue, S. Pierret, The unsteady temperature field in a turbine blade cooling channel, RTO AVT Symposium, 2001.

[6] F. Lemoine, Y. Antoine, M. Wolff and M. Lebouch, Simultaneous temperature and 2D velocity measurements in a turbulent heated jet using combined laser-induced fluorescence and LDA, Experiments in Fluids 26 (1999) 315–323.

[7] A. Y. C. Tropea, J. Foss, Handbook of Experimental Fluid Mechanics, Springer, 2007.

[8] M. C. Thurber, F. Grisch and R. K. Hanson, Temperature imaging with single- and dual-wavelength acetone planar laser-induced fluorescence, Optics Letters 22 (4) (1996) 251–253.

[9] M. Luong, W. Koban and C. Schulz, Novel strategies for imaging temperature distribution using Toluene LIF, Journal of Physics: Conference Series 45 (2006) 133–139.

[10] P. Lavieille, F. Lemoine, G. Lavergne and M. Lebouch, Evaporating and combusting droplet temperature measurements using two-color laser-induced fluorescence, Experiments in Fluids 31 (2001) 45–55.

[11] B. Peterson, E. Baum, B. Böhm, V. Sick, A. Dreizler, Evaluation of toluene lif thermometry detection strategies applied in an internal combustion engine, Applied Physics B 117 (1) (2014) 151–175. doi:http://dx.doi.org/10.1007/s00340-014-5815-0.

[12] S. P. Kearney and F. V. Reyes, Quantitative temperature imaging in gas-phase turbulent thermal convection by laser-induced fluorescence of acetone, Experiments in Fluids 34 (2003) 87–97.

[13] Lei Shi, Xiaoan Mao and Artur J Jaworski, Application of planar laser-induced fluorescence measurement techniques to study the heat transfer characteristics of parallel-plate heat exchangers in thermoacoustic devices, Measurement Science and Technology 21 (2010) 116.

[14] V. A. Miller , M. Gamba, M. G. Mungal and R. K. Hanson, Single- and dual-band collection toluene PLIF thermometry in supersonic flows, Experiments in Fluids 54 (2013) 1539–1551.

[15] C. Gessenhardt, C. Schulz and S.A. Kaiser, Endoscopic temperature imaging in a four-cylinder IC engine via two-color toluene fluorescence, Proceedings of the Combustion Institute 35 (2014) 36973705.

[16] M. C. Thurber, F. Grisch, B. J. Kirby and M. Votsmeier, Measurements and modeling of acetone laser induced fluorescence with implication for temperature imaging diagnostics, Applied Optics 37 (21) (1998) 4963–4978.

[17] A. Lozano, Laser-excited luminescent tracers for planar concentration measurements in gaseous jets, Ph.D. thesis, Stanford University (1992).

[18] R. A. Bryant, J. M. Donbar and J. F. Driscoll, Acetone laser induced fluorescence for low pressure/low temperature flow visualization, Experiments in Fluids 28 (2000) 471–476.

[19] S. G., B. J. McBride, Computer Program for Calculation of Complex Chemical Equilibrium Compositions and Applications, Nasa Reference Pubblication 1311, NASA (1994).

[20] W. Koban, J. D. Koch, R. K. Hanson and C. Schulz, Absorption and fluorescence of toluene vapor at elevated temperatures, Phys. Chem. Chem. Phys 6 (2004) 2940–2945.

[21] W. Koban, J. D. Koch, R. K. Hanson and C. Schulz, Oxygen quenching of toluene fluorescence at elevated temperatures, Applied Physics B 80 (2005) 777–784.

[22] M. C. Thurber, Acetone Laser-Induced Fluorescence for temperature and multiparameter imaging in gaseous flows, Ph.D. thesis, Stanford University (1999).

[23] S. Faust, M. Goschütz, S. A. Kaiser, T. Dreier, C. Schulz, A

comparison of selected organic tracers for quantitative scalar imaging in the gas phase via laser-induced fluorescence, Applied Physics B 117 (2013) 183–194.

[24] K. Tran, P. Guibert, C. Morin, J. Bonnety, S. Pounkin, G. Legros, Temperature measurements in a rapid compression machine using anisole planar laser-induced fluorescence, Combustion and Flame 162 (10) (2015) 3960 – 3970. doi:http://dx.doi.org/10.1016/j.combustflame.2015.07.033.

[25] S. Kaiser, M. Schild, C. Schulz, Thermal stratification in an internal combustion engine due to wall heat transfer measured by laser-induced fluorescence, Proceedings of the Combustion Institute 34 (2) (2013) 2911 – 2919. doi:http://dx.doi.org/10.1016/j.proci.2012.05.059.

[26] B. Standards, Measurements of fluid flow by means of pressure differential devices inserted in circular cross-section conduits running full - Part 1: General principles and requirements, Standard BS EN ISO 5167-1:2003, European Committee for Standardization (2003).

[27] B. Standards, Measurements of fluid flow by means of pressure differential devices inserted in circular cross-section conduits running full - Part 1: Orifice plates, Standard BS EN ISO 5167-2:2003, European Committee for Standardization (2003).

Advanced experimental aero-thermal investigations of wall-bounded swirling flows in three-dimensional ribbed tubes

Marco Virgilio

Turbomachinery and Propulsion Department, von Karman Institute for Fluid Dynamics, Belgium, marco.virgilio@vki.ac.be

Supervisor: Tony Arts

Professor and Head of Department, Turbomachinery and Propulsion Department, von Karman Istitute for Fluid Dynamics, Belgium, tony.arts@vki.ac.be

University Supervisor: Kevin Van Geem

Professor, Laboratory for Chemical Technology, Universiteit Gent, Belgium, Kevin.VanGeem@UGent.be

Abstract

The effects of helical ribs on both the flow field and the heat transfer have been investigated experimentally in circular cross section channels. Stereoscopic Particle Image Velocimetry (S-PIV) was applied in order to measure the 3 components of the mean and turbulent velocities. Moreover, steady-state Liquid Crystal Thermography (LCT) and Infrared Thermography (IRT) were used for studying the forced convection on the wall. In this paper, high turbulent kinetic energy and heat exchange are shown a few rib heights downstream of the obstacles.

Keywords: Helical ribs, Flow Field, Heat Transfer, Stereoscopic Particle Image Velocimetry, Liquid Crystal Thermography

1. Introduction

In petroleum refinery and particularly in thermal cracking of hydrocarbons for the production of ethylene, the reactors expect short residence time for endothermic reactions, so a high rate of heat transfer is required. One of the solutions may be the use of pipe turbulators, as in Fig. **??**, whose faultlessness has been tested in commercial plants. Generally speaking, they disrupt the boundary layer at the wall and make the flow temperature profile to be more homogeneous. As a consequence, the coking rate is minimized, the cracking volume maximized and both the run length and the tube life are extended since the wall temperature is kept relatively low. Hence, similarly as in turbomachinery [1], local obstacles help to enhance the heat transfer in the reactor tubes. The knowledge gained from turbomachinery will be useful in this environment. As a matter of fact, there is a massive need for increasing the gas turbine efficiency by means of rising the flow temperature. To maintain the blade integrity, at least, internal cooling is needed. To improve the forced convection on the blade walls, the internal channels need to be ribbed in order to enhance the heat transfer. Although it has been demonstrated by several authors that the increase of the Nu number is about more than 1.5 times the one seen in a smooth tube at the same Reynolds and Prandtl numbers [2], the ribbing technique is limited by the rise in the friction losses [3]. Therefore, a multi-objective optimization design is a reasonable method which can find out the best solution to the problem stated before. Anyway, the optimization tool needs the use of a fluid dynamic solver which has to be able to well simulate the turbulent structures generated at the wall. In this case, Large Eddy Simulations (LES) are supposed to be the best choice in terms of quality, in comparison with RANS, and time-saving, instead of DNS. Therefore, the chosen sub-grid scale model needs to be validated by doing measurements of the turbulent swirling flows. Afterward, optimizing techniques can be carried on for the design of chemical reactors, turbines internal cooling channels or heat exchangers in a more general sense.

The present experimental investigation focuses on the aero-thermal characterization of a helically corrugated cylindrical cooling channel. Empirical correlations for the evaluation of the friction factor and Nusselt number for ribbed geometries were proposed by Ravigururajan and Bergles [4] and Pethkool et al. [5]. Nevertheless, the correlations are based on heat transfer measurements affected by a significant lack of information, since they are obtained by point-wise techniques. Garcia et al. [6] have already provided 2D-PIV data for helically corrugated ducts but for flows whose regimes are laminar and transient without any detailed info about the heat transfer. On the other hand, Bonanni et al. [7] provided the heat transfer coefficient over the full surface of a rib-roughened circular channel by using transient LCT. In that study, the obstacles were placed perpendicularly to the main flow direction. Recently, LES were performed by Zhu [8] in a configuration similar to the ones studied in the present paper.

The investigation will be done experimentally with Stereo-Particle Image Velocimetry to measure the flow field. It allows an accurate full-field evaluation of the mean flow quantities together with the turbulence statistics. Moreover, the secondary flows and vortical structures are solved and the results are matched with the associated heat transfer at the inner wall. The latter measurements have been carried out by means of steady-state LCT.

Actually, the ambition of this Ph.D. research is to continue the work made by Mayo et al.[2] and to extend the investigation also to three-dimensional turbulators, understanding the complexity of wall-bounded turbulent swirling flows. Therefore, a well-documented test case for high-fidelity computations will be provided.

2. Experimental Setup

2.1. Velocity measurement setup

The flow field measurements have been made in a low-speed water tunnel (Fig. 2). The flow is accumulated in a settling chamber and the water level is kept constant thanks to an adjustable overflow channel which works as a by-pass. In such a way, the total inlet pressure can be chosen and kept constant, which means steady boundary conditions. The mass flow, chosen during the experiments, corresponds to a turbulent flow Reynolds number. Anyway, it is kept at low values, which are enough to allow corresponding LES computations. The water is discharged by the settling chamber into the inlet duct. In order to have the flow developed, the inlet section has a 150 mm internal diameter and a length of 15 diameters, according to Incropera [9]. Downstream of the inlet duct, there is the test section which is made of acrylic glass to obtain full optical access to the area of interest. The turbulence generator tested is made of ABS (Acrylonitrile Butadiene Styrene) and it is manufactured according to the stereolithography.

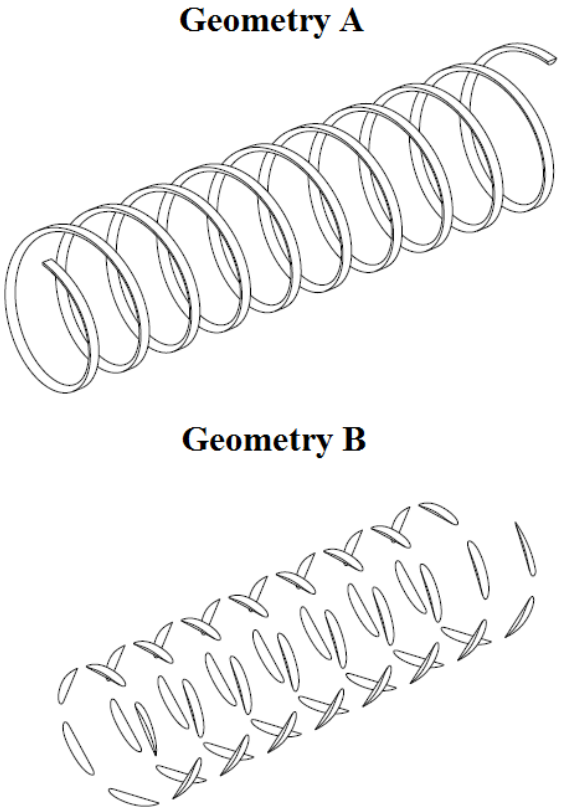

Figure 1: Obstacles of the ribbed channel

Initially, the rib tested by Mayo et al. (Geometry A) consisted in a semi-circle section swept throughout a helical pattern tangentially to the inner surface of the cylinder under test. The helix has a pitch of 63 mm repeated for 10 times and an angle of attack of 82°, while the semi-circle section has a constant height-to-diameter of 3.6%. The turbulator (Geometry B) tested in this paper (Fig. 1) has the same helix parameters stated before but the semicircle swept has a height which is changing through the helical pattern. The geometry of one obstacle is actually the solid intersection of the test section (i.e. a cylinder) with smaller cylinders (diameter of 10.8 mm) by moving their axes

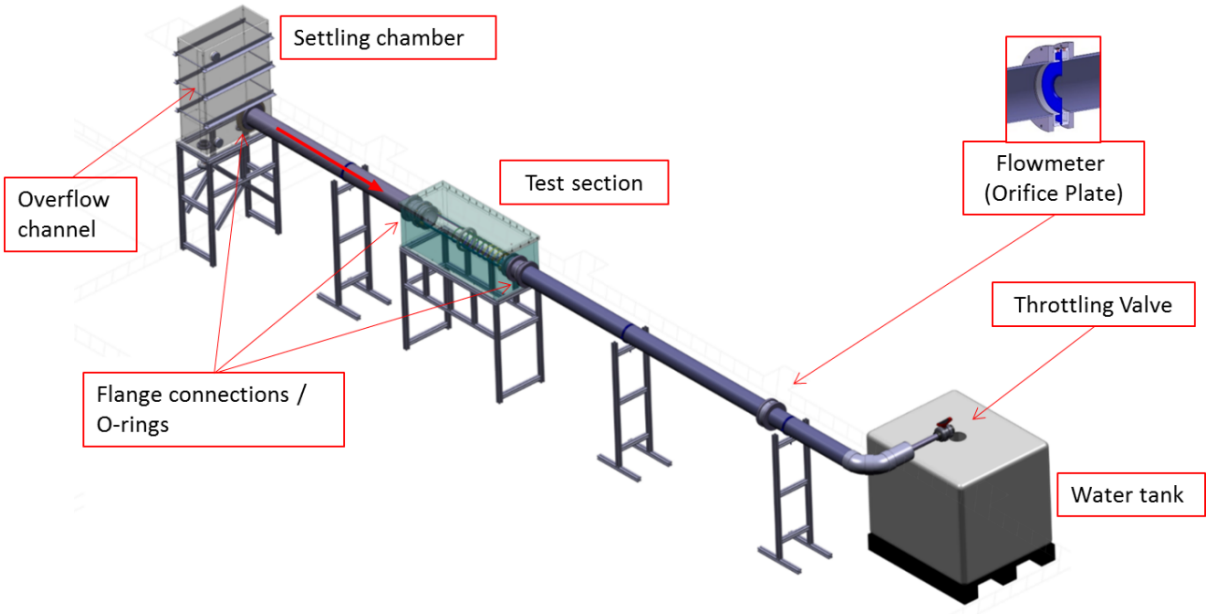

Figure 2: Facility for the S-PIV measurements.

in parallel . The intersection is made in order to have the maximum height-to-diameter of 3.6 % and a minimum of zero after a development of 20°in both the helix directions from the maximum height position on the surface. In such a way there are 6 obstacles in 1 helix pitch, and 50 obstacles in total, providing 8 full pitches. The start of the rib is located 440 mm downstream of the origin of the test section inlet. The S-PIV images are taken for the area between the obstacles far 5 and 6 times the pitch from the rib inlet. This choice has been taken by considering the fact that the typical development distance in low blockage ratio cooling channels is about 6 rib pitches [10]. To check the periodicity of the phenomenon, the same measurements have been made for the same area as before but switched of 1 pitch towards to the outlet of the ribbed test section. The channel is split longitudinally in two parts, to allow the spatial calibration of the 2 cameras. In order to match the refraction index of the solid wall and to minimize the images deformation, water has been chosen as working fluid. For the same reason as before, the test section is inserted into a transparent reservoir filled with water, in the interest of having a flat interface between the external air and the solid [11]. By measuring the static pressure drop given by an orifice plate, designed according to the ISO 5167 norm [12], it is possible to read the mass flow. The mass flow meter has been put 20 diameters downstream of the test section exit, and its dimensions have been chosen to minimize the relative measurement uncertainty, which turns to be 1.5% of the reading. A spherical valve is placed downstream of the orifice plate, allowing a coarse control of the flow regime. The fluid is finally collected in a large discharge chamber, and driven again to the settling chamber by means of a pump.

The investigated areas are illuminated by a Quantel Tween BSL 200 double pulse Nd:YAG laser which provides 70 mJ per pulse, that is the 33% of the nominal laser power. The combination of a telescope (focal length range of 300mm-2m), a cylindrical lens (20mm) and a mirror makes a focused light sheet of about 1 mm thickness to cover the region of interest between two obstacles. Two double-shutter CCD cameras with a sensor of 2360 x 1776 pix^2 are placed on the same side of the test section and equipped with Nikon Nikkor lenses of 50 mm focal length set to f/8. This choice of the cameras lenses (50 mm) let the image particle sizes to be between the range 2-5 pixels, which is optimal for minimizing the uncertainty coming from the cross-correlation algorithm [13]. In the interest of having a focused image all over the measurement plane, a Scheimpflug mount is used for each camera [14]. Most of the time, the angle between the cameras optical axes and the horizon is chosen to be 45°. Generally, bigger the angle, bigger is the sensitivity to the velocity components perpendicular to the laser sheet. On the other hand, the uncertainty on the

other two velocity components gets increased. Hence, the author chose to reduce the angle at 23°(Fig. 3), as suggested by the authors N. J. Lawson and J. Wu [15] and Mayo et al. [2]. The resulting overall Magnification Factor is about 29 pix/mm.

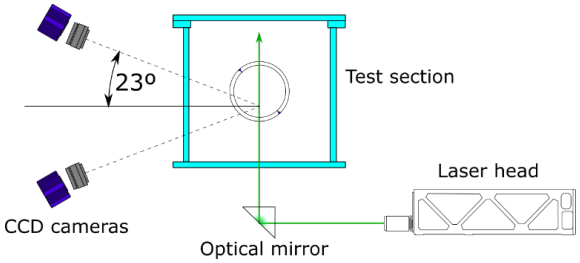

Figure 3: Set up of cameras and laser sheet for Stereo-PIV

The in-situ calibration of the image acquisition system is performed following the method proposed by Soloff et al. [16]. A dotted calibration grid is put inside the test section and positioned in the middle of the laser sheet by means of an adjustable micrometer support. The calibration plate is then displaced in two steps of 0.25mm each in the out-of-plane direction. The goal is to obtain a classical 3-D mapping function which makes the positions in the image system and in the real system to match. The partial derivatives of the functions in x,y and z are then used by the commercial software Davis 8.2, provided by Lavision, to compute the real particle displacement.

The S-PIV data will be used to validate LES results, so the target has been to investigate the statistics of the turbulent flow field [17]. To reach the convergence of the statistics, 1000 PIV realizations are acquired at a frequency of 1Hz [18], to have temporally uncorrelated events. In order to have a maximum particle displacement of about 10 pix [18], the separation time between the two frames of each PIV realizations has been set at 2.2 ms. The algorithm for the stereoscopic system processed the images in three refinement steps, with a final interrogation window size of 32 x 32 pix^2 and an overlap of 75%. In such a configuration, the system has a resolution of 1.1 x 1.1 mm^2. The seeding particles are Chospheric fluorescent polyethylene spheres of 10-45 μm diameter. A 532 nm notch filter is placed in front of each camera sensor in order to cut off the laser light, in such a fashion that only the fluorescent scattered light is recorded. By doing so, the background reflections are minimized and the signal to noise ratio has increased. The concentration of the particles is about 20 g/m^3 in order to have at least with a high probability 10 particles per window.

2.2. *Heat transfer measurement setup*

In heat transfer measurements the tested flow should have the same Prandtl number as in the real applications. Because of the complexity of building a facility with a reacting ethane flow, the chosen fluid has been air since is the simplest to work with. Anyway, the Large Eddy Simulations are supposed to be made with air as well, to validate how the code solves the energy equation. The facility (Fig. 4) works in the suction mode by operating a centrifugal blower at its exit. In this way, the inlet flow is not affected by the highly turbulent flow generated by the blower. Initially, the air enters the inlet duct, whose length is of 15 diameters. In such a way, the flow develops just before entering the test section, which is the same as the one used for the velocity measurement setup. Two additional K-type thermocouples are placed at the inlet and outlet sections in order to measure the temperature at the centre. The mass flow exiting the test section is directed through a U-bend towards the exit pipe. An orifice plate is placed in the exit pipe at a distance of 30 diameters downstream the U-bend. In this way, the operation of the mass flow meter is in agreement with the ISO 5167 norm [12]. The rotational speed of the blower can be changed so that the static pressure drop across the orifice plate corresponds to the required Reynolds number. Downstream of the mass flow meter, there is a settling chamber where the flow is discharged in. In such a system, it is possible to dump the possible fluctuations generated at the discharge side of the blower.

The inner surface temperature, T_w, has been measured by using the Liquid Crystal Thermography in the range 35-55 °C. Therefore, a layer of TLCs (Hallcrest Ltd) is firstly deposited on the inner wall of the cylinder under test, followed by a matt black paint layer to enhance the contrast, an acrylic adhesive of 0.06 mm thickness and an Inconel foil 600 of 0.025 mm thickness. The metal sheet extends to the full length of the test section and the obstacles are glued on the top of it. To increase the wall temperature, a DC voltage is applied to the Inconel foil and the heat transfer between the foil and the fluid is started. The Joule heating per unit area, q_{Joule}, is uniform since the metal alloy has a low resistivity temperature coefficient and the spatial variations of it under the present experimental conditions are below the 0.3%. The transparency of the Plexiglas and the black paint allow a Nikon D7100 digital SLR camera to acquire RGB intensities scattered by the TLCs. The camera lens is a Nikon AF DC-Nikkor 105 mm f/2D which with its big focal allows minimizing the angular aperture of

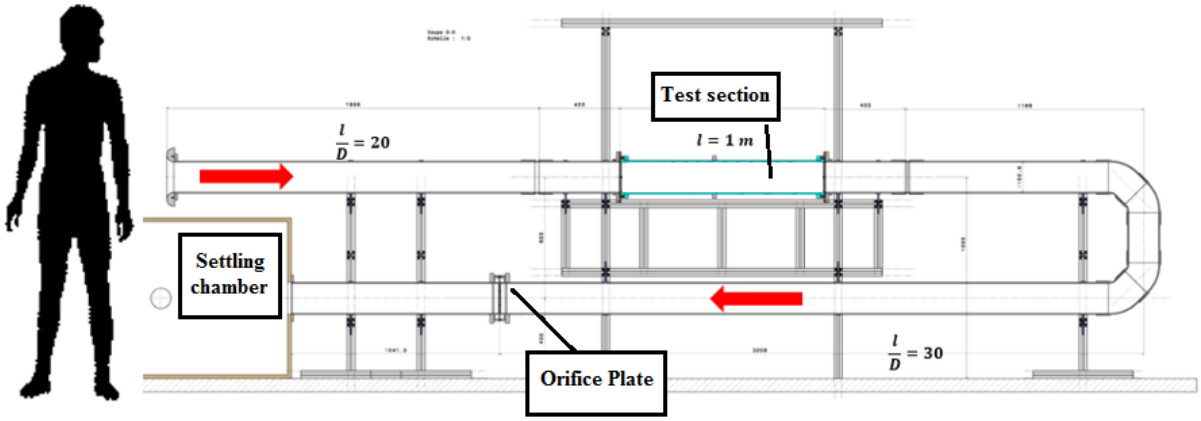

Figure 4: Facility for the TLCs measurements.

the camera. In such a way, the longitudinal variations of the recorded colours are kept as low as possible and so also the measurement uncertainty. Then, the SLR camera is focused on the test section from a distance of about 850 mm with an angle of 45°with respect to the horizontal. The ISO sensitivity has been set at 100 in order to enhance the signal to noise ratio of the images. The aperture and the shutter speed are set respectively at f/16 and 2 seconds, in order to have the images with the red, blue and green saturations as high as possible. The authors Kodzwa and Eaton [19] advice to work with high saturated images to minimize the temperature uncertainty given by the Liquid Crystals Thermography. The white balance of the camera has set at 4170 K, the same as for the led panel light. In such a fashion, the image colour range in the RGB space and the colour sensitivity of the camera are maximized [20].The test section is placed in a black box (Fig. 5), to avoid reflections coming from the environment, and below a diffusive LED light panel (Pan-70W). The part of the image processed is called Region of Interest (ROI) which consists on a rectangle whose dimensions are one helix pitch in the horizontal direction and 30°in the vertical direction of the image. The location of the Region of Interest in the stream-wise direction is established consistently with the S-PIV measurement area.

To evaluate the heat transfer by convection at the wall, the heat balance in each surface element of the Inconel needs to be solved. To do so, the temperature field at the inner and outer surfaces of the test section need to be measured. As stated before, the internal temperature of the ribbed pipe is given by the TLCs while the external cylinder temperature is provided by the infrared (IR) camera. The ThermaCAM SC3000 (Flir Systems) has a QWIP detector working in the infrared region of 8-9 μm. The IR images are taken with a spatial resolution of 1.1 mrad at a frequency of 50/60Hz. The evaluation of the Slit Response Function and the spatial frequency of the ROI suggest no images restoration. The test section is made of acrylic glass material, so the SLR is able to record the color distribution of the TLCs layer. For a specific temperature, angular position and illumination level on the curved surface, the liquid crystals scatter a predominant wavelength of the incident diffused light [21]. Therefore, the function who matches the TLCs colour properties and the temperature is obtained by doing a calibration in situ. During the calibration, the lower half of the cylinder is removed, to give an access to the infrared thermography. Hence, the IR camera is able to measure the temperature field on the inner surface of the pipe. On the other side, the SLR camera records the behaviour of the TLCs paint on the inner surface of the acrylic glass. With this approach, it is possible to match locally the temperature measured by the IR camera with the colours observed by the SLR camera in the same region (ROI). By means of the Hollingsworth equations [20], the red, blue and green intensities are converted in hue, saturation and intensity. To avoid heat flux reflection of the environment from the metal foil to the IR camera [22], a high emissivity vinyl (thickness of 0.1 mm) covers the inner surface of the cylinder. The IR camera itself has been calibrated both for the Plexiglas and for the vinyl materials, providing respectively ±0.5°C

and ±0.4°C extended uncertainties. The final calibration curves of the TLCs have been made for each row of the ROI and they consist in spline curves fitted to 18 calibration points. The corresponding uncertainties, with a level of confidence of 95%, take into account: the spatial variation of the Hue values over each row; the spatial variation of the temperature provided by the IR camera; the digital resolution of the SLC camera and the temperature uncertainty given by the IR camera. The major error source comes from the infrared thermography, which takes into account the errors in the IR camera calibration and the spatial variation of the temperature inside each row. This calibration methodology provides a resulting overall uncertainty on the temperature measurement between $\pm 0.46°C$ and $\pm 0.77°C$, depending on the row position inside the ROI. The extended uncertainty depends also on the temperature, and it results to be $\pm 0.46°C$ in the red region at 38.7°C ; $\pm 0.74°C$ in the green region at 46.5°C and $\pm 0.50°C$ in the blue region at 53.3°C. From this uncertainty analysis, it turns out that the biggest uncertainty is in the green region where the partial derivative $\partial T/\partial Hue$ has the biggest value. The chosen level of confidence is 95% respecting the terms of the ASME uncertainty nomenclature [23].

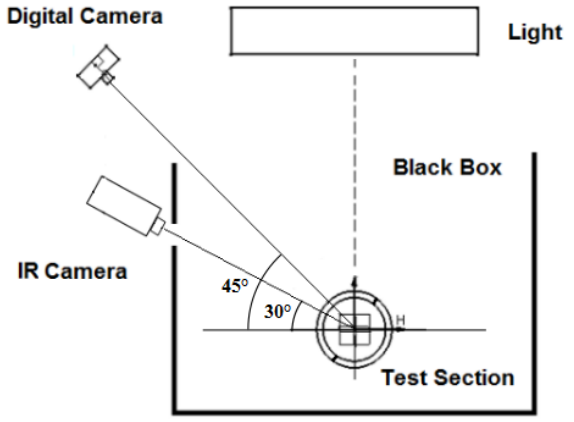

Figure 5: Images acquisition system and IR measurements layout

The Joule power per unit area (q_{Joule}) generated by the Inconel foil is transferred by convection (q_{conv}) to the flow and by conduction (q_{cond}) to the channel. Internal radiation fluxes are not considered since the elementary surfaces of the wall are put in a cavity with very low temperature differences. The equation to be solved is the following:

$$Q_{\text{conv}} = Q_{\text{Joule}} - Q_{\text{cond}} \tag{1}$$

Due to the non-uniformity of the conduction losses, the resulting heat transfer by convection per unit area is not perfectly uniform. The standard deviation of the q_{conv} fluxes for each surface element are equal to the 5.5%. The heat transfer coefficient, h, is defined as:

$$h(z,\theta) = \frac{q_{\text{conv}}(z,\theta)}{T_{\text{w}}(z,\theta) - T_{\text{c}}(z,\theta)} \tag{2}$$

where θ and z are the cylindrical coordinates along the pipe surface. Since the evaluation of the bulk Temperature is impossible without knowing its profile inside the swirling flow, all the properties and heat transfer coefficients are evaluated with the temperature of the flow at the centreline of the test section T_c. The latter is assumed to grow linearly from the inlet to the outlet section of the pipe. The dimensionless form of the convective coefficient is the Nusselt number, defined as:

$$Nu(z,\theta) = \frac{hD}{k_{\text{f}}} \tag{3}$$

where D is the pipe diameter and k_f is the thermal conductivity of the flow. It makes sense to compare the heat transfer in the ribbed cylinder with the one for a smooth channel, by means of the Enhancement Factor (EF):

$$EF(z,\theta) = \frac{Nu(z,\theta)}{Nu_0} \tag{4}$$

where Nu_0 is the Nusselt number of a fully developed flow in a smooth circular pipe, estimated from the Dittus-Belter correlation:

$$Nu_0 = 0.023 \times Re^{0.8} \times Pr^{0.4} \tag{5}$$

The reliability of the technique described before for heat transfer measurements has been validated in the work of the authors Mayo et al. [2] who applied the same measurements routine for a smooth channel without any turbulator inside. The results in terms of Nusselt number, for several Reynolds numbers, agree with those given by the correlation of Dittus-Belter. In the worst case, at a Reynolds number of about 2×10^5, the difference between measurements and correlation is of 7.4%.

2.3. Friction coefficient measurement setup

The friction losses evaluations have been made using the air tunnel used for the heat transfer measurements. Actually, this facility has two pressure taps, one upstream and one 2 diameters downstream of the

test section. An inductive pressure transducer (Validyne) measures the static differential pressure Δp_{static}. Out of it, the surface average of the wall shear tensor can be computed by using the formula as below:

$$\tau_{\text{wall}} = \frac{\Delta p_{\text{static}} \times r}{2 \times L} \tag{6}$$

where r and L are respectively, the inner radius of the test section and the distance between the two wall pressure taps. The pressure transducer has a Full Scale of ±86 Pa and provides an uncertainty of ±0.2 Pa. This low value has been provided thanks to the Ultra Low Differential Pressure calibrator DPI 610 LP which has a span of 250 Pa and an extended uncertainty of ±0.05% of the span. Therefore, the friction coefficient C_f, averaged on the ribbed surface, is computed according to the formula:

$$C_{\text{f}} = \frac{\tau_{\text{wall}}}{0.5 \times \rho \times u_b^2} \tag{7}$$

where ρ is the flow density and u_b is the bulk velocity given by the orifice plate. To validate the technique, the measurements made for the test section without any turbulator have been compared with the Blasius correlation for turbulent fully developed flows in smooth pipes [17]:

$$C_{\text{f}} = \frac{0.079}{Re^{0.25}} \tag{8}$$

3. Results

As expected, both the turbulators make the friction losses to increase, since the wall lost its smoothness. Regarding the geometry A, the friction factors are quite constant at a level of about 8 times the one given by the Blasius correlation for fully developed flows in smooth channels. For the case of geometry B, the C_{f} decreases with the Reynolds number at values lower than the ones before. As a matter of fact, the geometry B has been designed to decrease the pressure losses of this kind of turbulators. Fig. 6 shows a strange behaviour of such a turbulator when the Reynolds number is around 20000. Actually, the skin friction losses are bigger in comparison with the other geometry, at a value of 10 times the C_{f} for bare channels.

It might be explained by the change in the flow topology when passing from a Reynolds number of 20000 to bigger values, as shown in the heat transfer enhancement. The described behaviour is showed in the contours of Fig. 7 where the EF is plotted between

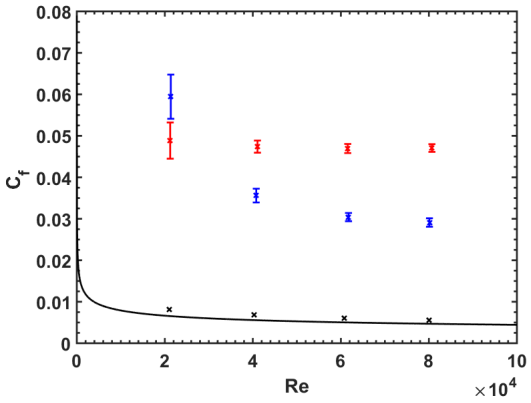

Figure 6: Friction factor as a function of Reynolds number: red crosses, geometry A; blue crosses, geometry B

the obstacles. The geometry A makes the flow to separate and reattach where the heat transfer shows its biggest value. This reattachment line follows the helix pattern imposed by the turbulator and it is set at a distance of about 4 times the rib's height. The surface averaged Nusselt number slightly increases with the Reynolds number, showing a maximum EF of about 1.72, with an extended uncertainty of 6% (Tab. 1). When the test section is equipped with the geometry B, the same phenomenon as before happens where the rib height is at the maximum value ($\theta = 0°$), but the reattachment length is slightly smaller (Fig. 10). Moving through the helix pattern (θ direction) toward the edge where the rib's blockage is null ($\theta = 20°$), the reattachment area does not follow any helix pattern, resulting to be a deformed line downstream the obstacle trailing edge. The higher the Reynolds number, the more is the deformation of the reattachment line. The area where the EF has its maximum value, corresponds to the impingement of the separated flow. This zone tends to get closer to the obstacle at the edge where $\theta = 20°$ and to get resized with increasing mass flows. The tendency of the surface averaged EF is to stay more or less constant with the Reynolds number at values slightly lower than the other geometry. Nevertheless, the maximum heat transfer enhancement has been shown for Re = 80000 at values comparable with the geometry A.

The flow field at the regime of Reynolds number equal to 20000 between the obstacles is provided by the Stereo-PIV measurements. The Fig. 8 plots the axial components of the velocity field at several locations between the obstacles. It is clear from the figure that the blockage provided by the geometry A is

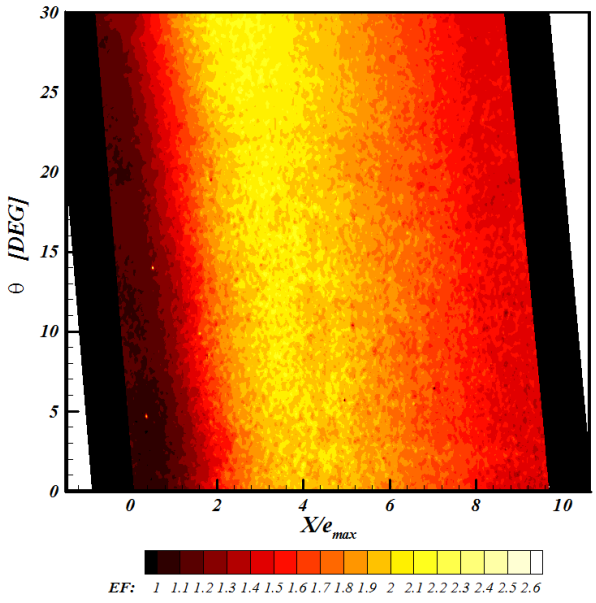

(a) EF field at Re = 20000 (geometry A)

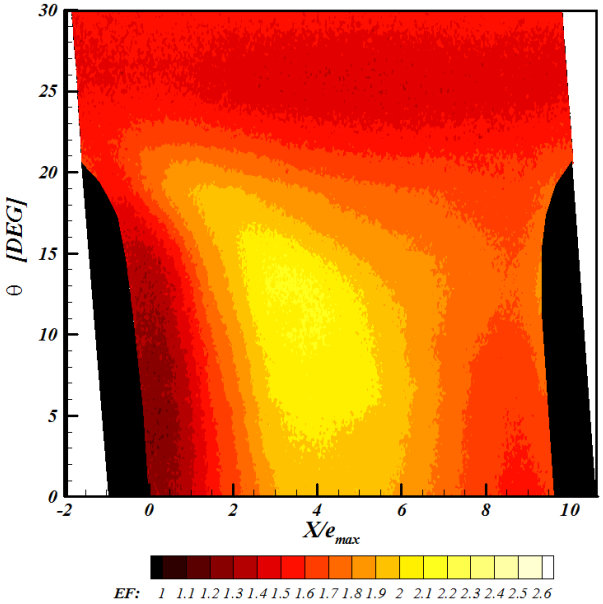

(b) EF field at Re = 20000 (geometry B)

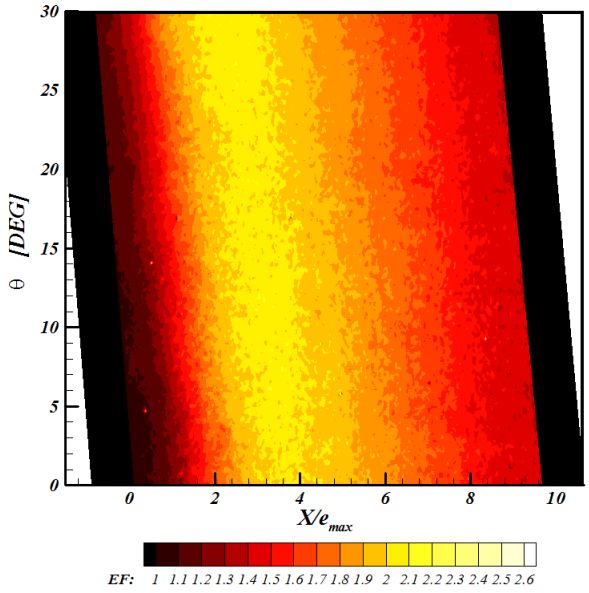

(c) EF field at Re = 40000 (geometry A)

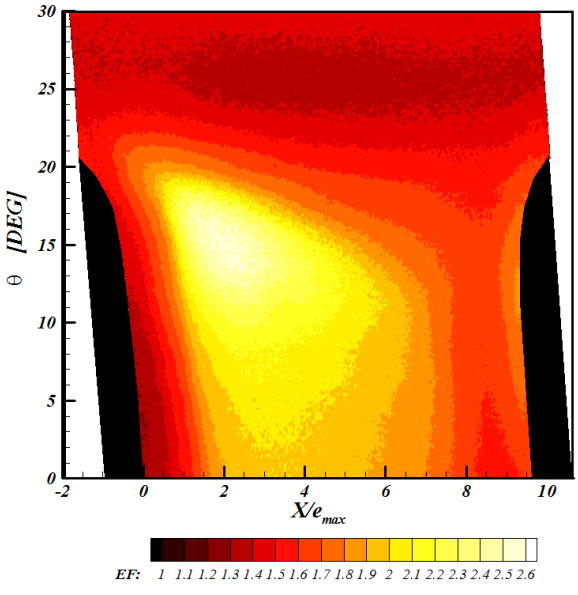

(d) EF field at Re = 40000 (geometry B)

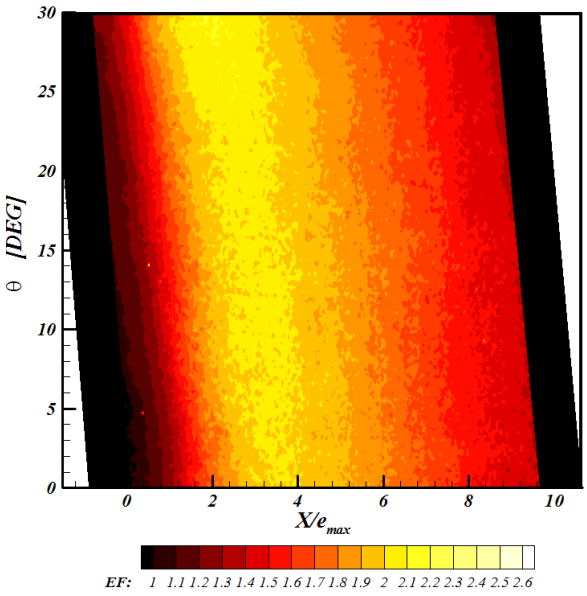

(e) EF field at Re = 60000 (geometry A)

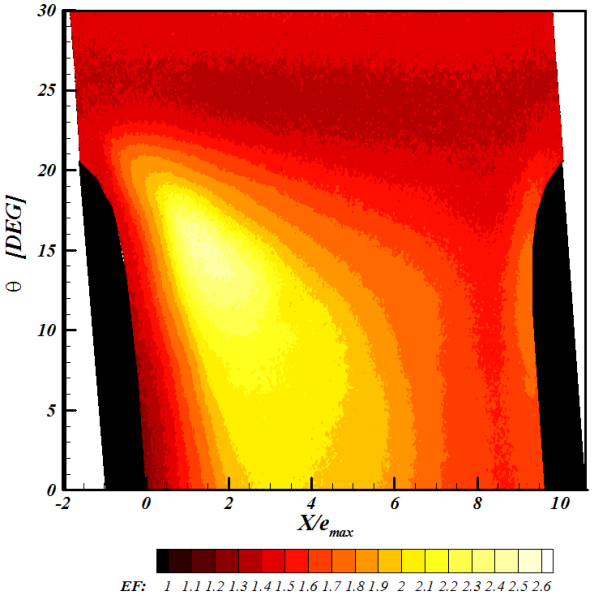

(f) EF field at Re = 60000 (geometry B)

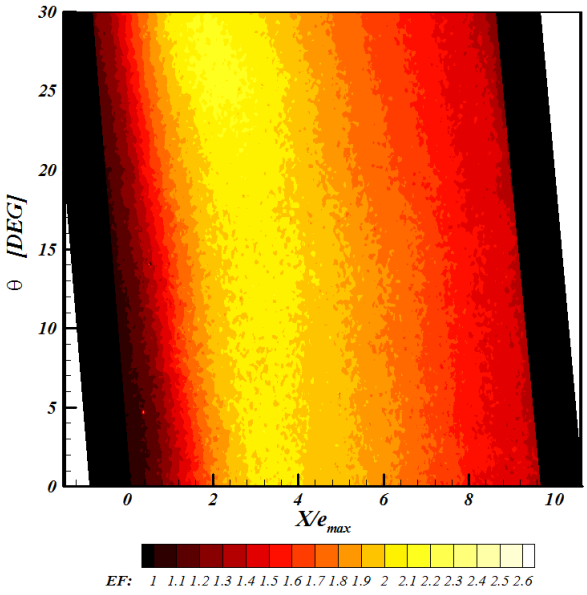

(g) EF field at Re = 80000 (geometry A)

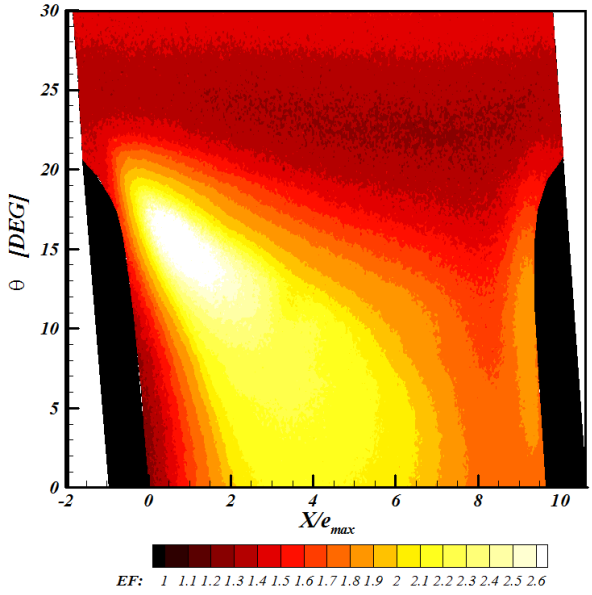

(h) EF field at Re = 80000 (geometry B)

Figure 7: EF contours between 2 obstacles of the 2 geometries as a function of Re number

Table 1: Surface averaged EF

Re number	$EF_{\text{geometry A}}$	$EF_{\text{geometry B}}$
20000	1.68±0.09	1.68±0.09
40000	1.70±0.07	1.70±0.07
60000	1.71±0.07	1.67±0.07
80000	1.72±0.08	1.70±0.09

higher than the one given by the other geometry.

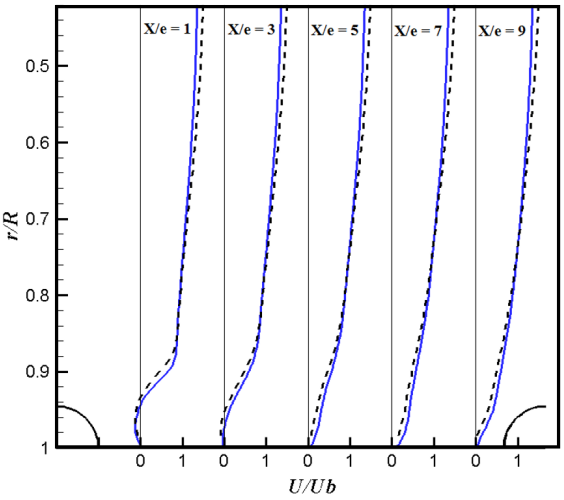

Figure 8: Axial velocity profiles at Re = 20000: blue solid, geometry A; black dashed, geometry B

The separation of the flow, followed by the impingement and recirculation bubble is better shown in the Fig. 9 where the streamlines are plotted on the top of the velocity azimuthal component distribution. The reattachment length results to be equal to the one argued by the EF contours, that is where X/e is about 4, for the geometry A and at a lower value, for the geometry B. Higher values for the swirl are given by the geometry A, since the turbulator has a profile that develops continuously through the helix pattern. The highest values for the azimuthal component are shown at the leading edge of the obstacles. In the case of the geometry B, the left side of the recirculation bubble has a negative swirl at the wall close to the trailing edge. This phenomenon is due to the discontinuity of the geometry blockage throughout the helix development.

The dimensionless Turbulent Kinetic Energy (k) fields defined as:

$$k = \frac{0.5 \times (u'^2 + v'^2 + w'^2)}{U_{\text{bulk}}{}^2} \tag{9}$$

where u', v' and w' are the velocity fluctuations in the three dimensions, is shown in Fig. 10, together with the EF plot between the obstacles. The geometry A provides a higher k than the geometry B, all over the flow field, with a maximum value of about 12.5% of the bulk velocity. The area is where the flow shows a high shear due to the separation from the obstacle. The same value has been measured for the other geometry, in the same position between X/e=2 and X/e=4. The remarkable difference is that, with the geometry B the dimensionless TKE, and so the turbulence levels, are lower in the zone far from the wall. Just behind the maximum value of the dimensionless TKE, the EF shows its peak, for both the cases (Fig. 10).

4. Conclusion

Data for the validation of Large Eddy Simulation on chemical reactors has been provided. The way the code solves the Navier-Stokes and the energy equation for the small scales can be verified with the results showed hereby. The measurements outcome, concerning the flow field and the heat transfer, show the importance of turbulators thought as well-performing cooling channels techniques. The induced 3-dimensional separation makes the flow to impinge on the wall allowing the enhanced heat transfer. Anyway, the topology of the flow and the increased turbulence produce more skin friction at the wall. An overall efficiency of the system, which takes into account both the results, can be evaluated by means of the equation below:

$$\eta = \frac{\frac{Nu}{Nu_{\text{S}}}}{\frac{(1+C_{\text{f}})}{(1+C_{\text{f}})_{\text{S}}}} \tag{10}$$

Actually, the global energetic efficiency (η) stated before, represents the ratio between the performances of the system with and without turbulator. The Tab. 2 shows its values at different Reynolds number for the two geometries. As a final remark, the two geometries provide the same energetic performances if considering their uncertainty's ranges. The statistical mean over the several values at different Re number turns to be 1.63, for both the geometries. The oncoming work will be concerning the performance evaluation given by dimpled channels in terms of heat transfer and friction losses.

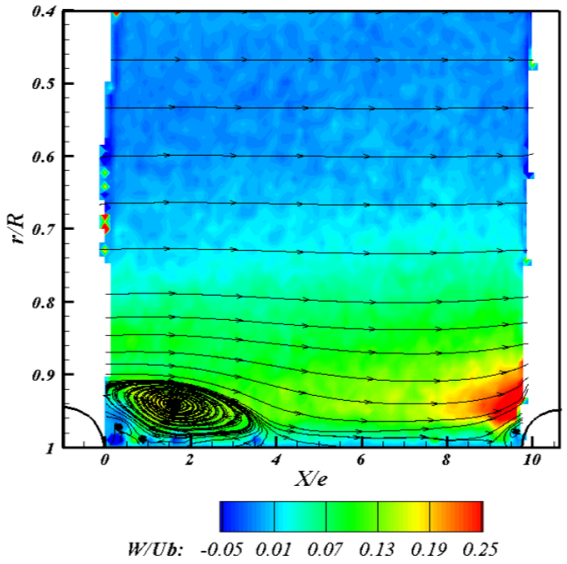

(a) Stream lines and azimuthal velocity field at Re = 20000 (geometry A)

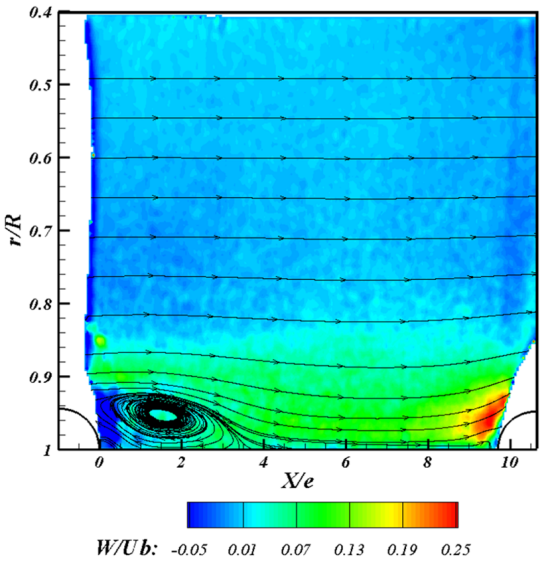

(b) Stream lines and azimuthal velocity field at Re = 20000 (geometry B)

Figure 9: Flow Field between 2 obstacles of the 2 geometries at Re = 20000

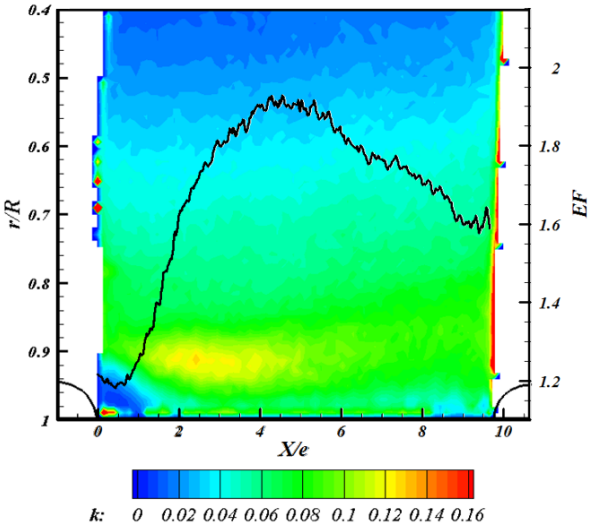

(a) Turbulent Kinetic Energy (k) field at Re = 20000 (geometry A)

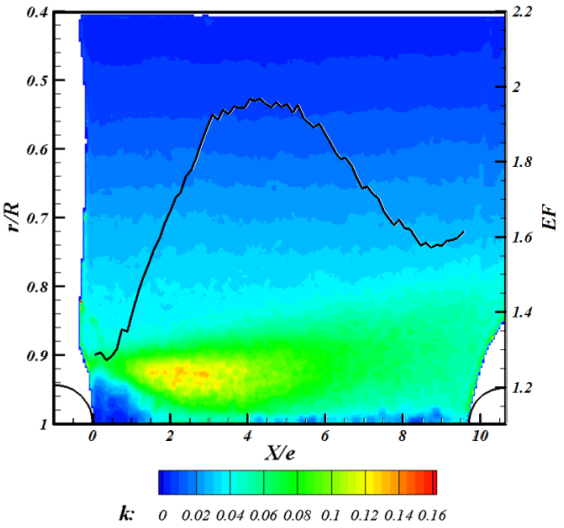

(b) Turbulent Kinetic Energy (k) field at Re = 20000 (geometry B)

Figure 10: TKE distibution between 2 obstacles of the 2 geometries at Re = 20000

Table 2: Global efficiency of the two geometries

Re number	$\eta_{\text{geometry A}}$	$\eta_{\text{geometry B}}$
20000	1.61	1.59
40000	1.63	1.65
60000	1.64	1.63
80000	1.65	1.66

Acknowledgments

The author wishes to thank CERFACS and the Laboratory for Chemical Technology in Gent University, for the initiative in performing the present experimental campaign. Also, the help and expertise of Ignacio Mayo Yage, Julien Desset, Grard Goossens and Jean-Christophe Desilve at VKI are highly appreciated.

References

[1] J. C. Han, S. Dutta and S. Ekkad, Gas Turbine Heat Transfer and Cooling Technology, Second Edition, Taylor and Francis, 2012.

[2] I. Mayo, B. C. Cernat, M. Virgilio, A. Pappa, T. Arts, Aerothermal Investigation of the Flow and Heat Transfer in a Helically Corrugated Cooling Channel, no. Proceedings of ASME Turbo Exp: Turbine Technical Conference and Expositiono, Seoul, South Korea, 2016.

[3] P. Ligrani, Heat Transfer Augmentation Technologies for Internal Cooling of Turbine Components of Gas Turbine Engines , International Journal of Rotating Machinery 2013.

[4] T. S. Ravigururajan and A. E. Bergles, Development and verification of general correlations for pressure drop and heat transfer in single-phase turbulent flow in enhanced tubes, Experimental Thermal and Fluid Science 70.

[5] S. Pethkool, S. Eiamsa-ard, S. Kwankaomeng and P. Promvonge, Turbulent heat transfer enhancement in a heat exchanger using helically corrugated tube, International Communications in Heat and Mass Transfer 38 (2011) 340–347.

[6] A. Garcia, J. P. Solano, P. G. Vicente and A. Viedma, Flow pattern assessment in tubes with wire coil inserts in laminar and transition regimes, Int. J. Heat Fluid Flow 28 (2007) 516–525.

[7] L. Bonanni, R. Da Soghe, B. Facchini, M. Micio, M. Pievaroli, L. Tarchi, L. Abba and M. Maritano, Heat transfer and friction in circular ducts with shaped ribs, no. Proceedings of the 10th European Turbomachinery Conference, Lappeenranta, Finland, 2013.

[8] M. Zhu, E. Riber, B. Cuenot, J. Bodart and T. Poinsot, Wall-resolved Large Eddy Simulation in refinery ribbed pipes, no. Center for turbulence research - Proceeding of the Summer program, 2014.

[9] F. P. Incropera, D. P. DeWitt, T. L. Bergman and A. S. Lavine, Foundamentals of Heat and Mass transfer, 6th ed., John Wiley & Sons, 2007.

[10] F. Coletti, T. Maurer, T. Arts and A. Di Sante, Flow Field investigation in rotating rib-roughened channel by means of particle image velocimetry, Experiments in Fluids 52 (2012) 1043–1061.

[11] C. W. H. van Doorne and J. Westerweel, Measurement of laminar, transitional and turbulent pipe flow using stereoscopic-PIV, Experiments in Fluids 42 (2007) 259–279.

[12] ISO 5167 - Measurement of fluid flow by means of pressure differential devices inserted in circular cross-section conduits running full, Tech. rep., International Organization for Standardization (2003).

[13] A. K. Prasad, Stereoscopic particle image velocimetry, Experiments in Fluids 29 (2000) 103–116.

[14] A. K. Prasad and K. Jensen, Scheimpflug stereocamera for particle image velocimetry to liquid flows, Appl. Optics 34 (1995) 7092–7099.

[15] N. J. Lawson and J. Wu, Three-dimensional particle image velocimetry: experimental error analysis of a digital angular stereoscopic system, Meas. Sci. Technol. 8 (1997) 1455–1464.

[16] S. M. Soloff, R. J. Adrian and Z. C. Liu, Distortion Compensation for generalised stereoscopic particle image velocimetry, Meas. Sci. Technol. 8 (1997) 1441–1454.

[17] S. B. Pope, Turbulent flows, Cambridge University Press, 2000.

[18] R. J. Adrian and J. Westerweel, Particle Image Velocimetry, Cambridge University Press, 2000.

[19] P. M. Kodzwa Jr. and J. K. Eaton, Angular effects on thermochromic liquid crystal thermography, Experiments in Fluids 43 (2007) 929–937.

[20] B. Cukurel, C. Selkan and T. Arts, Color theory perception of steady wide band liquid crystal thermometry, Experimental Thermal and Fluid Science 39 (2012) 112–122.

[21] N. Abdullah, A. R. A. Talib, A. A. Jaafar and M. A. M. Salleh, The basics and issues of thermochromic liquid crystal calibration, Experimental Thermal and Fluid Science 34 (2010) 1089–1121.

[22] G. M. Carlomagno and G. Cardone, Infrared thermography for convective heat transfer measurements, Exp. Fluids 49 (2010) 1187–1218.

[23] Test Uncertainty, Tech. rep., American Society of Mechanical Engineers, New York (2005).

DEVELOPMENT AND ADVANCED CFD AND OPTIMIZATION

Adjoint surface optimization for internal and external aerodynamics applications by means of OpenFOAM

Giacomo Alessi

Environmental and Applied Fluid Dynamics Department, von Karman Institute for Fluid Dynamics, Belgium, giacomo.alessi@vki.ac.be

Supervisors: Jeroen van Beeck and Tom Verstaete

Professor, Environmental and Applied Fluid Dynamics Department, von Karman Institute for Fluid Dynamics, Belgium, vanbeeck@vki.ac.be

Associate Professor, Turbomachinery and Propulsion Department, von Karman Institute for Fluid Dynamics, Belgium, tom.verstraete@vki.ac.be

University Supervisor: Bert Blocken

Part-Time Full Professor, Civil Engineering Department, Leuven University, Belgium, bert.blocken@bwk.kuleuven.be

Abstract

The pressure loss reduction inside the U-bends is of crucial importance to increase the performance of cooling systems of gas turbines. The optimization technique proposed is based on the continuous adjoint shape method and is implemented in an open-source framework. The calculated gradient of the objective function allows the modification of the body towards an optimum design that satisfies the constraints imposed.

Keywords: surface adjoint optimization, mesh morphing, open-source

1. Introduction

Nowadays the task of a designer consists more and more in the modification and improvement of existing designs. However, the designs complexity and the amount of parameters that could be modified complicate this task. The different parameters that play an import role are usually coupled and their effect on the design could be difficult to assess. As a consequence, the past decades have observed a large development of computational routines that autonomously look for improvements, i.e. the so-called optimization algorithm. The aim of these algorithms is to maximize the performance of a design by modifying its parameters, with minimal intervention from the designer. In order to evaluate the design performance, the optimization routine needs to be coupled with a solver for the physics under consideration, fluid dynamics in the present case. Therefore, the number of design parameters that can be taken into account represents a limitation, due to the numerous CFD evaluations required by most of these algorithms. The adjoint optimization method is particularly interesting in this aspect since its computational cost is independent from the number of design variables. Indeed, the optimized body can be obtained at a cost similar to two CFD evaluations independently from the number of design variables, considerably reducing the overall procedure time and the computational power needed. The application of the adjoint optimization method can be found in different fields, [1; 2; 3], and it is becoming more and more the tool of choice for gradient optimizations.

An example of application for internal aerodynamics will be presented in this work. The internal optimization carried out is linked to turbomachinery industrial applications, in particular to the cooling system of gas turbines [4]. The U-bend shape is particularly representative of the cooling system design, representing the major source of thermodynamic efficiency loss. The large number of parameters that plays a role in this application results in a conscious choice of the optimization method to be used. As an example, a classic trial-and-error approach would generate several configurations by varying a number of geometrical parameters, requiring an enormous number

of CFD evaluations. It would make the design process extremely time-consuming and it would most probably result in a design far from the optimal one. On the other hand, the adjoint method can handle numerous parameters and represents an efficient approach to the problem, making it the perfect candidate for the considered case.

2. The U-bend test case

Cooling systems of gas turbines, in most of the cases, use air bled from the high pressure compressor, leading to a penalty in thermodynamic efficiency. A proper design should maintain the desired thermal exchange minimizing the coolant mass flow rate, i.e. the air taken out from the compressor. The aim could be reached modifying the shape of the internal cooling passages in order to obtain a reduction of the pressure loss. Among the others, the U-bends that connect consecutive passages are of paramount importance since they present regions responsible for high pressure loss. As a consequence, design improvements can be obtained through the pressure loss minimization of the U-bends passage. The considered design and flow configuration has received particular attention both from research groups and industries, thus various approaches and optimization strategies have been applied to it [5; 6; 7].

The numerical domain considered in the present work is represented by a circular U-bend of square section (hydraulic diameter $D_h = 0.075[m]$), whose geometrical details can be found in [8; 9]. A velocity profile with a bulk velocity of $U_0 = 8.4[m/s]$ and a turbulence intensity of $T.I. = 5\%$ has been imposed at the inlet. A zero pressure boundary condition is applied to the outlet and a no-slip condition to the wall.

The numerical simulations have been performed using a 2D structured grid of 540x100 elements, assuring a maximum $y+$ value of 0.94. The Lauder-Sharma low-Reynolds $k-\epsilon$ turbulence model has been used. The velocity field obtained and its streamlines are shown in Fig. 1. The flow accelerates approaching the bend, it reaches the maximum velocity around the inner wall while it decelerates along the outer wall. The flow starts to separate before the end of the bend forming a long separation bubble.

The aim of the study is the minimization of the total pressure losses, thus the considered cost function J is represented by:

$$J = p_{Tin} - p_{Tout} = \left(p + \frac{1}{2}\rho U^2\right)_{in} - \left(p + \frac{1}{2}\rho U^2\right)_{out} \quad (1)$$

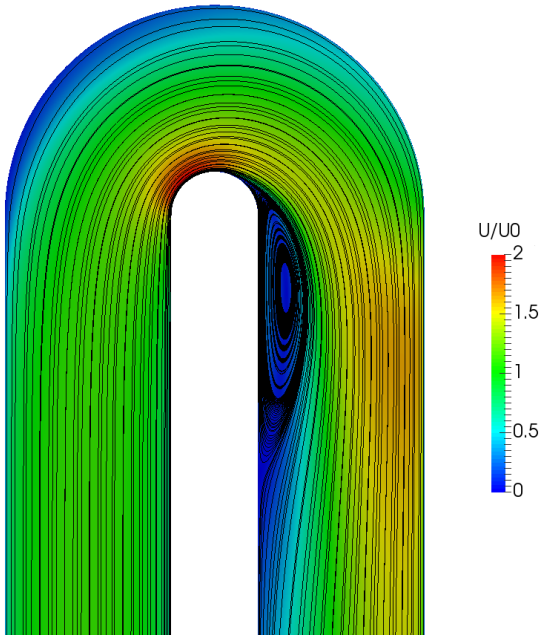

Figure 1: Velocity field and streamlines in the initial U-bend design.

3. The adjoint method in the context of shape optimization

In the adjoint formulation two systems of equations have to be solved, the Navier-Stokes equations and the adjoint equations. The first step of the optimization process is to solve the Navier-Stokes equations (primal system) to obtain convergent flow variables, as shown in Sec. 2; successively the convergent assessment is required for the adjoint variables. By solving both systems of equations, a surface sensitivity map can be extrapolated. The information contained in it suggests the modifications to perform on the body contour to increase the performance. Based on this information the geometry boundary can be modified. Eventually, as proposed in the present work (Sec. 4), a mesh morphing solver can be included in the optimization routine to allow automatic successive steps of the optimization process. A schematic loop of the optimization routine implemented is shown in Fig. 2.

3.1. Adjoint equations

Consider a general cost function J, depending on the flow variables $\mathbf{U}$ and p, respectively velocity and pressure, and on the design variables. The problem to consider is: minimize J such that the Navier-Stokes equations are satisfied. The direction of improvement can be evaluated from the solution of two equation systems: the Navier-Stokes and the adjoint one.

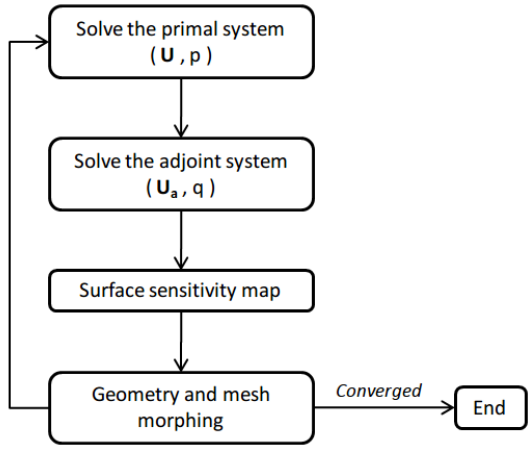

Figure 2: Optimization loop.

Following the derivation in [10], the adjoint equations, continuity and momentum, are:

$$\nabla \cdot \mathbf{U_a} = \frac{\partial J_\Omega}{\partial p} \tag{2}$$

$$\mathbf{U_a}\cdot\nabla\mathbf{U} - \mathbf{U}\cdot(\nabla\cdot\mathbf{U_a}) = \nabla\cdot(2\nu_{eff}D(\mathbf{U_a})) - \nabla q - \frac{\partial J_\Omega}{\partial \mathbf{U}} \tag{3}$$

The boundary conditions, derived for the following specified boundaries, are listed in Tab. 1.

Table 1: Adjoint boundary conditions.

Inlet and walls		
$\mathbf{U_a}_t = 0$	$U_{an} = -\frac{\partial J_\Gamma}{\partial p}$	$n \cdot \nabla q = 0$
Outlet		
$q = U_n U_{an} + \nu_{eff}(\mathbf{n} \cdot (\nabla \cdot U_{an})) + \frac{\partial J_\Gamma}{\partial U_n}$		
$U_n \mathbf{U_a}_t + \nu_{eff}(\mathbf{n} \cdot (\nabla \cdot \mathbf{U_a}_t)) + \frac{\partial J_\Gamma}{\partial \mathbf{U}_t} = 0$		

where: $\mathbf{U}$ and p represent velocity and pressure (primal variables); $\mathbf{U_a}$ and q are the adjoint velocity and adjoint pressure (adjoint variables); the subscripts Ω and Γ are referred respectively to the volume and boundary contributions of the cost function; while the subscripts t and n are respectively referred to the tangential and normal component.

As highlighted by the adjoint equations and its boundary conditions, the adjoint problem needs to be fed with information related to the cost function, making a one-to-one relation between the two. The cost function chosen for the U-bend optimization, i.e. the total pressure loss between inlet and outlet (Eq. 1), gives a contribution only to the boundary conditions, as well as for all the cost functions that are only defined along the boundaries. Those cost functions identify a class for which the adjoint equations do not vary with a cost function variation.

In the present work the variation of the effective turbulence viscosity with a design variation has been considered negligible, that is the so-called frozen turbulence assumption. It considers negligible the dependency of the turbulent quantities from the design variables. The use of the frozen turbulence assumption can have a significant influence on the obtained solution [11], on the other hand the use of an adjoint turbulence model would increase the complexity of the method. Despite the possible loss of accuracy, the use of this hypothesis leads to an overall validity of the solution obtained.

3.1.1. Surface sensitivity maps

The adjoint optmization method is a gradient-based method, hence it uses the information from the derivative of the objective function with respect to the design variables in its search for the minimum. The design variables chosen in the present work are represented by the normal displacement of each surface node, β , resulting in a very rich design space.

The gradient information takes the name of surface sensitivity map and can be evaluated from the solution of the primal and adjoint equations system, as in Eq. 4.

$$S = \frac{\partial J}{\partial \beta} = -\nu_{eff}\frac{\partial \mathbf{U_a}}{\partial \mathbf{n}}\frac{\partial \mathbf{U}}{\partial \mathbf{n}} \tag{4}$$

The surface sensitivity map is evaluated at the geometry walls and indicates the modifications to perform in order to improve the performance with respect to the chosen cost function. The design variable space is composed of the normal node displacement, thus the modifications must be performed in the direction normal to the surface itself. The sensitivity map obtained in the U-bend test case is shown in Fig. 3.

A positive sensitivity map region has to be moved away from the fluid to increase the performances, while a negative sensitivity value indicates that a performance improvement would be reached by moving those regions towards the fluid. On the other hand, modifications of a zero sensitivity map region will not influence the cost function.

The sensitivity map indicates the modifications to carry out in every single boundary point of the design. The cost is the solution of the adjoint equations

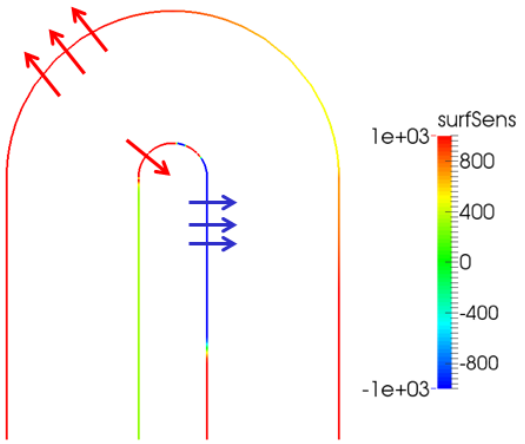

Figure 3: Surface sensitivity maps and improvement directions.

system that is similar to the one of the Navier-Stokes equations. Therefore, at a fixed cost, similar to two CFD evaluations, it is possible to obtain the gradient information for an arbitrary number of design variables, e.g. 686 design variables in the present work. Such a richness of the design variable space cannot be reached with other optimization methods, e.g. the random walking or genetic algorithm, in which the number of design variables that can be taken into account is limited to a few tens. A 3D extension of the U-bend would increase exponentially the number of design variables, keeping unchanged the cost of the gradient calculation. Therefore, the adjoint theory allows to carry out the optimization study decreasing considerably the computation cost of the procedure.

Before converting the gradient information into a real design variation, a preliminary step is needed. The surface sensitivity presents high frequency oscillation contents that would result in a rough design if not treated in a suitable way. The attainment of a smooth sensitivity is a crucial point to obtain a valid geometry deformation, and thus an admissible design. The application of the raw sensitivity would lead to boundary overlapping and mesh distortion problems after few iterations of the optimization loop. Moreover, the high frequency contents increase with the number of iterations, making indispensable the use of a smoother.

The choice of the smoothing strategy represents an optimization problem itself. Indeed, while is mandatory to get rid of the discontinuities, the main information content of the sensitivity must be preserved.

A weighted average smoothing has been used in the present work. In particular, the smoothed sensitivity $\overline{S}$ has been evaluated as follow:

$$\overline{S} = \sum_j \omega_j \sum_i \omega_i S_i \tag{5}$$

where the weight ω is calculated as:

$$\omega_i = l_i / l_{sum} \tag{6}$$

In Eq. 6 l_i is the inverse distance between face centers and boundary points and l_{sum} is the sum of the inverse distances. The same definition is used for w_j, where the distance to be considered is the one from the boundary points to the cell centers. The smoothing strategy used corresponds to successive weighted interpolations of the surface sensitivity from face centers to boundary points and vice versa, resulting in a weighted average that takes into account a stencil of three consecutive nodes.

The importance of the application of a smoothing function is highlighted in Fig. 4 and Fig. 5, which show the raw and smoothed sensitivity signal along the U-bend inner wall respectively after 1 and 100 iterations. The high frequency oscillations are already present at the first iteration step and become more pronounced with the iterations. Note how the smoothed signal still maintains the main information of the raw sensitivity.

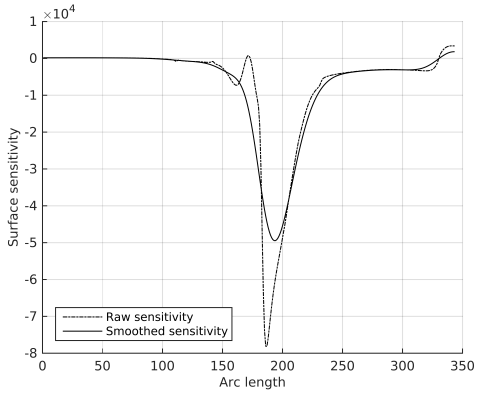

Figure 4: Raw and smoothed sensitivity signal along the U-bend inner wall at the first loop iteration.

4. Constrained morphing routine for an optimal design

The last step of the optimization process implemented includes the modification of the design and a link to a mesh morpher solver to allow successive

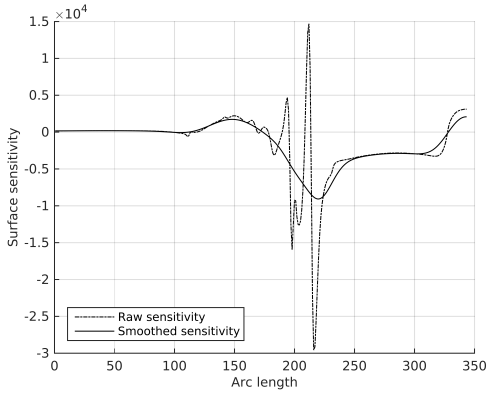

Figure 5: Raw and smoothed sensitivity signal along the U-bend inner wall after 100 loop iterations.

automatic steps towards the design improvement. Design modifications must take into account particular limitations intrinsic to the chosen design, e.g. aerodynamic and geometrical constraints. Moreover, the design feasibility must be guaranteed, hence rough surfaces cannot be accepted.

4.1. Design variation

Once the sensitivity oscillations have been ironed out, as shown in Sec. 3.1.1, it is possible to link its information to a design variation. In the present work the design is updated using a steepest descent algorithm, as in Eq. 7:

$$\mathbf{x_{i+i}} = \mathbf{x_i} + \alpha \overline{S}\,\mathbf{n} \tag{7}$$

where $\mathbf{x_i}$ and $\mathbf{x_{i+i}}$ represent the position vector of each node respectively before and after the boundary movement. The second term in the r.h.s. of the equation represents the differential displacement applied to each node. Indeed, it depends on the smoothed surface sensitivity map, $\overline{S}$, and it is applied in the direction normal to the surface, $\mathbf{n}$. The term includes an additional parameter, α, defined as follows:

$$\alpha = \frac{\epsilon}{max||\overline{S}||} \tag{8}$$

The role of the parameter is to normalize the sensitivity and to fix the maximum step size of the movement through the parameter ϵ. In the present work, ϵ is kept constant, so it has been used a steepest descent algorithm with fixed step size. Nevertheless, the surface sensitivity decreases its magnitude in its route to the optimum, hence the magnitude of the nodes movement decreases iteration by iteration and eventually becomes null if a local minimum is reached.

The choice of the right value for the parameter α represents a key point of the optimization process. After the attainment of fully convergent variables at the first iteration step, the present optimization algorithm has been run using partially converged variables to speed up the process. The strategy used is valid as long as the movement imposed is small enough to maintain the surface normals almost unaltered and to partially maintain the convergence level of the previous step. A big value of α would invalidate the strategy proposed and would lead to the worsening of the design, on the other hand a value that is too small would exponentially increase the computational time. Therefore, it represents another optimization problem itself, making impossible a choice of α a priori. Therefore, the choice of the suitable value to be assigned is left to the user, being the choice highly case-dependent. The results shown in the present work refer to a value of $\epsilon = 10^{-4}$. Note that at the end of the optimization process a fully convergent simulation is performed in order to verify the obtained result.

The algorithm described by Eq. 7 represents a classical steepest descent algorithm and allows a huge degree of freedom in the attainment of the optimized design. However, the majority of the designs must respect constraints, geometrical and aerodynamical, and the optimization is usually required in a limited region of the design. The constraints and limitations present in the U-bend test case are shown in Fig. 6.

The bounding box shown in Fig. 6 indicates the constraints to be satisfied and the zones of the U-bend that can take part in the optimization process. In order to fulfil the requirements, a constrained steepest descent algorithm has been implemented. The user has the freedom to choose between constrained and unconstrained optimization. In the latter, the definition of a bounding box is requested. Finally, the user can choose whether to perform the optimization in a limited region instead of in the whole design. Limitations in the optimization region are generally present, however could be of interest the evaluation of an unfeasible optimization covering the whole geometry. Indeed, it would enlarge the design space and it could lead to ideas for further design and different design strategy.

4.2. Mesh morphing strategy

The last step of the optimization process is represented by a link between the boundary movement and

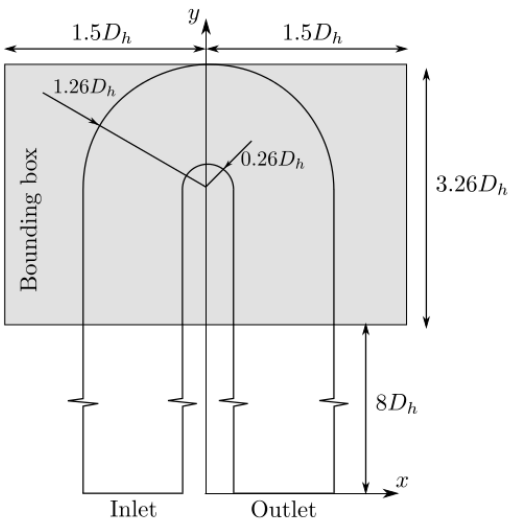

Figure 6: Constraints and limitations in the U-bend test case.

the mesh deformation. For the cases where the motion is solution-dependent, a mesh morpher based on the Laplace equation can be used in which the prescribed boundary movement represents the boundary condition for the internal cell motion. Details about the mesh morphing strategy can be found in [12].

The boundary movement prescribed, when using a Laplace equation based method, is not uniformly distributed in the inner mesh and can bring to deterioration of the mesh quality near the boundary. Indeed, unless a variable diffusivity in the Laplace equation is used, the largest cell movement is applied near the moving boundary. In the present work, a distance-based quadratic method has been chosen, so the diffusivity is function of the inverse square distance from the nearest boundary. A distance-based diffusivity improves the mesh quality near the boundaries: it redistributes the movement inside the domain allowing bigger deformations on the center of the domain where bigger cells are present.

However, the described strategy in not sufficient to avoid a local worsening of the mesh quality near the moving boundaries. The solver calculates the cell displacement based on a cell-centred approach and interpolates to obtain the points movement. However, boundaries with prescribed movement maintain their imposed value, leading to possible differences between those values and the ones of the internal points and eventually to highly distorted cells, especially for very thin layers. In order to maintain a good mesh quality, the strategy proposed by [13] has been followed. The method allows to maintain a fixed first layer height by extending the interpolation to the boundaries. The difference between the interpolated value on the boundary and the desired boundary condition is then propagated into the mesh.

The main concern about the use of a mesh movement solver is its capability to preserve the mesh quality. It is indeed of crucial importance for an automatic process to avoid the accumulation of error due to low mesh quality, especially when working with partially converged variables. The strategy described, together with the use of a suitable smoother and an appropriate step size for the boundary movement, allows the fulfilment of the mesh quality criteria. The cancellation of the high frequency noise in the sensitivity map is indeed fundamental in order to avoid overlapping of boundaries. However, the choice of the correct parameters to set is not straightforward and highly case-dependent, thus several attempts could be necessary before finding the most appropriate ones. In order to ensure the correctness of the process, thus avoiding to perform the optimization with a highly distorted mesh, a mesh quality check has been introduced after each mesh morphing step. The additional step assures that the mesh quality criteria are satisfied at each iteration step and decide whether to continue with successive iterations of the optimization loop or to end the process.

5. Optimization results

The application of the steps described outlines an optimization loop that should bring to an improvement of the design with respect to the objective function taken into account. In the present work, the optimization routine has been fed with a U-bend shape with the aim to reduce its total pressure loss. The outcome of the optimization routine is shown in Fig. 7 and Fig. 8. Fig. 7 shows the optimized shape obtained, the normalized velocity field in it and its velocity streamlines. The percentage variation of total pressure loss is shown in Fig. 8, i.e. the trend of the objective function during the optimization process.

Comparing the flow field in the original and in the optimized geometry (Fig. 1 and Fig. 7 respectively), the direction taken by the optimization routine to achieve its objective is highlighted. The body shape is modified in order to obtain a pressure drop minimization through the reduction of the separation bubble size that takes form after the bend. The separation region is indeed the main source of pressure

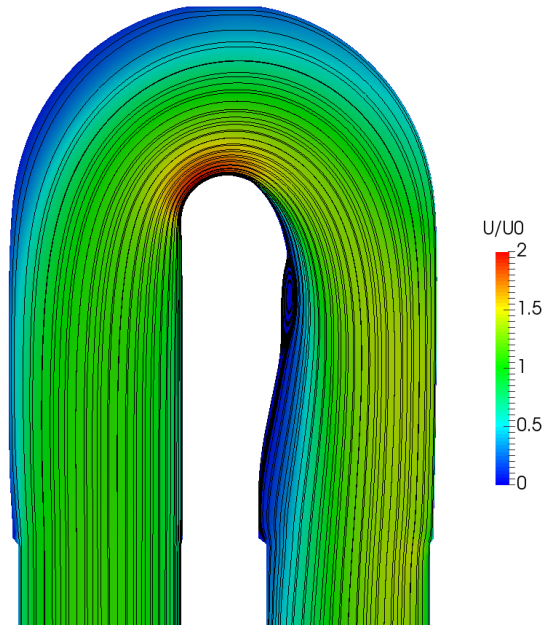

Figure 7: Optimized U-bend shape: velocity field and streamlines.

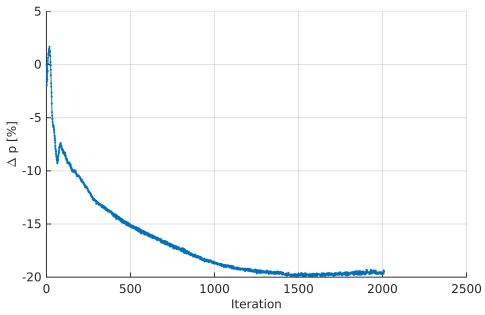

Figure 8: Optimization history: total pressure loss reduction during the loop iterations.

loss present in the proposed design, hence its suppression represents the target of the optimization routine. The optimized body allows to obtain a reduction of the pressure loss of the 20% in comparison with the initial design shape, as shown in Fig. 8. The optimization history converges in approximately 1500 iterations, where a local minimum is reached. The high number of iterations performed does not imply the use of an expensive computational routine. Indeed, the use of partially converged variables considerably speeds up the process, allowing to reach the minimum in a night-time period.

An analysis of the optimized U-bend shape verifies the characteristics discussed in the previous sections. A flat region is present at the top part of the bend, showing that the geometrical constraints imposed have been reached and satisfied. The external geometry looks smooth proving the effectiveness of the smoothing strategy used on the surface sensitivity. A kink highlights the passage from the design regions subjected to boundaries movement and the regions that are not allowed to take part in the optimization process. The rough transition between the two regions represents a limitation of the current routine. The discontinuity represents a limit to the capability of the optimizer, which indeed reaches a convergent optimization history when a recirculation bubble is still present. The use of a smoothing strategy along the borders would ensure continuity between the two regions, allowing further design improvement and acceptable external shapes.

The mesh morpher used has been showed to be robust enough so that the mesh quality criteria were satisfied at each iteration step.

A fully convergent simulation was carried out at the end of the optimization process; confirming the 20% improvement in the total pressure loss and thus verifying the validity of the approach used, i.e. the use of partially convergent variables at each iteration step.

6. Conclusion

The optimization of an internal flow application has been described in the present work. The U-bend test case has been optimized with respect to the total pressure loss. The use of an adjoint optimization strategy allowed to efficiently approach the problem, given the high number of design variables taken into account. The solution of the primal and adjoint problem gives information on the modifications to perform in order to improve the design, which has been attained trough the link to a constrained mesh morphing routine.

The optimization routine allowed to obtain a 20% of improvement of the cost function through the reduction of the separation bubble size that develops after the bend. However, the analysis of the flow field highlights that a small recirculation bubble is still present, probably due to the formation of a kink between the region subjected to optimization and the fixed one. Indeed, the presence of the discontinuity could lead the optimization routine to a local minimum. A smooth transition between the two regions would increase the degree of freedom of the optimizer, leading to further improvement of the design and to a faster optimization process.

Acknowledgments

This work was supported by the Fonds Wetenschappelijk Onderzoek Vlaanderen - FWO.

References

[1] A. Jameson, Aerodynamic Design via Control Theory, Journal of Scientific Computing.
[2] C. Othmer, Adjoint Methods for Car Aerodynamics, Journal of Mathematics in Industry.
[3] J.P. Goit and J. Meyers, Optimal Control of Wind Farm Power Extraction in Large Eddy Simulations, 32nd ASME Wind Energy Symposium, AIAA Journal DOI:10.2514/6.2014-0709.
[4] J. Han, S. Dutta, S. Ekkad, Gas Turbine Heat Transfer and Cooling Technology, Taylor and Francis, New York, 2000.
[5] T. Verstraete and J. Li, Multi-Objective Optimization of a U-bend for Minimal Pressure Loss and Maximal Heat Transfer Performance in Internal Cooling Channels, ASME Turbo Expo 2013: Turbine Technical Conference and Expositions Volume 3A: Heat Transfer.
[6] S. Zehner, H. Steinbrck, S.O. Neumann, B. Weigand, The Ice Formation Method: A Natural Approach to Optimize Turbomachinery Components, International Journal of Design & Nature 3 (2009) 259–272.
[7] H. Namgoong, C. Son, P. Ireland, U-bend Shaped Turbine Blade Cooling Passage Optimization, AIAA paper ISSMO 2008-5926.
[8] T. Verstraete and F. Coletti and J. Bulle and T. Vanderwielen and T. Arts, Optimization of a U-bend for Minimal Pressure Loss in Internal Cooling Channels Part I: Numerical Method, ASME paper GT2011-46541.
[9] F. Coletti, T. Verstraete, T. Vanderwielen, J. Bulle, T. Arts, Optimization of a U-bend for Minimal Pressure Loss in Internal Cooling Channels Part II: Experimental Validation, ASME paper GT2011-46555.
[10] E.M. Papoutsis-Kiachagias and K.C. Giannakoglou, Continuous Adjoint Methods for Turbulent Flows, Applied to Shape and Topology Optimization: Industrial Applications, Archives of Computational Methods in Engineering 23 (2) (2016) 255–299.
[11] A.S. Zymaris, D.I. Papadimitriou, K.C. Giannakoglou, C. Othmer, Continuous adjoint approach to the spalart-allmaras turbulence model for incompressible flows, Computers & Fluids (2009) 1528–1538.
[12] H. Jasak and Z. Tukovic, Automatic mesh motion for the unstructured Finite Volume Method, Transactions of FAMENA.
[13] http://www.openfoam.com/version-v3.0+/numerics.php.

Development of a hybrid multi-level optimization method

Arnaud Châtel

Turbomachinery and Propulsion Department, von Karman Institute for Fluid Dynamics, Belgium, arnaud.chatel@vki.ac.be

Supervisor: Tom Verstraete

Adjunct Professor, Turbomachinery and Propulsion Department, von Karman Institute for Fluid Dynamics, Belgium, tom.verstraete@vki.ac.be

University Supervisor: Grégory Coussement

Professor, Fluids Machines Department, Université de Mons, Belgium, Gregory.Coussement@umons.ac.be

Abstract

Nowadays, the engineering field makes extensive use of the optimization methods during the design procedures of new components in various scientific sectors. Moreover, the optimization problems become increasingly elaborate and complex to solve. Indeed, the optimizations are performed on geometries increasingly parametrized in order to explore larger design spaces. Since these optimizations require more computational resources and can be very time-consuming, the improvement of the optimization methods by themselves becomes a crucial challenge.

Therefore, the objective of the present project consists in the development of hybrid optimization methodology based on a multi-level approach in the parametrization enabling different levels of shape variety. In this algorithm, a coarse parametrization will control the geometry of the design by means of only few parameters, while finer models will use more parameters in order to allow a larger variability of the shapes. Moreover, the hybrid multi-level optimizations allow the design space exploration by the combination of gradient free methods operating on the coarse models with gradient based methods exploiting the finer parametrizations.

Given the objectives, the project will be decomposed in several steps. At first, an hybrid optimization algorithm will be developed and validated on analytical test cases specially designed to test the performances of optimization methods. Then, the hybrid method will be tested on typical turbomachinery applications and the multi-level approach in the parametrization will be implemented and validated on the same applications. Finally, in order to maximize the potential of the optimization methods, a dynamic strategy will be elaborated that selects the most significant parameters from the finer models to establish the coarse parametrization.

Optimization of the LS89 axial turbine profile using a CAD and adjoint based approach

Ismael Sànchez Torreguitart

Turbomachinery Department, von Karman Institute for Fluid Dynamics (VKI), Chaussée de Waterloo 72, 1640 Rhode-Saint-Genèse, Belgium, ismael.sanchez.torreguitart@vki.ac.be

Supervisor: Tom Verstraete

Queen Mary University of London, Mile End Road, E1 4NS, London, UK, t.verstraete@qmul.ac.uk

University Supervisor: Carles-David Segarra

Heat and Mass Transfer Technological Center (CTTC), Universitat Politcnica de Catalunya, segarra@cttc.upc.edu

Abstract

A single point CAD-based adjoint CFD optimization of the LS89 high pressure axial turbine vane cascade is performed herein. The gradients used for the optimization are obtained via a novel approach in which both the CAD kernel and grid generation VKI in-house tools are differentiated using Algorithmic Differentiation techniques, achieving a reduction of almost 12% and 16% in entropy generation and total pressure losses respectively.

Keywords: base pressure, profile losses, algorithmic differentiation, adjoint optimization

1. Introduction

Designing and optimizing a turbine vane is a complex iterative design process that can take significant time and effort. The use of relatively low-cost numerical shape optimisation methods has become more popular and have been widely used in turbomachinery applications. Within the different classes of optimization methods, the adjoint based methods are relatively low-cost gradient based optimization methods in computing the gradients for a large number of design variables [1]. Typically, the grid point coordinates have been used as design variables [2]. This approach offers a very rich design space but has some drawbacks that need to be considered. First, the connection to the CAD geometry is lost. This means that an additional step is required to transform the optimal shape defined by grid points back to smooth CAD shape. Secondly, although there are several successful methods that can be used to convert a cloud of grid points to CAD [3; 4], the fitting error can impair the optimality of the shape. Furthermore, this additional step can take significant time and it is not guaranteed that the final approximated CAD shape will meet the design requirements and constraints [5; 6]. Also, the use of a smoother is inevitable to avoid irregular shapes. To avoid these problems, in this work it is proposed to keep the CAD geometry in the optimization loop.

Changing the design variables from the grid coordinates to CAD-based parameters, such as axial chord length, stagger angle, trailing edge wedge angle, etc., requires an additional sensitivity computation step. The grid sensitivities, which are defined as the partial derivative of the grid coordinates with respect to the design variables, will need to be computed as well. This could be done by using finite differences but the accuracy of the gradients is dependent upon the chosen step size for each design variable. If the step size is too small the gradients are inaccurate due to limited arithmetic precision, whereas a too big step size would yield truncation errors. This work aims to circumvent these issues by making use of Algorithmic Differentiation (AD) [7] for the CAD kernel and the grid generation [8]. AD allows to compute the derivatives of an output of a program with respect to the inputs by applying the chain rule in an automatic fashion throughout the evaluation of the code. This means that the grid sensitivities will be accurate to machine

accuracy.

In this work, it is proposed to use a CAD-based adjoint-based optimization method for the LS89 [9; 10] high pressure axial turbine nozzle guide vane profile. The LS89 (Figure 1) was originally designed and optimized at the Von Karman Institute for Fluid Dynamics for a subsonic isentropic outlet Mach number of 0.9 (MUR45 conditions) by the inverse method [10]. [11] performed both single and multi-point optimisations on the LS89 but the total pressure loss reduction achieved was below 1%. The question arises whether the LS89 is to good already to be optimised any further. This paper addresses this and presents an adjoint optimization of the turbine profile, by using a novel CAD-based approach in which:

1. the optimal shape remains defined within the CAD tool. The optimization problem herein is expressed by CAD parameters that are directly used in defining the CAD geometry by means of Bézier and B-spline curves.
2. the in-house CAD and grid generation tools are automatically differentiated in forward mode to obtain the exact derivatives of the grid coordinates with respect to the CAD-based design parameters. This allows to accurately predict the sensitivities and circumvent the errors introduced by finite differences
3. the trailing edge thickness and axial chord length are kept fixed as manufacturing constraints and the exit flow angle is considered as an aerodynamic constraint.

A computer aided design and optimization tool for turbomachinery applications (CADO) [12] is used throughout this work.

2. CAD-based parametrisation

The construction of the turbine profile shown in Fig. 1 and 2 is based on the parametrization described by [13]. The profile is defined by a set of CAD-based or engineering based design parameters shown in Tab. 2 that are relevant to the aerodynamic performance (e.g. solidity, stagger angle, etc.) and the manufacturing requirements (e.g. axial chord length, trailing edge radius). First, a camber line is constructed. The points P_{LE},P_{mid}, P_{TE} define the control points of the 2nd order Bézier curve describing the camber line. The camber line is used to define the position of the control points of the SS and PS B-spline curves relative to it. The profile is constructed by two B-spline curves for the suction side (SS) and pressure side (PS) and a circular arc at the TE to close the profile. The normal distance of the first control point relative to the camber line is calculated in such a way that G2 geometric continuity (i.e. equal curvature) is maintained between the SS and PS B-splines at the Leading Edge.

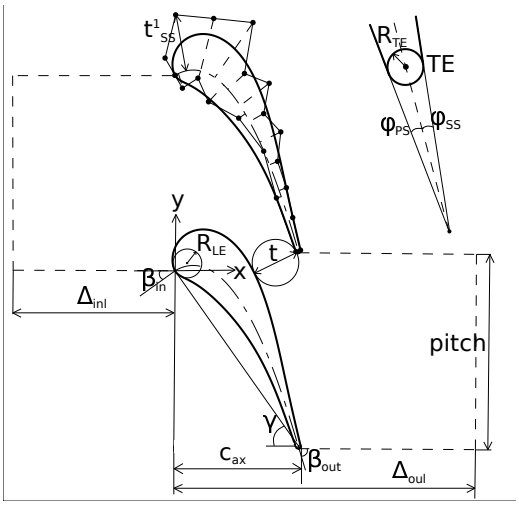

Figure 1: LS89 profile geometry

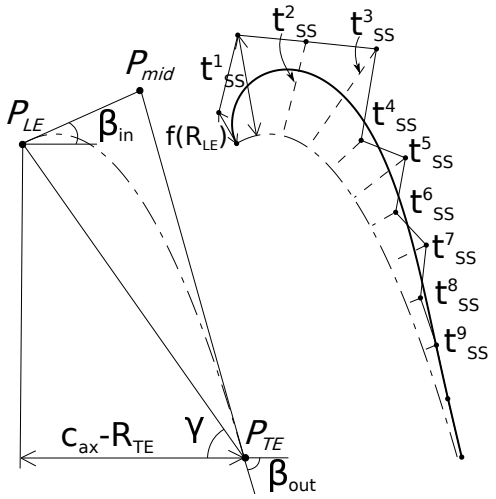

Figure 2: Construction of the suction side by a B-spline curve [8]

3. Optimisation

The purpose of the optimisation algorithm (Figure 3) is to reduce the entropy generation J_1 (Equation 1)

Table 1: Test conditions matrix

Test	q_{cw} kW m^{-2}	P_d Pa	h_e MJ kg^{-1}	T_e K	v_e m s^{-1}
1	160	16	7.5	3618	59.5
2	212	17	9.6	4476	69.0
3	280	19	12.0	5062	80.1
a	155	14	7.5	3601	56.4
b	211	16	9.6	4498	67.6
c	294	19	12.5	5137	80.0

Design parameters	Acronyms	Value
Solidity	σ	1.118
Axial Chord Length	c_{ax}	36.955 mm
Stagger Angle	γ	54.9°
LE Radius	R_{LE}	4.126 mm
TE Radius	R_{TE}	0.710 mm
TE Wedge Angle SS	φ_{SS}	4.0°
TE Wedge Angle PS	φ_{PS}	2.5°
Inlet Angle	β_{in}	0.0°
Outlet Angle	β_{out}	74.0°
Stretching Factors PS	k_{PS}	1.175
PS Thickness (x4)	t^1_{PS}, ..., t^4_{PS}	$\in$ (0.040, 6.650) mm
Stretching Factors SS	k_{SS}	1.1
SS Thickness (x9)	t^1_{SS}, ..., t^9_{SS}	$\in$ (2.565, 19.690) mm

Table 2: Design parameters used to define the LS89 baseline profile

whilst maintaining the exit flow angle J_3 (Equation 2) above or equal to the baseline value of $J_{3,ref} = 74.83$ deg, by modifying the design vector $\vec{\alpha}$. The flow state $\vec{U}$ and the design vector $\vec{\alpha}$ are coupled via the primal flow governing equations. The constrained optimisation problem is handled with the penalty method. The penalty term becomes active only if the exit flow angle is below the target value. The weighed cost function of the single point J_{SP} optimisation problem is given by Equation 3. The L-BFGS-B algorithm [14] available in the python SciPy package [15] is used to find the new design vector.

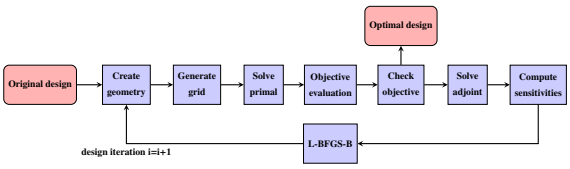

Figure 3: Optimisation flow chart

$$J_1(\vec{\alpha}, \vec{U}) = \frac{\int_{out} p\rho^{1-\gamma} V_x dy}{\dot{m}_{out}} \tag{1}$$

$$J_3(\vec{\alpha}, \vec{U} = atan\left(\frac{\overline{V_y}}{\overline{V_x}}\right) \tag{2}$$

$$J_{SP}(\vec{\alpha}, \vec{U}) = \frac{J_1}{J_{1,ref}} + J_{3,coef}\left(\frac{J_3}{J_{3,ref}} - 1\right)^2 \tag{3}$$

Grid generation

A multi-block structured grid is generated for every optimisation iteration (Figure 3). A mesh-independent sensitivity study was carried out in order to select an appropriate mesh for the optimization. One O-grid block is placed around the profile and there are six additional H-grid blocks, four of them distributed around the profile and the remaining two being used as the inlet and outlet blocks. [8] describes in more detail how the grid was generated.

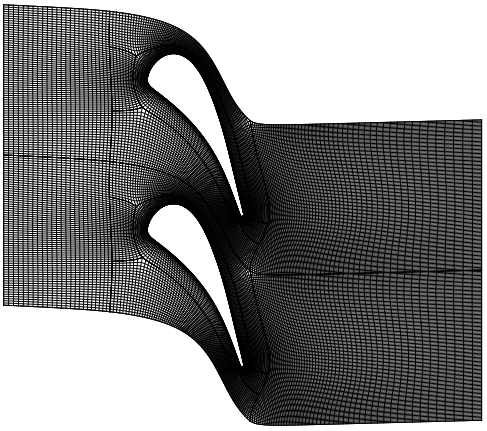

Figure 4: LS89 mesh [8]

Flow and Adjoint solvers

The flow solver employs a cell-centered finite volume discretization on multiblock structured grids. The three dimensional compressible Reynolds-Averaged Navier-Stokes (RANS) equations are solved with an implicit time integration scheme accelerated by local time-stepping and multigrid. The fluid is considered as a calorically perfect gas and the eddy-viscosity hypothesis is used to account for the effect of turbulence. Convective fluxes are computed using Roe's approximate Riemann solver [16] with a MUSCL-type reconstruction [17] of primitive variables to attain second order accuracy. Oscillations

near shocks are suppressed by a van-Albada type limiter [18]. The numerical dissipation of the scheme is controlled by the entropy correction of Harten [19] for both linear and non-linear eigenvalues. Viscous fluxes are calculated with a central discretization scheme, while the negative Spalart-Allmaras turbulence model [20] is used for the turbulence closure problem assuming fully turbulent flow from the inlet ($Re_{inlet} \approx 2x10^5$). Boundary conditions are imposed weakly by utilizing the dummy cell concept [21]. The hand derived discrete adjoint solver uses constant eddy viscosity assumption which is a valid approach for engineering design applications. The flow solver and its discrete adjoint counterpart use the stabilisation scheme described by [22].

Gradient computation

[8] showed the first results of differentiating the CAD kernel and grid generation tools using the AD tool ADOL-C [23]. In the work herein, the optimisation algorithm computes the grid sensitivities $\frac{d\vec{X}}{d\vec{\alpha}}$ for every optimisation step, using the forward vector mode as opposed to the forward scalar or reverse modes as it allows to compute $\frac{d\vec{X}}{d\vec{\alpha}}$ in one single evaluation of the primal at a relatively low cost. The performance sensitivities $\frac{dJ}{d\vec{\alpha}}$ for each cost function J_1 or J_3 are computed by doing a scalar product of the adjoint calculated sensitivities $\frac{dJ}{d\vec{X}}$ (ie. the derivative of the cost function with respect to the grid coordinates $\vec{X}$) with the grid sensitivities $\frac{d\vec{X}}{d\vec{\alpha}}$.

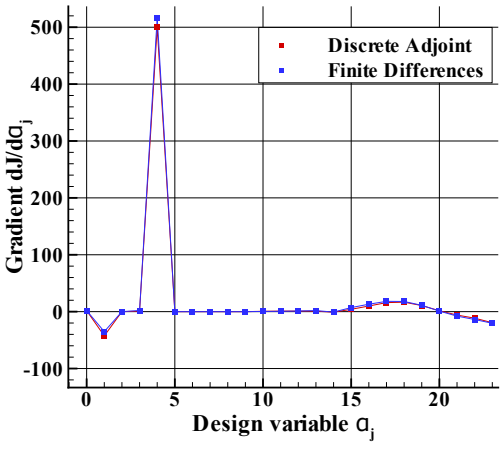

Figure 5: Entropy generation (J_1) gradients vs. Finite Differences

A suitable step size for each design variable was selected to compute the gradients with finite differences

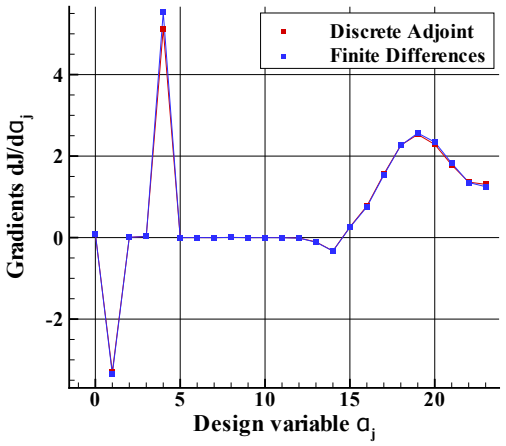

Figure 6: Exit flow angle gradients (J_3) vs. Finite Differences

and compare them against the gradients obtained by the discrete adjoint. Figure 5 and 6 show a good agreement with finite differences for both the entropy generation and exit flow angle.

4. Results

For the baseline geometry, Figure 8 shows a fairly good agreement between the M_{ise} predicted by CFD and the experimental data (MUR45 test condition, see [9]). The L-BFGS-B algorithm converges within 20 optimisation iterations. More cycles were performed but no further decrease in the objective function was obtained. Despite the fact that the mass flow for the optimal geometry has increased slighlty by 1.2%, the entropy generation is reduced by 11.6%, whilst maintaining the exit flow angle within ±0.1% of the baseline value.

Figure 7 shows significant shape differences between the LS89 and the optimal shape (which is referenced to as the LS89-II throughout this paper), the later being a more aft-loaded profile than the baseline design. The isentropic Mach number distributions is shown in Figure 8.

As the aft-loaded profile has significant rear suction side curvature, the flow is rapidly accelerated towards a higher peak Mach number than the baseline design, after which the flow is decelerated. This deceleration is then followed by a small acceleration before the flow is rapidly decelerated again and leaves the trailing edge at a significantly lower exit isentropic Mach number. The strong deceleration towards the end of the suction side suggests that the boundary layer will

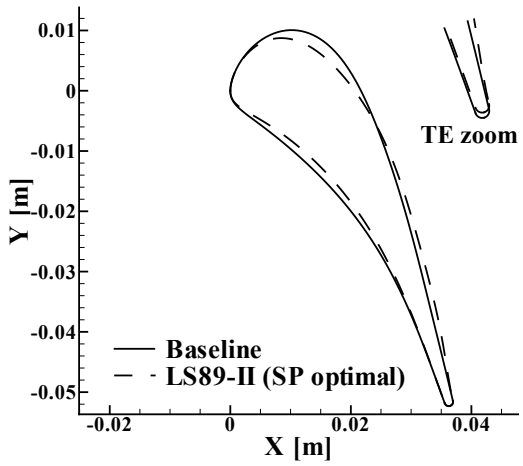

Figure 7: LS89 baseline and LS89-II optimal profiles

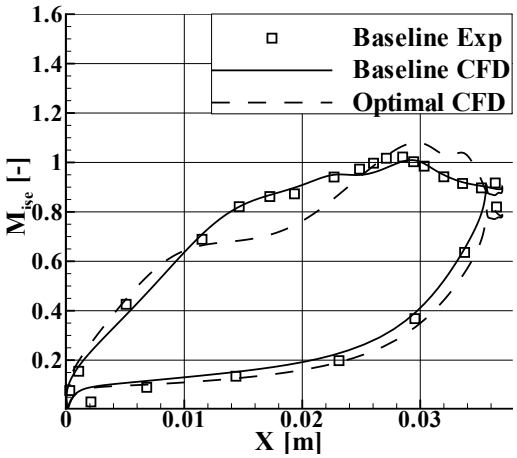

Figure 8: Isentropic Mach number comparison

be thicker and one would expect higher profile losses. However, the pressure losses figures shown in Table 5 show the opposite. The total pressure loss reduction between the inlet and the fully mixed-out flow at the outlet plane, expressed via $P_{01} - P_{02}$ or by the ζ_2 coefficient (see Equation 4), is of the order of 16.3%. The downstream total pressure loss profile, at the plane $X/c_{ax} = 1.433$, is shown in Figure 6. In the vertical axis the total pressure loss $P_{01} - P_{0X}$ between the inlet and a downstream plane at $x/c_{ax} = 1.433$ is expressed as a a percentage of the downstream dynamic head q_X at the $X/c_{ax} = 1.433$ plane. This figure shows that the total pressure loss generated in the wake is reduced significantly, although the loss is locally increased in the passage.

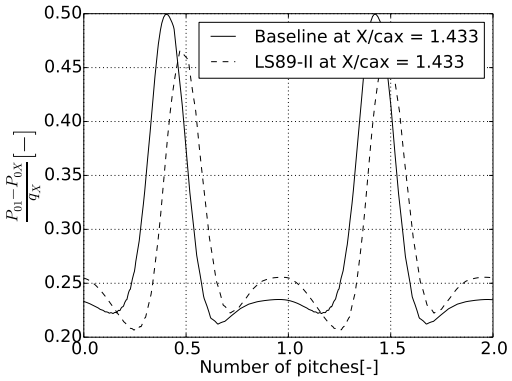

Figure 9: Total pressure loss downstream at $X/c_{ax} = 1.433$

$$\zeta_2 = 1 - \frac{1 - (\frac{p_2}{P_{02}})^{\frac{\gamma-1}{\gamma}}}{1 - (\frac{p_2}{P_{01}})^{\frac{\gamma-1}{\gamma}}} \tag{4}$$

In order to understand why the optimal shape is more efficient than the baseline, the following subsections will look into the loading, boundary layer parameters, base pressure and profile losses for each profile.

Zweifel loading coefficient

The total loading, which can be expressed as the integral of the $P_{PS} - P_{SS}$ over the axial chord length, has increased by 1% for the optimal shape as a result of the 1% increase in the pitch and having the same exit flow angle. The Zweifel loading coefficient Z_w [24] is a measure of how efficiently the profile is loaded. An efficient loaded profile would be one in which the pressure is stagnated over the pressure side and the velocity on the suction side is constant and equal to the downstream velocity. Equation 5 was used to calculate Zweifel, which increased from 0.67 for the baseline to 0.81 for the optimal and agrees with the Zweifel's design rule that says that loss is minimised for $0.8 < Z_w < 1$.

$$Z_w = \frac{\int_0^1 (p_{PS} - p_{SS}) \frac{dx}{c_{ax}}}{(P_{01} - p_b) c_{ax}} \tag{5}$$

Boundary layer parameters

The state of the boundary layer close to the trailing edge is deemed to have an impact on the profile losses (see Equation 6). Table 3 compares the boundary layer parameters between the baseline and optimal shapes for two locations on the suction side: at the

peak M_{ise} location and very close to the TE (approximately at $x = 0.03m$ and $x = 0.037m$ respectively, see Figure 8). The later location is defined herein as the point of the suction side slightly upstream of the TE circle. The boundary layer velocity profiles are shown in Figures 10 and 11 for both locations, showing that there is no boundary layer separation.

At the peak M_{ise} location, the boundary layer thickness δ for the optimal design is smaller than for the baseline, as expected due to the higher acceleration. When the flow decelerates from the peak M_{ise} location to the point just upstream of the trailing edge circle, the boundary layer thickness almost doubles for the baseline and triples for the optimal profile. The resulting δ of the optimal shape is 18% thicker than the baseline. The shape factor H is higher for the optimal than for the baseline design in both locations, which means that the optimal profile has stronger adverse pressure gradient. The shape factor for both designs are between the typical laminar Blasius boundary layer value ($H = 2.59$) and the turbulent values ($H = 1.3 - 1.5$).

From a boundary layer perspective, the optimal design would have higher profile losses due to the higher thickness displacement and momentum thickness. However, there is at least one more factor to be considered when determining the profile losses: the base pressure.

	LS89 at $M_{ise,max}$	LS89-II at $M_{ise,max}$	LS89 at $X_{SS,TE}$	LS89-II at $X_{SS,TE}$
$\delta/D_{TE}[-]$	0.501	0.390	0.939	1.11
$\delta^*/D_{TE}[-]$	0.104	0.079	0.206	0.346
$\theta/D_{TE}[-]$	0.0557	0.0405	0.1186	0.1780
$H[-]$	1.86	1.96	1.74	1.95

Table 3: Boundary layer parameters

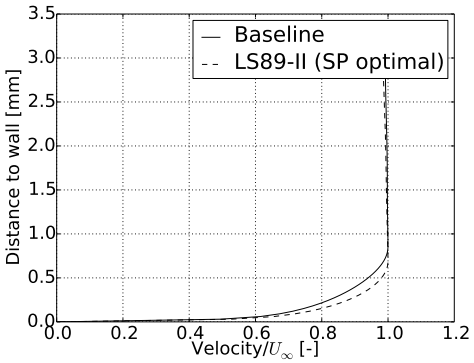

Figure 10: Boundary layer profiles on the suction side at peak Mach number location

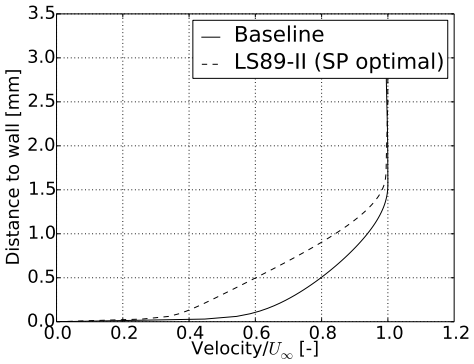

Figure 11: Boundary layer profiles on the suction side close to the TE

Base pressure

The base pressure, which is the static pressure at the mid point of the trailing edge is known to play an important role in the profile losses. Higher base pressures contribute to the reduction of the profile losses. The trailing edge pressure distribution shown in Figure 12 shows that the optimal shape has got 10 % higher base pressure. Higher base pressures are expected of an aft-loaded profile with significant rear suction side curvature and higher values of unguided or uncovered turning [25]. Also, it is generally thought that higher values of boundary layer thickness result in higher values of base pressure.

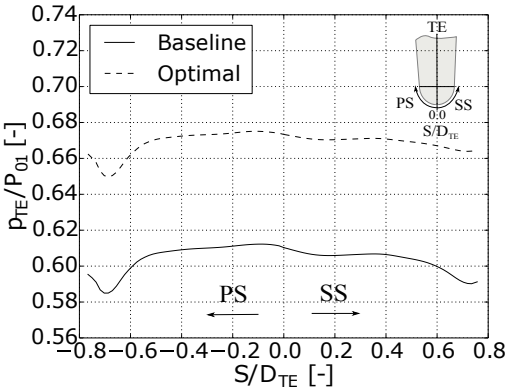

Figure 12: Optimal vs. Baseline trailing edge pressure distributions

Predicting the absolute values of the base pressure correctly can be very difficult due to the highly complex nature of the flow in the trailing edge. [27] showed that steady state simulations usually predict

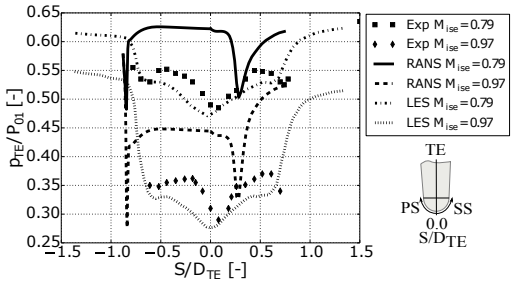

Figure 13: Trailing edge pressure distribution with the blade tested by [26]. LES results are from [27]

the wrong shape or distribution of pressure around the trailing edge, whereas LES or URANS capture much better the shape and the pressure values when compared to experimental data. The pressure distribution shown in Figure 12 is a nearly-uniform pressure around the trailing edge, which is suspected to be different to the real pressure distribution profile. However, it is believed that the base pressure delta difference between two steady state simulations, one for the optimal and the other for the baseline profiles, is a fairly good estimate of the real difference. The validity of this assumption has been investigated by performing two RANS simulations for the turbine profile that was tested by [26] at $M_{ise} = 0.79$ and 0.97 and comparing the base pressure delta between these two operating conditions against the experimental data and the LES results performed by [27] (Figure 13). The base pressure delta, which is taken at $S/D_{TE} = 0$ from Figure 13, is 0.18 for both the experiments and RANS and 0.20 for LES. This confirms that, despite the limitations of CFD in predicting the base pressure absolute values, RANS is able to capture very well the relative differences in base pressure between two operating conditions.

Profile losses

[28] showed that the profile losses for incompressible flow can be related to the base pressure coefficient and the boundary layer parameters, as shown in Equation 6. The relative effect of the base pressure coefficient is increased in compressible flow. The profile loss split is shown in Table 4. The higher δ^* and θ values of the optimal shape contribute to increasing the profile loss. However, the reduction in profile losses due to the 302.2% increase in the base pressure coefficient term dominates and explains the 30% reduction in profile losses.

$$\zeta_p = \frac{-C_b D_{TE}}{o} + 2\frac{\theta_{SS} + \theta_{PS}}{o} + \left(\frac{\delta^*_{SS} + \delta^*_{PS} + D_{TE}}{o}\right)^2 \quad (6)$$

	LS89	LS89-II (optimal)	Variation
$\frac{-C_b D_{TE}}{o}$ [-]	-0.0016	-0.0065	302.2%
$2\frac{\theta_{SS}+\theta_{PS}}{o}$ [-]	0.0066	0.0095	43.5%
$\left(\frac{\delta^*_{SS}+\delta^*_{PS}+D_{TE}}{o}\right)^2$ [-]	0.0010	0.0012	21%
ζ_p [-]	0.0060	0.0042	-30%

Table 4: Profile loss contribution for the LS89 (baseline) and LS89-II (optimal)

	Acronyms	LS89	LS89-II (optimal)	Variation
Entropy generation [Pa/(kg/m^3)]	J_1	826.7	731.0	-11.6%
Exit flow angle [deg]	J_3	74.89	74.89	-0.01%
Mass flow [kg/s]	$\dot{m}$	0.008	0.009	+1.2%
Total pressure losses [kPa]	$P_{01} - P_{02}$	2.47	2.07	-16.3%
Downstream loss coeff [-]	ζ_2	0.02986	0.02500	-16.3%
Profile losses [-]	ζ_p	0.0060	0.0042	-30%
Zweifel coefficient [-]	Z_w	0.67	0.81	+21.2%
Solidity [-]	σ	1.118	1.108	-0.9%
Pitch [m]	g	0.0575	0.0580	+0.9%

Table 5: Comparison between the LS89 (baseline) and LS89-II (optimal)

5. Conclusions

This paper presents an single point optimisation of the LS89 axial turbine cascade vane profile for the design downstream isentropic Mach number of 0.9. The results show that the total pressure losses and entropy generation can be reduced by 16% and nearly 12% respectively by going from an front to a rear loaded profile and by keeping the exit flow angle. Despite the increase in mass flow, loading, boundary layer thickness displacement and momentum thickness, the base pressure coefficient plays a dominant role herein and reduces the profile losses by 30%. The relative delta in base pressure predicted by the steady simulation between the optimal and baseline profiles is deemed to be representative of the real value, as RANS tends to capture well the relative differences between two designs. However, future unsteady studies or experimental investigations would be beneficial in order to confirm these findings.

6. Acknowledgments

This work has been conducted within the IODA project (http://ioda.sems.qmul.ac.uk). The authors would like to thank you the European Union for funding this work through the European Union HORIZON 2020 Framework Programme for Research and Innovation under Grant Agreement No. 642959.

References

[1] J. E. Peter, R. P. Dwight, Numerical sensitivity analysis for aerodynamic optimization: A survey of approaches, Computers & Fluids 39 (3) (2010) 373–391.

[2] A. Jameson, Efficient aerodynamic shape optimization, AIAA paper 4369 (2004) 2004.

[3] G. Becker, M. Schäfer, A. Jameson, An advanced nurbs fitting procedure for post-processing of grid-based shape optimizations, in: 49th AIAA Aerospace Sciences Meeting, Orlando, FL, USA, 2011.

[4] N. Leal, E. Leal, J. W. Branch, Simple method for constructing nurbs surfaces from unorganized points, in: Proceedings of the 19th international meshing roundtable, Springer, 2010, pp. 161–175.

[5] J. A. Samareh, Survey of shape parameterization techniques for high-fidelity multidisciplinary shape optimization, AIAA journal 39 (5) (2001) 877–884.

[6] V. Braibant, C. Fleury, Shape optimal design using b-splines, Computer Methods in Applied Mechanics and Engineering 44 (3) (1984) 247–267.

[7] A. Griewank, A. Walther, Evaluating derivatives: principles and techniques of algorithmic differentiation, Siam, 2008.

[8] I. Sanchez Torreguitart, T. Verstraete, L. Mueller, Cad kernel and grid generation algorithmic differentiation for turbomachinery adjoint optimization, in: 7th European Congress on Computational Methods in Applied Sciences and Engineering, Hersonissos, Crete, Greece, June, 2016.

[9] T. Arts, M. Lambertderouvroit, A. Rutherford, Aero-thermal investigation of a highly loaded transonic linear turbine guide vane cascade. a test case for inviscid and viscous flow computations, NASA STI/Recon Technical Report N 91 (1990) 23437.

[10] R. Van den Braembussche, O. Léonard, L. Nekmouche, Subsonic and transonic blade design by means of analysis codes, Computational Methods for Aerodynamic Design (Inverse) and Optimization, AGARD CP 463.

[11] H. Montanelli, M. Montagnac, F. Gallard, Gradient span analysis method: Application to the multipoint aerodynamic shape optimization of a turbine cascade, Journal of Turbomachinery 137 (9) (2015) 091006.

[12] T. Verstraete, Cado: A computer aided design and optimization tool for turbomachinery applications, in: 2nd Int. Conf. on Engineering Optimization, Lisbon, Portugal, September, 2010, pp. 6–9.

[13] S. Pierret, Designing turbomachinery blades by means of the function approximation concept based on artificial neural network, genetic algorithm, and the navier-stokes equations, Ph.D. thesis, Von Karman Institute for Fluid Dynamics (12 1999).

[14] C. Zhu, R. H. Byrd, P. Lu, J. Nocedal, Algorithm 778: L-bfgs-b: Fortran subroutines for large-scale bound-constrained optimization, ACM Transactions on Mathematical Software (TOMS) 23 (4) (1997) 550–560.

[15] E. Jones, T. Oliphant, P. Peterson, et al., SciPy: Open source scientific tools for Python, [Online; accessed 2016-09-11] (2001–).
URL `http://www.scipy.org/`

[16] Roe P.L., Approximate Riemann Solvers, Parameter Vectors, and Difference Schemes, Journal of Computational Physics 43 (1981) 357–372.

[17] van Leer B., Towards the Ultimate Conservative Difference Scheme, V. A Second Order Sequel to Godunov's Method, Journal of Computational Physics 32 (1) (1979) 101–136.

[18] Venkatakrishnan V., On the Accuracy of Limiters and Convergence to Steady State Solutions, in: AIAA Conference, no. 93-0880, 1993.

[19] Harten A.; Hyman J.M., Self-Adjusting Grid Methods for One-Dimensional Hyperbolic Conservation Laws, Journal of Computational Physiscs 50 (2) (1983) 235–269.

[20] Allmaras S.R.; Johnson F.T.; Spalart P.R., Modifications and Clarifications for the Imlementation of the Spalart-Allmaras Turbulence Model, in: ICCFD7-1902, 7th International Conference on Computational Fluid Dynamics, 2012.

[21] Blazek J., Computational Fluid Dynamics: Principles and Applications, 2nd Edition, Elsevier Science Ltd, Amsterdam, 2001.

[22] S. Xu, D. Radford, M. Meyer, J.-D. Müller, Stabilisation of discrete steady adjoint solvers, Journal of Computational Physics 299 (2015) 175–195.

[23] A. Walther, A. Griewank, A package for the automatic differentiation of algorithms written in c/c+, URL https://projects.coin-or. org/ADOL-C.

[24] O. Zweifel, The spacing of turbo-machine blading, especially with large angular deflection, Brown Boveri Rev. 32 (12) (1945) 436–444.

[25] C. Sieverding, M. Stanislas, J. Snoek, The base pressure problem in transonic turbine cascades, in: ASME 1979 International Gas Turbine Conference and Exhibit and Solar Energy Conference, American Society of Mechanical Engineers, 1979, pp. V01BT02A019–V01BT02A019.

[26] C. H. Sieverding, H. Richard, J.-M. Desse, Turbine blade trailing edge flow characteristics at high subsonic outlet mach number, Journal of turbomachinery 125 (2) (2003) 298–309.

[27] S. Vagnoli, T. Verstraete, B. Mateos, C. Sieverding, Prediction of the unsteady turbine trailing edge wake flow characteristics and comparison with experimental data, Proceedings of the Institution of Mechanical Engineers, Part A: Journal of Power and Energy (2015) 0957650915592074.

[28] J. D. Denton, Loss mechanisms in turbomachines, in: ASME 1993 International Gas Turbine and Aeroengine Congress and Exposition, American Society of Mechanical Engineers, 1993, pp. V002T14A001–V002T14A001.

Experimentally and numerically driven optimization of high performance instrumentation for real engine testing

Aude Lahalle

Turbomachinery and Propulsion Department, von Karman Institute for Fluid Dynamics, Belgium, aude.lahalle@vki.ac.be

Supervisor: Fabrizio Fontaneto

Assistant Professor, Turbomachinery and Propulsion Department, von Karman Institute for Fluid Dynamics, Belgium, fontaneto@vki.ac.be

University Promoter: Herve Jeanmart

Professor, Institute of Mechanics, Materials and Civil Engineering, Universite Catholique de Louvain, Belgium, herve.jeanmart@uclouvain.be

Abstract

During the development phase of an aircraft engine, extensive ground and flight instrumentation testing is performed. The performance of the instrumentation is quantified in terms of Recovery Factor (RF). Experimental data only provide measurement at the sensor location, but no information is available for the flow field taking place in and around the probe.

The scope of the present paper is to numerically investigate the flow field taking place inside and around a three Kiel heads rake. The study will focus on the description of the flow field and providing qualitative data. Each head has an elliptical casing and contains a pressure sensor (pneumatic pressure tap) and a temperature sensor (thermocouple).

Steady-state RANS simulations have been realized for two different Mach numbers (M = 0.30 and M = 0.65), providing a complete mesh and turbulence models sensitivity analysis. The simulated flow field demonstrated that regardless of the Mach number, the flow topology is very similar. The validity of the experimental calibration was then assessed by performing a Reynolds number investigation and by varying the external flow field. Four Reynolds number were investigated at M = 0.65 and confirmed that the experimental calibrations are independent from Reynolds number. Then, two engine geometries were reproduces, and simulations at M = 0.30 and M = 0.65 were realized. The results supported the calibrations results as still valid when the instrumentation was mounted in real engines.

Keywords: CFD, multi-port pressure port, real engine conditions

Nomenclature

Subscripts

Adim.	Adimensionalized
is	Isentropic
meas	Measured quantity
real	Real quantity

Greek

α, α'	[°]	Inclination angle
ΔP_0	[Pa]	$\Delta P_0 = P_{0,Real} - P_{0,Meas.}$
ΔT_0	[K]	$\Delta T_0 = T_{0,Real} - T_{0,Meas.}$
ϵ	[$m^2 s^{-2}$]	Turbulent dissipation rate
ω	[s^{-1}]	Specific turbulent dissipation rate

Latin

A_1, A_2	[m^2]	Inlet and outlet surfaces
AR	[-]	Area Ratio, AR = A_2/A_1
c	[m]	Chord length
D_{EXIT}	[m]	Nozzle exit diameter
k	[$m^2 s^{-2}$]	Turbulent kinetic energy
h	[m]	Altitude
l	[m]	Turbulent length scale
M	[-]	Mach number
$\dot{m}$	[$kg.m^{-3}$]	Mass flow rate

MF	[-]	Mass Factor
MR	[-]	Mass flow Ratio
P	[Pa]	Pressure
Re	[m^{-1}]	Lengthless Reynolds number
Re_c	[-]	Reynolds number
$Re_{c,Adim.}$	[-]	Non-dimensionalized Reynolds number
SST	[-]	Shear Stress Transport
RF	[-]	Recovery Factor
T	[K]	Temperature
TO	[-]	Take-Off

1. Introduction

During the development phase of an aircraft engine, extensive ground and flight testing is performed on the engine as well as on its components. On one hand, testing serves as a validation activity for the numerical simulations usually performed during the design phase of a new aero-engine component. On the other hand, testing stands as a fundamental benchmark of the performance of the engine, prior to its submission to the certification agency and therefore prior to its commercialization. In-house ground and flying testing is therefore crucial at every phase of the development of an aero-engine and strongly depends on the quality of the performed measurements. To this extent, the typically employed instrumentation undergoes an extremely precise calibration process targeting the evaluation of the so-called Recovery Factor (RF) - Eq.1 - at different flow conditions. The RF might be evaluated at variable Mach number, variable Reynolds number and/or at different flow angles. Since modern aircraft engines are heavily instrumented, the calibration phase corresponds to a substantial time and budget item.

$$RF = \frac{X_{meas}}{X_{real}} \tag{1}$$

Hypothetically, the impact of the instrumentation on the development budget of a new aero-engine component could be drastically reduced by suppressing the calibration of the instrumentation. This could be achieved by means of probes exhibiting RF values so high that the correction introduced by the RF (X_{real} = $X_{measured}$/RF) would fall within the uncertainty of the measurement itself or at a further extent result in the precise control of RF value. Generally speaking, the RF is subject to a number of parameters: e.g. geometry, dimensions and scaling effect, manufacturing repeatability, etc... Hence, in order to achieve a high RF, one must take into account several interdependant disciplines: from the aerodynamics of the internal field to the structural design, as well as the manufacturing technology. For that reason, a design methodology targeting high RF probes should be defined. Therefore, a thorough study of all the parameters affecting the RF should be performed as it will highlight the sensitivity of the RF to each parameter. The present paper is configured as a preliminary study towards the definition of a design methodology for extremely high performance instrumentation. It will first introduce the measurement environment of calibrated ground and flying testing instrumentation which was built during the last years at the von Karman Institute for Fluid Dynamics (VKI). The experimental data will then be used to trigger numerical simulations in order to provide a detailed analysis on the flow-field generated by a typical total temperature and total pressure probe for ground and flying testing campaigns.Then simulations will be performed to verify the validity of the experimental calibrations for different conditions then the experimental rig. A Reynolds number investigation will be realized, reproducing cruise conditions of a typical commercial compressor. Finally, engine-like geometries will be reproduced to determine the effect of constraining geometries on the performance of the probe.

2. Highly reliable instrumentation calibration

Over the two past years, VKI has developed a reliable calibration procedure for total temperature and/or pressure engine instrumentation in terms of Mach number and/or flow angles. The measurements were performed in VKIs high speed calibration facility, C4 (Figure 1), and deliver pressure and temperature RFs respectively referred to as RF_P - Eq. 2 - and RF_T - Eq. 3.

$$RF_P = \frac{P_{0,measured}}{P_{0,real}} = 1 - \frac{\Delta P_0}{P_{0,real}} \tag{2}$$

$$RF_T = \frac{T_{0,measured}}{T_{0,real}} = 1 - \frac{\Delta T_0}{T_{0,real}} \tag{3}$$

This facility, a highly versatile atmospheric discharge calibration nozzle, consists of a circular convergent nozzle characterized by a contraction ratio of 14.75 with an outlet diameter, D_{EXIT}, of 50mm. The discharge Mach number at the nozzle exit, which can vary between 0.1 and sonic conditions, is regulated by means of a needle valve allowing the operator to control the total pressure upstream of the nozzle, the outlet static pressure being equal to atmospheric condition.

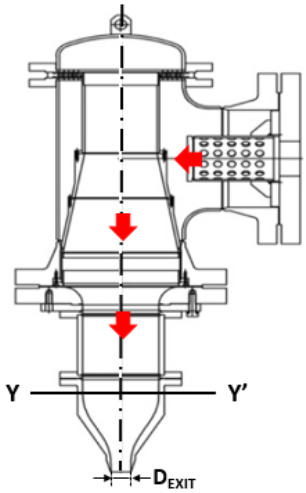

Figure 1: Experimental facility: C4

C4 is equipped with total temperature and total pressure instrumentation located at the inlet of the nozzle (uniformly spread over the nozzle circumference along CUT YY' in Figure 1) after a series of mesh-wires screens. The nozzle inlet total pressure, $P_{0,real}$, is connected to a Validyne differential transducer and referenced to atmospheric conditions. The total pressure measured by the probe, $P_{0,measured}$, is connected to a Validyne referenced to the nozzle inlet. The nozzle inlet total temperature, $T_{0,real}$, is acquired using Platinum Resistance Thermometers (RTDs - PT100), while the total temperature acquired by the probe, $T_{0,measured}$, is measured in differential by means of a referenced thermocouple with respect to $T_{0,nozzle}$. Further details on the experimental setup and measurement chain can be found in [1].

3. Global flow field

The extensive experimental database includes several types of probe geometries, different sensors and several flow conditions. However, no information on the flow field topology taking place inside and around the heads is available. Indeed, typical calibrated probes exhibit dimensions which are too small to allow instrumentation inside the head without perturbing the sensors. As a result, numerical simulations were employed to reconstitute the experimental setup and obtain the flow field in and around a typical VKI calibrated probe.

The simulated probe (Figure 2) is a VKI model based on typical encountered probe geometries: three heads ([A] in Figure 2) are mounted on a 35mm long stem ([B] in Figure 2) and fixed to the experimental set-up by a mounting support ([C] in Figure 2). The probe is instrumented with a total temperature sensor (thermocouple) and a total pressure sensor (pneumatic pressure tap). The heads have an elliptical casing which displays a hydraulic diameter of 2.77mm. They are composed of a shrouded inlet section and two exit ventilation holes located on its sides leading to a nominal area ratio of 0.25. The particularity of this probe is the inclination of the heads with respect to each other.

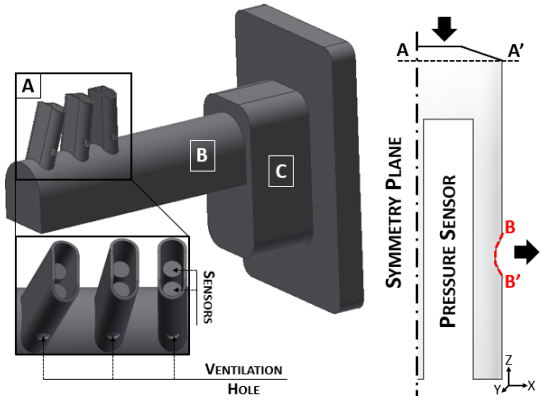

(a) Probe nomenclature (b) Head #2

Figure 2: Probe geometry

In an effort to reduce the numbers of cells constituting the mesh, the dimensions of the thermocouple and the pressure sensor have been assumed identical, which allowed to adopt a symmetry plane (Figure 3). The numerical setup (Figure 4) is defined in order to reproduce the experimental setup, and given that C4 discharges to the atmosphere, a portion of the surroundings of the facility needed to be included in the numerical domain. The domain was limited to a cylindrical form, with a height of $34D_{EXIT}$ and a diameter of $20D_{EXIT}$ [2,3]. The central head (i.e. head #2) was aligned and centered in the core of the jet, at a distance of $0.7D_{EXIT}$.

Aschenbruck, Hauptmann and Seume [4] have investigated the influence of a multi-hole pressure probe on the flow field in axial- turbines as did Herbst et al. [5]. Experimentally obtained pressure measurements as well as CFD computations were compared. Simulations with and without probe displayed good agreement in flow areas with low gradients. Based on the results, the authors concluded that when encountering differences between probe measurements and numerical results, they were caused by the po-

tential effect of the probe. CFD can also be used to calibrate probes, as did Guzman, Fletcher and Hooper [6]. They have investigated numerically, using an in-house CFD code, the flow field behavior around a four-hole Cobra probe. Numerical results have been compared with experimental results and have shown good agreement quantitatively and qualitatively. This investigation has demonstrated the effectiveness of using computational analysis to provide information for engineering design purposes. However, no investigations have been carried out on the effect of the flow field on calibrated instrumentation, and in particular on the flow features occurring inside the Kiel heads which directly affects the RF.

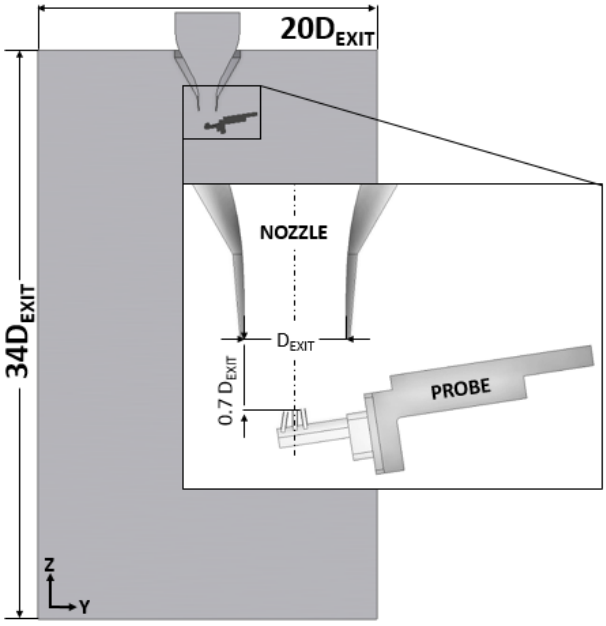

Figure 3: Numerical domain

3.1. Grid details

The unstructured mesh (Figure 5), consisting of hexahedral cells and prism-layers close to the walls, is generated with the grid generator HEXPRESS^{TM} [7] by NUMECA.

The quality of the mesh has been secured by respecting a maximum skewness of 0.7 in the critical areas, and a maximum aspect ratio of 142. The first cell size has been imposed targeting a y^+ of 30 on the walls constituting the probe and the internal walls of the nozzle. Particular attention has been given to the mesh refinement of the heads ([1] in Figure 5) in order to ensure a sufficient number of cells between the heads. Furthermore, starting from the core of the jet

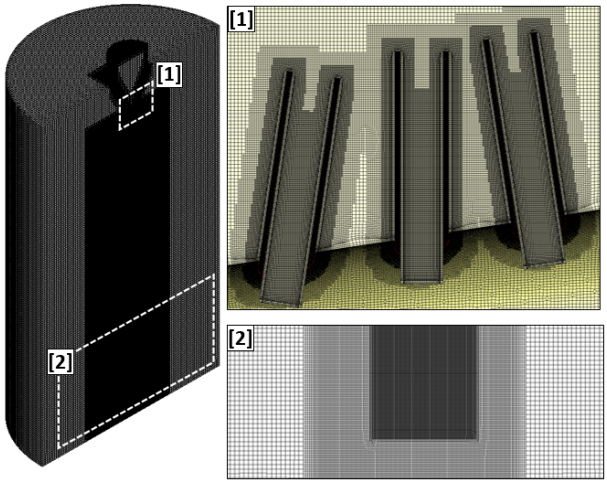

Figure 4: Global view of the mesh

until the surroundings of the shear layer of the jet, a progressive cell size increase has been imposed ([2] in Figure 5).

3.2. Boundary conditions

The boundary conditions (Figure 5), for both tested jet Mach numbers (M_1 = 0.30 and M_2 = 0.65), are set to match the experimental one and have been summarized in Table 1. Since total quantities are measured at the inlet (along CUT YY' in Figure 1), total pressure (P_0), total temperature (T_0) and velocity flow angle have been imposed at the inlet of the nozzle ([1] in Figure 5). Given the large size of the domain the boundaries of the numerical domain, as well as the nozzle and the probe, have been set to an adiabatic wall condition ([2] in Figure 5), while the bottom of the domain ([3] in Figure 5) has been set as an outlet condition, with an averaged imposed static pressure (P).

M [-]	P_0 [Pa]	T_0 [T]	P [Pa]	k [m^2s^{-2}]	ϵ [m^2s^{-3}]
0.30	106668	300	100165	1.6	9.5
0.65	133132			7.1	87.7

Table 1: Boundary conditions for numerical simulations

The experimental setup does not provide turbulent quantities as C4 is not equipped with turbulence measuring instrumentation. Therefore, the hypothesis that

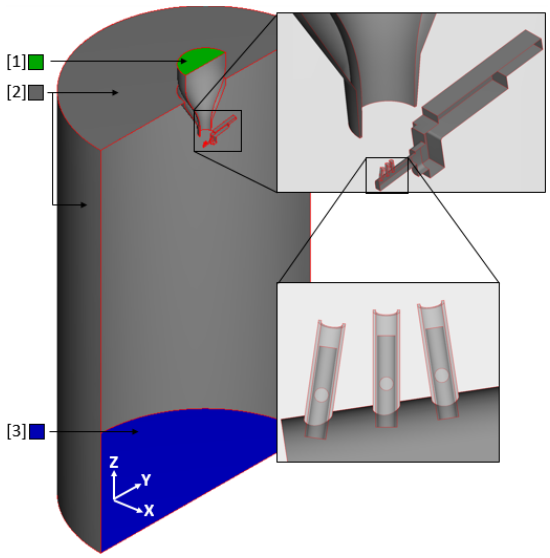

Figure 5: Boundary conditions for the numerical domain

the flow turbulence at the inlet is isotropic combined with an assumed 1% turbulent intensity lead to the computation of the turbulent kinetic energy, k, at the nozzle inlet. Finally, the turbulent dissipation rate, ϵ, was obtained using Eq.4 and assuming the turbulent length scale (l) is proportional to the hydraulic diameter of the nozzle inlet ($l = 0.1D_h$).

$$\epsilon = C_\mu \frac{k^{3/2}}{l} \tag{4}$$

3.2.1. *Flow solver and numerical methods*

The simulations have been performed using the commercial RANS-based code FINE/OPEN 4.3 [8,9] owned by NUMECA with the 2nd order central scheme. The mesh quality has been verified by performing a mesh sensitivity study. The simulations focus on the flow field occurring in and around the probe which is imposed by the jet. For this reason, the mesh sensitivity was quantified in terms of MR (Mass flow Ratio), a non-dimensional parameter defined by Eq.5:

$$MR = \frac{\dot{m}_{INLET}}{\dot{m}_{is,OUTLET}} \tag{5}$$

The inlet mass flow, $\dot{m}_{INLET}$, results from the imposed experimental conditions, while the exit isentropic mass flow of the nozzle, $\dot{m}_{is,OUTLET}$, is computed considering the ratio between the total pressure imposed at the inlet and the extracted average static pressure at the outlet of the nozzle. The total temperature is considered identical as the one at the inlet of the nozzle given the adiabatic assumption. Figure 6 summarizes the comparison of three different meshes (grid #1: 13.2 million cells, grid #2: 28 million cells and grid #3: 50 million cells) in terms of MR for two jet Mach numbers ($M_1 = 0.30$ and $M_2 = 0.65$).

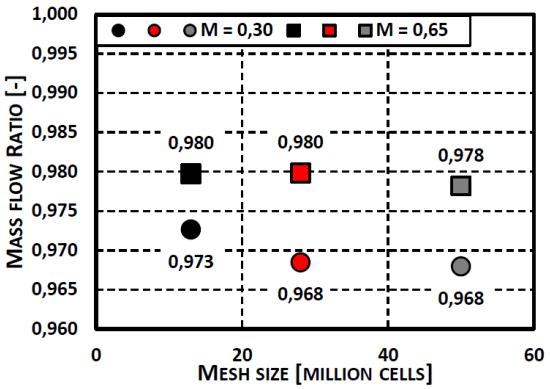

Figure 6: Mesh sensitivity analysis for $M_1 = 0.30$ and $M_2 = 0.65$ in terms of MR

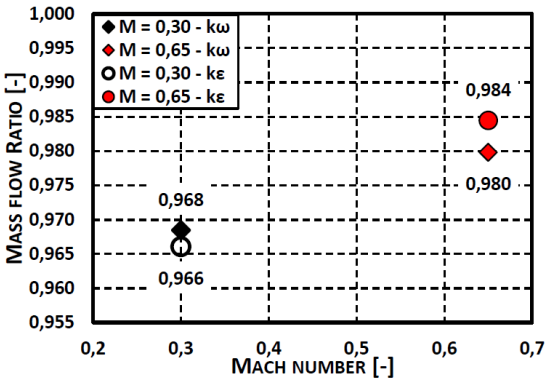

Figure 7: Turbulent model analysis for $M_1 = 0.30$ and $M_2 = 0.65$ in terms of MR

The numerical set-up has been kept identical along the investigation. Both series of simulations exhibit an asymptotic behavior as the mesh is refined. As a result from the mesh sensitivity, and in an effort to reduce the computational effort, the turbulence model investigation (Figure 7) was lead on the intermediate grid (grid #2: 28 million cells) to determine which model would be most suitable. Two models have been considered: the k-ω Shear Stress Transport (SST) [10,11] and the k-ϵ [12,13]. The first one captures well the flow separation and adverse pressure gradients, while the second displays higher stability. In terms of MR,

both models displayed very similar results for both jet Mach numbers. As a result given the geometry of the domain, and more specifically the one of the probe, the k-ω SST will be selected for future simulations.

3.2.2. Results

This paragraph will present a qualitative overview of the numerical results obtained on the finest grid (grid #3: 50 million cells with k-ω SST turbulence model) starting from a macroscopic point of view and ending with an analysis of the flow field occurring around the heads. Nevertheless, for future simulations, the mesh sensitivity suggests that the intermediate mesh will suffice with respect to the accuracy requirements.

Globally, the flow topology is identical for both jet Mach numbers (M_1 = 0.30 in Figure 8 and M_2 = 0.65 in Figure 9): a strong acceleration takes place at the sharp tip of the stem, a large recirculation area takes place downstream of the stem and a wake develops further downstream. The presence of a large wake downstream of the stem suggests that the shape of the stem should be modified during an optimization process in order to reduce the downstream flow disturbance. In addition, the flow exiting the ventilation holes mixes with the main flow, resulting in a highly three dimensional flow field. The flow being subsonic, any perturbation is transported upstream to the exit of the nozzle. The probe creates a potential effect which perturbs the core of the jets streamlines. As a consequence the streamlines are curved and the static pressure at the nozzle exit might differ from the ambient one. However, the simulations have demonstrated that the choice of positioning the probe with respect to the nozzle exit (i.e. 35mm downstream), is coherent, as the static pressure corresponds to the ambient one within 0,003%. The probe exhibits the particularity of having multiple heads which are inclined with respect to each other. The distance between each heads and the positioning of one head with respect to the others are clearly two parameters which must be taken into account during the design process.

Figure 11 (resp. Figure 12) represents the total pressure field for M_1 = 0.30 (resp. M_2 = 0.65) normalized by the maximum total pressure. A cut was done along the axis of each individual head in order to highlight the interaction between the external flow field and the flow field taking place at each ventilation hole. All heads exhibit a separation bubble taking place on the top corner. For head #1 and head #2, the separation zone grows along the wall of the head and mixes with the flow ejected by the ventilation hole as well as with the separation bubble present on the stem. For head #3, the flow reattaches along the wall upstream of the ventilation hole. These different behaviors result from the presence of vortices taking place between heads #1 and #2, and between heads #2 and #3 ([A] in Figure 9 and Figure 10). The aforementioned vortices have been highlighted in Figure 13: for each head the vortical structures have been plotted in a different color. The vortices generated between heads #2 and #3 grow and in turn affect the flow field surrounding head #2. Similarly, the vortex generated between heads # 1 and #2 affect the flow field of head #1. In addition, the velocity streamlines have been plotted in the symmetry plane in order to emphasize the impact of the vortices taking place between each heads. Furthermore, the open separation bubble present over the stem drives the static pressure field, including close to the ventilation holes, which influences the RF of the different heads.

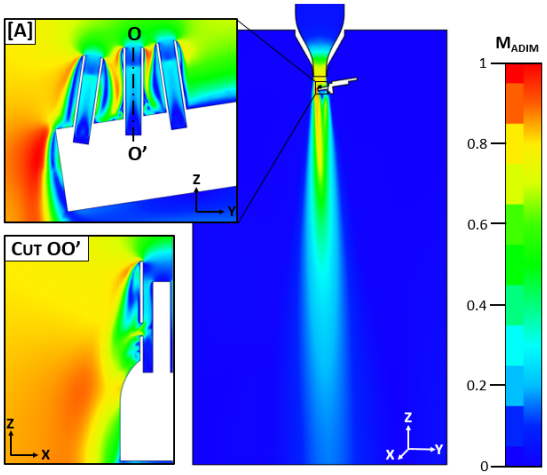

Figure 8: Normalized Mach number flow field for M_1 = 0.30

The design of a stem with a more aerodynamic profile (smoother corners, less blunt-shaped body and contoured trailing edge) such as a symmetric airfoil-like profile could reduce the perturbation linked to the probe. Such stem would create a narrower wake, thereby reducing the recirculation zone located downstream of the stem. Furthermore, the static pressure field created by such an airfoil-like stem could mitigate the effects of the vortices discussed in Figure 13. A solid multi-head probe design targets a constant RF value for every head. However, the external aerodynamic effect on each individual head is consequent, and results from the mutual effect of the heads incli-

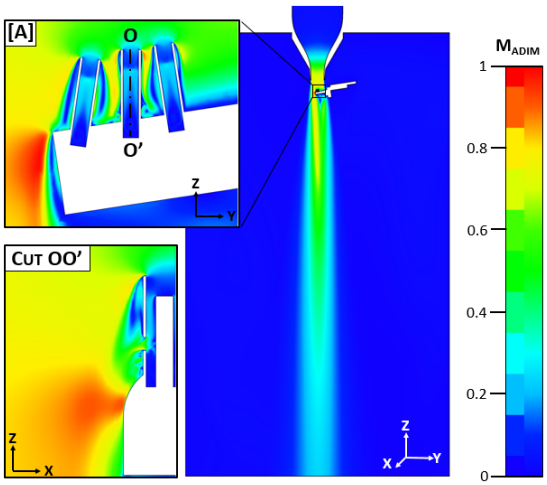

Figure 9: Normalized Mach number flow field for $M_2 = 0.65$

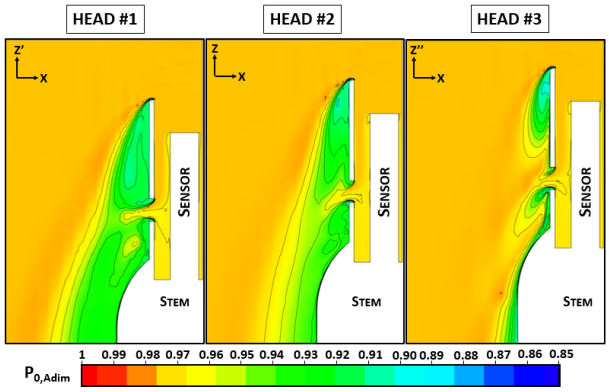

Figure 10: Normalized total pressure flow field for M_1=0.30 for cuts along axis of heads #1 to 3

nation. Therefore, the positioning and inclination of the heads along the stem and the effect of the stem must be considered during an optimization process.

In order to quantify the influence of the external flow field on the exiting ventilation holes, a non-dimensional parameter - the Mass Factor (MF) ratio, was introduced:

$$\mathrm{MF} = \frac{\dot{m}_{\mathrm{AA'}}}{\dot{m}_{\mathrm{is,BB'}}} \tag{6}$$

The mass flow, $\dot{m}_{AA}$, is extracted from the CUT AA' in Figure 3, while an isentropic exit mass flow, $\dot{m}_{is,BB'}$ is computed using extracted data from the simulations along CUT BB' in Figure 3. The isentropic mass flow uses the ratio of the total pressure extracted from the head inlet and the averaged static pressure

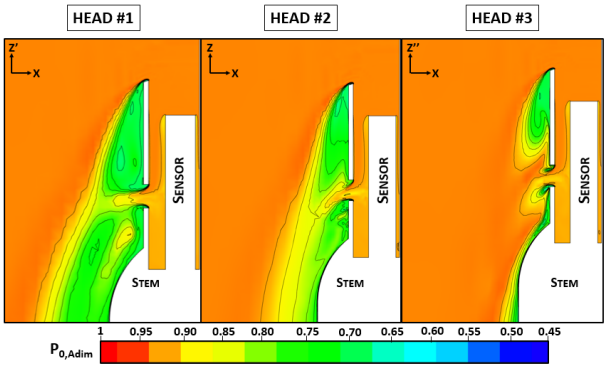

Figure 11: Normalized total pressure flow field for M_2=0.65 for cuts along axis of heads #1 to 3

at the corresponding ventilation hole. The total temperature is considered as identical as the inlet of the nozzle given the adiabatic assumption. The resulting MFs, obtained on grid #3 with k-ω SST, are summarized in Table 2.

M [-]	**HEAD #1**	**HEAD #2**	**HEAD #3**
0.30	0.75	0.67	0.72
0.65	0.80	0.71	0.77

Table 2: Comparison of the MF values for heads #1, #2 and #3 for M = 0,30 and M = 0,65 for k-ω SST

For both Mach numbers heads #1 and #3 exhibit similar values, while head #2 displays a lower value than heads #1 and #3. Head #2 is aligned and centered in the core of the jet, while head #1 (resp. head #3) has an inclination of -8° (resp. 8°). Kiel-shrouded heads, such as the simulated head, should display an insensitivity to yaw (resp. pitch) flow angle for a range of 20 (resp. 10) [16]. The experimental data has shown that these elliptical heads display an insensitivity range for pitch angles which varies between 5 and 8°. The similar values heads #1 and #3 show most likely provide from their similar inclination with respect to head #2. Furthermore, the typical 10° insensitivity to pitch flow angle does not apply to this particular three-heads probe, and could be linked to the close proximity of the heads. This statement raises the question of calibration procedure: a multi-head probe designed in such a way that several heads fit very closely together questions the necessity of calibrating each head individually rather than all together at the same time. Furthermore, the design of the head should take into

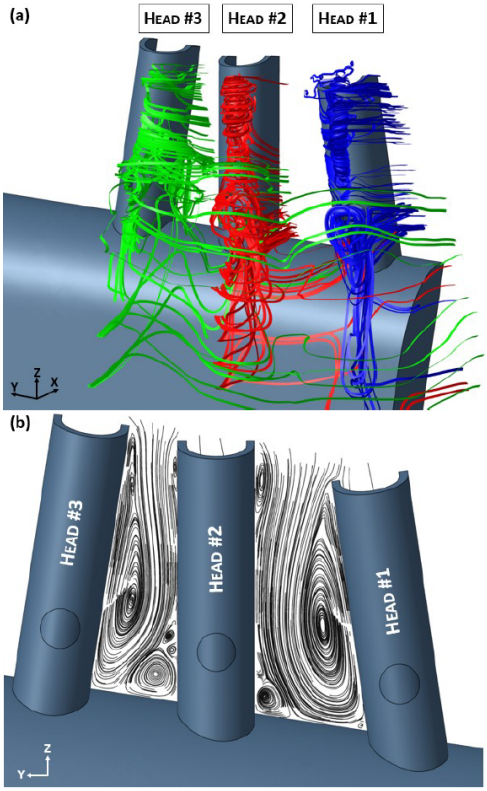

Figure 12: Fine Mesh - M_2 = 0.65 - (a) Vortical structures for each head - (b) Velocity streamlines in the symmetry plane between the heads

consideration the desired performance of it, but also its location along the stem and its insensitivity to the neighboring heads.

These simulations have highlighted the influence of the external flow on the performance of each individual head. Detailed simulations have been run focusing in particular on the internal flow field of each heads, however these investigations will not be discussed in the present paper. The following paragraphs will investigate the influence of the external flow on the flow field. In the second phase on this paper the influence of the Reynolds number will be discussed as well as the results of simulations performed in real engine conditions.

4. Reynolds number influence

The experiments performed in the C4 facility correspond to the Reynolds number order of typical Take-Off (TO) conditions for a commercial aircraft. The knowledge of the Reynolds number for a particular phase of the engine is considerable in terms of boundary layer development, flow separation and frictional losses. These behaviors set the flow field surrounding the probe and its heads, and in turn most likely affect the RF.

During its cycle an engine operates at a large range of Reynolds number, and in particular, the Reynolds number can decrease significantly from the TO phase to a high-altitude cruise phase. The C4 facility is composed of an atmospheric pressure discharge nozzle therefore coupling the Reynolds number with the Mach number. In order to only quantify experimentally the effect of the Reynolds number on the RF a closed-loop facility such as VKI's S1 facility. From a numerical point of view, it is however possible to assess the effect of the Reynolds number on the RF by adapting the experimental boundary conditions to simulate different Reynolds numbers for a given Mach number. The following paragraphs will introduce the results of simulations performed for M = 0,65 varying the Reynolds number.

4.1. Reynolds number investigation test cases

The same numerical domain as in 3 was considered and the numerical set up detailed in 3.2.1 was kept identical. The mesh employed for the simulations was similar to grid #1 in 3.1.

The Reynolds number, Re_c, was computed using as reference length the blade chord, c, of the VITAL test model calibrated in VKI's R4 facility. In a compressor, for cruise conditions, the typical Reynolds number encountered reaches 200 000, however for the simulations the Reynolds number varied from 50 000 to 350 000 (Table 3).

CASE	**Re**$_c$	**P**$_{0,INLET}$	**P**$_{OUTLET}$	**T**$_0$
	[-]	[Pa]		[K]
TO	3.5E5	133 143	100 284	300.0
CASE A	2E5	74 222	55 000	300.0
CASE B	2E5	133 143	100 284	477.5
CASE C	1E5	37 111	27 938	300.0
CASE D	5E4	18 556	13 969	300.0

Table 3: Boundary conditions for Reynolds number investigation - M = 0.65

The TO case is considered as the reference case as the boundary conditions derive from the experiments. For case A (resp. B) the experimental total temperature (resp. total pressure) has been kept identical as for the TO case, while the total pressure

(resp. total temperature) has been derived from a typical Reynolds number for a compressor in cruise conditions, i.e. 200 000. Finally, two additional Reynolds number were considered for cases C and D, keeping the total temperature equal to the experimental one, as for case A, while the total pressure was derived from the Reynolds number.

4.2. Results

The investigation was carried out for a unique Mach number (M = 0,65) but varying the Reynolds number (50 000 $\leq$ Re_c $\leq$ 350 000). The Reynolds number, as well as the Mach number distribution along the axis of the flow field is illustrated by Figure13. Despite different inlet conditions, the Mach number distribution is very similar for all cases, while the Reynolds number distribution highlighted a few differences between the different cases.

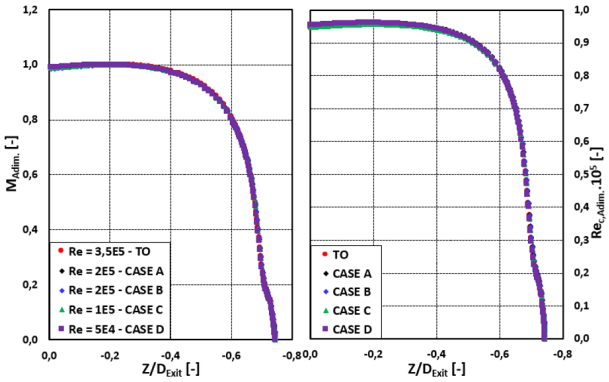

Figure 13: Comparison for different Reynolds number of the Mach number and Reynolds number distribution along z axis

The Reynolds number has been normalized, $Re_{c,Adim.}$, by the maximum Reynolds number of each case, which allows a fair comparison between the different cases. From Figure 13 it appears that the flow field is identical for all cases. As a result, one can conclude that the flow field does not depend on the Reynolds number. Therefore, the calibration of the instrumentation in the C4 facility is valid for the complete cycle of an engine component.

Particular attention is also given to the flow behavior inside the probe's head, especially for head #2. Figure 14 highlights the position of different cuts along the Z-axis, and correspond to the head's inlet (CC'), the top of the sensor (DD'), a distance at midway between the top of the sensor and the ventilation

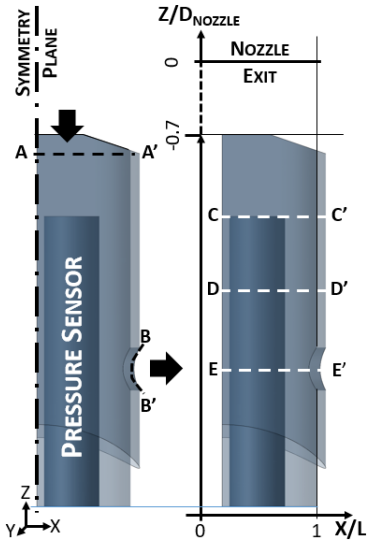

Figure 14: Cuts along Z axis for head #2

hole (EE') and finally the centerline of the ventilation hole.

Figure 13 illustrates the comparison of the Mach number distribution for the different Reynolds along different cuts. Globally at the inlet of the head (Figure 13.A), for all cases, the flow has decelerated to an average of M = 0,14. The rise of Mach number at X/L = 0,85 is related to the presence of a chamfer at the head inlet which creates a local increase of Mach number. Further downstream (Figure 13.B) the flow slightly accelerate due to the presence of the sensor, but no significant changes are noticed between the different cases. The Mach number distribution is asymmetric between X/L = 0,66 and X/L = 1. As the flow separates on the sensor's sharp corner, the passage between the sensor and the head's inner casing is reduced and results in a local acceleration of the flow. At mid-distance between the sensor's top and the centerline of the ventilation hole (Figure 13.C), as the flow accelerates furthermore, the flow reattaches and the peak Mach number has shifted towards the inner casing of the heads (X/L=0,9). As the flow approaches the ventilation hole ((Figure 13.D), the velocity profile changes significantly and displays an almost linear profile along the centerline of the ventilation hole. For the TO case and CASE D for which the Reynolds number is respectively the highest and lowest of the investigated Reynolds number, the velocity profiles differ from CASES A, B and C. The flow entering the head is almost completely evacuated through the ventilation holes. However a small por-

tion of the flow isn't, and instead reaches the bottom of the casing which created a recirculation bubble. As the Reynolds number varies, the strength of the recirculation bubble is impacted by the mainstream Reynolds number, which impacts the velocity distribution along the ventilation centerline.

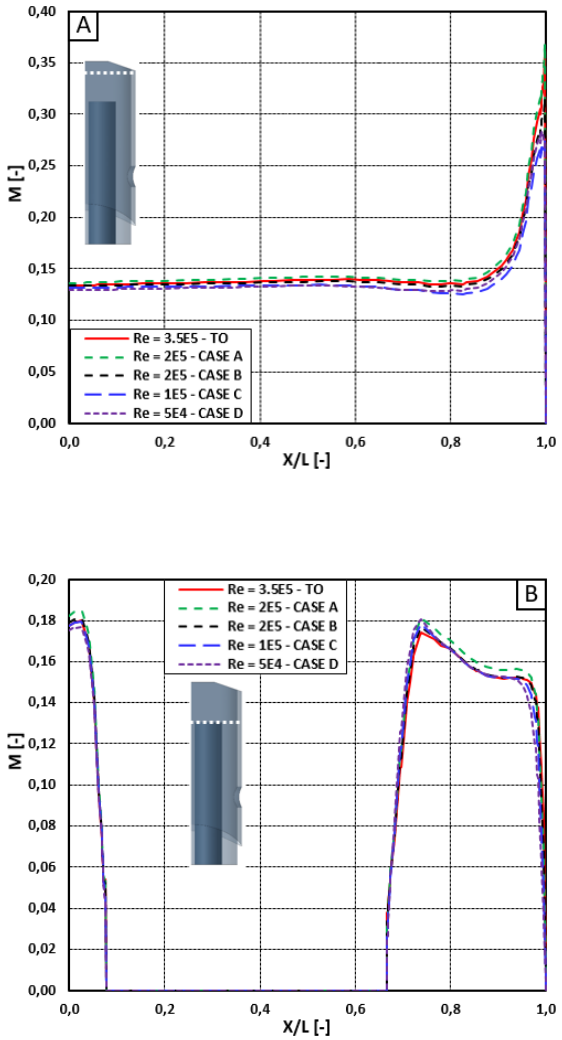

As in 3.2.2, the MF (Eq.6) was computed and plotted for each investigated case in Figure 16. The MF seems to behave asymptotically as the Reynolds number increases. Nevertheless the lowest MF lags behind 3,4% of the asymptotic trend. Figure 16 confirms that the experimentally calibrated elliptical probe is almost Reynolds number independent. The calibrations performed for ground conditions in the C4 facility can be used with few corrections for different Reynolds numbers.

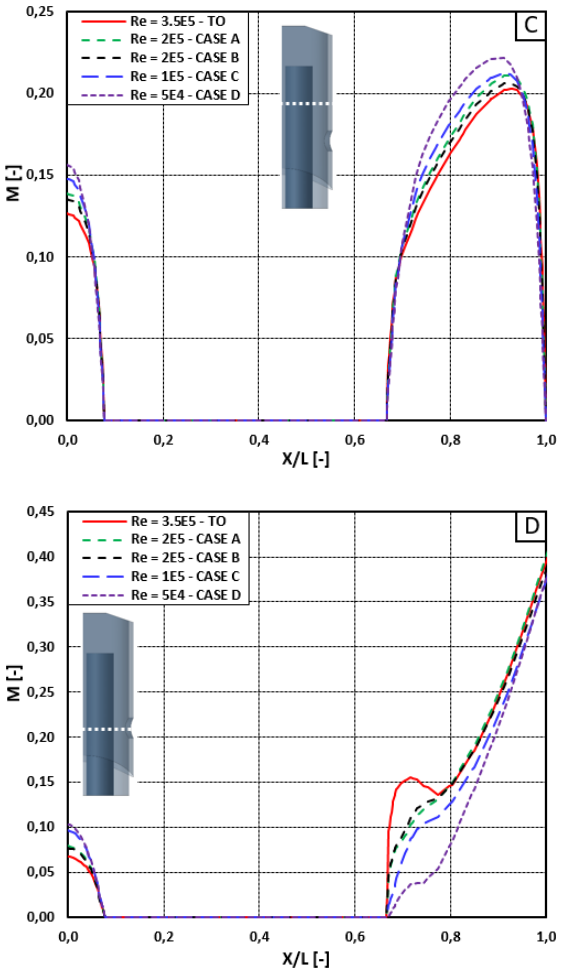

Figure 15: Mach number distribution for different Reynolds number along CUT AA' (A), CC' (B), DD' (C) and EE' (D)

5. Real engine investigation

The previous paragraphs have validated the experimental calibration of the elliptical probe for the complete cycle of an engine component, e.g. for different Reynolds conditions. The numerical domain has been kept identical as the experimental rig, which is a calibration performed by means of an open-jet. However, the instrumentation calibrated in the C4 facility equips real engines, therefore one can question the validity of the calibration as the flow field in an engine differs significantly from an open-jet. Indeed, for example, a compressor exhibits a geometry similar to a constant height converging annulus. Such geometry provides a flow field with a continuously accelerating flow which is less likely to separate. As a conse-

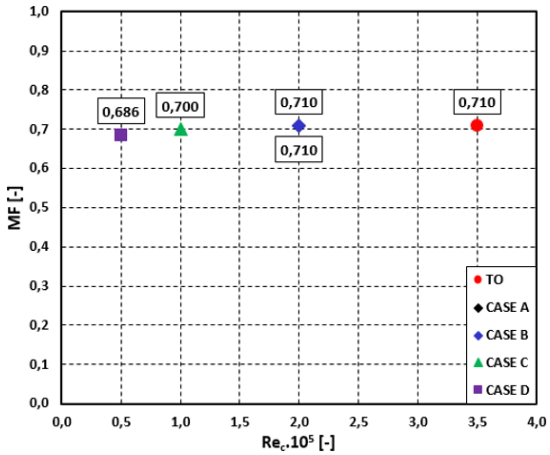

Figure 16: Comparison of MF values for the different investigated Reynolds number

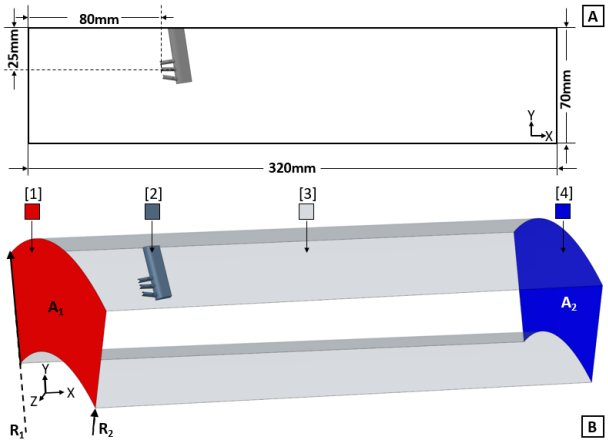

Figure 17: Geometry details for GEOM. B-a

quence, the wake encountered downstream of the stem (3.2.2) might display a shorter length. The following paragraphs will reproduce real engine conditions and perform numerical simulations to assess the validity of the experimental calibration.

5.1. Investigated geometries and boundary conditions

The geometry described in 3 will constitute the first geometry (e.g. GEOM. A) as the numerical domain reproduces the experimental rig. In addition, two other geometries will be investigated, first a constant-height converging annulus shaped duct (e.g. GEOM. B-a and GEOM. B-b), second a constant-height annulus shaped duct (e.g. GEOM. C).

5.1.1. Geometry

As for GEOM. A, in an effort to reduce the mesh size, only a quarter of both annulus was considered. In addition, since the probe described in 3 is symmetric only half of the quarter constitutes the geometry of interest. The probe is located at 80mm from the inlet (Figure 17.A), which corresponds to 25% of the domain's length, and has been positioned such as the central head, i.e. head #2 is aligned with the flow field. The radial distance, R, and inclination, α, of the probe with respect tot the engine's axis is kept identical as the manufacturer's. A comparison of the different geometries is illustrated by Figure18 to help the reader understand.

5.1.2. Numerical set-up

A hexahedral mesh constitued of 15 million cells and targeting a $y^+ \leq 5$ near the probe has been generated using the same grid generator as in 3.1. The numerical methods have been kept identical as 3.2.1. The boundary conditions have been computed assuming that the engine was flying at an altitude h= 10 000m at a speed of M = 0,78. The characteristics of the compressor correspond to typical values for a last stage compressor: PR = 40:1 and $\eta_{TT,is}$ = 0,80.

The boundary conditions have been computed such as the Mach number at the inlet of the probe correspond to M = 0,30 and M = 0,65. Total pressure, total temperature have been imposed at the inlet ([1] in Figure 17.B), the velocity being assumed normal to the surface. The probe ([2] in Figure 17.B), the hub and the shroud ([3] in Figure 17.B) have been considered as adiabatic walls, and an average static pressure is imposed at the outlet ([4] in Figure 17.B). Two symmetry planes complete the set of boundary conditions.

The boundary conditions for both Mach numbers are summarized in Table 4 as well as the ratio between the inlet surface (A_1 in Figure 17.B) and outlet surface (A_2 in Figure 17.B), e.g. AR.

The boundary conditions are implicitly related to the inclination of the duct with respect to the engine's axis. For M = 0,30, the boundary conditions were computed in adequation with the manufacturer's characteristic inclination, α. However, for the boundary conditions corresponding to M = 0,65, the inclination has been modified as the outlet surface was choked for the initial inclination. An iterative process on the inclination angle was undertaken in order to reach M = 0,65 at the probe inlet with non- chocked conditions at the outlet surface. In order to reach them, the initial inclination angle, α, was reduced of 75%, to α'.

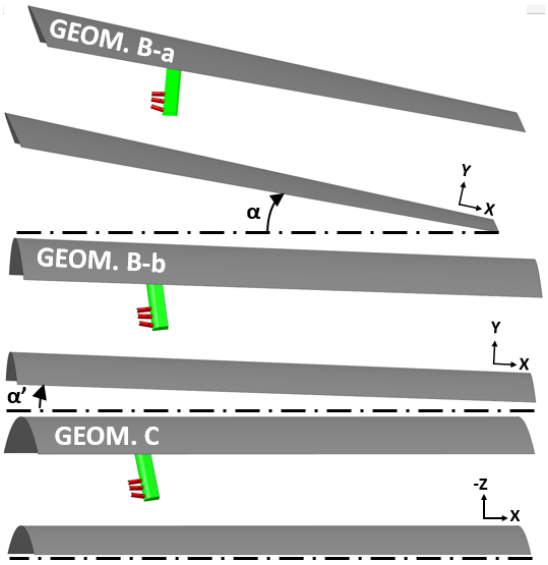

Figure 18: Comparison of the different annulus geometries (from top to bottom): GEOM.B-a, GEOM.B-b and GEOM. C

		$P_{0,INLET}$ [Pa]	$T_{0,INLET}$ [K]	P_{OUTLET} [Pa]	AR [-]
M = 0,30	A	106 668	300	100 165	NA
	B-a	$1{,}510^6$	835,1	985 391	2,28
	C			1 404 184	1
M = 0,65	A	133 132	300	100 165	NA
	B-b	$1{,}510^6$	835,1	1 027 237	1,09
	C			1 125 221	1

Table 4: Boundary conditions for real engine conditions

5.2. *Results*

Two Mach numbers were tested (M = 0,30 and M = 0,65) for the three different geometries and the results will focus on the central head, i.e. head #2.

The major difference between GEOM. A and GEOM. B-a and GEOM. C is related to the constrain of the flow. In an open-jet, as in GEOM. A, one expects the flow to expand, while the engine geometry is designed to guide the flow. Moreover, the converging aspect of GEOM.B-a results in a constant acceleration of the flow which differs significantly from GEOM. A. Nevertheless, the velocity profile along the Z-axis and centered on head #2 (Figure 19.A) reveals that the flow is relatively similar for GEOM. A and C for which the flow starts decelerating at Z/D_{EXIT} = -0,3. For GEOM.B-a, the flow decelerates later (Z/D_{EXIT} = -0,4), at results from the constant acceleration of the converging duct. By the time the flow enters head#2, the velocity for all the geometries has reached a common value of M = 0,09. The velocity profile inside the head (Figure 19.A) exhibits differences between the cases, but they are low ($\Delta M \approx 0{,}01$).

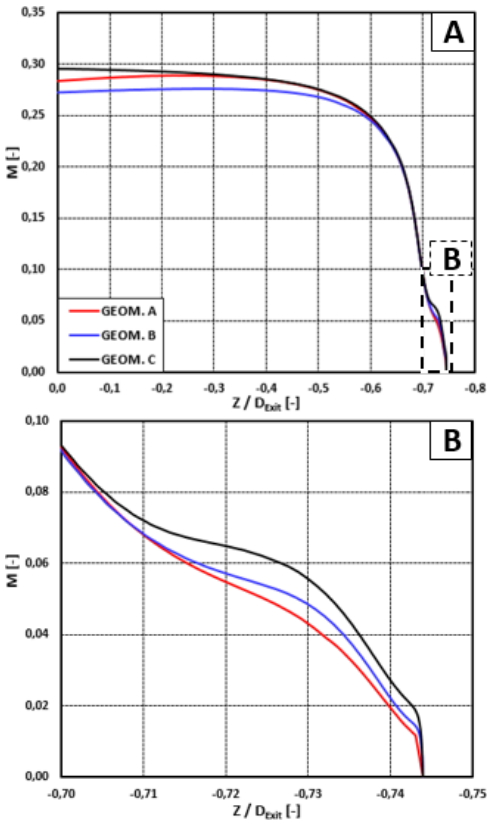

Figure 19: Comparison of Mach number distribution along Z axis for M = 0,30

For GEOM. A, the probe is submitted to several large recirculation bubbles (Figure20.A) resulting from the interaction of the jet with the probe, but also from the mutual interaction of the flow exiting the heads (3.2.2). These interactions produce vortical structures illustrated by Figure12. These flow behaviours are present for GEOM.B-a and GEOM.C but, the confined aspect of the geometry limits their impact on the global flow field, and growth. For GEOM.B-a (resp.GEOM. C), as the duct is converging (resp. with a constant height), the Mach number surrounding the stem of the probe is higher (Figure20.B-a and (Figure20.C). As the Mach number is increased to M = 0,65 (Figure 21) the trends are

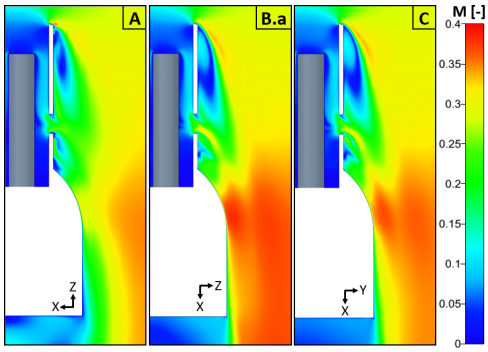

Figure 20: Comparison of the Mach number distribution for geometries A, B-a and C for M = 0,30

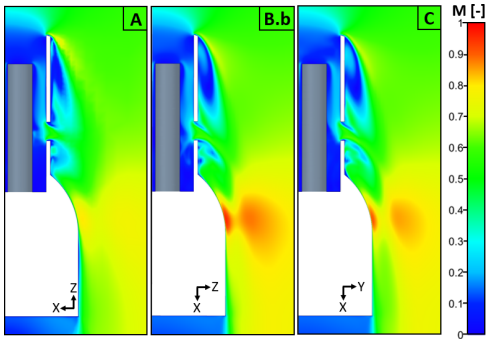

Figure 21: Comparison of the Mach number distribution for geometries A, B-a and C for M = 0,65

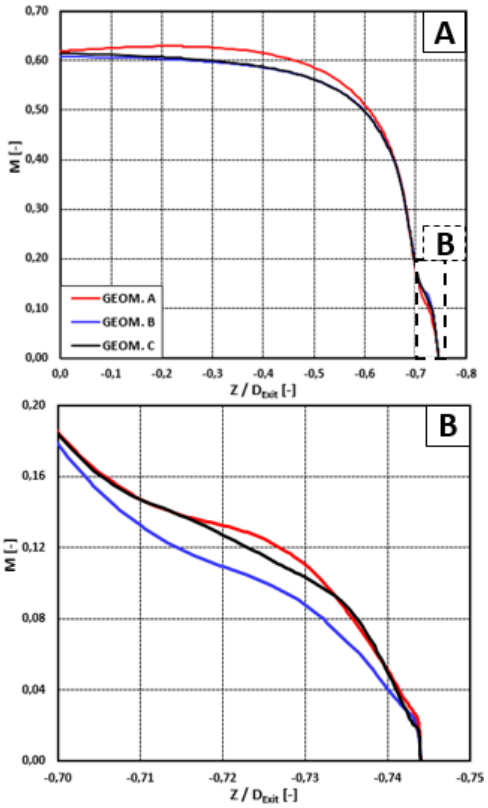

Figure 22: Comparison of Mach number distribution along Z axis for M = 0,65

confirmed.

Figure 22 illustrated the velocity profile along the Z-axis and centered on head#2 for the three different geometries. As for M = 0,30, the differences between the three cases are quite small. The velocity keeps constant for GEOM.A until Z/D_{EXIT} = -0,3, while for GEOM.B-b and C, the flow decelerates steadily until Z/D_{EXIT} = -0,6. Nevertheless all cases display a head inlet velocity of M = 0,18. As for M = 0, 30, the flow inside the head is very similar for the three cases with at maximum a difference in Mach number of $\Delta M \approx$ 0,02. As the Mach number, the effect of the external condition is more important.

In order to quantify the effect of the external conditions, the MFs have been computed for the three different geometries and at both Mach numbers. The results are illustrated by Figure 23. At M = 0,30 the scatter between the different MF values is greater than at M = 0,65. However, the geometries for the converging annulus at M = 0,30 and M = 0,65 are different. Therefore, one cannot conclude on the effect of GEOM. B on the external flow field. It seems however, that at at low Mach number, i.e. M = 0,30, the acceleration resulting from the converging duct degrades the performance of the heads, even though its impact is lower than 1%. Nevertheless, for higher Mach numbers, the MFs are relatively close, implying that the external flow field has little effect on the performance of the probe. Therefore the calibrations performed in the C4 facility can be used with little correction when mounted in real engines.

6. Conclusions

Steady-state RANS numerical simulations have been performed for two Mach numbers: M = 0,30 and M = 0,65. The investigation was lead on a three Kiel heads rake, each head designed with an elliptical casing. Three different investigations were carried out on this probe.

The first set of simulations on the full experimental setup, reproduced the flow field taking place in and around a probe and used experimental data as boundary conditions and validation data. For both Mach

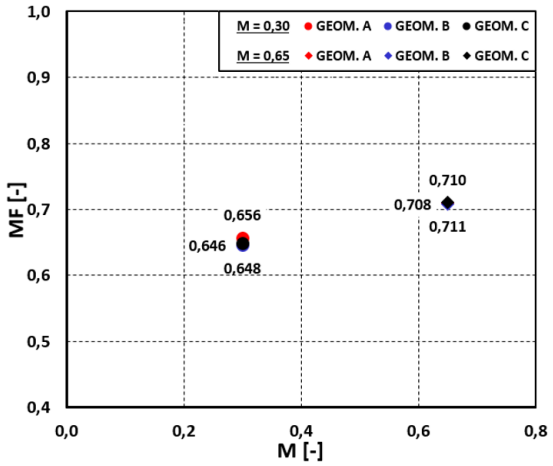

Figure 23: MF as a function of Mach number for real engine conditions

numbers the flow topology is similar. However, three conclusions can be drawn. For this investigated multi-heads probe, the results have demonstrated a strong mutual interaction of the heads with each other. Indeed, the proximity and/or inclination of the heads strongly affects the internal flow field of the heads as shown by Figure and Figure . Therefore, for short probes with multiple heads, the heads equipping the probe should be calibrated altogether. Secondly, as the effect of the head is so strong, more attention should be given during the design phase of the probe to the development of a more aerodynamic stem. A more airfoil-like shape would guide the flow, particularly it would reduce the effect of the vortexes, and in turn would less disturb the ejected flow by the ventilation holes. Finally, designing a stem with an airfoil-like shape would reduce the thick wakes present in Figure and Figure , and also diminish the large recirculation areas.

Secondly simulations have been performed varying the Reynolds number from 50 000 to 350 000 for a constant Mach number (M_2 = 0,65). The velocity profiles and MFs are not affected by the Reynolds number variation. Therefore, the calibration performed in the C4 facility are considered Reynolds number independent and therefore valid regardless of the engine's operating point.

Finally, the numerical domain was modified to reproduce engine-like geometries (i.e. converging duct and constant radius duct) for two Mach numbers (M_1 = 0,30 and M_2 = 0,65). Few differences are observed in terms of MF despite varying velocity profiles inside the head. Thus, the experimental calibrations realized in the C4 facility are still valid when the instrumentation is mounted in the engine.

References

[1] F. Fontaneto and A. Lahalle, 2016, "*Highly reliabe aerodynamic calibration for ground and flight testing total temperature probes*", in XXIII Biannual Symposium on Measuring Techniques in Turbomachinery Transonic and Supersonic Flow in Cascades and Turbomachines, Stuttgart, Germany.

[2] Ball C.G., Fellouah H. and Pollard A., 2012, *The Flow Field in Turbulent Round Free Jets*, Progress in Aerospace Sciences, **50**, pp. 1-26.

[3] Kaushik M., Kumar R. and Humrutha G., 2015, *Review of Computational Fluid Dynamics Studies on Jets*, 2015, American Journal of Fluid Dynamics, **5 (3A)**, pp. 1-11.

[4] Aschenbruck J., Hauptmann T. and Seume J.R., 2015, *Influence of a Multi-Hole Pressure Probe on the Flow Field in Axial Turbines*, in Proceedings of 11th European Conference on Turbomachinery Fluid Dynamics & Thermodynamics, Madrid, Spain.

[5]Herbst F., Bluemel S., Fakiolas E. and Seume J.R., 2011, *Numerical Investigation of the Interaction between Probe, Flow and Blading in an Axial-Turbine*, in International Gats Turbine Congress, Osaka, Japan.

[6] Guzman M. M., Fletcher C. A. J. and Hooper J. D., 1994, *Computational Investigation of Cobra Probe Operation*, International Journal of Numerical Methods for Heat & Fluid Flow, **4 (5)**, pp.425-445.

[7] Hexpress Users Manual, NUMECA International, Brussels, Belgium.

[8] FINE/Open Users Manual, NUMECA International, Brussels, Belgium.

[9] FINE/Open Theoretical Manual, NUMECA International, Brussels, Belgium.

[10] Menter F.R., 1992, *Influence of Freestream Values on k- Turbulence Model Predictions*, AIAA Journal, **30(6)**, pp.1657-1659.

[11] Menter F.R., 1992, *Performances of Popular Turbulence Models for Attached and Separated Adverse Pressure Gradient Flows*, AIAA Journal, **30(6)**, pp. 2066-2072.

[12] Menter F.R., 1994, *Two-Equation Eddy-Viscosity Turbulence Models for Engineering Applications*, AIAA Journal, **32(8)**, pp. 1598-1605.

[13] Menter F.R., 1993, *Zonal Two Equations k-Turbulence Models for Aerodynamic Flows*, in 24th Fluid Dynamics Conference, Orlando, Florida, USA.

[14] Yang Z. and Shih T.H., 1993, *A k-ϵ Model for Turbulence and Transitional Boundary Layer*, Near-Wall Turbulent Flows, R.M.C. So., C.G. Speziale and B.E. Launder (Editions), Elsevier-Sceince Publishers B.V., pp. 165-175.

[15] Hakimi N., 1997, *Preconditioning Methods for Time Dependent Navier-Stokes Equations*, PhD Thesis, Dept. of Fluid Mechanics, Vrije Universiteit Brussel.

[16] Smout P. D. and Cook S. C., 1996, *Simple Instrumentation Rake Designs for Gas Turbine Engine Testing* in International Gas Turbine and Aeroengine Congress & Exhibition, Birmingham, UK.

Turbocharger design and optimization by adjoint method coupled with CHT analysis

Alberto Racca

Turbomachinery and Propulsion Department, von Karman Institute for Fluid Dynamics, Belgium, alberto.racca@vki.ac.be

Supervisors: Tony Arts and Tom Verstraete

Professor Head of Dept., Turbomachinery and Propulsion Department, von Karman Institute for Fluid Dynamics, Belgium, arts@vki.ac.be

Visiting Professor, School of Engineering and Materials Science, Queen Mary University of London, UK, t.verstraete@qmul.ac.uk

University Supervisor: Lorenzo Casalino

Associate Professor, Mechanical and Aerospace Engineering Department, Politecnico di Torino, Italy, lorenzo.casalino@polito.it

Abstract

The design of turbochargers for modern automotive applications requires the solution of a highly constrained problem in which targets of extended operative range and performance are coupled with the need of improved synergies with surrounding engine subsystems. The optimization of Variable Geometry Turbines (VGT) demands a multidisciplinary and multipoint approach aimed at improving the machine efficiency while complying with the restrictions imposed by the wide thermal spectrum experienced during various driving conditions. Conjugate Heat Transfer (CHT) describes the process of thermal interaction between a solid body and its surrounding fluid. The numerical simulation of CHT involves the simultaneous solution of both domains in a closely coupled manner. The implementation of this analysis in industrial optimization processes is usually not undertaken due to its computational cost. The present PhD program focuses on the application of CHT analysis to the optimization of VGT turbochargers by introduction of thermal evaluations in an adjoint-based shape optimization framework. The goal is to demonstrate the possibility of enhancing the system efficiency by improving the effectiveness of the optimizer in its design choices thanks to the increased fidelity in performance prediction, the reduction of current safety margins on applied constraints and the minimization of heat losses. Gradient based optimization methods - if using the adjoint method to compute sensitivities - have a clear advantage over gradient-free techniques (e.g. Evolutionary Algorithms) because allowing a faster identification of the optimum of an objective function. Moreover, adjoint methods result in less computationally expensive evaluations of the sensitivity of the objective function with respect to variations of the control parameters by decoupling of the gradients calculation through the state equation. Therefore this methodology offers a suitable optimization framework for the implementation of high-fidelity analyses such as CHT, especially when considering rich design spaces. The development of the procedure is approached through several steps. A heat transfer solver is first generated and radiation term is included to evaluate the large heat dissipation occurring through the turbine scroll. A Fluid-Structure Interface is then designed in order to transfer temperature and heat fluxes information between the fluid and solid domains and to deal with interpolation issues between the two regions. A Conjugate Heat Transfer computation is then implemented using the partitioned hFFB method. The discrete adjoint formulation is applied to the problem and automatic differentiation techniques are introduced for gradients calculation. Finally an adjoint one-shot method is investigated in order to reveal the possibility of reducing the computational cost of the evaluation process in favor of an anticipated introduction of CHT analysis during the optimization. The design of VGT turbochargers is approached by studying the stator-rotor interactions through implementation of a mixing plane. The highly perturbed flow field generated at totally closed VGT vanes position is examined by introduction of stabilization techniques and their influence on the optimizer effectiveness is analyzed. Finally the CHT analysis is tested in several operative conditions, with focus on its application to the turbine scroll and vanes channel.

Adjoint optimization of turbomachinery components under mechanical constraints

Marc Schwalbach

Turbomachinery and Propulsion Department, von Karman Institute for Fluid Dynamics, Belgium, marc.schwalbach@vki.ac.be

Supervisor: Tom Verstraete

Visiting Professor, School of Engineering & Materials Science, Queen Mary University of London, United Kingdom, t.verstraete@qmul.ac.uk

Adjunct Professor, Turbomachinery and Propulsion Department, von Karman Institute for Fluid Dynamics, Belgium, tom.verstraete@vki.ac.be

University Supervisor: Nicolas R. Gauger

Professor, Scientific Computing, Technische Universität Kaiserslautern, Germany, nicolas.gauger@scicomp.uni-kl.de

Abstract

This paper summarizes work done within the framework of an adjoint multidisciplinary optimization for turbomachinery components. Adjoint models for the linear stress and vibration analysis are implemented by the discrete adjoint method using algorithmic differentiation. It is also shown that the design space of the implemented adjoint models can be extended to compute sensitivities relevant to composite material applications.

Keywords: adjoints, algorithmic differentiation, linear stress analysis, vibration analysis, composite materials, turbomachinery

1. Introduction

In the field of turbomachinery, state of the art adjoint optimization methods focus on aerodynamic cost functions and constraints [1; 2; 3]. Structural constraints are often considered *a posteriori* rather than within the optimization. As a result, the optimized shape may be aerodynamically optimized, but structurally infeasible. This can lead to expensive design re-iterations. To avoid this, an adjoint multidisciplinary optimization (MDO) framework is required that can converge towards aerodynamically optimal designs that obey the structural constraints. An adjoint implementation within such a framework is discussed in section 2.

Structural constraints of prime importance in the design of turbomachinery components are stress and vibration. Centrifugal forces caused by high rotational speeds lead to significant stresses and deformations, while the unsteady pressure forces from the surrounding fluid can cause unwanted vibrations. Taking these effects into account within a structurally constrained optimization is paramount. This project works with the VKI's in-house MDO framework *CADO* [4]. Previous work within this PhD project involves the implementation of an adjoint cold-to-hot CAD deformation for this framework [5]. This deforms the CAD geometry based on the structural deformations caused mainly by centrifugal forces. An adjoint structural solver for stress and vibration analysis is required to include the structural constraints within an adjoint MDO. These are discussed in sections 3 and 4, respectively.

Composite material applications are gaining more traction in turbomachinery due to their light weight and customizable material properties. The structural solver described in this paper is extended to offer the capability of composite material vibration analysis. Here an extended design space is used to evaluate sensitivities with respect to composite material properties as well, enabling simultaneous material optimizations

in addition to traditional shape optimizations. This is explored in section 5.

2. Adjoint Multidisciplinary Optimization

Multidisciplinary optimization methods seek to converge towards an optimal design that adheres to cost and constraint functions from multiple domains, e.g. fluid and structure. For turbomachinery applications, this is of great importance, as most components experience high centrifugal forces and unsteady pressure loads. Optimization methods used to achieve this goal can be classified into two categories: gradient-free and gradient-based methods.

Gradient-free optimization methods are widely used and have been successfully applied in turbomachinery applications [6; 7]. Due to their non-intrusive nature requiring only function evaluations, they are relatively straightforward to implement and can be used to work with codes that are treated as a *black box*. Unfortunately, these methods suffer from the curse of dimensionality. The cost of performing a gradient-free optimization is proportional to the number of design parameters m, which can be significantly large. Additionally, a high amount of iterations is typically required to converge towards an optimum.

On the other hand, gradient-based optimization methods use the gradients of the cost function $\sigma \in \mathbb{R}$ with respect to the design $\boldsymbol{x} \in \mathbb{R}^m$

$$\frac{\partial \sigma}{\partial \boldsymbol{x}} \in \mathbb{R}^m \tag{1}$$

to converge towards an optimum with less iterations. Computing the gradient can be an expensive task using methods such as finite differences, where $m + 1$ evaluations of the cost fuction would be required for a first order approximation. With large design spaces, computing the gradient easily becomes infeasible.

The adjoint method, which was applied in aerodynamic optimization by Pironneau [8] and later by Jameson [9; 10], offers an efficient alternative for computing gradients. The key difference is that gradients can be computed at a cost proportional to the number of outputs n, rather than the number of inputs m. In most turbomachinery optimization problems, the case is usually that the number of design parameters m is far greater than the number of cost functions and constraints n, such that $n \ll m$. Utilizing this method boils down to deriving an adjoint model of the form

$$\bar{\boldsymbol{x}} = \frac{\partial \sigma}{\partial \boldsymbol{x}}^T \bar{\sigma}, \tag{2}$$

where the bar notation $\bar{\boldsymbol{x}}$ is used to define an adjoint variable. The adjoint model is then *seeded* by setting the adjoint of the input $\bar{\sigma} = 1$. Running the adjoint model will result in

$$\bar{\boldsymbol{x}} = \frac{\partial \sigma}{\partial \boldsymbol{x}}^T, \tag{3}$$

so that the needed gradient can be extracted from the adjoint variable $\bar{\boldsymbol{x}}$.

There exist two general approaches for implementing the adjoint model. First, there is the *continuous adjoint* approach [11], which derives an adjoint model from the continuous *primal* equations, e.g. the Navier-Stokes equations. The continuous adjoint model is then discretized to be solved numerically. However, deriving a continuous adjoint model is a meticulous and arduous task. Alternatively, the *discrete adjoint* approach derives an adjoint model from the discretized set of equations. A discrete adjoint model can be derived using the source code transformation method *algorithmic differentiation* (AD), using a procedure referred to as *reverse AD*. A list of different AD tools can be found on the community's webpage `www.autodiff.org`. In this work, the operator-overloading AD tool CoDiPack [12] is used. The interested reader is referred to [13; 14] for more information on algorithmic differentiation.

AD can also be used to derive the tangent model of a code using the chain rule of differentiation. The tangent model has the form

$$\dot{\sigma} = \frac{\partial \sigma}{\partial \boldsymbol{x}} \dot{\boldsymbol{x}}, \tag{4}$$

where the dot notation $\dot{\boldsymbol{x}}$ is used to denote a tangent variable. The tangent variable is seeded with a unit vector, which is a vector where all vector components are 0, except the i-th component, which is 1. Seeding

$\dot{\boldsymbol{x}}$ with the i-th unit vector,

$$\dot{\boldsymbol{x}} = \begin{pmatrix} 0 \\ \vdots \\ 0 \\ 1 \\ 0 \\ \vdots \\ 0 \end{pmatrix}, \tag{5}$$

and plugging this into the tangent model (4), computes the derivative

$$\dot{\sigma} = \frac{\partial \sigma}{\partial x_i}. \tag{6}$$

For m input parameters, m tangent models would have to be run to compute the entire gradient. This method is also referred to as *forward AD* and has a computational cost of $O(m) \cdot cost(F)$, where $cost(F)$ denotes the cost of evaluating the primal function. Big O notation is used to describe that the cost of computing the gradient is

$$cost(gradient) \leq c \cdot m \cdot cost(F), \quad c \in \mathbb{R}, \tag{7}$$

where usually the constant $c \in [2, 2.5]$ for forward AD, depending on the platform. Reverse AD would compute the same gradient at a cost of $O(n) \cdot cost(F)$, i.e. $O(1) \cdot cost(F)$, since the number of outputs $n = 1$ in this example. For reverse AD, the constant c is expected to be within the range $c \in [3, 4]$. From a computational effort point of view, the main difference is that the cost of computing a gradient using the tangent method is proportional to the number of inputs m, while the cost of using the adjoint method is proportional to the number of outputs n.

While AD can be applied on a structural solver in a black-box fashion, two important components must be treated manually - the iterative linear solver for the linear stress analysis and the iterative eigenvalue solver for the vibration analysis. Failure to do so could lead to incorrect gradients, higher memory requirements, and longer run times. This treatment is discussed in sections 3 and 4, respectively.

3. Adjoint Linear Stress Analysis

The governing equations of a linear stress analysis is a linear system of equations of the form

$$A\boldsymbol{u} = \boldsymbol{b}, \tag{8}$$

where $A \in \mathbb{R}^{m \times m}$ is the stiffness matrix, $\boldsymbol{u} \in \mathbb{R}^m$ the vector of displacements, and $\boldsymbol{b} \in \mathbb{R}^m$ the load vector [15]. The stiffness matrix A and the load vector $\boldsymbol{b}$ are computed from the material properties and boundary conditions, such as fixed nodes, point loads, or distributed loads. Turbomachinery applications typically apply centrifugal loads.

For the structural constraints, the maximum von Mises stress $\sigma_{max}(\boldsymbol{u}) \in \mathbb{R}$ is considered. In order to be able to differentiate the constraint function, the maximum von Mises stress is determined using a continuous function, such as the p-norm or the Kreisselmeier-Steinhauser function [16].

Table 1: Linear stress analysis chain of operations

Step	Input	Description	Output
1	$\boldsymbol{x}$	Linear system assembly	A, $\boldsymbol{b}$
2	A, $\boldsymbol{b}$	Linear system solve	$\boldsymbol{u}$
3	$\boldsymbol{u}$	Cost function evaluation	σ_{max}

Table 2: Adjoint linear stress analysis chain of operations

Step	Input	Description	Output
1	$\bar{\sigma}_{max}$	Cost function evaluation	$\bar{\boldsymbol{u}}$
2	$\bar{\boldsymbol{u}}$	Linear system solve	$\bar{A}$, $\bar{\boldsymbol{b}}$
3	$\bar{A}$, $\bar{\boldsymbol{b}}$	Linear system assembly	$\bar{\boldsymbol{x}}$

For design variables $\boldsymbol{x} \in \mathbb{R}^m$, the gradient

$$\frac{\partial \sigma_{max}}{\partial \boldsymbol{x}} \in \mathbb{R}^m \tag{9}$$

is required to take stress constraints into consideration in a gradient-based optimization. Using the design variables $\boldsymbol{x}$ as an input, the structural solver's chain of operations can be listed as in table 1. First, the stiffness matrix A and the load vector $\boldsymbol{b}$ are computed in the assembly phase to set up the linear system (8). The linear system is then solved for the displacements $\boldsymbol{u}$, which are used to evaluat the cost fuction, e.g. the maximum von Mises stress σ_{max}. The reverse order gives us the adjoint chain of operations of table 2, which would be seeded with $\bar{\sigma}_{max} = 1$. The resulting gradient is then given by the adjoint variable

$$\bar{\boldsymbol{x}} = \frac{\partial \sigma_{max}}{\partial \boldsymbol{x}}^T. \tag{10}$$

While the linear system assembly and the cost function evaluation within this chain of operations can be easily differentiated using AD, the linear system solve, which usually consists of an iterative solver, requires special treatment. Differentiating an iterative linear solver using a black-box approach means that its adjoint would use the same number of iterations and the same Krylov subspace. This may lead to wrong results, which will propagate through the adjoint model. As described in [17], the adjoint model of a linear solver can be treated in such a way that its resulting adjoint variables can be computed as

$$\bar{\boldsymbol{b}} = A^{-T}\bar{\boldsymbol{u}}, \quad \bar{A}_{i,j} = -u_j\bar{b}_i. \tag{11}$$

Due to the symmetric positive definite properties of the stiffness matrix A, this can be further simplified to a linear system

$$A\bar{\boldsymbol{b}} = \bar{\boldsymbol{u}}, \tag{12}$$

where the same stiffness matrix A of the primal problem can be recycled. The resulting adjoint variables $\bar{\boldsymbol{b}}$ and $\bar{A}$ can then be plugged into the algorithmically differentiated cost function to compute $\bar{\sigma}_{max}$, wich will contain the gradient (9).

3.1. Gradient Accuracy and Runtime Comparison

The gradient (9) computed using the adjoint method is validated by comparing it with the gradient computed using finite differences and forward AD. As an accuracy test case, a rotating cantilever beam with $m = 270$ degrees of freedom (figure 1) is used. As is shown in figure 2, the gradient computed using the adjoint method matches the gradients computed using forward AD and finite differences.

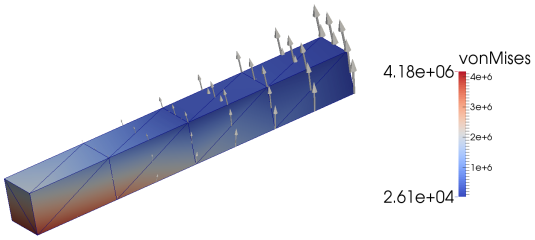

Figure 1: Rotating cantilever beam testcase

Runtime tests were done using an axial fan geometry [18] with approximately $m \approx 200,000$ degrees of freedom, which is shown in figure 3. The time

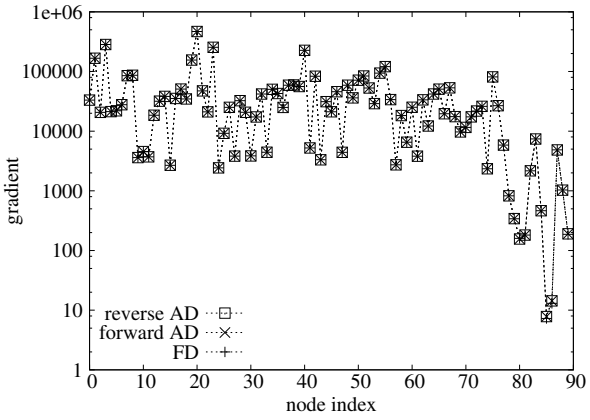

Figure 2: Maximum von Mises stress sensitivitiy $|\frac{\partial\sigma_{max}}{\partial \boldsymbol{x}}|$. Comparison of adjoint vs forward AD vs FD

taken to compute the entire gradient (9) is measured. As a reference, the time it takes to complete one cost function evaluation T and the memory required M is measured as well. Using finite differences or forward AD, e.g., it is estimated that computing the gradient would cost approximately $m \cdot T$. Using the adjoint method, we are able to compute the gradient at a relative cost of $2.1 \cdot T$ with a relative memory requirement of $6.4 \cdot M$. The sensitivities (9) are visualized in figure 4.

4. Adjoint Vibration Analysis

A free vibration analysis takes the form a generalized eigenvalue problem

$$(A - \lambda_k B)\,\boldsymbol{u}_k = 0, \tag{13}$$

where B is the mass matrix, λ_k is the k-th eigenfrequency, $\boldsymbol{u}_k$ is the k-th eigenvector, and A is the same stiffness matrix used in the stress analysis. An iterative eigenvalue solver can be used to solve this system.

Applying vibrational constraints within a gradient-based optimization requires the gradients of the eigenfrequencies with respect to the design variables

$$\frac{\partial\lambda_k}{\partial \boldsymbol{x}} \in \mathbb{R}^m, \quad k = 0, .., p-1, \tag{14}$$

where p denotes the number of eigenfrequencies computed. Starting with the design variables $\boldsymbol{x}$ as our input, the chain of operations can be enumerated as in table 3. First, the stiffness and mass matrices A, B

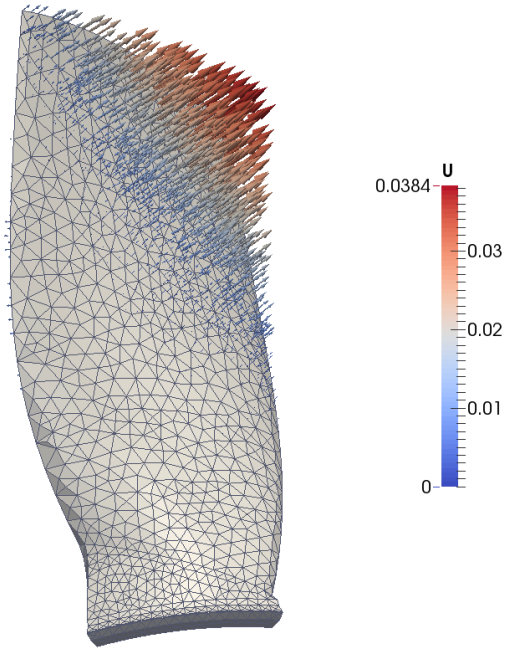

Figure 3: Rotating axial fan test case

are computed. These are then used to set up the generalized eigenvalue problem of (13), which is solved for the k-th eigenfrequency λ_k and eigenmode $\boldsymbol{u}_k$. For the vibration constraint, we are only interested in the eigenfrequency sensitivities. Again, the adjoint model goes in the reverse direction as in table 4. Seeding the adjoint model with $\bar{\lambda_k} = 1$, would give us the sensitivities of the k-th eigenvalue from the adjoint variable

$$\bar{\boldsymbol{x}} = \frac{\partial \lambda_k}{\partial \boldsymbol{x}}^T . \tag{15}$$

Table 3: Vibration analysis chain of operations

Step	Input	Description	Output
1	$\bar{\boldsymbol{x}}$	Assembly	A, B
2	A, B	Generalized eigenvalue solve	λ_k

Similarly to the manual treatment of the iterative linear solver in section 3, the adjoint model of the iterative solver for the generalized eigenvalue solver can be derived as:

$$\bar{A}_{i,j} = \bar{\lambda_k} u_{k,i} u_{k,j} \tag{16}$$

$$\bar{B}_{i,j} = -\bar{\lambda_k} \lambda_k u_{k,i} u_{k,j} \tag{17}$$

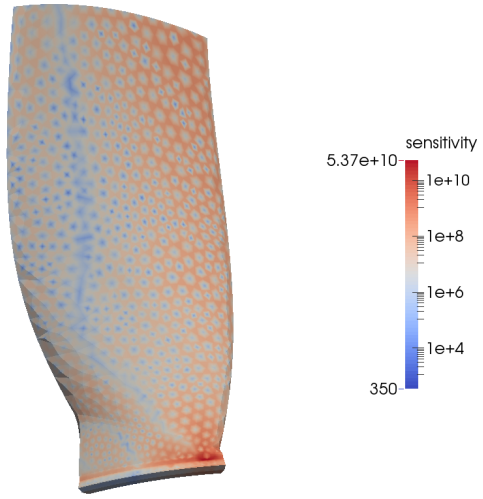

Figure 4: Maximum von Mises stress sensitivities $|\frac{\partial \sigma_{max}}{\partial \boldsymbol{x}}|$

Table 4: Adjoint vibration analysis chain of operations

Step	Input	Description	Output
1	$\bar{\lambda_k}$	Generalized eigenvalue solve	$\bar{A}$, $\bar{B}$
2	$\bar{A}$, $\bar{B}$	Assembly	$\bar{\boldsymbol{x}}$

An adjoint generalized eigenvalue solve is thus replaced by (16) and (17), cutting the gradient evaluation costs significantly. The resulting adjoint variables $\bar{A}$ and $\bar{B}$ are then plugged into the adjoint mass and stiffness matrix assemblies, which are differentiated using AD. Note that the stiffness matrix assembly from the linear stress analysis can be recycled here.

4.1. Gradient Accuracy and Runtime Comparison

The same gradient accuracy test case used in section 3.1 is used to validate the vibration analysis gradients. The gradients (14) are computed using the adjoint method, finite differences, and forward AD. Comparisons for the 2nd and 5th eigenvalues are shown in figures 5 and 6. The gradients computed using the adjoint method match the gradients computed using finite differences and forward AD.

Similar runtime measurements are done using the axial fan geometry of section 3.1. Since the stiffness matrix A can be recycled from the linear stress analysis, its assembly is not considered in the

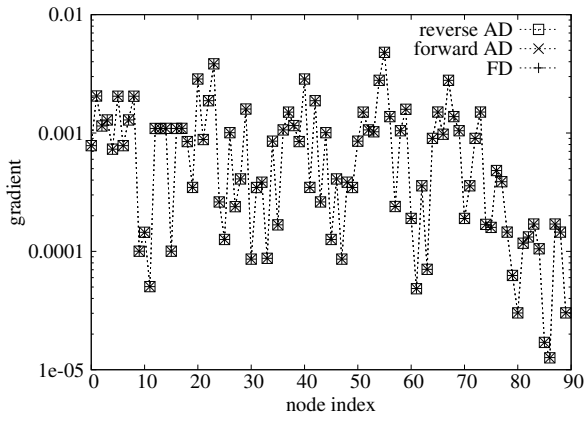

Figure 5: Eigenfrequency sensitivitiy $|\frac{\partial \lambda_1}{\partial \boldsymbol{x}}|$. Comparison of adjoint vs forward AD vs FD

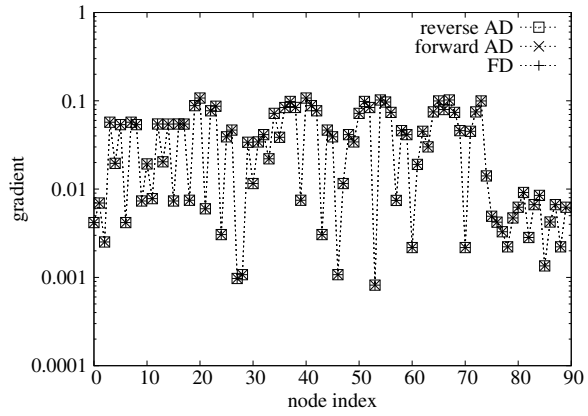

Figure 6: Eigenfrequency sensitivitiy $|\frac{\partial \lambda_4}{\partial \boldsymbol{x}}|$. Comparison of adjoint vs forward AD vs FD

time measurements. The adjoint vibration evaluations are significantly cheap compared to the forward vibration evaluations. Performing $p = 10$ adjoint evaluations to compute the the sensitivities (14) for 10 eigenfrequencies, costs only $\approx 11\%$ of the runtime of a single forward evaluation. This is mainly due to the fact that the eigenvalue solver, which makes up the majority of the runtime (99.5%), has been taken out of the adjoint model and replaced by direct evaluations (16) and (17). The gradient results for the second eigenfrequency λ_1 are shown in figure 7.

5. Extension to Composite Shell Elements

The structural solver's program structure, and in particular its discrete adjoint, is generalized to allow

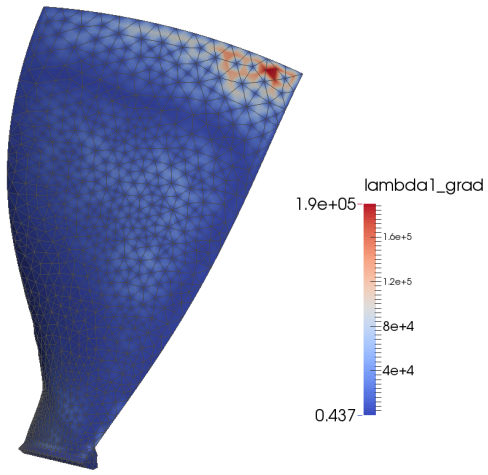

Figure 7: Eigenfrequency sensitivities $|\frac{\partial \lambda_1}{\partial \boldsymbol{x}}|$

the definition of different functions for the evaluation of matrices A and B, inputs $\boldsymbol{x}$, and cost function σ. This is particularly interesting when exploring more specific structural problems. For instance, isotropic materials have constant material properties and the stiffness and mass matrices A and B are dependent on design variables $\boldsymbol{x}$, e.g. the node coordinates. The maximum von Mises stress σ_{max} is evaluated as the cost function. In constrast, composite material matrices A and B rely on additional input parameters related to the material's composition. Typically, a cost function, such as the Tsai-Wu criterion $\sigma_{TW} \in \mathbb{R}$, is used to evaluate the composite structural analysis. For a more detailed discussion on composite materials and their optimization emthods, the interested reader is referred to [19; 20].

5.1. Integration into Structural Solver Framework

The linear stress analysis (sec. 3), the vibration analysis (sec. 4), and their respective adjoints consist of just a few main building blocks that can be adjusted according to the specific application at hand. These blocks are mainly composed of the following:

- input $\boldsymbol{x}$
- stiffness matrix A
- mass matrix B
- cost function σ

Each of these building blocks can be defined as separate functions within an element class that can

be overridden by derived classes. The results shown in sections 3.1 and 4.1 were achieved using isotropic elements.

Composite element support is achieved by implementing composite-specific definitions and functions for $\boldsymbol{x}$, A, B, and σ. This was done by defining isotropic and composite element subclasses that derive from a common element class, as depicted in figure 8. The derived classes then define their own functions for inputs, stiffness matrix, mass matrix, and cost function. By AD'ing the superclass, the differentiation is automatically implemented for the derived classes. As long as the overall structure of the linear stress and vibration analysis does not change, no additional differentiation is required for the subclasses. This showcases the advantages of code extensibility that an operator-overloading AD tool can provide. As the code evolves, developers can focus on the implementation of the primal problem and need to worry less about the differentiation.

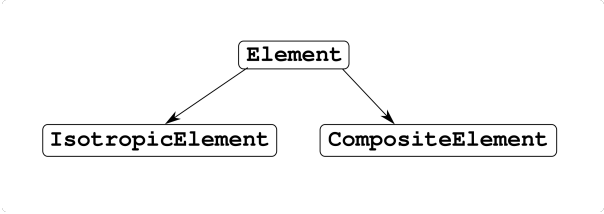

Figure 8: Inheritance for element class

5.2. Extension of Design Space

Composite material applications based on first-order shear deformation theory (FSDT) offer additional lamination parameters $V \in \mathbb{R}^l$ as design parameters [21]. Sensitivities with respect to the lamination parameters,

$$\frac{\partial \sigma_{TW}}{\partial V} \in \mathbb{R}^l, \tag{18}$$

could be taken into consideration alongside sensitivities with respect to node coordinates to perform concurrent shape and material optimization. In this sense, the design space can be extended to include lamination parameters:

$$\boldsymbol{x}^* := (\boldsymbol{x}, V), \quad \boldsymbol{x}^* \in \mathbb{R}^{n+l} \tag{19}$$

Accordingly, the dependency of the stiffness and mass matrices changes such that

$$A = A(\boldsymbol{x}^*), \quad B = B(\boldsymbol{x}^*). \tag{20}$$

The same adjoint implementations described in sections 3 and 4 can be used to perform a sensitivity analysis with respect to the extended design space. The resulting sensitivities using the adjoint linear stress analysis and adjoint vibration analysis are

$$\frac{\partial \sigma_{TW}}{\partial \boldsymbol{x}^*} \in \mathbb{R}^{n+l}, \quad \frac{\partial \lambda_k}{\partial \boldsymbol{x}^*} \in \mathbb{R}^{n+l}. \tag{21}$$

5.3. Gradient Accuracy

The vibration analysis gradients with respect to the extended design space $\boldsymbol{x}^*$ computed using the adjoint method, finite differences, and forward AD were compared. The results for the vibration sensitivities with respect to a lamination parameter are shown in figure 9 and the resulting gradients show a good agreement with one another.

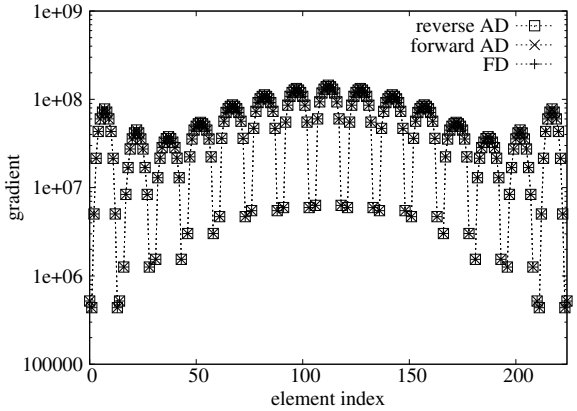

Figure 9: Eigenfrequency sensitivities $|\frac{\partial \lambda_0}{\partial V_{11}}|$

6. Conclusion

Discrete adjoint models have been implemented for both the linear stress analysis and the free vibration analysis. Special care is taken to treat the iterative solvers of the linear stress analysis and vibration analysis manually to reduce errors and improve performance. The extensibility of the adjoint structural solver has been demonstrated by extending the design space by additional material design variables used in composite material design. The gradients computed using the adjoint method have an excellent agreement with the gradients computed using finite differences

or forward AD.

Future work will bridge the gap between the structural solver's computational mesh and the CAD geometry by the implementation of a discrete adjoint mesh deformation. This will enable the computation of structural sensitivities with respect to CAD design parameters directly. Additionally, the links between the fluid and structure domains, e.g. interpolating pressure forces from the fluid domain onto the structural domain, need to be differentiated as well to support an adjoint fluid-structure interaction problem.

Acknowledgments

The authors would like to acknowledge the financial support of the European Commission through the IODA (*Industrial Optimal Design using Adjoint CFD*) project under grant agreement number 642959.

References

[1] S. Willeke, T. Verstraete, Adjoint optimization of an internal cooling channel u-bend, in: ASME Turbo Expo 2015: Turbine Technical Conference and Exposition, American Society of Mechanical Engineers, 2015.

[2] J. Luo, C. Zhou, F. Liu, Multipoint design optimization of a transonic compressor blade by using an adjoint method, Journal of Turbomachinery 136 (5) (2014) 051005.

[3] B. Walther, S. Nadarajah, Constrained adjoint-based aerodynamic shape optimization of a single-stage transonic compressor, Journal of turbomachinery 135 (2) (2013) 021017.

[4] T. Verstraete, Cado: a computer aided design and optimization tool for turbomachinery applications, in: 2nd Int. Conf. on Engineering Optimization, Lisbon, Portugal, September, 2010, pp. 6–9.

[5] M. Schwalbach, T. Verstraete, Towards multidisciplinary adjoint optimization of turbomachinery components, in: V. P. M. Papadrakakis, V. Papadopoulos, G. Stefanou (Ed.), Proceedings of the VII European Congress on Computational Methods in Applied Sciences and Engineering, Crete, 2016, pp. 3999 – 4010.

[6] L. Mueller, Z. Alsalihi, T. Verstraete, Multidisciplinary optimization of a turbocharger radial turbine, Journal of Turbomachinery 135 (2) (2013) 021022.

[7] T. Verstraete, Multidisciplinary turbomachinery component optimization considering performance, stress, and internal heat transfer, Ph.D. thesis, von Karman Institute (2008).

[8] O. Pironneau, On optimum design in fluid mechanics, Journal of Fluid Mechanics 64 (01) (1974) 97–110.

[9] A. Jameson, Aerodynamic design via control theory, Journal of scientific computing 3 (3) (1988) 233–260.

[10] A. Jameson, J. Reuther, Control Theory Based Airfoil Design Using the Euler Equations, AIAA paper 94-4272, 5th AIAA/US AF/NAS A/ISSMO Symposium on Multidisciplinary Analysis and Optimization, Panama City Beach, FL.

[11] A. Jameson, S. Shankaran, L. Martinelli, Continuous adjoint method for unstructured grids, AIAA journal 46 (5) (2008) 1226–1239.

[12] T. Albring, M. Sagebaum, N. R. Gauger, Development of a consistent discrete adjoint solver in an evolving aerodynamic design framework, AIAA 2015-3240.

[13] A. Griewank, A. Walther, Evaluating derivatives: principles and techniques of algorithmic differentiation, Siam, 2008.

[14] U. Naumann, The art of differentiating computer programs: an introduction to algorithmic differentiation, Vol. 24, Siam, 2012.

[15] G. Dhondt, The Finite Element Method for Three-Dimensional Thermomechanical Applications, John Wiley & Sons, 2004.

[16] G. Kreisselmeier, R. Steinhauser, Systematic control design by optimizing a vector performance index, in: International Federation of Active Controls Symposium on Computer-Aided Design of Control Systems, 1979.

[17] M. Tadjouddine, S. A. Forth, A. J. Keane, Adjoint differentiation of a structural dynamics solver, in: Automatic Differentiation: Applications, Theory, and Implementations, Springer, 2006, pp. 309–319.

[18] C. Chahine, T. Verstraete, L. He, Multidisciplinary Design Optimization of an Aero-Engine Fan Blade with Consideration of Bypass and Core Performance, Proceedings of the 11th World Congress on Structural and Multidisciplinary Optimization (June) (2015) 5–10.

[19] E. J. Barbero, Finite element analysis of composite materials using AbaqusTM, CRC press, 2013.

[20] Z. Gürdal, R. T. Haftka, P. Hajela, Design and optimization of laminated composite materials, John Wiley & Sons, 1999.

[21] S. T. IJsselmuiden, Optimal design of variable stiffness composite structures using lamination parameters, TU Delft, Delft University of Technology, 2011.

Full HAWT rotor CFD simulations using different RANS turbulence models compared with actuator disk and experimental measurement

Nikolaos Stergiannis

Department of Environmental and Applied Fluid Dynamics, von Karman Institute for Fluid Dynamics, Belgium, nikolaos.stergiannis@vki.ac.be

Supervisor: Jeroen van Beeck

Professor, Department of Environmental and Applied Fluid Dynamics, von Karman Institute for Fluid Dynamics, Belgium, vanbeeck@vki.ac.be

University Supervisor: Mark C. Runacres

Associate Professor, Thermo and Fluid dynamics (FLOW), Faculty of Engineering, Vrije Universiteit Brussel, Belgium, marc.runacres@vub.ac.be

Abstract

The development of large-scale wind energy projects has created the demand for increasingly accurate and efficient models that limit a project's uncertainties and risk. Wake effects are of great importance and are relevant for the optimization of wind farms. Despite a growing body of research, there are still many open questions and challenges to overcome. In computational modelling, there are always numerous input parameters such as material properties, geometry, boundary conditions, initial conditions, turbulence modelling etc. whose estimation is difficult and their values are often inaccurate or uncertain. Due to the lack of information of several sources, e.g., uncertainties present in operating conditions as well as in the mathematical modelling, the computational output is also uncertain. It is therefore very important to validate the mathematical models with experiments performed in controlled conditions. In the present paper, the single wake characteristics of a Horizontal-Axis Wind Turbine Rotor (HAWT) and their spatial evolution are investigated with different Computational Fluid Dynamics (CFD) modelling approaches and compared to experimental measurements.

The steady state 3-D Reynolds-Averaged Navier Stokes (RANS) equations are solved in the open-source platform OpenFOAM, using different turbulence closure schemes. For the full-rotor CFD simulations, the Multiple Reference Frames (MRF) approach was used to model the rotation of the blades. For the simplified cases, an actuator disk model was used with the experimentally measured thrust (C_T) and power (C_P) coefficient values. The performance of each modelling approach is compared with experimental wind tunnel wake measurements from the 4th blind test organized by NOWITECH and NORCOWE in 2015. Numerical results are compared with experimental data along three horizontal lines downstream, covering all the wake regions. The full wind turbine rotor simulations show good agreement to the experimental data, especially in the near wake. They predict more details of the flow field in contrast with the "U" shaped velocity deficit downstream of the ADM. Wake predictions are shown to be very sensitive to the choice of the RANS turbulence model. For most cases, the ADM under-predicts the velocity deficit, except for the case of *RNG k-ε* which showed excellent performance in the mid and far wake.

Keywords: RANS, MRF, turbulence modelling, full-rotor CFD simulation, actuator disk model, wake effects.

1. Introduction

During the lifetime of a wind farm, the operating wind turbines have to deal with multiple interactions. Part of the wind's kinetic energy is extracted by the rotors, resulting in a velocity deficit and increased levels of turbulence downstream [1]. In full wake

conditions, the power losses of a downstream wind turbine can easily reach 40% [2] while in extreme cases observed in very large offshore arrays, even 60% [3; 4; 5]. Considering the total annual power production of a wind farm, by averaging over all wind sectors, wake effects can cause losses from 8% onshore to 20% offshore [4].

The wind turbines in a row are exposed to single or multiple upstream wake flows, resulting in power losses and additional loads from increased turbulence fluctuations [6; 7; 8; 9; 10; 11; 12]. To optimize a wind farm over a certain spatial area and reach the maximum potential production of the installed wind turbines, we have to understand the physics involved in the process of making torque from wind and be able to predict effectively the wake effects. The estimation of the wake characteristics helps the developers to optimize the final wind farm layout under the prevailing winds, ensuring improved power extraction and working conditions for the downstream wind turbine generators. Wake optimization can benefit the project's lifetime OPerational EXpenses (OPEX), since operating wind turbine generators are expected to be more reliable with less total failures [10].

To predict wakes, several linear models have been developed and applied in industry [13; 14; 15; 16]. However, despite their ease of use, all these models are based on simple assumptions and experimental observations. On the other hand, Computational Fluid Dynamics (CFD) simulations provide more sophisticated methods, such as the 3-dimensional solution of the Navier-Stokes equations, that represent the flow field with great accuracy [17]. Although CFD simulations can be performed on both steady and unsteady state problems, it is common and acceptable to use, with certain limitations, the assumption of steady state approach to resolve a time-varying (unsteady state) problem when one is interested in the mean values of the flow. The wind turbine is rotating at a constant tip-speed-ratio, with fixed yaw and blade pitch angles and the inflow is uniform with small wind speed variations reflected in the turbulence intensity. Therefore, the flow can be treated as steady in the frame of rotation, a common approach in turbomachinery research [18; 19]. The drawback of the steady state frozen-rotor approach is that the rotating wake is always in the same position. The numerical solution of the Reynolds-Averaged Navier-Stokes (RANS) equations uses a statistical description of the flow, where flow quantities are split in an average and a fluctuation. To express the Reynolds stresses in terms of the mean flow quantities and close the system of equations, several turbulence models have been developed. The use of a two-equation turbulence closure model [20; 21] is a common approach, with reasonable computational cost, for industrial applications involving flows of high Reynolds numbers. Methods that are inherently unsteady, such as Detached Eddy Simulation (DES), Large Eddy Simulation (LES) and Direct Numerical Simulation (DNS) can be more accurate but the high computational cost makes them less suitable for use in industrial applications. However, following the technological growth, the computational cost is expected to decrease in years to come and the usage of CFD will be increasingly affordable for optimizing complex industrial applications.

2. Mathematical model

2.1. Statement of the problem

The physical problem under investigation is the flow over two identical wind turbines in a row under the controlled conditions of a wind tunnel. The current study focuses on predicting the single wake characteristics and development using different CFD modelling approaches.

2.2. Governing equations

The governing equations solved of the flow field are the continuity and conservation of momentum equations:

$$\frac{\partial \rho}{\partial t} + \nabla \cdot (\rho \vec{u}) = 0 \tag{1}$$

$$\frac{\partial (\rho \vec{u})}{\partial t} + \nabla \cdot (\rho \vec{u}\vec{u}) = -\nabla p + \nabla \cdot \tau + \vec{S_M} \tag{2}$$

where ρ is the air density, $\vec{u}$ is the fluid velocity vector, p the pressure, τ the shear stress tensor and $\vec{S_M}$ a momentum source term. The stress tensor is related to the strain rate as:

$$\tau = \mu \left[\nabla \vec{u} + \left(\nabla \vec{u} \right)^{\mathrm{T}} - \frac{2}{3} \cdot \delta \cdot \nabla \vec{u} \right] = 0 \tag{3}$$

where δ is Kronecker's delta and μ is the dynamic viscosity of the fluid.

2.3. The Multiple Reference Frame formulation

The multiple reference frame (MRF) approach was used to model the internal rotating frames in a stationary computational mesh and reference frame. The velocities in the inertial and rotating reference frames,

using the notation I for inertial and R for rotating, are related by:

$$\vec{u}_{\mathrm{I}} = \vec{u}_{\mathrm{R}} + \vec{\Omega} \times \vec{r} \tag{4}$$

The acceleration is expressed as:

$$\left[\frac{d\vec{u}_{\mathrm{I}}}{dt}\right]_{\mathrm{I}} = \left[\frac{d\vec{u}_{\mathrm{R}}}{dt}\right]_{\mathrm{R}} + \frac{d\vec{\Omega}}{dt}\times\vec{r} + 2\vec{\Omega}\times\vec{u}_{\mathrm{R}} + \vec{\Omega}\times\vec{\Omega}\times\vec{r} \tag{5}$$

The incompressible RANS equations for steady flow in the rotating frame of reference can be written in terms of the relative velocity:

$$\nabla \cdot \vec{u}_{\mathrm{R}} = 0 \tag{6}$$

$$\nabla\cdot(\vec{u}_{\mathrm{R}}\otimes\vec{u}_{\mathrm{R}}) + 2\vec{\Omega}\times\vec{u}_{\mathrm{R}} + \vec{\Omega}\times\vec{\Omega}\times\vec{r} = -\nabla\left(\frac{p}{\rho}\right) + \nu(\nabla\cdot\nabla)\vec{u}_{\mathrm{R}} \tag{7}$$

2.4. Turbulence modelling

Two-equation turbulence models have been widely tested over the years and have been proven as an accepted compromise between accuracy and computational cost. In the present work, the performance of several two-equation turbulence models on wake expansion is tested and compared with measurements. A short description of each turbulence model and the constants used is given below.

2.4.1. Standard k-ε

The standard k-ε turbulence model [22] is based on transport equations for the turbulence kinetic energy, k and its dissipation rate, ε. The model parameters used are given in Table 1, following Launder et al [23].

Table 1: Constants of the *standard* k-ε turbulence model

C_μ	C_1	C_2	σ_k	σ_ε
0.09	1.44	1.92	1.0	1.3

2.4.2. Realizable k-ε

In the *realizable* k-ε turbulence model of Tsan-Hsing Shih et al, a modified model dissipation rate equation and realizable eddy viscosity formulation is used. A detailed description of the turbulence model is given in [24]. The model constants are given in Table 2.

Table 2: Constants of the *realizable* k-ε turbulence model

C_μ	A_0	C_2	σ_k	σ_ε
0.09	4.0	1.9	1.0	1.3

2.4.3. RNG k-ε

The *RNG* k-ε turbulence model was developed by Yakhot et al [25] using the Re-Normalisation Group (RNG) methods in the Navier-Stokes equations in order to account for smaller scales of turbulence. The main difference and advantage compared to the *standard* k-ε turbulence model, is that the model attempts to account for the different scales of motion through a modified epsilon equation, instead of determining the eddy viscosity from a single turbulence length scale. The model constants are given in Table 3.

2.4.4. Wilcox (1988) k-ω

The k-ω turbulence model is a two-equation turbulence model that uses the turbulence kinetic energy k and the specific rate of dissipation ω to predict turbulence. The model has been improved over the years with several versions and modifications [21; 26], but in our cases we are using the Wilcox (1988) version [27] that is implemented in OpenFOAM [28]. The model constants are given in Table 4.

Table 4: Constants of the *standard* k-ω turbulence model

C_μ	σ_k	σ_ω	β^*	β	γ
0.09	0.5	0.5	0.09	0.072	0.52

2.4.5. Menter (2003) k-ω SST

The k-ω *SST* turbulence model, also known as Menter's Shear Stress Transport turbulence model, was introduced in 1994 by F.R. Menter [29]. It is a two-equation turbulence model that uses k-ω in the inner region of the boundary layer and switches to k-ε in the free shear flow to improve the predictions of adverse pressure gradients. The model also has other modified versions [30]. The updated model of 2003 [31] with a different expression to derive the eddy viscosity was used. The model constants are given in Table 5.

2.5. Wind turbine modelling

In the case of actuator disk model, wind turbine rotors are approximated as momentum sinks (see eq. 2) to represent the axial thrust force T, associated with

Table 3: Constants of the *RNG k-ε* turbulence model

C_μ	C_1	C_2	σ_k	σ_ε	η_0	β
0.0845	1.42	1.68	0.71942	0.71942	4.38	0.012

Table 5: Constants of $k-\omega\ SST$ turbulence model

σ_{k1}	σ_{k2}	$\sigma_{\omega1}$	$\sigma_{\omega2}$	β^*	β_1	β_2	γ_1	γ_2	α_1
0.85	1.0	0.5	0.856	0.09	0.075	0.0828	5/9	0.44	0.31

a constant uniform thrust coefficient C_T over the rotor area:

$$T = 0.5\rho C_T A U_{\text{ref}}^2 \tag{8}$$

where A is the surface area of the rotor-disk, ρ the air density, U_{ref} the undisturbed reference free-stream velocity and C_T the thrust coefficient of the rotor.

Once the U_{ref} is known, C_T can be estimated through the thrust curve of the wind turbine generator considered as uniform over the rotor area [6; 32; 17]. However, in operating conditions, the flow across the rotor is very complex with varying span-wise properties, due to the blade characteristics, rotational velocity, turbulence, finite number of blades and also other flow characteristics related to non-uniform inflow conditions, atmospheric boundary layer shear and so on.

To overcome the limitations of the standard actuator disk model, several more advanced models like the rotating actuator disk, generalized actuator disk, actuator line model, actuator surface, have been proposed [17; 33]. The drawback of the advanced models is mainly that they need several input variables such as airfoil data, detailed blade geometry which most of the times are not available or confidential for industrial applications. Finally, most of the advance models require time resolved CFD simulations which increase the final computational cost [2].

The standard actuator disk model that was used in this study is implemented in OpenFOAM based on the axial induction factor a:

$$a = 1 - \frac{C_P}{C_T} \tag{9}$$

where C_P is the power coefficient. The thrust force can then be expressed as:

$$T = 2\rho A a(1-a) U_{\text{ref}}^2 \tag{10}$$

For all the cases under investigation, a constant uniform reference wind speed of 11.5 m/s has been used. The coefficients C_P and C_T have been provided from the wind tunnel measurements and were used as inputs to the simplified models. While it is true that the induction factor is calculated from both thrust and torque, the model is purely axial and does not include rotation.

3. The 4th blind test experiment

The 4th Blind Test (BT4) experiment was organized by NOWITECH and NORCOWE in 2015. The total power output from two in-line turbines was investigated under the influence of different inlet conditions and turbine separation distance [34].

The axial separation distance between the turbines was set to $x/D = 2.77$, $x/D = 5.18$ and $x/D = 9.00$, where the diameter $D = 0.894$ m. Furthermore, three different inflow conditions at the inlet of the test section were tested:

- Low-turbulence uniform inflow (CASE-A): No grid at the inlet to the test section. At the position of the upstream turbine the turbulence intensity measured was $TI = 0.23\%$. The mean wind speed was uniform across the test section, apart from small wall boundary layer effects.

- High-turbulence uniform inflow (CASE-B): An evenly spaced grid at the tunnel inlet generated a higher turbulence intensity level of $TI = 10.0\%$ at the location of the upstream turbine. The mean wind speed was uniform across the test section.

- High-turbulence shear inflow (CASE-C): A turbulence grid with increasing vertical distance between the horizontal bars was installed at the inlet of the test section, creating a non-uniform shear flow with a mean turbulence intensity of $TI = 10.0\%$ over the rotor swept area of the upstream turbine.

At the experiment, the high turbulence intensity CASE-B was tested on three different downstream axial separation distances. In our study, the CASE-B3 of high TI and with axial separation distance of $x/D = 9.00$ was chosen, mainly because more measured data were available downstream and additionally to eliminate the impact of the second wind turbine on the single wake expansion of the first turbine. For the simulations, a uniform inlet velocity profile of 11.5 m/s was considered, similar to the inlet velocity profile of the wind tunnel. The two wind turbines are identical and constructed with the same aluminium blades, using the NREL S826 airfoil section from root to tip.

4. Full rotor CFD simulations

To address the question of how much information is lost with the simplified models, results are compared with more advanced CFD simulations that include the full wind turbine rotor geometries and their hubs.

4.1. Computational domain

The computational domains were designed to match the exact wind tunnel dimensions to represent the experimental setup and account for possible blockage effects (Fig. 1). Particularly for the CASE-B3, the domain have been extended by 3.7 m in length (30% of total) to avoid any numerical oscillations from the outlet at the far wake measurements downstream. The MRF regions are cylindrical and they are located inside the stationary rectangular region of the computational domain. The cyclic Arbitrary Mesh Interface (AMI) was used in between the rotating and the non-rotating mesh regions. To limit any possible impact of the interfaces with the flow field, the MRF regions have been extended further downstream. In all the cases under investigation, the rotating frame regions include the rotor-hub geometries and all the wake regions downstream.

The `blockMesh` utility of OpenFOAM platform was used to generate a multi-block hexahedral computational mesh of 670k cells. That mesh was further modified and refined in regions of interest with the `snappyHexMesh` utility. Different refinements have been tested in the rotor-wake region with the actuator disk models using the k-ε turbulence model, to achieve a mesh independent solution. The hexahedral mesh elements of the background mesh (M1 = 0.67Mi cells) were doubled at each coordinate on every new level of refinement. The final computational meshes that have been generated and tested are given in Table 6. Steady state solutions using RANS and second order schemes, converged with residuals below 10^{-4}. The axial velocity over the line L1 = $2.77D$ at the near wake was used as reference. The maximum error between the M3 (fine) and M4 (very fine) computational meshes was observed at the rotor centre position ($z = 0$), where the velocity deficit of the single wake had a relative difference of 0.025 m/s. Therefore, the M3 (fine) mesh with two internal regions using two levels of refinement, proved to be a good compromise of accuracy and computational cost, and was chosen for all the CFD simulations.

Table 6: Size of the tested computational meshes in millions ($\times 10^6$)

M1	M2	M3	M4
0.67	2.91	11.9	92.6

For the full-rotor cases, before the snapping of the mesh to the surfaces, several local refinements have been done also at the blades (level 6) and the hubs (level 5) of the wind turbines. Between all the refinement levels, four cells have been used to ensure a smooth transition. (Fig. 2, bottom-left). Four cell-layers were also added normal to the surfaces of the geometries with an expansion ratio of 1.5 (Fig. 2, bottom-right) to ensure a global average y^+ value smaller than 50. The global cell size at the centered block of the mesh was 0.0675 m^3. According to each refinement level, those cells have been refined to 0.016875 m^3 (level 1) and 0.003375 m^3 (level 2), whereas the cells close to the geometries had a global size of 0.00105 m^3 (level 5) at the hub and 0.0007 m^3 (level 6) at the surface of the blades. The final fine computational mesh size was approximately 30Mi cells for the full-rotor CFD simulations and 14Mi cells for the ADM cases.

At the design condition for a Tip Speed Ratio (TSR) $\lambda = \Omega R / U_{\text{ref}} = 6$, the Reynolds number at the tip is $Re_c = \lambda U c_{\text{tip}} / \nu \approx 10^5$, where c_{tip} the chord length at the tip and ν the kinematic viscosity of air. Therefore the above cell sizes ensure that high-Reynolds wall functions can be applied at the first cells above the walls.

4.2. Solution methodology and boundary conditions

All the simulations have been performed in the open-source CFD platform OpenFOAM, using the steady state incompressible solver `simpleFoam`

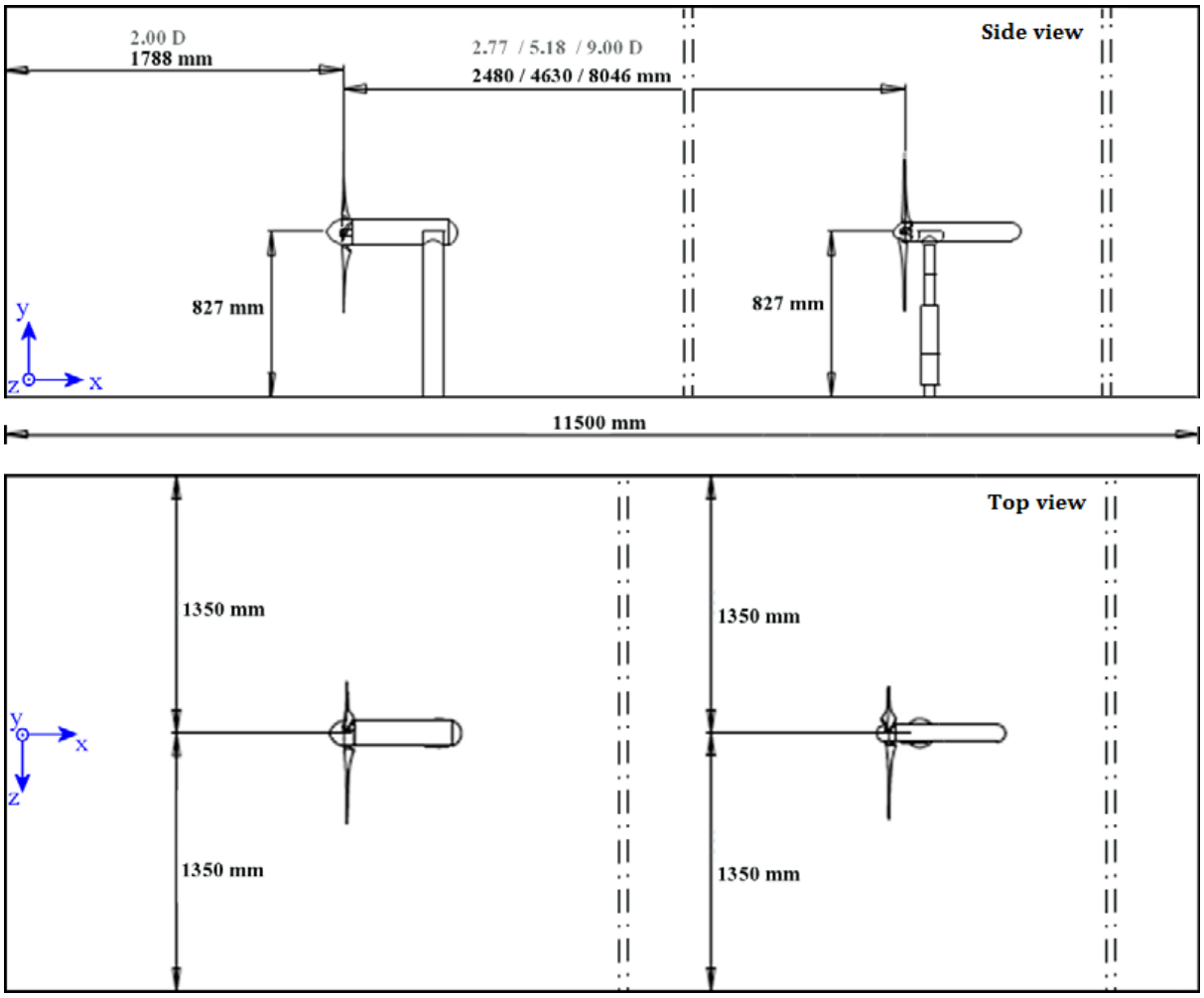

Figure 1: Wind tunnel dimensions and wind turbine positioning at the reference coordinate system. [34]

which is based on the Semi-Implicit Method for Pressure-Linked Equations (SIMPLE) algorithm [35].

Initial values and inlet values for the turbulence characteristics were estimated by using the experimental measured TI and the turbulent length scales ℓ of each case with the following expressions:

$$k = \frac{3}{2}\left(\overline{U}TI\right)^2 \tag{11}$$

$$\varepsilon = C_\mu^{0.75}\frac{k^{1.5}}{\ell} \tag{12}$$

$$\omega = C_\mu^{-0.25}\frac{\sqrt{k}}{\ell} \tag{13}$$

where $\overline{U} = U_{\text{ref}} = 11.5$ m/s and the density of air $\rho = 1.25$ kg/m^3. The boundary conditions that were used are summarized in Tables 7 and 8.

Table 7: Inflow and outflow boundary conditions

	Dirichlet	von Neumann
	Fixed value	Zero gradient
Inlet	$\vec{u}, k, \varepsilon, \omega$	p
Outlet	$p = 0$	$\vec{u}, k, \varepsilon, \omega$

Table 8: Other boundary conditions

Sides, top and bottom	Slip condition
Blades, hubs	Wall functions
Actuator discs	Momentum sinks
Rotating frame WT1	TSR: $\lambda = 6$
Rotating frame WT2	TSR: $\lambda = 4 - 5$

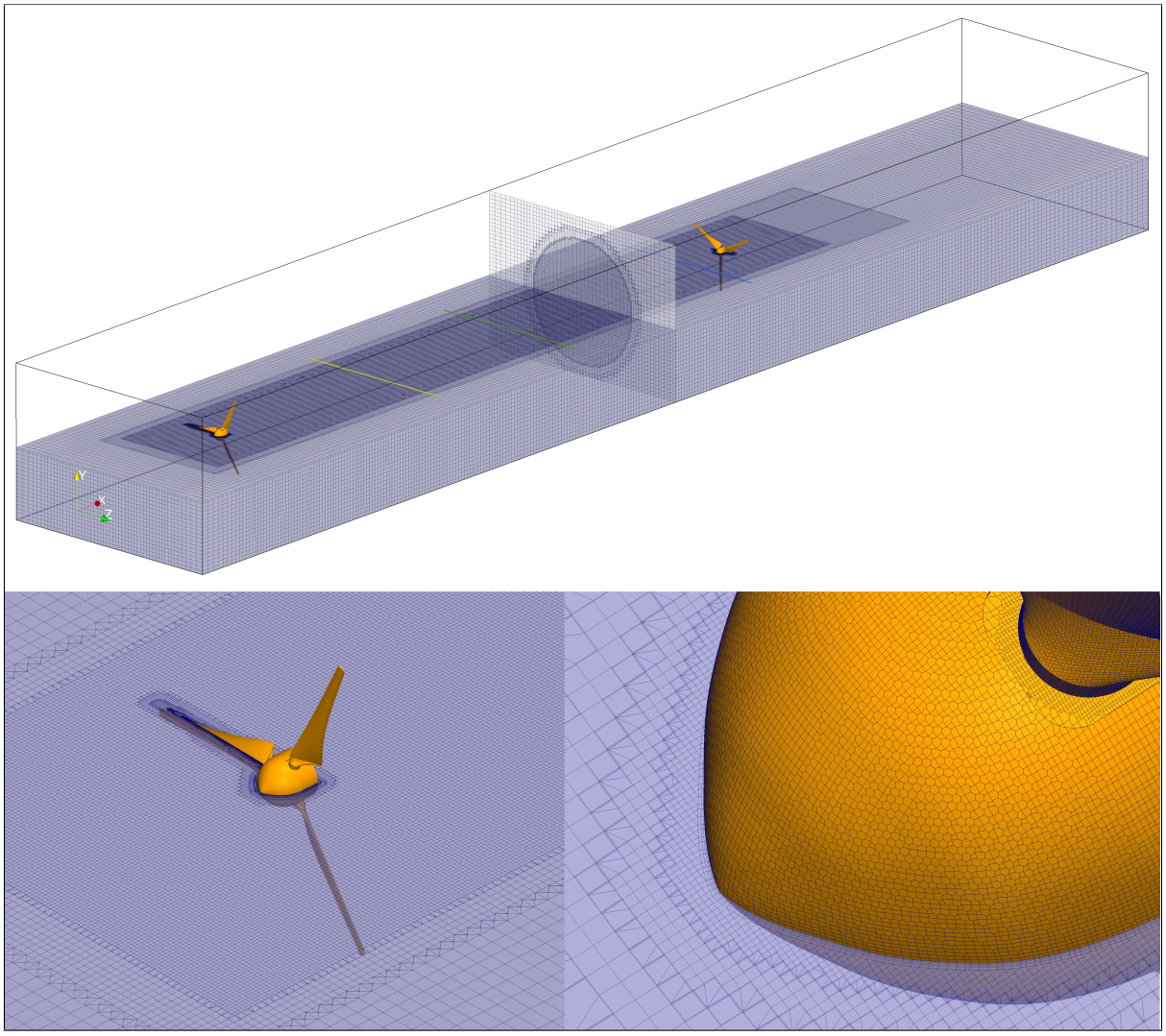

Figure 2: The fine mesh (M3) that was used for the CFD simulations. Top: details of the multi-block mesh and refinements that were generated with `blockMesh` and `snappyHexMesh` utilities. The three horizontal lines represent the measurements at the hub height h_{hub} = 0.827 m over the L1 (yellow) = 2.77D, L2 (green) = 5.18D and L3 (blue) = 8.5D lines downstream of the first rotor. bottom-left: rotor-wake region using a refinement of level 2. bottom-right: surface cells and surface layers close to the geometry.

5. Results and discussion

Results of the wake expansion for all the cases are presented below. Two CFD modelling approaches (full-rotor and actuator disk) have been tested using incompressible, steady state RANS and several turbulence models. All the cases converged after approximately 6000 iterations and were run for 10000 iteration Fig. 3. Pressure residuals converged below 10^{-3}, velocity components below 10^{-5} and turbulence variables below 10^{-6}. Bounded second-order numerical schemes were used for all the quantities, except for k, ε and ω in which a blended first-second order numerical scheme was chosen for numerical stability. Results in all wake regions show that both CFD approaches are very sensitive to the choice of turbulence model. A total number of 128 processors of 2.2 GHz and AMD x86_64 architecture was used. The computational time was approximately 98 hours for the full-rotor CFD simulations and 52 hours for the ADM and 10000 iterations. The total number of cells per processor was approximately 250k cells for the full-rotor and 110k cells for the ADM respectively.

Full-rotor simulations are capable to represent the flow field close to the wind turbine (Fig. 5), but they

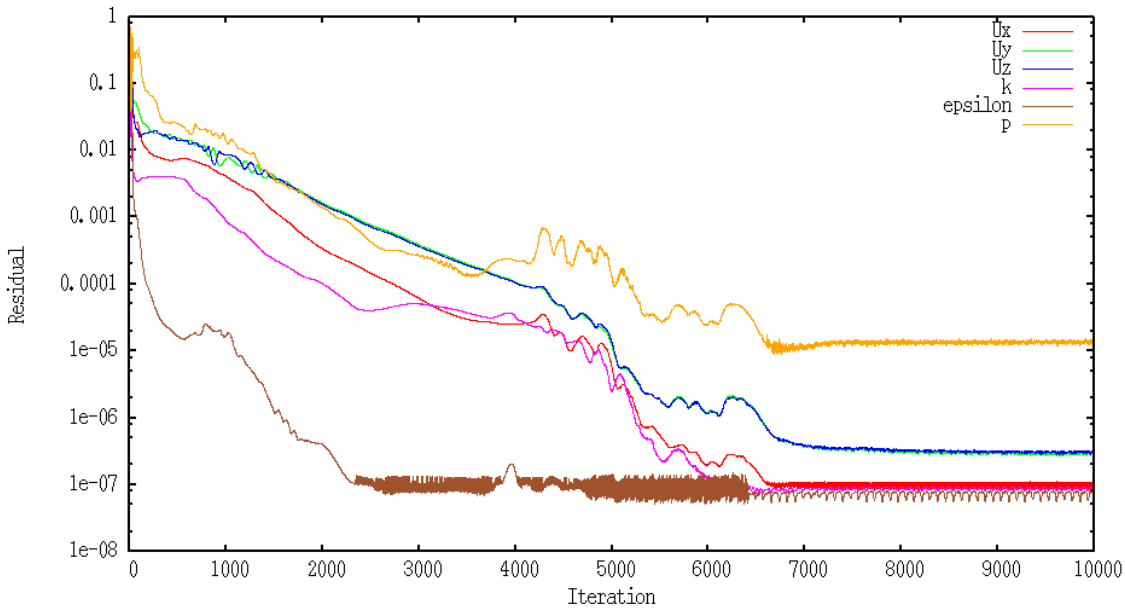

Figure 3: Residuals of the full-rotor CFD simulation using the $k-\varepsilon$ *RNG* turbulence model

are over-estimate the velocity deficit at the far wake (Fig. 10).

The actuator disk model under-estimates the velocity deficit in most cases, except for the $k-\varepsilon$ *RNG* turbulence model which shows excellent performance at the mid and far wake (Fig. 9).

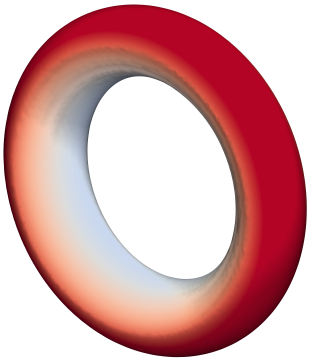

Figure 4: Iso-surfaces of the Q criterion colored by velocity for the case of actuator disk model, using RANS and the $k-\omega$ turbulence model

5.1. *Predictions of axial velocity, turbulence kinetic energy (TKE), and vorticity*

In order to compare and study the differences between the simplified ADM and the full-rotor CFD simulations, slices of the velocity, turbulence kinetic energy and of vorticity at the xz-plane and at the hub height ($h_{\text{hub}} = 0.827$ m) are given for all the turbulence models. The slices of the full-rotor CFD simulations have been azimuthally averaged. It should be noted that the size of the computational domain is similar for both approaches. The smaller extent of the full-rotor slices is a consequence of the rotor not being in the centre of the (y,z) plane. As the radial grid used in the azimuthal averaging is obviously centered on the rotor, the extent of the domain in radial coordinates is smaller than in Cartesian coordinates. This explains the differences in size between the top and lower groups of panels in Fig. 6-8.

The actuator disk model is more sensitive to the different turbulence models compared to the full-rotor simulations. Results of the ADM confirm that it is implemented correctly, since it represents a uniform momentum sink, as observed in Figures 6a, 7a and 8a. Strong velocity gradients are expected at the disk circumference where the free-stream flow will interact with the boundaries of the disk region of decelerated flow (momentum sink). The iso-surfaces of the Q criterion (Fig. 4), are in agreement with the slices of vorticity (Fig. 8a) in which the strong effect of the shear stresses at the edge of the disk area is apparent. Results of TKE (Fig. 7a) for the ADM case show that the $k-\omega$ and the $k-\omega$ SST turbulence models are less sensitive to the shear stresses caused by the free stream flow at the disk circumference, in contrast with

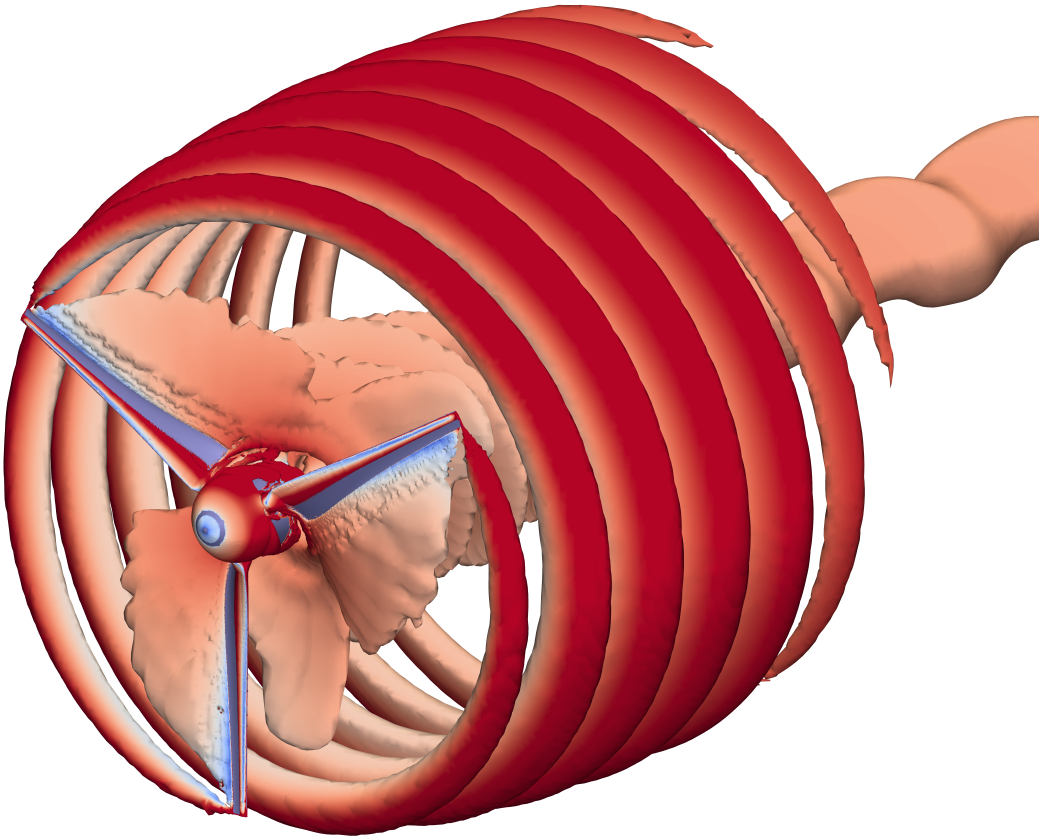

Figure 5: Iso-surfaces of the Q criterion colored by velocity for the case of full-rotor CFD simulation, using RANS and the $k-\omega$ turbulence model

the group of $k-\varepsilon$ turbulence models. Instead, we observe that there is enhanced turbulence production at the low-pressure region, behind the disk, where a pressure drop is also present. The wakes of the modified $k-\varepsilon$ turbulence models produce more TKE and vorticity at the blades-tip positions. The enhanced turbulence kinetic energy will increase the mixing between the free-stream layers of the flow and the inner wake flow. More enhanced mixing will cause stronger interaction between the regions and finally a faster recovery of the velocity downstream. The connection between the production of turbulence and of the wake recovery can be observed also in the slices of turbulence (Fig. 7a) and of velocity (Fig. 6a). It is more dominant in the case of $k-\omega$ turbulence model, where the over-predicted turbulence production was observed, with faster mid and far wake velocity recovery. We conclude that for the case of the ADM, a choice from the $k-\varepsilon$ turbulence models group is recommended.

The full-rotor simulations show large wake development downstream of the first wind turbine with all the turbulence models (Fig. 6b). That behaviour is related to the severe under-estimation of the turbulence intensity (Fig. 7b). Preliminary tests showed that the small turbulence production downstream is also related to the absence of nacelles and towers. The TKE production in the wake of the second wind turbine is greater at the blade-tip positions downstream compared to the single wake predictions of the first. We can observe that the surrounding turbulence at the position of the second wind turbine is smaller as we are approaching the outlet. The fact that the turbulence intensity decays downstream is known and observed also in several experiments performed in wind tunnels [34]. That is also confirmed by the slices of vorticity (Fig. 8b), despite the small difference at the tip-vortexes of the second wind turbine which operates under the wake effect of the upstream rotor. A further investigation is needed to quantify the impact of the turbulence intensity at the inlet. In our case, we

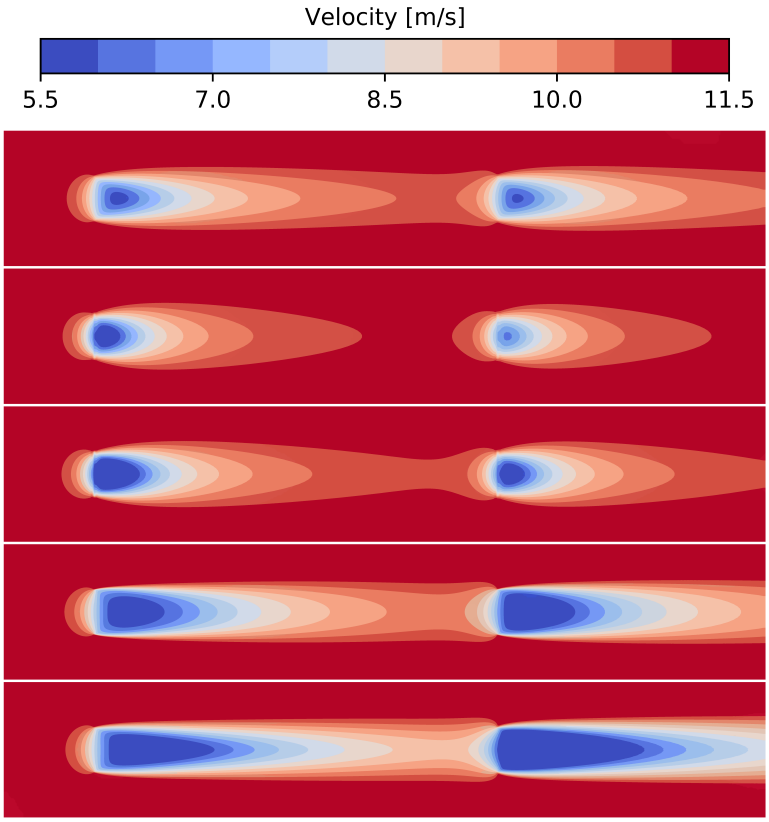

(a)

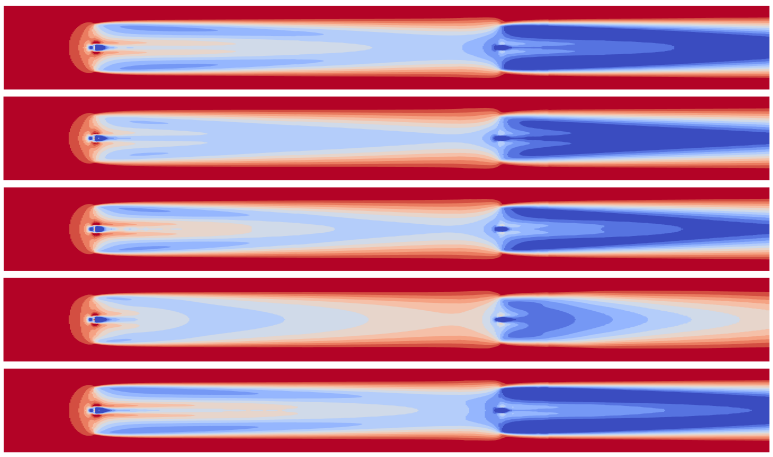

(b)

Figure 6: Contours of velocity [m/s] for the ADM (a) and full-rotor (b) cases at the xy-plane and h_{hub}. From top to bottom: $k-\varepsilon$, $k-\omega$, $k-\omega$ SST, $k-\varepsilon$ *Realizable*, $k-\varepsilon$ *RNG*.

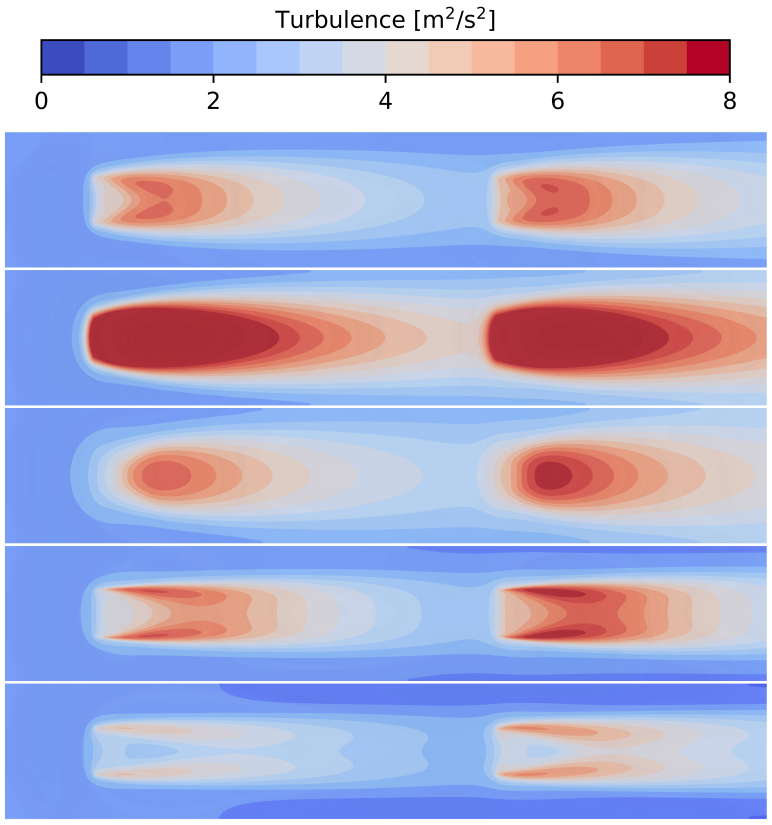

(a)

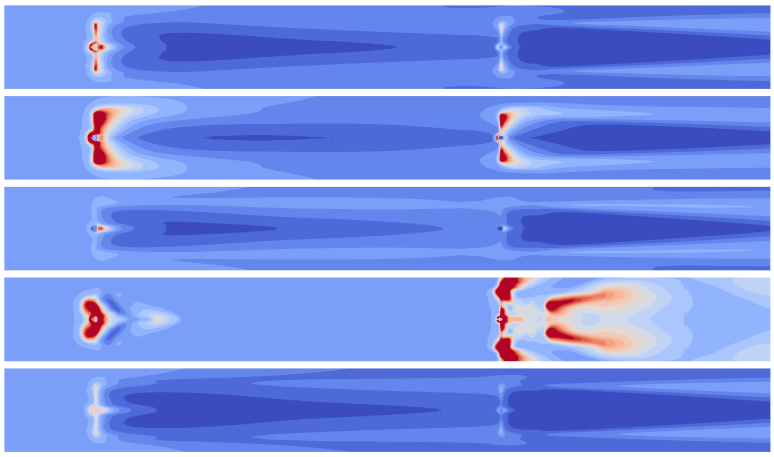

(b)

Figure 7: Contours of turbulence k [m^2/s^2] for the ADM (a) and full-rotor (b) cases at the xy-plane and h_{hub}. From top to bottom: $k-\varepsilon$, $k-\omega$, $k-\omega$ *SST*, $k-\varepsilon$ *Realizable*, $k-\varepsilon$ *RNG*.

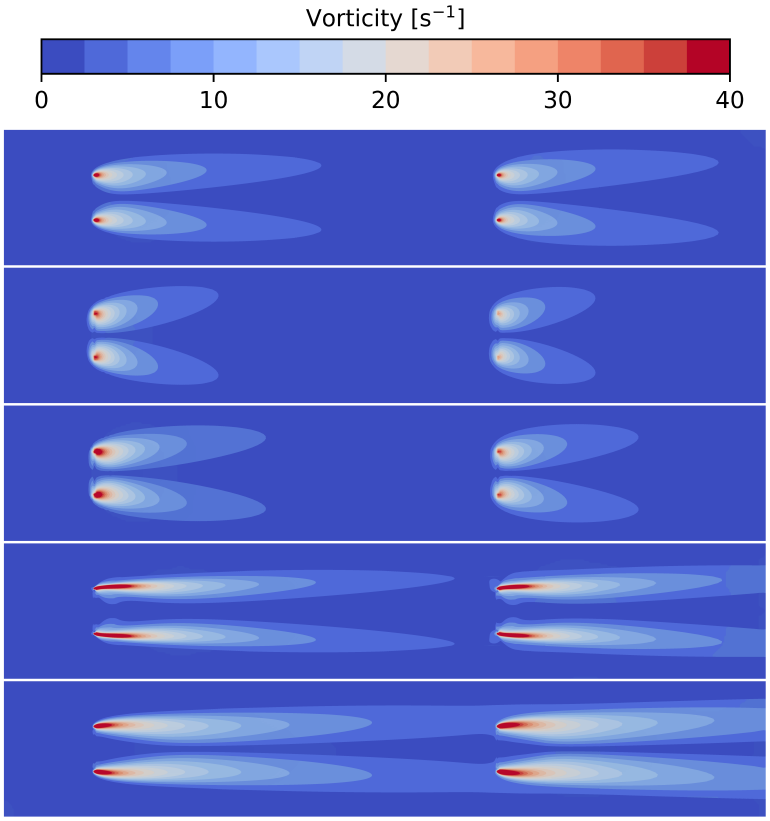

(a)

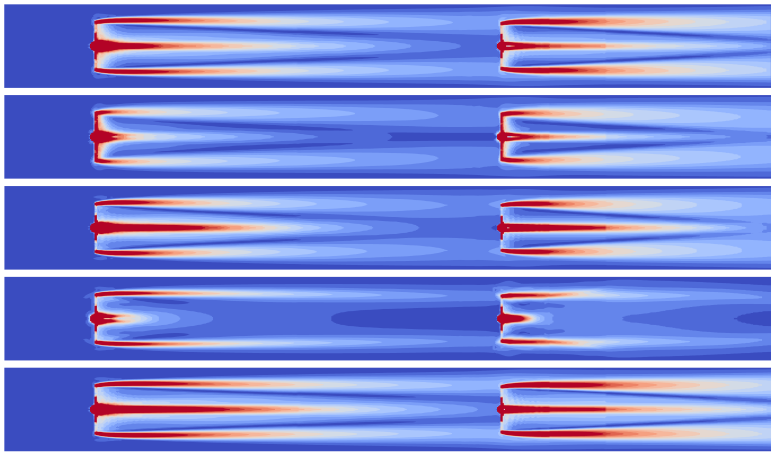

(b)

Figure 8: Contours of vorticity [s^{-1}] for the ADM (a) and full-rotor (b) cases at the xy-plane and h_{hub}. From top to bottom: $k-\varepsilon$, $k-\omega$, $k-\omega$ *SST*, $k-\varepsilon$ *Realizable*, $k-\varepsilon$ *RNG*.

used a given turbulence length scale and a $TI = 10\%$, provided by the experiment. However, those measurements have been performed at the position of the first wind turbine rotor. It is proposed to investigate the turbulence decay under the absence of rotors, at the position of the first wind turbine.

The contour of TKE (Fig. 7) for the $k-\varepsilon$ *Realizable* model shows an unphysical behavior of turbulence production at the position of the second wind turbine and further downstream. Therefore, this case is considered unreliable and needs further investigation.

5.2. Comparison against measurements

Velocity profiles in the wake of the upstream wind turbine rotor are compared with measurements along three horizontal lines at the hub height ($h_{\text{hub}} = 0.827$ m), covering an horizontal span width from $z = -0.944$ m to $z = 0.944$ m. The three horizontal lines L1, L2, L3 are located $2.77D$ (near), $5.18D$ (mid) and $8.5D$ (far wake) downstream of the first wind turbine rotor respectively. Plots of normalized velocity $U^* = U_{\text{wake}}/U_{\text{ref}}$ over the rotor's radial distance (z/R) are compared against the BT4 experimental data (Fig. 9, 10).

The correct implementation of the ADM is also validated from the symmetrical U-shaped velocity profile that was expected at the wake region and over horizontal lines at h_{hub} if a uniform momentum sink of constant thrust is applied [6; 17]. The plots of normalized velocity (Fig. 9) verify that behaviour for all the turbulence models.

The ADM under-estimates the velocity deficit at all the wake regions downstream for most turbulence models, except from the $k-\varepsilon$ *RNG* which shows a superb agreement with the measurements (Fig. 9). Nevertheless, as already discussed in section 5.1, results of the ADM are very sensitive to the choice of turbulence model. Quantitatively, over the line L1 at the near wake, the maximum relative difference between the $k-\omega$ and $k-\varepsilon$ turbulence models is 4.046 m/s (equal to a relative difference of 0.352 in normalized velocities). The relative difference between the turbulence models decreases as we move further downstream. At the mid wake over line L2, the relative difference is 2.635 m/s and at the far wake, over line L3, 1.653 m/s.

The full wind turbine rotor simulations predict more accurately the near wake, capturing also the shape of the velocity deficit (Fig. 10). At the mid wake, the $k-\varepsilon$ and the $k-\varepsilon$ *RNG* maintain the "W-shaped" horizontal velocity profile, whereas the other models are in better agreement with the measurements. In the far wake region, over line L3, all the models fail to predict correctly the velocity deficit and overestimate it. The $k-\varepsilon$ *Realizable* turbulence model shows excellent agreement at the mid and far wake regions, but as already discussed in section 5.1, it is unreliable. Preliminary results suggest that the impact of tower will increase the TKE at wake, resulting to a better agreement at the far region. A further study on the performance of different turbulence models including the nacelle and tower will be performed by the authors in the future. It is concluded that for full-rotor CFD approach, the group of $k-\omega$ turbulence predicts the velocity deficit more accurately, with the $k-\omega$ SST showing slightly better performance.

6. Conclusion

The wake expansion of a wind turbine was investigated under controlled conditions of a wind tunnel, using different CFD modelling approaches. The OpenFOAM open-source platform was used, with the multiple reference frame (MRF) utility (for the case of the full wind turbine rotor) and the standard actuator disk model to solve the 3-dimensional, incompressible, steady state RANS. Five RANS turbulence models have been tested on both cases (full rotor and actuator disk). The models were compared with experimental data at three downstream positions over horizontal lines at hub height.

On average, the actuator disk models under-predict the velocity deficit in the wake. The under-prediction of the far wake by ADM was observed also by other studies [6; 36; 32; 7]. Especially for the downstream distance of five diameters, which is of high interest since it is commonly used by industry as a separation distance in wind farms, results show that there is a failure to capture accurately the velocity deficit with the standard actuator disk model for most turbulence models. However, good results are obtained with an appropriate turbulence model: the $k-\varepsilon$ *RNG* shows excellent agreement in the mid and far wake.

Full-rotor simulations show very good agreement in the near and mid wake. On the other hand, they all over-estimate the velocity deficit in the far wake, which is related to the severe under-estimation of the turbulence intensity by the full-rotor simulations. Preliminary calculations that we have performed, suggest that including the tower and nacelle might lead to better prediction of the far wake. This topic needs further investigation. Also, it would be worthwhile to investi-

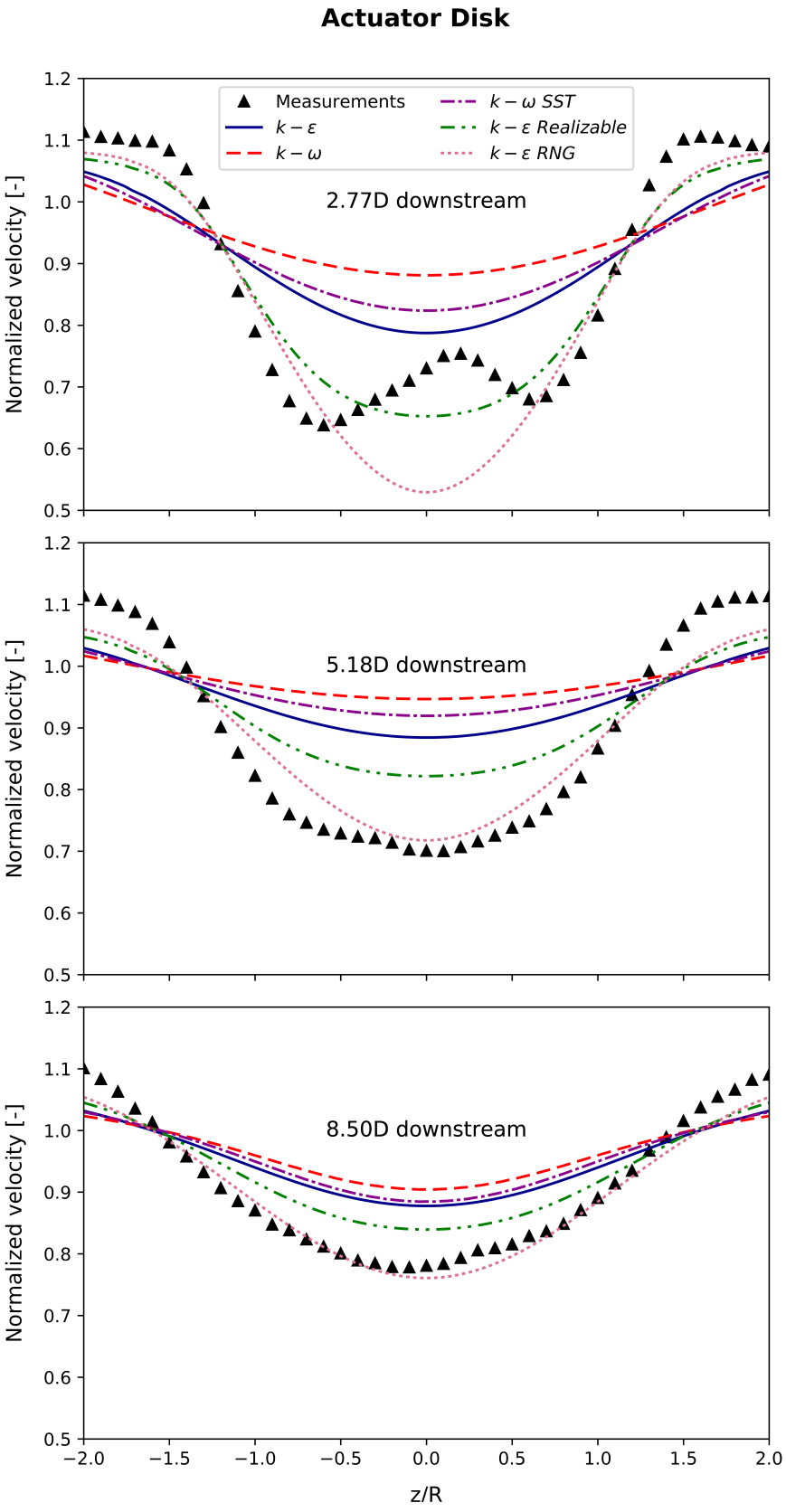

Figure 9: Results of actuator disk model CFD simulations, using several turbulence models against measurements. From top to bottom: line L1, L2 and L3 respectively.

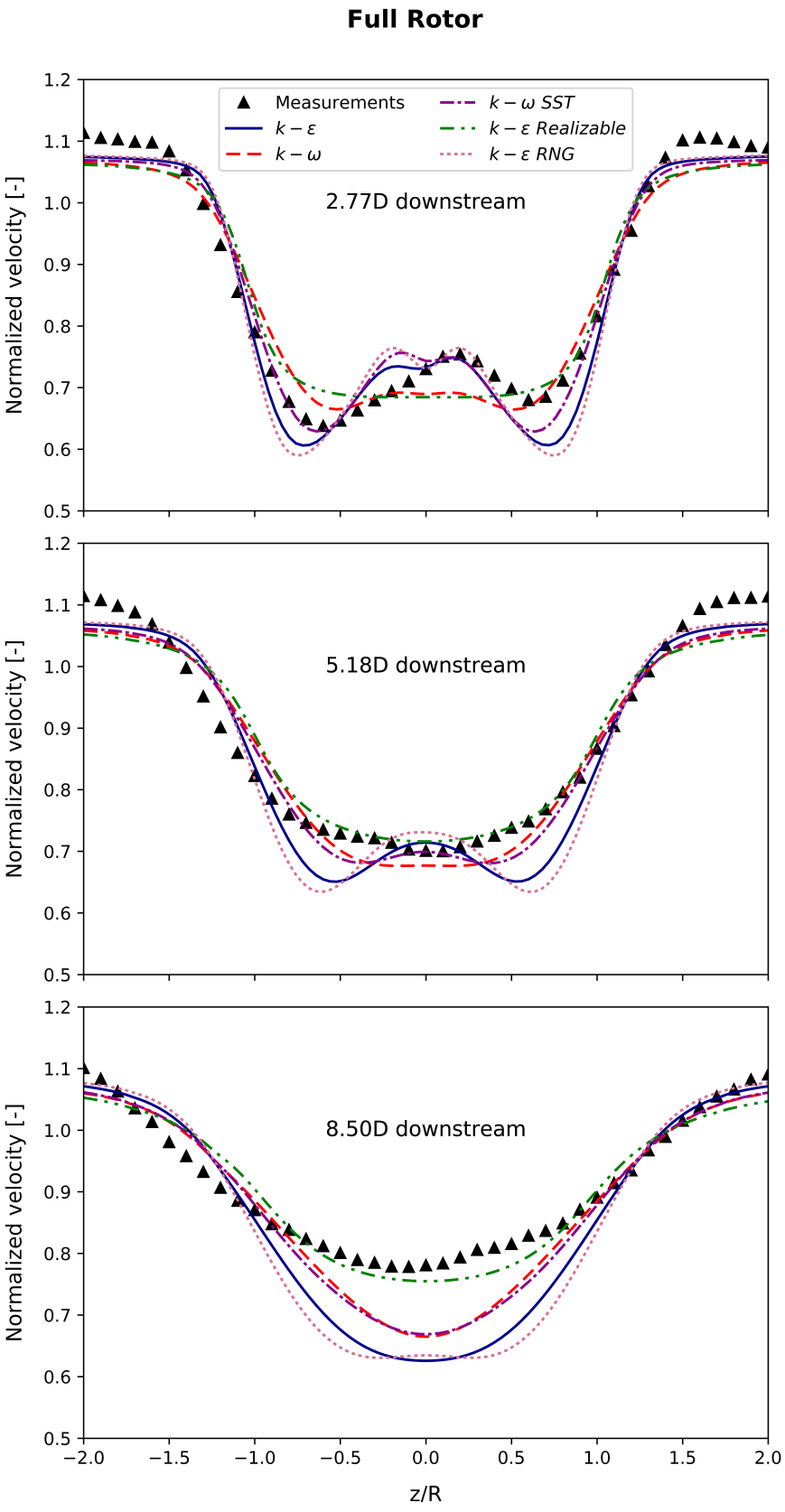

Figure 10: Results of full-rotor CFD simulations, using several turbulence models against measurements. From top to bottom: line L1, L2 and L3 respectively.

gate the impact of different inflow turbulence intensities on the results.

Acknowledgments

This work has been funded by INNOVIRIS, the Brussels Institute for the promotion of scientific research and innovation, in the framework of the DOCTIRIS program and under the research project: ***"Non-deterministic advanced CFD modelling of wind turbine wakes and their interaction with applications to wind farms including complex terrain effects"***.

The authors acknowledge the Norwegian Technical National University (NTNU) for providing the experimental data of Blind Test 4 and professors Lars Roar Sætran and Per-Åge Krogstad for their support.

References

[1] L. J. Vermeer, J. N. Sørensen, A. Crespo, Wind turbine wake aerodynamics, Progress in Aerospace Sciences 39 (6-7) (2003) 467–510. doi:10.1016/S0376-0421(03)00078-2.

[2] B. Sanderse, S. P. Pijl, B. Koren, Review of computational fluid dynamics for wind turbine wake aerodynamics, Wind Energy 14 (7) (2011) 799–819. doi:10.1002/we.458.

[3] K. Walker, N. Adams, B. Gribben, B. Gellatly, N. G. Nygaard, A. Henderson, M. Marchante Jimémez, S. R. Schmidt, J. Rodriguez Ruiz, D. Paredes, G. Harrington, N. Connell, O. Peronne, M. Cordoba, P. Housley, R. Cussons, M. Håkansson, A. Knauer, E. Maguire, An evaluation of the predictive accuracy of wake effects models for offshore wind farms, Wind Energy 19 (2016) 979–996. doi:10.1002/we.1871.

[4] R. J. Barthelmie, K. Hansen, S. T. Frandsen, O. Rathmann, J. G. Schepers, W. Schlez, J. Phillips, K. Rados, A. Zervos, E. S. Politis, P. K. Chaviaropoulos, Modelling and measuring flow and wind turbine wakes in large wind farms offshore, Wind Energy 12 (2009) 431–444. doi:10.1002/we.348.

[5] R. J. Barthelmie, S. T. Frandsen, K. Hansen, J. G. Schepers, K. G. Rados, W. Schlez, A. Neubert, L. E. Jensen, S. Neckelmann, Modelling the impact of wakes on power output at nysted and horns rev, EWEC 2009.

[6] K. G. Rados, S. Mosfilis, N. Stergiannis, A. Tourlidakis, G. Caralis, A. Zervos, Cfd modeling approaches of wind turbine single and multiple wakes, in: European Wind Energy Conference and Exhibition 2012, EWEC 2012, Vol. 3, 2012, pp. 1842–1849.

[7] J. M. Prospathopoulos, E. S. Politis, K. G. Rados, P. K. Chaviaropoulos, Evaluation of the effects of turbulence model enhancements on wind turbine wake predictions, Wind Energy 14 (2011) 285–300. doi:10.1002/we.419.

[8] R. J. Barthelmie, O. Rathmann, S. T. Frandsen, K. S. Hansen, E. S. Politis, J. M. Prospathopoulos, K. G. Rados, D. Cabezón, W. Schlez, J. Phillips, A. Neubert, J. G. Schepers, S. P. van der Pijl, Modelling and measurements of wakes in large wind farms, Journal of Physics: Conference Series 75 (1) (2007) 012049. doi:10.1088/1742-6596/75/1/012049.

[9] G. C. Larsen, J. Højstrup, H. A. Madsen, Wind field in wakes, Proceedings: European Wind Energy Conference and Exhibition 1996, Gothenberg, Sweden (1996) 764–768.

[10] G. C. Larsen, I. Carlen, J. G. Schepers, Fatigue life consumption in wake operation, Proceedings: European Wind Energy Conference and Exhibition 1998, Dublin, Ireland, Irish Wind Energy Association (1998) 605–610.

[11] G. C. Larsen, H. A. Madsen, N. N. Sørensen, Mean wake deficit in the near field, Proceedings: European Wind Energy Conference 2003, Madrid, Spain, EWEA.

[12] M. Magnusson, K. G. Rados, S. G. Voutsinas, A study of the flow down stream of a wind turbine using measurements and simulations, Wind Engineering 20 (1996) 389–403.

[13] N. O. Jensen, A note on wind turbine interaction, Risø-M-2411, Risoe National Laboratory, Roskilde, Denmark (1983) 16 pp.

[14] I. Katic, J. Højstrup, N. O. Jensen, A simple model for cluster efficiency, Proceedings: European Wind Energy Association Conference and Exhibition, Rome, Italy (1986) 407–409.

[15] J. F. Ainslie, Calculating the flow field in the wake of wind turbines, Journal of Wind Engineering and Industrial Aerodynamics 27 (1988) 213–224.

[16] K. G. Rados, G. Larsen, R. Barthelmie, W. Schlez, B. Lange, J. G. Schepers, T. Hegberg, M. Magnusson, Comparison of wake models with data for offshore windfarms, Wind Engineering 25 (2002) 271–280.

[17] R. Mikkelsen, Actuator disc methods applied to wind turbines, Ph.d thesis, Technical University of Denmark (2003).

[18] E. Van Der Weide, G. Kalitzin, J. Schluter, G. Medic, D. J. J. Alonso, On large scale turbomachinery computations, Center for Turbulence Research Annual Research Briefs.

[19] D. G. Holmes, B. J. Moore, S. D. Connell, Unsteady vs. steady turbomachinery flow analysis: exploiting large-scale computations to deepen our understanding of turbomachinery flows, in: SciDAC Conference, Denver, CO, 2011, pp. 1–13.

[20] N. C. Markatos, The mathematical modelling of turbulent flows, Applied Mathematical Modelling 10 (1986) 190–220.

[21] D. C. Wilcox, Turbulence modeling for CFD, 1st Edition, Vol. 93, DCW Industries, 1993. doi:0963605151.

[22] B. E. Launder, D. B. Spalding, The numerical computation of turbulent flows, Computer Methods in Applied Mechanics and Engineering 3 (2) (1974) 269–289. doi:10.1016/0045-7825(74)90029-2.

[23] B. E. Launder, A. Morse, W. Rodi, D. B. Spalding, Prediction of free shear flows: A comparison of the performance of six turbulence models, in: NASA. Langley Res. Center Free Turbulent Shear Flows, Vol. 1, 1973, pp. 361–426.

[24] T. Shih, W. Liou, A. Shabbir, Z. Yang, J. Zhu, A new k-epsilon eddy viscosity model for high reynolds number turbulent flows, Computers and Fluids 10 (3) (1995) 227–238.

[25] V. Yakhot, S. A. Orszag, S. Thangam, T. B. Gatski, C. G. Speziale, Development of turbulence models for shear flow by a double expansion technique, Physics of Fluids 4 (7) (1992) 1510–1520.

[26] D. C. Wilcox, Formulation of the k-w turbulence model revisited, AIAA Journal 46 (11) (2008) 2823–2838. doi:10.2514/1.36541.

[27] D. C. Wilcox, Reassessment of the scale-determining equation for advanced turbulence models, AIAA Journal 26 (1988) 1299–1310.

[28] OpenFOAM, openfoam.org (2016).
URL `www.openfoam.org`

[29] F. R. Menter, Two-equation eddy-viscosity turbulence models for engineering applications, AIAA 32 (8) (1994) 1598–1605.

[30] A. Hellsten, Some improvements in menter's k-omega sst turbulence model, 29th AIAA, Fluid Dynamics Conference (1998) 1–11doi:10.2514/6.1998-2554.

[31] F. R. Menter, M. Kuntz, R. Langtry, Ten years of in-

dustrial experience with the sst turbulence model, Turbulence Heat and Mass Transfer 4 4 (2003) 625–632. doi:10.4028/www.scientific.net/AMR.576.60.

[32] G. Crasto, A. R. Gravdahl, F. Castellani, E. Piccioni, Wake modeling with the actuator disc concept, Energy Procedia 24 (2012) 385–392. doi:10.1016/j.egypro.2012.06.122.

[33] Y.-T. Wu, F. Porté-Agel, Large-eddy simulation of wind-turbine wakes: Evaluation of turbine parametrisations, Boundary-Layer Meteorology 138 (2011) 345–366.

[34] L. Sætran, J. Bartl, Invitation to the 2015 "Blind test 4" Workshop Combined power output of two in-line turbines at different inflow conditions (2015).

[35] S. V. Patankar, D. B. Spalding, A calculation procedure for heat, mass and momentum transfer in three-dimensional parabolic flows, International Journal of Heat and Mass Transfer 15 (1972) 1787–1806.

[36] K. Vafiadis, N. Stergiannis, A. Tourlidakis, K. G. Rados, Computational investigation of horizontal axis wind turbine wake, in: European Wind Energy Conference and Exhibition, EWEC 2013, Vol. 3, 2013, pp. 1692–1700.